AES 2023 Torremolinos - Spain

The 9th International Conference on Antennas and Electromagnetic Systems

June 5 – 8, 2023
Torremolinos - Spain

Proceedings

ISSN 2491-2417

aesconference.org

AES 2023 Torremolinos - Spain

The 9th International Conference on Antennas and Electromagnetic Systems

Edited by

Enrique Márquez Segura | University of Malaga, Spain
Said Zouhdi | Paris-Saclay University, France

TABLE OF CONTENT

ORGANIZATION I COMMITTEES

Conference Chairs

Enrique Márquez Segura
University of Malaga, Spain

Said Zouhdi
Paris–Saclay University, France

International Advisory Committee

Yahia Antar, Canada
Christos Christopoulos, UK
Tie Jun Cui, China
Peter de Maagt, Netherlands
Apostolos Georgiadis, Spain
D. V. Giri, USA
Xun Gong, USA
Lixin Guo, China
Yang Hao, UK
Nathan Ida, USA
Koichi Ito, Japan
Ahmed Kishk, Canada
Kwai Man Luk, Hong Kong
Andrea Massa, Italy
Alain Sibille, France
Ari Sihvola, Finland
Paul Smith, Australia
J(Yiannis) C. Vardaxoglou, UK
Junhong Wang, China

Technical Program Committee

Christos Argyropoulos, USA
Silvio Ernesto Barbin, Brazil
Xavier Begaud, France
Yangjian Cai, China
Pai-Yen Chen, USA
Christophe Craeye, Belgium
Tian Sen Jason Horng, Taiwan
Zhirun Hu, UK
Ruey-Bing Hwang, Taiwan
Sungtek Kahng, Korea
Ali Khenchaf, France
Sebastien Lallechere, France
Allen M. Larar, USA
Howard Lee, USA
Jensen Li, Hong Kong
Jean-Marc Lopez, France
Ozlem Ozgun, Turkey
Oscar Quevedo-Teruel, Sweden
Eva Rajo-Iglesias, Spain
Blaise Ravelo, China
Junsuk Rho, Korea
Josaphat T. Sri Sumantyo, Japan
Van Yem Vu, Viet Nam
Amir I. Zaghloul, USA
Kuang Zhang, China
Qi-Jun Zhang, Canada
Linjie Zhou, China
Arkady Zhukov, Spain

Special Sessions Organizers

Jeremy Barton, Canada
Mario Ferraro, Italy
Angelo Freni, Italy
Yongxin Guo, Singapore
Enrique Márquez Segura, Spain
Paola Pirinoli, Italy
Vaibhav Thakore, Canada
Maxim Zhadobov, France
Arkady Zhukov, Spain

Sponsors

Université Paris-Saclay is a research university based in Paris, France. Université Paris-Saclay offers a comprehensive and varied range of Undergraduate, Master's and PhD degrees, renowned internationally thanks to the University's reputation for research excellence and the commitment of its academic staff. The University's constituent faculties, institutes and component institutions all contribute to the curricula with cutting-edge specialised courses in Science and Engineering, Life Sciences and Health, and Social Sciences and Humanities.
Université Paris-Saclayis ranked 1st in France and 16th in the world according to the Academic Ranking of World Universities (ARWU).

AEM - Advanced Electromagnetics is a free, peer-reviewed, Gold Open Access journal. It covers recent international research results in the general field of Electromagnetic Waves, Antennas and Propagation. Authors of articles published in Advanced Electromagnetics retain the copyright of their articles and are free to reproduce and disseminate their work (under a Creative Commons Attribution License). AEM is widely indexed and has a Scopus CiteScore of 2.2 (2021).

PLENARY SPEAKERS

Shanhui Fan

Stanford University, USA

Electromagnetics for Energy Applications

Shanhui Fan is the Joseph and Hon Mai Goodman Professor in the School of Engineering, a Professor of Electrical Engineering, a Professor of Applied Physics (by courtesy), and a Senior Fellow of the Precourt Institute for Energy, at the Stanford University. He received his Ph. D in 1997 in theoretical condensed matter physics from the Massachusetts Institute of Technology (MIT). His research interests are in fundamental studies of solid state and photonic structures and devices, especially photonic crystals, plasmonics, and meta-materials, and applications of these structures in energy and information technology applications. He has published over 600 refereed journal articles, has given over 380 plenary/keynote/invited talks, and holds over 70 US patents. He has cofounded two companies aiming to commercialize high-speed engineering computations and radiative cooling technology respectively. Prof. Fan received a National Science Foundation Career Award (2002), a David and Lucile Packard Fellowship in Science and Engineering (2003), the U. S. National Academy of Sciences W. O. Baker Award for Initiatives in Research (2007), the Adolph Lomb Medal from the Optical Society of America (2007), a Vannevar Bush Faculty Fellowship from the U. S. Department of Defense (2017), a Simons Investigator in Physics (2021), and the R. W. Wood Prize from Optica (2022). He is a Web of Science Highly Cited Researcher since 2015, and a Fellow of the IEEE, the American Physical Society, the Optical Society of America, and the SPIE.

Electromagnetics for Energy Applications

Electromagnetic fields represent one of the most important carriers of energy. The ability to control electromagnetic fields therefore play an essential role in the generation, transport, and utilization of energy. In this talk, we review our efforts in advancing electromagnetic technology for energy applications. Examples include radiative cooling, nighttime power harvesting, and the use of non-reciprocity to reach the ultimate efficiency limit of solar energy harvesting.

Yongxin Guo

National University of Singapore, Singapore

Efficient Wireless Power Transfer for IoTs and Biomedical Applications

Yongxin Guo is currently a Full Professor at the Department of Electrical and Computer Engineering, National University of Singapore (NUS). Concurrently, He is Director, Center for Peak of Excellence on Smart Medical Technology at NUS Suzhou Research Institute and Co-Director, Center for Smart Sensing and Artificial Intelligence, NUS Chongqing Research Institute. He has authored or co-authored over 500 international journal and conference papers and 4 book chapters. He holds over 50 granted/filed patents in USA, China and Singapore. His current research interests include RF sensing, antennas and electromagnetics in medicine ; wireless power for biomedical applications and internet of things ; wideband and small antennas for wireless communications ; and RF and microwave circuits and MMIC modelling and design. He has graduated 19 PhD students at NUS.

Dr. Guo is a Fellow of IEEE and a Fellow of Academy of Engineering, Singapore. He is serving as Editor-in-Chief, IEEE Journal of Electromagnetics, RF and Microwave in Medicine and Biology for the term of 2020-2023. He served as the IEEE Fellow Evaluation Committee for IEEE Engineering in Medicine and Biology Society (2019-2020). Dr Guo was the Chair for IEEE AP-S Technical Committee on Antenna Measurement in 2018-2020. He served as Associate Editor for IEEE Antennas and Propagation Magazine (2018-2020), IEEE Journal of Electromagnetics, RF and Microwave in Medicine and Biology (2017 – 2020), Electronics Letters (2015-2019), IEEE Antennas and Wireless Propagation Letters (2013-2018), and IET Microwaves, Antennas & Propagation (2014-2017). He has served as General Chair/Co-Chair for a number of international conferences. He was the recipient of 2020 IEEE Microwave and Wireless Components Letters Tatsuo Itoh Prize of the IEEE Microwave Theory and Techniques Society. He was elected as a Distinguished Lecturer of IEEE Antennas and Propagation Society for the term of 2022-2024.

Efficient Wireless Power Transfer for IoTs and Biomedical Applications

Wireless power transfer (WPT) plays an increasingly important role in internet of things (IoTs) and biomedical applications. With the rapid development of 5G and IoTs, the dense deployment of sensor nodes become more popular. Various wireless power application scenarios will be introduced. Our recent research progress on near-field inductive and capacitive WPT and far-field WPT will be reported. Adaptive rectifier design and reconfigurable diode topology will be explained. Waveform-optimized WPT together with reconfigurable diode topology will be further illustrated.

Yahya Rahmat-Samii

University of California - Los Angeles, USA

Yahya Rahmat-Samii is a Distinguished Professor, a holder of the Northrop-Grumman Chair in electromagnetics, a member of the U.S. National Academy of Engineering (NAE), a Foreign Member of the Chinese Academy of Engineering (CAE) and the Royal Flemish Academy of Belgium for Science and the Arts, the winner of the 2011 IEEE Electromagnetics Field Award, and the Former Chairman of the Electrical Engineering Department, University of California at Los Angeles (UCLA), Los Angeles, CA, USA. He was a Senior Research Scientist with the Caltech/NASA's Jet Propulsion Laboratory. He has authored or coauthored more than 1100 technical journal and conference papers and has written over 36 book chapters and six books and is the holder many patents. He has more than 20 cover-page IEEE publication articles.

Prof. Rahmat-Samii is a fellow of IEEE, AMTA, ACES, EMA, and URSI. He was a recipient of the Henry Booker Award from URSI, in 1984, which is given triennially to the most outstanding young radio scientist in North America, the Best Application Paper Prize Award (Wheeler Award) of the IEEE Transactions on Antennas and Propagation in 1992 and 1995, the University of Illinois ECE Distinguished Alumni Award in 1999, the IEEE Third Millennium Medal and the AMTA Distinguished Achievement Award in 2000. In 2001, he received an Honorary Doctorate Causa from the University of Santiago de Compostela, Spain. He received the 2002 Technical Excellence Award from JPL, the 2005 URSI Booker Gold Medal presented at the URSI General Assembly, the 2007 IEEE Chen- To Tai Distinguished Educator Award, the 2009 Distinguished Achievement Award of the IEEE Antennas and Propagation Society, the 2010 UCLA School of Engineering Lockheed Martin Excellence in Teaching Award, and the 2011 campus-wide UCLA Distinguished Teaching Award. He was also a recipient of the Distinguished Engineering Educator Award from The Engineers Council in 2015, the John Kraus Antenna Award of the IEEE Antennas and Propagation Society and the NASA Group Achievement Award in 2016, the ACES Computational Electromagnetics Award and the IEEE Antennas and Propagation S. A. Schelkunoff Best Transactions Prize Paper Award in 2017. Rahmat-Samii was the recipient of the prestigious Ellis Island Medal of Honor in 2019. The medals are awarded annually to a group of distinguished U.S. citizens who exemplify a life dedicated to community service. These are individuals who preserve and celebrate the history, traditions, and values of their ancestry while exemplifying the values of the American way of life and are dedicated to creating a better world. Among the receipts of this honor are seven US presidents to name the few. He is listed in Who's Who in America, Who's Who in Frontiers of Science and Technology and Who's Who in Engineering. He has been a plenary and millennium session speaker at numerous national and international symposia. He has been the organizer and presenter of many successful short courses worldwide. Many of his students have won major theses and conference paper awards.

He has had pioneering research contributions in diverse areas of electromagnetics, antennas, measurements and diagnostics techniques, numerical and asymptotic methods, satellite and personal communications, human/antenna interactions, RFID and implanted antennas in medical applications, frequency-selective surfaces, electromagnetic band-gap and meta-material structures, applications of the genetic algorithms and particle swarm optimizations. He was the 1995 President of the IEEE Antennas and Propagation Society and 2009–2011 President of the United States National Committee (USNC) of the International Union of Radio Science (URSI). He has also served as an IEEE Distinguished Lecturer presenting lectures internationally.

The Art, Science and Engineering of Modern Antenna Measurements and Diagnostics : From Marconi's First Measurements to Today's Incredible Advances

Starting with Marconi's first antenna pattern measurements, we then discuss modern planar near-field antenna measurements as a novel paradigm linking electromagnetic theory, sampling techniques, back projection and FFT. Based on the fundamental electromagnetic principles, the underlying concepts governing simulations, designs and operations of planar-near field measurements and diagnostics techniques will be highlighted. Modern measurement systems such as plane-polar, bi-polar and robotics

scanning systems will be presented. Representative measurement results of reflector, array, reflectarray and lens antennas will be presented for diverse applications including planetary missions, radars for remote sensing, and Cubesats. Finally, the topics of diagnostics and phaseless antenna measurement techniques and algorithms will be touched upon..

Eva Rajo-Iglesias

University Carlos III of Madrid, Spain

Eva Rajo-Iglesias was born in Monforte de Lemos, Spain, in 1972. She received the M.Sc. degree in telecommunication engineering from the University of Vigo, Spain, in 1996, and the Ph.D. degree in telecommunication engineering from the University Carlos III of Madrid, Spain, in 2002. She was a Teacher Assistant with the University Carlos III of Madrid from 1997 to 2001. She joined the Polytechnic University of Cartagena, Cartagena, Spain, as a Teacher Assistant, in 2001. She joined University Carlos III of Madrid as a Visiting Lecturer in 2002, where she has been an Associate Professor with the Department of Signal Theory and Communications since 2004. Since 2018 she is Full Professor in the same department. She visited the Chalmers University of Technology, Göteborg, Sweden, as a Guest Researcher, in 2004, 2005, 2006, 2007, and 2008, and has been an Affiliated Professor with the Antenna Group, Signals and Systems Department, since 2009 to 2016. She has co-authored more than 75 papers in JCR international journals and more than 120 papers in international conferences. Her current research interests include microstrip patch antennas and arrays, metamaterials, artificial surfaces and periodic structures, gap waveguide technology and MIMO systems. Dr. Rajo-Iglesias was the recipient of the Loughborough Antennas and Propagation Conference Best Paper Award in 2007, the Best Poster Award in the field of Metamaterial Applications in Antennas, at the conference Metamaterials 2009, the 2014 Excellence Award to Young Research Staff at the University Carlos III of Madrid and the Third Place Winner of the Bell Labs Prize 2014. She is currently an Associate Editor of the IEEE Antennas and Propagation Magazine and has served as Associate Editor of the IEEE Antennas ans Wireless Propoagation Letters (2011-2017).

Designing Antennas with Gap Waveguide Technology : Exploring New Trends

A brief introduction to the foundational principles of gap waveguide technology, followed by an overview of traditional designs of directive antennas using corporate fed arrays will be presented. Subsequently, novel applications of this technology in the millimeter frequency bands will be explored, which include the implementation of alternate periodic structures replacing the conventional bed of nails. Finally, the potential of combining this technology with established technologies like microstrip, as well as the design of other types of antennas as leaky wave antennas, will be discussed. In this way, an overview of different on going research lines connected to this technology will be presented.

Wen Tong

Huawei Wireless, Canada

cmWave-MIMO : towards the 1K-element-array paradigm

Wen Tong is the CTO, Huawei Wireless. He is the head of Huawei wireless research. In 2011, Dr. Tong was appointed the Head of Communications Technologies Labs of Huawei, currently, he is the Huawei 5G chief scientist and leads Huawei's 10-year-long 5G wireless technologies research and development.

Prior to joining Huawei in 2009, Dr. Tong was the Nortel Fellow and head of the Network Technology Labs at Nortel. He joined the Wireless Technology Labs at Bell Northern Research in 1995 in Canada.

Dr. Tong is the industry recognized leader in invention and standardization of advanced wireless technologies, he is the key contributor to 3GPP since its inception. Dr. Tong was elected as a Huawei Fellow and an IEEE Fellow. He was the recipient of IEEE Communications Society Industry Innovation Award for "the leadership and contributions in development of 3G and 4G wireless systems" in 2014, and IEEE Communications Society Distinguished Industry Leader Award for "pioneering technical contributions and leadership in the mobile communications industry and innovation in 5G mobile communications technology" in 2018. He is also the recipient of R.A. Fessenden Medal. For the past three decades, he had pioneered fundamental technologies from 1G to 5G wireless and Wi-Fi with more than 450 granted US patents.

Dr. Tong is a Fellow of Canadian Academy of Engineering, Fellow of Royal Society of Canada, and he serves as Board of Director of Wi-Fi Alliance, he is the committee member for "IEEE Fellow Committee".

cmWave-MIMO : towards the 1K-element-array paradigm

In this talk, we present the development of massive MIMO antenna technologies for the emerging 6G and associated challenges. The overall system performance and antenna design-choice in terms of spectrum and channel propagation properties are discussed. We explore the centimeter wave spectrum for the 6G massive MIMO. The candidate frequency range is from 7GHz to 15GHz, we discuss the new propagation properties and ultra-large antenna element array architecture, namely, the 1K-element-array paradigm for both base-station and user-equipment.

KEYNOTE SPEAKERS

Andrea Fratalocchi

KAUST, Saudi Arabia

Universal light encoders : artificial intelligent optical hardware for real-time hyperspectral imaging and ultrasensitive detection

Andrea Fratalocchi is a Full Professor (from Jan 2023) in the Computer, Electrical, and Mathematical Sciences and Engineering Division at KAUST University. He joined KAUST in January 2011 as Assistant Professor and was promoted to Associate Professor in July 2016. Before joining KAUST, Andrea Fratalocchi was a Research Fellow at the Sapienza University of Rome under a KAUST Fellowship Award. From 2007 to 2009, Andrea Fratalocchi worked as a post-doctoral researcher at Sapienza University under a "New Talent" Award from the research center "Enrico Fermi." In 2012 he was appointed as Editor of Nature Scientific Report. In 2017, he won the Middle East GCC Enterprise Award as the best electrical engineer of the year. In 2019, he became a Fellow of the Institute of Physics (IOP), a Senior Member of the IEEE, and a Fellow of the Optical Society of America (OSA) : "For pioneering innovations in the use of complex optical systems and the development of creative technologies in clean energy harvesting, bio-imaging, and advanced optical materials". According to the standardized citations index collected by Plos (https ://doi.org/10.1371/journal.pbio.3000918).

Andrea Fratalocchi is in the top 2% of Optics worldwide. Andrea Fratalocchi authored more than 200 publications, including three books and six patents. Andrea Fratalocchi is the co-founder of Pixeltra (www.pixeltra.com), a startup company implementing a revolutionary artificial intelligent hardware and software hyperspectral technology for security, food safety, and biomedical applications.

Universal light encoders : artificial intelligent optical hardware for real-time hyperspectral imaging and ultrasensitive detection

I will summarize present and future research in the field of universal light encoders (ULEs), which represent artificial intelligent optical hardware implementing arbitrary user-defined functionalities in ultrathin metasurfaces. ULEs process information at the speed of light and can be integrated into any conventional monochrome camera for machine vision, transforming the system into an optical neural network processor. I will discuss applications of ULEs in the implementation of HyplexTM, a high-resolution hyperspectral imaging camera and a universal platform for ultrasensitive detection.

Mona Jarrahi

University of California Los Angeles, USA

Hyperspectral Terahertz Imaging Using Plasmonic Detectors

Mona Jarrahi is a Professor of Electrical and Computer Engineering at the University of California Los Angeles. She has made significant contributions to the development of ultrafast electronic and optoelectronic devices and integrated systems for terahertz, infrared, and millimeter-wave sensing, imaging, computing, and communication systems by utilizing novel materials, nanostructures, and innovative plasmonic concepts. Her scientific achievements have been recognized by several prestigious awards including the Presidential Early Career Award for Scientists and Engineers ; Friedrich Wilhelm Bessel Research Award from Alexander von Humboldt Foundation ; Moore Inventor Fellowship from the Gordon and Betty Moore Foundation ; Kavli Fellowship by the USA National Academy of Sciences, Grainger Foundation Frontiers of Engineering Award from the USA National Academy of Engineering ; Breakthrough Award from Popular Mechanics Magazine ; Research Award from Okawa Foundation ; Early Career Award in Nanotechnology from the IEEE Nanotechnology Council ; Outstanding Young Engineer Award from the IEEE Microwave Theory and Techniques Society ; Booker Fellowship from the USA National Committee of the International Union of Radio Science ; Lot Shafai Mid-Career Distinguished Achievement Award from the IEEE Antennas and Propagation Society ; Early Career Award from the USA National Science Foundation ; Young Investigator Awards from the USA Office of Naval Research, the Army Research Office, and the Defense Advanced Research Projects Agency. Prof. Jarrahi is a Fellow of IEEE, OSA and SPIE societies and has served as a distinguished lecturer of IEEE, traveling lecturer of OSA, and visiting lecturer of SPIE societies.

Hyperspectral Terahertz Imaging Using Plasmonic Detectors
This talk gives an overview of advancements in hyperspectral terahertz imaging systems, which utilize plasmonic photoconductive terahertz detectors to provide significantly higher signal-to-noise ratio levels.

Maria Kafesaki

University of Crete, Greece

Cylinder- and multi-coated-cylinder-systems as multifunctional metamaterials : An Effective Medium description

Maria Kafesaki is Associate Professor in the Dept. of Materials Science and Technology of the University of Crete and Adjunct Researcher at the Institute of Electronic Structure and Laser (IESL) of Foundation for Research and Technology Hellas (FORTH). She obtained her Ph.D. in 1997, at the Physics Department of the University of Crete, Greece, on elastic wave propagation in complex media. She has worked as a post-doctoral researcher in the Consejo Superior de Investigaciones Cientificas in Madrid, Spain, and in IESL of FORTH (1997-2001). Her current research is on the area of electromagnetic wave propagation in periodic and random media, with emphasis on photonic crystals and metamaterials, where she has large theoretical and computational experience. She has more than 110 publications in refereed journals (with more than 6500 citations and h-index=42, according to Web of Science), and more than 70 invited talks at international conferences and schools. She has participated in many European projects as well as in the organization of many international conferences and schools. She is a Fellow of the Optical Society of America. Figure : A simple PT-symmetric chiral bi-layer. Under oblique incidence of circularly polarized (CP) waves the bi-layer eigenvalues σ indicate the existence of a mixed phase and two exceptional points, highly tunable by the incidence angle.

Cylinder- and multi-coated-cylinder-systems as multifunctional metamaterials : An Effective Medium description

We discuss an effective medium approach for analyzing metamaterials composed of cylindrical scatterers/meta-atoms, either simple or coated/multi-coated. We demonstrate the potential of this approach in THz systems made of polaritonic cylinders as well as in graphene-based nanotubes. In both cases we demonstrate a reach palate of optical responses, including negative index and hyperbolic metamaterial response.

Enrica Martini

University of Siena, Italy

Recent advances in metasurface antennas design and modelling

Enrica Martini received the Laurea degree (cum laude) in telecommunication engineering from the University of Florence, Italy, in 1998. From 1998 to 1999 she worked at the University of Florence under a one-year research grant from the Alenia Aerospazio Company, Rome, Italy. In 2002, she received the PhD degree in informatics and telecommunications from the University of Florence and the Ph.D. degree in electronics from the University of Nice-Sophia Antipolis, under joint supervision. In 2002, she was appointed Research Associate at the University of Siena, Italy. In 2005, she received the Hans Christian Ørsted Postdoctoral Fellowship from the Technical University of Denmark, Lyngby, Denmark, and she joined the Electromagnetic Systems Section of the Ørsted DTU Department until 2007. From 2007 to 2017 she was a Postdoctoral Fellow at the University of Siena, Italy. In 2012, she co-founded the start-up Wave Up Srl, Siena, Italy, of which she was the CEO from 2016 to 2018. From 2019 to 2021 she was an assistant professor at the University of Siena, Italy. She is currently an Associate Professor with the Department of Information Engineering and Mathematics, University of Siena, Siena, Ital Dr. Martini coordinated tasks of various research projects funded by national and international governmental institutions, as well as by industry. Her research interests include metasurfaces and metamaterial characterization, metasurface-based antennas and microwave devices, electromagnetic scattering, antenna measurements and tropospheric propagation. Dr. Martini was a co-recipient of the 2016 Schelkunoff Transactions Prize Paper Award, of the Best Paper Award in Antenna Design and Applications at the 11th European Conference on Antennas and Propagation in 2017, of the Best Poster Award at the Metamaterials Congress in 2019 and of the Best Paper Award in Electromagnetics at the 15th European Conference on Antennas and Propagation in 2021.

Recent advances in metasurface antennas design and modelling

This contribution provides an overview of the recent advances in the field of modulated metasurface antennas. After reviewing the most advanced analytical and numerical models, different designs and realizations will be presented, including antennas with shaped pattern, dual polarized, multibeam and beam scanning antennas.

Taiichi Otsuji

Tohoku University, Japan

Graphene-based van der Waals 2D heterostructure materials and devices for terahertz wireless communications

Taiichi Otsuji is a Full Professor at the Research Institute of Electrical Communication (RIEC), Tohoku University, Sendai, Japan. He received the Dr. Eng. degree in electronic engineering from Tokyo Institute of Technology, Tokyo, Japan in 1994. From 1984 to 1999 he worked for NTT Laboratories, Kanagawa, Japan. In 1999 he joined Kyushu Institute of Technology as an associate professor, being a professor in 2002. He joined RIEC, Tohoku University, in 2005. His current research interests include terahertz electronic, photonic and plasmonic materials/devices and their applications. He has authored and co-authored 300 peer-reviewed international journal papers and more than 600 international conference proceedings including 210 invited presentations, and holds 13 Japanese and 8 US patents. He is the recipient of the Outstanding Paper Award of the 1997 IEEE GaAs IC Symposium in 1998, the Prizes for Science and Technology in Research Category, the Commendation for Science and Technology by the MEXT, Japan, in 2019, and the 59th Achievement Award of the IEICE (Institute of Electronics, Information, and Communication Engineers), Japan, in 2022. He has served as an IEEE Electron Device Society Distinguished Lecturer since 2013. He is a Fellow of IEEE, OPTICA (former OSA, Optical Society of America), and JSAP (Japan Society of Applied Physics).

Graphene-based van der Waals 2D heterostructure materials and devices for terahertz wireless communications

This paper reviews recent advances in the research and development of graphene-based van der Waals 2D heterostructure materials and devices for terahertz wireless communications.

Willie J. Padilla

Duke University, USA

Physics Informed Deep Learning In Metamaterials

Willie J. Padilla is a professor at Duke University with a master's degree and doctorate in physics. He received a Young Investigator Award from the Office of Naval Research and a Presidential Early Career Award for Scientists and Engineers. Padilla is a fellow of the American Physical Society, Optical Society of America and Kavli Frontiers of Science. He is also a Web of Science Highly Cited Researcher in physics for 2018 and 2019. He heads a group working in the area of metamaterials with a focus on machine learning, computational imaging, spectroscopy and energy, and has published more than 200 peer-reviewed journal articles.

Physics Informed Deep Learning In Metamaterials

Deep learning has had profound impacts in electromagnetic metamaterials, however there are several,drawbacks including. Through incorporation of prior knowledge, physics informed deep neural networks (PINNs),have the capability to solve many of the outstanding problems in deep learning and may additionally learn new,physics of systems under study. We discuss three different studies using physics informed deep learning and,describe the future of the field is also given.

Atif Shamim

KAUST, Saudi Arabia

On-Chip Antennas - The Last Barrier to True RF System-on-Chip

Atif Shamim received his MS and PhD degrees in electrical engineering from Carleton University, Canada in 2004 and 2009 respectively. He was an NSERC Alexander Graham Bell Graduate scholar at Carleton University from 2007 till 2009 and an NSERC postdoctoral Fellow in 2009-2010 at Royal Military College Canada and KAUST. In August 2010, he joined the Electrical and Computer Engineering Program at KAUST, where he is currently an Associate Professor and principal investigator of IMPACT Lab. He was an invited researcher at the VTT Micro-Modules Research Center (Oulu, Finland) in 2006. His research work has won best paper awards in IEEE ICMAC 2021, IEEE IMS 2016, IEEE MECAP 2016, IEEE EuWiT 2008, first prize in IEEE IMS 2019 3MT competition and IEEE AP-S Design Competition 2022, finalist/honorable mention prizes in IEEE AP-S Design Competition 2020, IEEE IMS 2017 (3MT competition), IEEE IMS 2014, IEEE APS 2005. He has been selected as the Distinguished Lecturer for IEEE AP-S (2022-2024). He has won the Kings Prize for the best innovation of the year (2018) for his work on sensors for the oil industry. He was given the Ottawa Centre of Research Innovation (OCRI) Researcher of the Year Award in 2008 in Canada. His work on Wireless Dosimeter won the ITAC SMC Award at Canadian Microelectronics Corporation TEXPO in 2007. Prof. Shamim also won numerous business-related awards, including 1st prize in Canada's national business plan competition and was awarded OCRI Entrepreneur of the year award in 2010. He is an author/co-author of around 300 international publications, an inventor on more than 40 patents and has given close to 100 invited talks at various international forums. His research interests are in innovative antenna designs and their integration strategies with circuits and sensors for flexible and wearable wireless sensing systems through a combination of CMOS and additive manufacturing technologies. He is a Senior Member of IEEE, founded the first IEEE AP/MTT chapter in Saudi Arabia (2013) and served on the editorial board of IEEE Transactions on Antennas and Propagation (2013-2019), and as a Guest Editor for IEEE AWPL Special issue (2019), and is currently serving as an Associate Editor for IEEE Journal of Electromagnetics, RF and Microwaves in Medicine and Biology. He serves on numerous IEEE committees such IEEE Technical committees on Antenna Measurements (AP-S), Microwave Controls (MTT-S 13), and Additive Manufacturing (CRFID). Find out more details at (https ://cemse.kaust.edu.sa/impact).

On-Chip Antennas - The Last Barrier to True RF System-on-Chip

In the last decade, the increased level of integration provided by silicon technologies and emerging applications at millimeter wave frequencies has helped to achieve true System-on-Chip solutions bringing the antennas on the chip. This is because antenna sizes at these frequencies become small enough for practical on-chip realization. However, there are a number of challenges to overcome, for instance dealing with silicon substrate high conductivity and permittivity, metal stack-up and layout restrictions, and on-chip characterization through delicate probes, etc.

Fredrik Tufvesson

Lund University, Sweden

Channel modelling and characterization for communication and sensing in a 6G era

Fredrik Tufvesson received his Ph.D. in 2000 from Lund University in Sweden. After two years at a startup company, he joined the department of Electrical and Information Technology at Lund University, where he is now professor of radio systems. His main research interests is the interplay between the radio channel and the rest of the communication system with various applications in wireless systems such as massive MIMO, mm wave communication, vehicular communication and radio based positioning. Fredrik has authored around 90 journal papers and 140 conference papers, he is fellow of the IEEE and recently he got the Neal Shepherd Memorial Award for the best propagation paper in IEEE Transactions on Vehicular Technology and the IEEE Communications Society best tutorial paper award.

Channel modelling and characterization for communication and sensing in a 6G era

6G is expected to be based on distributed and co-located ultra-massive MIMO at frequencies ranging from one or a few GHz to hundreds of GHz. It will support both communication and sensing applications and should at the same time offer extreme reliability, enormous data rates, and ultra-low latencies. In this talk, we discuss channel characteristics, channel models, and the implications on 6G. Based on measurement examples, we point out possible directions and limitations and what we really can expect from the various frequency bands.

Ventsislav K. Valev

University of Bath, UK

Chiroptical harmonic scattering : predicted in 1979 and demonstrated four decades later

Ventsislav K. Valev is a Full Professor and a Research Fellow of the Royal Society, in the Physics Department of the University of Bath, where he serves as the Head of Department. He is also an Associate Fellow of Homerton College, in the University of Cambridge.

Valev was born in Bulgaria. He studied physics at the University of Western Brittany (France), with a final year at the University of Cardiff (Wales), as an Erasmus student. He received his PhD in 2006, from the Radboud University Nijmegen (the Netherlands). Subsequently, he was a post-doc and a Research Fellow at the KU Leuven University (Belgium). In 2012, he became a Research Fellow in the Cavendish Laboratory at the University of Cambridge and, in 2013, he joined Homerton College, as a Research Associate. Since 2014, he has been working at the University of Bath, where he arrived as a Reader and a Research Fellow of the Royal Society. In 2019, he was promoted to professor and in 2021 he became the Director of Research for the Department of Physics. He was appointed Head of Department in 2022.

Valev's research group focuses on the interaction between powerful laser light and nanostructured materials. He builds laser experiments to study novel materials, such as plasmonic nanostructures, metamaterials, 2D materials and quantum optical materials. He explores the physics of photons, electrons and magnetism confined to tiny volumes of space – nanoparticles or 2D sheets. He aims to discover new properties and to test theoretical predictions, seeking out new and useful intersections between classical electromagnetism and quantum mechanics. His investigations are both fundamental and applied, with potential benefits for the pharmaceutical, food, perfume, and agrochemical industries.

Chiroptical harmonic scattering : predicted in 1979 and demonstrated four decades later
Chiroptical harmonic scattering (CHS) was predicted in 1979, but an experimental observation of this effect remained elusive for 40 years. A first form of CHS was reported in 2019 ; it was demonstrated that light scattered at the second-harmonic from Ag nanohelices dispersed in water could reveal the chirality of the nanohelices. Observations in other systems (metal and semiconductor) and at the third-harmonic quickly followed. Now, we show the effect in high refractive index dielectrics.

TUTORIALS

Prof. Willie J. Padilla

Duke University, USA

Tuesday 6th June
15:00 - 16:00 — Playamar

Introduction to Deep Learning Techniques for Artificial Electromagnetic Materials

Willie J. Padilla is a professor at Duke University with a master's degree and doctorate in physics. He received a Young Investigator Award from the Office of Naval Research and a Presidential Early Career Award for Scientists and Engineers. Padilla is a fellow of the American Physical Society, Optical Society of America and Kavli Frontiers of Science. He is also a Web of Science Highly Cited Researcher in physics for 2018 and 2019. He heads a group working in the area of metamaterials with a focus on machine learning, computational imaging, spectroscopy and energy, and has published more than 200 peer-reviewed journal articles.

Introduction to Deep Learning Techniques for Artificial Electromagnetic Materials
Deep neural networks (DNNs) have enhanced and transformed traditional research methods and are driving scientific advance. Deep learning has shown immense potential in the field of artificial electromagnetic materials (AEM) research, with applications spanning electromagnetic metamaterials, metasurfaces, photonic crystals, and plasmonics. In this brief tutorial we review the status of the field with a focus on recent advances, key limitations, and future directions. Strategies, guidance, evaluation, and limits of using deep networks for both forward and inverse AEM problems are presented.

GUIDELINES FOR PRESENTERS I IN-PERSON

In-person Oral Presentations

Each session room is equipped with a stationary computer connected to a LCD projector. Presenters must load their presentation files in advance onto the session computer. Technician personnel will be available to assist you.

Scheduled time slots for oral presentations are 15 mn for regular, 20 mn for invited presentations, 30 mn for keynote talks and 35 mn for plenary talks, including questions and discussions. Presenters are required to report to their session room and to their session Chair at least 15 minutes prior to the start of their session.

The session chair must be present in the session room at least 15 minutes before the start of the session and must strictly observe the starting time and time limit of each paper.

In-person Poster Presentations

Presenters are requested to stand by their posters during their session. One poster board, A0 size (118.9 x 84.1 cm), in portrait orientation, will be available for each poster. Pins or thumbtacks are provided to mount your posters on the board. All presenters are required to mount their papers 30mn before the session and remove them at the end of their sessions. Posters must prepared using the standard AES poster template (available on the conference website).

GUIDELINES FOR PRESENTERS I **ONLINE**

All Oral presentations will be in person with option for remote viewing via Zoom.

Poster sessions will be hybrid, consisting of both in person and virtual presentations. Instructions for **virtual poster presenters** can be found here : guidelines).

USEFUL INFORMATION

Venue

AES 2023 will be held at :
Palacio de Congresos y Exposiciones de la Costa del Sol
3 Calle Mexico, 29620 Torremolinos (Spain)

https://palacio-congresos.es

Opened in October 1970, the Palacio de Congresos y Exposiciones de Torremolinos (Congress and Exhibition Centre) was the result of a project designed in 1967 by the architects Rafael de la Hoz and Gerardo Olivares James. The building, which became the state heritage property in 1971.

The complex is built on an estate of 70,000 square meters, of which 18,000 square meters are gardens. Situated in a privileged location in the municipality of Torremolinos and located in the upper area of the town on a hill overlooking the sea, the Congress Center is an icon of Malaga's coastal landscape.

The building is arranged in a circular format around which the various auditoriums, meeting rooms, administrative offices and annexed buildings are distributed. The central hall is presided over by its most iconic visual symbol, an emblem of convention and business tourism in Spain : a large translucent dome with an unprecedented crystal lamp hanging from the center of the exposed radial roof, falling like drops in a waterfall spilling over the center of the composition.

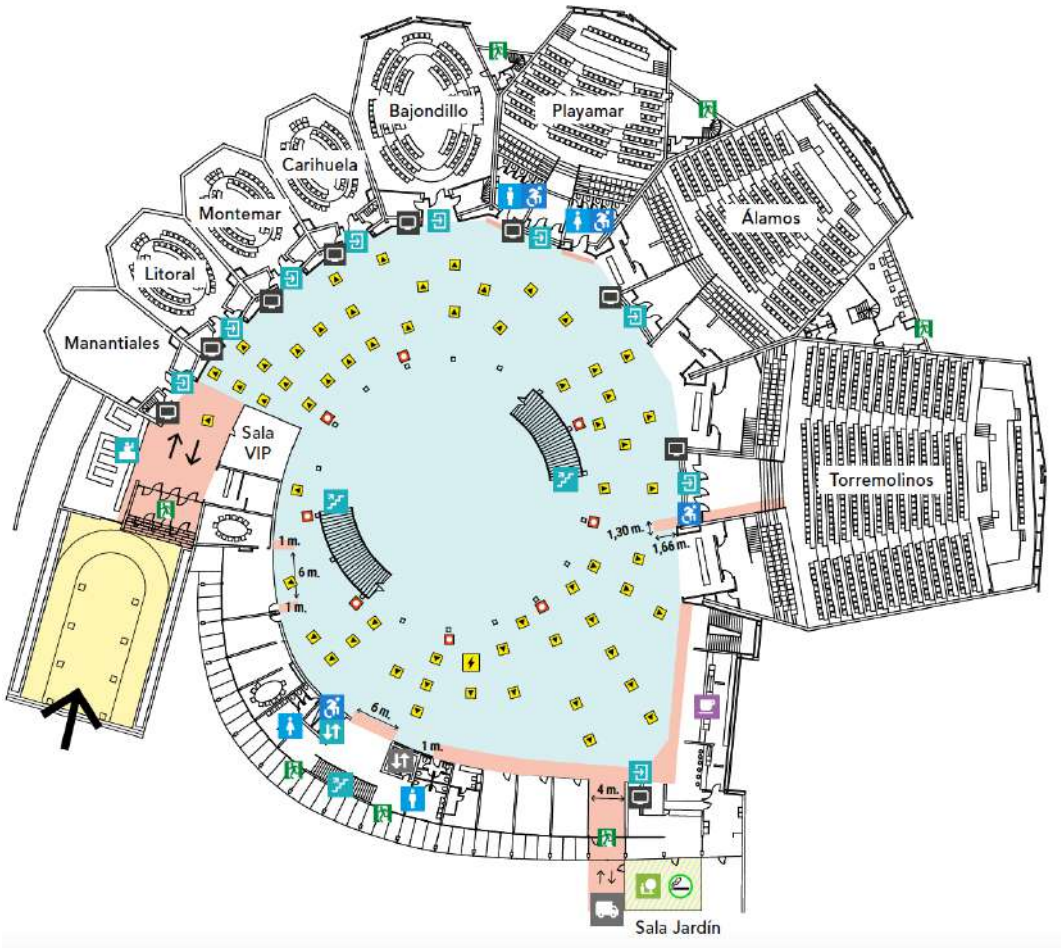

Getting to Venue

Getting to Torremolinos from Malaga Airport

Torremolinos is around 8km away from Malaga international airport. You can go from the airport to the city center by taxi, by train or by bus.

Taxi

The airport has a well-signposted taxi rank outside the arrivals area of Terminal T3. Make sure that the taxi driver has started the taximeter at the beginning of the journey (minimum fare). We recommend requesting a receipt for any complaint or claim.

Train

The new suburban train station in the new Terminal T3 building links the airport with Torremolinos city centre and other cities like Benalmadena and Fuengirola in one direction, and it links Malaga city center in the other direction.

The train station is situated underground and accessed via escalators. It is well signposted and can be reached via the square outside arrivals or outside departures. Before the station entry barriers you will see several self-service tickets machines on your right where you can buy your tickets.

The first train to Torremolinos leaves the airport at 05 :32, leaving every 20-30 minutes until the last train at 23.42. Line : C1. Estimated travel time : 10 minutes.

Bus

You will find the bus stop straight in front of you outside the arrivals area of Terminal T3 on the side of the road where there are a couple of shelters with seats. You will also see a ticket office in the left hand corner of the arrivals forecourt where you should purchase your tickets for the journey. Line : Torremolinos-Benalmadena-Airport. Estimated travel time : 30 minutes.

Getting to Torremolinos from Malaga train station

There are two train stations in the centre of Malaga : Maria Zambrano and Centro Alameda. Maria Zambrano station provides high-speed (AVE) and long-distance links to many Spanish cities like Barcelona, Cordoba, Madrid, Santiago de Compostela, Seville, etc, as well as local and regional routes.

You can take Line C1 from any of the two stations to reach Torremolinos. The estimated travel time is 20 minutes. You can check the timetables on the website of the national rail company RENFE

Getting to Torremolinos from Malaga bus station

Malaga bus station is located at the street "Paseo de los Tilos" very near Maria Zambrano train station. So it will be very easy to take a bus or a train from this station. You can take bus line Malaga-Torremolinos. Estimated travel time : 20 minutes.

TABLE OF CONTENTS

Plenary presentation

Keynote presentation

Tutorial

Spatiotemporal effects in multimode optical fiber

Additive manufacturing for electromagnetic devices

Antennas, EM and Smart Sensing Technologies for Biomedical and Healthcare Applications

Advances in Sensor Technologies Involving Electrodynamics and Magnetism

Smart Electromagnetic Skins and their Applications

Nanoscale Electrodynamics

Antenna theory and design

Array antennas, active, adaptive and reconfigurable antennas

Analytical, Computational and numerical techniques

Imaging, inverse scattering and remote sensing

Metamaterials, metasurfaces, FSS and EBG

Nanophotonics, plasmonics and quantum optics

Optics and Photonics

Optoelectronics, Photonic Materials and Devices

Scattering and diffraction

Propagation theory

Material Characterization and non-destructive testing

Plenary presentation

Electromagnetics for Energy Applications

Shanhui Fan[1]

[1]Department of Electrical Engineering, Ginzton Laboratory, Stanford University, Stanford, CA 94305, USA

Abstract: Electromagnetic fields represent one of the most important carriers of energy. The ability to control electromagnetic fields therefore play an essential role in the generation, transport, and utilization of energy. In this talk, we review our efforts in advancing electromagnetic technology for energy applications. Examples include radiative cooling, nighttime power harvesting, and the use of non-reciprocity to reach the ultimate efficiency limit of solar energy harvesting.

Efficient Wireless Power Transfer for IoTs and Biomedical Applications

Yongxin Guo[1,2]

[1]National University of Singapore, Singapore
[2]National University of Singapore Suzhou Research Institute, China
Yongxin.guo@nus.edu.sg

Abstract: Wireless power transfer (WPT) plays an increasingly important role in internet of things (IoTs) and biomedical applications. With the rapid development of 5G and IoTs, the dense deployment of sensor nodes become more popular. Various wireless power application scenarios will be introduced. Our recent research progress on near-field inductive and capacitive WPT and far-field WPT will be reported. Adaptive rectifier design and reconfigurable diode topology will be explained. Waveform-optimized WPT together with reconfigurable diode topology will be further illustrated.

cmWave-MIMO : towards the 1K-element-array paradigm

Wen Tong

Huawei Technologies, Canada
*corresponding author: tongwen@huawei.com

Abstract:
In this talk, we present the development of massive MIMO antenna technologies for the emerging 6G and associated challenges. The overall system performance and antenna design-choice in terms of spectrum and channel propagation properties are discussed. We explore the centimeter wave spectrum for the 6G massive MIMO. The candidate frequency range is from 7GHz to 15GHz, we discuss the new propagation properties and ultra-large antenna element array architecture, namely, the 1K-element-array paradigm for both base-station and user-equipment. The 6G centimeter-wave MIMO signal processing represents the new opportunities and challenges to advance the classical MIMO technology.

Designing Antennas with Gap Waveguide Technology: Exploring New Trends

E. Rajo-Iglesias[1]

[1]University Carlos III of Madrid, Spain

[*]corresponding author: eva.rajo@uc3m.es

Abstract: A brief introduction to the foundational principles of gap waveguide technology, followed by an overview of traditional designs of directive antennas using corporate fed arrays will be presented. Subsequently, novel applications of this technology in the millimeter frequency bands will be explored, which include the implementation of alternate periodic structures replacing the conventional bed of nails. Finally, the potential of combining this technology with established technologies like microstrip, as well as the design of other types of antennas as leaky wave antennas, will be discussed. In this way, an overview of different on going research lines connected to this technology will be presented.

The Art, Science and Engineering of Modern Antenna Measurements and Diagnostics: From Marconi's First Measurements to Today's Incredible Advances

Yahya Rahmat-Samii
Distinguished Professor
Department of Electrical and Computer Engineering
University of California, Los Angeles, USA
rahmat@ee.ucla.edu, www.antlab.ee.ucla.edu

Abstract: Starting with Marconi's first antenna pattern measurements, we then discuss modern planar near-field antenna measurements as a novel paradigm linking electromagnetic theory, sampling techniques, back projection and FFT. Based on the fundamental electromagnetic principles, the underlying concepts governing simulations, designs and operations of planar-near field measurements and diagnostics techniques will be highlighted. Modern measurement systems such as plane-polar, bi-polar and robotics scanning systems will be presented. Representative measurement results of reflector, array, reflectarray and lens antennas will be presented for diverse applications including planetary missions, radars for remote sensing, and Cubesats. Finally, the topics of diagnostics and phaseless antenna measurement techniques and algorithms will be touched upon.

Keynote presentation

Universal light encoders: artificial intelligent optical hardware for real-time hyperspectral imaging and ultrasensitive detection

A. Fratalocchi[1,2]

[1]PRIMALIGHT, Faculty of Electrical and Computer Engineering, King Abdullah University of Science and Technology (KAUST), Thuwal 23955-6900, Saudi Arabia
Andrea.fratalocchi@kaust.edu.sa

Abstract: I will summarize present and future research in the field of universal light encoders (ULEs), which represent artificial intelligent optical hardware implementing arbitrary user-defined functionalities in ultra-thin metasurfaces. ULEs process information at the speed of light and can be integrated into any conventional monochrome camera for machine vision, transforming the system into an optical neural network processor. I will discuss applications of ULEs in the implementation of Hyplex^{TM}, a high-resolution hyperspectral imaging camera and a universal platform for ultrasensitive detection.

Universal light encoders (ULEs) represent a class of artificial intelligent hardware trained to implement any user-defined input-output function. These components comprise nanostructured metasurfaces with suitably engineered nanoresonators with controllable features of 20 nm scale. The physical set of nanostructures acts as an equivalent hidden layer of artificial neural networks' universal approximators, which process information at the speed of light without requiring electronics. These systems implement basic optical circuitry and more advanced systems that perform machine learning functionalities directly in hardware.

In this Keynote talk, I will discuss present and future research in this field of science. I will begin by discussing optical ULEs' motivation and fundamental design and their training with both software and machine learning hardware approaches. I will then briefly summarize the recent applications of this technology in hyperspectral imaging (HI) and bio-sensing.

In HI, I will discuss the implementation of a camera for acquiring and processing real-time hyperspectral videos in high resolution at 30 frames per second for machine vision segmentation and object-tracking in ground and airborne applications. In the field of bio-sensing, I will discuss the fundamentals and applications of ULEs in implementing an integrated platform technology that opens to ultrasensitive detection below 10^-15 Mol.

References

1. Getman, F, Makarenko, M, Burguete-Lopez, A, Fratalocchi, A, "Broadband vectorial ultrathin optics with experimental efficiency up to 99% in the visible region via universal approximators", Light: Science & Applications, vol. 10, no. 1, pp. 47, 2021.
2. Makarenko, M., Wang, Q., Burguete-Lopez, A., Getman, F. Fratalocchi, A., "Robust and Scalable Flat-Optics on Flexible Substrates via Evolutionary Neural Networks", Advanced Intelligent Systems, pp. 2100105, 2021.
3. Makarenko, M. Burguete-Lopez, A., Wang, Q., Getman, F, Giancola, S., Bernard, G, Fratalocchi, A., "Real-time Hyperspectral Imaging in Hardware via Trained Metasurface Encoders", Conference on Computer Vision and Pattern Recognition (CVPR), Jul. 2022.

Recent advances in metasurface antennas design and modelling

E. Martini

Department of Information Engineering and Mathematics, University of Siena, Siena, Italy
martini@dii.unisi.it

Abstract: This contribution provides an overview of the recent advances in the field of modulated metasurface antennas. After reviewing the most advanced analytical and numerical models, different designs and realizations will be presented, including antennas with shaped pattern, dual polarized, multibeam and beam scanning antennas.

Metasurface antennas are based on the controlled conversion of a non radiative surface wave (SW) into a radiative leaky wave [1]. The SW is launched by a feeder, and the conversion is performed by a modulated artificial surface, or metasurface (MTS), imposing locally periodic boundary conditions (BCs) for the electromagnetic field. In the microwave range, this latter is typically realized by printing metallic sub-wavelength elements positioned on a regular lattice over a grounded dielectric slab. Metasurface antennas are characterized by an extremely low profile, light weight, moderate losses and low-cost fabrication. A key point for the accurate characterization and design of MTS antennas is the possibility to effectively characterize the MTS through homogenized BCs of impedance type, which is due to the electrically small size of its constitutive elements. This allows for an effective multiscale design approach, that starts from a continuous impedance profile to finally provide the precise layout of the metalisation. The continuous impedance profile is obtained through the rigorous analysis of the periodic problem that locally approximates the real profile, while its implementation is performed by using proper impedance maps which relate the equivalent tensor impedance to the geometrical parameters of the patches. As a result of this design approach, it is possible to accurately control the amplitude, phase and polarization of the radiating aperture field [2].

The versatility of this class of antennas will be illustrated through the presentation of the most recent designs, including antennas with shaped pattern, dual polarized, multibeam and beam scanning antennas. It will be also shown how, differently from other leaky wave antennas, metasurface antennas based on *anisotropic* BCs do not present the open stop band problem, and can be therefore designed to efficiently radiate also at broadside [3]. This is not true, on the other hand, for MTS antennas based on *isotropic* BCs. This behavior will be justified based on the rigorous analysis of the homogenized model and numerically verified on practical structures.

References

1. Minatti, G., F. Caminita, E. Martini and S. Maci, “Flat Optics for Leaky-Waves on Modulated Metasurfaces: Adiabatic Floquet-Wave Analysis,” in *IEEE Trans. Antennas Propagat.*, vol. 64, no. 9, pp. 3896-3906, Sept. 2016.
2. M. Faenzi, G. Minatti, D. González-Ovejero, F. Caminita, E. Martini, C. Della Giovampaola, S. Maci, “Metasurface antennas: New models, applications and realizations,” *Scientific Reports* 9.1, pp. 1-14, 2019.
3. Giusti, F., S. Maci and E. Martini, “Complete Open-Stopband Suppression for Anisotropic Modulated Metasurfaces Scanning Through Broadside,” *2022 Sixteenth International Congress on Artificial Materials for Novel Wave Phenomena (Metamaterials)*, Siena, Italy, 2022, pp. X-166-X-168.

On-Chip Antennas: The Last Barrier to True RF System-on-Chip

Atif Shamim
King Abdullah University of Science and Technology (KAUST), Saudi Arabia

Abstract: Antennas are integral part of wireless communication devices and traditionally have remained off the Integrated Circuits (ICs which are also commonly known as chips) resulting in large sized modules. In the last decade, the increased level of integration provided by silicon technologies and emerging applications at millimeter wave frequencies has helped to achieve true System-on-Chip solutions bringing the antennas on the chip. This is because antenna sizes at these frequencies become small enough for practical on-chip realization. Though, there are a number of benefits of putting antennas on-chip, such as monolithic integration resulting in compact systems, robustness due to absence of bond wires or other connection mechanisms between the antenna and the circuits, lower cost due to mass manufacturing in standard CMOS processes, etc. However, there are a number of challenges to overcome, for instance dealing with silicon substrate high conductivity and permittivity (resulting in poor radiation efficiency), metal stack-up and layout restrictions, and on-chip characterization through delicate probes, etc. Furthermore, the co-design of circuits and antenna which sometime have contradicting requirements need knowledge of both the domains. This talk aims to discuss the above challenges in detail as well as the proposed solutions. In particular, many design examples will be shown for the gain and radiation efficiency enhancement of on-chip antennas through artificial magnetic conductors. The talk will conclude with the upcoming trends in the field of on-chip antennas.

Graphene-based van der Waals 2D heterostructure materials and devices for terahertz wireless communications

T. Otsuji[1*]

[1]Research Institute of Electrical Communication, Tohoku University, Japan
[*]corresponding author: otsuji@riec.tohoku.ac.jp

Abstract: This paper reviews recent advances in the research and development of graphene-based van der Waals 2D heterostructure materials and devices for terahertz wireless communications.

The authors' theoretical discovery of THz laser transistors in 2007 [1-4] was realized in 2018 [5] as a distributed-feedback dual-gate graphene-channel field-effect transistor (DFB-DG-GFET). However it had small output power (single-mode emission at 5.2 THz with ~0.1 μW output intensity) and operated at a low lasing threshold temperature (100K). Various approaches have been introduced and discussed to realize room temperature, dry-cell battery operating, and intense THz lasing with fast direct modulation, based on graphene plasmonic metamaterials The proposed designs include (i) replacement of the laser photonic cavity with a plasmonic cavity enormously improving the THz photon field confinement with larger gain overlapping [6], (ii) introduction of THz amplification of stimulated emission via current-driven instability of graphene Dirac plasmons (GDPs) [7-12], and (iii) controlling the parity and time-reversal symmetry of GDPs enabling ultrafast direct gain-switch modulation [13-15]. Possible device structures and design constraints were discussed as a promising pathway towards coherent light sources for future 6G- and 7G-class THz wireless communication systems. The graphene plasmonic metamaterial solutions offer new ways for designing efficient devices for future robust far-infrared and THz plasmonic device technology. New physical models should meet new important challenges for theoretical physics and provide a full quantitative description of current-driven plasma phenomena in graphene and other 2D systems with Dirac-like energy band structure.

The author acknowledges Drs. S. Boubanga-Tombet, C. Tang, A. Satou, V. Ryzhii, K. Wojciech, D. Yadav, K. Narahara, M. Ryzhii, V. Mitin, and M.S. Shur for their contributions. This work was supported by JSPS KAKENHI # 21H04546 and 20K20349, Japan. The device process responsible for the author was carried out at the Laboratory for Nanoelectronics and Spintronics of RIEC, Tohoku University, Japan.

References

1. Ryzhii, V., Ryzhii, M., Otsuji, T. "Negative dynamic conductivity in optically pumped graphene," J. Appl. Phys., Vol. 101, 083114, 2007.
2. Ryzhii M, Ryzhii V. "Injection and population inversion in electrically induced p-n junction in graphene with split gates," Jpn. J. Appl. Phys., Vol. 46, L151-L153, 2007.
3. Otsuji T, Boubanga-Tombet S, Satou A, Ryzhii M, Ryzhii V. "Terahertz-wave generation using graphene-toward new types of terahertz lasers," IEEE J. Selected Topics in Quantum Electron., Vol. 19, 8400209, 2013.
4. Ryzhii V, Ryzhii M, Mitin V, Otsuji T. "Toward the creation of terahertz graphene injection laser," J. Appl. Phys., Vol. 110, 094503, 2011.
5. Yadav D, Tamamushi G, Watanabe T, Mitsushio J, Tobah Y, Sugawara K, Dubinov AA, Satou A, Ryzhii M, Ryzhii V,

Otsuji T. “Terahertz light-emitting graphene-channel transistor toward single-mode lasing,” Nanophotonics, Vol. 7, 741–752, 2018.

6. Dubinov A A, Sleshkin V Ya, Morozov SV, Ryzhii V, Otsuji T. “Terahertz plasmon-emitting graphene-channel transistor,” Opto-Electron. Rev., Vol. 27, 345-347, 2019.
7. Boubanga-Tombet S, Knap W, Yadav Y, Satou A, But DB, Popov VV, Gorbenko IV, Kachorovskii V, Otsuji T. “Room temperature amplification of terahertz radiation by grating-gate graphene structures,” Phys. Rev. X, Vol. 10, 031004, 2020.
8. Boubanga-Tombet S, Satou A, Yadav Y, But DB, Knap W, Popov VV, Gorbenko IV, Kachorovskii V, Otsuji T. “Paving the way for tunable graphene plasmonic THz amplifiers,” Frontiers in Phys., Vol. 7, 726806, 2021.
9. Ryzhii V, Ryzhii M, Mitin V, Shur MS, and Otsuji T. “S-shaped current-voltage characteristics of n+-i-n-n+ graphene field-effect transistors due to the Coulomb drag of quasi-equilibrium electrons by ballistic electrons,” Phys. Rev. Appl., Vol. 16, 014001, 2021.
10. Ryzhii V, Ryzhii M, Mitin V, Shur MS, and Otsuji T. “Coulomb drag mechanism of terahertz plasma instability in n+-i-n-n+ graphene FETs with ballistic injection,” Appl. Phys. Lett., Vol. 119, 093501, 2021.
11. Ryzhii V, Ryzhii M, Satou A, Mitin V, Shur MS, and Otsuji T, “Ballistic injection terahertz plasma instability in graphene n+-i-n-n+ field-effect transistors and lateral diodes,” Phys. Status Solidi A, Vol. 219, 2100694, 2022.
12. Ryzhii V, Ryzhii M, Satou A, Otsuji T, Mitin V, and Shur MS. “Effect of Coulomb carrier drag and terahertz plasma instability in p+-p-i-n-n+ graphene tunneling transistor structures,” Phys. Rev. Appl., Vol. 16, 064054, 2021.
13. Bender CM, Boettcher S. “Real spectra in non-Hermitian Hamiltonians having PT symmetry,” Phys. Rev. Lett., Vol. 80, 5243-5246, 1998.
14. Ramezani H, and Kottos T. “Unidirectional nonlinear PT-symmetric optical structures,” Phys. Rev. A, Vol. 82, 04383, 2010.
15. Miri M-A, Alu A. “Exceptional points in optics and photonics,” Science, Vol. 363, 42, 2019; Krasnok A, Alu A. “Active nanophononics,” Proc. IEEE, Vol. 108, 628-564, 2020.
16. Otsuji T, Boubanga-Tombet SA, Satou A, Yadav D, Fukidome H, Watanabe T, Suemitsu T, Dubinov AA, Popov VV, Knap W, Kachorovskii V, Narahara K, Ryzhii M, Mitin V, Shur MS, and Ryzhii V. "Graphene-based plasmonic metamaterial for terahertz laser transistors," Nanophotonics, Vol. 11, 1677-1696, 2022.

Cylinder- and multi-coated-cylinder-systems as multifunctional metamaterials: An Effective Medium description

Ch. Mavidis[1,2], A. Tasolamprou[1], M. Kafesaki[1,2]

[1] Foundation for Research and Technology Hellas (FORTH), Institute of Electronic Structure and Laser, N. Plastira 100, 70013 Heraklion, Crete, Greece

[2] University of Crete, Dept. of Materials Science and Technology, 70013 Heraklion, Crete, Greece

[*]corresponding author: kafesaki@iesl.forth.gr

Abstract: We discuss an effective medium approach for analyzing metamaterials composed of cylindrical scatterers/meta-atoms, either simple or coated/multi-coated. We demonstrate the potential of this approach in THz systems made of polaritonic cylinders as well as in graphene-based nanotubes. In both cases we demonstrate a reach palate of optical responses, including negative index and hyperbolic metamaterial response.

In recent years, high-index dielectric metamaterials and metamaterials made of resonant materials (e.g. phonon-polartion materials) have gained significant attention due to their ability to support multiple tailorable subwavelength resonances avoiding the high losses inherent to metallic metamaterials. The accurate description of such metamaterials as effective media requires approaches applicable beyond the quasistatic regime, i.e. in regimes where the wavelength inside the meta-atoms is comparable to their size. The common though effective medium approaches, such as Maxwell-Garnett, fail to accurately describe wave propagation in this regime. While different extensions of the Maxwell-Garnett approach have been developed for systems of spherical scatterers [1], none such approach exists for systems of cylindrical scatterers, to the best of our knowledge.

In this study, we introduce an effective medium approach that accurately describes wave propagation in metamaterials made of cylindrical scatterers beyond the quasi-static regime. Our approach is based on the Coherent Potential Approximation (CPA) method, which is well-known in the Solid State Physics community. We build on the work of Yu et al. [2] and extend the approach to coated and multi-coated cylinders with the potential to incorporate a metasurface at each interface. The cylinders can be made of any resonant isotropic material, including dielectric, metals, and polaritonic materials, while the metasurfaces can have both magnetic and electric surface impedance (applicable, e.g., to graphene sheets, patterned or unpatterned).

Application of our CPA-based approach to various cylinder-based systems has shown a rich and interesting metamaterial response. As an example, we demonstrate this response in the case of SiC cylinders in air [3] and in systems of graphene-based nanotubes [4]. In both systems we reveal a very rich response including regons of hyperbolic dipersion relation, negative refractive index and engineerable near-zero permittivity or permeability.

We acknowledge funding by the EU projects PHOTOMETA, NANOPOLY, VISORSURF, as well as from Hellenic Foundation for Research and Innovation.

References

1. R. Ruppin, “Evaluation of extended Maxwell-Garnett theories,” Optics Commun., Vol. 182, 273, 2000.

2. Y. Wu, J. Li, Z.-Q. Zhang, and C. T. Chan, “Effective medium theory for magnetodielectric composites: Beyond the long-wavelength limit”, Phys. Rev. B, Vol. 74, 08511, 2015.
3. Ch. P. Mavidis, A. C. Tasolamprou, E. N. Economou, C M. Soukoulis, and M Kafesaki, “Polaritonic cylinders as multifunctional metamaterials: Single scattering and effective medium description”, Phys. Rev. B, Vol. 102, 155310, 2020.
4. Ch. Mavidis, A. C. Tasolamprou, M. Kafesaki, “Effective medium description for coated and multicoated cylinders”, http://arxiv.org/abs/2302.08227, submitted to Phys. Rev. B

Chiroptical harmonic scattering: predicted in 1979 and demonstrated four decades later

Ventsislav K. Valev[1]

[1] Centre for Nanoscience and Nanotechnology, University of Bath, Bath, BA2 7AY, United Kingdom
*corresponding author: v.k.valev@bath.ac.uk

Abstract: Chiroptical harmonic scattering (CHS) was predicted in 1979, but an experimental observation of this effect remained elusive for 40 years. A first form of CHS was reported in 2019; it was demonstrated that light scattered at the second-harmonic from Ag nanohelices dispersed in water could reveal the chirality of the nanohelices. Observations in other systems (metal and semiconductor) and at the third-harmonic quickly followed. Now, we show the effect in high refractive index dielectrics.

Chirality – the lack of mirror symmetry – is a fundamental geometric property of nature. It is exhibited by many life-related molecules and most of the building blocks of biology are chiral, including amino acids, DNA, sugars, proteins, etc. Since much of the bio-machinery of life is chiral, it is not surprising that most of the new drugs that arrive on the market nowadays are chiral. As the world population grows and globalization facilitates the propagation of germs, antibiotic resistance has become one of the top 10 threats to humankind. At the same time, the cost associated with new drug discoveries has become a challenge.

Against this background, a surprising new direction of potential therapeutic innovation has emerged – chiral inorganic nanoparticles. These have been shown to interact successfully with the immune system[1] and to kill viruses using light commands. Chiral nanoparticles are highly complex and have a large parameter space. In order to characterize them, new methods to probe chirality in tiny volumes of liquid are needed.

In 1979, Prof David Andrews published a theory predicting that, upon illuminating chiral (meta)molecules with circularly polarized light, the intensity of light scattered at higher harmonics would depend on the chirality of the scatterers.[3] However, for four decades this theory remained unobserved experimentally and Andrews started referring to it as an “impossible theory”. In 2019, my team reported the first experimental observation of the effect – Chiroptical Harmonic Scattering – at the second harmonic, from Ag nanohelices. Our paper settled the 40-year old scientific question.[4] We later reported the effect from chiral Au nanocubes[5], from semiconductor (CdTe) nanoparticles[6] and at the third harmonic wavelength (together with Andrews).[7] The new effect is highly sensitive and it allowed the first characterization of the chirality of a single nanoparticle (on average) floating freely in a liquid environment.[5,8]

In this talk, the progress so far and the future challenges will be presented.

V.K.V. acknowledges support for this work from the Royal Society through the University Research Fellowships and the Royal Society grants PEF1\170015 and RGF\EA\180228, as well as the STFC grant ST/R005842/1. Acknowledged also is funding and support from the Engineering and Physical Sciences Research Council (EPSRC) Centre for Doctoral Training in Condensed Matter Physics (CDT-CMP), Grant No. EP/L015544/1 and EP/T001046/1.

References

1. Xu, L., Wang, X., Wang, W. et al. “Enantiomer-dependent immunological response to chiral nanoparticles”, Nature

Vol. 601, 366–373, 2022.

2. Gao, R., Xu, L., Sun, M. et al. “Site-selective proteolytic cleavage of plant viruses by photoactive chiral nanoparticles”, Nat Catal Vol. 5, 694–707, 2022.
3. L. D. Andrews, T. Thirunamachandran, “Hyper−Raman scattering by chiral molecules”, J. Chem. Phys. Vol. 70, 1027, 1979.
4. J. T. Collins, K. R. Rusimova, D. C. Hooper, H.-H. Jeong, L. Ohnoutek, F. Pradaux-Caggiano, T. Verbiest, D. R. Carbery, P. Fischer, V. K. Valev, “First Observation of Optical Activity in Hyper-Rayleigh Scattering”, Phys Rev. X Vol. 9, 011024, 2019.
5. L. Ohnoutek, N. H. Cho, A. W. A. Murphy, H. Kim, D. M. Răsădean, G. D. Pantoș, K. T. Nam, V. K. Valev, “Single Nanoparticle Chiroptics in a Liquid: Optical Activity in Hyper-Rayleigh Scattering from Au Helicoids”, Nano Lett. Vol 20, 5792–5798, 2020.
6. L. Ohnoutek, J.-Y. Kim, J. Lu, B. J. Olohan, D. M. Răsădean, G. Dan Pantoș, N. A. Kotov, V. K. Valev, “Third harmonic Mie scattering from semiconductor nanohelices”, Nat. Photonics Vol 16, 126-133, 2022.
7. L. Ohnoutek, H.-H. Jeong, R. R. Jones, J. Sachs, B. J. Olohan, D. M. Răsădean, G. Dan Pantoș, D. L. Andrews, P. Fischer, V. K. Valev, “Optical activity in third-harmonic Rayleigh scattering: a new route for measuring chirality”, Laser. Photonics. Rev. Vol 12, 2100235, 2021.
8. L. Ohnoutek, R. R. Jones, X. Zheng, H.-H. Jeong, V. K. Valev, “Second harmonic Rayleigh scattering optical activity of single Ag nanohelices in liquids”, Nanoscale Vol. 14, 3888-3898, 2022.

Physics Informed Deep Learning In Metamaterials

W.J. Padilla[1*], O. Khatib[1], S. Ren[1], Christian Nadell[1], and J.M. Malof[2]

[1]Department of Electrical and Computer Engineering, Duke University, USA
[2]Computer Science Department, University of Montana, USA
[*]corresponding author: willie.padilla@duke.edu

Abstract: Deep learning has had profound impacts in electromagnetic metamaterials, however there are several drawbacks including. Through incorporation of prior knowledge, physics informed deep neural networks (PINNs) have the capability to solve many of the outstanding problems in deep learning and may additionally learn new physics of systems under study. We discuss three different studies using physics informed deep learning and describe the future of the field is also given.

Deep learning has had profound impacts in electromagnetic metamaterials from accelerated learning to inverse design. Although the universal approximation theorem indicates that deep learning is a universal solver and therefore can be applied to solve any problem, there are several drawbacks including, required large training datasets, unknown size of required datasets, and black box models (no access to any physics learned by the model). However, through incorporation of prior knowledge, physics informed deep neural networks have the capability to solve many of the outstanding problems in deep learning and may additionally learn new physics of systems under study. We overview the approach and taxonomy of informed deep learning and show three different studies where we verify the great potential for metamaterial problems. An overview and future of the field is also given.

Some types of prior knowledge of the problem under study may be incorporated into a deep neural network. There are three possible steps in the standard workflow of neural networks where prior information may be input, including: feature engineering, neural network (NN) architecture, and regularization. Here feature engineering refers to any modification of the data one may do prior to using it as input to the NN. Neural network architecture means that we may modify the design of the NN to incorporate knowledge. Lastly, we may use a particular loss function for regularization that involves some prior knowledge. The particular types of knowledge that we can input into deep NNs include: differential equations, algebraic equations, knowledge graphs, simulations results, and human feedback. These different knowledge types may be input into the aforementioned regions of a NN, and thus there are many possible PINN configurations possible.

We have studied and report on three different PINNs. The first is a conventional feedforward neural network where we have incorporated prior knowledge into the feature engineering step and have demonstrated improved results. [1] Our second study modifies the neural network architecture where we incorporated a Lorentz oscillator model. We directly show our PINN uses 4x less data than a conventional NN with similar performance. [2] Lastly we show a PINN where we use a convolutional NN and directly use a Green's function. We show excellent results and generalizability.

We have explored three different options for incorporating prior knowledge into neural networks. Our results demonstrate reduced dataset sizes and improved performance compared to conventional neural networks. We discuss the future of this exciting field.

The authors acknowledge support from the Department of Energy under U.S. Department of Energy (DOE) Office of Science (DESC0014372).

References

1. Nadell, C. C., Huang, B., Malof, J. M., and Padilla, W. J., “Deep learning for accelerated all-dielectric metasurface design,” Opt. Exp. Vol. 27, 27523, 2019.
2. Khatib, O., Ren, S., Malof, J. M., and Padilla, W.J. “Learning the Physics of All-Dielectric Metamaterials with Deep Lorentz Neural Networks,” Adv. Opt. Mat. Vol. 10, 2200097, 2022.

Hyperspectral Terahertz Imaging Using Plasmonic Detectors

(Invited talk)

Mona Jarrahi

University of California, Los Angeles, USA
mjarrahi@ucla.edu

Abstract: This talk gives an overview of advancements in hyperspectral terahertz imaging systems, which utilize plasmonic photoconductive terahertz detectors to provide significantly higher signal-to-noise ratio levels.

Terahertz waves have unique specifications that enable unprecedented sensing functionalities for personal health monitoring, environmental monitoring, and security screening as well as pharmaceutical, industrial, and agricultural product quality control. This is because most molecules have unique spectral signatures in the terahertz frequency range and many optically opaque materials are relatively transparent to terahertz waves. Additionally, terahertz photons are sufficiently low energy that they don't cause any damage or ionization especially for biomedical sensing applications. Although unique potentials of terahertz waves have been recognized for quite a while, the low efficiency, higher costs, and bulky nature of traditional terahertz systems has impeded their usage in practical applications. In this talk, I will give an overview of advancements in hyperspectral terahertz imaging systems, which utilize plasmonic photoconductive terahertz detectors [ref] to provide several orders of magnitude higher signal-to-noise ratio levels compared to the state-of-the art.

References

1. N. T. Yardimci, D. Turan, M. Jarrahi, "Efficient Photoconductive Terahertz Detection Realized by Plasmonic Nanocavities," APL Photonics, 6, 080802, 2021
2. P. K. Lu, D. Turan, M. Jarrahi, "High-sensitivity telecommunication-compatible photoconductive terahertz detection through carrier transit time reduction," Optics Express, 28, 26324-26335, 2020
3. D. Turan, N. T. Yardimci, M. Jarrahi, "Plasmonics-enhanced photoconductive terahertz detector pumped by Ytterbium-doped fiber laser," Optics Express, 28, 3835-3845, 2020
4. N. Wang, S. Cakmakyapan, Y.-J. Lin, H. Javadi, M. Jarrahi, "Room-temperature heterodyne terahertz detection with quantum-level sensitivity," Nature Astronomy, 3, 977–982, 2019
5. N. T. Yardimci, D. Turan, S. Cakmakyapan, M. Jarrahi, "High-Responsivity and Broadband Photoconductive Terahertz Detector Based on a Plasmonic Nanocavity," Applied Physics Letters, 113, 251102, 2018
6. N. T. Yardimci, M. Jarrahi, "Nanostructure-Enhanced Photoconductive Terahertz Emission and Detection," Small, 14, 1802437, 2018
7. N. T. Yardimci, M. Jarrahi, "High Sensitivity Terahertz Detection through Plasmonic Nano-Antenna Arrays," Scientific Reports, 7, 42667, 2017
8. C. W. Berry, N. Wang, M. R. Hashemi, M. Unlu, M. Jarrahi "Significant Performance Enhancement in Photoconductive Terahertz Optoelectronics by Incorporating Plasmonic Contact Electrodes," Nature Communications, 4, 1622, 2013

AES 2023, TORREMOLINOS - SPAIN, 5 – 8 JUNE 2023

Channel modelling and characterization for communication and sensing in a 6G era

F. Tufvesson

Dept. of Electrical and Information Technology, Lund University, Box 118, SE-221 00 Lund, Sweden
corresponding author: fredrik.tufvesson@eit.lth.se

Abstract: 6G is expected to be based on distributed and co-located ultra-massive MIMO at frequencies ranging from one or a few GHz to hundreds of GHz. It will support both communication and sensing applications and should at the same time offer extreme reliability, enormous data rates, and ultra-low latencies. In this talk, we discuss channel characteristics, channel models, and the implications on 6G. Based on measurement examples, we point out possible directions and limitations and what we really can expect from the various frequency bands.

Tutorial

AES 2023, TORREMOLINOS - SPAIN, 5 – 8 JUNE 2023

Introduction to Deep Learning Techniques for Artificial Electromagnetic Materials

Willie J. Padilla

University Duke University, USA

*corresponding author: willie.padilla@duke.edu

Abstract: Deep neural networks (DNNs) have enhanced and transformed traditional research methods and are driving scientific advance. Deep learning has shown immense potential in the field of artificial electromagnetic materials (AEM) research, with applications spanning electromagnetic metamaterials, metasurfaces, photonic crystals, and plasmonics. In this brief tutorial we review the status of the field with a focus on recent advances, key limitations, and future directions. Strategies, guidance, evaluation, and limits of using deep networks for both forward and inverse AEM problems are presented.

Spatiotemporal effects in multimode optical fiber

Light by light manipulation in multimode fibers

T. Mansuryan[1], A. Tonello[1], Y. Arosa Lobato[3], M. Ferraro[2], M. Zitelli[2], F. Mangini[2], Y. Sun[2], B. Wetzel[1], K. Krupa[4], S. Wabnitz[2], V. Couderc[1]

[1]Université de Limoges, XLIM, UMR 7252, 123 Avenue A. Thomas, 87060 Limoges, France

[2] DIET, Sapienza University of Rome Via Eudossiana 18, 00184 Rome, Italy

[3] University of Santiago de Compostela, Praza do Obradoiro S/N, Santiago de Compostela, 15782 Coruña, Spain

[4] Institute of Physical Chemistry, Polish Academy of Sciences, ul. Kasprzaka 44/52, 01-224 Warsaw, Poland

*corresponding author: Vincent.couderc@xlim.fr

Abstract: We demonstrate that a low-intensity beam can be severely cleaned or distorted by a high-energy pump beam copropagating in a multimode optical fibre at different wavelengths. Thus, the M^2 coefficient of the weak beam is either enhanced or degraded relative to the pump intensity, allowing an ultra-fast light-by-light control. This unconventional development extends the concept of the self-cleaning process where a single beam undergoes a significant brightness improvement under its own peak power.

Providing additional degrees of freedom, a multimode beam propagation has been attracting a great interest, as it allows unveiling various new processes based on its highly complex dynamics [1-4]. Among others, Kerr-induced beam self-cleaning is one of the most debating phenomenon recently discovered. It permits changing a speckled structure into a quasi-single mode beam by using the light intensity itself. Such a self-transformation can be explained in terms of four-wave-mixing interactions, so far, demonstrated only at a single wavelength due to a nonlinear non-reciprocity of the mode coupling process [4]. This behaviour arises from a presence of self-phase-modulation differently impacting high-order and low-order modes. However, up to now this process seems resulting only in particular, Rayleigh-Jeans, energy distribution without allowing an on-demand control of the energy distribution over the guided modes [5].

In this paper, we demonstrate experimentally that an incoherent speckled propagation of a weak beam can be controlled by means of a cross-phase-modulation enabled by an additional high power pump beam at a different wavelength, instead. We show that the change in modal energy distribution leading to the brightness enhancement (i.e. M^2 decrease) (see figure 1(a)), can be controlled and properly adapted. Interestingly, we notice a monotone evolution of the entropy while improving M^2 coefficient. Differently from previous studies we also show that by modifying the initial modal structure of the pump wave it is possible to obtain the opposite effect, observed as a beam defocusing or a beam degradation (i.e. M^2 increase) (see figure 1(b)), due to a change of modal energy distribution to the benefit of high-order modes. Our findings allow to generalise the concept of light control by light in multimode optical fibers. Numerous applications ranging from ultrafast focus control for nonlinear imaging or beam quality control for lidar can be addressed. A further extension of the light self-organization approach to the time domain can also be envisaged while allowing to control, for instance, multimode laser dynamics based on amplifying fibers or supercontinum generation in passive fibers. We believe that our results may also add new building blocks and strengthen the research activity in thermodynamic-based description of beams propagation in complex media since a large number of modes may lead to averaging approach, as well [6].

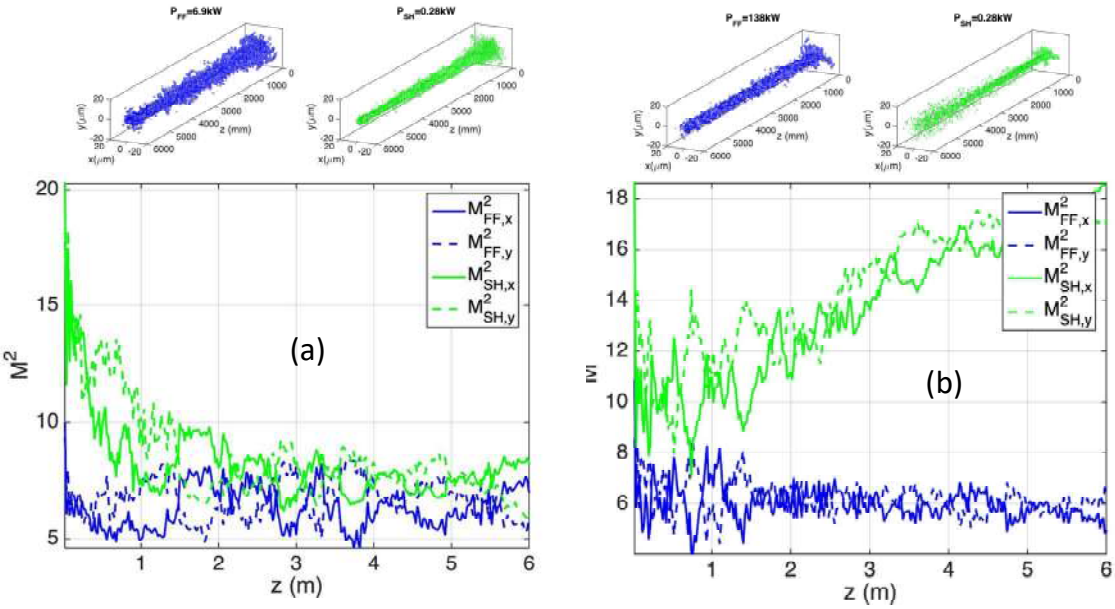

Figure 1: Numerical simulations of the M² coefficient evolution of a weak and a strong beams (pump) copropagating in a graded index optical fiber for two different cases. (a) cross-cleaning of the weak beam because of the pump beam intensity; (b) cross-defocusing of the weak beam because of the pump beam intensity

References

1. A. Picozzi, G. Millot, and S. Wabnitz, "Nonlinear virtues of multimode fibre," Nat. Photonics 9, 289-291, 2015.

2. L. G. Wright, W. H. Renninger, D. N. Christodoulides, and F. W. Wise, "Spatiotemporal dynamics of multimode optical solitons," Opt. Express 23, 3492-3506, 2015.

3. K. Krupa, A. Tonello, A. Barthelemy, V. Couderc, B. M. Shalaby, A. Bendahmane, G. Millot, and S. Wabnitz, "Observation of geometric parametric instability induced by the periodic spatial self-imaging of multimode waves," Phys. Rev. Lett. 116, 183901v, 2016.

4. K. Krupa, A. Tonello, B. M. Shalaby, M. Fabert, A. Barthelemy, G. Millot, S. Wabnitz, and V. Couderc, "Spatial beam self-cleaning in multimode fibres," Nat. Photonics 11, 234-241, 2017.

5. Hamed Pourbeyram, Pavel Sidorenko, Fan O. Wu, Nicholas Bender, Logan Wright, Demetrios N. Christodoulides, and Frank Wise, "Direct observations of thermalization to a Rayleigh–Jeans distribution in multimode optical fibres," Nat. Physics, 18, 685-690, 2022.

6. M. Ferraro, F. Mangini, F. O. Wu, M. Zitelli, D. N. Christodoulides, and S. Wabnitz, "Calorimetry of photon gases in nonlinear multimode optical fibers," arXiv:2212.12781v1 [physics.optics] (2022).

Twists and turns of light propagation in periodically modulated waveguide arrays

Alejandro B. Aceves[1]

[1]Department of Mathematics, Southern Methodist University, Dallas TX, USA
*corresponding author: aaceves@smu.edu

Abstract: The ability to modulate the topology of waveguide arrays in the direction of propagation presents unique opportunities to explore new physics and applications in nonlinear photonics. Here we present some of our recent theoretical work for periodically modulated nonlinear waveguides.

Light propagation in nonlinear optical media continues to advance in diverse platforms, advancing both in understanding new phenomena that could lead to novel applications. One such type of platforms in that of topological photonics, whereas the name suggests, refers to light propagation in media with unique geometries. Applications such as topological insulators show much promise to advance novel all optical logic gates. In particular for both photonic crystals and waveguide arrays, recent work has shown novel physics if the PC cores or the waveguide arrays are twisted in the direction of propagation [1,2]. The work shown here [3,4] was motivated by the experimental efforts of Rechtsman's group [2] on the physical process of quantized Thouless pump. Their discovery of soliton mobility in an adiabatically modulated waveguide array having three units (cores) per cell. Adiabaticity means this quantized transport effect, which happens at certain powers, can be understood as a bifurcation process. In this work, we remove adiabaticity and instead study coherent light transport and localization phenomena for the same topological structure described by the equations,

$$i\frac{dU_n}{dz} + J_n(z)U_{n+1} + J_{n-1}(z)U_n + |U_n|^2U_n = 0 \qquad (1)$$

with the coupling functions $J_n(z)$ being periodic

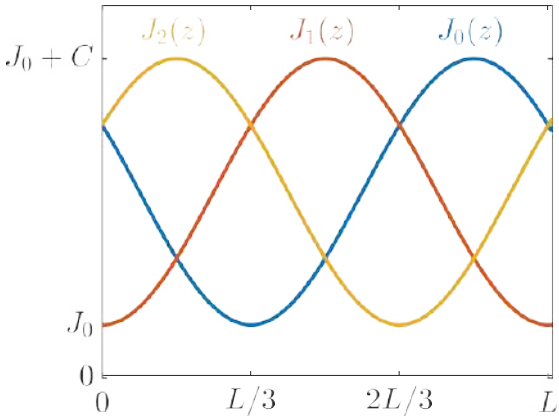

FIG. 1: Coupling functions $J_0(z)$, $J_1(z)$, and $J_2(z)$ of z-dependent nearest-neighbor couplings over one spatial period L.

We will present different regimes of coherent structures propagation (discrete solitons) in two regimes: trapped (localized) and traveling.

A.A acknowledges his collaborators on this effort: Ross Parker, Jesus Cuevas-Maraver and Panayotis Kevrekidis. He has been supported by the NSF grant DMS-1909559.

References

1. R. Beravat , G.K.L. Wong, M.H. Frosz, X.M. Xi and P.St.J. Russell, "Twist-induced guidance in coreless photonic crystal fiber: A helical channel for light", Science Advances 2, 2016.
2. Jürgensen, M., Mukherjee, S. and Rechtsman, M. C., "Quantized nonlinear Thouless pumping", Nature 596, 63–67, 2021; M. Jürgensen M and Rechtsman M.C, "Chern number governs soliton motion in nonlinear Thouless pumps". Phys. Rev. Lett. 128, 113901, 2022.
3. Parker R, Aceves A, Cuevas-Maraver J. and Kevrekidis P.G, "Floquet solitons in square lattices: Existence, stability, and dynamics", Phys. Rev. E **105**, 044211, 2022
4. Parker R, Cuevas-Maraver J., Kevrekidis P.G. and Aceves A, "Standing and Traveling Waves in a Model of Periodically Modulated One-dimensional Waveguide Arrays", submitted for publication, 2023.

Stabilization of light bullets in multimode graded-index fibers: Analytical versus numerical characterization

P. Parra-Rivas*, Y. Sun, M. Ferraro, F. Mangini, M. Zitelli, and S. Wabnitz

Dipartimento di Ingegneria dell'Informazione, Elettronica e Telecomunicazioni, Sapienza Universita di Roma, via Eudossiana 18, 00184 Rome, Italy

*Corresponding author: pedro.parra-rivas@uniroma1.it

Abstract: We study the stabilization of light bullets in multimode fibers with graded-index profiles using variational approaches and numerical simulations. With pure Kerr self-focusing non-linearity, spatiotemporal solitons are stable for low energies, and the agreement of our both approaches is excellent. With increasing energy, however, the light bullet undergoes wave collapse. We study arresting mechanisms of this collapse considering other types of nonlinear contributions, such as quintic self-defocusing nonlinearity, and higher-order dispersion effects.

The emergence and dynamics of solitons continuously attract tremendous attention. Solitons propagate without suffering any shape modification and emerge from the interplay between linear and nonlinear processes, which separately would cause the wave to decay. These solitary waves arise in a plethora of different natural contexts, including hydrodynamics, plasma and condensed matter physics, biology, and nonlinear optics, to cite a few [1]. In nonlinear optics, these particle-like objects may emerge in nonlinear media due to a double balance between dispersive or diffractive effects and light confinement on in either time or space, leading to temporal or spatial solitons, respectively [2]. In this context, light confinement may be related with the nonlinear dependence of the refractive index with the light intensity (optical Kerr effect), which yields to spatial self-(de)focusing and temporal self-phase modulation (SPM). The previous spatial and temporal effects can be coupled and occur simultaneously, such that dispersion and diffraction counteract Kerr nonlinearity at once, leading to light confinement in space-time, and therefore to the formation of coherent spatiotemporal solitons, also known as *light bullets* (LBs) [3]. In bulk Kerr media these states undergo different types of instabilities such as wave collapse and are therefore unstable [2,3].

Singly-pass systems with a parabolic refractive index dependence, such as multimode (MM) graded-index (GRIN) fibers, have been shown to support LBs formation [4]. Here, the parabolic potential created by the GRIN structure leads to such stabilization. Different studies have tackled this problem utilizing variational approaches based on the Lagrangian formalism applied to the Gross-Pitaevskii equation (GPE) [5,6]. However, a systematic full 3D numerical characterization was lacking. Here, we extend the work presented in [5] by using a combination of Lagrangian and Hamiltonian formalisms. This allows us to characterize the stability of LBs using different approaches including the Vakhitov-Kolokolov and Lyapunov criteria [2]. To do so, we consider anomalous second-order dispersion (SOD) with self-focusing Kerr nonlinearity.

Figure 1 shows the dependence of the LB peak intensity with the energy (E) for the anomalous SOD/self-focusing regime. The red line corresponds to the analytical results obtained from the variational computations, while the blue dots represent the numerical results obtained from full 3D numerical simulations, applying a split-step method, of the GPE. For low energy values, the agreement between analytical and

numerical computations is excellent. Increasing E, however, the deviation of the numerical results from the analytical ones is more notable. Eventually, the concentration of energy due to the self-focusing Kerr effect leads to wave collapse (see vertical blue lines) below the analytical upper LB existence limit (see red dot). This disagreement has not been pointed out before and shows some of the limitations of variational approaches.

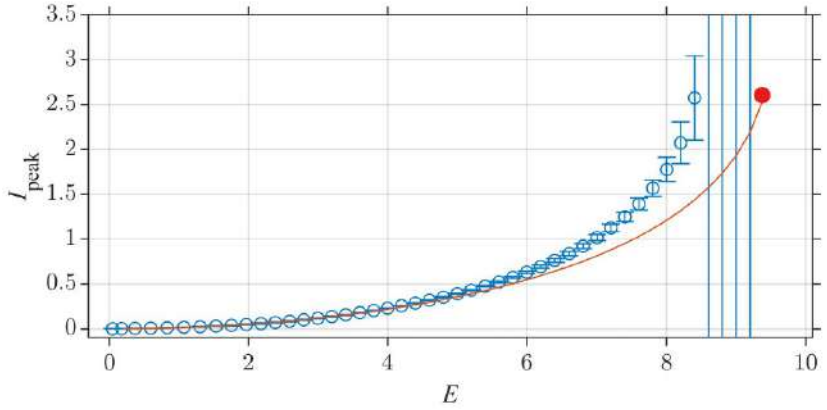

Figure 1. (a) Comparison between peak intensity vs. energy dependence using variational approaches (red line) and direct numerical simulations (see blue dots). The red dot marks the analytical upper limit for LB existence. Vertical blue lines correspond to wave collapse.

We are currently studying the effects that other types of nonlinear contributions, such as quintic self-defocusing nonlinearities, and high-order dispersion effects may have on the extension of the LB existence region. Preliminary results show that these elements have positive effects on the LBs stabilization. Our findings are key to understanding the formation of LBs in passive multimode cavities where the spatiotemporal dynamics are much more complex [7].

This work was supported by the European Research Council (740355), Marie Sklodowska-Curie Actions (101064614,101023717), Ministero dell'Istruzione, dell'Universita e della Ricerca (R18SPB8227).

References

[1] Dauxois, T., Michel Peyrard, "*Physics of Solitons"*, Cambridge University Press (2006).

[2] Kivshar, Y. S. and Agrawal, G. P., "*Optical solitons: From fibers to photonic crystal*", Academic Press (2003).

[3] Silberberg, Y., "*Collapse of optical pulses"*, Opt. Lett. 15, 1282-1284 (1990).

[4] Renninger, W. H., Wise F. W., "*Optical solitons in graded-index multimode fibres*", Nat. Commun. **4**, 1719 (2013).

[5] Yu, S.-S., *et al.*, *Spatio-temporal solitary pulses in graded-index materials with Kerr nonlinearity*, Op. Comm., **119**, 167–170, (1995).

[6] Shtyrina, O. V., *et al., "Coexistence of collapse and stable spatiotemporal solitons in multimode fibers"*, Phys. Rev. A, **97**, 013841, (2018).

[7] Sun. Y, *et al.,* "*Robust three-dimensional high-order solitons and breathers in driven dissipative systems: a Kerr cavity realization*", arXiv:2212.13052v1.

Random lasing in multimode diode-pumped graded-index fiber with fs-inscribed 3D refractive-index structures

A.G.Kuznetsov[1], A.A.Wolf[1], Zh.Munkueva[1,2], A.V.Dostovalov, S.A. Babin[1,2]

[1]Institute of Automation and Electrometry SB RAS, 1 Koptyug Ave., Novosibirsk, Russia, 630090
[2]Novosibirsk State University, Novosibirsk, Russia, 630090
[*]corresponding author: babin@iae.nsk.su

Abstract: We review our recent results on the random Raman lasing based on femtosecond (fs) pulse written randomly spaced scattering points (Rayleigh reflector) and random array of fiber Bragg gratings (FBGs) in multimode graded-index (GRIN) fiber directly pumped by multimode laser.

Raman fiber lasers (RFLs) based on multimode graded-index (GRIN) fibers allow for direct pumping by laser diodes (LDs) in all-fiber scheme [1], see also [2] for a review. An attractive feature of such lasers is a possibility to efficiently convert a highly multimode pump radiation into a Stokes beam generation, the quality of which turns out to be much better than that for the original pump beam, thanks to the Raman beam cleanup effect [8] treated as the main reason. The use in the laser cavity of output couplers based on a fiber Bragg grating (FBG) inscribed by femtosecond pulses in the near-axis area of the GRIN fiber core, corresponding to the fundamental mode, makes it possible to further enhance the effect of beam cleaning for the generated Stokes radiation. So, in a single-stage resonator consisting of FBG pair resonantly reflecting Stokes beam at a wavelength of 976 nm at >100 W pumping by multimode LD with beam quality $M^2 \approx 34$ at 940 nm, high-quality ($M^2 \approx 2$) Stokes beam has been obtained in 1-km GRIN fiber with record pump-to-Stokes brightness enhancement factor of 73 [3]. For a random lasing of the 1st Stokes wave in multimode GRIN fiber with low-quality pumping much higher pump power is required. So, more than 300 W power of random lasing at the first Stokes wavelength of 1120 nm has been obtained in 120-m GRIN fiber at ~700 W multimode pumping by fiber combined Yb-doped fiber lasers at 1070 nm [4], however the threshold pump power for such Raman laser is as high as ~500 W.

Here we review our recent results on the random Raman lasing based on femtosecond (fs) pulse written randomly spaced scattering points (artificial Rayleigh reflector) or random array of short fiber Bragg gratings (FBGs) in graded-index (GRIN) fiber which is directly pumped by multimode laser diode. The artificial random structures help to reduce the pumping threshold for random lasing and allow for the beam quality improvement, similarly to regular FBG with spatial filtering properties [3]. Note that much better output characteristics of random lasing are achieved in the latter case (random grating array). The fabricated 1D-3D random arrays form a half-open cavity together with the input highly-reflective regular FBG. Above the threshold pump power of ~100W from a multimode 940-nm laser diode with beam quality M^2~34, random lasing of the 1st-order Stokes beam was obtained with output power reaching ~30 W at maximum pumping. The output beam quality parameter varies with FBG distribution in the fiber cross-section and its best value amounts to M^2~2, while the linewidth narrows to 0.1-0.2 nm. The main mechanisms of spatio-spectral beam narrowing in this configuration will be discussed.

The authors acknowledge financial support of Russian Science Foundation (grant №21-72-30024).

References

1. Wolf, A.A., Nemov, I.N., Dostovalov, A. V., Tyrtyshnyy, V.A., Myasnikov, D. V., Babin, S.A. “Generating high-quality beam in a multimode LD-pumped all-fiber Raman laser,” Opt. Express, Vol. 25, 12581–12587, 2017.
2. Babin, S.A., Zlobina, E.A., Kablukov, S.I. “Multimode Fiber Raman Lasers Directly Pumped by Laser Diodes,” IEEE J. Sel. Top. Quantum Electron., Vol. 24, 1–10, 2018.
3. Kuznetsov, A.G., Kablukov, S.I., Podivilov, E.V., Babin, S.A. “Brightness enhancement and beam profiles in an LD-pumped graded-index fiber Raman laser,” OSA Continuum, Vol. 4, 1034, 2021.
4. Chen, Y., Fan, C., Yao, T., Xiao, H., Leng, J., Zhou, P., Nemov, I.N., Kuznetsov, A.G., Babin, S.A. “Brightness enhancement in random Raman fiber laser based on a graded-index fiber with high-power multimode pumping,” Opt. Lett. Vol. 46, 1185, 2021.

Reduced model for nonlinear multimode dynamics in photonic crystal structures

F. R.Talenti[1,2*], A. De Rossi[1], and S. Wabnitz[2]

[1]Thales Research and Technology, Campus Polytechnique, 1 Avenue Augustin Fresnel, 91767 Palaiseau, France
[2]Dipartimento di Ingegneria dell'Informazione, Elettronica e Telecomunicazioni, Sapienza University of Rome, 00184 Rome, Italy
[*]corresponding author: francescorinaldo.talenti@uniroma1.it

Abstract: We recently introduced a novel technique for the systematic design of multimode photonic crystal (PhC) cavities with a prescribed dispersion curve, based on a well-established 1D reduced model. This is particularly interesting in the view of miniaturizing parametric generators of nonclassical light, optical nanocombs, and mode-locked laser sources. Here we apply our model to the study of nonlinear multimode interactions.

Introduction

The route towards the demonstration of optical frequency comb (OFC) generation in PhC structures [1] has been paved since a few years. The main interest comes from the minimal footprint of PhCs, resulting in ultra-low operational power levels, possibly leading to nonlinear quantum sources. The optical parametric oscillator (OPO), which can be seen dynamically as the very first stage of an OFC, has been reported only recently [2]. Nevertheless, the residual nonzero dispersion of real fabricated samples, leading to largely unequally spaced neighboring cavity modes, makes the demonstration of PhC-OFC – which is composed of equally spaced frequency components - particularly challenging [3]. Both fabrication tolerances and intrinsic geometrical characteristics are responsible for this shortcoming. In a recent paper [4], we presented a novel self-consistent systematic technique, permitting to efficiently tailor the cavity dispersion management directly at the design stage. In order to do that, we set up a simple 1D reduced model (RM), which approximates a wide class of multimode PhC resonators to a distributed feedback (DFB) mirror. Interestingly, the model is also capable of describing nonlinear parametric interactions between the resonant modes of the resonators, thus describing the overall intra-cavity field evolution. In what follows, we show how we can simulate the PhC-OPO dynamics, which enables us to predict OFC generation under realistic experimental situations.

Nonlinear multimode interactions in PhCs

The RM of ref. [4] can be generalized to embed nonlinear cross- (γ_x) and self- ($\gamma_{+,-}$) phase modulation terms:

$$\begin{cases} \partial_t A^+ = & (\mathcal{D}_2\partial_x^2 - iv_g\partial_x)A^+ - \mathcal{K}A^- + i(\gamma_x|A^-|^2A^+ + \gamma_+|A^+|^2A^+) \\ \partial_t A^- = & (\mathcal{D}_2\partial_x^2 + iv_g\partial_x)A^- - \mathcal{K}A^+ + i(\gamma_x|A^+|^2A^- + \gamma_-|A^-|^2A^-) \end{cases}, \quad (1)$$

where $A^{+,-}$ are two counter-propagating waves, linearly coupled by means of a DFB mirror (K). v_g and D_2 are the group velocity and the second order dispersion, respectively. In red we highlight nonlinear terms. In Figure I, we report the cold cavity spectrum (a), and the nonlinear evolution of the field (b). In (a) we colored the three fundamental modes interacting nonlinearly, while grey dashed lines indicate higher-order modes, whose contribution can be neglected for weakly nonlinear systems. Here we report a general physical situation using arbitrary units, by setting v_g(x)=1 a.u., and neglecting leading-order dispersion terms. The coupling is chosen in such a way to shape the parabolic potential well, which is depicted in red in panel (a). The field is treated by means of a modal decomposition analysis on the OPO triplet $\omega_{+,-,0}$. We can see how nonlinear terms work as a tea spoon, mixing the stationary eigen solutions of the system. As the $\gamma_{x,+,-}$ terms increase, the coupling between modes is stronger and, eventually, it is no longer fully described by a pure OPO interaction, since higher-order modes also partecipate in the wave mixing process.

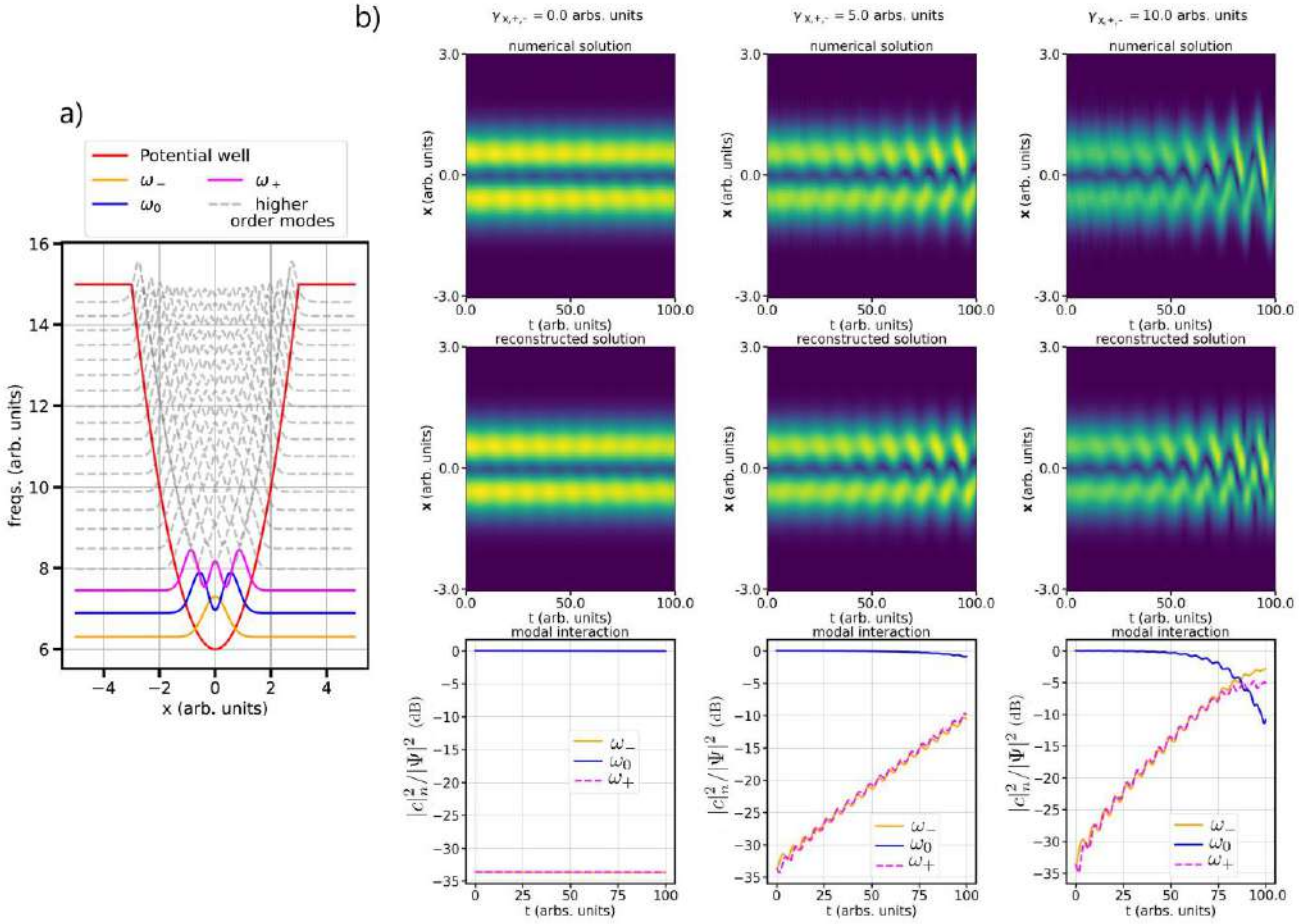

Figure I: a) Cold PhC cavity spectrum. The colored modes $\omega_{-,0,+}$ are interacting nonlinearly. Higher-order modes, not participating to the nonlinear interaction, are colored in grey, while in red we illustrate the effective potential well. b) Nonlinear frequency mixing dynamics of the OPO triplet. On top of each column we report the results of the corresponding nonlinearity level. The first row is the numerical solution of the dynamical evolution of the system. The horizontal axis represents time t, while on the vertical axis we show the spatial coordinate x. The intracavity field intensity is color mapped, from blue (cold, low intensity) to yellow (warm, high intensity). With an identical system of coordinates, on the second row we illustrate the reconstructed solutions from a modal decomposition analysis. Finally, on the bottom row we show the modal evolution which leads, at each given instant, to the decomposition of the intracavity field for the OPO triplet.

Conclusion

In conclusion, we presented an application of a reduced model recently introduced for the systematic design of PhC structures, and the optimization of their geomtry [1]. Because of its generality, our analysis can also be extended to describe parametric nonlinear interactions in a wide class of multimde PhC resonators.

References

1. Combrié, S. et al., “Comb of high-Q resonances in a compact photonic cavity”. Laser & Photonics Reviews, 2017.
2. Marty, G et al., “Photonic crystal optical parametric oscillator”, Nat. Photonics 15, 53–58 (2021).
3. Chopin, A. et al., "Canonical Resonant Four-Wave-Mixing in Photonic Crystal Cavities: Tuning, Tolerances and Scaling," IEEE Journal of Selected Topics in Quantum Electronics, vol. 29, no. 1: Nonlinear Integrated Photonics, 2023.
4. Talenti, F. R. et al., “Fast dispersion tailoring of multimode photonic crystal resonators”, Phys. Rev. A 106, 023505, 2022.

Controlling optical thermalization via spectral engineering: A Kinetic Equation Approach

T. Kottos*

Wave Transport in Complex Systems Lab, Department of Physics, Wesleyan University, USA
*corresponding author: tkottos@wesleyan.edu

Abstract: We utilize a kinetic equation approach together with a nonlinear scaling theory for the analysis of optical thermalization in multimode nonlinear photonic networks. We show that spectral engineering, either via band-gap design or via disorder, molds the thermalization process and the formation of the thermal states. Further isomorphisms with the theory of spin networks reveals the existence of optical phase transitions of the thermal equilibrium states, which resemble a paramagnetic to ferromagnetic and to a spin-glass phase transition.

In physics, one often encounters problems involving a great number of interacting modes. Such problems naturally arise in statistical mechanics, hydrodynamics, matter-waves, and more. An emerging framework is in photonics, where light propagation in non-linear or disordered multimode optical structures have recently attracted a lot of attention. On the fundamental side there are many unanswered questions associated with the energy exchange between the modes and the role of the underlying spatio-temporal complexity, originating from the disorder, the network topology, the complex nonlinear intermodal interactions and mode-dependent losses. Brute force computational attempts to answer these questions are either impossible (due to the large number of degrees of freedom involved) or unsatisfactory as far as the understanding of the underlying physics that dictates the energy redistribution. At the same time, there is a pressing need from modern technologies to develop theoretical tools that will allow us to tailor the intermodal energy exchange and harvest it to our advantage. If this endeavor is successful, it will give rise to a next generation of high-power light sources, high-resolution imaging schemes, and high-speed telecommunication systems.

A prominent photonic framework where the above fundamental questions are interlinked with technological developments appear in the multi-core fibers (MCFs) and multi-mode fibers (MMFs). These systems have recently been exploited as alternatives to single mode fibers – the latter experiencing information capacity limitations, imposed by amplifier noise and fiber non-linearities. What makes multicore and multimode fibers attractive is the possibility to utilize the multiple cores/modes as extra degrees of freedom in order to carry additional information -- thus increasing the information capacity of a single fiber. Of course, MCFs and MMFs also suffer from the above-mentioned challenges (e.g. disorder-induced or/and nonlinearity-induced mode mixing). It is, therefore, imperative to develop theories that take into consideration the role of band-structures of an underlying linear structure, the potential presence of disorder and their interplay with non-linearities in the modal mixing and provide a quantitative description of light transport in such multimode photonic systems.

We have addressed these questions, by implementing a kinetic equation (KE) approach together with a newly developed scaling theory, to the optical beam propagation in such multimoded nonlinear settings. Our analysis is able to highlight the importance of spectral engineering and band-gap structures, disorder, and connectivity between the nodes of the optical nonlinear network. We have found that an engineered band-gap dispersion leads to an optical beam thermal state that is described by a generalized Rayleigh-Jeans distribution. Its formation is controlled by the size of the underlying band-gap of the linear system. The KE allows us also to evaluate the relaxation times towards such thermal states. In case that disorder is introduced into the linear structure, the

thermalization process is hindered. We have developed a universal one-parameter scaling theory that predicts an exponential suppression of the relaxation rate for increasing disorder. The one-parameter scaling variable that controls the relaxation rate, describes the resilience of spatially localized modes to form “localization” clusters against non-linear interactions which tends to desegregate them. Finally, we have shown that appropriate connectivity of the underlying linear system might lead to the presence of various phases of the optical thermal state that share similar features as the paramagnetic, ferromagnetic and spin-glass phase encountered in spin systems.

We acknowledge partial support from Simons Foundation grant no MPI 733698.

References

1. A. Y. Ramos, C. Shi, L. J. Fernandez-Alcazar, D. N. Christodoulides, T. Kottos, “Theory of localization-hindered thermalization in nonlinear multimode photonics,” submitted, 2023.
2. C. Shi, T. Kottos, B. Shapiro, “Controlling Opyical beam Thermalization via Band-Gap Engineering,” Phys. Rev. research, Vol. 3, 2973, 2021.
3. A. Ramos, L. Fernandez-Alcazar, T. Kottos, B. Shapiro, “Optical Phase Transitions in Photonic Networks: a Spin-System Formulation,” Phys. Rev. X, Vol. 10, 031024, 2020.

Two-waves thermalization and calorimetry experiments in nonlinear multimode optical fibers

Mario Ferraro[1,*], Fabio Mangini[1], Fan O. Wu[2], Mario Zitelli[1], Demetrios N. Christdoulides[2], and Stefan Wabnitz[1]

[1]DIET, Sapienza University of Rome, 00184 Rome, Italy

[2]CREOL, University of Central Florida, 32816 Orlando, Florida, USA
[*]corresponding author: mario.ferraro@uniroma1.it

Abstract: We carried out two-waves thermalization and calorimetry experiments in nonlinear multimode optical fibers. Our results extend the thermodynamic description of the beam self-cleaning effect, enabling a new paradigm for the all-optical control of the spatial profile of intense multimode laser beams.

The thermodynamic theory of light propagation in weakly nonlinear multimode optical systems allows for describing laser beams in analogy with a gas of particles [1]. In such a thermodynamic framework, the nonlinearity is responsible of the interaction among the gas of photons, which leads to the establishment of a thermal equilibrium after a sufficiently long propagation distance. Recently, the gas-like representation has been applied to the spatial beam self-cleaning (BSC) effect [2], which consists on the spontaneous formation of a bell-shaped intensity profile at the output of graded-index (GRIN) multimode optical fibers (MMF) [3]. The BSC effect, which is driven by the Kerr nonlinearity, can be described as resulting from the thermalization of the multitude of fiber modes, leading to a mode power distribution which obeys the Rayleigh-Jeans (RJ) law.

Hence, BSC is associated with the transformation of a nonequilibrium system at the fiber input (Fig. 1a) into a state of equilibrium, i.e., of maximum entropy, at the fiber output (Fig. 1b). Note that virtually all ~~the~~ experimental demonstrations of BSC use linearly polarized light at the fiber input. At the same time, it is well-known that light progressively loses its degree of polarization upon propagation in a MMF [4]. Therefore, in Fig. 1a,b, we represent the input state as a gas which occupies half of the modal volume, i.e., only the modes with a given polarization are populated at the fiber input. Whereas, at thermal equilibrium, the gas homogeneously occupies the whole modal volume; moreover, it is possible to define thermodynamic parameters such as the gas temperature (T) and chemical potential (μ). Remarkably, the value of thermodynamic parameters is only determined by the injection conditions of the input laser beam. As a consequence, one may somehow associate a temperature even to a nonequilibrium state, such as the input state. Note that such a temperature has a pure statistical meaning, i.e., it cannot be measured with a thermometer.

Experimentally, in short fiber spans, i.e., whose typical length is of the order of a few meters, BSC is observed whenever the input power is high enough to ensure that interactions among the gas particles lead to a thermal equilibrium within the limited propagation distance. Typically, one observes a transformation from a speckles (Fig. 1c) into a bell-shaped beam (Fig. 1d), whenever the input peak power of the laser pulses reaches values of the order of few tens of kilowatts.

Here we extend the thermodynamic description of BSC in MMF to two-wave thermalization (for more details, see Ref.[5]). We carried out experiments where two orthogonally polarized infrared beams are simultaneously injected into the core of a standard GRIN MMF. Such an input condition is represented in Fig. 1e in the same fashion as in Fig. 1a,b. In particular, in Fig. 1e, the particles of the two gases are shown with different colors, since the two beams were prepared so that they have different values of T and μ at the fiber

input. In analogy with the single gas system, maximization of entropy of the gas mixture leads to the establishment of a thermal equilibrium, where the system eventually reaches a single temperature. Moreover, being the particles indistinguishable, at thermal equilibrium, the two gases are associated with the same value of the chemical potential. Consequently, the particles are depicted with the same color in Fig. 1f.

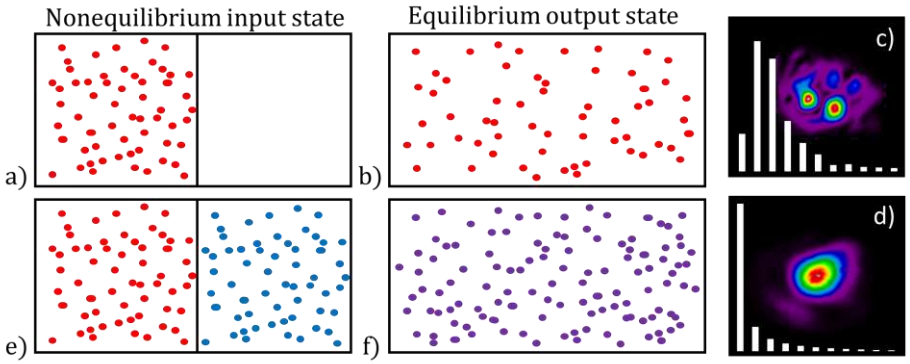

Fig. 1. (a) Representation, in the thermodynamic framework, of a linearly polarized beam at the input of a MMF. (b) Depiction of the equilibrium state corresponding to BSC which is reached at the fiber output. (c) Intensity profile of the beam at the output of a GRIN MMF when the input peak power is lower than the BSC threshold. (d) Intensity profile of a self-cleaned beam. The histograms in (c) and (d) represent the distribution of the mode powers, sorted by their propagation constants. In (d) the monotonic trend obeys the RJ law. (e) Representation of the fiber input when two orthogonally polarized beams with different values of T and μ are simultaneously injected. (f) Equilibrium state resulting from two-wave thermalization.

Our experiments verified the theoretical expectation: we found that the experimentally determined temperature and chemical potential of the photon gas mixture are independent of the output polarization direction (i.e., T and μ are the same in both the left and right sides of the box in Fig. 1f). Moreover, we experimentally verified that the value of entropy of the equilibrium state is grater than that at the fiber input. Finally, we demonstrate that the equilibrium values of T and μ can be varied according to the laws of classical calorimetry, e.g., by acting on the temperature or mass of any of the two gases at the fiber input. In this regard, our results pave the way for novel signal processing functionalities based on MMFs, such as the all-optical control of the spatial profile of intense multimode laser beams.

We acknowledge the financial support of the European Research Council (740355), Ministero dell'Istruzione, dell'Università e della Ricerca (R18SPB8227), and Sapienza University (Avvio alla Ricerca Grants: AR2221815ED243A0, AR2221815C68DEBB).

References

1. F. O. Wu, A. U. Hassan, and D. N. Christodoulides, Nat. Photonics 13, 776–782 (2019)
2. F. Mangini et al., Opt. Express 30, 10850–10865 (2022)
3. K. Krupa et al., “Spatial beam self-cleaning in multimode fibres," Nat. Photonics 11, 237–241 (2017)
4. K. Krupa, et al., Optics letters 44.1, 171-174 (2019)
5. Ferraro, M., et al. "Calorimetry of photon gases in nonlinear multimode optical fibers." arXiv: 2212.12781 (2022)

Thermodynamic fluctuations in optical nonlinear systems

K. G. Makris[1,2*], G. G. Pyrialakos[3], Fan O. Wu[4] and D. N. Christodoulides[3]

[1]*ITCP-Physics Department, University of Crete, Heraklion, 71003, Greece*

[2]*Institute of Electronic Structure and Laser (IESL) FORTH, Heraklion, 71110, Greece*

[3]*Ming Hsieh Department of Electrical and Computer Engineering,*
University of Southern California, Los Angeles, California 90089, USA

[4]*CREOL, College of Optics and Photonics, University of Central Florida, Orlando, FL 32816, USA*

[*]corresponding author: makris@physics.uoc.gr

Abstract: In the context of the new area of optical thermodynamics of weakly nonlinear systems, we provide a fluctuation theory based on grand canonical ensemble. Our theory is generic and can be applied to any weakly nonlinear and non-integrable system (for example planar waveguide, optical fiber, photonic lattice) that contains a finite number of supermodes. By employing non-equilibrium statistical mechanics we also study the out-of-equilibrium behaviour.

In recent years, considerable effort has been devoted to the study of nonlinear highly multimoded optical systems [1]. The physical motivation behind these theoretical and experimental efforts has been the search for high-power optical sources that has been enabled by a sequence of new developments in multimode technologies pertaining to both guided wave structures and optical cavities. Understanding and predicting the complex nonlinear response of such systems especially when hundreds or thousands of modes are involved, is a challenging task. In the best case, all relevant approaches are mostly based on complicated nonlinear optical simulations, that make the description of realistic multimode fibers a formidable task. Thus a theory that explains and predicts such a complex behavior is still missing.

Quite recently however, a self-consistent theoretical framework has emerged, what we call *"Optical Thermodynamics"* [2–6]. In particular, optical thermodynamic theory is capable of describing such complex phenomena by means of thermodynamics of the system's supermodes. A complete set of thermodynamical variables was determined and thus was able to describe and accurately predict the equilibrium behavior of the multimoded system. The equation of state, the entropy and the Rayleigh-Jeans modal occupancies distribution was derived axiomatically either on thermodynamical grounds [2–4] or equivalently on statistical mechanical foundations [5, 6]. Such an approach is universal since it can be applied to any weakly nonlinear optical multimode system of finite number of supermodes that involves a finite number of conserved quantities. We can derive the fundamental relations that govern the grand canonical ensemble through maximization of the Gibbs entropy at equilibrium. In this classical picture of statistical photo-mechanics, we obtain analytical expressions for the probability distribution, the grand partition function, and the relevant thermodynamic potentials.

The first part of the talk is devoted to the understanding of the role of equilibrium fluctuations and the second

part to develop a non-equilibrium description of the system. In order to achieve our first goal we are going to rely on the grand canonical formalism [5] and directly calculate the relevant fluctuations based on the grand partition function expression. For states far from equilibrium, we develop a Langevin type of approach for the projection modal coefficients and derive effective stochastic equations that govern every supermode. Our analytical expressions are compared with direct numerical results of system-bath simulations, in all cases, and the agreement is excellent.

In conclusion, by means of statistical mechanics, we have established a solid foundation for the optical thermodynamics for equilibrium and non-equilibrium states. This formulation was carried out in the grand canonical ensemble picture and is applicable to any nonlinear arrangement involving conserved quantities such as the power, Hamiltonian, and a finite set of distinguishable modes. The equilibrium expressions for the fluctuations of power, Hamiltonian and modal occupancy number were found in excellent agreement with direct bath-system simulations. Even more interestingly, we were able to apply a Langevin type of formalism in order to understand the non-equilibrium behavior of our system. Our results universally apply to any other weakly nonlinear highly multimoded bosonic arrangement.

Acknowledgements: This project was funded by the European Research Council (ERC- Consolidator) under the grant agreement No. 101045135 (Beyond Anderson).

References

1. L. G. Wright, D. N. Christodoulides, and F. W. Wise, Nat.Phot. **9**, 306 (2015).
2. F. O.Wu, A. U. Hassan, and D. N. Christodoulides, Nat.Phot. **13**, 776 (2019).
3. M. Parto, F. O. Wu, P. S. Jung, K. G. Makris, and D. N. Christodoulides,Opt.Lett. **44**, 3936 (2019).
4. F. O. Wu, P.S.Jung, M.Parto, M. Khajavikhan, and D. N. Christodoulides, Comm.Phys. **3**, 1 (2020).
5. K. G. Makris, Fan. O. Wu, P. S. Jung, and D.N. Christodoulides, Opt.Lett. **45**, 1651 (2020).
6. F. O. Wu, Q. Zhong, H. Ren, P. S. Jung, K. G. Makris, and D. N. Christodoulides, Phys.Rev.Lett.**128**, 123901 (2022).

Multimode dissipative spatiotemporal solitons in coherently driven passive nonlinear cavities with parabolic potentials

Y. Sun[1,*], P. Parra-Rivas[1], C. Milián[2], Y. V. Kartashov[3], M. Ferraro[1], F. Mangini[1], M. Zitelli[1], R. Jauberteau[1], F. R. Talenti[1], and S. Wabnitz[1,4]

[1]DIET, Sapienza University of Rome, 00184 Rome, Italy
[2]Institut Universitari de Matematica Pura i Aplicada, Universitat Politecnica de Valencia, 46022 Valencia, Spain
[3]Institute of Spectroscopy, Russian Academy of Sciences, Troitsk, Moscow, 108840, Russia
[4]CNR-INO, Istituto Nazionale di Ottica, Via Campi Flegrei 34, 80078 Pozzuoli, Italy
[*]corresponding author: yifan.sun@uniroma1.it

Abstract: We show the presence of stable high order light bullets in a coherently driven passive multimode Kerr cavity with a three-dimensional potential. These states have very rich multimode features, which are unveiled by decomposing the nonlinear solutions on the three-dimensional linear eigenmodes of the cavity.

Solitons are defined as self-sustained localized packets of light or matter waves that propagate in nonlinear media. In the realm of nonlinear optics, a spatiotemporal localized light wave, commonly referred to as a light bullet (LB), emerges as a result of the delicate balance between nonlinearity, diffraction, and dispersion. However, the formation of steady-state LB in three-dimensional settings is a well-known challenge due to the presence of high-order perturbation effects and inherent instabilities, such as wave collapse [1]. Nevertheless, the aforementioned detrimental effects can be mitigated through various mechanisms, including the utilization of saturable and competing nonlinearities [2], twisted lattices [3], and graded refractive index (GRIN) distribution [4]. Moreover, LBs can be stabilized in the presence of dissipation, as exemplified in optical cavities with a saturable absorber and subsequently in the context of multimode fiber lasers utilizing external phase modulation [5]. Phase modulation can be incorporated in externally driven cavities by utilizing intracavity synchronous modulators [6,7]. This results in the creation of a temporal trapping potential that facilitates stable solitons and LBs in the case of 1D [8] and 3D settings [9], respectively.

In this work, we uncover the existence of a rich variety of LBs of different orders in the context of multimode externally driven Kerr cavities with the added influence of parabolic potentials. We examine the stability of various high-order LBs and classify them in terms of their bifurcation diagram. By decomposing the LBs into three-dimensional linear eigenmodes, we can obtain the evolution of the modal energies of high-order LBs. We attribute the origin of the high-order LBs primarily to the corresponding high-order modes.

In the mean-field approximation, the dynamics of the electric field envelope $A(x, y, \tau, t)$ propagating within the cavity is governed by an extended dimensionless Lugiato-Lefever (LL) equation with a 3D parabolic potential

$$\frac{\partial A}{\partial t} = \mathrm{i}\left(\nabla_\perp^2 + \frac{\partial^2}{\partial \tau^2}\right)A - \mathrm{i}\left(x^2 + y^2 + C\tau^2\right)A + \mathrm{i}|A|^2 A - (1 + \mathrm{i}\delta)A + P, \tag{1}$$

where δ is the cavity detuning parameter, P is the pumping rate, $\nabla_\perp^2 = \partial_{xx} + \partial_{yy}$ accounts for diffraction, $\partial_{\tau\tau}$ accounts for dispersion, $(x^2 + y^2)$ is the transverse parabolic index profile (or spatial potential), and $C\tau^2$ originates from synchronous phase modulation.

Figure 1(a) shows the bifurcation diagram of LB energy vs. detuning δ. Four examples of LB states for the negative detuning values $\delta = -1,\ -4,\ -8,\ -11.5$ are plotted in Fig. 1(i-iv), respectively. The two shells (i.e., isosurfaces) with different colors, represent different field intensities $I_1 = 3$ (red), and $I_2 = 0.1$ (blue). The four states that we consider represent the first high-order LBs. They are separated by the three peaks visible in the bifurcation diagram. Apart from these LBs, we also observe wave collapse and three-dimensional breathers in the red and blue regions, respectively. Numerical continuation and direct numerical simulation are used to calculate these states. By decomposing these solutions on the three-dimensional linear eigenmodes, we obtain modal energy E_n ($n = 1,\ 2,\ \ldots$), which is plotted in Fig. 1(b). As the detuning δ decreases for each n-th order bullet, its modal energy E_n increases until it reaches a peak value where a phase transition of LB order occurs.

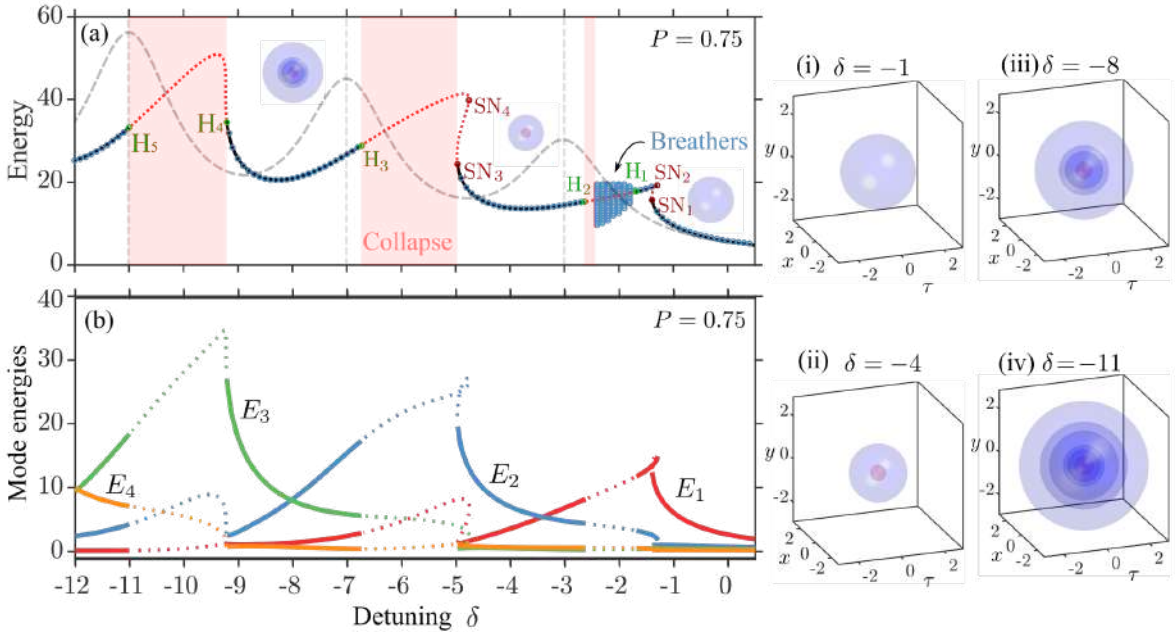

Figure 1. (a,b) Bifurcation diagrams showing the field energy of the bullets $E(t)$ in (a) and their modal energy $E_n(t)$ in (b), vs. δ, for the pump $P = 0.75$ in (a). Solid black (dashed red) lines represent stable (unstable) solutions obtained by numerical continuation. Blue circles superimposed on solid lines are solutions from direct numerical simulations. The collapse regions are marked by red areas, and breather amplitudes are marked by sparse blue circles. The gray dashed curve corresponds to the linear states of the cavity. Here, $C = 1$.

This work reveals the presence of a diverse range of LBs with high orders in multimode externally driven Kerr cavities with parabolic potentials. Through our analysis, we evaluate the stability of multiple high-order LBs and categorize them. By projecting the LBs into linear three-dimensional eigenmodes, we trace the origin of the high-order LBs to their corresponding high-order modes.

We acknowledge the financial support of the European Research Council (740355), Ministero dell'Istruzione, dell'Università e della Ricerca (R18SPB8227), Marie Sklodowska-Curie Actions (101064614, 101023717), Grant PID2021-124618NB-C21 MCIN/AEI/ 10.13039/501100011033 and "ERDF A way of making Europe", and Sapienza University (Avvio alla Ricerca Grants: AR2221815ED243A0, AR2221815C68DEBB).

References

1. Y. Silberberg, Opt. Lett. 15, 1282-1284 (1990)
2. Y. V. Kartashov, G. E. Astrakharchik, B. A. Malomed, and L. Torner, Nat. Rev. Phys. 1, 185 (2019)
3. C. Milián, Y. Kartashov, and L. Torner, Phys. Rev. Lett. 123, 133902 (2019).
4. O. V. Shtyrina, M. P. Fedoruk, Y. S. Kivshar, and S. K. Turitsyn, Phys. Rev. A 97, 013841 (2018)
5. V. L. Kalashnikov and S. Wabnitz, Laser Phys. Lett. 19, 10510 (2022)
6. A. K. Tusnin, A. M. Tikan, and T. J. Kippenberg, Phys. Rev. A 102, 023518 (2020).
7. N. Englebert, N. Goldman, M. Erkintalo, N. Mostaan, S.-P. Gorza, F. Leo, and J. Fatome, arXiv:2112.10756 (2021)
8. Y. Sun, P. Parra-Rivas, M. Ferraro, F. Mangini, M. Zitelli, R. Jauberteau, F. R. Talenti, and S. Wabnitz, Opt. Lett. 47, 6353 (2022)
9. Y. Sun, P. Parra-Rivas, C. Milián, Y. V. Kartashov, M. Ferraro, F. Mangini, M. Zitelli, R. Jauberteau, F. R. Talenti, and S. Wabnitz, arXiv:2212.13052 (2022).

Additive manufacturing for electromagnetic devices

Iterative correction of phase errors in flat distributed dielectric lenses using full-wave modeling

Carey Rappaport* **and Ann Morgenthaler**

Northeastern University, Boston, MA , USA
*rappaport@neu.edu

Abstract: Distributed dielectric lenses offer significant packaging and performance advantages over conventional uniform dielectric lens antennas, but often exhibit unexpected phase errors following ray-based design. The current investigation considers an improved design process using full-wave modeling of wave propagation through a lens that measures the phase errors and feeds back a correction to the dielectric profile of the lens. The design process proceeds iteratively until the best possible performance is reached for the optimal lens antenna.

Design Method

Assume the desired lens is flat, circular, with uniform thickness d, and unity dielectric constant at radius $\rho = \rho_0$, fed by a point source at height h, as indicated in Fig. 1. Initially, a *radially varying* dielectric lens will have relative dielectric constant $\varepsilon'(\rho)$ that is independent of height z. Lens are typically designed using the simplified condition that rays from the feed follow a path from $(0, h)$ to the top lens surface $(\rho, 0)$, and then trace straight down to the outer surface (ρ, d). In reality, there is always ray refraction and bending.

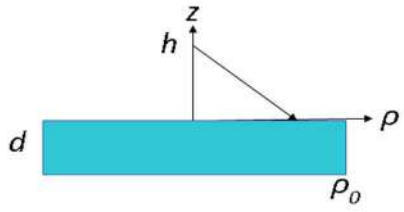

Figure 1: Flat circular lens geometry

To generate a plane wave output with collimated rays, the phase of all exiting rays must be the same. Equivalently, the electrical path length, $\int_0^S \sqrt{\epsilon'} ds$ through the lens S to the outer surface must be constant, which occurs when:

$$\varepsilon'(\rho) = \left(1 + \frac{\sqrt{(h/\rho_0)^2+1} - \sqrt{(h/\rho_0)^2+(\rho/\rho_0)^2}}{d/\rho_0}\right)^2 \quad (1)$$

inside the lens. Note that the distances are normalized to the radius of the lens, and that $\varepsilon'(\rho_0) = 1$ at that point.

For a 60 GHz, 100 mm ($2\rho_0 = 20\ \lambda$) diameter, 20 mm ($d = 4\ \lambda$) thick lens with feed point at $h = 50$ mm, the dielectric constant profile is shown in Fig. 2 in the ρ-z plane. The maximum $\varepsilon'(\rho = 0)$ is 4.2.

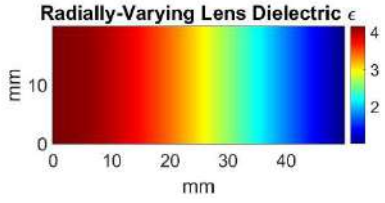

Figure 2: Flat circular lens dielectric constant profile

The electric field from a 60 GHz point source that is scattered by the distributed dielectric lens is modeled with the Finite Difference Frequency Domain (FDFD) method and is shown in Fig. 3. There is significant backscatter with medium intensity waves leaving the lens to the upper right.

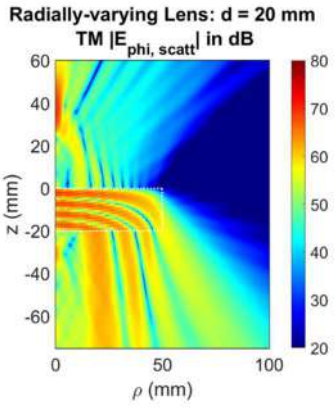

Figure 3: Field scattered by a flat circular radially varying lens

The backscatter can be ameliorated by grading the dielectric constant in thickness as well as radius, producing a *3D distributed lens*. Assuming rays trace straight through the lens and accumulate phase by $\int_0^d \sqrt{\epsilon'} dz$,

the index of refraction $\sqrt{\epsilon'(\rho, z)}$ dependence is hypothesized to be parabolic with z, growing from unity (matched) at the top lens surface to a maximum n_{max} at $z = -d/2$, and then symmetrically falling back to unity at the bottom surface at $z = -d$:

$$\sqrt{\epsilon'(\rho, z)} = \begin{cases} 1 + n_{max}\left(\frac{z}{\rho_0}\right)^2, & -d/2 \le z \le 0 \\ 1 + n_{max}\left(\frac{d}{\rho_0} - \frac{z}{\rho_0}\right)^2, & -d \le z \le -d/2 \end{cases} \quad (2)$$

To determine n_{max}, the index of refraction in (2) is integrated in z from $-d$ to 0 and set equal to $d\sqrt{\epsilon'(\rho)}$ from (1). The solution is: $n_{max} = 3(-1 + \sqrt{\epsilon'(\rho)})/(d/2\rho_0)^2$. The resulting distribution, shown in Fig. 4 with $n_{max} = -75 + 75\sqrt{\epsilon'(\rho)}$ and maximum $\epsilon' = 16.9$, presents a match to free space at the top and bottom surfaces while keeping the phase change vertically straight through the lens with the same radial variation as the previous lens.

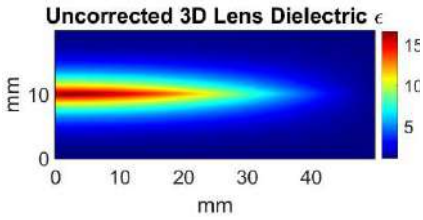

Figure 4: 3D Flat circular lens dielectric constant profile

The FDFD-modeled propagation through this 3D-varying lens indicates near plane wave behavior on exiting the lens, but there is still phase error across the bottom aperture. The red curve in Fig. 5 indicates almost -π phase change from $\rho = 0$ to $\rho = \rho_0$. Using this detailed phase information enables a correction to the dielectric constant distribution, namely, by adjusting n_{max} in (2). First, fit a fourth order even polynomial in ρ/ρ_0 to the error in Fig. 5, then set it equal to the integral of (2) less the nominal value $d\sqrt{\epsilon'(\rho)}$ and solve for n'_{max}. Iterate the modeling with varying proportions of the original n_{max} and the corrected n'_{max} until the phase variation is minimized (see Fig.5, blue curve, with 0.1 radian phase variation across the aperture). For $d = 0.4\rho_0$ and $h = 2\rho_0$ the corrected $n_{max} = -83.71 + 75\sqrt{\epsilon'(\rho)} + 14.71(\rho/\rho 0)^2 - 4.93(\rho/\rho 0)^4$, with $\sqrt{\epsilon'(\rho)}$ given in (1).

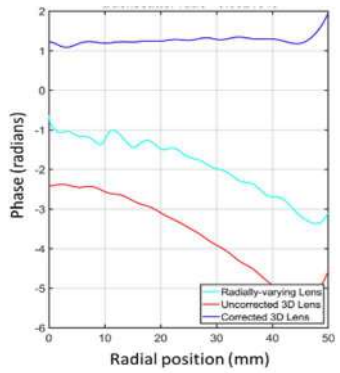

Figure 5: Phase error for radially varying, 3D uncorrected, and 3D corrected flat lenses

Results and Conclusions

The computed wave pattern in Fig. 6 shows extremely parallel phase fronts below the bottom exit surface of the lens (white box). The 60 GHz farfield patterns of the three lenses: radial varying, 3D uncorrected, and 3D corrected are shown in Fig. 7, along with the ideal uniformly excited aperture with the same circular dimensions $\rho_0 = 50$ mm =10 λ. The pattern of the corrected lens (blue) approaches the ideal (green), with less than 3 dB peak gain reduction, but with lower sidelobes.

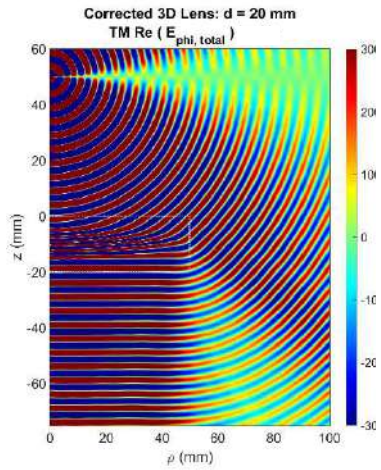

Figure 6: Real part of the total electric field excited by a right circular polarized point source at (0, 50) mm with 3D phase corrected lens (white)

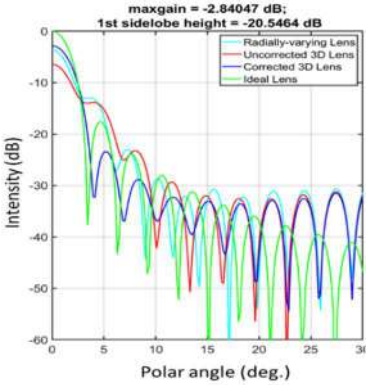

Figure 7: Modeled farfield patterns for radially varying, uncorrected, corrected, and ideal uniform aperture

It has been shown that with full-wave modeling of waves exiting a distributed dielectric lens, it is possible to perturb the dielectric distribution to correct phase errors and generate near-perfect patterns.

Advanced Computational Electromagnetics Code for Efficient Synthesis and Design of Coupled-Resonator Microwave Circuits

V. de la Rubia

Departamento de Matematica Aplicada a las TIC, ETSI de Telecomunicacion, Universidad Politecnica de Madrid, Spain
valentin.delarubia@upm.es

Abstract: This work deals with a new methodology for coupled-resonator microwave circuits. The frequency response of the impedance matrix of the device under analysis is obtained in pole-residue form by means of a full-wave solver, namely, the finite element method (FEM), with a model order reduction (MOR) layer on top of it to get the frequency response with ease.

This impedance matrix stands for electromagnetics, i.e., no circuit approximation is taken into account to solve Maxwell's equations. Wrapping the physical information included in the pole-residue representation of the impedance matrix for the microwave filter under analysis, a linear dynamical system can be identified, which provides valuable design information. To some extent, in the narrowband limit, this dynamical system is similar to a circuit representation.

This new dynamical system stands upon electromagnetics, giving rise to an electromagnetically generated coupling matrix for coupled-resonator microwave circuits. Several applications, such as microwave filters, diplexers and antennas, will show the capabilities of this new technique.

Electromagnetics today underpins all modern information and communication technologies. Increasing deployment of telecommunication services is urging RF industry to carry out better and better electrical designs, where a single device is no longer conceived to perform a single functionality, but rather multiple tasks at the same time.

Unfortunately, much electrical design activity is still based on brute-force computational simulations to predict the actual physical behavior of electromagnetic (EM) devices. These time-consuming simulations are repeated, changing the device characteristics until satisfying stricter specifications of emerging information and communications technologies.

Efficient microwave circuit and antenna design is still an open problem. Several ad-hoc techniques are available for each EM device, most of them based on approximations. However, the current EM designs are challenging enough to use approximate design methodologies and costly full-wave optimization loops, typically using commercial EM software, are employed instead.

In this work we propose to use computational electromagnetics (CEM) as an actual design tool, rather than just an analysis one. This can be achieved by shrinking CEM into a simple parameterized equivalent circuit form, from which an electrical engineer can get actionable design insights.

Numerical codes, such as finite-element and integral equation-based solvers, provide a reliable and accurate prediction of electromagnetics, but at the expense of extremely large computational time since an extremely large matrix system has to be solved. A

model-order reduction (MOR) technique is capable of shrinking these large matrix systems into a fairly small-size reduced matrix system, which is small enough depending on the underlying electromagnetic complexity of the original system. In other words, the electromagnetic information is compressed to the minimum size by means of MOR. This is a huge advantage as the electromagnetic response can now be obtained in real time.

Any electromagnetic device, ranging from microwave circuits, antennas to silicon photonics is based upon the uprising of the dominant electromagnetic eigenmodes [1] which, in turn, are built up by adequately putting local resonators or local modes together, with a specific coupling topology [2]. Bringing all these local resonators together with the specific interaction among them is at the heart of carrying out electromagnetic design [3]. Having control over these local resonators is indeed the key and quantifying their couplings is a challenging problem in electromagnetics [4].

This work aims to find out new efficient synthesis and design techniques for microwave circuits and antennas by means of advanced CEM codes to solve Maxwell's equations numerically, focusing on coupled-resonator EM circuits. Not only the CPU time in EM simulations needs to be reduced, but also the number of analyses within the optimization loop until an EM design is obtained.

We show an electromagnetically generated coupling matrix for coupled-resonator microwave circuits by means of a single full-wave simulation. This result provides valuable design information. Several applications, such as microwave filters, diplexers and antennas, will show the capabilities of this new technique during the presentation.

References

1. V. de la Rubia and M. Mrozowski, “A compact basis for reliable fast frequency sweep via the reduced-basis method,” IEEE Trans. Microwave Theory Tech., vol. 66, no. 10, pp. 4367–4382, 2018.
2. V. de la Rubia, "Description of Microwave Circuits via the Reduced-Basis Method Giving Physical Insight," in IEEE Transactions on Antennas and Propagation, vol. 70, no. 11, pp. 10554-10568, Nov. 2022.
3. V. de la Rubia, "EM-Based Design of Microwave Filters and Diplexers: Full-Wave Coupling Matrix and Its Narrowband Counterpart," 2022 52nd European Microwave Conference (EuMC), Milan, Italy, pp. 60-63, 2022.
4. V. de la Rubia. (2023) Full-wave coupling matrix results in MATLAB. [Online]. Available: https://drive.upm.es/s/cnTXeZjrXYsxmbK

Review of patch antennas for wireless applications using ink-jet printing technique

Mohamad Hosein Rasekhmanesh[1], Asrin Piroutiniya[1], José Luis Masa-Campos[1], Enrique Márquez-Segura[2], Eduardo García-Marín[1], Juan Córcoles[1], Jorge A. Ruiz-Cruz[1]

[1] Group of Radio-Frequency, Circuits, Antennas and Systems (RFCAS), Department of Electronics and Communication Technologies, Universidad Autonoma de Madrid, 28049, Madrid, Spain, {mohamad.rasekhmanesh, asrin.piroutiniya }@estudiante.uam.es, {joseluis.masa, eduardo.garciam, juan.corcoles, jorge.ruizcruz }@uam.es

[2] Telecommunication Research Institute (TELMA), E.T.S. Ingeniería de Telecomunicación, Universidad de Málaga, 29016 Málaga, Spain {ems}@ic.uma.es

Abstract: This study focused on a double-stacked array antenna with patch elements disposed linearly and circularly. Using the inkjet printing method, the single patch antenna was created for the 5 GHz band. The goal is to print conductive silver ink on a thin Kapton film to produce microstrip lines. High-impact polyester (HIPS) is utilized as a substrate to secure the Kapton layers, which increases the impedance matching bandwidth while also enhancing mechanical stability.

Antenna design:

Fig. 1 shows the suggested method for introducing a double-stacked patch antenna that is described in [1]. Although this technique increases overall thickness, it improves antenna bandwidth in terms of impedance matching, which makes it worthwhile to use. As per the manufacturer [2], the electric constant of the HIPS and Kapton substrates are 2.4 and 3.4 respectively.

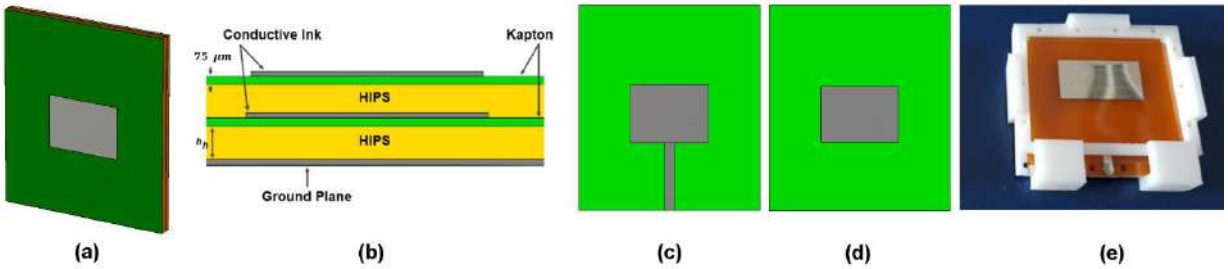

Fig. 1) Stacked patch antenna configuration a) Perspective view, b) side view of the antenna including ground plane, conductive ink, Kapton and HIPS substrate, c) front view of the bottom layer and d) top layer, e) manufactured antenna.

In a subsequent step, the idea of designing a stacked linear array antenna was discussed based on the proposed design principles. The proposed antenna's ultimate design is displayed in Fig. 2. As shown in this figure, the first layer includes the feeding network, which is intended to excite eight radiating patches. In order to obtain a compact design and enhance the impedance matching, double quarter-wavelength ($\lambda/4$) transmission lines with a corner-cut T-junction power divider were used in each step of this feeding network.

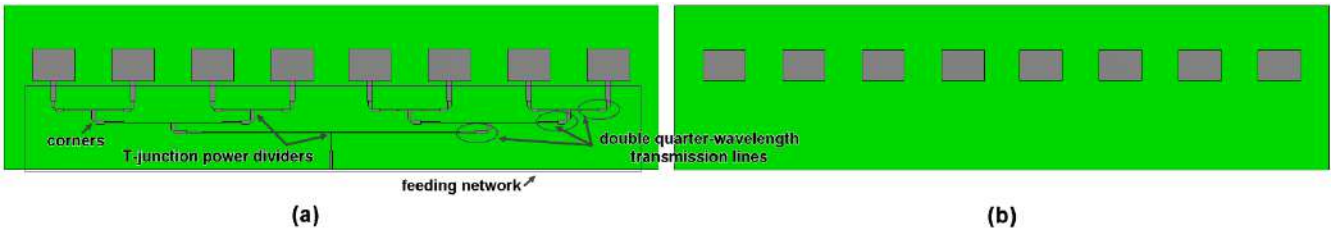

Fig. 2) Front view of the stacked linear array antenna including the a) bottom and the b) top layers.

So far, the concept of a directional stacked antenna design employing a combination of the ink-jet printing method to put the silver conductive ink on Kapton films and the 3D printing method to manufacture the HIPS has been presented. This approach has a lot of potential, so it might be expanded to include more complex structures. An example is the omnidirectional antenna design, which is covered in more detail in this section.

It has always been fascinating to think of conformal array antennas as small, inexpensive structures. The orientation of the elements, as the primary distinction between conformal and linear array antennas, makes it feasible to obtain an omnidirectional radiation pattern in the azimuth plane with this arrangement of the radiating elements. The formulation for an N-faced prism is taken from [3] and is as follows:

$$\vec{E}_{array}(\theta,\emptyset) = \sum_{n=1}^{N} \vec{E}_n(\theta,\emptyset) I_n e^{j\left[\left(\frac{2\pi}{\lambda_0}\right).\ \mathrm{r}\ .\ sin\theta cos(\emptyset-\emptyset_n)+a_n\right]}$$

Where $\vec{E}_{array}(\theta,\emptyset)$ shows the conformal array antenna's radiated E-field, $\vec{E}_n(\theta,\emptyset)$, I_n, and a_n represent, respectively, the radiated E-field, feeding amplitude, and phase of the n*th* single radiating element and r is the radius of the circle, which also points to the distance between the center of the circle and the center of each element. Accordingly, an initial idea of presenting a conformal array antenna by bending the concept that is presented in Fig. 2 based on designing a linearly stacked array antenna with eight elements has been shown in Fig. 3.

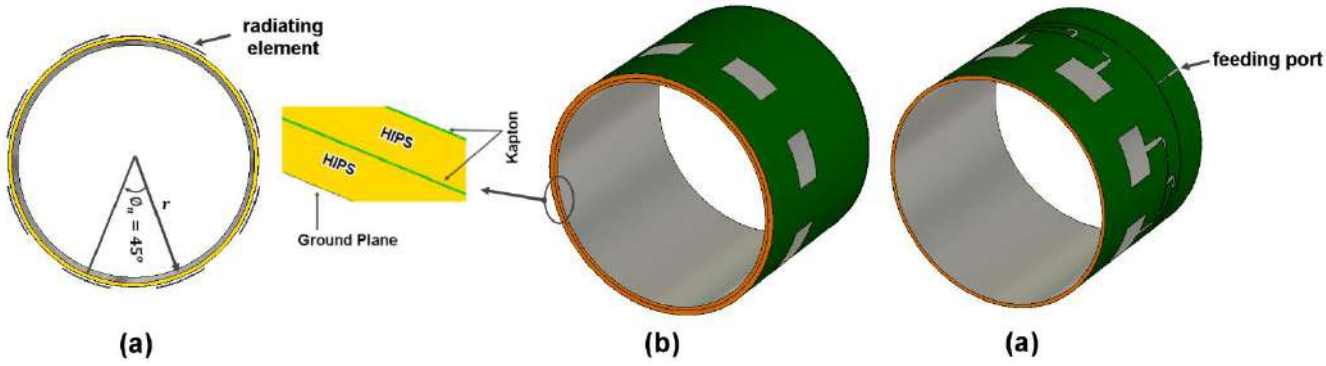

Fig. 3) Stacked conformal array configuration. a) front view, b) perspective view of the top layer and c) perspective view of the bottom layer.

References

1. E. García-Marín, E. Márquez-Segura, P. Sánchez-Olivares, J. L. Masa-Campos, J. A. Ruiz-Cruz and C. Camacho-Peñalosa, "Ink-jet Implementation of Stacked-Patch Antenna for Wireless Applications," 2019 IEEE MTT-S International Microwave Workshop Series on Advanced Materials and Processes for RF and THz Applications (IMWS-AMP), pp. 151-153, 2019.
2. M. Pérez-Escribano and E. Márquez-Segura, "Parameters Characterization of Dielectric Materials Samples in Microwave and Millimeter-Wave Bands," *IEEE Transactions on Microwave Theory and Techniques*, vol. 69, pp. 1723-1732, 2021.
3. P. Sanchez-Olivares, P. P. Sanchez-Dancausa and J. L. Masa-Campos, "Circularly conformal patch array antenna with omnidirectional or electronically switched directive beam," *IET Microw. Antennas Propag.*, vol. 11, pp. 2253-2259, 2017.

Stereolithography to generate OAM waves using dielectrics.

M.A. Balmaseda-Marquez[1*], S. Moreno-Rodriguez[1], Á. Palomares-Caballero[1], C. Molero, J.F. Valenzuela-Valdés[1], P. Padilla[1]

[1*]Department of Signal Theory, Telematics and Communications, Universidad de Granada (CITIC-UGR), 18071 Granada, Spain.
[*]corresponding author: migbalmar@ugr.es

Abstract: Metal prototypes has always played an important role, with low tolerances and fulfilling the high standards of investigation [1]. 3-D printing is emerging as an alternative with technologies such as stereolithography. In this work it will be seen the application of this technique in the fabrication of dielectric transmitarrays (TA) with the capability of producing orbital angular momentum waves (OAM).

Summary:

Orbital angular momentum waves were proposed by Allen et al [2] in 1992. This type of wave has different modes, which are orthogonal one to another when the mode differs. Since then, the generation of this modes have been pursued, being the multimodal generation the principal target. Many ways of creation have been achieved in previous years using high-cost systems as multi-arrays antennas or monolithic metallic prototypes [3]. Stereolithography emerged as a solution to create 3D printed devices in dielectric with the capability of generate OAM.

Stereolithography (SLA) emerged during the 1970s as a system that can build 3D objects by two intersecting radiation beams through both photochemically cross-linking or degrading polymers [4]. The process begins with an STL file, by slicing it the 3D model is converted to 2D slices that contain the information needed to generate each layer. The fundament of this process is the curing reaction of resins; the reaction is initiated by supplying the energy of UV light and it occurred two stages during the curing: gelation and vitrification [5]. The gelation is a transition between the liquid resin to a rubber state. Then, the vitrification occurred, being a thermo-reversible process that leads to the transition from rubber to a glassy solid resin [6].

The choice of this technique to our problem is not trivial. After a careful design studying the phase shift introduce by each part of the cell, the unit cell presented in Fig.1 is developed:

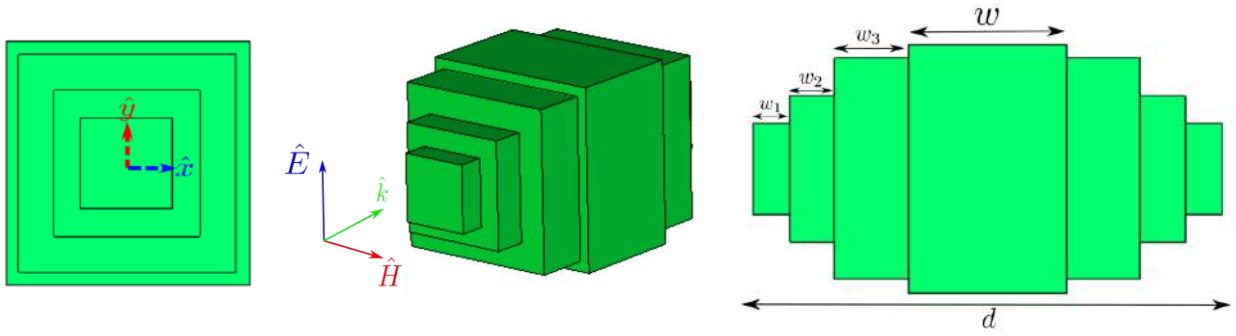

Fig.1 Front (left), perspective (center) and side (right) view of the unit cell proposed.

While the dimension ω can vary from 0.42mm to 4.38mm (to introduce different phase shifts), dimensions ω1 to ω4 are fixed, being its function to adapt the impedance to the dielectric. The goal was to obtain four different phase shifts in order to have a 2-bit configuration. With this unit cell we create a transmitarray (40x40) which has the ability to generate OAMs. Our choice of material was the *Grey V4* with a permittivity of Er = 2,6.

Once the final design is decided and the STL file is generated, it is used the *Formlabs 3* [7] to 3D print our model. The tolerance of our printing is about 25μm (XY plane) and the layer thickness is about 50μm. This kind of machine use *low force stereolithography.* In this type of SLA, the printer uses a flexible film which bows gradually as the part is lowered, reducing the pressure in the overall system. It is important to set a correct arrangement of supports depending on the type of geometry we have. For example, if the structure has gaps or non-bulky parts, it is needed to correct the possible deviations of the printing. When the printing is done, a post-processing must be carried out, depending on the material used. First of all, the prototype must be washed to remove any resin residues. Then, the cured occurred, leaving it the time needed to entangle the polymer. Some pictures of final results can be seen in Fig.2. We expect to obtain a flat TA with the capability of generate a certain OAM mode.

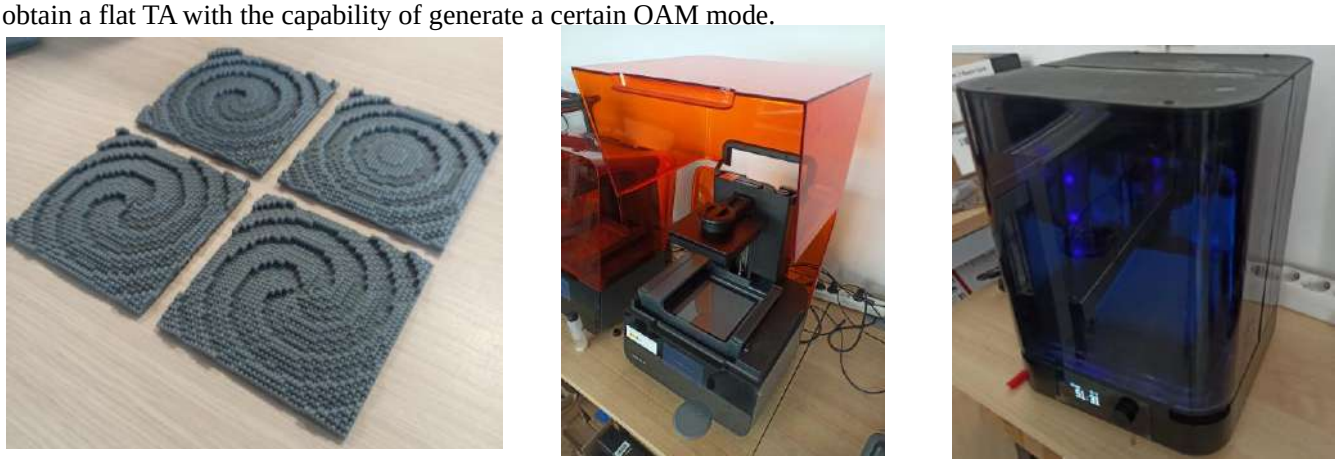

Fig.2. Several OAMs lenses (left). Formlabs 3 (middle) and curing machine (right)

References

1. Ahmed, N. (2019). Direct metal fabrication in rapid prototyping: A review. Journal of Manufacturing Processes, 42, 167–191. doi:10.1016/j.jmapro.2019.05.001
2. L. Allen, M. W. Beijersbergen, R. Spreeuw, and J. Woerdman, “Orbital angular momentum of light and the transformation of Laguerre-Gaussian laser modes,” Physical Review A, vol. 45, no. 11, p. 8185, 1992.
3. Zhang, Wang, Yuan, & Burokur. (2020). A Review of Orbital Angular Momentum Vortex Beams Generation: From Traditional Methods to Metasurfaces. Applied Sciences, 10(3), 1015. doi:10.3390/app10031015
4. Huang, J., Qin, Q., & Wang, J. (2020). A Review of Stereolithography: Processes and Systems. Processes, 8(9), 1138. doi:10.3390/pr8091138.
5. Olayan, H.B.; Hami, H.S.; Owen, E.D. Photochemical and Thermal Crosslinking of Polymers. J. Macromol. Sci. Part C Polym. Rev. 1996, 36, 671–719.
6. Cadenato, A.; Salla, J.M.; Ramis, X.; Morancho, J.M.; Marroyo, L.M.; Martin, J.L. Determination of gel and vitrification times of thermoset curing process by means of TMA, DMTA and DSC techniques. J. Therm. Anal. 1997, 49, 269–279
7. Formlabs (8 March 2023). *Introducing the Form 3 and Form 3L, Powered by Low Force Stereolithography. https://formlabs.com*

3D-Manufacturing of Reflectarrays through the process of Stereolithography plus Metallization

I. Parellada-Serrano[1*], J. Velasco[1], Á. Palomares-Caballero[1], C. Molero[11], P. Padilla[1], J. F. Valenzuela-Valdés[1]

[1] Department of Signal Theory, Telematics and Communications, University of Granada (CITIC-UGR), 18071 Granada, Spain.
[*]corresponding author: parellada@ugr.es

Abstract: Recently, 3D-printing has flooded our lives as an option to materialize our own ideas and designs. This has reached the professional spheres, such as antennas and communications engineering, where this way of manufacturing has given the opportunity to create different types of reflectarrays (RAs) with innovative designs, as the one we present here. The fast production also allows an accelerated trial-and-error process.

Summary:

Even though stereolithography (SLA) emerged during the 1970s, the technical possibilities were scarce. From that time to the 2010s, antennas and other electronic devices, such as RAs, were frequently prototyped in structures that combined metallic and dielectric materials, being manufactured through PCB techniques [1-3]. RAs consist of a group of elements which, suitably distributed, and normally illuminated by a horn, allow the beam to be redirected. Nonetheless, over the last few years numerous 3D-print approaches have emerged, being now when SLA is being exploited. In the same way, many RAs based on fully-dielectric or fully-metallic structures are being seen in [4] and [5], respectively.

Here, we present a full-metal RA which consists of a unit cell which is periodically placed along x- and y-directions. It includes a triangular resonator that is inserted in the vertical wall along the propagation direction (z-direction). A view of the unit cell can be seen in Fig. 1. We take two pairs of values for *z1* and *z2*, having the two types of cells that make up the RA. Thanks to the quick improvement of 3D-printing techniques, we have the possibility to test different resonator shapes, both for electromagnetic behaviour and feasibility of printing, reaching a tradeoff between these factors.

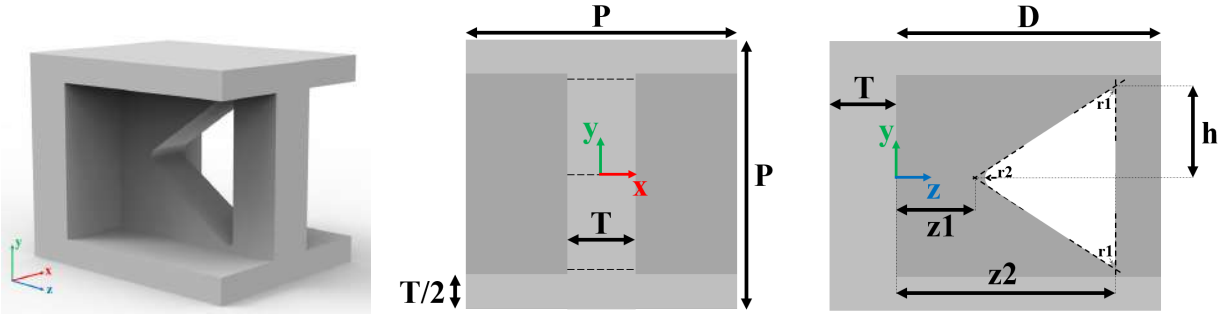

Fig. 1. Perspective (left), frontal (center) and lateral (right) view of the unit cell.

Once we have our design, we use the *Formlabs Form 3* [6] to print it. It is a professional brand not oriented for home use. A crucial step in 3D-printing, and even more in SLA, is the arrangement of supports, as they are needed for complex geometries, which may include gaps. The orientation of the model is also decisive because

the side facing to the printing platform will be the one that the supports will be attached to. Another aspect related to the orientation is that models with a high surface and a low thickness, as is our case, tend to bend if they are printed on that large surface, due to the direction of the printing layers and the heat produced by the UV light. To avoid this, it is better to print it edgewise.

When the print is finished, a postprocess must be carried out, that consist of a wash and cure of the piece. Depending on the resin used, times and temperatures vary. Mainly, we use three types of resins, also branded by *Formlabs*. One of them is the standard *Grey V4*; the second, named *High Temp,* has a higher heat deflection temperature, useful for precise prototypes; and the last one, *Castable Wax*, has a 20% wax that allows the omission of the postprocessing. After some testing, the best option was the *Grey V4*.

At this point, we have finished the first stage of our RA, which is shown in Fig. 2. There, it can be seen all the rings formed by the two types of cells, that is crucial for the beamforming. The metallization process is carried out by the French company *Jet Metal* [7]. They apply a micrometric layer of some conductive material. In our case, we usually request a 3µm of silver, which is enough to avoid deterioration due to the skin-effect.

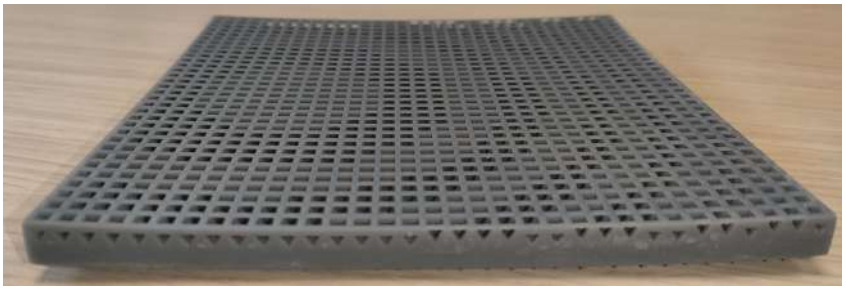

Fig. 2. 3D-printed Reflectarray prototype.

To sum up, since we work with 3D-printing, our production line has improved its efficiency. The independence acquired to check the feasibility of our designs has saved a lot of time and money.

References

1. Encinar, J. A. “Design of two-layer printed reflectarrays using patching of variable size”, IEEE Trans. Antennas Propag., 49, 1403-1410, 2001.
2. Robustillo, P., Zapata, J., Encinar, J. A., Arrebola, M. “Design of a Contoured-Beam Reflectarray for a EuTELSAT European Coverage Using a Stacked-Patch Element Characterized by an Artificial Neural Network”, IEEE Antennas Wirel. Propag. Lett., 11, 977-980, 2012.
3. Arrebola, M., Encinar, J.A., Barba, M. “Multifed Printed Reflectarray With Three Simultaneous Shaped Beams for LMDS Central Station Antenna”, IEEE Trans. Antennas Propag., 56, 1518-1527, 2008.
4. Li, B., Mei, C.Y., Zhou, Y., Lv, X. “A 3-D-Printed Wideband Circularly Polarized Dielectric Reflectarray of Cross-Shaped Element”, IEEE Antennas Wirel. Propag. Lett., 19, 1734–1738, 2020.
5. Palomares-Caballero, Á., Molero, C., Padilla, P., García-Vigueras, M., Gillard, R. “Wideband 3-D-Printed Metal-only Reflectarray for Controlling Orthogonal Linear Polarizations”, IEEE Trans. Antennas Propag., 71, 2247-2258, 2023.
6. Formlabs. *Introducing the Form 3 and Form 3L, Powered by Low Force Stereolithography*. https://formlabs.com
7. Jet Metal. https://www.jetmetal-tech.com/

The Manufacturing Methods Comparison for a Ka – Band Slotted Waveguide Antenna

Alicja Schreiber[1], Bernd Gabler[1]*S*

[1]Microwave and Radar Institute, German Aerospace Center (DLR), Oberpfaffenhofen, Germany
*Alicja.Schreiber@dlr.de

Abstract

This paper describes three manufacturing technologies at the example of a single Ka – band slotted waveguide antenna designed for an airborne synthetic aperture radar system. The prototype reference is machined by milling and compared with samples of two different 3D printing techniques. The antennas are fabricated and measured. The mechanical as well as the electromagnetic characteristics of the manufactured antennas are investigated. The individual results are shown and compared with design goal and simulated data.

1. Introduction

There are many different methods to fabricate an antenna and new ones are still being discovered, since the technical possibilities continuously improved in the recent years. These include, above all, additive processes, which promise many advantages over conventional production methods [1], [2]. This technique offers the possibility of creating sophisticated geometries, producing very small structures as well as potential material savings and weight reduction. On the other hand, like any other manufacturing technology, the 3D printing has its limitations. One of the main constraints of this process is the challenge of achieving both sufficient metallization and a smooth surface. The maximum part size of the printed components that can be achieved can also be an issue, since printers have limited available workspace, which is mostly smaller than that in a machining process.

In order to verify the usability of the 3D printing process for antennas in higher frequency bands, a single Ka-band slotted waveguide antenna (SWA) is designed and fabricated using the 3D selective laser sintering (SLS) process with both metal and synthetic material and compared with a brass prototype in conclusion.

2. Antenna under test

The AUT is an 8-slot end-fed single ridge slotted waveguide antenna made in a standing wave configuration and designed for a center frequency of f_0 = 35.5 GHz [3], [4]. Fig. 1 illustrates the simulation model of the designed antenna. The longitudinal slots are arranged in a broad wall of the waveguide in such a way that the current flow is interrupted, resulting in a potential difference that ultimately causes the slots to radiate.

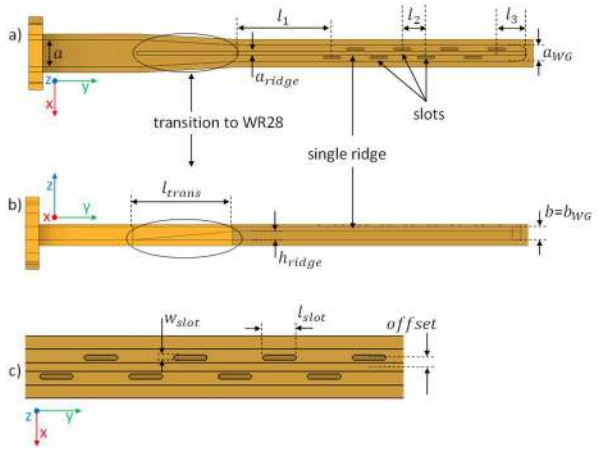

Figure 1: The simulation model of the AUT a) bottom view b) side view c) enlarged view of the radiation section.

To enable the in-phase radiation, the slots are positioned alternately with a distance to each other that equals the half-guided wavelength (l_2). The slot impedance is matched to that of the waveguide by optimum positioning with appropriate slot offset to the middle waveguide line ($offset$), resulting in maximum power being coupled into the slot. To ensure that this power is actually radiated, the slots are operated at resonance for a certain length (l_{slot}), which is set to the half-free space wavelength. To simplify the comparison and reduce sources of error, the antenna has a uniform amplitude distribution, with each slot placed at the same distance from the middle line of the waveguide and from each other. The input impedance matching can be controlled by changing the geometrical dimensions of the slot (l_{slot}, w_{slot}) as well as by adjusting the distance between the last slot and the short waveguide wall (l_3), which is set to the quarter guided wavelength. In order to be able to measure the antenna, the transition from the single ridge to the standard waveguide size WR28 has also been developed.

The simulation and optimization are done with 3D electromagnetic field simulator Ansys HFSS. Table 1 summarizes the geometric dimensions of the simulated brass antenna model.

Table 1: The parameters of simulated antenna model.

Parameter	*Value*	*Description*
a	7.112 mm	Standard waveguide WR28 width
b	3.556 mm	Standard waveguide WR28 height
a_{WG}	4.2 mm	Waveguide width
b_{WG}	3.556 mm	Waveguide height
a_{ridge}	1 mm	Ridge width
h_{ridge}	2.25 mm	Ridge height
l_{slot}	3.856 mm	Slot length
w_{slot}	0.6 mm	Slot width
t_{Wall}	0.3 mm	Wall thickness
$offset$	1.228 mm	Slot offset to the middle line
l_1	21 mm	Input length
l_2	5.146 mm	Distance between two slots
l_3	6.65 mm	Distance to the waveguides short
l_{trans}	22.15 mm	Transmission length

The demands on the manufacturing processes increase with frequency. This is because the dimensions of the components to be produced are in the millimeter range, as can be seen from the listed data. A reduction in antenna performance is already caused by small deviations from the specified geometry, or surface imperfections inside the waveguide. Therefore, low fabrication tolerances are an essential requirement for the manufacturing process. Another point is to make the antenna from as few parts as possible. Thus, every connection is a potential source of error due to the risk of inaccurate joining. Furthermore, the cost factor has to be considered during the production.

As mentioned in previous section, the AUT is designed for an airborne application [5]. In this case, the manufacturing process has to meet additional requirements. This includes the total weight of the antenna. It must be ensured that the weight of all systems used is evenly distributed and does not interfere with aerodynamics. However, as the antennas in the Ka-band range are rather small, this requirement is not dominant for the design process. A very important property is the stability and strength of the material. During the flight, it is exposed to different forces and vibrations and must not break or tear. The environmental conditions of the airborne campaigns are varying during the flight and are depending on the type of mission. In this way, the antenna must be able to deliver the same performance under different outdoor conditions, there must be no corrosion or deformation due to temperature differences or air humidity.

3. Technology

In this section, three different fabrication techniques are presented, for producing the antenna under test.

3.1. Milling

In a milling process, the material is removed from a metal piece until a desired geometry is achieved. In this case, a rotating tool with geometrically determined cutting shape is used to remove material by machining. This technique offers high dimensional accuracy with tolerances of approximately ± 0.125 µm and produces parts with smooth surface properties. However, milling machining process has several key design limitations, including tool access and clearances, holding or mounting points, as well as the inability to machine square corners due to tool geometry. Some geometries are even impossible to manufacture with this fabrication method, as the tools are not able to access all surfaces of part. On the other hand, milling machines can produce parts with smoother surfaces than 3D printed part, which is an important factor for high frequency application.

Fig. 2 depicts a sample of the AUT that is fabricated from a MS58 brass using an in-house workshop milling machine. Brass is an alloy of copper and zinc and is characterized by good corrosion resistance, ductility and thermal conductivity. The value of the electric conductivity depends on the amount of zinc in the alloy and decreases with increasing zinc content. For the here presented antenna this parameter is equal to $\sigma_{CuZn39Pb3} = 15 \times 10^6\, S/m$. With this technology, the slotted waveguide antenna cannot be made in one piece. The total antenna is therefore milled from two parts, that are soldered to each other in a vapor phase process using a solder paste no-clean SMDLTLFP10T5. Related to this process, there is a certain risk of unwanted gaps occurring when the parts are joined. In order to ensure the correct assembly procedure, adjustment pins are added to the lower part of the waveguide.

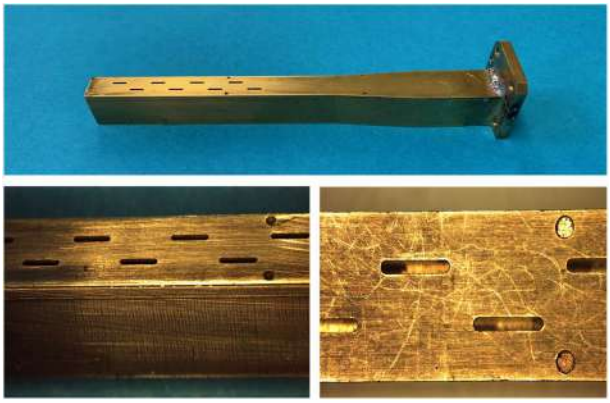

Figure 2: The fabricated brass antenna and its enlarged views.

Fig. 3a shows the enlarged view through a measurement microscope of one slot of the manufactured antenna with its geometrical dimensions, while Fig. 3b verifies the correct distance between two slots. As can be seen from these pictures, both the geometrical size (l_{slot}, w_{slot}) of the slot and the distance between two slots (l_2) agree very well with the parameters listed in the Table 1. The exact distance from the slot to the centerline of the waveguide cannot be determined using this measurement method.

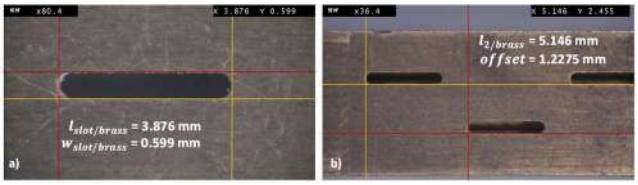

Figure 3: The microscope views of the fabricated brass antenna with their geometrical dimensions.

However, under the assumption that the slots are placed symmetrically to the centerline of the waveguide, the distance between the edges of opposite slots can be estimated. This counts under the prerequisite that the number is ideally equal twice the offset resulting distance agrees with the ideal simulated parameter ($offset$) very well.

3.2. 3D SLS Metal Print

The 3D printing technology is an additive manufacturing process, where components are built layer by layer. There are numerous ways to produce parts using this technology, which differ from the type of substance, for building components and moreover the manufacturing process itself. Typical materials for 3D printing are plastics, synthetic resins, ceramics and specially processed metals.
The presented antennas are made by selective laser sintering (SLS) process, where a powdery material is brought into the desired shape by laser sintering. Due to the additive nature of 3D printing, layer height determines the smoothness of the printed surface and the minimum feature size, which a printer can produce. The minimum wall thickness of SLS 3D printed parts is limited by the size of the laser spot and manufacturing tolerances are typically ± 0.300 mm, which causes potential issue for components of very small geometrical structures. Since this process allows manufacturing components from one piece, it is ideally suited for highly complex, topology-optimized geometries. However, according to the requirements of the AUT design parameters, it was impossible to achieve a thickness of 0.3 mm that does not collapse along its length. Therefore, the model of the antenna is modified before printing. The front of the antenna is therefore thickened to 0.5 mm. Since this process results in a change in the impedance of the antenna, both the geometric dimensions of the slots and their position need to be adjusted to achieve the desired performance. All modified parameters of the 3D printed antennas are summarized in Table 2.

Table 2: The modified parameters for 3D print process.

Parameter	*Value*	*Description*
t_{Wall}	0.5 mm	Wall thickness
l_{slot}	3.93 mm	Slot length
w_{slot}	0.6 mm	Slot width
$offset$	1.25 mm	Slot offset to the middle line
l_2	5.15 mm	Distance between two slots

The 3D metal printed antenna, which is illustrated in Fig. 4, is made from Inconel, a precipitation-hardening nickel-chromium alloy.

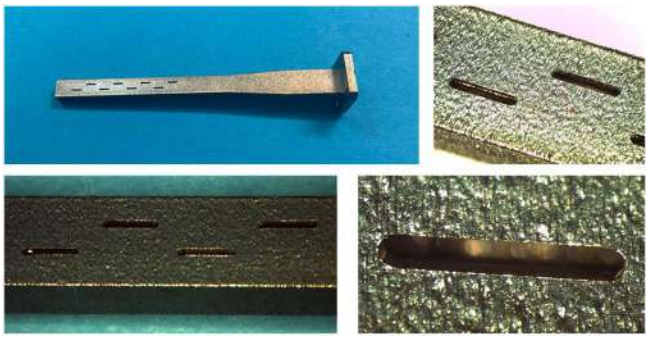

Figure 4: The fabricated 3D metal printed antenna and its enlarged views.

The Inconel has an excellent mechanical property and offers an optimal combination of high strength and good workability. With its good resistance to corrosion, the material is suitable for use in extreme environments. When heated, the material forms a thick, stable oxide layer that protects the surface. However, from the electrical point of view, such a layer acts as an isolator, which causes higher conductive losses. The exact value for the electrical properties of any alloy is difficult to determine, as it depends on the composition of the metals. Inconel that used in the frame of this work is mainly composed of nickel and chromium, resulting in an electric conductivity that is varying between $\sigma_{Inconel} = 7.7 - 13.9 \times 10^6\ S/m$. The 3D metal printed antenna is manufactured in one piece. In a first attempt, the slots were printed as well, but the result was unsatisfactory. Therefore, the slots are machined after the printing by means of a milling machine. However, it needs to be considered that this process is a potential source of error with respect to the exact position of the slots. It was also decided to mill the flange for achieving a flat surface that ensures a no-gups connection to the waveguide to coax adapter.

Fig. 5a illustrates the enlarged view of one of the slots of the manufactured 3D metal printed antenna with its geometrical dimensions. The position of the slots in relation to each other are seen in Fig. 5b. The shape of the slot as well as its position deviate somewhat from the values listed in Table 2. In particular, the length of the slots and their distance from the center line of the waveguide affect how the electromagnetic wave is coupled into the slots and radiated through them. Dimensional imperfections result in an antenna performance degradation.

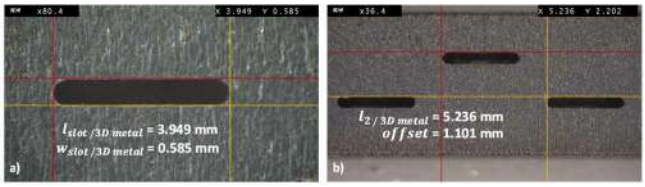

Figure 5: The microscope views of the fabricated 3D metal printed antenna with their geometrical dimensions.

3.3. 3D SLS Synthetic Material Print

The 3D synthetic material printed antenna is made from PA12, which is a versatile, strong, and durable thermoplastic also called Nylon12. The antenna is coated using a galvanic process with a copper sheet of 10 µm, which is considered sufficient with regard to skin effect. The skin depth for the copper coated antenna for the antenna center frequency is equal to 0,11 µm. Among the metals that are used for manufacturing the antennas in the frame of this work, copper shows the highest value for the electric conductivity of $\sigma_{Cu} = 58 \times 10^6\, S/m$. In order to properly dispose the copper residues from the antenna, a grid structure was added to the antenna's side, which has no electrical influence on their functionality. In the Fig. 6 the fabricated 3D thermoplastic antenna is depicted.

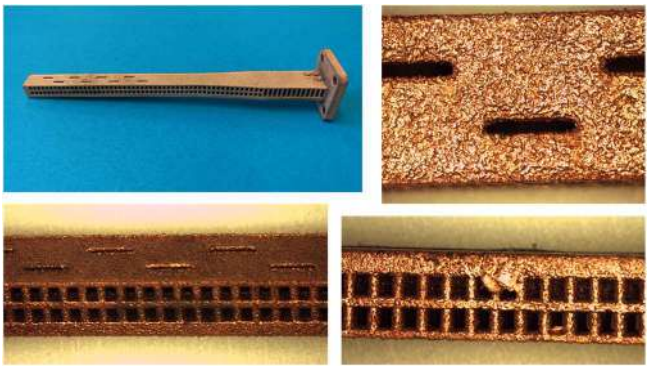

Figure 6: The fabricated 3D SLS printed synthetic material antenna and its enlarged views.

As can be seen from the pictures, copper residues are presents in some places in the antenna, which are difficult to remove after the galvanic process without risk of damaging the metal layer. In contrast to materials used in stereolithography (SLA) process that become brittle over time, the SLS antenna is mechanically stable. Fig. 7a illustrates the enlarged view of a single slot from a 3D thermoplastic printed antenna with its geometrical dimensions, while Fig. 7b overlays the specified dimensions between two slots to the realized structure. Since the slots of this type have no sharp edges, the exact geometry cannton easily be determined. The obtained values are therefore subject to a certain degree of uncertainty. Nevertheless, the parameters deviate from the simulated data. All slots of the antenna are measured, resulting in a relatively large variations over their length, width and position of the slots could be determined in this antenna.

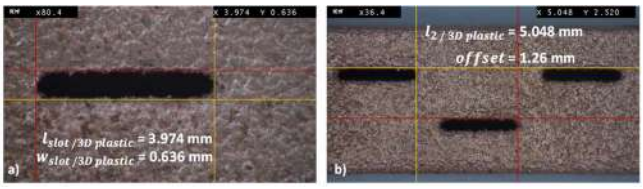

Figure 7: The microscope views of the fabricated 3D SLS printed synthetic material antenna with their geometrical dimensions.

4. Measurement vs. simulation

The antenna radiation characteristics are verified by far-field measurements in a Compact Antenna Test Range (CATR) at the DLR Microwaves and Radar Institute. Fig. 8 depicts the radiation patterns of all manufactured antennas and the simulated data in co-polarization at the center frequency.

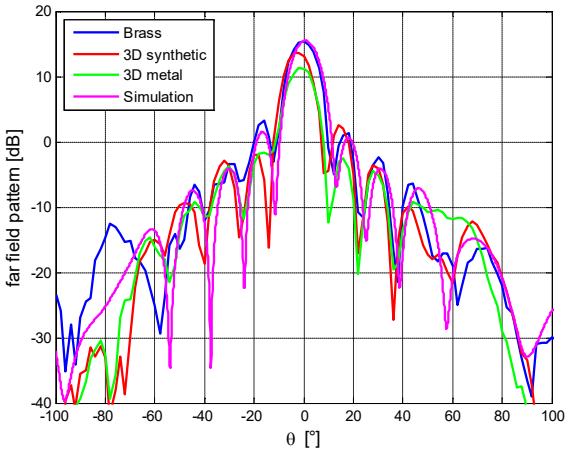

Figure 8: The measured co-polar radiation pattern for φ=0° of manufactured antennas and the simulated data.

Compared to the brass antenna, which agrees well with the simulation results, both 3D printed antennas have a slight pointing shift, as well as a higher total loss. For the waveguides that are not filled with dielectric, losses are generally caused by the wall currents in the finitely conductive waveguide material. This is mainly from the skin effect [6], which leads to an increase in specific resistance according to the material. With increasing electric conductivity, the value of the resistance decreases. Copper shows higher conductivity values compared to brass and nickel. However, the copper oxide layer that forms on metal sheet leads to its reduction, which is most probably the case for the 3D plastic printed antenna. Due to the low electrical conductivity value of Inconel, the 3D metal printed antenna achieves reduced gain compared to the copper coated antenna. Theoretically, the difference is approximately only 0.1 dB. As can be seen from Fig. 8, this antenna type achieves only 12 dBi gain and shows the largest differences to the simulated data.

The surface roughness also plays a major role in relation to the losses, since rough surfaces represent a longer path for the current and thus elevates resistance, which leads to an increase of losses. Compared to the milled brass antenna, the SLS printed antennas that are described in this paper, have a relatively rough surface, which is clearly visible in the pictures above. This implies that the losses are in consequence higher. The sidelobes level for both printed antennas are unbalanced. This is most likely from imperfection in the phase, which arise by incorrect placement of the slots on the waveguide top side.

In Fig. 9 the reflection coefficients for the manufactured antennas are depicted and compared with the simulation data.

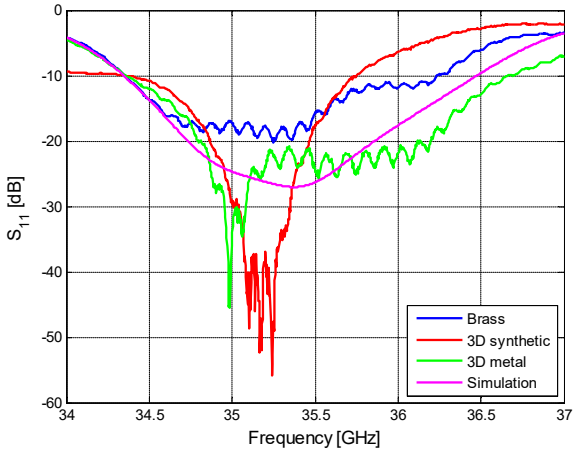

Figure 9: The measured and simulated reflection coefficient at the antenna input.

The simulated 10 dB bandwidth for the antenna is about 2 GHz with the resonance frequency at f_0=35.5 GHz. From this diagram, it can be seen that only the 3D metal printed antenna completely matches the simulated results. The 3D plastic antenna has a slightly narrower bandwidth than the brass antenna. The reason for that is the incorrect length of the slot, which causes the shift of the resonant frequency in the low frequency range

In Fig. 10, the radiation efficiency is depicted, which is measured by means of the radiometric hot-cold measurement method [7].

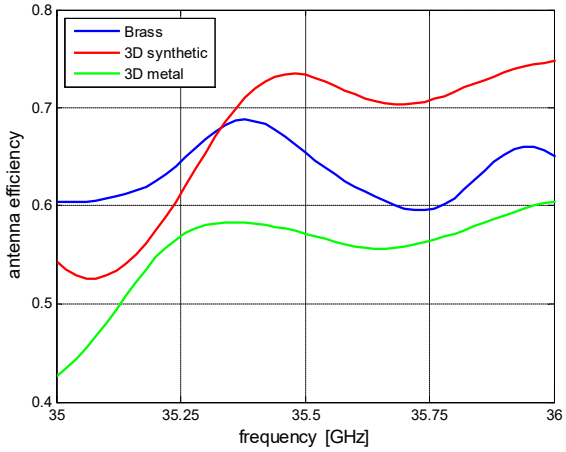

Figure 10: The simulated and measured reflexion coefficient for manufactured antennas.

The brass antenna has a tolerably constant progression over the desired frequency band, while the 3D printed antennas prove to be more stable in upper frequency range. The radiation efficiency for the 3D metal printed antenna is relatively low, especially in the lower frequency range. Since the slot offset for this antenna does not correspond to the simulated value, the slot impedance is not optimally matched to the waveguide impedance and therefore the maximum power is not coupled into the slot.

5. Conclusions

To prove the applicability of the additive manufacturing method for antennas that are operating in higher frequency bands, two 3D SLS printed antennas based on two different materials have been fabricated and compared with the milled brass antenna in both mechanical and electromagnetic point of view.

Compared to conventional fabrication methods, such as milling or eroding, complex components can be manufactured in one piece using 3D printing technology. However, the implementation of quality control is difficult due to the limited access for visual inspection. In addition, the components design needs an individual adaption to the selected 3D printing process and the end result depends strongly on print process settings. On the other hand, printed elements are lighter, which is an important factor for the airborne applications, but not that significant in this frequency range. Ultimately, the use of the additive manufacturing methods must be verified during the development process.

Acknowledgements

The authors thank the Golden Device team for supporting this work by providing numerous 3D synthetic material technology antenna samples.

References

[1] D. Helena, A. Ramos, T. Varum and J. N. Matos, Antenna Design Using Modern Additive Manufacturing Technology: A Review, *inSIEEESAccess*, vol.8, pp. 1777064-177083, 2020.

[2] T. D. Ngo, A. Kashani, G. Imbalzano, K. T. Q. Nguyen and D. Hui, Additive manufacturing (3D printing): A review of materials, methods, applications and challenges, *Compos.SB,SEng.*, vol. 143, pp. 172-196, Jun. 2018.

[3] L. Jossefson and S. R. Rengarajan, Slotted Waveguide Array Antennas, *TheSInstitutionSofSEngineeringSandS Technology*, 2018.

[4] R. Enjiu, M. P. Perotoni, Slotted Waveguide Antenna Design Using 3D Simulation, *MicrowaveSJournal*, July 2013.

[5] R. Horn, A. Nottensteiner, A. Reigber, J. Fischer and R. Scheiber, F-SAR-DLR's new multifrequency polarimetric airborne SAR, *IGARSS*, 2009.

[6] L.F. Giacoletto, Frequency-and Time Domain Analysis of Skin Effects, *IEEES TransactionsS ofS Magnetics*, Vol.32, No. 1, January 1996.

[7] J. Ashkenazy, E. Levine and D. Treves, Radiometric measurement of antenna efficiency, *ElectronS Lett*, Vol.21, no.3, 1985.

Antennas, EM and Smart Sensing Technologies for Biomedical and Healthcare Applications

AES 2023, TORREMOLINOS - SPAIN, 5 – 8 JUNE 2023

Millimeter-Waves for Breast Cancer Detection: State-of-the-Art and Perspectives

S. Di Meo[1*], G. Matrone[1], and M. Pasian[1]

[1]Department of Electrical, Computer and Biomedical Engineering, University of Pavia, Italy
[*]corresponding author: simona.dimeo@unipv.it

Abstract: In this contribution, we present the work done and ongoing at the University of Pavia on the design of a millimeter-wave imaging system for breast cancer detection.

Breast cancer is one of the most diagnosed diseases among women worldwide. Nowadays, X-ray mammography is considered the gold standard for breast cancer detection; however, its limitations are driving interest in new diagnostic modalities. Among the most promising techniques, the use of microwaves has been proposed for imaging of the breast [1], based on dielectric contrast between healthy and neoplastic tissues [2-3]. In order to improve the resolution of the currently proposed microwave imaging systems, at the University of Pavia we have been working for years on a new imaging system in the mm-wave regime. In particular, we (A.) measured the dielectric properties of human breast *ex-vivo* tissues up to 50 GHz; (B.) carried out a numerical and simulative feasibility study of such an imaging system; (C.) developed and characterized (both dielectrically and mechanically) several tissue-mimicking breast phantoms, and (D.) tested the imaging prototype on our produced phantoms, also combining mm-waves, ultrasounds and ultrasounds elastography. In the following, we present the main achievements about these steps, and in (E.) we present the ongoing activities.

A. Dielectric characterization of human breast ex-vivo tissues

In collaboration with the European Institute of Oncology in Milan, we performed two experimental campaigns on more than 300 *ex-vivo* healthy and cancerous breast samples from 100 women aged 14-89 years. Measurements were done with an open-ended coaxial probe in the frequency range [0.5-50] GHz on samples at room temperature. The results of these two experimental campaigns showed a significant dielectric contrast in the whole investigated bandwidth between healthy and malignant tissues, even when healthy tissues with high fibro-glandular content are considered. More details can be found in [2-3].

B. Numerical feasibility study of the mm-wave imaging system

Based on the significant dielectric contrast between healthy and neoplastic tissues, we performed a numerical feasibility study of the mm-wave imaging system both in a linear and conformal configuration. In particular, through link-budget evaluation in different scenarios (i.e., different breast types), we evaluated aspects such as the optimal number of antennas in the array maximizing the signal-to-noise ratio, the maximum penetration depth, as well as the achievable resolution for this type of system. Details in [4].

C. Bi-modal tissue-mimicking breast phantoms

To test the mm-wave imaging prototype, we studied and dielectrically characterized several recipes based on low-cost, easily handled and safe components, i.e. based on the use of deionized water, sunflower oil, dishwashing liquid and solidifying agent such as gelatin or agar. The dielectric properties of the produced phantoms were measured in the frequency range [0.5-50] GHz and were compared with those of the corresponding human breast *ex-vivo* tissues, showing the good capability of our recipes in mimicking all breast tissues types, by changing only the percentage of oil in the mixtures. More details can be found in [5].

In addition, healthy and diseased tissues have different mechanical properties [6] and to produce increasingly

realistic phantoms (to be used in combined imaging systems), we characterized the mechanical properties of our phantoms under different experimental conditions. In particular, starting from the recipes proposed in [5], we increased the phantom stiffness by increasing the gelatin volume percentage within the mixture, always monitoring its dielectric properties. More details can be found in [7].

D. Multi-modal imaging combining mm-waves, ultrasounds and ultrasounds elastography

We tested the mm-wave imaging prototype on these phantoms. In particular, we used two double-ridge waveguides with mono-modal frequency bandwidth from 18 to 40 GHz to synthesize an array consisting of 24 radiators. All measurements were made without the coupling medium and we experimentally demonstrated the possibility of reaching targets up to 3 cm in a phantom with losses. More details can be found in [8].

In addition, a triple-mode scan, using millimeter waves, and ultrasound waves, to obtain B-mode and quasi-static elastography images of a phantom of human breast tissues was done. A homogeneous phantom composed of non-toxic, low-cost and easy-to-handle materials ([5]) was produced, with an inclusion made of water and agar. These are intended to mimic, in terms of dielectric properties, healthy adipose tissues and neoplastic tissues, respectively. The resulting images obtained from millimeter-wave, ultrasound B-mode and quasi-static elastography acquisitions are shown in Fig. 1a, Fig. 1b and Fig. 1c, respectively. More details can be found in [9].

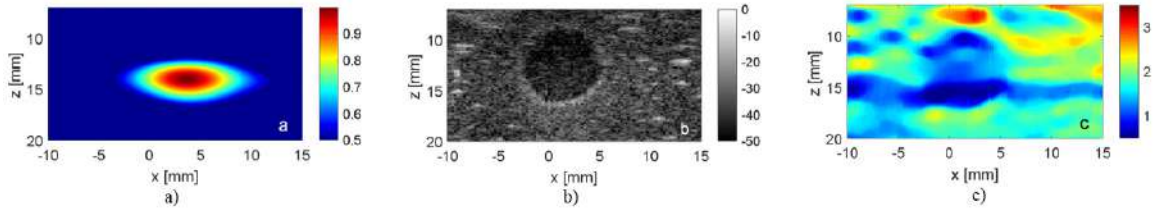

Figure 1. a) mm-wave, b) ultrasound B-mode and c) elastography images of the phantom [9].

E. Ongoing activities

We are currently dealing with the aspects related to the presence of the skin, both in terms of producing the phantom and removing the associated artifact in the mm-wave image. In parallel, we are working on characterizing, in addition to dielectric and mechanical properties, the acoustic properties of our phantoms. More details and results will be presented at the conference.

References

1. N. K. Nikolova, “Microwave imaging for breast cancer,” *IEEE Microw. Mag.*, vol. 12, no. 7, pp. 78–94, Dec. 2011.
2. A. Martellosio, et al, "Dielectric Properties Characterization from 0.5 to 50 GHz of Breast Cancer Tissues," IEEE TMTT, Vol. 65, No. 3, pp. 998-1011, March 2017.
3. S. Di Meo, et al, "Dielectric properties of breast tissues: Experimental results up to 50 GHz," *EuCAP 2018*, London, UK, April 9-13, 2018.
4. S. Di Meo, et al, "On the Feasibility of Breast Cancer Imaging Systems at Millimeter-Waves Frequencies," *IEEE TMTT*, Vol. 65, No. 5, pp. 1795-1806, May 2017.
5. S. Di Meo, et al, "Tissue-mimicking materials for breast phantoms up to 50 GHz," *IOP Phys. in Med. and Biol.*, Vol. 64, 055006, Feb. 2019.
6. A. Samani et al, “Elastic moduli of normal and pathological human breast tissue: an inversion-tecnique-based investigation of 169 samples,” IOP Physics in Medicine & Biology, vol. 52, pp. 1565-1576, 2007.
7. S. Di Meo, A. Cannatà, S. Morganti, G. Matrone, and M. Pasian, "On the dielectric and mechanical characterization of tissue-mimicking breast phantoms," IOP Physics in Medicine and Biology, Vol. 67, 155018, July 2022
8. S. Di Meo, et al, "Experimental Validation on Tissue-Mimicking Phantoms of Millimeter-Wave Imaging for Breast Cancer Detection," Applied Sciences, Vol. 11, No. 1, pp. 432, Jan. 2021.
9. S. Di Meo et al, "Combining Millimeter-Wave Imaging, Ultrasound and Elastography in a New Multimodal Approach for Breast Cancer Detection: Initial Experimental Results," IEEE EMBC 2020, Montreal, Canada, July 20-24, 2020.

A systematic study of the electromagnetic occupational exposure in healthcare applications

S. D'Agostino[1], M. Colella[1], M. Liberti[1] and F. Apollonio[1]

[1]Department of Information Engineering, Electronics and Telecommunications (DIET), Sapienza University of Rome, Italy
[*]corresponding author: simona.dagostino@uniroma1.it

Abstract: This paper aims to study how to improve occupational health and safety conditions in the healthcare environment; in particular we will focus on a systematic evaluation of the exposure to the variable magnetic field produced during a transcranial magnetic stimulation (TMS) treatment. Four exposure conditions are provided based on two virtual human body models, in the case of a circular coil applicator. Results of the induced electric field inside the human body models show that in some cases exposure limits are exceeded and lead us to possible safety suggestions.

Introduction

The study began by carefully reviewing real exposure scenarios of clinicians, as the reference material used is company user manuals, websites, papers, and measurement campaigns[1]. We collected approximately 70 images of these scenarios to identify all the possible positions assumed by clinicians during TMS treatments. Furthermore, since the coil must be held in place in proximity of the patient's head, the operator often uses hands to hold it during treatment. This can potentially introduce critical issues with operator's limb exposure that were confirmed by some results obtained in a previous study[1,2]. To reduce these local risks, a dosimetric approach to provide useful suggestions is carried out, as no technical standard devices are currently available for TMS.

Models and methods

As *a source model*, it is considered a circular coil model 9784-00 of Magstim powered with Magstim200[1] and BiStim system; at the maximum stimulator output (100%MSO) the two systems deliver current pulses assimilated to pure sinusoids at equivalent frequencies of 3 kHz (5.6 kA) and 1 kHz (9.7 kA), respectively. *The Human models* used to reproduce the operator, are two posable versions of the male models, called Duke (34-year-old, 1.77 m, 70.2 kg) and Jeduk (33-year-old, 1.62 m, 64.5 kg), both members of the Virtual Population (ViP., v.3.0)[3]. Concerning the *exposure scenario*, in order to conduct a local analysis of the exposure of the clinician's hands, two different way of gripping the coil are considered for each human model. For Duke, the clinician is assumed to hold the coil with one hand (right and left are assessed separately) with two different ways of gripping (defined as Closed and Open). For Jeduk model, a more realistic conditions are evaluated, with both hands involved in the exposure, as well as two different holding modes (related to the orientation of the right hand and named defined as "Alfa" and "Beta"). Finally, the 99th percentile of the induced electric (E-) field in the human model was assessed by comparing it with the limit of ICNIRP 2010[4] guidelines (i.e., 1.13 V/m for these frequencies).

Results

First, we have evaluated the local maps of the induced E-field due to the TMS exposure of the hands, considering the four conditions described before (Figure 1).

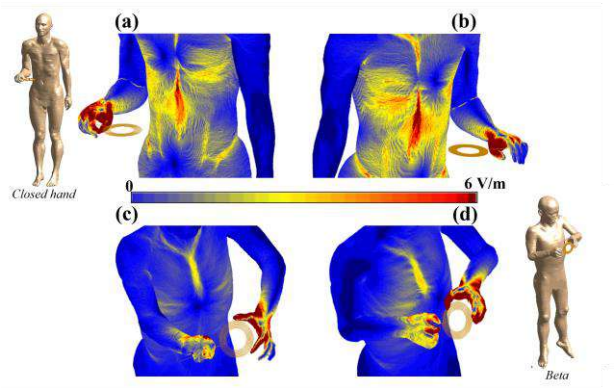

Figure 1. *E-field maps: (a) Duke right Closed hand, (b) Duke left Open hand, (c) Jeduk Alfa with coil handle perpendicular to the body surface, and (d) Jeduk Beta with the handle parallel to the body surface.*

These distributions of the E-field show how, in all the cases, a large portion of the hand exceeds the limit confirming the criticality of the proximity in use of the device. The extent of the exposure becomes clearer by analyzing the 99th percentiles of the E-field evaluated in the hand and forearm, as reported in Table I.

Table 1. 99th percentiles of induced E-field (V/m)

	Duke		**Jeduk**			
	Closed	*Open*	*Alfa*		*Beta*	
Hand	*right*	*left*	*right*	*left*	*right*	*left*
70% MSO	21.36	15.17	7.33	15.88	6.97	21.67
50% MSO	15.26	10.84	5.23	11.34	4.98	15.48
30% MSO	9.15	6.50	3.14	6.81	2.99	9.29

Discussions

For all the exposure conditions here considered, the circular coil causes an induced E-field that exceeds the suggested limits, also considering the lowest level of MSO used in practice in clinics (30% MSO). Excluding the implausible 100%MSO[5], the percentage variation respect the limits ranges between +164.6% up to +1790%. These results indicate the need to explore new method for shielding the hand by using for example a dedicated glove. In conclusion, we demonstrate how, risk assessment in healthcare workplace can be effectively approached using computational methods with ultimate goal to identify possible flaw of knowledge and suggesting new protocol for assessing exposure to devices such as TMS, which currently lack standardizations.

References

1. D'Agostino S, Colella M, Liberti M, Falsaperla R, Apollonio F. Systematic numerical assessment of occupational exposure to electromagnetic fields of transcranial magnetic stimulation. *Med Phys*. 2022;49(5):3416-3431. doi:10.1002/mp.15567
2. D'Agostino S, Colella M, Liberti M, Falsaperla R, Apollonio F. Dosimetric assessment of clinical staff exposed to magnetic field produced by a transcranial magnetic stimulation circular coil. *2021 34th Gen Assem Sci Symp Int Union Radio Sci URSI GASS 2021*. 2021;(September):2021-2024. doi:10.23919/URSIGASS51995.2021.9560280
3. Gosselin M-C, Neufeld E, Moser H, et al. Development of a new generation of high-resolution anatomical models for medical device evaluation: the Virtual Population 3.0. *Phys Med Biol*. 2014;59(18):5287-5303. doi:10.1088/0031-9155/59/18/5287
4. ICNIRP. Guidelines for limiting exposure to time-varying electric and magnetic fields (1 Hz TO 100 kHz). *Health Phys*. 2010;99(6):818-836. doi:10.1097/HP.0b013e3181f06c86
5. Groppa S, Oliviero A, Eisen A, et al. A practical guide to diagnostic transcranial magnetic stimulation: Report of an IFCN committee. *Clin Neurophysiol*. 2012;123(5):858-882. doi:10.1016/j.clinph.2012.01.010

Antenna / body interactions at mmWaves

Maxim Zhadobov

[1]IETR / CNRS, Rennes, France
maxim.zhadobov@univ-rennes.fr

Abstract: Millimeter-wave technologies are upcoming for 5G/6G communications as well as for body-centric applications, including wireless sensors networks and wireless body-area networks. The corresponding new usages and services increasingly involve near-field interaction of radiating devices with the human body, both in terms of body impact on wireless device performance as well as in terms of user exposure. This presentation will provide an overview of challenges and recent advances in the field of antenna / human body interactions in the millimeter-wave (mmWave) band. It will highlight the key challenges related to the design of tissue-equivalent models, multi-physics measurements, exposure assessment and compliance testing, age-dependent effects, and micro-scale dosimetry, as well as to design of advanced exposure systems for in vitro and in vivo studies.

A Radar And Camera-based Cuff-less And Calibration-free Blood Pressure Estimation Method

Bo Wang[1], Zhi Zheng[1], Haotian Shi[1], and Yongxin Guo[1*]

[1]National University of Singapore, Singapore
[*]corresponding author: eleguoyx@nus.edu.sg

Abstract: A cuff-less calibration-free BP estimation method with fusion from a radar and a camera is proposed. The waveform features and health information are used as inputs to convolutional neural network (CNN) models to estimate BPs. The models are first trained on the Medical Information Mart for Intensive Care III (MIMIC-III) database and then transferred to the non-contact setup. The proposed method provides a feasible way to realize calibration-free, cuff-less BP estimation.

Blood pressure (BP) is an important vital sign my medical diagnosis. Pulse transit time (PTT)-based methods [1][2] can realize cuff-less BP estimation, but it is yet limited by subject-dependent calibration. In this paper, a cuff-less, calibration-free BP estimation system is designed with fusion from a radar and a camera. A radar is used to capture the thorax heartbeat signal, and a camera monitors the pulse from the palm simultaneously. The proposed cuff-less measurement method is applicable to different scenarios, and an example of robot setup are shown in Figure 1.

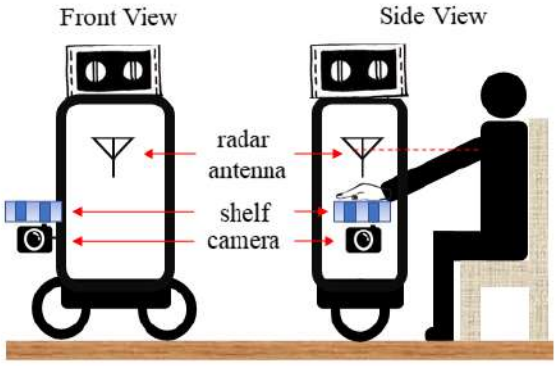

Figure 1 Sketch map of the system setup on a robot

The proposed method utilize non-contact sensors to realize cuff-less measurement. The radar captures the heartbeat signal by sensing the chest wall movements caused by cardiac activities. The camera extract pulse wave from the palm by analyzing the skin color change caused by the pulse wave. In the robot setup, the subject only needs to sit in front of the robot, facing the antenna and put his or her hand in front of the camera. The signals in 30 seconds are recorded in the experiment.

A convolution neural network (CNN) is used as the calibration-free BP estimation model. The subject's health information and waveform features are used as inputs to the model. The health information includes the age, gender, hypertension history, weight, height, etc. A series of features, including the heart rate, time features, area features, and PTT features, are extracted from the pulse waves. To solve the problem of limited number of data samples to train the model, a model transfer scheme is adopted. The model is first trained on the data samples generated from

Medical Information Mart for Intensive Care III (MIMIC-III) dataset, and then transferred to the non-contact setup. In the MIMIC-III data set, the data are captured by electrocardiogram (ECG) and photoplethysmography (PPG). Since all measurements are modified by cardiac activities, the waveforms measured by ECG and PPG can be transferred to the waveforms measured by the radar and the camera, which supports the feasibility of the model transfer scheme. As is shown in Table I, the experiment results show that the proposed method provides a feasible way to realize the cuff-less, calibration-free BP estimation.

TABLE I Estimation Performance

Group	No. of subjects	Systolic BP (mmHg)			Diastolic BP (mmHg)		
		Mean Error	Mean Average Error	Standard Deviation	Mean Error	Mean Average Error	Standard Deviation
Subjects with hypertension	46	25.14	25.99	20.50	10.24	14.73	8.95
Subjects with hypotension	20	-5.81	11.76	8.23	-16.9	14.58	8.83
Subjects with BP in the normal range	128	7.74	12.66	12.21	3.89	7.93	6.65
Total	194	10.47	15.73	15.01	3.16	10.23	7.93

References

[1] C. C. Y. Poon and Y. T. Zhang, "Cuff-less and noninvasive measurements of arterial blood pressure by pulse transit time," *Annu. Int. Conf. IEEE Eng. Med. Biol. - Proc.*, vol. 7 VOLS, no. May 2014, pp. 5877–5880, 2005.

[2] R. Shriram, A. Wakankar, N. Daimiwal, and D. Ramdasi, "Continuous cuffless blood pressure monitoring based on PTT," *ICBBT 2010 - 2010 Int. Conf. Bioinforma. Biomed. Technol.*, pp. 51–55, 2010.

Design and Optimization of Transmission Coils for Magnetic Resonance Coupling Human Body Communication

Ziliang Wei[1], Yupei Zheng[1], Bingheng Chen[1], Yueming Gao[1*], Yadong Yin[1], Jiejie Yang[1], Sio Hang Pun[2] and Mang I Vai[2]

[1] Provincial Key Laboratory of Medical Instrument and Pharmaceutical Technology, Fuzhou University, China
[2]State Key Laboratory of Analog and Mixed-Signal VLSI, University of Macau, China
[*]corresponding author: fzugym@gmail.com

Abstract: This summary presents an optimization approach for designing coils of magnetic resonance coupling human body communication. The optimal configuration of various coils is examined and attained by means of electromagnetic simulations. Subsequently, experiments are conducted to validate the feasibility of the most effective scheme. The results indicate that the strongest correlation (α= 0.01) is found between the inner diameter and its inductance. Moreover, it is evinced that an increased coil inductance results in a reduced transmission loss.

The emergence of human body communication technology has greatly aided in the refined management of medical, rehabilitation and physical health fields. Magnetic Resonance Coupling Human Body Communication (MRC-HBC) is an innovative technology that enables efficient single-carrier communication, and is anticipated to introduce new prospects and challenges in the realm of wearable devices and near-field communication [1, 2]. In MRC-HBC, signals are transmitted by resonating the system, which consists of transceiver coils and the human body, at the same frequency. Therefore, the design and optimization of the transceiver coil is a critical aspect of the MRC-HBC system. However, existing research has paid relatively little attention to the development of transmission coils. M. Nath et al. [3] explored the distinctions and associations between the magnetic coupling HBC and the EQS-HBC through simulations and basic coil experiments. E. Wen et al. [4] compared human channel characteristics measured by the Bluetooth approach and the coil approach to showcase the benefits and feasibility of magnetic coupling HBC. G. Alvarez et al. [5] explicated the coupling mechanism between the coil and the human body through an equivalent circuit model, and investigated the effect of coil configuration on the arm. In summary, the majority of current research endeavors to demonstrate the feasibility of magnetic coupling HBC or explain the conduction mechanism of electrical signals, while only limited research has been dedicated to a comprehensive design of transmission coils. Therefore, this study proposes a coil optimization method for maximizing inductance, which is subsequently experimentally validated for its effectiveness and reliability.

The inductance of the coil is indicative of the extent of variation in magnetic flux generated by changes in current. As per the definition of inductance and Faraday's law (1), it is evident that a higher coil inductance indicates a stronger magnetic field intensity generated by the coil at a given input current, resulting in enhanced energy storage and transmission capacity. For MRC-HBC, coils conforming to wearable devices deserve to possess the greatest possible inductance while also being as miniaturized as possible.

$$Li = N \cdot \Phi = N \cdot \int_s \mathbf{B} \cdot \mathrm{d}\mathbf{s} \tag{1}$$

Table1. Optimal Combination of *s*, *w* and d_{in} and Correlation Analysis

	Inductance	Correlation coefficient	Significance level
s	0.5mm	0.192	α=0.01
w	0.5mm	0.055	α=0.05
d_{in}	13.5mm	0.357	α=0.01

Table2. Inductances for Different Geometries of Coils

	Rectangular	Hexagonal	Octagonal	Circular
Simulation	6.31μH	5.81μH	5.64μH	5.35μH
Measurement	6.12μH	5.61μH	5.43μH	5.23μH
Error	3.11%	3.54%	3.81%	2.21%

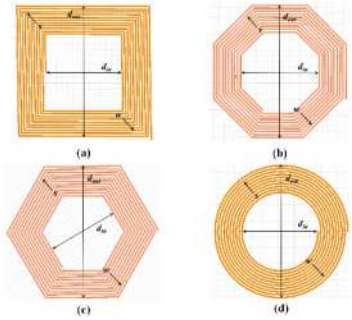

Fig. 1. An array of diverse coil geometries

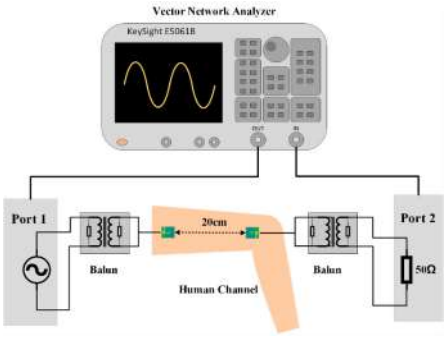

Fig. 2. In vivo measurement setup

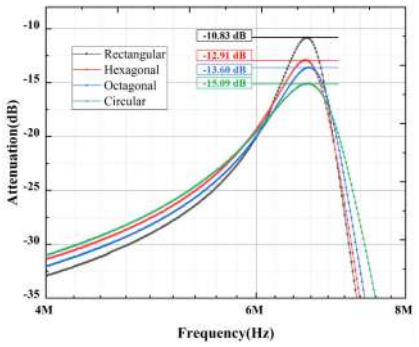

Fig. 3. Transmission loss among various coil geometries @6.78MHz

For this purpose, we initially conducted simulations and optimizations of coil inner diameter (d_{in}), wire width (w) and wire spacing (s) in HFSS, with the aim of obtaining the maximum inductance for a rectangular coil with the same area. The model was developed based on planar coil theory, and the maximum inductance was parametrically scanned as an objective function. The resulting data was then analyzed for correlation. Table 1 reveals that, for a fixed area and an equal number of turns, the inner diameter of the coil displays the most significant correlation with the inductance. Moreover, while holding all other parameters constant, we investigated the influence of distinct geometries (rectangular, hexagonal, octagonal, and circular) on inductance, as depicted in Figure 1. The simulation results indicate that the rectangular coil produces the maximum inductance.

To substantiate the accuracy of the simulation findings, four printed circuit board coils with the parameters delineated in Table 1 were constructed in the specified geometries, and their inductances were measured utilizing a vector network analyzer (Keysight E5061B). The simulation and measurement results are presented in Table 2. The error between the simulated and measured values for all geometries remains below 4%, indicating the reliability of the simulation results. Moreover, we conducted *inSvivo* experiments to validate our hypothesis that using a higher coil inductance for MRC-HBC results in a lower transmission loss at the resonant frequency (6.78MHz). The measurement setup is depicted in Figure 2. The experimental findings substantiate our conjecture (as depicted in Figure 3), wherein the rectangular coil, possessing the most substantial inductance, displayed the minimal transmission loss of 10.83dB. Conversely, the circular coil, characterized by the least inductance, manifested the maximal transmission loss of 15.09dB. This preliminary study validates the significance of inductance in MRC-HBC transmission, refines and optimizes the transmission coil design, thereby offering novel reference points for future wearable device communication and near-field communication endeavors.

References

1. N. Golestani and M. Moghaddam, “Theoretical Modeling and Analysis of Magnetic Induction Communication in Wireless Body Area Networks (WBANs),” *IEEESJ.SElectromagn.SRFSMicrow.SMed.SBiol.*, Vol. 2, No. 1, 48–55, 2018.
2. T. Ogasawara, A. Sasaki, K. Fujii, and H. Morimura, “Human Body Communication Based on Magnetic Coupling,” *IEEESTrans.SAntennasSPropagat.*, Vol. 62, No. 2, 804–813, Feb. 2014.
3. M. Nath, A. K. Ulvog, S. Weigand, and S. Sen, “Understanding the Role of Magnetic and Magneto-Quasistatic Fields in Human Body Communication,” *IEEESTrans.SBiomed.SEng.*, Vol. 69, No. 12, 3635–3644, 2022.
4. E. Wen, D. Sievenpiper, and P. Mercier, “Channel Characterization of Magnetic Human Body Communication,” *IEEES Trans.SBiomed.SEng.*, Vol. 69, No. 2, 569–579, Feb. 2022.
5. G. A. Alvarez-Botero, Y. K. Hernandez-Gomez, and H. Lobato-Morales, “On the Orientation of Signal Excitation for Magnetically Coupled Human Body Communication,” *IEEESTrans.SInstrum.SMeas.*, Vol. 71, 1–9, 2022.

Bioimpedance-based Muscle Activity Monitoring

Pan Xu[1], Wanting He[2], Wei Ma[1], Ting Liu[1], Yipeng Liao[1], Željka Lučev Vasić[3], Mario Cifrek[3], and Yueming Gao[1*]

[1]College of Physics and Information Engineering, Fuzhou University, China
[2]School of Advanced Manufacturing, Fuzhou University, China
[3]Faculty of Electrical Engineering and Computing, University of Zagreb, Croatia
[*]corresponding author: fzugym@gmail.com

Abstract: This summary proposed a new method for continuous monitoring of finger flexor activity. The bioimpedance measurement scheme for muscle dynamic monitoring is determined by analysis of finite element electromagnetic simulations with an upper arm model. In vivo experiments were conducted to verify the accuracy of the simulation, followed by constructing a long and short-term memory network to characterize the muscle activity level by bioimpedance. The results indicate that the bioimpedance technique has the potential to track muscle activity continuously.

Muscle fatigue is a physiological phenomenon characterized by a decline in muscle strength and an inability to maintain established movements [1]. It occurs commonly in sports, fitness, and rehabilitation training [1]. Appropriate exercise promotes health, but free radicals produced by excessive exercise will cause an imbalance in the body's oxidative and antioxidant capacity [2]. Continuous monitoring of muscle activity is an effective method of avoiding muscle injury and developing proper training plans. Shin et al. [3] used bioimpedance (BI) data at multiple frequencies to track muscle changes in patients with stroke. Li et al. [4] measured local BI changes during the progression of muscle fatigue to verify that BI can be a biomarker of muscle status. None of the above studies have

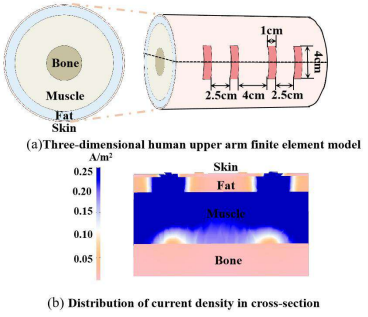

Fig.1. The FEM model

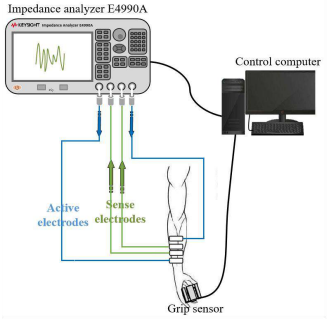

Fig.2. Experimental diagram

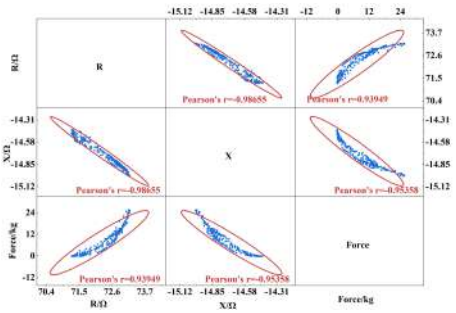

Fig.3. Correlation Analysis

validated whether BI has the potential to track muscle activity continuously. This summary designs muscle-sustained contraction experiments based on electromagnetic simulations to achieve mapping from BI to muscle activity.

The electrode configuration is an important influence on measuring surface BI. It is necessary to conduct an electromagnetic simulation of the electrode arrangement to determine the availability of the scheme. First, we used VINNO portable ultrasound Q5-7L (Suzhou, China) to collect the thickness of each tissue layer of the subject's forearm (from the wrist joint to the elbow joint) and calculated the average value as a basis for modeling. We constructed a human forearm finite element (FEM) electric field model in COMSOL Multiphysics 5.4. The forearm was equated to a four-layer cylinder, where the thickness of each tissue layer was set as follows: skin: 0.15 cm, fat: 0.9 cm, muscle: 3 cm, and bone: 3.4 cm. The dielectric parameters of each tissue layer were obtained from the database [5][6]. The FEM model is shown in Fig. 1(a). To track the changes in finger flexor muscle group activity

caused by finger flexion and extension, electrodes were pasted to the skin of the finger flexor muscle, with the two external electrodes as excitation electrodes and the two internal electrodes as sensing electrodes. The electromagnetic simulation follows the following principles: 1) Make the excitation current flow through the target area but not affect the sensing electrodes' work; 2) Make the excitation signal flow through the muscle layer as much as possible. We finally designed the electrode arrangement as shown in Fig. 1(a). In the electromagnetic simulation, the excitation current signal amplitude is 1 mA, the frequency is 50 kHz. After electromagnetic calculations, the current density distribution in the transverse slice of the model is shown in Fig. 1(b). The results showed that most of the current passed through the muscle layer, while almost no current passed through the bone layer. Therefore, this electrode configuration scheme meets the experimental requirements, and the measured impedance information mainly originates from the muscle layer.

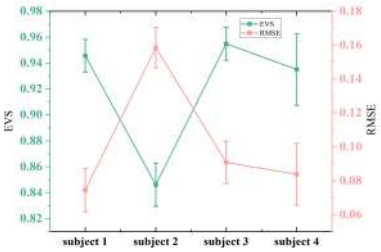

Fig.4. Predicted results

We conducted in vivo experiments based on the simulation results. The Keysight Agilent E4990A impedance analyzer (Keysight Technologies, USA) was used to obtain the impedance parameters of the finger flexor muscle. We used a tensile force transducer (DYLY-103, Freud, China) to simultaneously collect grip force, representing the different finger flexor muscle activity levels. Four subjects were asked to perform finger flexion and extension movements, and the experimental diagram is shown in Fig. 2. We conducted a correlation analysis between the resistance R, reactance X, and the grip force. The results are shown in Fig. 3, the red ellipse in the figure represents the 95% confidence interval. The results showed that R and X were highly correlated with grip force, and the absolute values of Pearsson's r were all greater than 0.93. It validated the results of the electromagnetic simulations and demonstrated the ability of BI to track changes in muscle activity.

To further verify impedance parameters can be used to characterize the degree of muscle activities, we restored the muscle activities by impedance parameters using a long and short-term memory network. The effect evaluated by explained variance score (EVS) with root mean square error (RMSE). After normalizing the data, R&X was used as the input to the network, and force was used as output. 75% of the data was used as the training set, and 25% was used as the test set. The prediction results for the four subjects are shown in Fig. 4. The average EVS of the subjects was 0.9204 ± 0.0502, and RMSE was 0.1027 ± 0.0380. In this paper, we designed an experimental scheme based on the simulation results and achieved the accurate reduction from BI to muscle activity with the help of artificial intelligence. It provides a more lightweight and simple design solution for wearable muscle continuous monitoring.

References

1. Wan, J. J., Z. Qin, and P. Y. Wang et al., "Muscle fatigue: general understanding and treatment," *Exp. Mol. Med.*, Vol. 49, No. 10, e384 – e384, 2017.
2. Appell, H. J., J. M. C. Soares and J. A. R. Duarte, "Exercise, muscle damage and fatigue," *Sports Med.*, Vol. 13, No. 2, 108 – 115, 1992.
3. Li, X., L. Li, and H. Shin et al., "Electrical impedance myography for evaluating paretic muscle changes after stroke," *IEEE Trans. Neural Syst. Rehabil. Eng.*, Vol. 25, No. 11, 2113 – 2121, 2017.
4. Li, L., H. Shin, and X. Li et al., "Localized electrical impedance myography of the biceps brachii muscle during different levels of isometric contraction and fatigue," *Sensors*, Vol. 16, No. 4, 581, 2016.
5. Gabriel, S., R. W. Lau and C. Gabriel, "The dielectric properties of biological tissues: III. Parametric models for the dielectric spectrum of tissues," *Phys. Med. Biol.*, Vol. 41, No. 11, 2271 – 2293, 1996.
6. Andreuccetti D., R. Fossi and C. Petrucci, "An Internet resource for the calculation of the dielectric properties of body tissues in the frequency range 10 Hz-100 GHz," *Inst. Appl. Phys.*, 1997.

Space-Division-Based Stroke Classification and Localization Using Wearable Microwave Sensing Technique

Zheng Gong[1] and Yifan Chen[1,2]*

[1]University of Waikato, New Zealand
[2]University of Electronic Science and Technology of China, China
*corresponding author: yifan.chen@uestc.edu.cn

Abstract: A novel microwave medical sensing method is proposed for fast stroke classification and localization, which utilizes space division of the region under examination (i.e., the head). The space division is enabled by the generalized scattering matrix theory and incorporates the brain anatomy. Then a novel decision tree learning method is proposed, which facilitates efficient stroke feature identification for classification. The classification accuracy and localization efficiency are shown to be greatly improved compared to the traditional method.

In microwave medical sensing (MMS), signals scattered from a region under examination (RUE) such as the human head are related to the RUE's geometric shape, internal structure, and electromagnetic properties. A wearable MMS system is shown in Fig. 1(a). The RUE structure is often highly complex, and it is difficult to characterize the spatial property of an anomaly without reconstructing the image. To solve this problem, we propose a novel space-division-based stroke classification and localization method. As shown in Fig. 1(b), the RUE is an enclosed area A, whereas the receiving antennas are outside A. Assume that there is an anomaly in the RUE; this feature will influence the electromagnetic responses at the receiving antennas. According to medical knowledge and anatomical structure, RUE is divided into multiple subareas by spatial partitioning. The generalized scattering matrix (GSM) theory is utilized to conduct an electromagnetic analysis on the space division, merging some of the subareas. The merging aims to ensure that the electromagnetic responses of different subareas are independent of each other. Thus, any anomaly present in a certain subarea will introduce highly location-selective signatures. Subsequently, if the RUE A is divided into several subareas, $A = \{A_1, \ldots, A_i, \ldots, A_I\}$. Each subarea separately satisfies the electromagnetic independence requirement based on GSM [1]. When an anomaly occurs in a certain A_i, this feature will produce a specific electromagnetic response. Based on this response, we can obtain the location information of the disease.

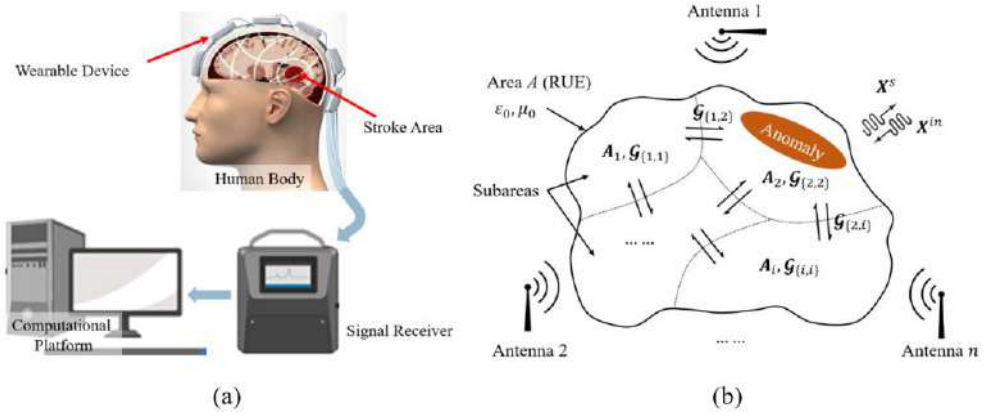

Fig. 1. (a) Architecture of the proposed system. (b) Pictorial illustration of the space-division-based method.

For each A_i, a stroke incidence probability α_i is assigned according to expert knowledge, where the risk set of A is $\alpha = \{\alpha_1, ..., \alpha_i, ..., \alpha_I\}$. Without loss of generality, let us assume that the subareas are sorted in risk so that A_1 has the highest risk in A and $\alpha_1 \geq \alpha_2 \geq \ldots \geq \alpha_I$. We now proceed to construct a decision-tree-based classifier. The criterion for decision-making is the incidence probability, where the highest-risk subarea should be selected.

Thus we first check A_1 for stroke classification. In this case, the root node has two branches, which are $\{A_1\}$ and $\{A_2, ..., A_i, ..., A_I\}$. If the stroke area is not in A_1, we would continue to the subarea with the second highest incidence probability A_2. As such, the detection sequence is obtained based on the incidence risks. Next, as there are two types of stroke, intracranial haemorrhage (ICH) and ischemic strok (IS). Linear discriminant analysis is utilized to distinguish ICH from IS due to its efficiency.

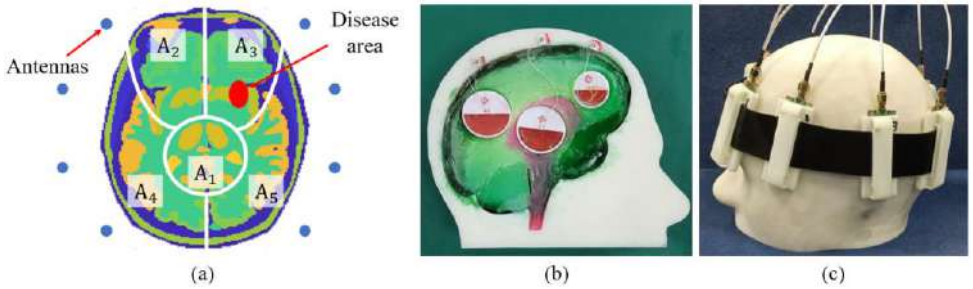

Fig. 2. (a) Brain structure and space division. (b) Head-mimicking phantom. (c) Wearable antenna array.

The brain area is divided into five subareas based on GSM and brain anatomy: basal ganglia region (BGR) A_1, left forebrain A_2, right forebrain A_3, left hindbrain A_4, right hindbrain A_5, as shown in Fig. 2(a). Then we define the incidence probabilities of these subareas as α_1 = 46%, α_2 = 20%, α_3 = 20%, α_4 = 7%, α_5 = 7% [2]. The disease area is randomly introduced to these subareas according to their corresponding incidence probabilities. Half of the manufactured human brain is shown in Fig. 2(b), and the experimental system setup with the wearable antenna array is shown in Fig. 2(c).

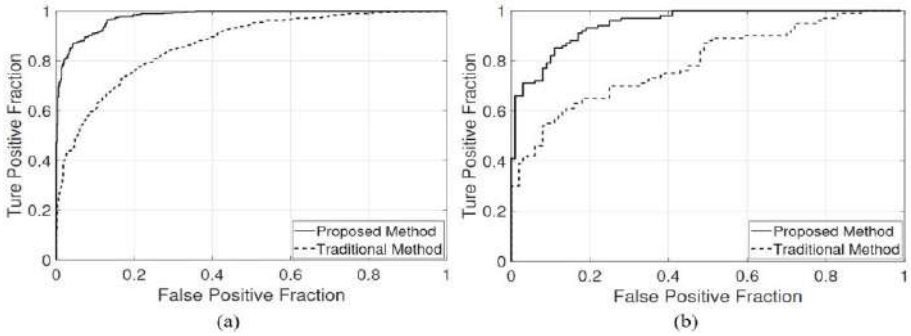

Fig. 3. (a) Simulation and (b) experimental results for proposed and traditional methods.

There are 1000 and 200 groups of simulation and experimental results in the database, respectively, and half of those are IS and the other half are ICH. The training set accounts for 70% of the database, whereas the test set accounts for 30%. For the classification performance, the receiver operating characteristic (ROC) curves of the proposed and traditional methods are shown in Fig. 3. For simulation results, the areas under the curve (AUCs) for the proposed and traditional methods are 0.97 and 0.85, respectively, which exhibits a 14.1% performance improvement. The localization accuracy of the proposed method is 94.2%. For experimental results, the AUC for the proposed and traditional methods are 0.93 and 0.78, respectively, which exhibits a 19.2% performance improvement. The localization accuracy of the proposed method is 90.5%. In addition, due to the decision tree learning method, the diagnosis time is significantly reduced, with a 21.1% efficiency improvement.

References

1. C. Wan and J. A. Encinar, "Efficient computation of generalized scattering matrix for analyzing multilayered periodic structures," *IEEE Trans. Antennas Propag.*, vol. 43, no. 11, pp. 1233–1242, 1995.
2. C. Nag, K. Das, M. Ghosh, and M. Khandakar, "Prediction of clinical outcome in acute hemorrhagic stroke from a single CT scan on admission," *North Amer. J. Med. Sci.*, vol. 4, no. 10, p. 463, 2012.

Advances in Sensor Technologies Involving Electrodynamics and Magnetism

Giant Magnetoimpedance Effect in amorphous microwires: from phenomenology to non-destructive composites monitoring

A. Zhukov[1,2,3,4], P. Corte-Leon[1,2,4], M. Ipatov[1,2], J.M. Blanco[2,4] and V. Zhukova[1,2,4]

[1] Dpto. de Polímeros y Materiales Avanzados, University of Basque Country, UPV/EHU, San Sebastian, Spain

[2] Dpto. de Fisica Aplicada, EIG, University of Basque Country, UPV/EHU, San Sebastian, Spain

[3]IKERBASQUE, San Sebastian and Bilbao, Spain

[4] EHU Quantum Center, University of the Basque Country, UPV/EHU, Spain.

[*]corresponding author: arkadi.joukov@ehu.es

Abstract: We provide extensive studies of the factors affecting the giant magnetoimpedance, GMI, effect value and magnetic field dependence in amorphous magnetic microwires. The high GMI effect as well as best magnetic softness have been observed in Co-rich microwires. However, specially designed postprocessing allows also to improve substantially the GMI effect and magnetic softness in less expensive Fe-rich microwires. The frequency dependence of the GMI effect is also substantially affected by the wire diameter. Considerable GMI effect is reported in thin microwires in the GHz frequency range. A new sensing technology is proposed that involves free space microwave spectroscopy using ferromagnetic microwires inclusions, exhibiting the GMI effect at GHz frequencies, for stress, temperature, and magnetic field monitoring in composites. The influence of conductive carbon fibers can be avoided by applying a low frequency modulation magnetic field, allowing to obtain the microwave signal from the composites containing carbon fibers.

Studies of the GMI effect have attracted considerable attention in the last few years owing to it suitability for various technological applications [1,2]. The origin of the GMI effect was explined in terms of the classical skin effect of a magnetic conductor as the penetration depth dependence of the AC current flowing through the magnetically soft conductor on applied magnetic field [1-3]. Commonly, the GMI effect is described as the magnetoimpedance ratio, ΔZ/Z, defined as:

$$\Delta Z/Z = [Z(H) - Z(H_{max})]/Z(H_{max}), \quad (1)$$

being H_{max} - the axial magnetic DC-field.

Cylindrical shape and high circumferential permeability observed in amorphous wires are quite favorable for achievement of high GMI effect [1-3]. With increasing the frequency, the GMI peaks are shifted to larger fields where sample is magnetically saturated. At this frequency range strong changes of the sample's impedance have been discussed in terms of the ferromagnetic resonance (FMR)[4,5]. Recently major attention is focused on high frequencies (GHz range) GMI applications owing to the development of thinner magnetically soft materials and recent tendency in miniaturization of magnetic field sensors [1,4]. Thus, thin microwire inclusions with the GHZ range GMI effect have been proposed for the development of tunable composites that allow wireless monitoring of stresses, temperature, and magnetic field [1, 5].

The purpose of this paper is present last results on the GMI effect in soft magnetic wires at high

frequencies and explore the application of such microwires in carbon containing tunable composites with thin microwires inclusions.

We measured magnetic field, H, dependences of impedance, Z, and ΔZ/Z(H) dependences in magnetic microwires prepared by the Taylor-Ulitovsky method in the frequency, *f*, range up to GHz frequencies. In amorphous materials characterized by the absence of magneto-crystalline anisotropy the main sources of magnetic anisotropy are the shape and magnetoelastic anisotropy, K_{me}, determined by the magnetostriction coefficient, λ_s, and the internal stresses, σ_i, by the relation [1]:

$$K_{me} = 3/2\ \lambda_s \sigma_i, \qquad (2)$$

Vanishing λ_s – values and better magnetic softness are observed in Co_xFe_{1-x} ($0 \leqslant x \leqslant 1$) or Co_xMn_{1-x} ($0 \leqslant x \leqslant 1$) systems at $0{,}03 \leq x \leq 0{,}08$ [1]. From ΔZ/Z(H) dependencies measured in Co-rich microwires with $\lambda_s \approx 0$ with but with different diameters, d (d=25.6 μm and d=10.8μm) was observed that thicker microwires present higher ΔZ/Z ratio at f=100 MHz. However, at 700 MHz higher ΔZ/Z ratio is observed for thinner microwire. Accordingly, there is arelationship between the optimal frequency for the GMI performance and the wire diameter: a trade-off between wire dimensions and frequency is required [1,4]. The diameter reduction must be associated with the increasing of the optimal GMI frequency range [1]. Magnetic softness and GMI of Fe-rich microwires with high and positive λ_s – values can be substantially improved by stress-annealing allowing induction of transverse magnetic anisotropy [1].

The integration of such ferromagnetic microwires into composite materials significantly modify the effective microwave response, allowing to obtain tunable composite material [5]. In the case of the composites containing carbon fibers, the surrounding conductive carbon fibers interfere in the microwave signal generated by ferromagnetic microwires. However, low frequency magnetic field modulation allows to detect the microwave signal from ferromagnetic microwires inclusions. These results demonstrate the capability for the integration of ferromagnetic microwire inclusions into structural carbon composite parts for wireless monitoring of external stimuli, such as applied stress, temperature or magnetic field.

References

[1] Zhukov, A., Corte-Leon, P., Gonzalez-Legarreta, L., Ipatov, M., Blanco, J.M., Gonzalez, A., Zhukova, V. “Advanced functional magnetic microwires for technological applications”, J. Phys. D: Appl. Phys., vol. 55, 253003, 2002.

[2] Phan, M.-H., Peng, H.-X. “Giant magnetoimpedance materials: Fundamentals and applications”, Prog.Mater. Science vol. 53, 323–420, 2008

[3] Panina L.V. and Mohri, K. “Magneto-impedance effect in amorphous wires”” Appl. Phys. Lett. vol. 65, 1189-1191, 1994.

[4] Ménard, D., Britel, M., Ciureanu, P. and Yelon,A. “Giant magnetoimpedance in a cylindrical conductor,” J. Appl. Phys., vol. 84, 2805–2814, 1998.

[5] Makhnovskiy, D., Zhukov, A., Zhukova, V. and Gonzalez, J. “Tunable and self-sensing microwire composite materials incorporating ferromagnetic microwires,” Advances in Science and Technology, Vol. 54, 201–210, 2008.

Sensing carbon fiber composites with continuous ferromagnetic microwires - electromagnetic and mechanical characterization

R. B. Garcia-Etxabe[1*], D. Pineda[1], B. Muniozguren[1], J. Malm[2], C. Johansson[2], V. Zhukova[3], M. Ipatov[3] and A. Zhukov[3,4]

[1]GAIKER Technology Centre, Basque Research and Technology Alliance (BRTA), Spain
[2]RISE Research Institutes of Sweden, Digital Systems, Göteborg, Sweden
[3] Dept. Advanced Polymers and Materials, and Dept. Appl. Phys. University of Basque Country, UPV/EHU, 20018 San Sebastian
[4]IKERBASQUE, Basque Foundation for Science, 48011 Bilbao, Spain

[*]corresponding author: etxabe@gaiker.es

Abstract: Short glass-coated ferromagnetic microwires have demonstrated their potential use as wireless sensors for structural composite parts. On the other hand, continuous microwires facilitate their integration into carbon non-crimp fabrics and the automation of the embedding process into industrial parts. However, composites with both carbon fibers and microwires inclusions have been studied in a very few papers. In this work we provide new experimental results on studies of the composites with glass-coated microwires aligned with the requirements of carbon composites. This work focuses on the free space microwave measurements of the composites made from the carbon fibers and ferromagnetic microwires inclusion focusing on electromagnetic properties and mechanical properties of continuous glass coated Co-rich ferromagnetic microwires.

One of the common problems in composite materials is wireless monitoring of stresses or temperature. Usually, the composites monitoring is performed by different sensors like pressure transducers and dielectric sensors or though the piezoelectric fibers with diameters of 10 to 100 μm [1]. However, employed sensors are not wireless or require plates for supplying electrical field, occupying a significant space. One of the recently proposed solutions for composites monitoring is a new sensing method involving free space microwave spectroscopy using inclusions of ferromagnetic microwires presenting high frequency magnetoimpedance with high sensitivity to applied stress, temperature and magnetic field [2]. Among the different families of magnetic wires, microwires with metallic nucleus diameters of 0.2 - 100 μm covered by insulating and flexible glass-coating and therefore presenting excellent mechanical and corrosive properties, are most suitable for the wireless monitoring of stresses and temperature of composites [3].

The integration of such ferromagnetic microwires into composite materials significantly modify the effective microwave response, making it possible to obtain a new tunable and self-sensing composite material [2]. The mechanical stress dependence of the magnetic switching field in glass coated microwires has enabled the development of sensors for bending or strain monitoring [4]. Magnetoimpedance (MI) and coercivity of microwires and its response to electromagnetic fields can be used to develop wireless stress sensors for composite materials [5]. Generally, highest MI effect is observed in Co-rich microwires [6]. However, previously only microwave behavior of composites with both carbon fibers and Fe-rich microwires have been reported in a very few papers [7].

In this paper, we present new experimental results on wireless monitoring of composites containing both

carbon fibers and ferromagnetic glass-coated microwires obtained during the development of the INFINITE (Horizon Europe) project. The INFINITE project aims to develop the know-how to develop and incorporate advanced sensing technology for the aerospace sector and demonstrate the capability for the integration of embedded sensors in structural carbon composite parts. However, several challenges have been found during the project development. Thus, the surrounding conductive carbon fibers interfere in the microwave signal generated by ferromagnetic microwires, making it difficult to be measured. On the other hand, the manufacturing processes involved require the use of continuous fibers, as yarns and non-crimped fabrics, and continuous and microwires are preferred.

Glass-coated Co-rich microwires with vanishing magnetostriction coefficients, λ_s, have been prepared by Taylor-Ulitovsky technique described elsewhere [3]. Hysteresis loops of single microwires have been measured using fluxmetric methods previously described elsewhere [6]. Additionally, we used the free space microwave measurement system, previously described elsewhere [2]. The reflection (R) and transmission (T) coefficients were measure in free-space. The experimental set-up consists of a pair of broadband horn antennas (1-17 GHz) and a vector network analyzer. The composites were placed in 60 x 60 cm^2 window to avoid the edge effects. In spite of the influence of the conductive carbon fibers, application of an external low frequency modulated magnetic field allows to sensitive and stable extraction of the response signal (R and T coefficients) from the ferromagnetic microwires inclusions.

In this work, the mechanical properties of Co-rich microwires have been also experimentally measured by determining the modulus and tensile strength and their resistance to bending deformation.

INFINITE project receives funding in the European Commission's Horizon 2022 Research Program under Grant Agreement Number 101056884.

References

1. Nelson, L. J. "Smart piezoelectric Fibre composites", Mat. Sci. and Tech., vol. 18, 1245-1256, 2002
2. Makhnovskiy, D., Zhukov, A., Zhukova, V. and Gonzalez, J. "Tunable and self-sensing microwire composite materials incorporating ferromagnetic microwires," Advances in Science and Technology, Vol. 54, 201–210, 2008.
3. Zhukov, A., Corte-Leon, P., Gonzalez-Legarreta, L., Ipatov, M., Blanco, J.M., Gonzalez, A., Zhukova, V. "Advanced functional magnetic microwires for technological applications", J. Phys. D: Appl. Phys., vol. 55, 253003, 2002.
4. Sabol, R., Rovnak, M., Klein, P., Vazquez, M. and Varga R., "Mechanical Stress Dependance of the switching field in amorphous microwires," IEEE Transactions on magnetics, Vol. 51, No. 1, 2015.
5. P. Marín, "Wireless Stress Sensor Based on Magnetic Microwires," Chapter from the book Magnetic Sensors – Development Trends and Applications, 2017.
6. Gonzalez-Legarreta, L., Corte-Leon, P., Zhukova, V., Ipatov, M., Blanco, J. M., Gonzalez, J., Zhukov, A. "Optimization of magnetic properties and GMI effect of Thin Co-rich Microwires for GMI Microsensors", Sensors, vol. 20, 1558, 2020.
7. Y. Luo, F. X. Qin, F. Scarpa, J. Carbonell, M. Ipatov, V. Zhukova, A. Zhukov, J. Gonzalez, L. V. Panina, and H. X. Peng, "Left-handed metacomposites containing carbon fibers and ferromagnetic microwires", AIP Advances vol. 7, 056110, 2017.

Magnetic properties and applications of glass-coated ferromagnetic microwires

V. Zhukova[1,2,3], P. Corte-Leon[1,2,4], M. Ipatov[1,2], J.M. Blanco[2,4] and A. Zhukov[1,2,3,4]

[1] Dpto. de Polímeros y Materiales Avanzados, University of Basque Country, UPV/EHU, San Sebastian, Spain

[2] Dpto. de Fisica Aplicada, EIG, University of Basque Country, UPV/EHU, San Sebastian, Spain

[3]EHU Quantum Center, University of the Basque Country, UPV/EHU, Spain.

[4]IKERBASQUE, San Sebastian and Bilbao, Spain

[*]corresponding author: valentina.zhukova@ehu.es

Abstract: The impact of post-processing on soft magnetic properties and the giant magnetoimpedance (GMI) effect of Fe- and Co-based glass-coated microwires is evaluated. A remarkable improvement of magnetic softness and GMI effect is observed in Fe-rich glass-coated microwires subjected to stress annealing. Frequency dependence of GMI ratio of stress-annealed Fe-rich microwires has been discussed considering frequency dependence of the skin penetration depth, δ, as well as magnetic anisotropy distribution within the metallic nucleus. Annealed and stress-annealed Co-rich microwires present rectangular hysteresis loop and single and fast domain wall propagation. However, Co-based stress-annealed microwires present high magnetoimpedance ratio. Observed stress-induced anisotropy and related changes of magnetic properties are discussed considering internal stresses relaxation and "back-stresses"

Development of magnetic sensors is focused on the miniaturization of their size, improvement of their features and on finding of new materials. Among new magnetic materials a family of thin wire with reduced dimensions recently gained considerable attention [1]. Glass-coated magnetic microwires prepared using the Taylor-Ulitovsky technique with thin metallic nucleus (typically with diameters 0.5 to 50 μm) covered by flexible, insulating and biocompatible glass are therefore quite interesting for sensor applications [2]. This technique allows preparation of the thinnest rapidly quenched wires with amorphous or crystalline structure of metallic nucleus. Good magnetic properties can be observed either in crystalline or in amorphous magnetic wires, but amorphous magnetic wires present several advantages, such as superior mechanical properties, the absence of the microstructure defects (grain boundaries, crystalline texture, dislocations, point defects,…) [2] and hence precise post-processing is not required.. Particularly, amorphous microwires can present giant magneto-impedance (GMI) or magnetic bstability. In the case of glass-coated microwires the magnetoelastic anisotropy contribution becomes relevant since the preparation process involves not only the rapid quenching itself, but also simultaneous solidification of the metallic nucleus surrounded by non-magnetic glass-coating with rather different thermal expansion coefficients [2].

The purpose of this paper is present last results on tailoring of soft magnetic properties and GMI effect in glass-coated microwires paying special attention to achievement of high GMI effect and on optimization of domain wall dynamics.

Studied Co-rich and Fe-rich as-prepared microwires present rather different magnetic properties and hence GMI effect: Fe-rich microwires present perfectly rectangular hysteresis loops exhibiting magnetic

bistability and coercivity, H_c, of the order of 50 A/m. In contrast Co-rich microwires present linear hysteresis loops with an order of magnitude lower H_c.

Stress annealing of Fe based microwires allows considerable magnetic softening (H_c decrease) and inducing of transverse magnetic anisotropy. Magnetic properties are considerably affected by the stress, σ_m, applied during the stress annealing: induced transverse magnetic anisotropy becomes more noticeable with increasing of σ_m -values. Accordingly, remarkable improvement of GMI ratio is observed in stress-annealed Fe–rich ($Fe_{75}B_9Si_{12}C_4$) microwires: improvement of $\Delta Z/Z$ –values by an order of magnitude is achieved.

As recently reported elsewhere [1] upon annealing the hysteresis loop of Co-rich microwires becomes rectangular presenting considerable magnetic hardening.. However, stress-annealed Co-rich microwires ($Co_{69.2}Fe_{4.1}B_{11.8}Si_{13.8}C_{1.1}$) microwires present lower coercivity as compared to annealed without stress Co-rich microwires.

Hysteresis loops of Co-rich microwires observed after stress-annealing at low annealing temperature or σ_m –values present features similar to that of Fe-rich microwires and annealed Co-rich microwires, i.e. rectangular shape that must be related to presence of single and large Barkhausen jump and induced magnetic bistability. Therefore, similarly to annealed without stress Co-rich microwires, stress-annealed Co-rich microwires present single domain wall (DW) propagation.

Consequently, stress annealing of ferromagnetic microwires allows achievement of interesting combination of magnetic properties. In the Fe-rich microwires stress-annealing allows remarkable improvement of magnetic softness and GMI effect. Stress-annealed Co-rich microwires can simultaneously present single and fast domain wall (DW) propagation and high GMI effect.

References

[1] Zhukov, A., Corte-Leon, P., Gonzalez-Legarreta, L., Ipatov, M., Blanco, J.M., Gonzalez, A., Zhukova, V. “Advanced functional magnetic microwires for technological applications”, J. Phys. D: Appl. Phys., vol. 55, 253003, 2002.

[2] Herzer, G., Amorphous and nanocrystalline soft magnets, in Proceedings of the NATO Advanced Study Insititute on Magnetic Hysteresis in Novel Materials, Mykonos, Greece, 1-12 July 1996 ed. George C. Hadjipanayis, NATO ASI Series (Series E:Applied Sciences) Vol. 338, pp.711-730. Kluwer Academic Publishers (Dordrecht/Boston/London) 1997.

Non-plane Surface Magnetic Structures in Cylindrical Magnetic Microwires

A. Chizhik[1*], P. Corte-Leon[1,2], V. Zhukova[1,2], J. Gonzalez[1], P. Gawronski[3] and A. Zhukov[1,2,4]

[1]Department of Polymers and Advanced Materials: Physics, Chemistry and Technology, Facultad de Quimica, Universidad del País Vasco UPV/EHU, San Sebastian, Spain

[2]Department Applied Physics I, EUPDS, UPV/EHU, 20018, San Sebastian, Spain

[3]AGH University of Science and Technology, Faculty of Physics and Applied Computer Science, 30-059, Krakow, Poland

[4]IKERBASQUE, Basque Foundation for Science, Bilbao, Spain

[*]corresponding author: oleksandr.chyzhyk@ehu.es

Abstract: We studied the magneto-optical and magnetic behavior of Co- and Fe-rich microwires that were stress-annealed at temperatures distributed along the microwire length. There was a transformation of the magnetic structure across zones subjected to annealing at different temperatures. We propose a route to design graded magnetic anisotropy in a magnetic microwire.

We report the magneto-optical and magnetic study of Co-rich and Fe-rich microwires stress-annealed with graded magnetic anisotropy distributed along the microwire length. The graded magnetic anisotropy has been obtained by stress-annealing of microwires at variable annealing temperatures [1]. The transformation of the magnetic structure was fixed as it moved through the regions subjected to annealing at different temperatures (Fig. 1). Changes on the surface and in the volume were found in two types of the investigated microwires. The formation or the transformation of magnetic structures was observed depending on the type of microwire. For the first time, the effect of annealing on the magnetic system was recorded at a sufficiently low annealing temperature.

The magnetostriction coefficient that determines the features of the magnetic structures has opposite signs in Fe- and Co-rich microwires. These two classes of complementary materials form the basis for a wide class of magnetic sensors. A comparative analysis of surface and volume magnetic reversal processes was a supplementary objective of this study.

A spatial distribution of circular, elliptic, spiral and axial magnetic structures was observed. In particular, in Co-rich microwires, the existence of two different types of helical magnetic structure with a distributed degree of helicity was fixed by the MOKE microscopy.

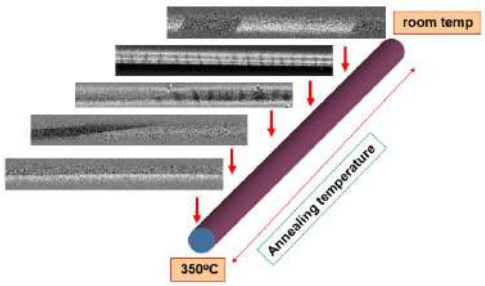

Fig. 1. Magnetic structures distribution along the microwire.

A theoretical analysis was performed on the basis of the assumption that, for a magnetostrictive microwire, the cylindrical symmetry of the wire limits the stress to radial, circumferential and axial components (i.e., a different

stress along each axis). The results of calculation are presented in Figure 2 as a half-tube. The colours (red and blue) correspond to two opposite axial magnetization orientations.

This analysis has demonstrated that the domain structure consists of two types of domain structures (Fig. 2). The domains of the type I (red colour) consist of inner parts and outer parts that leads to their low mobility. The superficially located domains of the type II have a higher mobility. All this determines the diversity of the magnetization reversal process in microwires.

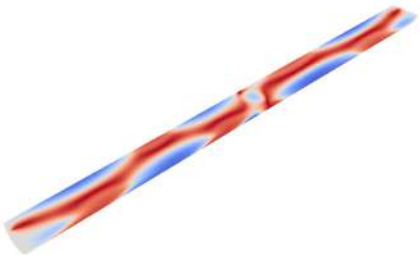

Fig. 2. Calculated images of domain structure inside the microwire.

The observer variety of magnetic structures could be used to expand the possibilities of fine tuning a magnetic system in the search for optimal magnetic structures in microwires used in magnetic sensors.

References

1. P. Corte-León, P., V. Zhukova, J.M. Blanco, A. Chizhik, M. Ipatov, J. Gonzalez, A. Fert, A. Alonso and A. Zhukov, “Engineering of domain wall propagation in magnetic microwires with graded magnetic anisotropy,”Applied Materials Today, Vol. 26, 101263, 2022.

Smart Electromagnetic Skins and their Applications

Preliminary study of reconfigurable Orbital Angular Momentum beams with Liquid Crystal metasurface at mmWave

P. de la Rosa[1,2*], R. Guirado[1], G. Perez-Palomino[1], M. Caño-García[2], E. Carrasco[1]

[1] Applied Electromagnetism Group (GEA), Information Processing and Telecommunications Center (IPTC), ETSI Telecomunicación, Universidad Politécnica de Madrid, Spain
[2]CEMDATIC, ETSI Telecomunicación, Universidad Politécnica de Madrid, Spain
[*]Corresponding author: p.delarosa@upm.es

Abstract

Generation of beams carrying orbital angular momentum can be of great interest if achieved in the mmWave range, since it has the potential to generate orthogonal channels. A preliminary approach to its generation using Liquid Crystal metasurfaces and a potential simplification of their addressing are presented.

Introduction

The Orbital Angular Momentum (OAM) of a beam is related to a helical phase profile orthogonal to the propagation direction. The electric field of the beam can be described by:

$$E(r,\theta) = A(r) \cdot e^{jl\theta} \quad (1)$$

where $A(r)$ is the amplitude component, l is the topological charge and θ is the azimuthal angle. It can be derived from it, that at the beam axis, a singular point of zero intensity (termed vortex) emerges from the superposition of all phase values ranging from 0 to $2\pi \cdot l$. The topological charge, l, describes the number of intertwined helices in a wavelength. The existence of such vortices in light beams was first described by Berry [1], and has since attracted increasing interest mainly in optical wavelengths owed to their vast range of applications [2]. Of the many applications, it is of special interest the ability of vortex carrying beams (VBs) to be used in communications, since beams with equal frequency and polarization, but different topological charge are orthogonal to each other. However, in RF, this phenomenon has not yet been studied in depth [3][4], since the beam collimation in RF, compared to that of a laser, is not enough to receive the whole ring pattern intrinsic to VBs.

Two main techniques are used, in optics, to generate beams carrying vortices, which are Spatial Light Modulators (SLMs) and purposed built Spiral Phase Plates (SPPs) [2], of which both passive and reconfigurable devices exist. Analogous devices could be designed in RF to achieve its generation.

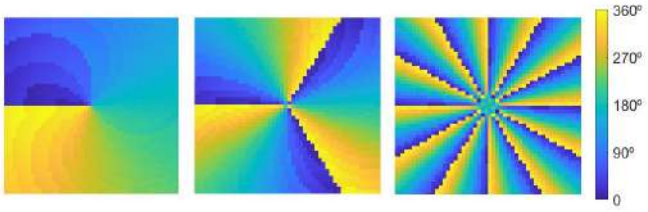

Figure 1. Phase profiles of reflected beams using the S parameters for the planar incident beam and l = 1, 3, 12

Liquid Crystal (LC) based reflectarray antennas could be a good candidate to reproduce the behavior of such optical devices at mmWave, stemming from LC's inherent reconfigurability, feasible addressing techniques and low costs. Limitations regarding the addressing appear when trying to achieve 3-D beam reconfigurability [5] using direct addressing of each pixel, which becomes increasingly difficult as the total number of pixels in a 2D matrix increases.

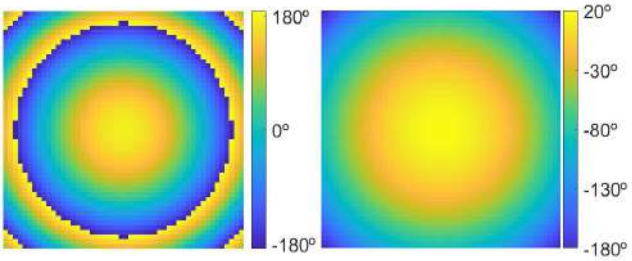

Figure 2. Incident beams phase profile.

Through this work, a preliminary approach to the generation of OAM carrying beams at mmWave is presented. First, a general approach with 2-D addressing (for 3-D beam reconfigurability) is presented, followed by a short overview of the potential design of purposed built reflectarrays with custom electrodes, that would allow for a substantial simplification of the addressing techniques while maintaining the functionality.

Preliminary Results

A reflectarray cell [6] has been simulated using CST Studio for different LC dielectric permittivities, which induces a varying phase delay with 360º range over a 5 GHz approximate bandwidth. Simulations take into account the behavior and losses of the LC. With it, a reflectarray antenna has been simulated which allows for the generation of different topological charge VBs (Fig. 1). Two incident beams have been considered (Fig. 2), one with sharper phase profile (20 cm distance from the cell), to reproduce the behavior of a reflectarray, and another one with a phase profile closer to that of a planar wave (200 cm distance from the cell), to reproduce the behavior of a reconfigurable intelligent surface (RIS).

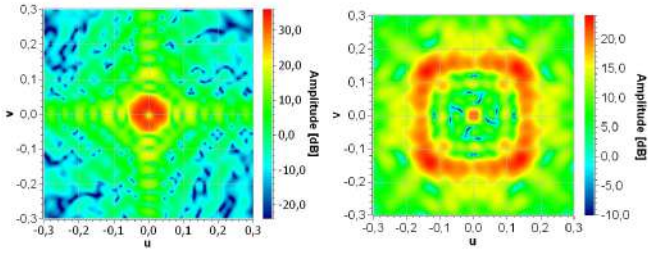

Figure 3. Far field radiation pattern simulated using GRASP for l = 1, 12, where the vortex at the beam axis can be seen, and follows the expected increase in size [3]

The simulation results show the expected azimuthal variation of the phase profile (Fig. 1), with certain aberrations resulting from the discretization in pixels of the RIS. Additionally, the amplitude profile shows the expected vortex at the beam axis (Fig. 3), for two generated VBs with different topological charge.

All simulations have been done assuming individual addressing of each pixel of a 50x50 matrix, which in practice would entail a very complex 2-D addressing to achieve such results. However, by using the azimuthal phase variation, electrodes resembling pie slices [3] could be designed and more directly addressed, thus greatly simplifying the generation of VBs.

This work was supported in part by the Spanish Ministry of Science and Innovation and the Spanish Agency for Research within projects ENHANCE-5G (PID2020-114172RB-C22/AEI/10.13039/501100011033) and TSI-063000-2021-83, and by the European Union's Horizon 2020 Framework Programme for Research and Innovation: ARIADNE project, under grant agreement no.871464. R. Guirado acknowledges the support of a fellowship from "La Caixa" Foundation (ID 100010434). The fellowship code is LCF/BQ/DR21/11880029. M. Cano-García is grateful to Spanish government grant (BG20/00136).

References

1. Berry, M. V. et al. "Optical vortices evolving from helicoidal integer and fractional phase steps." J. Opt. A: Pure Appl. Opt., Vol. 6, No. 2, 259–268, 2004.

2. Caño-García, M. and X. Quintana. et al. "Dynamic multilevel spiral phase plate generator," Sci Rep, Vol. 8, No. 1, 15804, 2018.

3. Tamburini, F. et al. "Encoding many channels on the same frequency through radio vorticity: first experimental test," New J. Phys., Vol. 14, No. 3, 033001, 2012.

4. Tamagnone, M. et al. "Comment on `Encoding many channels on the same frequency through radio vorticity: first experimental test'," New J. Phys., Vol. 14, No. 11, 118001, 2012.

5. Perez-Palomino, G. et al. "Liquid Crystal Based Beam Scanning Reflectarrays and Their Potential in SATCOM Antennas: 11th European Conference on Antennas and Propagation," EUCAP., Proceedings, 3428-3431, 2017.

6. Perez-Palomino, G. et al. "Design and Demonstration of an Electronically Scanned Reflectarray Antenna at 100 GHz Using Multiresonant Cells Based on Liquid Crystals," IEEE TAP., Vol. 63, No. 8, 3722-3727, 2015

Reflection Loss Assessment of Reflecting Intelligent Surfaces

F. Costa[1], **M. Borgese**[2]

[1]Dipartimento di Ingegneria dell'Informazione, Università di Pisa, Italy
[2]Research and Development Department, SIAE MICROELETTRONICA, 20093 Cologno Monzese, Italy
[*]corresponding author: filippo.costa@unipi.it

Abstract: Reconfigurable Reflecting Intelligent Surfaces represent a valid solution for future 6G communications but face practical implementation challenges such as limited tuning range of diodes and losses caused by their presence. The paper focuses on the impact of diode series resistor on RIS performance, highlighting the importance of minimizing losses.

In recent years, Reflecting Intelligent Surfaces (RISs) have become a highly investigated solution for wireless communication systems [1]. The concept behind RISs is to manipulate the phase and amplitude of incident signals by adjusting the impedance of the surface [2], [3]. This can be achieved by using reconfigurable RISs, which allow for dynamic changes to the impedance and reflectivity in real-time [4], [5].

The reconfigurable nature of RISs brings numerous benefits to wireless communication systems, such as improved spectral efficiency, increased coverage, and reduced interference [6]. There are various methods to achieve reconfigurability in RISs, including using Varactor Diodes [7]–[9], PIN Diodes [10], [11], and MEMS [12].

By applying a varying bias voltage to varactor diodes, the impedance of the surface can be adjusted, resulting in a range of reflection coefficients for incident signals. However, there are also challenges associated with reconfigurable RISs. One of these challenges is the limited tuning range of varactor diodes, which restricts the range of impedances that can be realized by the RIS [13]. Additionally, the high series resistance of the diodes can result in substantial reflection losses, which can negatively impact the overall performance of the RIS.

In addition to losses caused by the presence of diodes, there are other factors that affect the efficiency of Reflecting Intelligent Surfaces (RISs). For example, the use of materials such as glass-reinforced epoxy laminate (FR4), which are cost-effective but also have high loss properties, can result in losses. Furthermore, the flow of current on imperfect conductors and losses in the active components can lead to ohmic losses. Minimizing the effect of these losses is critical, and it has been found that a small periodicity of the lattice is an effective way to achieve this [14]. In fact, designing the pattern with a small period not only reduces losses but also leads to a wider bandwidth for the RIS, thus improving its overall performance [15], [16]

Studies in the literature have investigated the behavior of varactor diodes, the key components of RISs, at microwave frequencies. However, it has been discovered that the actual resistor value of the diodes is significantly different from the one specified in the data sheet, and the series resistance is often much higher than expected [17]. Given these findings, it is critical to assess the reflection losses of RISs when the series resistor exceeds 2 ohms.

This paper aims to provide a comprehensive evaluation of the reflection losses of RISs, focusing on the impact of the diode series resistor on the performance of the RIS.

References

[1] Q. Wu and R. Zhang, 'Towards Smart and Reconfigurable Environment: Intelligent Reflecting Surface Aided Wireless Network', *IEEE Commun. Mag.*, vol. 58, no. 1, pp. 106–112, Jan. 2020, doi: 10.1109/MCOM.001.1900107.

[2] S. Abeywickrama, R. Zhang, Q. Wu, and C. Yuen, 'Intelligent Reflecting Surface: Practical Phase Shift Model and Beamforming Optimization', *IEEE Trans. Commun.*, vol. 68, no. 9, pp. 5849–5863, Sep. 2020, doi: 10.1109/TCOMM.2020.3001125.

[3] D. Dardari, 'Communicating With Large Intelligent Surfaces: Fundamental Limits and Models', *IEEE J. Sel. Areas Commun.*, vol. 38, no. 11, pp. 2526–2537, Nov. 2020, doi: 10.1109/JSAC.2020.3007036.

[4] C. Pan *et al.*, 'Reconfigurable Intelligent Surfaces for 6G Systems: Principles, Applications, and Research Directions', *IEEE Commun. Mag.*, vol. 59, no. 6, pp. 14–20, Jun. 2021, doi: 10.1109/MCOM.001.2001076.

[5] E. Björnson, Ö. Özdogan, and E. G. Larsson, 'Reconfigurable Intelligent Surfaces: Three Myths and Two Critical Questions', *IEEE Commun. Mag.*, vol. 58, no. 12, pp. 90–96, Dec. 2020, doi: 10.1109/MCOM.001.2000407.

[6] C. Huang, A. Zappone, G. C. Alexandropoulos, M. Debbah, and C. Yuen, 'Reconfigurable Intelligent Surfaces for Energy Efficiency in Wireless Communication', *IEEE Trans. Wirel. Commun.*, vol. 18, no. 8, pp. 4157–4170, Aug. 2019, doi: 10.1109/TWC.2019.2922609.

[7] A. Araghi *et al.*, 'Reconfigurable Intelligent Surface (RIS) in the Sub-6 GHz Band: Design, Implementation, and Real-World Demonstration', *IEEE Access*, vol. 10, pp. 2646–2655, 2022, doi: 10.1109/ACCESS.2022.3140278.

[8] R. Fara, P. Ratajczak, D.-T. Phan-Huy, A. Ourir, M. Di Renzo, and J. de Rosny, 'A Prototype of Reconfigurable Intelligent Surface with Continuous Control of the Reflection Phase', *IEEE Wirel. Commun.*, vol. 29, no. 1, pp. 70–77, Feb. 2022, doi: 10.1109/MWC.007.00345.

[9] F. Costa and M. Borgese, 'Electromagnetic Model of Reflective Intelligent Surfaces', *IEEE Open J. Commun. Soc.*, vol. 2, pp. 1577–1589, 2021, doi: 10.1109/OJCOMS.2021.3092217.

[10] J.-B. Gros, V. Popov, M. A. Odit, V. Lenets, and G. Lerosey, 'A Reconfigurable Intelligent Surface at mmWave Based on a Binary Phase Tunable Metasurface', *IEEE Open J. Commun. Soc.*, vol. 2, pp. 1055–1064, 2021, doi: 10.1109/OJCOMS.2021.3076271.

[11] H. Yang *et al.*, 'A 1-Bit 10×10 Reconfigurable Reflectarray Antenna: Design, Optimization, and Experiment', *IEEE Trans. Antennas Propag.*, vol. 64, no. 6, pp. 2246–2254, Jun. 2016, doi: 10.1109/TAP.2016.2550178.

[12] F. Yang, P. Pitchappa, and N. Wang, 'Terahertz Reconfigurable Intelligent Surfaces (RISs) for 6G Communication Links', *Micromachines*, vol. 13, no. 2, Art. no. 2, Feb. 2022, doi: 10.3390/mi13020285.

[13] F. Costa and M. Borgese, *Circuit Modelling of Reflecting Intelligent Surfaces*. 2021, p. 550. doi: 10.1109/SPAWC51858.2021.9593104.

[14] F. Costa and A. Monorchio, 'Closed-Form Analysis of Reflection Losses in Microstrip Reflectarray Antennas', *IEEE Trans. Antennas Propag.*, vol. 60, no. 10, pp. 4650–4660, Oct. 2012, doi: 10.1109/TAP.2012.2207318.

[15] D. M. Pozar, 'Wideband reflectarrays using artificial impedance surfaces', *Electron. Lett.*, vol. 43, no. 3, p. 1, 2007.

[16] F. Costa, S. Genovesi, and A. Monorchio, 'On the Bandwidth of High-Impedance Frequency Selective Surfaces', *IEEE Antennas Wirel. Propag. Lett.*, vol. 8, pp. 1341–1344, 2009, doi: 10.1109/LAWP.2009.2038346.

[17] K. Omoto, T. Tomura, and H. Sakamoto, 'Proof-of-Concept on Misalignment Compensation for 5.8-GHz-Band Reflectarray Antennas by Varactor Diodes', *IEEE Access*, vol. 9, pp. 54101–54108, 2021, doi: 10.1109/ACCESS.2021.3071090.

Preliminary Results on Conformal Reflective Surfaces for Urban Scenarios

M. Beccaria[1*], A. Mazzinghi[2], A. Massaccesi[1], A. Freni[2] and P. Pirinoli[1]

[1]Department of Electronics and Telecommunications, Politecnico di Torino, Turin, Italy
[2]Department of Information Engineering, University of Florence, Florence, Italy
[*]corresponding author: michele.beccaria@polito.it

Abstract: In this communication, the results of a preliminary analysis on the possibility to use a curved passive smart electromagnetic skin working at millimeter waves to be mounted on street light or stop light poles are presented. In particular, the radiation properties of the curved surface are studied and compared with those of a planar solution, taking also into account the visual impact and the possibility to rotate the surface around the supporting pole.

The need for the next generation of communication systems to provide huge data rates with very low latency, ubiquitous mobile ultra-broadband connectivity, seamless coverage, and reduced power consumption pushed the research interest to find new solutions to satisfy these requirements. If, on one side, the use of the mm-wave frequencies presents several advantages, on the other, the larger attenuation and stronger interaction with obstacles along the propagation path can cause a degradation of the services in those regions that are not in the line-of-sight of the base station antennas. To limit their spread, Smart Electromagnetic Skins (SESs) can be introduced in the environment in which the propagation occurs [1-2]. They are very thin surfaces, consisting of many elements with resonant or subwavelength size, able to provide anomalous reflections. Depending on the scenario in which they are introduced, they could be passive structures [3], but, if necessary, they could also include active elements to provide coverage reconfigurability [4]. Usually, SESs are assumed planar to be integrated on walls of buildings. However, this solution is not always feasible, as for example, in historical city centers or on buildings with plenty of windows. Thus, other supporting structures must be used, such as the street light or the stop light poles (see the scheme in Fig. 1a). For the latter cases, the use of a curved instead of a planar reflecting surface seems convenient to reduce its visual impact and allow the SES to be illuminated by the field arriving from different base stations.

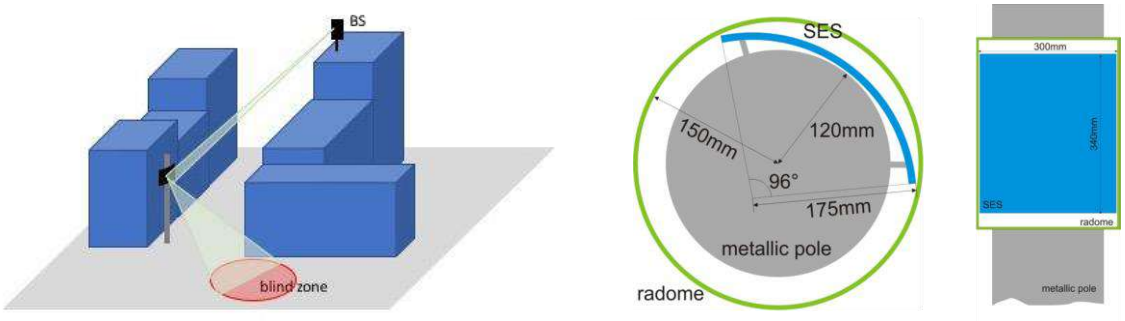

(a) (b)

Figure 1: (a) Example of the considered environment, where the SES is used to cover blind zones for the base station antenna. (b) Top and side view of the SES.

To assess the feasibility and the performance of a curved SES, a configuration as the one shown in Fig. 1b,

designed to be mounted on a light pole with a diameter of 240 mm and protected by a radome concentric to the pole, with a diameter of 300 mm, is considered. Note that in the present analysis the effect of the radome on the performance of the SES is assumed negligible, but it is used to have an indication of the size of the reflecting surface that can be introduced between it and the pole.

Even if SESs can be realized either with resonant or sub-wavelength unit-cells, here the first choice is adopted. Moreover, since the required bandwidth is less than 10%, a simple re-radiating element is selected, i.e., a square patch printed on a single layer of Dicald527, with thickness h = 0.8 mm, relative dielectric constant $\varepsilon_r = 2.55$ and losses characterized by $\tan\delta = 0.017$. The unit-cell has a size equal to $\lambda/2$ at the upper bound of the considered frequency range f = 27.5 GHz. The surface, that has size of 300 mm × 340 mm, is therefore discretized with 55×62 elements.

The performance of the curved SES is compared with that of two different planar reflecting surfaces with the same height of the curved one. The first one has a width of 180 mm to stay between the pole and the radome. The width of the second configuration is instead fixed in such a way that the reflected main beam has the same HPBW of the curved SES, and it is equal to 266 mm. In Fig. 2a the top and side views of the two planar SESs are shown. The three configurations are designed to provide a reflection in the direction ($\theta_r = 110°, \varphi_r = 30°$) with respect to the coordinate system indicated in Fig. 2a, when an incident plane wave is impinging on the surface with angles ($\theta_{inc} = 90°, \varphi_{inc} = -20°$) and then their radar cross section (RCS) is evaluated. The obtained patterns in the plane $\theta_r = 110°$ are plotted in Fig. 2b. It is worth noting that the curved SES has a maximum RCS comparable to that of the larger planar SES, which however is too large to stay behind the radome.

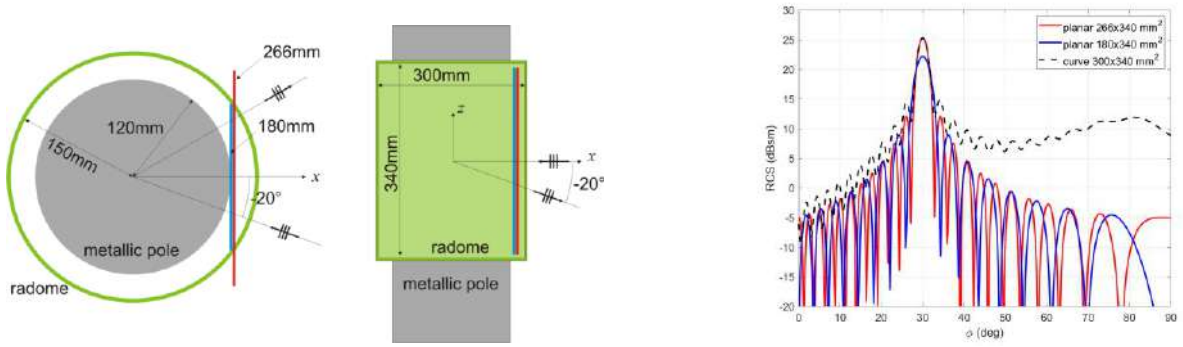

(a) (b)

Figure 2: (a) Top and side view of the planar SESs. (b) Evaluated RCS in the $\theta_r = 110°$ plane.

References

1. Erricolo, D., A. Rozhkova and A.C. Stutts, "Towards Smart Electromagnetic Environments," Computing, Comm. and IoT Applications, 2021, pp. 361-366.
2. Oliveri, G., F. Zardi, P. Rocca, M. Salucci and A. Massa, "Building a Smart EM Environment -AI-Enhanced Aperiodic Micro-Scale Design of Passive EM Skins," IEEE Trans. Ant. and Propag., Vol. 70, No. 10, 8757-8770, 2022.
3. Martinez-de-Rioja, E., et al. "Passive intelligent reflecting surfaces based on reflectarray panels to enhance 5G millimeter-wave coverage," Int. Journal of Microw. and Wireless Tech., pp. 1-12, 2022.
4. Degli-Esposti, V., E.M. Vitucci, M. Di Renzo and S. Tretyakov, "Reradiation and Scattering from a Reconfigurable Intelligent Surface: A General Macroscopic Model," IEEE Trans. Ant. and Propag., Vol. 70, No. 10, 8691-8706, 2022.

Smart Skin-Enabled Communications Exploiting Surface Waves

T. Arshed, S. Maci, and E. Martini*

Department of Information Engineering and Mathematics, University of Siena, Siena, Italy
*corresponding author: martini@dii.unisi.it

Abstract: This contribution presents an innovative approach based on the use of smart electromagnetic skins to meet the stringent requirements of future wireless networks in complex environments experiencing non line of sight conditions. The approach is based on the combination of radiative wave and surface wave propagation, enabled by artificial surfaces properly designed to perform efficient wave conversion and routing.

The continuous grow of the request for massive and ubiquitous multimedia information access calls for new communication paradigms, capable to satisfy latency, reliability and data rate requirements beyond the capacity of existing 5G systems. One of these is based on the concept of Smart Radio Environment (SRE), in which the environment is controlled and programmed jointly with the transmitters and receivers, rather than something to compensate for. The key technology underpinning SREs is represented by smart skins, or metasurfaces (MTSs), artificial surfaces consisting of electrically small elements that can be designed to control electromagnetic fields. MTSs do not require signal processing nor signal amplification processes, so they have an extremely low power consumption, and they can process EM signals directly at the speed of light, dramatically reducing latency and complexity with respect to corresponding fully digital solutions. In this context, the most popular approach relies on the use of large surfaces re-route radio waves intelligently toward intended user terminals, possibly in a dynamic and programmable way [1]. An alternative approach, that has been proposed in [2], uses engineered MTSs to guide surface waves (SWs) to reduce losses related to open-space radio propagation.

In this paper we discuss how open-space radio propagation and SW propagation can be conveniently combined to address “see around the corner” issues in complex wireless scenarios. The basic idea is to first convert the signal coming from the base station into a SW mode, then guide the SW along a desired path and finally transform it into a radiative wave directed towards the intended user. The building block for the effective realization of this functionality is the MTS realizing an efficient conversion between radiative wave and SW and vice versa [3]-[4]. This conversion is based on a periodic modulation of the equivalent boundary conditions (BCs), that, through the generation of a series of Floquet modes, will couple space and surface waves, according to the same mechanism exploited to design leaky wave antennas [5]. A systematic design procedure will be presented to maximize conversion efficiency and minimize spurious radiation towards undesired directions. The design is first performed at homogenized BCs level and then converted into a practically realizable structure consisting of metallic patches printed over a grounded dielectric slab.

The proposed solution is aimed to assist the wireless connectivity, reliability, throughput, and localization especially in complex indoor environments, with a low-cost, zero-latency, full-duplex, low-complexity, and green technology.

E. Martini gratefully acknowledges the support of the University of Siena through the funding of a Curiosity driven (F-CUR) project in the framework of the program PSR 2021.

References

1. Di Renzo, M., Debbah, M., Phan-Huy, DT. et al., "Smart radio environments empowered by reconfigurable AI meta-surfaces: an idea whose time has come," *J Wireless Com Network* 2019, 129, 2019.
2. Wong, K. -K., K. -F. Tong, Z. Chu and Y. Zhang, "A Vision to Smart Radio Environment: Surface Wave Communication Superhighways," in *IEEE Wireless Communications*, Vol. 28, No. 1, pp. 1064–1076, February 2021.
3. Sun, S., Q. He, S. Xiao, Q. Xu, X. Li, and L. Zhou, "Gradient-index meta-surfaces as a bridge linking propagating waves and surface waves," *Nat. Mater*. 11, pp. 426, 2012.
4. Tcvetkova, S. N., D.-H. Kwon, A. Díaz-Rubio, and S. A. Tretyakov, "Near-perfect conversion of a propagating plane wave into a surface wave using metasurfaces," *Phys. Rev. B*, 97, 115447 – Published 28 March 2018.
5. Minatti, G., F. Caminita, E. Martini and S. Maci, "Flat Optics for Leaky-Waves on Modulated Metasurfaces: Adiabatic Floquet-Wave Analysis," in *IEEE Transactions on Antennas and Propagation*, vol. 64, no. 9, pp. 3896-3906, Sept. 2016.

Some Notes on the Electromagnetic Field Processing in the Deep Physical Layer

Marco Donald Migliore

DIEI,
University of Cassino and Southern Lazio
*corresponding author, E-mail: mdmiglio@unicas.it

Abstract

Antennas and Electromagnetic field Processing Devices (EPD) are discussed, considering their role in the OSI stack of the next generations of personal communication systems. The physical layer is divided into two layers, the 'Surface Physical Layer', which will be called simply the Physical Layer (PL), and the 'Deep Physical Layer' (DPL). According to this 'extended OSI' model, antennas are 'cross-layer' devices, while EPDs are 'signal processing' devices operating at the DPL, wherein the 'signal' is the electromagnetic field configuration.

1. Introduction

The challenging objectives of the next generation of personal communication systems require extremely aggressive use of the communication channel with active control of it. In this new vision, the communication channel becomes a resource that can be dynamically optimized, with a great impact on the performance of the communication system. Radiating systems interact intelligently with the environment, playing an active role in the communication system.

The starting point of the analysis carried out in this presentation is to use a physical approach to information theory [1] for the analysis of such structures. The basic idea is to split the Physical Layer, introducing a layer below the physical layer, called the Deep Physical Layer, wherein information is not yet an abstract quantity, but a *physical* quantity, defined as the number of distinguishable configurations of the observable (in the specific case the electromagnetic field) in the presence of noise at the receiver side [2].

This opens new challenges in the study of the physical processing of information in the communication channel and the analysis of the impact of these systems on the communication process.

2. The Deep Physical Layer

The OSI model (Fig. 1) gives a complete view of the communication process. In the OSI model the data stream is divided into seven layers starting from the highest level, the "application" layer, down to the lowest level, the "physical layer" (PL), which describes the implementation of the transmission of bits through the communication channel. Each intermediate layer represents a conceptual 'discontinuity' in the complex procedures required for communication.

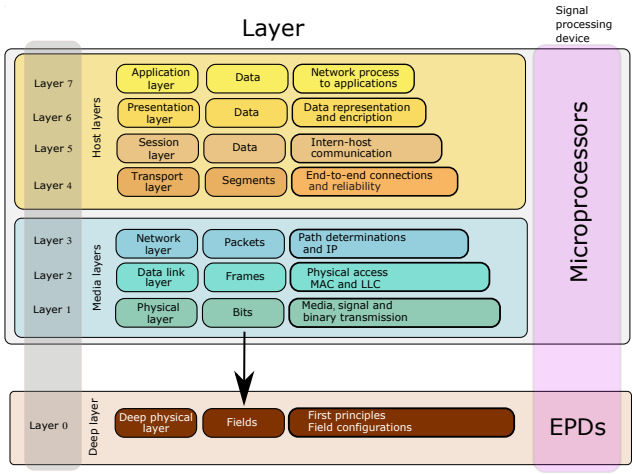

Figure 1: In the extended OSI layer, antennas are 'cross layer' devices, while RISs (Reflecting Intelligent Surfaces) are special EPDs (Electromagnetic field Processing Devices) able to perform signal processing at the Deep Physical Layer level

If we look at the physical layer, we can note that the analysis of the communication process at this level is performed using statistical models. This is a well-established approach, routinely applied by the signal processing community with great success.

However, the first step that any communication system does before starting the communication is to identify the channel state. In practice, this changes the perspective of the communication systems from a statistical approach to a deterministic approach, 'observing' the actual state of the channel. This indicatedn that inside the physical layer, there is a 'conceptual' discontinuity.

Loosely speaking, in the physical layers two 'worlds' coexist. In a world, information is an abstract concept related to the Shannon mutual information. This is the world of the *mathematical* theory of information. However, there is a further world where information is encoded in a physical observable, that obeys the rule of physics. Loosely speaking, this is the world of the *physical* theory of information. Here, limitations are fixed by the laws governing our universe and hence are unbreakable.

All this suggests dividing the physical layer into two parts, an upper part, the "surface physical layer," which in the following will be called simply the Physical Layer (PL)

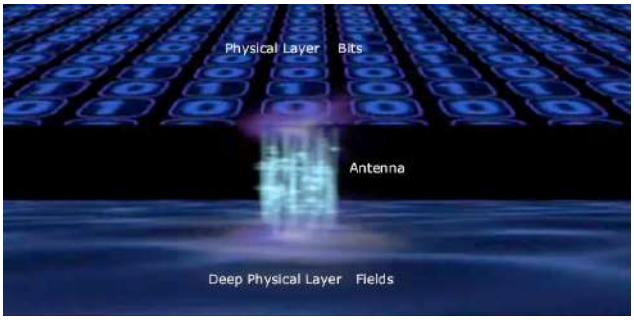

Figure 2: A prictorial view of the roel of the antennas in the extended OSI layer; antenna is the 'gate' between the Physical Layer (PL) and the Deep Physical Layer (DPL). In this sense, antennas can be seen as 'cross-layer' devices.

for the sake of simplicity, and a lower part, the "Deep Physical Layer" (DPL) [1]. While in the upper part, information is represented by abstract quantities, at the DPL, information is associated with physical observables. In particular, the amount of information is defined as the number of distinguishable electromagnetic field configurations on the receiver.

In this 'extended' OSI model the DPL is treated the same way as the other layers of the stack. In particular, as in the other layers, also in the DPL it is possible to do some 'signal processing' to optimize the communication process [4]. The only difference is that at the DPL the 'signal' is the electromagnetic field configuration, and the devices at the DPL directly modify the electromagnetic field configuration. We will call these devices Electromagnetic field Processing Devices (EPDs) [3]..

3. The role of Antennas in the DPL

As discussed above EPDs directly modify the electromagnetic field configuration in the DPL. In this view, antennas can be seen as quite special EPDs.

Indeed, the role of the antennas is to 'connect' the PL with the DPL (Fig. 2). In this sense, they 'translate' bits in different electromagnetic field configurations and viceversa [4].

All this also suggests a bottom-up vision of the communication systems.

The DPL contains all the resources regarding space/time/polarization degrees of freedom of the electromagnetic field that the communication system can use to encode information [1]. EPDs allow the maximization of these resources by increasing the number of possible distinguishable field configurations by the receiver.

The different distinguishable configurations of the field must be converted into 'bits' to be processed by the layers above the DPL. The antenna does this conversion.

As a consequence, while before the use of EPD the propagation channel was the bottleneck, the use of EPD shifts such a bottleneck toward the antennas. It is worth noting that this view also suggests a 'cross-layer' approach for

Figure 3: A pictorial view of an EPD; it consists of an array of electromagnetic controllable scattering elements optimized to maximize the capacity of the wireless system. The DPL contains all the resources regarding space/time/polarization degrees of freedom of the electromagnetic field that the communication system can use to encode information while EPDs allow the maximization of these resources by increasing the number of possible distinguishable field configurations by the receiver, acting as 'lenses' for physical information.

antenna synthesis, in which the radiating system is designed considering a double goal: controlling the distribution of the radiated power density in the space and maximizing the channel capacity [4].

4. The role of EPDs in the DPL

As noted above, the role of the EPD is to maximize the resources the DPL makes available to the upper layers [3].

An EPD consists of several electronically controllable scattering elements. The general architecture is similar to the one used in the Reflecting Intelligent Surfaces (RIS) [5]. However, there are some differences.

The goal of EPDs is the maximization of the channel capacity, and their synthesis is driven by information-based goals [6]. The solution maximizes the number of MIMO spatial subchannels [7], giving quite complex field configurations on the EPD. Instead, the main goal of the RIS is extending the wireless connection to overcome the limitations of the high-frequency communication systems, as in 5G FR2 or in the THz band that will be used in the next-generation 6G communication systems. RIS is based on reflection, allowing more classic synthesis methods to be used.

Also, the field of application of EPDs and RISs is different. RISs are highly effective in mmW and THz frequencies, where their use at lower frequencies, where scattering mitigates the coverage problems, is more attractive at the lower frequencies, where increasing the MIMO spatial subchannels allow increasing the capacity balancing the narrower bandwidth available, while is less appealing. at very high frequencies, where extremely large bandwidth allows very high bit rates.

EPDs and RISs share the use of controllable devices. Indeed, EPDs can also be obtained as an array of RISs, i.e.,

of reflecting controllable surfaces [7] organized to maximize the capacity of the wireless system [3] (Fig. 3).

Loosely speaking, RIS devices give optimal field processing when field configurations have only one spatial degree of freedom, [4]. More complex field elaboration must be carried out to maximize the channel capacity if more than one degree of freedom is available.

5. Conclusions

Introducing the Deep Physical Layer in the OSI model allows for quantifying the amount of information transmitted by the communication systems in terms of electromagnetic field configurations. Put simply, in the DPL, *information is physical*.

In this model, the role of the antennas is to 'connect' the upper layer of the physical layer with the DPL, 'mapping' bits in different configurations of the electromagnetic field and vice-versa.

Processing at the DPL is made by devices called Electromagnetic Field Processing Devices (EPDs), which consist of arrays of controllable reflecting devices organized to maximize the capacity of the wireless system [3]. They act as 'lenses' instead of 'mirrors,' as in RIS devices, for information.

A simple "proof of concept" of EPD is the ADAM architecture, in which several controllable scattering elements are placed in proximity of a MIMO antenna, obtaining a 6 bits local controllable environment [6]. Experiment tests confirmed the effectiveness of the use of EPD. In particular, the prototype allowed almost half the transmitted power without reducing the performance in terms of channel capacity, with a positive impact not only on the communication network, reducing energy consumption, but also on the environment, lowering the level of the electromagnetic field [7]. The ADAM architecture is the starting point for developing new devices under investigation in the microwave laboratory of Cassino University.

References

[1] Migliore, M. D. "On electromagnetics and information theory." IEEE transactions on antennas and propagation 56.10 (2008): 3188-3200

[2] Migliore, M. D. "The world beneath the physical layer: An introduction to the deep physical layer." IEEE Access 9 (2021): 77106-77126.

[3] Migliore, M. D. "Information Flows at the Deep Physical Layer Level." A Glimpse Beyond 5G in Wireless Networks. Cham: Springer International Publishing, 2022. 59-87.

[4] Migliore, M. D. "Horse (electromagnetics) is more important than horseman (information) for wireless transmission." IEEE Transactions on Antennas and Propagation 67.4 (2018): 2046-2055

[5] Martini, E., and S. Maci. "Theory, analysis, and design of metasurfaces for smart radio environments." Proceedings of the IEEE 110.9 (2022): 1227-1243

[6] Migliore, M.D., D. Pinchera, F. Schettino. "Improving channel capacity using adaptive MIMO antennas." IEEE Transactions on Antennas and Propagation 54.11 (2006): 3481-3489

[7] Pinchera, D., Wallace, J. W., Migliore, M. D., Jensen, M. A. "Experimental analysis of a wideband adaptive-MIMO antenna", IEEE transactions on antennas and propagation, (2008). 56(3), 908-913

Characterization and Optimization of Intelligent Reflective Surfaces in mm-Wave Band including the Reflection Produced by the Building Structure

Á. F. Vaquero[1,2], E. Martinez-de-Rioja[3], M. Arrebola[1*], and J. A. Encinar[4]

[1]Department of Electrical Engineering, Universidad de Oviedo, Spain
[2]Instituto de Telecomunicações, Universidade de Lisboa, Portugal
[3]Dep. of Signal Theory and Communications and Telematic Systems and Computing, Universidad Rey Juan Carlos, Spain
[4]Information Processing and Telecommunications Center, Universidad Politécnica de Madrid, Spain
[*]Corresponding author: arrebola@uniovi.es

Abstract

This work presents the design and optimization of a passive Intelligent Reflective Surface (IRS) based on a reflectarray technology to improve the coverage in a mm-Wave 5G scenario. A preliminary design is performed to achieve a wide beam in azimuth and elevation. The IRS is placed on a building façade and its effect is electromagnetically characterized for different materials. The design is then improved by optimizing the IRS considering the wall where it is placed.

1. Introduction

In the recent years, Smart Electromagnetic Skins (SMEs) have been proposed to overcome the issues related to signal propagation because of the physical barriers in the deployment of novel wireless networks in mm-Wave scenarios [1]. Namely, Intelligent Reflective Surfaces (IRS) are used to enhance 5G FR2 coverage avoiding the installation of multiple base stations (BS). An IRS is a planar surface made up of phase-shifting elements that reflect the impinging signal radiated from the BS into a desired direction (specular or another direction). The reflected field could be either a beam pointing or even a shaping beam. Active or passive phase-shifting elements can be used in the panel, mainly depending on the reconfiguration required by the coverage. Moreover, IRS has been also proposed to introduce beam tilting in a pointing direction to overcome the so-called blind zones, which are defined as an area of poor or even null coverage [2]. When the IRS is based on passive elements it is called SME.

IRS have been proposed for both urban and indoor scenarios [3], [4]. In both cases, the walls are usually the most suitable placements for installing the reflective surface. In a general scenario, the BS is far away from the IRS, therefore only a small fraction of the radiated power provided by the BS is captured by the IRS. This small fraction must be properly managed to enhance the coverage. Owing to the BS is far away, the surroundings of the IRS are also strongly illuminated so that the spillover on the building façade cannot be negligible.

The reflection produced by the surrounding wall should be characterized and considered for an accurate modeling of the coverage provided to the devices of the users as Figure 1 shows. If this effect is not taken into account the coverage could be not the desired one, having a significant distortion in the coverage link. Thus, the coverage synthesis and the IRS design should be carried out considering this major effect. Moreover, the limits in the achievable coverage should be also studied, to avoid unfeasible goals in the design and optimizations process.

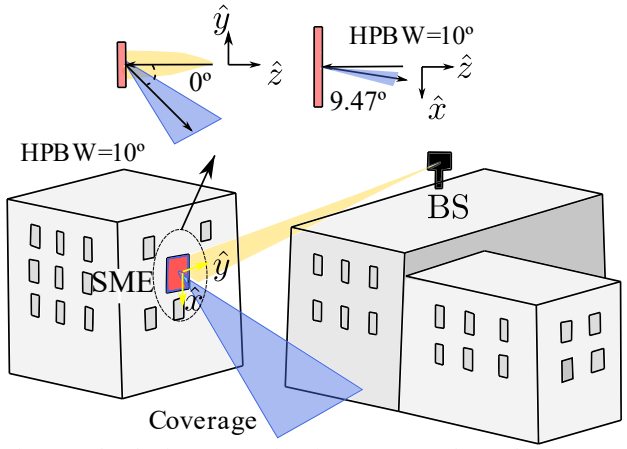

Figure 1. Sketch of a 5G scenario using an IRS to enhance the coverage. The BS illuminates the IRS that generates a coverage to overcome a blind area.

2. Smart Electromagnetic Skin Design

2.1. Scenario and Smart Electromagnetic Skin Optics

The Intelligent Reflective Surface is based on a passive panel, so that it is called a Smart Electromagnetic Skin. In this case, the SME is designed for an outdoor scenario. The aim is placing the panel in a building face to enhance the coverage provided by a base station. A similar case as the one of Figure 1 is proposed for this design. The BS is placed at 30 m in the **z**-direction and at height of 5 m in the **x**-direction. The panel is used to enhance the coverage in the specular direction since there is a blind area with poor coverage due to physical barriers (wall, building, etc.).

The panel does not only reflect the incident wave but also to produce a broad beam in both azimuth and elevation. The specifications in terms of beam pointing and half-power beamwidth (HPBW) are shown in Figure 1. Mainly, the panel operates at 27.7 GHz widening the beam 10º in both azimuth and elevation, resulting in a square coverage. Since the

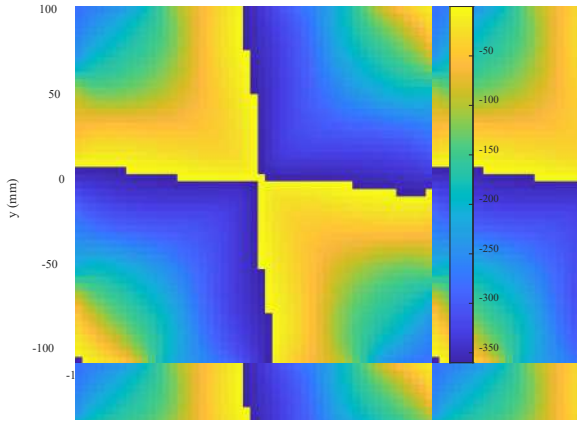

Figure 2. Phase-shift distribution of the elements of the SME obtained after the POS.

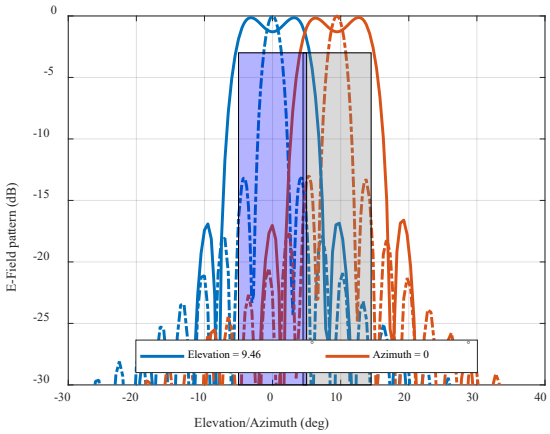

Figure 3. Normalized E-field pattern computed in the main cuts of the coverage for the V-polarization before (dotted line) and after (solid line) the synthesis at 27.7 GHz.

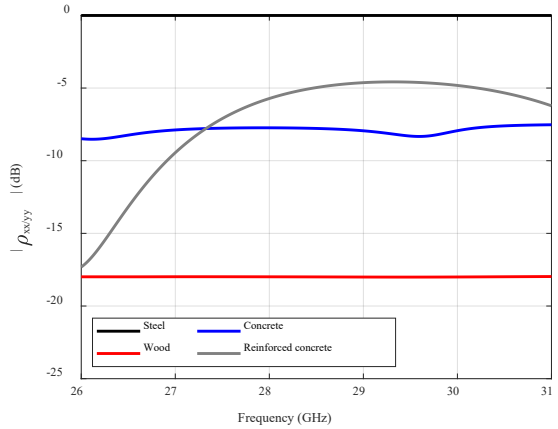

(a)

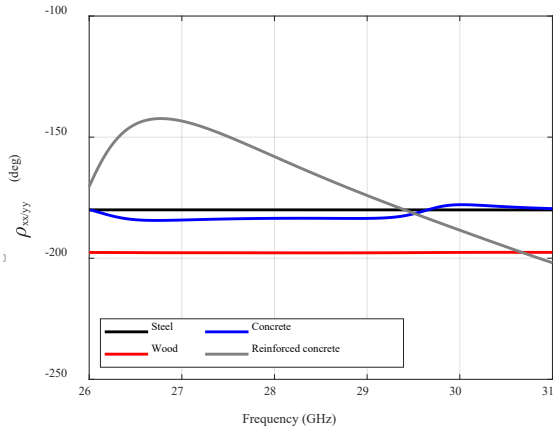

(b)

Figure 4. Reflection coefficient of the analyzed materials at several frequencies considering normal incidence (a) amplitude (dB) (b) phase (deg).

incident wave is reflected in the specular, the outgoing angles are 9.47º in elevation and 0º in azimuth.

The panel is dual-linearly polarized considering the horizontal polarization (H) defined according to the **y**-axis, while the vertical polarization (V) is defined in the **x**-axis.

To achieve the desired specifications the reflective SME is comprised of 50 x 50 elements of periodicity 4.29 x 4.29 mm^2.

2.2. Design procedure

As a first attempt, the SME is designed to radiate a pencil beam in the desired direction following (1) to compute the phase-shift of the elements:

$$\phi(x_l, y_l) = k_0(|\boldsymbol{d}_l| - (x_l \cos\varphi_0 + y_l \sin\varphi_0)\sin\theta_0) \quad (1)$$

where k_0 is the wavenumber in vacuum, (θ_0, φ_0) are the pointing direction of the pencil beam, in this case 9.47° and 0° , respectively. $\boldsymbol{d}_l$ is the distance from the feed $(x_{BS}, y_{BS}, z_{BS}) = (-5, 0, 30)$ m and the l th element, and (x_l, y_l) are the coordinates of the lth element referred to the center of the SME.

This solution provides a narrow beam whose half-power beamwidth is around 2º. Therefore, this configuration does not provide a successful solution, requiring widening the beam in both azimuth and elevation to fulfill the specifications

To obtain the broadened beam, the phase-shift distribution of the SME computed using (1) is synthesized using a Phase-Only Synthesis (POS) technique. The aim is to synthesize the phase of the reflection coefficients of the elements to finally find a proper distribution that radiates the desired pattern. To do so, the classical technique based on the Intersection Approach [5],[6] is used to reach the broadened beam with a ripple lower than 3 dB. Note that, during this process, the elements are modeled as ideal elements and the output of the synthesis is the phase-shift distribution that produces the desired co-polar pattern.

The synthesis procedure is based on a multi-stage process to improve the convergence of the algorithm. This procedure is commonly used when dealing with a large number of elements (in this case 2500), since the elements are the number of unknowns to be solved in the synthesis for each polarization. Figure 2 shows the phase-shift distribution that should introduce each element in both linear polarizations. Then, Figure 3 shows the main cuts of the co-polar pattern of the starting point and the synthesized phase-shift distribution for the V-polarization. Since the synthesis is based on ideal

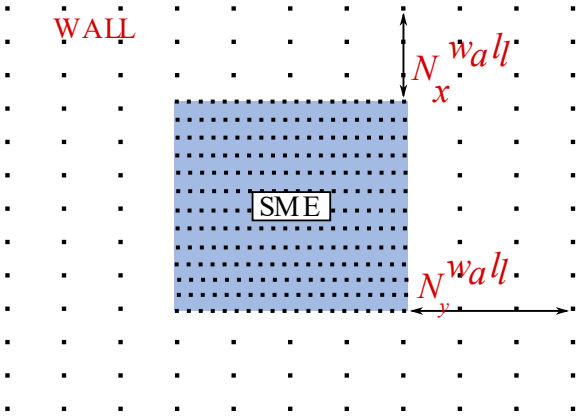

Figure 5. Sketch of the discretization of the whole array (SME plus wall).

elements, the results for the H-polarization are nearly the same.

In the light of these results, the beam is properly widened in both directions, reaching a square coverage of 10º by 10º. Furthermore, the ripple is quite low, having an almost flat-top beam in both azimuth and elevation. Therefore, it satisfies the requirements of ripple.

3. Electromagnetic response of the wall

The SME is designed for an outdoor scenario, so that the panel will be installed in a building façade. Considering that the BS is far away and provides a beam with wide HPBW (in this case about 12°), the incident field will have a strong illumination also in the surrenders of the SME, producing a high spillover. Comparing the electrical size of the SME and the façade, the SME will only capture a low fraction of the radiated power, while the spillover will be high. Therefore, the reflection produced by the wall should be analyzed to evaluate its influence on the coverage.

To do so, the wall should be firstly characterized. We have evaluated different materials to obtain their electromagnetic response. In this case, the materials analyzed are concrete ($\epsilon_r = 5.45, \tan\delta = 0.0021$), reinforced concrete ($\epsilon_r = 12.8, \tan\delta = 0.0021$), wood $\epsilon_r = 1.54, \tan\delta = 0.033$) and steel ($\sigma = 7.69 * 10^6$ S/m). The electromagnetic characterization of the materials is extracted from the libraries of CST Microwave Studio [7].

Those materials are analyzed in CST Microwave Studio to obtain the reflection coefficient. The analysis is carried out considering a block of 120-mm thick made up of the corresponding material under analysis. The block is analyzed considering local periodicity environment, ant it is illuminated by a uniformed-linearly-polarized plane wave propagating in the **z**-direction. The four materials are analyzed within a band of 4 GHz, from 26 to 30 GHz.

Note that the analysis is carried out using a uniformed-linearly-polarized plane wave, since the distance between the BS and the SME is large enough to consider the real incident field as a plane wave. Furthermore, the angles of incidence on both SME and surrounding area will be low enough to only consider normal incidence.

Figure 4 shows the amplitude and phase of the reflection coefficients (ρ_{xx} and ρ_{yy}). As might be expected, the greater

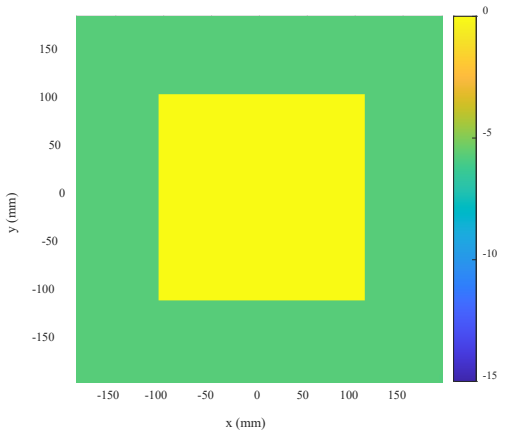

(a)

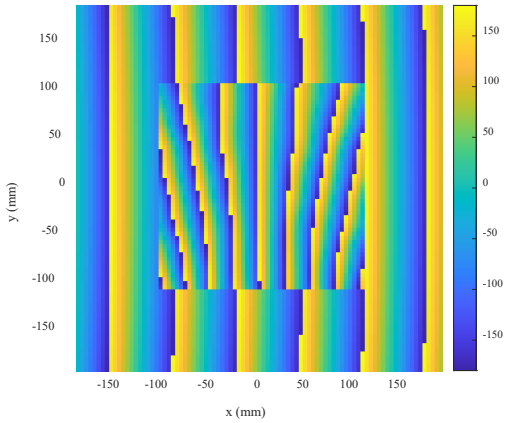

(b)

Figure 6. (a) Normalized amplitude (dB) and (b) phase (deg) of the reflected field onto the SME surface and the wall at 27.7 GHz.

the presence of steel (or other metals), the greater the reflection produced. The response of steel can be approximated by the reflection produced by a Perfect Electrical Conductor (PEC), while the wood might be considered as transparent since it barely reflects the wave (at least within this bandwidth).

4. Effect of the wall on the coverage

4.1. Computation of the wall in the radiation pattern

Once the electromagnetic characterization of the wall is obtained, its influence on the coverage can be obtained. We are going to assume that the panel is centered in a wall. Now, the wall and the SME will be assumed as a whole, having a larger SME. To do so, the wall is also divided into unit cells, considering the same periodicity of the SME. The new SME (wall plus SME) is comprised of $N_x \times N_y$ elements that are extended $N_x^{wall} \times N_y^{wall}$ elements in **x-** and **y**-direction, respectively. Therefore, the total size of the new SME is $(N_x + 2N_x^{wall}) \times (N_y \times 2N_y^{wall})$. Figure 5 shows further details on how the elements are distributed.

The radiated field of the whole SME is computed by means of contributions [8]. The aperture is divided into subdomains

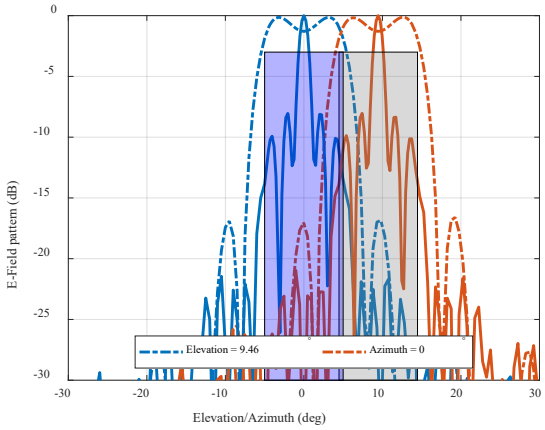

Figure 7. Normalized E-field pattern computed in the main cuts of the coverage for the V-polarization (dotted line) after the synthesis only considering the SME (solid line) after the synthesis considering the wall at 27.7 GHz.

that are associated to a single element of the SME. Then, the radiated field can be expressed as

$$\boldsymbol{E}_R(\boldsymbol{r}) = \sum_{n=1}^{N_x}\sum_{m=1}^{N_y} \boldsymbol{E}_{SME}^{mn}(\boldsymbol{r}) + \sum_{p=1}^{N_x^{wall}}\sum_{l=1}^{N_y^{wall}} \boldsymbol{E}_{wall}^{pl}(\boldsymbol{r}) \qquad (2)$$

where $\boldsymbol{E}_{SME}$ is the contribution of the nm-th elements of the original SME at the observation point $\boldsymbol{r}$, and $\boldsymbol{E}_{wall}$ is the contribution of the pl-th element of the wall.

Both contributions $\boldsymbol{E}_{SME}$ and $\boldsymbol{E}_{wall}$ can be computed using the classical theory of planar apertures, since the SME and wall are considered as a planar radiating aperture. Those contributions require knowing the tangential field onto the aperture surface. The tangential field is obtained from the incident field and the reflection matrix $\bar{\boldsymbol{R}}$. In this case, we must consider two reflection matrices, one for the SME elements (4), and one for the wall elements (5). In the case of the SME the elements are modeled as ideal phase shifters, so that they are lossless and only introduce a delay in the incident wave. Moreover, only the co-polar pattern is computed. This approximation is valid since the losses of the elements are quite low in reflective surfaces. However, in the wall the elements are fully characterized considering the reflection coefficients as a complex number. It is important to consider the loss of the material, otherwise there will be no difference between steel or wood, just on the introduced delay. Furthermore, the elements of the wall introduce the same phase delay and loss, since all of them are under normal incidence.

$$\bar{\boldsymbol{R}}_{SME} = \begin{pmatrix} \rho_{xx}^{mn} & \rho_{xy}^{mn} \\ \rho_{yx}^{mn} & \rho_{yy}^{mn} \end{pmatrix} = \begin{pmatrix} e^{j\phi_{xx}^{mn}} & 0 \\ 0 & e^{j\phi_{yy}^{mn}} \end{pmatrix} \qquad (4)$$

$$\bar{\boldsymbol{R}}_{wall} = \begin{pmatrix} \rho_{xx}^{pl} & \rho_{xy}^{pl} \\ \rho_{yx}^{pl} & \rho_{yy}^{pl} \end{pmatrix} = \begin{pmatrix} |\rho_{xx}|e^{j\phi_{xx}} & 0 \\ 0 & |\rho_{yy}|e^{j\phi_{yy}} \end{pmatrix} \qquad (5)$$

4.2. Distortion on the coverage produced by the wall

To compute the effect of the wall we assume that the wall has an area of 0.480×0.480 m^2, being the SME area 0.215×0.215 m^2 (it is centered in the wall as Figure 5 shows). Therefore, the wall extends the array in 20 elements from each edge of the SME, so that the new array is 90×90 elements. Figure 6 shows the reflected field considering the whole array, for the case of concrete. It should be noted that the illumination taper at the edge of the SME is less than 1 dB. The amplitude of the reflected field along the SME surface barely changes, having a uniform reflection, while the amplitude in the wall is attenuated due to the losses of the material (reinforced concrete). The phase clearly changes in the area wherein the SME is placed, while the wall only introduces a delay in the incident field (being the same delay for each cell).

Applying (2) to compute the radiated field, we obtain the radiation pattern shown in Figure 7. This radiation pattern is clearly distorted regarding Figure 3, mainly due to the strong specular reflection produced by the wall. Although the field level increases, the shaped beam is shattered.

5. Conclusions

In this work, a SME is proposed to enhance the coverage of a 5G network in mm-Wave band. A synthesis technique is used to obtain a phase-shift distribution of the SME elements that generates a widened beam. Specifically, a flat-top beam of $10° \times 10°$ in azimuth and elevation, with the aim of covering a blind coverage area. The antenna is designed and the effect on the radiation pattern is evaluated once it is placed on a façade. For this purpose, a simple model based on the Principle of Superposition is introduced, which allows taking into account the field reflected by the wall (spillover). It is observed that the shaped beam is shattered, mainly because the contribution of the wall is much higher than the one of the SME. For this reason, the design of SME or, in general IRS, must consider the environment where the antenna is located. Therefore, the optimization or synthesis processes used in the antenna design must be extended to include these new effects. Additionally, the used of higher directivity beams to illuminate the IRS (or SME), as well as the use of larger aperture should be also analyzed to overcome those effects.

Acknowledgements

This work was supported by MICIN/AEI/10.13039/501100011033 within projects PID2020-114172RB-C21-2; by the Spanish Ministry of Universities and European Union (NextGenerationEU fund) under project MU-21-UP2021-03071895621J; by Gobierno del Principado de Asturias under project AYUD/2021/51706; and by de Comunidad de Madrid within the Multiannual Agreement Framework with Universidad Rey Juan Carlos, Line of Action 1, Young Researchers R&D Project INCREASE-5G (Ref. F858).

References

[1] G. Oliveri, P. Rocca, M. Salucci, and A. Massa, Holographic Smart EM Skins for Advanced Beam Power Shaping in Next Generation Wireless Enviroments, *IEEE Journal on Multiscale and Multiphysics*

Computational Techniques, vol. 6, pp. 171-182, Oct. 2022.

[2] K. Zheng, D. Wang, Y. Han, X. Zhao, and D. Wang, Performance and measurements analysis of a commercial 5G millimeter-wave network, *IEEE Access*, vol. 8, pp. 163996-164011, 2020.

[3] E. Martinez-de-Rioja, Á. F. Vaquero, M. Arrebola, E. Carrasco, J. A. Encinar and M. Achour, Passive Dual-Polarized Shaped-Beam Reflectarrays to Improve Coverage in Millimeter-Wave 5G Networks, *2021 15th European Conference on Antennas and Propagation (EuCAP)*, Dusseldorf, Germany, pp. 1-5, 2021.

[4] E. Martinez-de-Rioja *et al*., Enhancement of 5G Millimeter-Wave Coverage in Indoor Scenarios by Passive Shaped-Beam Reflectarray Panels, *2022 16th European Conference on Antennas and Propagation (EuCAP)*, Madrid, Spain, pp. 1-5, 2022.

[5] O. M. Bucci, G. D'Elia, and G. Romito, Power synthesis of conformal arrays by a generalized projection method, *IEE Proc. Microw. Antennas Propag.*, vol. 142, no. 6, pp. 467-471, Dec. 1995.

[6] D. R. Prado *et al*., Efficient Crosspolar Optimization of shaped-beam dual-polarized reflectarrays using full-wave analysis for the antenna element characterization, *IEEE Transactions on Antennas and Propagation*, vol. 65, no. 2, pp. 623-635, Feb. 2017.

[7] Systèmes, Dassault, CST microwave studio [Computer program], Available at : http://www.cst.com [Accessed : 14 October 2022].

[8] Á. F. Vaquero, M. Arrebola, M. R. Pino, R. Florencia, and J. A. Encinar, Demonstration of a reflectarray with near-field amplitude and phase constraints as Compact Antenna Test Range probe for 5G new radio devices, *IEEE Transactions on Antennas and Propagation*, vol. 69, no. 5, pp. 2715-2726, May 2021.

Nanoscale Electrodynamics

Terahertz Waveforms in the Atom-Scale Gap of a Scanning Tunnelling Microscope

L. Z. Kastner[1], D. Peller[1], C. Roelcke[1], T. Buchner[1], A. Neef[1], J. Hayes[1], F. Bonafé[2], D. Sidler[2], M. Ruggenthaler[2], A. Rubio[2,3,4], J. Repp[1] and R. Huber[1]

[1]Department of Physics and Regensburg Center of Ultrafast Nanoscopy, University of Regensburg, Germany
[2]MPSD, MPG, Hamburg, Germany; [3]CCQ, Flatiron Institute, New York, USA; [4]UPV/EHU, San Sebastían, Spain
Author e-mail address: lukas.kastner@ur.de

Abstract: Measuring ultrafast, near-field waveforms on atomic length scales has remained an open challenge. Using a molecular switch as a local field sensor, we sample the temporal shape and strength of atomically confined light field transients. This allows us to quantitatively determine the instantaneous field strength in units of V/m with sub-cycle precision.

Tailored nanostructures like antennas, nanoparticles and tips can confine and enhance electromagnetic waveforms in sub-wavelength volumes. Such nanoscale optical fields have revolutionized (bio)chemical and medical detection[1], augmented photoenergy harvesting[1], and allowed for femtosecond scanning tunneling microscopy (STM)[2,3], with real-space resolution down to the sub-molecular level[3]. However, when light interacts with nanostructures, a complex interplay of plasmonic propagation, near-field screening, geometrical phase retardation and antenna enhancement determines the time-dependent near fields making an a priori prediction of local waveforms extremely challenging. Moreover, non-classical femtosecond dynamics such as tunneling has been predicted to shape local fields[4]. Far-field transients can be directly sampled in the time domain by electro-optic detection. In contrast, quantitative measurements of ultrafast atom-scale near fields have remained a major challenge. Since light-matter interaction crucially depends on the absolute strength of local fields as well as their temporal evolution, a parameter-free method to directly measure and calibrate atom-scale waveforms has been highly desirable.

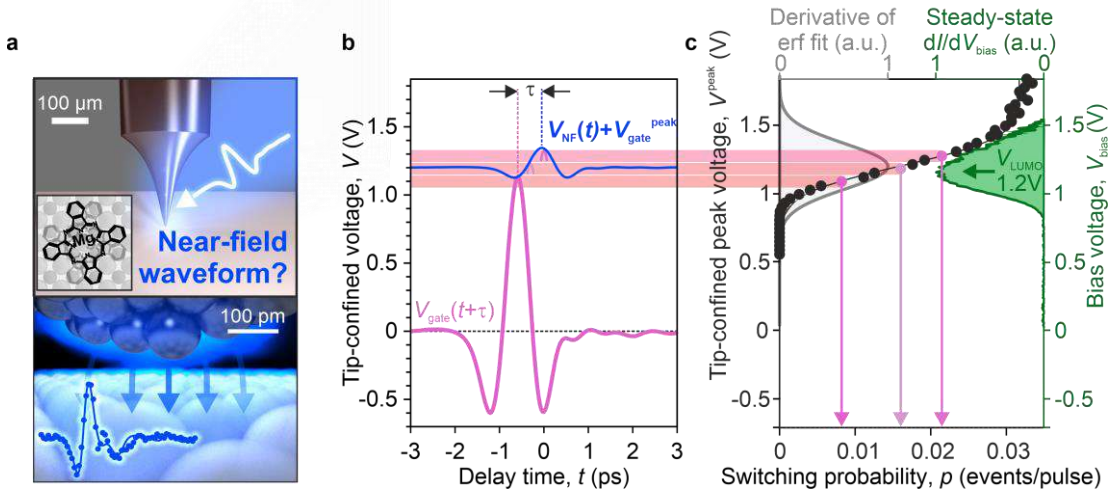

Fig. 1. **a**, A THz waveform is coupled into an STM junction where the ultrafast voltage applied by the near-field waveform is detected using a single-molecule switch (inset) as an atom-scale voltage gauge. **b**, A test transient, $V_{NF}(t)$, is superimposed with a gate waveform, $V_{gate}(t)$, (pink curve) for different delay times, τ. Thereby, the field crest at the maximum of the interference sum samples the test waveform (blue curve). **c**, Calibration scheme. The switch's reaction rate depends on the local THz-induced peak voltage (data points). Comparing the derivative of this error function (gray curve) with steady-state tunnel spectroscopy (green curve) gauges the THz-induced voltage quantitatively.

We demonstrate a direct quantitative detection of atomic-scale near-field waveforms with femtosecond precision in a novel pump-probe sampling scheme[5]. A single-cycle pulse in the terahertz (THz) range of the electromagnetic spectrum is focused onto the Ångström-scale junction of an STM, where the light fields induce an ultrafast voltage[2,3,5,6]. The idea is to use the field crest of a second THz pulse as a sub-cycle gate. When we vary the delay time between the two pulses, the peak voltage of the interference transient directly traces the test waveform. Hence, we can stroboscopically resolve the time evolution of our test waveform, if we manage to measure the local instantaneous peak voltage. To this end, we employ a bistable molecule as a high-precision, atom-scale and quantitative voltage sensor and build on state-selective lightwave-driven STM[3,7]. Using the voltage-dependent switching rate of the molecular rotor, we directly sample the temporal shape and strength of atomically confined light-field transients quantified in units of volts[5]. The far-field waveform (Fig. 2a, red) focused on the STM junction differs markedly from the atomic near-field transient (data points). The 1/f-scaling of the field enhancement redshifts the central frequency and a clear phase shift can be observed. These and more subtle features of the transfer from the far field to the near field are reproduced by a classical numerical calculation (Fig. 2b). First principles TDDFT simulations[8] corroborate assumptions made in our analysis and confirm that the instantaneous peak voltage can be extracted very accurately by our atomic-scale sensor.

Our ultrafast, local sampling technique opens the doors to exploring the validity limits of classical nano-optics directly on sub-Å and femtosecond scales. Moreover, this lays the foundation for calibrated simulations, which connect macroscopic light and Å-scale waveforms. Moreover, atomically defined and calibrated waveforms can now be utilized to shed light on the dynamics of single molecules, atomic defects or novel quantum materials by means of ultrafast nanoscopy and spectroscopy.

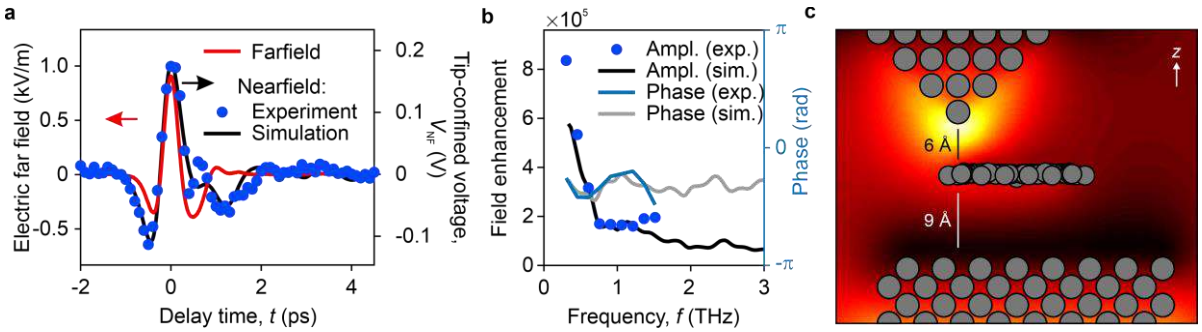

Fig. 2. **a**, Far-field waveform coupled into the junction (red). Resulting tip-confined voltage transient (data points) and a scaled classical simulation of the near-field waveform (black curve). **b,** Transfer function for amplitude and phase determined experimentally and using a classical simulation. **c**, First principles TDDFT simulations[8] of the dynamical Hartree potential.

References

1. Barnes, W.L., A. Dereux and T. W. Ebbesen, "Surface plasmon subwavelength optics", Nature 424, 824 (2003).
2. Cocker, T.L. *et al.*, "An ultrafast terahertz scanning tunnelling microscope", Nat. Photon. 7, 620 (2013).
3. Cocker, T.L., D. Peller *et al.*, "Tracking the ultrafast motion of a single molecule by femtosecond orbital imaging", Nature 539, 263 (2016).
4. Jestädt, R. *et al.*, "Light-matter interactions within the Ehrenfest-Maxwell-Pauli-Kohn-Sham framework: fundamentals, implementation, and nano-optical applications", Adv. Phys. 68, 225 (2019).
5. Peller, D. *et al.*, "Quantitative sampling of atomic-scale electromagnetic waveforms", Nat. Photon. 15, 143–147 (2021).
6. Yoshida, S. *et al.*, "Subcycle Transient Scanning Tunneling Spectroscopy with Visualization of Enhanced Terahertz Near Field", ACS Photonics 6, 1356 (2019).
7. Peller, D. *et al.*, "Sub-cycle atomic-scale forces coherently control a single-molecule switch", Nature 585, 58 (2020).
8. Tancogne-Dejean, N. *et al.*, "Octopus, a computational framework for exploring light-driven phenomena and quantum dynamics in extended and finite systems", J. Chem. Phys. 152, 124119 (2020).

First-principles electromagnetics simulation for nonlinear nanophotonics: method and applications

M. Uemoto[1*] and K. Yabana[2]

[1]Department of Electrical and Electronic Engineering, Graduate School of Engineering, Kobe University, Japan
[2] Center for Computational Sciences, University of Tsukuba, Japan
[*]corresponding author: uemoto@eedept.kobe-u.ac.jp

Abstract: Electron dynamics simulation based on the first-principles time-dependent density functional theory (TDDFT) is utilized to theoretically predict linear and nonlinear, ultrafast optical properties of various materials. In this work, we propose computational methods for coupled dynamics of electrons and electromagnetic fields and apply them to analyze interactions between intense and ultrashort laser pulses and nanoscale optical structures such as nanofilms, nanoparticles, and metasurfaces.

Ultrafast and nonlinear optical phenomena induced under intense laser pulses have been an essential topic in the current frontier of optical sciences. In the research field of nanophononics, artificial nanoscale structures, particularly the semiconductor-based "all-dielectric" nanoparticles and metasurfaces, have been intensively studied in recent years as a new platform for nonlinear optics, such as harmonic generations. Computational electromagnetics simulations based on Maxwell's equations, such as the time-domain finite difference (FDTD) method, have become an indispensable tool in the design of nanophotonics devices. However, the conventional method requires empirical optical constants of media and its application is limited to events caused by weak intensity light with linear and low-order perturbative nonlinear optical responses.

We investigate a theoretical and computational method of electron dynamics based on time-dependent density functional theory (TDDFT) [1] and apply to various material systems [2-5], such as atoms, molecules, and bulk solids. The TDDFT can successfully predict linear dielectric function [3], low-order nonlinear susceptibilities [4], and non-perturbative nonlinear phenomena such as tunnel ionization, saturable absorption, and high harmonic generations (HHGs). We further develop a coupled method combining the first-principles TDDFT and the electromagnetic simulation that we call the “Maxwell+TDDFT multiscale method”, to describe light-matter interaction in the nanoscale materials [5].

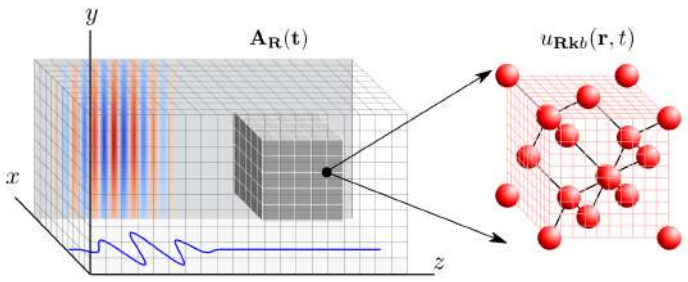

Figure 1: Image of Maxwell+TDDFT multiscale method. Macroscopic electromagnetic field is solved using course grid system (left) while microscopic electron dynamics is calculated using fine grid system (right).

The conceptual illustration of our Maxwell+TDDFT coupling is shown in Fig. 1. Using the course grid system, the macroscopic electromagnetic field is described by the Maxwell equation for the vector potential $\mathbf{A}_{\mathbf{R}}(t)$:

$$-\nabla_{\mathbf{R}} \times \nabla_{\mathbf{R}} \times \mathbf{A}_{\mathbf{R}}(t) + \frac{1}{c^2}\frac{\partial^2}{\partial t^2}\mathbf{A}_{\mathbf{R}}(t) = \frac{c}{4\pi}\mathbf{J}_{\mathbf{R}}(t),$$

where **R** is the macroscopic coordinate. The source term $\mathbf{J}_{\mathbf{R}}(t)$ represents current density induced in the media, which is given by the microscopic electron dynamics. At each grid point **R**, the individual electron dynamics is governed by the time-dependent Kohn-Sham (TDKS) equation:

$$i\frac{\partial}{\partial t}u_{b\mathbf{kR}}(\mathbf{r},t) = \left\{\frac{1}{2}\left[-i\nabla_{\mathbf{r}} + \mathbf{k} + \frac{1}{c}\mathbf{A}_{\mathbf{R}}(t)\right]^2 + V_{\mathbf{R}}(\mathbf{r},t)\right\}u_{b\mathbf{kR}}(\mathbf{r},t),$$

where $u_{b\mathbf{kR}}$ are the Bloch orbitals of electrons and $V_{\mathbf{R}}$ is the effective potentials including the ionic, Hartree and exchange-correlation terms. Calculation of the coupled equations provides the light propagation and materials response simultaneously.

As a demonstration of the Maxwell+TDDFT multiscale calculation, we consider an intense laser excitation of the periodic array of semiconducting (silicon) nanospheres with a diameter R~250 nm [see Fig. 2(a)-(b)]. The incident laser frequency is set as 1.55 eV, which is smaller than the direct band gap of silicon. Under the strong intensity (I=10^{12} W/cm^2) pulse, two photon and three photon absorption process leads the carrier excitations at a focal region. [See Fig 2(c)]. At each blue cell shown in Fig. 2(b), TDDFT calculation of silicon is carried out ("macroscopic grid points"). Since there are about 16,000 macroscopic grid points, the calculation requires huge computing resources.

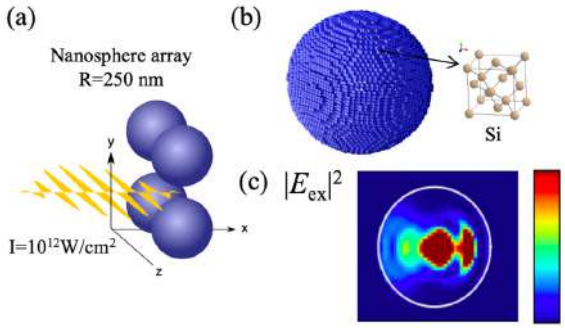

Figure 2: (a) illustration of periodic nanostructure (b) multiscale model (c) profile of excitation energy at t=18.4 [fs].

Alternatively, it is possible to perform the electrodynamics calculation using semiconducting Bloch equation that involves the density matrix ρ, ground state eigenenergies ε and transition dipole moments p;

$$i\frac{\partial}{\partial t}\rho_{bb'}^{(\mathbf{k},\mathbf{R})}(t) = \left[\epsilon_b(\mathbf{k}) - \epsilon_{b'}(\mathbf{k})\right]\rho_{bb'}^{(\mathbf{k},\mathbf{R})}(t) + \frac{1}{c}\mathbf{A}_{\mathbf{R}}(t)\cdot\left\{\sum_j\left[\mathbf{p}_{bj}(\mathbf{k})\rho_{jb'}^{(\mathbf{k},\mathbf{R})}(t) - \rho_{bj}^{(\mathbf{k},\mathbf{R})}(t)\mathbf{p}_{jb'}(\mathbf{k})\right]\right\}.$$

By using it, computational costs can be significantly reduced compared to TDDFT. It allows us to describe further complex processes including realistic all-dielectric nanophotonics devices. The methods we have been developing are implemented in an open-source program package "SALMON" (Scalable Ab initio Light–Matter simulator for Optics and Nanoscience) [6-7]. We expect it will provide a useful platform enabling to gain a deeper understanding of the underlying physics and insights that is useful for the design of future optical devices.

References

1. E. Runge, E. K. U. Gross, Phys. Rev. Lett. **52**, 997 (1984)
2. K. Yabana, G. F. Bertsch, Phys. Rev. B **54**,4484 (1996)
3. G. F. Bertsch, J. -I. Iwata,A.Rubio, K. Yabana, Phys. Rev. B **62**, 7998 (2000)
4. M. Uemoto,Y. Kuwabara, S. A. Sato, K. Yabana, J. Chem. Phys. **150**, 094101 (2019)
5. K. Yabana, T. Sugiyama, Y. Shinohara, T. Otobe, G. F. Bertsch, Phys. Rev. B **85**, 045134 (2012)
6. M. Noda *et al*., Comput. Phys. Comm. **235**, 356-365 (2019)
7. SALMON TDDFT project official website: https://salmon-tddft.jp/

Terahertz Scanning Tunneling Microscopy: Exploring Ultrafast Dynamics in Materials down to the Atomic Scale

F. A. Hegmann*

Department of Physics, University of Alberta, Edmonton, Alberta T6G 2E1, Canada
*corresponding author: hegmann@ualberta.ca

Abstract: Terahertz scanning tunneling microscopy (THz-STM) enables imaging of ultrafast phenomena in materials down to the atomic scale. In THz-STM, picosecond-duration THz pulses are antenna-coupled to the sharp metal tip of an STM, and the resulting field enhancement at the junction produces a sub-picosecond transient tunnel current that can be used to probe ultrafast dynamics on the nanoscale. How THz-STM works, recent experiments, and future directions are discussed.

The ability to directly probe ultrafast phenomena on the nanoscale is essential to our understanding of excitation dynamics in materials and in the development of new device technologies. However, achieving this capability has been challenging and is the focus of research in many labs around the world. Terahertz scanning tunneling microscopy, or THz-STM, is a powerful new technique that enables direct imaging of sub-picosecond dynamics in materials down to the atomic scale. [1-26].

In THz-STM, terahertz pulses (Fig. 1a) are focused onto the sharp metal tip of an STM (Fig. 1b), which behaves like an antenna that greatly enhances the THz pulse electric field that is coupled to the tip at the tunnel junction. The resulting terahertz voltage transient across the junction produces sub-ps duration tunnel currents that can have a net rectified component due to the inherent nonlinearity in the current-voltage (I-V) characteristic of the tunnel junction (Fig. 1c), which can be a function of the bias-dependence of the local density of states as well as the electron concentration and tip-induced band-bending effects in the sample.

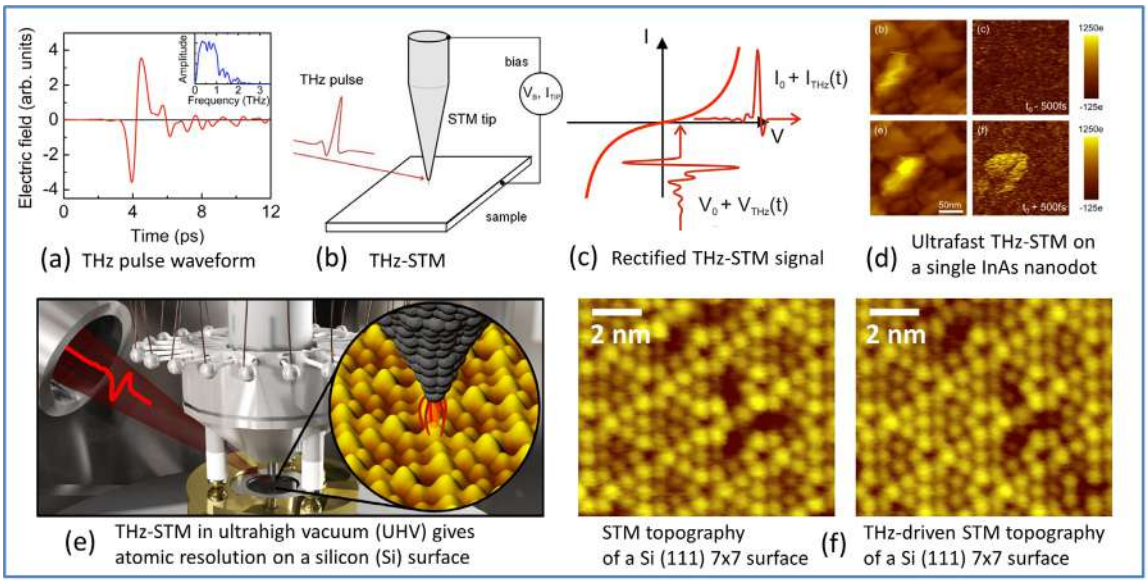

Figure 1. THz pulses (a) coupled to a STM (b) produce transient tunnel currents (c). (d) THz-STM of single InAs nanodots [1] and (e,f) a silicon surface with atomic resolution [2].

THz-STM was first demonstrated by Cocker et al. [1], showing the photoexcitation dynamics in a single InAs nanodot with simultaneous 0.5 ps time resolution and 2 nm spatial resolution under ambient conditions (Fig. 1d). Operation in ultrahigh vacuum (Fig. 1e) allows for THz-pulse-induced tunnel currents confined to single atoms (Fig. 1f), as reported for THz-STM of silicon surfaces [2] and single pentacene molecules [3]. THz-STM has recently been used to study metal surfaces [4], graphene nanoribbons [5], 2H-MoTe2 and Bi2Se3 [6], and C60 films [7], as well as for applying localized forces to single molecules [8] and inducing luminescence in materials [9]. Much work has focused on characterizing the near-field waveform [10-15], coherent control of tunnel currents [2,6,13,14], modeling the THz-STM signal [2,4,16], increasing bandwidth [15] and efficiency [17], thermal and nonthermal tunneling effects [18], and achieving attosecond time resolution [19,20]. THz-STM has also been the subject of several recent review articles [21-26].

Funding support from NSERC, CFI, Alberta Innovates, and ATUMS is acknowledged.

References

1. T. L. Cocker, V. Jelic, M. Gupta, S. J. Molesky, J. A. J. Burgess, G. De Los Reyes, L. V. Titova, Y. Y. Tsui, M. R. Freeman, and F. A. Hegmann, Nat. Photon. 7, 620 (2013).
2. V. Jelic, et al., Nat. Phys. 13, 591 (2017).
3. T. L. Cocker, et al., Nature 539, 263 (2016).
4. Y. Luo, V. Jelic, et al., Phys. Rev. B 102, 205417 (2020).
5. S. E. Ammerman, et al., , Nat. Commun. 12, 6794 (2021).
6. S. Yoshida, et al., ACS Photonics 6, 1356 (2019).
7. S. Yoshida, et al., ACS Photonics 8, 315 (2021).
8. D. Peller, et al., Nature 585, 58 (2020).
9. K. Kimura, et al., ACS Photonics 8, 982 (2021).
10. P. H. Nguyen, et al., Phys. Can. 71, 157 (2015).
11. D. Peller, et al., Nat. Photon. 15, 143 (2021).
12. J. Takeda and I. Katayama, Nat. Photon. 15, 70 (2021).
13. K. Yoshioka, et al., Nat. Photon. 10, 762 (2016).
14. K. Yoshioka, et al., Nano Lett. 18, 5198 (2018).
15. M. Müller, et al., ACS Photonics 7, 2046 (2020).
16. S. E. Ammerman, et al., Phys. Rev. B 105, 115427 (2022).
17. M. Abdo, et al., ACS Photonics 8, 702 (2021).
18. N. M. Sabanés, et al., ACS Nano 16, 14479 (2022).
19. M. Garg and K. Kern, Science 367, 411 (2020).
20. M. Garg, et al., Nat. Photon. 16, 196 (2022).
21. T. L. Cocker, V. Jelic, R. Hillenbrand, and F. A. Hegmann, Nat. Photon. 15, 558 (2021).
22. T. L. Cocker and F. A Hegmann, in J Lloyd-Hughes, et al, “The 2021 ultrafast spectroscopic probes of condensed matter roadmap”, Journal of Physics: Condensed Matter 33, 353001 (2021).
23. T. Tachizaki, et al., APL Mater. 9, 060903 (2021).
24. R. Gutzler, et al., Nat. Rev. Phys. 3, 441 (2021).
25. M. Peplow, Nature 544, 408 (2017).
26. Y. Tian, et al., Surf. Rev. Lett. 25, 1841003 (2018).

In situ control and nanofocusing of extreme ultraviolet

A. Korobenko[1*], S. Rashid[2], C. Heide[3], A. Yu. Naumov[1], D. A. Reis[3], P. Berini[2,4,5], P. B. Corkum[1], and G. Vampa[1]

[1]Joint Attosecond Science Laboratory, National Research Council of Canada and University of Ottawa, Canada

[2]Center for Research in Photonics, University of Ottawa, Ottawa K1N 6N5, Canada

[3]Stanford PULSE Institute, SLAC National Accelerator Laboratory, USA

[4]School of Electrical Engineering and Computer Science, University of Ottawa, Canada

[5]Department of Physics, University of Ottawa, Canada

[*]corresponding author: akoroben@uottawa.ca

Abstract: We integrate coherent short-wavelength high-order harmonics from a MgO crystal, with a nanostructured element etched onto the surface of the crystal itself, allowing us to control the emitted extreme ultraviolet light. Using this technique, we achieve focusing of the radiation down to 150 nm waist radius. Future developments may demonstrate nanoscale laser ablation and miniaturization of extreme ultraviolet coherent sources on a chip.

Modern technology heavily relies on the processes occurring on a length scale of 10 nm. Addressing this length scale with light requires operating in the extreme ultraviolet (XUV) as dictated by the diffraction limit. Using the traditional, *ex situ* approach, where the XUV generation and control are separated, is complicated by the need of bulky and expensive equipment.

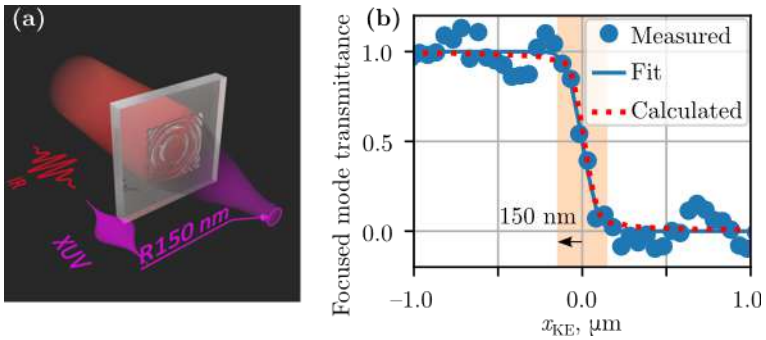

Figure 1. (a) High-NA in situ focusing of XUV from a structured dielectric. (b) Knife-edge measurement of a waist size.

Here we report on a different, *in situ* approach, with both generation and control of the XUV taking place in a single, chip-scale device. We fabricate a structure on the surface of a magnesium oxide crystal. When illuminated by the femtosecond laser, it emits coherent radiation in the extreme ultraviolet spectral range through a high harmonic generation process. The phase and amplitude profile, imprinted by the structure onto the generated light, leads to the rapid focusing of the latter with unprecedentedly high numerical aperture of 0.35, and to its eventual convergence down to a waist radius of 150 nm.

In the future, shorter wavelength harmonics and higher numerical aperture structures will bring the size of focal spot achieved with our technique, down to the sub-100 nm scale. The unique combination of short

wavelength, small focus and high intensity, inherent to the method, will enable many applications, such as direct laser nanostructuring and nonlinear imaging with chemical specificity, element-specific imaging, and photoelectron spectro-nanoscopy.

We acknowledge the support from the W. M. Keck Foundation, the Alexander von Humboldt foundation, the Joint Center for Extreme Photonics, the U.S. Defense Threat Reduction (Grant No. 1-19-1-0026), U.S. Air Force Office of Scientific Research (Grant No. FA9550-16-1-0109) and the Natural Sciences and Engineering Research Council of Canada.

References

1. Korobenko A., Rashid S., Heide C., Naumov A. Yu., Reis D. A., Berini P., Corkum P. B., and Vampa G., "In-Situ Nanoscale Focusing of Extreme Ultraviolet Solid-State High Harmonics," Phys. Rev. X, Vol. 12, 041036, 2022.
2. Korobenko A., Rashid S., Heide C., Naumov A. Yu., Reis D. A., Berini P., Corkum P. B., and Vampa G., "Generation of structured coherent extreme ultraviolet beams from an MgO crystal," Opt. Exp., Vol. 29, No. 15, 24161–24168, 2021.

Thermodynamic limits for radiative heat engines

M. Giteau, M. F. Picardi, and G. T. Papadakis*

ICFO - Institut de Ciencies Fotoniques, The Barcelona Institute of Science and Technology, Castelldefels (Barcelona) 08860, Spain

*corresponding author: georgia.papadakis@icfo.eu

Abstract: The efficiency of any heat engine is bounded by the well-known Carnot efficiency. While achieving high efficiency is of interest for energy production, engines that operate close to the Carnot efficiency usually have vanishing power output. Operating at maximum power, however, leads to significantly degraded efficiencies, thus imposing a trade-off between power and efficiency. In this talk, we evaluate this trade-off for heat engines that exchange heat radiatively with a hot source, which includes thermophotovoltaic systems.

Thermodynamic limits set the bounds for any heat engine operating between thermal sources. Particularly, the maximum efficiency of a heat engine that operates between a hot source and a cold bath is given by the Carnot limit [1]. Among heat engines, a peculiar example is given by radiative heat engines, which receive heat in the form of thermal radiation. One practical implementation of such engines is thermophotovoltaic systems, where a photovoltaic cell converts the thermal radiation emitted by a hot source into electricity. Thermophotovoltaics is a very active and promising research field, with many impressive results reported recently, both in terms of efficiency [2], [3] and power density [4]. Aside from solar radiation, thermophotovoltaics can convert heat from any other source, which results in a large applicability of this technology in waste-heat recovery. Therefore, it is becoming increasingly important to determine figures of merit in order to compare experimental results between each other, as well as to evaluate their performance relative to optimal configurations.

We consider a hot emitter at temperature T_H and a cold bath at temperature T_C exchanging power through a heat engine in steady-state condition. The emitter and the converter exchange energy radiatively, while the converter is in thermal contact with the cold bath. We call P_H and P_E the power densities emitted by the hot source and by the engine, respectively. The heat engine generates an output power density W, with an accompanying heat flux Q. The general system is schematically represented in Fig. 1 (a).

We define a first figure of merit $\rho = W/\sigma T_H^4$ as the output power density normalized to the power density emitted by a blackbody emitter at temperature T_H, where σ is the Stefan-Boltzmann constant. Meanwhile, the second figure of merit is the efficiency $\eta = W/(P_H - P_E)$, where the denominator accounts for the net heat drawn from the emitter. We aim at maximizing the ρ for any given value of η, once T_H and T_C are fixed, to estimate the maximum power output attainable when operating at a given conversion efficiency.

In doing so, we derive three general thermodynamic bounds for radiative energy conversion (Fig. 1 (b)). The first is the absolute limit, corresponding to an isentropic conversion process and requiring an infinite number of engines connected non-reciprocally (analogous to the Landsberg limit for sunlight conversion [6]). This is indicated, in Fig. 1 (b), as “Nonreciprocal”. The second is obtained by combining an infinite number of engines without breaking reciprocity (in analogy to what in solar energy conversion is called multicolor limit [7]), in Fig. 1(b) this

is reported as “Reciprocal”. Finally, the third corresponds to the performance bounds using a single engine (endoreversible or blackbody limit for solar conversion [8]), denoted as “Blackbody” in Fig. 1 (b). We observe that the introduction of nonreciprocity leads to significantly higher upper bounds, while the difference between one engine and an infinite number of reciprocal engines is marginal.

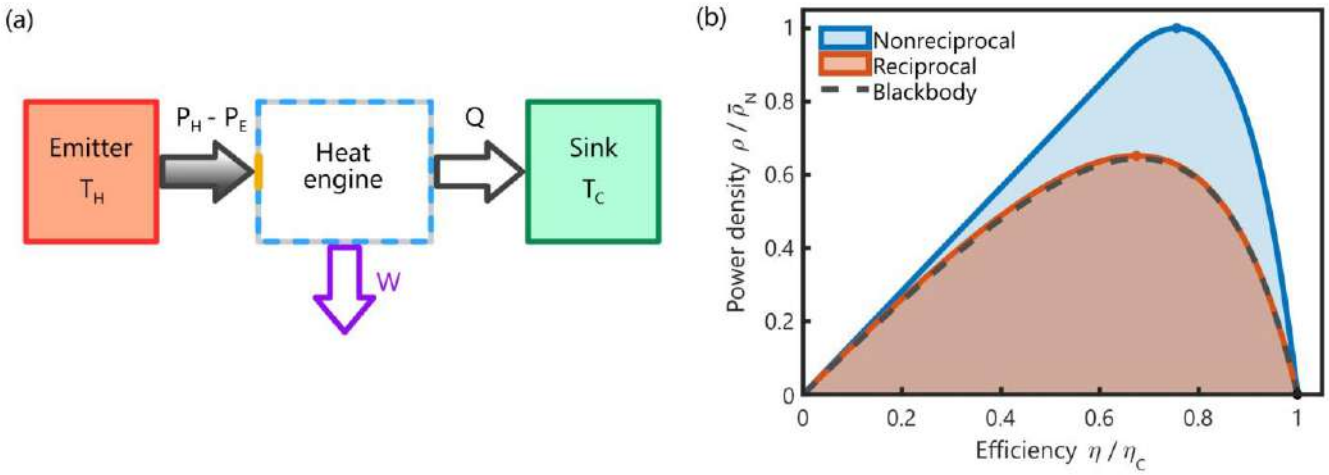

Figure 1: Thermodynamic limits of radiative heat conversion. In (a) a schematics of a radiative heat engine operating between two thermal reservoirs is depicted. (b) Thermodynamic performance bounds of radiative energy conversion, in terms of the maximum power output achievable for any given efficiency, for the three different engine configurations. The plotted curves are calculated for $T_H = 600$ K and $T_C = 300$ K.

References

1. N. Shiraishi, K. Saito, and H. Tasaki, “Universal Trade-Off Relation between Power and Efficiency for Heat Engines,” *Phys. Rev. Lett.*, vol. 117, no. 19, p. 190601, Oct. 2016, doi: 10.1103/PhysRevLett.117.190601.
2. B. Lee *et al.*, “Air-Bridge Si Thermophotovoltaic Cell with High Photon Utilization,” *ACS Energy Lett.*, pp. 2388–2392, Jun. 2022, doi: 10.1021/acsenergylett.2c01075.
3. A. LaPotin *et al.*, “Thermophotovoltaic efficiency of 40%,” *Nature*, vol. 604, no. 7905, Art. no. 7905, Apr. 2022, doi: 10.1038/s41586-022-04473-y.
4. E. López, I. Artacho, and A. Datas, “Thermophotovoltaic conversion efficiency measurement at high view factors,” *Solar Energy Materials and Solar Cells*, vol. 250, p. 112069, Jan. 2023, doi: 10.1016/j.solmat.2022.112069.
5. A. Datas, “Optimum semiconductor bandgaps in single junction and multijunction thermophotovoltaic converters,” *Solar Energy Materials and Solar Cells*, vol. 134, pp. 275–290, Mar. 2015, doi: 10.1016/j.solmat.2014.11.049.
6. P. T. Landsberg and G. Tonge, “Thermodynamic energy conversion efficiencies,” *Journal of Applied Physics*, vol. 51, no. 7, pp. R1–R20, Jul. 1980, doi: 10.1063/1.328187.
7. M. A. Green, *Third Generation Photovoltaics Advanced Solar Energy Conversion*. Berlin; Heidelberg: Springer, 2003.
8. A. D. Vos, “Reflections on the power delivered by endoreversible engines,” *J. Phys. D: Appl. Phys.*, vol. 20, no. 2, p. 232, Feb. 1987, doi: 10.1088/0022-3727/20/2/014.

Antenna theory and design

Antenna Design Optimization Using Machine Learning

C.J. Reddy[1]

[1]Altair Engineering, Inc, USA
cjreddy@altair.com

Abstract:
Antennas are critical part of any wireless system for maximizing efficiency and data rates. Machine learning (ML) is a method of data analysis that automates analytical model building. Antennas are becoming more and more complex each day with increase in demand for their use in variety of devices (smart phones, autonomous driving to mention a couple); antenna designers can take advantage of ML to generate trained models for their physical antenna designs and perform fast and intelligent optimization on these trained models. Using the trained models, different optimization algorithms and goals can be run quickly, in seconds, for comparison of different designs.

In CAE and in antenna simulation the availability of data is the main challenge. Fortunately, clever design exploration methods such as space filling Design of Experiment (DoE) approaches can enable the antenna designer to use ML technologies favorably in the antenna design process [1,2]. Using the trained models, different optimization algorithms and goals can be run quickly, in seconds, for comparison and for types of different studies, such as for example stochastic analysis for tolerance studies etc. (Figure 1). This talk presents the process of fast and intelligent optimization by Design Exploration and machine learning. Examples to showcase the advantages of using machine learning for antenna design and optimization will be presented.

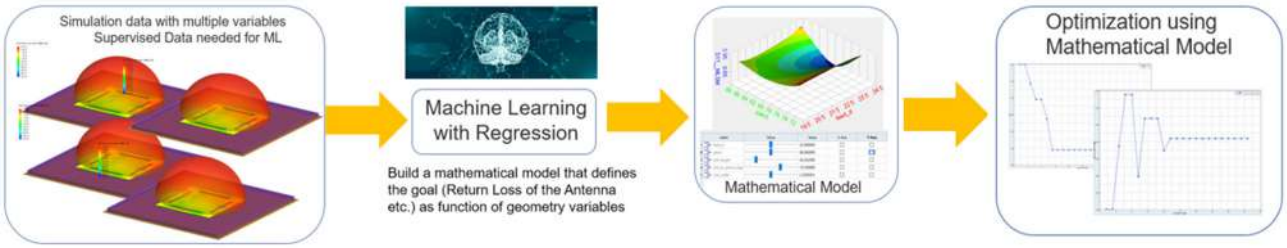

Figure 1. Antenna Design Optimization Process via Machine Learning

References

1. G. Gampala and C. J. Reddy, "Fast and Intelligent Antenna Design Optimization using Machine Learning," 2020 International Applied Computational Electromagnetics Society Symposium (ACES), 2020, pp. 1-2, doi: 10.23919/ACES49320.2020.9196193.
2. C. Maeurer, P. Futter and G. Gampala, "Antenna Design Exploration and Optimization using Machine Learning," 2020 14th European Conference on Antennas and Propagation (EuCAP), 2020, pp. 1-5, doi: 10.23919/EuCAP48036.2020.9135530.

AES 2023, TORREMOLINOS - SPAIN, 5 – 8 JUNE 2023

Applications of reflectarray antennas using frequency and polarization independent beamforming

Jose A. Encinar*, and Daniel Martinez-de-Rioja

Information Processing and Telecommunications Center, Universidad Politecnica de Madrid, Spain
*corresponding author: jose.encinar@upm.es

Abstract: Some recent applications based on the reflectarray's properties of independent beamforming at two frequencies and two polarizations are described. The applications include, reflectarrays generating separate beams for each polarization, operating at dual frequency (transmit and receive) for Telecomm satellites, and reflectarray panels to eliminate "blind zones" in the deployment millimeter-wave 5G networks.

Reflectarrays, contrary to reflector antennas, offer the possibility of independent beamforming for each polarization in multi-frequency operation, by using reflectarray cells with various conductive printed elements that can be tuned to allow an independent phase control for each frequency and polarization. Some recent applications, which exploit this unique property of reflectarrays, are presented.

Several applications have been proposed for satellite antennas. The first one was a reflectarray able to generate independent beam for DBS, covering North America in V-polarization and Europe in H-polarization, see Fig. 1. A 1-m breadboard was designed, manufactured and tested to produce a contoured beam for a European coverage in H-polarization, and a pencil beam to illuminate the East Coast in North America in V-polarization [1]. The gain requirements were fulfilled in a 10% bandwidth for both coverages.

A 43-cm reflectarray antenna was developed [2] to generate four adjacent beams per feed, each in a unique frequency-polarization pairing, see Fig. 2. This design has applications to multi-beam antennas for spot-coverage. The design method combines the beam squint effect with the independent phase control in each linear polarization. This approach is suitable for multi-beam antennas to generate a cellular coverage with frequency and polarization reuse, enabling a reduction of required antennas and feeds for the whole coverage.

More recently, a 90-cm parabolic reflectarray has been demonstrated to generate two beams per feed in orthogonal Circular Polarization (CP), operating at two frequency bands (20 GHz for transmit and 30 GHz for receive) [3], see Fig. 3. The measured radiation patterns (see Fig. 4) show the six beams generated by three feeds operating in dual-CP. This results are satisfactory and validate the concept of generating two spaced beams in the orthogonal CP by a single feed, changing the polarization of the beam in Tx and Rx. This concept can be suitable for multispot satellites in Ka-band, enabling to reduce the number of onboard antennas, from four conventional reflectors to two reflectarrays.

Finally, reflectarray panels have been proposed as Reconfigurable Intelligent Surfaces (RIS) to address the problem of "blind zones" in the deployment millimeter-wave 5G networks, see Fig. 5. Passive RIS are designed to illuminate the blind zone by redirecting and shaping the reflected beam received from a nearby Base Station (BS), by using a phase-only pattern synthesis [4]. The reflectarray based RIS can be deployed at reduced cost, with

low visual impact (installed on walls or ceilings) and without requiring any energy supply. Moreover, they are designed in dual-linear polarization to compensate the different reflecting properties under oblique incidence and to apply polarization diversity. They can also be designed to generate different coverages in two frequency bands, as 28 GHz and 38 GHz. Finally, reconfigurable reflectarray panels based on liquid crystals [5] can be used to dynamically reconfigure the coverage, according to the users' demand.

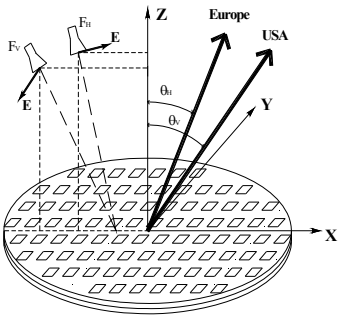

Figure 1. Reflectarray with different beams for V and H polarization.

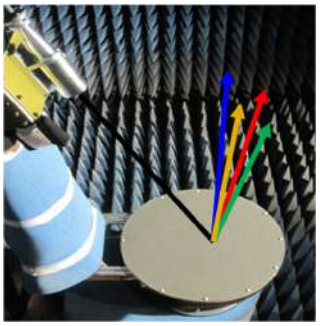

Figure 2. Reflectarray generating 4 beams per feed.

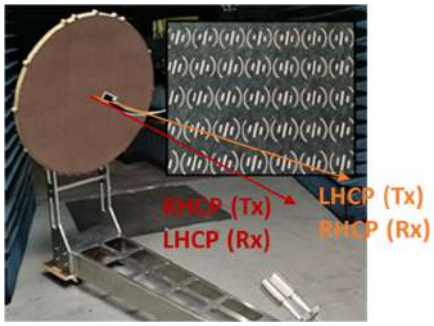

Figure 3. Reflectarray generating 2 beams per feed at Tx and Rx frequencies.

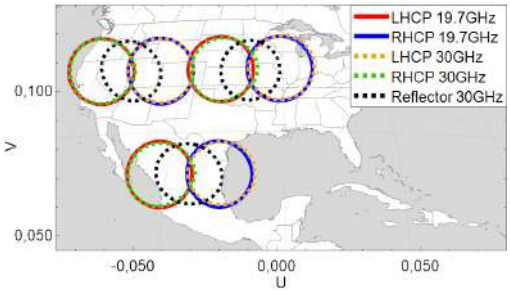

Figure 4. Six beams generated by 3 feeds in dual-CP.

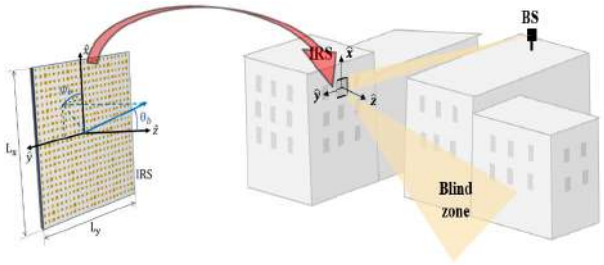

Figure 5. Reflectarray panels as RIS for mm-wave 5G.

This work has been supported by the Spanish Ministry of Science and Innovation and the Spanish Research Agency within projects PID2020-114172RB-C21-2/ and PDC2021-120959-C21AEI/10.13039/501100011033, and by the Spanish Ministry of Economic Affairs and Digital Transformation within the project DISRADIO TSI-063000-2021-82. The last two granted by the NextGenerationEU under the Recovery plan for Europe and the Recovery and Resilience Facility.

References

1. Encinar, J.A. et al., "Dual-Polarization Dual-Coverage Reflectarray for Space Applications," IEEE Transactions on Antennas and Propagation, vol. 54, no. 10, pp. 2827-2837, Oct. 2006.
2. Martinez-De-Rioja, D., E. Martinez-De-Rioja, J. A. Encinar, R. Florencio and G. Toso, "Reflectarray to Generate Four Adjacent Beams per Feed for Multispot Satellite Antennas," in IEEE Trans. on Antennas and Propagat. vol. 67, no. 2, pp. 1265-1269, Feb. 2019.
3. Martinez-de-Rioja, D. et al., "Transmit–Receive Parabolic Reflectarray to Generate Two Beams per Feed for Multispot Satellite Antennas in Ka-Band," IEEE Trans. on Antennas and Propagat., vol. 69, no. 5, pp. 2673-2685, May 2021.
4. Vaquero, Á. F. et al., "Reflectarray-based Intelligent Reflecting Surface to Improve mm-Wave 5G coverage in outdoor scenarios," 2022 IEEE Intl. Symp. on Antennas and Propagation (AP-S/URSI), Denver, CO, USA, 2022, pp. 794-795
5. Guirado, R. et al., "Dynamic Modeling of Liquid Crystal-Based Metasurfaces and Its Application to Reducing Reconfigurability Times," in IEEE Trans. on Antennas and Propagat., vol. 70, no. 12, pp. 11847-11857, Dec. 2022.

Multiband Substrate Integrated Waveguide Dielectric Resonator Antenna for 4G and 5G Applications

I. K. C. Lin[1] **and M. H. Jamaluddin**[1*]

[1]Wireless Communication Centre, Faculty of Electrical Engineering, Universiti Teknologi Malaysia, 81310 Johor Bahru, Johor, Malaysia

[*]corresponding author: haizal@fke.utm.my

Abstract: In this work, Substrate Integrated Waveguide with a Dielectric Resonator Antenna is introduced in a more compact size to operate in the 4G bands for LTE Band 3 (1.8 GHz), LTE Band 7 (2.6 GHz) and covers 5G Band n77 (3.7 GHz). A U-shaped slot cut is introduced in order to produce multiple frequency of operation. Simulation is done using Ansys HFSS (High Frequency Structure Simulator) version 2019. Simulated impedance bandwidths are 21.51% (1.67- 2.07 GHz) at 1.8 GHz, 4.63% (2.53-2.65 GHz) at 2.6 GHz and 7.57% (3.56-3.84GHz) at 3.7 GHz and good radiation pattern performance were obtained.

I. Introduction

A compact multiband antenna is favored in today's wireless communication era [1]. A multiband resonance can be obtained by the multiple slots [2] using Substrate Integrated Waveguide (SIW). In this paper, a rectangular Dielectric Resonator Antenna (DRA) excited by a U-shaped slot using Substrate Integrated Waveguide is proposed in this paper for 4G and 5G applications to have higher bandwidth and higher gain.

II. Research Methodology

The 3D model view of a single port SIW fed DRA is shown in Fig. 1. A FR4 substrate with a permittivity of 4.6, a loss tangent of 0.019 and with a thickness of 1.6 mm is used. A DRA's permittivity of 10 and a loss tangent of 0.0019 is used in this work. Its dimensions for 1.8 GHz are calculated in [1]. It is excited in respective mode by the U-shaped cut configuration, located in the top wall of SIW operating in TE10 mode. The SIW and microstrip transition design parameters are calculated from a conventional waveguide WR 430 in [3], [4], [5].

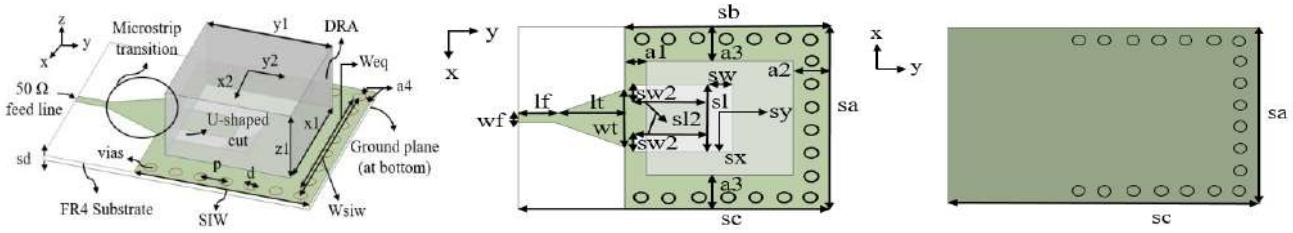

(a) (b) (c)

Fig. 1 Single port SIW with a DRA geometry (a) Overall 3D view (b) Top view (c) Back view

Table 1 Optimised design parameters

Parameter	sa	sb	sc	sd	x1	y1	z1	x2	y2	lf	lt	wf	wt	sw
Value (mm)	64	56	85	1.6	40	40	21	0	-2	10	19	2.95	20	7

Parameter	sl2	sw2	sx	sl	sy	d	p	a1	a2	a3	a4	Weq	Wsiw
Value (mm)	20	6	0	23	-2	4	8	6	10	12	2	52	56

III. Result and Discussion

The simulated results of the proposed antenna are discussed. The simulated impedance bandwidths are 21.51% (1.67-2.07 GHz) at 1.8 GHz, 4.63% (2.53-2.65 GHz) at 2.6 GHz and 7.57% (3.56-3.84 GHz) at 3.7 GHz, as shown in Fig. 2(a). Less than -22 dB of return loss is found within the bands of interest. Simulated normalised radiation patterns of E-plane and H-plane for each frequency is depicted in Figs. 2(b), 2(c) and 2(d).

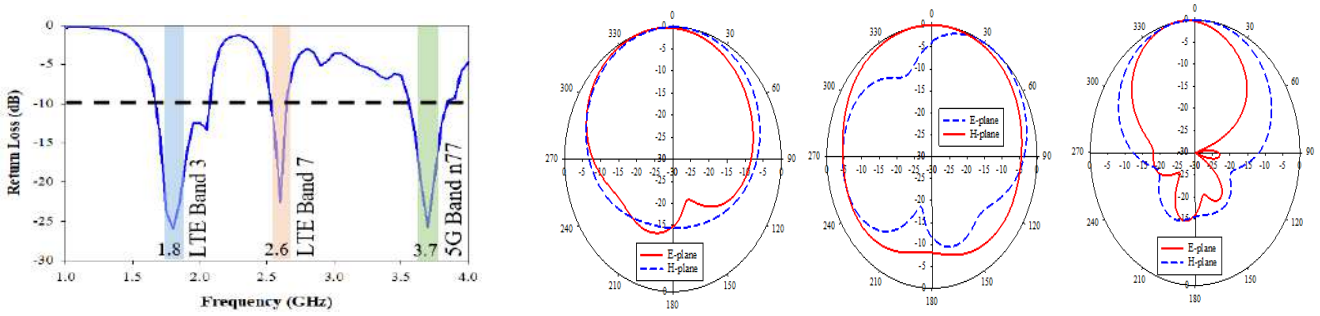

(a) (b) (c) (d)

Fig. 2 Simulated antenna performance (a) return loss (b) normalised radiation patterns at 1.8 GHz (c) normalised radiation patterns at 2.6 GHz (d) normalised radiation patterns at 3.7 GHz

IV. Conclusion

A multiband SIW singly fed with a DRA and a U-shaped cut is presented in this paper. The antenna exhibits good characteristics where impedance bandwidths are 21.51% at 1.8 GHz, 4.63% at 2.6 GHz and 7.57% at 3.7 GHz. More than 4.5 dBi of gain and at least 74% of antenna efficiency are found within the bands of interest. The proposed antenna can be a good candidate for 4G and 5G applications.

Acknowledgements

This study was supported by the Fundamental Research Grant Scheme (FRGS) awarded by the Ministry of Education of Malaysia (Investigation of Low Cost Substrate-Based Antenna Using Three-Dimensional Printing Technology for Fifth Generation Wireless System) –FRGS/1/2021/TK0/UTM/02/60).

References

1. Lin, I. K. C., M. H. Jamaluddin, A. Awang, R. Selvaraju, M. H. Dahri, L. C. Yen and H. A. Rahim, “A Triple Band Hybrid MIMO Rectangular Dielectric Resonator Antenna for LTE Applications,” IEEE Access, Vol. 7, 122900-122913, 2019.
2. Ashraf, N., O. Haraz, M. A. Ashraf and S. Alshebeili, “28/38-GHz dual-band millimeter wave SIW array antenna with EBG structures for 5G applications,” in International Conference on Information and Communication Technology Research (ICTRC), 5–8, 2015.
3. Iqbal, A., J. J. Tiang, S. K. Wong, M. Alibakhshikenari, F. Falcone and E. Limiti, “Miniaturization Trends in Substrate Integrated Waveguide (SIW) Filters: A Review,” IEEE Access, Vol. 8, 223287–223305, 2020.
4. Kumar, P., S. Dwari, S. Singh and N. K. Agrawal, “Design Investigation of a Laminated Waveguide Fed Multi-Band DRA for Military Applications,” Frequenz, Vol. 72, No. 1–2, 7–14, 2018.
5. Kumar, H., R. Jadhav and S. Ranade, “A Review on Substrate Integrated Waveguide and its Microstrip Interconnect,” IOSR J Electron Commun Eng, Vol. 3, No. 5, 36–40, 2012.

On The Performance of Minkowski Fractal Resonator for Ku-Band Applications

Mustafa Mahdi Ali [1,2], Taha A. Elwi [3], Enrique Márquez-Segura [1,]

[1]Telecommunication Research Institute (TELMA), E.T.S. Ingeniería de Telecomunicación, Universidad de Málaga, Málaga, Spain.
[2]Electrical Engineering Department, College of Engineering, Mustansiriyah University, Iraq.
[3] International Applied and Theoretical Research Center (IATRC), Baghdad Quarter, Iraq.
*corresponding author, E-mail: ems@ic.uma.es

Abstract

The proposed resonator is applied for Ku-band applications based on a two-port network configuration. The resonator is based on metamaterial behavior using Minkowski fractal design. It is found that the proposed resonator shows an excellent bandwidth obtaining a reflection coefficient below -10dB around the target frequency of 15.6GHz. Such achievement is obtained considering 3-unit cells. The resonator performances in terms of S-parameters are obtained from CST MWS and HFSS software packages for assessment. It is found that the proposed resonator establishes a cut-off frequency bandwidth out of the pass band between 14GHz and 15.5GHz with matching coupling of -15dB. It is noteworthy that the proposed resonator occupies an area of 30mm×35mm when printed on Roger substrate 5880 of 0.8mm thickness with a low dielectric constant of 2.2.

1. Introduction

Researchers has been attracted to use composite right/left-handed structures due to their unique performance and useful characteristics [1]. These structures are characterized by their effective size reduction with enhanced electromagnetic properties over a wide band of frequencies [2]. However, they suffer from bandwidth limitations at certain frequencies because of parasitic coupling and field gradient at certain edges and slots [3]. Therefore, many researchers applied their studies on eliminating those phenomena. One of those solutions, for instance, is the introduction of fractal geometries due to their self-design property that depends on traces geometries instead of slots within a limited area that magnify the current intensity by increasing electrical path [4]. Thus, the researchers in [5] applied a Hilbert shape to create a miniaturized microstrip antenna at C-band applications. Later, the same Hilbert geometry but with a third order was introduced for microwave sensing applications at low frequency bands, as in [6], where a design of a Hilbert shape metamaterial for gain enhancement of a printed dipole antenna for Wi-Fi applications was presented.

Another geometry with interesting properties based on Minkowski shape was proposed to develop several microwave devices for different applications. For example, a design of a compact dual band microstrip filter was proposed in [7] for modern communication systems. Another design was proposed based on interdigital based on Minkowski fractal geometry for bandpass filter design at sub-6 GHz. The use of such fractal is to maintain size reduction with minimum field fringing from sharp edges [8]. On the other hand, a design of a multistage resonator was proposed in [9] for dual band passband filter applications. The closed ring stepped impedance resonators are usually inductively excited to realize effectively permeable behaviors with high magnetic field intensity [10].

One of the most famous fractal types is Koch geometry that was modified for different microwave applications [11]. In [12] a design of MIMO antenna at millimeter wave was proposed based on the third order of Koch geometry. Therefore, it was a similar design that was proposed in [13], based modified metamaterial Koch geometry to suite the applications of MIMO systems at 5G and sub-6 GHz applications.

In this paper, a design of a stepped closed ring resonator based on Minkowski is proposed for Ku band applications. The geometrical details of the proposed resonator are introduced in section two. In section three, an analytical circuit model is proposed. The design methodology is discussed in section four. For validation, two different commercial electromagnetic simulator packages are invoked to optimize the proposed design as seen in section five. Finally, the paper is concluded in section six.

2. Geometrical details

In this section, the proposed resonator design based the Minkowski fractal of the second order is thoroughly discussed. As seen in Fig.1, the proposed resonator is attached to 50Ω transmission line with a separation distance of coupling about tenth of the substrate thickness [5].

Now, such distance is considered to ensure the electrostatic charges accumulation with enough capacitive coupling and minimum field gradient [6]. The transmission line is invoked to activate TEM-mode excitation; in which, the electric and magnetic fields is quasi perpendicular to each other with respect to the propagation [5]. The proposed Minkowski fractal geometry is picked among many other fractals to maintain stepped iterations in a way keeping continuous

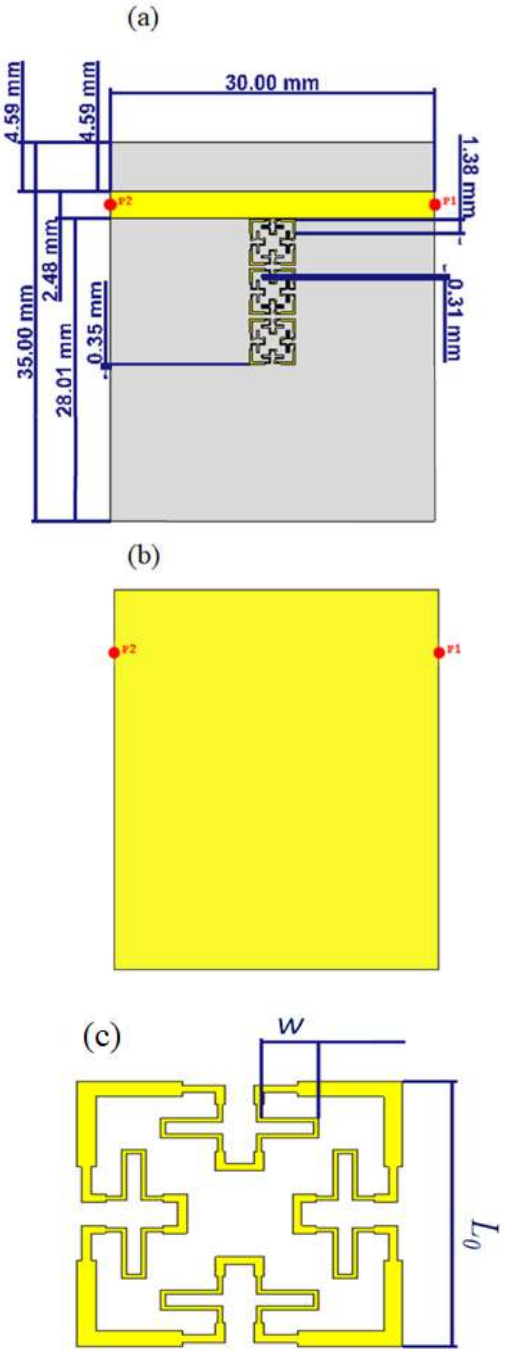

Figure 1: Resonator geometrical details: (a) front view of the whole structure, (b) back view showing the complete ground plane, and (c) detail of the unit cell showing the main parameters w and L_0.

consistency of impedance variation [7]. This is because the high symmetry with respect to the width and length that realizes symmetrical variation in the relative constitutive parameters [8]. The proposed microwave resonator is discussed with all geometrical details in this section. The proposed fractal is designed to realize a frequency resonance around 15.6GHz. This frequency resonance can be calculated according to fractal perimeter, which can be obtained according to [10] as

$$P_n = \left(1 + 2\frac{w}{L_0}\right) P_{n-1}, \qquad (1)$$

where P_n is the perimeter of the n-th iteration fractal structure, w, and L_0 are as depicted in Fig.1.

3. Design methodology

In this section, a parametric study is involved to determine the optimal design by using the relevant parameter as the transmission line geometry, the order of the Minkowski unit cell used and the number of unit cells.

3.1. Substrate length

The proposed transmission line structure is designed to obtain a close value around 50Ω for characteristic impedance. This can be calculated directly from [11] analytically based on the transmission line width. However, the authors evaluated the S-parameters in terms of S11 and S12 through full-wave analysis based on commercial software package of CST microwave studio [12]. Therefore, the effect of substrate dimension is changed with an increase of substrate length (Ls) starting from 0mm to 20mm where the initial substrate dimension is 15mm. In such case the effective dimensions would be accumulatively varied from 15mm to 35mm with step of 5mm. It is found from the obtained results insignificant variations in the S-parameters due to the fact of field fringing is negligible when the trace line is much less than the substrate dimensions [14]. Fig.2 shows the obtained results from the proposed parametric study in terms of S11 and S12 spectra.

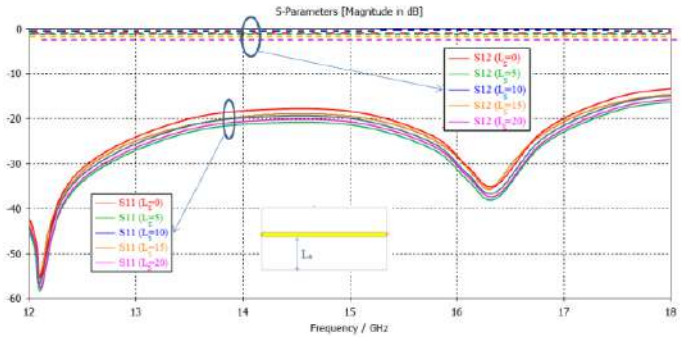

Figure 2: Evaluated S-parameters based varying the substrate dimension in terms of S11 and S12 frequency response.

3.2. Minkowski Order Effects

Based on transmission line theory that was explained in [15], the authors evaluated the effective S-parameters parameters. These parameters describe the inherent characteristics of the proposed fractal structure at the resonance frequency band. Therefore, the authors computed

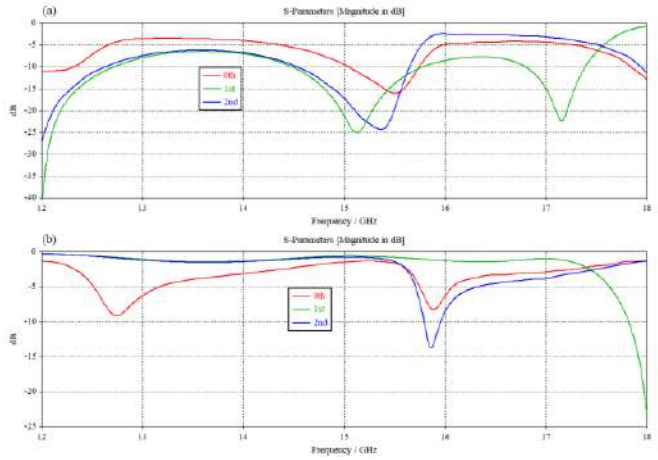

Figure 3: Evaluated S-parameters based varying the order effect in terms: (a) S11 and (b) S12 frequency response.

in terms of S11 and S12 spectra. These calculations are applied to the proposed Minkowski starting from the zeroth up to the second order. In this analysis the authors mounted the proposed unit cell on a substrate enclose to the transmission line to evaluate the unit cell S-parameters. Therefore, the generated waves inside such transmission line are excited from two wave guides ports to mimic TEM-like free space environment [15]. Thus, the unit cell S-parameters would be used to characterize the basic properties in terms of bandwidth, frequency resonance, and losses as shown in Fig.3.

It is found from the proposed results of S12 spectra; the second order provides a frequency resonance at 15.6GHz that effectively eliminated the first mode of the zeroth order and the resonance band of the first order, effectively. It is obvious that the second order combined these bands without new mode generation. This reveals no need to increase complexity of the design to consider the third order with high complexity and implementation difficulty.

3.3. Number of unit cells

The proposed resonator is constructed from number of proposed unit cells. Therefore, it is very logical to study the effect of increasing the number of unit cell on the performance of proposed resonator. In such case the variation in the S-parameters with respect to the unit cell number increase from 1 to 5 with step of 1 is realized for each case in Fig. 4. It has been found from such study that increasing the unit cell repetition would increase the proposed resonator bandwidth with greater slope at edges. In the same context, each individual unit cell performs separately as an L-C branch; therefore, increasing the unit cell number increases the number of L-C branches [11].

4. Validation and Discussion

After arriving to the optimal design, authors invoked another software package based on HFSS simulations for validation.

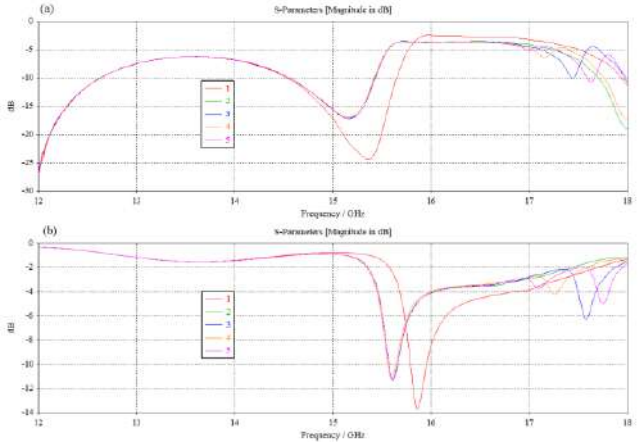

Figure 4: Evaluated S-parameters based varying the unit cell number in terms: (a) S11 and (b) S12 frequency response.

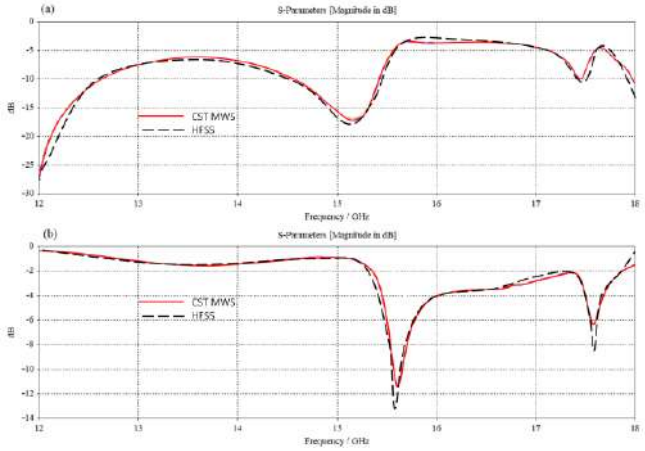

Figure 5: The proposed resonator results validations based on CST MWS and HFSS software simulations.

We found from the obtained results an excellent agreement between the results of CST and HFSS simulations, using different numerical algorithms to assess the model. It is clear that the proposed resonator shows an excellent bandwidth with well-acceptance and maximum transmission around 15.6GHz with S12 below -10dB. The maximum reflection magnitude in terms of S11 is found to be -5dB at the frequency band of interest. Such observations reveal that the proposed resonator behaves an excellent passband filter. As seen in Fig.5, the obtained results from both CST and HFSS simulations are presented. It is found the achieved results from both software packages agree very well to each other.

Finally, a comparison between their proposed resonator and other published results to indicate the achieved advancements over other resonators has been carried out. The proposed resonator is found to show minimum reflection coefficient in terms of S11 in comparison to other published results. Such achievement is attributed to the advantages of using Minkowski fractal unit cell structure. The comparison is extended between different published

results in terms of S11 and S21 parameters at the frequency resonance (f_r) as shown in Table 1.

Table 1: Comparison between the proposed resonator results and other published results.

Ref.	S_{11}/dB	S_{12}/dB	f_r/GHz
[1]	-1.6	-15	2.1
[2]	-2.5	-30	5.7
[3]	-5.0	-40	2.95
[4]	-3.6	-20	2
[4]	-1.3	-15	1.4
[5]	-2.4	-38	4.05
[6]	-4.5	-12	3.5
[7]	-2.9	-13/-21	0.75/1.24
[8]	-1.9	-19	2.14
[9]	-1.6	-16	3.75
[10]	-1.1	-30	4.1
[11]	-1.2	-40	0.8
[12]	-2.3	-22	1.1
[13]	-3.0	-18	2.96
[14]	-1.8	-19	2.23

5. Conclusion

The proposed work is designed based on a printed microwave resonator which is developed for Ku-band. It is designed based on a single column array of 3 unit cells of Minkowski fractal design. Therefore, the proposed design is found to provide a pass band around 15.6GHz with S12 about -12dB. The proposed work is designed using CST MWS to optimize the resonator bandwidth parametrically. The proposed resonator occupies an area about 35×30mm2 when printed on Roger 8550 substrate of 0.8mm thickness. The proposed work is found to show an excellent performance in comparison to identical resonators that were published in the literature. For validations, the proposed resonator performances are evaluated using HFSS. Finally, the results from CST MWS and HFSS are found to agree to each other excellently.

References

[1] S. Arain, P. Vryonides, M. A. B. Abbasi, A. Quddious, M. A. Antoniades and S. Nikolaou, "Reconfigurable Bandwidth Bandpass Filter With Enhanced Out-of-Band Rejection Using π -Section-Loaded Ring Resonator," *IEEE Microwave and Wireless Components Letters*, vol. 28, no. 1, pp. 28-30, Jan. 2018.

[2] T. Cheng and K. -W. Tam, "A Wideband Bandpass Filter With Reconfigurable Bandwidth Based on Cross-Shaped Resonator," *IEEE Microwave and Wireless Components Letters*, vol. 27, no. 10, pp. 909-911, Oct. 2017.

[3] X. -K. Bi, X. Zhang, S. -W. Wong, S. -H. Guo and T. Yuan, "Design of Notched-Wideband Bandpass Filters with Reconfigurable Bandwidth Based on Terminated Cross-Shaped Resonators," *IEEE Access*, vol. 8, pp. 37416-37427, 2020.

[4] M. A. Sanchez Soriano, R. Gomez Garcia, G. Torregrosa Penalva, "Reconfigurable-bandwidth bandpass filter within 10–50%" *IET Microwave Antenna*, vol. 7, pp. 502–509, Nov. 2012.

[5] A. L. Borja, J. Carbonell, J. L. Martinez, "A controllable bandwidth filter using varactor-loaded metamaterial-inspired transmission lines" *IEEE Antennas Wireless Propagation,* vol. 10, pp. 1575–1578, May. 2013.

[6] N. Chen, S. K. Jeng, "Reconfigurable bandpass filter with separately relocatable passband edge" *IEEE Microwave Wireless Components Letter*, vol. 22, pp. 559–561, Sep. 2012.

[7] X. M. Wang, X. K. Bi, S. H. Guo. "Synthesis design of equal-ripple and quasi-elliptic wideband BPFs with independently reconfigurable lower passband edge" *IEEE Access*, vol. 8, pp. 76856–76866, Oct. 2020.

[8] R. Gomez-Garcia, A. C. Guyette, D. Psychogiou, "Quasi-elliptic multi-band filters with center-frequency and bandwidth tenability" *IEEE Microwave Wireless Components Letter*, vol. 26, pp. 192–194, Dec. 2019.

[9] B. C. Huang, N. W. Chen, S. K. Jeng, "A reconfigurable bandpass filter based on a varactor-perturbed, T-shaped dual-mode resonator", *IEEE Microwave Wireless Components Letters*, vol. 24, pp. 297–299, Jun. 2017.

[10] M. Sanchez-Renedo, R. Gomez-Garcia, J. L. Alonso, "Tunable combline filter with continuous control of center frequency and bandwidth", *IEEE Transactions Microwave Theory and Techniques*, vol. 53, pp.191–199, Jan. 2005.

[11] P. W. Wong and I. C. Hunter, "Electronically Reconfigurable Microwave Bandpass Filter," *IEEE Transactions on Microwave Theory and Techniques,* vol. 57, no. 12, pp. 3070-3079, Dec. 2009.

[12] H. -J. Tsai, N. -W. Chen and S. -K. Jeng, "Center Frequency and Bandwidth Controllable Microstrip Bandpass Filter Design Using Loop-Shaped Dual-Mode Resonator," *IEEE Transactions on Microwave Theory and Techniques*, vol. 61, no. 10, pp. 3590-3600, Oct. 2013.

[13] H. Guo, J. Ni and J. Hong, "Varactor-Tuned Dual-Mode Bandpass Filter With Nonuniform Q Distribution," *IEEE Microwave and Wireless Components Letters*, vol. 28, no. 11, pp. 1002-1004, Nov. 2018.

[14] C. Schuster, A. Wiens, F. Schmidt, "Performance analysis of reconfigurable bandpass filters with continuously tunable center frequency and bandwidth" *IEEE Transactions on Microwave Theory and Techniques*, vol. 65, pp. 4572–4583, Sep. 2017.

T. A. Elwi, "A Further Investigation on the Performance of the Broadside Coupled Rectangular Split Ring Resonators," *Progress in Electromagnetics Research Letters*, vol. 34, pp. 1-8, Oct. 2012.

Investigation of Compact Antenna Test Range Symmetry Requirements

M. Dirix[1*] and S. F. Gregson[2, 3]

[1]Antenna Systems Solutions, Spain
[2]Next Phase Measurements, USA, [3]Queen Mary University London, UK
[*]corresponding author: mdirix@asysol.com

Abstract: The optimal design of a compact antenna test range (CATR) is constrained by many factors including electrical performance, available space, and facility cost. This trade-off has implications for the location of certain critical components which include the reflector, antenna under test positioner, and feed positioner. This paper presents the results of a recent study that examined the effect on measurement accuracies of utilising three commonly used configurations for the CATR feed position, namely floor-, corner- and side-fed. Here, particular attention is paid to the effect of range symmetry on measured test antenna co- and cross-polar patterns.

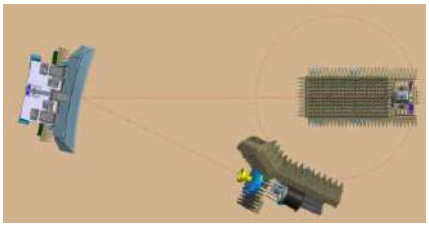

Figure 1. Layout of a corner fed CATR

While over the air (OTA) testing is performed almost exclusively in the direct far-field in the sub-6 GHz FR1 bands, the CATR has become the de facto standard test methodology for mm-wave massive multiple input multiple output (Massive MIMO) antennas for the 5G New Radio communication systems [1]. This is especially true for mm-wave, FR2, OTA test applications which have greatly intensified the demand for CATRs, and particularly those having small quiet zone (QZ) sizes, *e.g.* ranging from 0.3 to 0.6 m in diameter. This, coupled with the frequent need to collocate multiple test systems needed for production testing, has further increased the desire for highly space efficient designs. Here, the position of the feed within a CATR can be seen to be a particularly important factor in these considerations as, for example, corner-fed CATRs provide an easy way to reduce the overall length of the setup whilst incurring only a comparatively minimal impact on the width as is illustrated in Figure 1. Indeed each of the floor-, corner-, and side-fed CATR configurations place different constraints in terms of the physical envelope required by the respective systems, whilst also yielding subtly different properties of the resulting, collimated, pseudo plane-wave [2].

In this paper, we compare and contrast the electrical performances of these three commonly employed range configurations by means of an accurate numerical simulation that provides the “measured” antenna pattern for a known CATR and AUT pair. Details of the simulation technique together with its verification are left to the open literature [3, 4, 5] A floor fed blended rolled edge (BRE) single offset parabolic reflector with a 4 m focal length was designed and optimised using the techniques developed in [6, 7, 8, 9]. The CATR design was then fed from the floor, corner, and side with the edge treatments being kept consistent between three cases with the CATR quiet-zone (QZ) field distribution being predicted at 5 GHz for each. Here, a frequency towards the bottom of the operational frequency of this design was chosen as this is the region in which the QZ will have the largest differences as here the reflector is electrically smallest. These can be seen presented in Figure 2. While the symmetry of the copolar field distribution is more easily derived from the one-dimensional line plots (a), (c) and (e), the overall cross-polar pattern and its symmetry is more discernible from the two-dimensional false colour checkerboard plots (b), (d),and (f). Inside the QZ field, two different simulated test antennas are considered. The first antenna is a WR187 pyramidal horn which was placed with its aperture at the centre of the QZ and centre of rotation of the φ over θ positioner. This represents a very simple case and provides a good baseline for further evaluation of the algorithm, however here only a small and typically optimal portion of the QZ is occupied by the antenna during an acquisition. The “second” antenna comprised the same pyramidal horn, only here its aperture was displaced by 0.25 m in the positive z-direction away from the positioner rotation origin which means the antenna traverses across a larger

portion of the QZ during its measurement as the AUT is rotated from -90° to +90° in azimuth. This is the most commonly used acquisition mode, with even a conventional "model tower" ϕ over θ type positioning system utilising the same horizontal motion [3]. Then, for each of the three CATR configurations, the RMS dB difference level was calculated between the ideal "reference" far-field pattern of the AUT and the simulated "measured" pattern to provide a single quantitative measure of similarity [3]. A further test involved performing a "flip test" on each of the patterns to obtain a measure of symmetry within the measurement, which replicates a test that is often performed in antenna test system validation campaigns [3]. Finally, the lower bound sensitivity for the simulation, which was found to be at circa -88 dB for the copolar pattern and significantly lower for the cross-polar pattern, was determined by illuminating the AUT with a perfect plane wave, and then comparing this with the reference far-field pattern. Here, the sensitivity of the simulation technique was established as more than 20 dB below the pattern level for all cases considered.

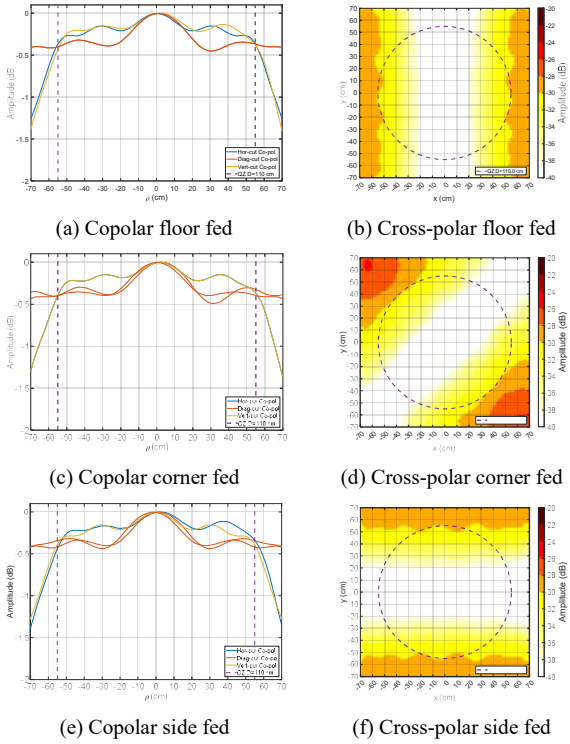

(a) Copolar floor fed (b) Cross-polar floor fed

(c) Copolar corner fed (d) Cross-polar corner fed

(e) Copolar side fed (f) Cross-polar side fed

Figure 2. BRE CATR Quiet-Zone Field Distribution.

In Table 1 the RMS dB difference levels are shown for comparison of the various configurations. Here it can be seen that the pattern accuracy of the offset pyramidal horn has degraded by *circa* 10 dB from the centred horn, which is caused by the larger part of the QZ that the offset horn traverses through during the measurement. However, more interesting is that the differences between the CATR setups remains within 2 dB for all three cases, and is largely independent of the position of the horn. Further investigation of Table 1 shows that for the offset horn case, the accuracy of the measured copolar patterns is very similar, even though the flip test clearly shows a much greater degree of symmetry for the floor fed case. In essence, this just means that the left and right hand sides of the pattern will have the exact same error. Lastly, while looking at the furthest right column of Table 1, it shows that as expected from the field distribution presented in Figure 2, the floor fed case performs the worst in terms of cross-polar accuracy, and the side-fed case shows the best performance for antenna centred in the QZ and φ over θ positioner. It should be noted here that this will only be true for an azimuth scanning, which as noted above, is the most commonly used setup, including using a conventional "model tower" ϕ over θ type positioner.

RMS difference (dB)	Centred Pyramidal Horn	Offset Pyramidal Horn		
	Co-Pol.	Co-Pol.	Co-Pol. Flip	Cx-Pol.
Floor Fed	-63	-53	-139	-59
Corner Fed	-61	-54	-56	-62
Side Fed	-60	-54	-54	-130

Table 1: Measurement accuracy presented as RMS dB difference levels.

In summary, this paper has used an end-to-end measurement simulation to compare the measurement accuracies of several common CATR feed configurations. It was shown that the expected measurement error between the three configurations is comparable, where range symmetry is only expected to result in a symmetric constellation of said errors. Thus, we have established that conventional flip tests can yield unduly optimistic estimations of accuracy if not interpreted correctly. This paper has been able to confirm that the best cross-polar accuracies can be obtained when using a side fed CATR arrangement when the AUT is not located at the origin of the measurement coordinate system.

References

[1] Y. Hu, S. Wang and S. An, "Over the Air Testing and Error Analysis of 5G Active Antenna System Base Station in Compact Antenna Test Range," 2019 Photonics & Electromagnetics Research Symposium - Fall (PIERS - Fall), Xiamen, China, 2019, pp. 1007-1010, doi: 10.1109/PIERS-Fall48861.2019.9021378.

[2] A. D. Olver, "Compact antenna test ranges," 1991 Seventh International Conference on Antennas and Propagation, ICAP 91 (IEE), York, 1991, pp. 99-108 vol.1.

[3] C. Parini, S. Gregson, J. McCormick, D. Janse van Rensburg and T. Eibert, Theory and Practice of Modern Antenna Range Measurements, 2nd Expanded Edition ed., vol. 1, London: IET Press, 2020.

[4] C. Parini, R. Dubrovka and S. Gregson, “Compact Range Quiet Zone Modelling: Quantitative Assessment using a Variety of Electromagnetic Simulation Methods,” in Loughborough Conference on Antennas and Propagation, Loughborough, 2015.

[5] C. Parini, R. Dubrovka and S. Gregson, “CATR Quiet Zone Modelling and the Prediction of 'Measured' Radiation Pattern Errors: Comparison using a Variety of Electromagnetic Simulation Methods,” in AMTA 37th Annual Meeting & Symposium, Long Beach California, 2015.

[6] I. Gupta and W. Burnside, “A Method to Design Blended Rolled Edges for Compact Range Reflectors,” The Ohio State University, ElectroScience Laboratory, Columbus, 1989.

[7] S. Gregson, M. Dirix and R. Dubrovka, “Efficient Optimization of the Blended Rolled Edge of a Rectangular Single Offset Fed Compact Antenna Test Range Reflector Using Genetic Evolution” in EuCAP, Madrid, 2022.

[8] M. Dirix, S. Gregson and R. Dubrovka, “Genetic Evolution of the Reflector Edge Treatment of a Single Offset-Fed Compact Antenna Test Range for 5G New Radio Applications,” in AMTA Annual Meeting and Symposium, Daytona Beach, Florida, 2021.

[9] M. Dirix, S. Gregson and R. Dubrovka, “Genetic Optimization of Edge Treatments of Single Offset Reflector Compact Antenna Test Ranges,” in AMTA Annual Meeting and Symposium, Denver, CO, 2022.

Investigation of the textile technology impact's on the RF performances of a fully textile offset parabolic antenna design

L. MERCIER[1,2*], B. AGNUS[1], Y. HERVE[1] and S .CARRAS[3]

[1]SCIENTEAMA, 27 rue des Glengarrians, 14610 Villons les buissons, France
[2]LATMOS/IPSL, UVSQ Université Paris-Saclay, Sorbonne Université, CNRS, France
[3]FILIX SAS, Rue Saint-Aventin, F-10150 Creney-prés-Troyes, France, stephane.carras@filix.fr
[*] Léa MERCIER: lea.mercier@scienteama.fr

Abstract: This paper details the analysis of a fully textile offset parabolic antenna that operates around 8 GHz. The performances of the textile design are compared to that of a reference counterpart antenna provided by CNES. The objective of this study is to observe the impact of the textile technology on the deterioration of the radio-frequency performances of the antenna and to highlight the ratio between the effective gain of the antenna and the weight of the design.

In the constantly evolving space sector, new technologies have been introduced due to the need of new lightweight and resistant materials while dealing with space condition as vacuum, high temperature variation or also shock and vibrations during the launch. Especially in the design of new type of integrated antenna's deployable and reconfigurable for communications or planetary scientific objectives (sounding radar, Ground Penatrating Radar...) according to the needs of the given mission. At the meantime, the IoT (Internet of Things) increased tremendously in recent years, which has increased the interest and the integration of textile antennas with flexible structure in different sectors such as smart clothing or medical industry. SCIENTEAMA company develops ultra light and flexible electronic devices using technology based on processed textile fibers supplied by FILIX® company [1][2][3]. These textile materials have been designed in the context of the research project on innovative textile, FIL HARMONIQUE initiated in 2017 [1][2].Textile antennas using this technology have already been realized and tested in RF (Radio-Frequency) radiation. In IOT or WLAN (Wireless Local Area Network) configurations [3] but not yet for space applications.

In order to evaluate the performance of such a technology and its potential compatibility with the space industry, a collaboration has been initiated between SCIENTEAMA and CNES. With as a preliminary study to compare the RF performances of a reference antenna provided by CNES [4] with known characteristics to the exact same design with identical parameters made with our materials. An offset parabolic antenna operating between 8,025 GHz and 8,4 GHz has been selected by CNES for the analyze, with a 200 mm Z-projected diameter. The main objectives are to assess the impact of textile technology but also to highlight the gain of this promising new technology in terms of mass/gain ratio.

Two different versions of this antenna have been made with processed textile fibers in distinct textile structures in order to study also their effect on RF performances. Also, they must be able to operate at temperature ranging between -85°C and +85°C. The solution used for the antennas conception allows surface conditions that comply with RF specifications, while maintaining lightweight structures. The technology, which is neither a weaving nor a membrane, provides radiation properties for RF devices. The technique used also enables the antenna to be folded and unfolded using shape memory wires embedded in the structure [3].

Both models have been tested with the same source and feed positioner as the standard antenna for characterizing the antennas under the exact same conditions by CNES [4]. The weight of the antennas is 25.3 g and 29.3 g, depending on the applied textile structure and their thickness (around 1,55 mm). We will present and analyze the experimental data obtained of both textile prototypes and reference counterpart antenna.

Acknowledgements: Acknowledgement is made to the CNES for its contribution, especially the supply of the test platform and the realization of the antennas characterization.
We are grateful to the FILIX® company for providing the textile materials required for the conception of the antenna and the France Normandy Region support for this research work.

References

1. S. Carras, B. Agnus, B. Ravelo and B. Nsom, “Experimentation of an Ambient Micro-Energy Harvester Pillow”, Proc. Congrès Français de Mécanique 2019, Brest, France, 26-30 Août 2019, pp. 1-8.
2. Z. Xu, B. Ravelo, B. Agnus and S. Carras “Substrate microgrid fiber effects on microstrip line,” Proc. AES 2018 symposium, round-trip marseille cruise, june 24 – july 1, 2018
3. B. Agnus, S. Carras, B. Ravelo, "Improvement of Textile Antenna System Wireless Link Budget with Parabolic Textile Reflector", Proc. AES 2019, the 7th Advanced Electromagnetics Symposium, Lisbon, Portugal, 24-26 July 2019, pp. 1-
4. K. Elis, M. Romier, L. Feat, D. Belot, “Etude d’une antenne à pointage mécanique en bande X utilisant un guide d’onde coudé non-dépolarisant”,XXIèmes Journées Nationales Micro-ondes 14-17 mai 2019 – Caen

Review on Dual BP-NGD Phase Shifter Application for Beam Steering Antenna Design

(Invited talk)

B. Ravelo[1*], S. Ngoho[2], F. Wan[1], T. Gu[1], F. Haddad[3], M. Guerin[3], and W. Rahajandraibe[3]

[1]Nanjing University of Information Science & Technology (NUIST), Nanjing 210044, Jiangsu, China
[2]Association Française de Science des Systèmes (AFSCET), 151 Bd de l'Hôpital, Paris 75013, France
[3]Aix-Marseille University, CNRS, University of Toulon, IM2NP UMR7334, 13007 Marseille, France
[*]Corresponding author: blaise.ravelo@yahoo.fr

Abstract: Recent study reveals an application of dual bandpass (BP) type negative group delay (NGD) circuit for beam steering antenna array (BSAA) design. The innovative BSAA is based on frequency independent microwave phase shifter. The operation principle in function of the BP-NGD center frequency and bandwidth is described. An illustrative recent result showing simultaneous steering in two different directions by means of NGD value in dual-band frequency is reviewed. The proposed dual BP-NGD microwave function is particularly useful in the future for 5G and 6G communication system.

1. Introduction of BP-NGD description for microwave signal synchronization

An unfamiliar electronic circuit susceptible to operate with NGD effect was investigated [1]. Thanks to the behavioral analogy with filter theory, a BP type NGD microwave function was identified [1]. The NGD can be analytically understood by means of GD definition from f-frequency dependent transmission coefficient S_{21} associated to PS expression $\phi(f)= \arg[S_{21}(jf)]$:

$$2\pi \cdot GD(f) = -\frac{\partial \phi(f)}{\partial f} \tag{1}$$

The outstanding BP-NGD circuit can be used to synchronize microwave signals for 5G communication system [2]. The proposed dual BP-NGD can be potentially employed for WSN Tx-Rx system performance improvement owing to the principle illustrated by Fig. 1. In this scenario, a tri-band NGD circuit having center frequency and bandwidth $(f_k,\Delta f_k)_{k=\{1,2,3\}}$ is expected to synchronize signals transmitted by WS_k by reducing propagation from distance d_k.

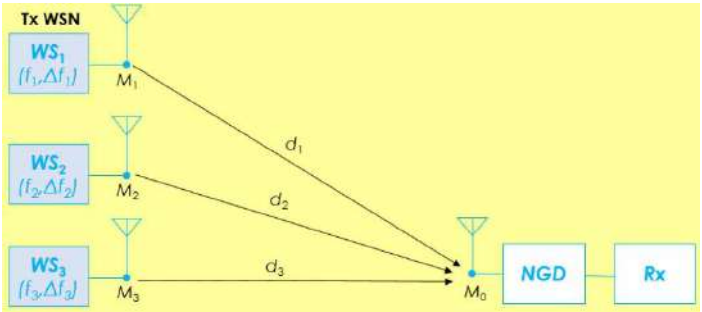

Fig. 1: Illustrative Tx-Rx multi-WSN scenario of synchronization by using BP-NGD circuit [2].

By assuming that $GD(f \in [f_k \pm \Delta f_k / 2]) < 0$, the following equation explains how the synchronization can be performed:

$$t_k = d_k / velocity + GD(f_k) \quad (2)$$

2. BSAA design principle with dual BP-NGD frequency independent PS

The unfamiliar BP-NGD circuit was also used for frequency independent PS design [3-4]. We remind that the classical BSAA operating through bandwidths B_1 and B_2 at two frequencies f_1 and f_2 which are associated to PS values $\phi_1=\phi(f_1)$ and $\phi_2=\phi(f_2)$, respectively, can be represented by Fig. 2(a). The BP-NGD PS was recently exploited to design BSAA with outstanding control of radiation center frequencies and bandwidths as illustrated by Fig. 2(b) [5].

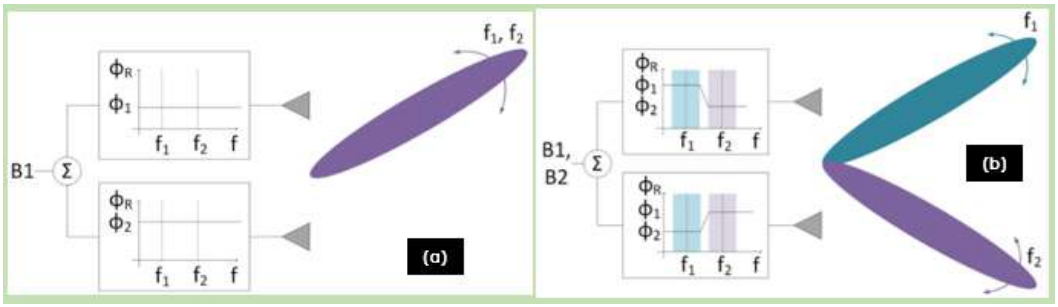

Fig. 2: Illustration of (a) classical and (b) dual band NGD BSAA [5].

The BSAA BP-NGD design principle of the multi-beam phased array is described. The design feasibility is illustrated with dual BP-NGD circuit. A proof-of-concept (PoC) of BP-NGD circuit is simulated and analyzed. Based on the PoC, simulations with separate beam steering positions at different frequencies are also analyzed. The innovative SBAA behavior is discussed.

3. Conclusion

An innovative application of dual BP-NGD circuit for BSAA design is reviewed. After description of BP-NGD unfamiliar microwave function, the design principle is illustrated. Simulations with dual BP-NGD PoC explain the feasibility of the SBAA design. The developed concept is useful in the future for designing SAA-NGD system of innovative multi-beam antenna for the improvement of RF and microwave system.

References

1. Ravelo, B., "Similitude between the NGD function and filter gain behaviours," Int. J. Circ. Theor. Appl., Vol. 42, No. 10, 1016–1032, 2014.
2. Lalléchère, S., L. Rajaoarisoa, L. Clavier, R. Sanchez Galan, and B. Ravelo, "Bandpass NGD function design for 5G microwave signal delay synchronization application", CRAS, Tome 22, no. S1, 53-71, 2021.
3. Ravelo, B., G. Fontgalland, H. S. Silva, J. Nebhen, W. Rahajandraibe, M. Guerin, G. Chan, and F. Wan, "Original Application of Stop-Band Negative Group Delay Microwave Passive Circuit for Two-Step Stair Phase Shifter Designing," IEEE Access, Vol. 10, No. 1, 1493-1508, 2022.
4. Ravelo, B., M. Guerin, J. Frnda, F. E. Sahoa, G, Fontgalland, H. S. Silva, S. Ngoho, F. Haddad, and W. Rahajandraibe, "Design Method of Constant Phase-Shifter Microwave Passive Integrated Circuit in 130-nm BiCMOS Technology with Bandpass-Type Negative Group Delay," IEEE Access, Vol. 10, No. 1, 93084-93103, 2022.
5. Ravelo, B., G. Fontgalland, A. P. B. Dos Santos, H. S. Silva, N. M. Murad, F. Haddad, M. Guerin, and W. Rahajandraibe, "Dual stop-band type NGD network design for true time-delay based multi-beam steerer application," PIER B, Vol. 98, 107-123, 2023.

Optimizing a pyramidal horn together with a dielectric lens for an airborne X-band transmitter

J.Kuster[1*], F.Christophe[2], A.Penarier[1], and P.Nouvel[1]

[1]IES, CNRS - Montpellier University, France
[2]Aresia, France
*corresponding author, E-mail: Jonathan.kuster@umontpellier.fr

Abstract

The design of a pod-mounted transmitter is subject to specific radiation pattern constrains, to be fulfilled in a strongly limited volume. The step-by-step definition of the antenna is described.

1. Introduction

The antenna will be housed in a pod of internal diameter 250 mm and protected by a radome to be optimized separately. The antenna to be designed has to cope with radiation pattern requirements as indicated below:

Table 1: Radiation pattern requirements.

Frequency band (GHz)	Beamwidth horizontal	Beamwidth vertical	Gain (dBi)	Near SLL (dB)	Far SLL (dB)
8.5-9.6	<10°	>30°	>20	<-15	<-25

The horizontal beam width requires the width of the antenna to be close to the pod diameter. A further requirement is the capability of the main beam to be mechanically scanned from the axis of the pod up to at least 40° laterally, which adds a constrain to the length of the antenna, see figure 1. Due to power handling capability, the antenna has to be fed by a waveguide, chosen to be flexible to avoid rotary joint issues.

First, in terms of antenna selection, a pyramidal horn of thickness smaller than width –close to a sectoral horn- appears to approach the radiation pattern requirements [1]. Nevertheless, the criteria of quasi-plane wave front at the aperture doesn't appear achievable without a length of the horn prohibiting wide enough angular scan, see (figure 1a) [1]. Therefore, compensating the spherical wave front of a reduced length horn through a plano-convex dielectric lens was selected [2]. Secondly, since mechanical scan remained still insufficient (figure 1b), the next improvement was to add a dielectric prism to deflect the main beam out of the plane of symmetry of the horn (figure 1c). Numerical simulations with a 3D electromagnetic commercially available code implementing Finite Integration Method with the Perfect Boundary Approximation were performed.

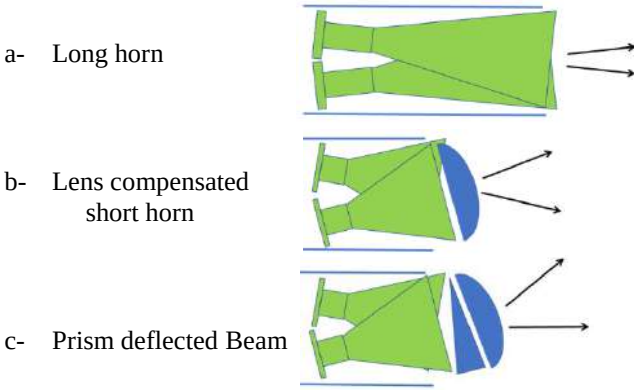

Figure 2 : Principles for mitigating the size limited angular scan (radome not shown)

This article presents the different steps to achieve an antenna that meets the different constraints imposed by the specifications.

2. Preliminary antenna selection

Without taking into account the size of the antenna, a preselection of several kinds of antennas has been made.
For the realization of this project, high peak power was considered, to be generated by a magnetron. This leads to feed the antenna through a waveguide. In the literature [1], several types of antennas can be found which meet this criterion. From radiation pattern and footprint considerations, sectoral horn antennas were first selected.

Because of its simplicity of construction and dimensioning, the horn antenna is the most widely used antenna for microwaves [1], fed by a waveguide. At the end of this waveguide, the edges are flared to obtain a larger opening. The angle, cross-section and length of the flare play an important role in the radiation pattern. This gradually increasing aperture also prevents mismatch from guided to free space propagation.

2.1. Sectoral E plane

The sectoral horn in E plane corresponds, on the one hand, to the flaring of the guide sections perpendicular to the E field. On the other hand, the edges of the guide parallel to the E field keep the same dimension, as shown below.

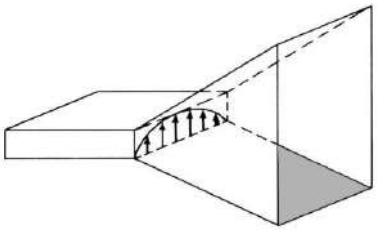

Figure 3 : Geometry of a sectoral E horn antenna [1]

Thanks to this aperture, the radiation in the E plane is thin and wide in the H plane. We have dimensioned a sectoral E plane horn from a WR112 guide (12.63 x 28.50mm).
First, we considered that the horn will be installed in a 250 mm diameter cylinder: this leads us to choose an aperture width of 240 mm. In a second phase, following the main laws of illumination for a rectangular aperture and assuming that the plane E follows a uniform and equiphase law [2], we obtain :

$$HPBW = 50.8\frac{\lambda}{\ell}, \quad (1)$$

With λ the wavelength, ℓ the aperture width of the horn and $HPBW$ is the half-power beam width in degrees. Taking an average frequency of 9 GHz, we obtain HPBW = 7°, with a peak sidelobe at -13.2 dB. We are now interested in the distance Re from the center of phase of the horn to the center of its aperture. We seek the smallest possible length, while having secondary lobes lower than -15 dB. From the universal E-plane radiation pattern [1], for an E-plane sectoral antenna, we derive a parameter s of one eighth and side lobes less than -15 dB for angles greater than 15°.
This parameter corresponds to a coefficient given in the literature [1].

$$s = \frac{\ell^2}{8\lambda Re}, \quad (2)$$

Thus, depending on this parameter, and using relationship (2) we obtain a length Re of 172 cm.

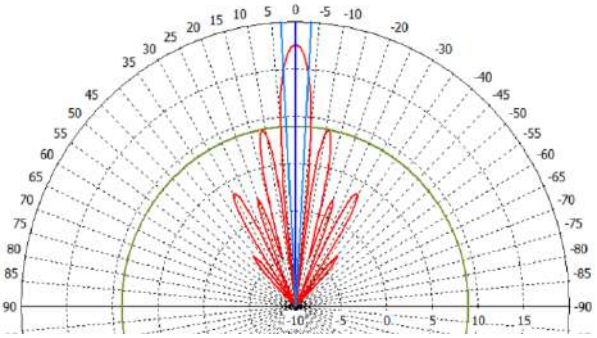

Figure 3 : Radiation diagram in E-plane (in blue the half-power beam width, in green the peak side lobe level)

We carry out a simulation with the dimensions determined previously, the result is presented in figure 3. The simulation results show parameters in agreement with those obtained analytically. Nevertheless, the side lobes are too high (-8 dB peak value) and do not meet the specifications. In addition, the length of the horn does not allow for the expected angular deflection.

2.2. Sectoral H plane

The H-plane sectoral horn is defined by flaring the guide sections parallel to the E-plane, with constant dimension in the perpendicular plane, resulting in a wide beam in the E plane and a thin beam in the H plane.

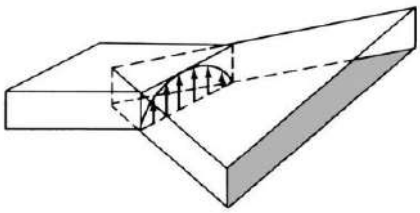

Figure 4 : Geometry of a sectoral H horn antenna [1]

We start from a WR112 guide to shape the horn and we keep an aperture width of 240 mm. Since the illumination now follows a cosine law [2], we obtain in a first step a -3 dB beam width of 9.6°, as well as a peak sidelobe equal to -23dB for a frequency of 9 GHz. In a second step, reference is made to the universal H-plane radiation pattern for an H-plane sectoral antenna: a parameter s of one quarter is determined for same conditions as in E-plane, this parameter s is also obtained from the literature [1]. A length Rh of 86 cm is now required to reduce the side lobes below -15 dB.
The simulation of the horn is shown in figure 5. The cross-

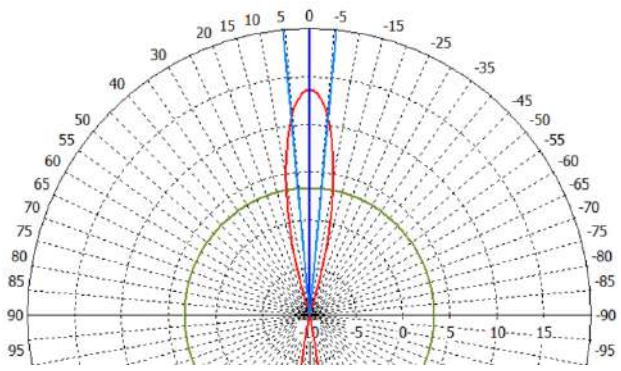

Figure 5 : Radiation diagram in H plane (In blue the half power beam width, in green the peak side lobe level)

sectional plane is this time quite conclusive at the level of the side lobes. It also matches the data obtained theoretically. Nevertheless, the vertical aperture has to be adjusted, which is performed in the next section.

It is now clear that H-plane sectoral horn is preferred to E-plane not only for side lobes level but also for horn length consideration.

2.3. Transition from a sectoral horn to a pyramidal horn

In parts 2.1 and 2.2 we studied the radiation pattern in the horizontal plane parallel to the flared sides of the horn. But the above defined H-plane sectoral horn has a gain of only 13.7 dBi due to its very wide but unnecessary beam width of 111° in the vertical plane. We therefore have to consider increasing the vertical aperture to increase the gain, i.e. turning the sectoral into a pyramidal horn. Following [1], the gain equation for a non-equiamplitude aperture is given by :

$$G = \frac{4\pi}{\lambda^2} * S * f_g, \quad (3)$$

With G the gain of the antenna, S the aperture surface, f_g the gain factor depending on the illumination law of the aperture (in our case, this coefficient is 0.81). Thus, for a gain of 20.7 dBi at 9 GHz and an horizontal aperture of 240 mm a vertical aperture of 55 mm is obtained. The simulation figure 6 shows the resulting vertical radiation pattern with 32° of half power beam width.

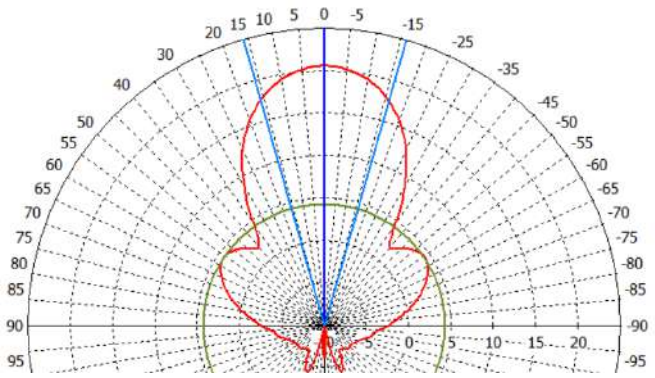

Figure 6 : Section of the radiation pattern in E-plane

3. Reduction of the length of the horn

As seen in the previous section, the length of the horn becomes our main problem to meet the specifications. To reach the angular deflection, a shortening of the horn length is necessary. We first performed a simulation by reducing the length of the horn down to 200 mm, while keeping the same aperture. The degradation on the beam in the horizontal plane is such that the main lobe widens to 16.9 degrees: this leads to a loss of 4 dB on the gain of the antenna. In order to compensate for these degradations, we now add a lens. The objective of this lens is to compensate the spherical phase front at the aperture, therefore thin the beam and increase the gain.. By pure geometric rule, if we place ourselves in the H plane and look in the direction of propagation, we determine that the wave at the center of the aperture travels 17.6 mm further than on the edges of the horn. This distance difference generates a phase shift of 190° at a frequency of 9 GHz. We consider using rexolite (refractive index 1.59) for the lens, for its low loss at microwave frequencies and high resistance to environmental constraints. With these different data, geometrical considerations show that a planospherical lens of radius Rh = 332.3 mm and as center, the center of phase of the horn, is able to achieve the required phase front compensation at the aperture of the horn. To avoid reflections generated by the refractive index of the lens, matching layers a quarter wavelength thick and refractive index 1.26 are also included in the overall simulation presented in the figure below.

The results are quite satisfactory: when we look at the line-of-sight section, the compensation of the phase shift by the lens is obvious. This compensation is reflected in the radiation diagram, with a thinning of the main beam and a gain greater than 21 dBi.

To conclude, the lens fulfills its objective by compensating for the shortening of the horn. With such horn dimensions, angular scanning becomes feasible. However, practical implementation of the matching layers is now to be considered.

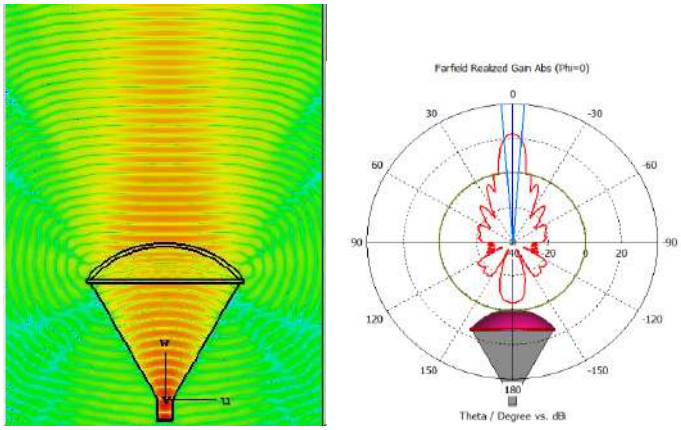

Figure 7 : Electric field inside and outside the device (left) and radiation diagram at 9 GHz for phi 0° (right)

4. Corrugated matching layers

The matching layers realized in the previous simulations are ideal, but not realizable in homogeneous rexolite. A solution is to create an artificial dielectric material, i.e. make periodic holes or grooves within the dielectric structure.

In order to be equivalent to an homogeneous medium, the period of the corrugations must not exceed the spacing p defined by the following equation:

$$p = \frac{\lambda}{n_s + n_i * \sin(\theta_i)}, \quad (4)$$

With n_s , the refractive index of the rexolite, n_i =1 the refractive index in free space and θ_i the maximum angle of incident radiation, we find a spacing that must be less than 16 mm. There are two choices since corrugation can be achieved by periodic material substitution in 1 or 2 dimensions.. For practical reasons we chose to dig cylindrical holes in the lens according to spacing p.

Following this, an optimization was made through computation of the effect of varying the diameter and

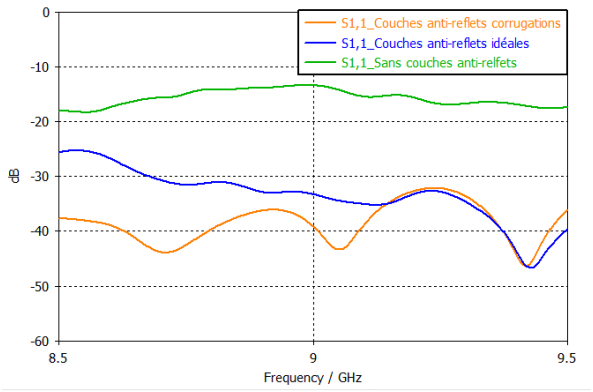

Figure 8 : Reflection coefficient without matching layer (green), with periodic holes (blue), with periodic grooves (orange)

spacing of the holes, in order to obtain the structure with the lowest reflection coefficient. Below we can see a comparison of the coefficient for a simulation without matching layers, and with layers of periodic holes or grooves .

Figure (8) confirms the advantages of the matching layers. Moreover, we observe that we obtain slightly better results with corrugated grooves.

5. Beam deflection

Having achieved the design of a compact, high peak power antenna meeting the required radiation pattern, we further want to extend the potential beam deflection. Such a 15° beam deflection should allow a mechanical scan of +/- 25° of the antenna to create a beam scan of -10/+40° with respect to the axis of the cylinder, meeting a further requirement for the system.. Such beam deflection could result from the insertion of a dielectric prism into the horn. Like the lens, the prism is expected to be made of rexolite.

A representation of the antenna is given figure 9 with lens, prism and matching layers assembled. Obviously, prism and lens may be implemented from a single piece of rexolite, with matching layers at the input of the prism and the output of the lens.

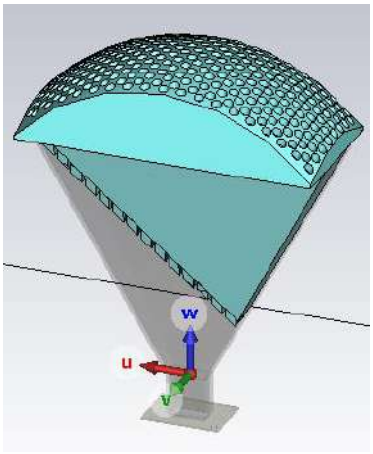

Figure 9 : Final design of pyramidal horn

Again the sizing of the prism is done by simulation, starting with a thin prism, allowing to observe jointly beam deflection and potential radiation pattern degradation, and further increasing the thickness of the prism. . The figures below shows the final result: we obtain a 15° beam deflection without changing the main characteristics of the radiation pattern.

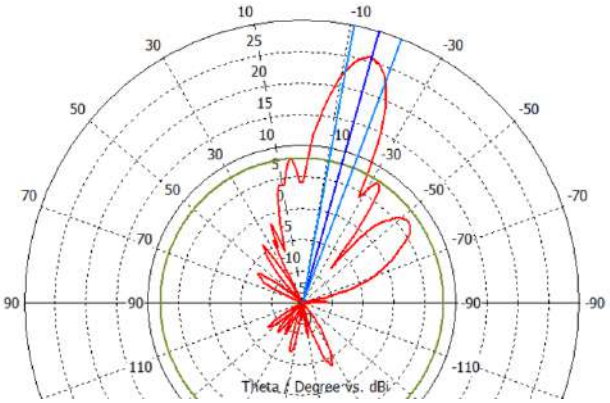

Figure 10 : Radiation diagram at 9 GHz for phi 0°

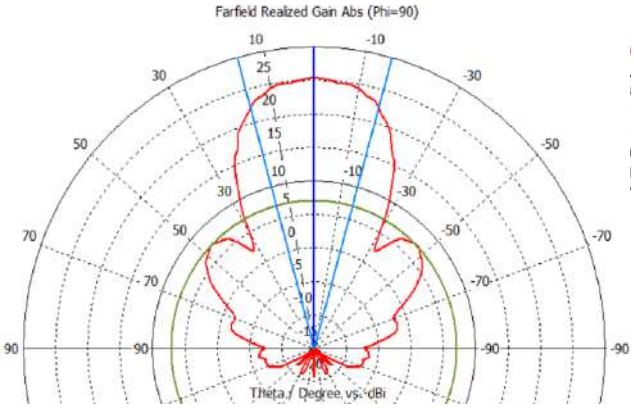

Figure 11 : Radiation diagram at 9 GHz for phi 90°

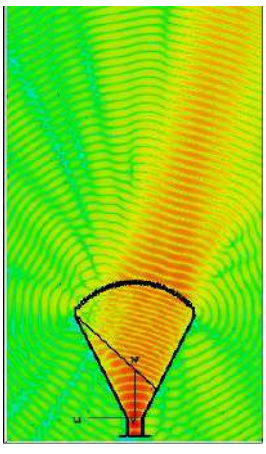

Figure 12 : Electric field inside and outside the device combining horn, lens and prism

6. Conclusion

To conclude, the step-by-step design of a horn and dielectric antenna has been shown theoretically to meet the specifications, taking into account various practical constraints. A physical realization of this antenna is underway..

Acknowledgements

The authors would like to thank Région Occitanie / Pyrénées-Méditerranée (HERMES platform) and the European Regional Development Fund (FEDER) for partial funding of this work.

References

[1] Balanis, C. A. Antenna theory: analysis and design. John wiley & sons. pp 639-782. 2015.

[2] Robert S.E. Antenna theory and design. Institute of Electronics & Electrical Enginneers. pp 79-99 & 482-545.2003

[3] Wheeler, Jordan D., et al. "Antireflection coatings for submillimeter silicon lenses." Millimeter, Submillimeter, and Far-Infrared Detectors and Instrumentation for Astronomy VII. Vol. 9153. SPIE, 2014.

Array antennas, active, adaptive and reconfigurable antennas

Deep-learning-assisted reconfigurable metasurface antenna for real-time holographic beam steering

Hyunjun Ma[1], Jin-soo Kim[1], Jongho Choe[1], and Q-Han Park[1*]

[1]Department of physics, Korea University, Seoul, 02841, Korea
[*]corresponding author: qpark@korea.ac.kr

Abstract: We propose a deep-learning-based method for the control of a reconfigurable metasurface antenna. We modeled the metasurface as a collection of dipoles with states of varying polarizability and used a deep autoencoder neural network combined with a scattering equation and Born approximation to generate on-demand far-field maps. Our proposed autoencoder exhibits higher accuracy and a much faster speed compared with the conventional GA approach and allows for the real-time operation of a reconfigurable metasurface antenna for beam steering.

We propose a metasurface antenna capable of real-time holographic beam steering. An array of reconfigurable dipoles can generate on-demand far-field patterns of radiation through the specific encoding of meta-atomic states i.e., the configuration of each dipole. Suitable states for the generation of the desired patterns can be identified using iteration, but this is very slow and needs to be done for each far-field pattern. Here, we present a deep-learning-based method for the control of a metasurface antenna with point dipole elements that vary in their state using dipole polarizability. Instead of iteration, we adopt a deep learning algorithm that combines an autoencoder with an electromagnetic scattering equation to determine the states required for a target far-field pattern in real-time. The scattering equation from Born approximation is used as the decoder in training the neural network, and analytic Green's function calculation is used to check the validity of Born approximation. Our learning-based algorithm requires a computing time of only around 100 μs to determine the 900 meta-atomic states, thus enabling the real-time operation of a holographic antenna.

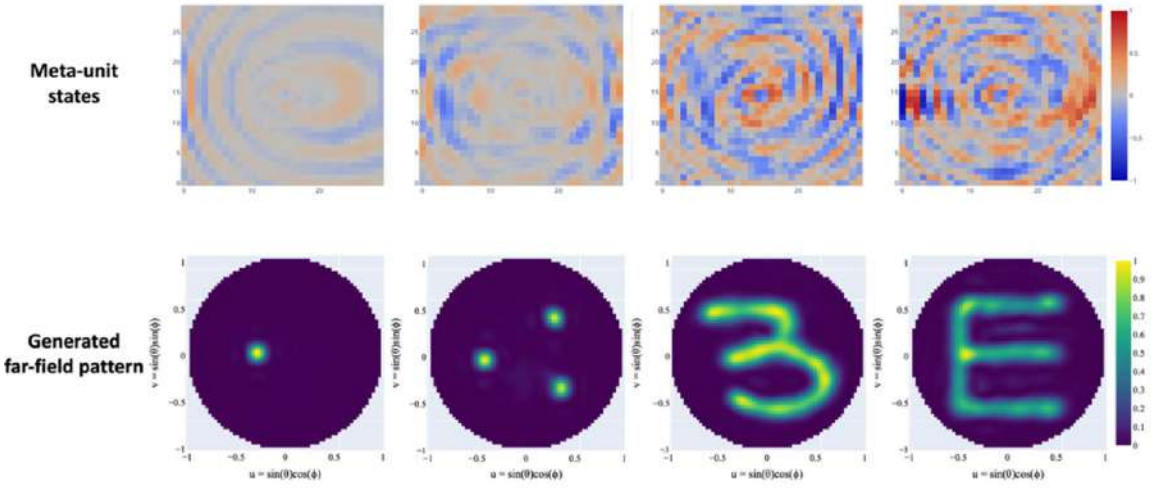

State patterns generated by the neural network, and the calculated far-field map from the Green's function

References

1. Ma, H. J. et al. "Deep-learning-assisted reconfigurable metasurface antenna for real-time holographic beam steering" ,submitted, 2023

Origami foldable and deployable reflectarray antennas for CubeSats

T. Tomura[1]

[1]Tokyo Institute of Technology, Japan
*corresponding author: tomura@ee.e.titech.ac.jp

Abstract: This paper presents origami foldable and deployable reflectarray antennas for CubeSats. To enable the reflectarray antennas, there is two key technology: creaseless reflection elements and deformation compensation reflectarray. In this paper, these technologies are shown in detail with design and measurement results.

Folding patterns are shown in Fig. 1 and are composed of mountain and valley folding lines. Array lattice is shown in the same figure and designed so that the boundaries coincide with the folding lines. Most of them match with the array lattice but some cross the array element [2]. Figure 2 shows the shape of the reflection element which does not cross the folding lines and it is composed of four triangular patches with notches. Changing the dimension of the patch and the notch reflection phase can be tuned. These reflection elements enable creaseless design of reflectarray antennas.

Figure 3 shows the deformation compensation reflectarray antennas and the reflection elements are composed of a rectangular patch and a varactor diode. Depending on the deformation amount, bias voltage to the varactor diode is controlled to compensate for the deformation. Using a solid reflectarray prototype, the gain increment is confirmed [3].

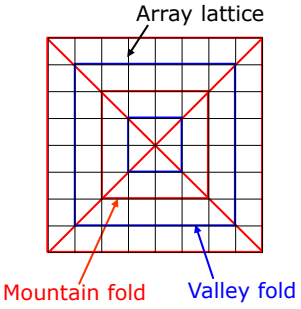

Fig. 1 Folding patterns

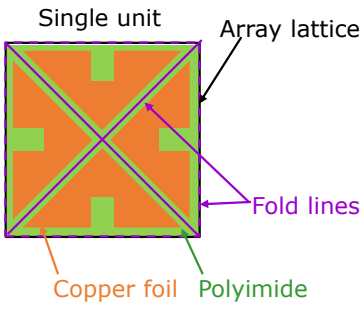

Fig. 2 Creaseless patch shape

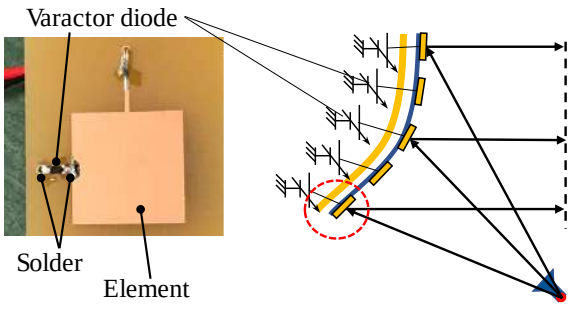

Fig. 3 Deformation compensation reflectarray

This work was supported in part by the Telecommunications Advancement Foundation, the Japan Society for the Promotion of Science (JSPS) KAKENHI under Grant JP20H00281 and Grant JP20H02146, DLab Challenge 2022 of Tokyo Institute of Technology.

References

1. K. Ikeya, et al., “Significance of 3U CubeSat OrigamiSat-1 for space demonstration of multifunctional deployable membrane,” Acta Astronautica, vol. 173, pp. 363--377, Aug. 2020.
2. T. Tomura, et al., “Two-layer pop-up origami deployable membrane reflectarray antenna stowed in 1U CubeSat,” AIAA/USU Conf. Small Satellites, SSC22-WKVI-05, Aug. 2022.
3. K. Omoto, T. Tomura, and H. Sakamoto, “Proof-of-concept on misalignment compensation for 5.8-GHz-band reflectarray antennas by varactor diodes,” IEEE Access, vol. 9, pp. 54101--54108, Apr. 2021.

The Wide-band SIW Antenna Arrays for 5G Mm-wave Applications

Huanhuan Huang[1,2], Yanzhong Yu[1*], Xuehua Lin[1], Jing Tian[1]

[1]College of Physics & Information Engineering, Quanzhou Normal University, Fujian, China
[2]School of Advanced Manufacturing, Fuzhou University, Jinjiang, China
*yuyanzhong059368@163.com

Abstract

In this paper, a broadband antenna array with high gain is presented. The array element has obtained a gain of 6.19dB and wide impedance bandwidth of more than 8.8GHz (from 25.8 GHz to 34.6GHz). A gain of 13dB is achieved in the 1 ×4 array. The working band of the four elements array can cover the mm-wave band. The proposed arrays with good symmetry of radiation patterns and wide bandwidth are proper for 5G mm-wave communication.

1. Introduction

With the generational development and technological innovation of mobile communication, the occupancy rate of mobile terminals is getting higher and higher, which leads to the requirement for a higher channel capacity and transmission rate of the mobile communication system[1,2]. The existing frequency band is already very congested, it is urgent to adopt the new communication frequency band such as millimeter wave for 5G to expand the limited bandwidth[3].

Therefore, millimeter wave technology has attracted much attention from communication researchers. The ref[4] has proposed a 1×4 millimeter array with a gain of 12.06dBi and a symmetrical pattern. A compact dual band antenna that works at the mm-wave frequency(from 27GHz to 38GHz) is presented in ref[5]. To meet the requirements of 5G, the antenna also needs to be with higher gain and a wider working band.

The SIW technology can suppress the loss of the surface wave and reduce interference by suppressing the leakage of the electromagnetic signal[6,7]. A linear MIMO antenna array is proposed in this article, the designed array has achieved wide working bandwidth, high gain, and good pattern consistency.

Section 2 has described the construction and the simulation result of the array element. The numerical results of the two elements array and four elements array are discussed in section 3. The conclusion is given in section 4.

2. Simulation of structure

The material of the substrate is Rogers5880. The element is formed by substrate1(0.762mm), substrate2(1mm), ground, patch1, patch2, coaxial cable, copper cylinders, and pec cylinders, as presented in Figure. 1. The feeding method of the antenna element is coaxial cable. The dimension parameters of the element are given in Table 1.

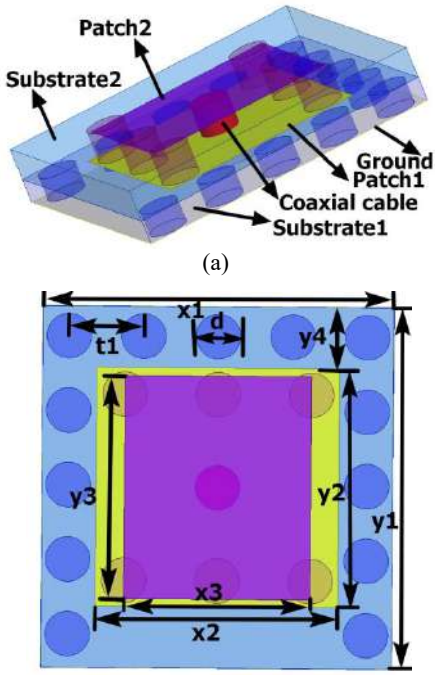

Figure 1: Configurations of the array element. (a) perspective view. (b) top view

Table 1: The Parameters Of The Element.

Parameters	Value(mm)	Parameters	Value(mm)
x1	9.7	y1	9.4
x2	6.4	y2	6.5
x3	6	y3	5
y4	1.85	t1	2
t2	2.5	d	1.2

The simulation results of the element are given in Figure. 2. The working frequency of the antenna element is from 24.27GHz to 34.9GHz which covers the Chinese 5G mm-wave band of 24.75GHz to 27.5GHz. The return loss of the element can reach -48.1dB and the Z parameter of the element is 50.45-0.002i at the center frequency point (25.8 GHz). A gain of 6.19dB is obtained at the center frequency of 25.8GHz. The VSWR band of less than 2 is from

24.2GHz to 35.1GHz which can cover the entire working bandwidth. The designed element has good impedance matching and gain.

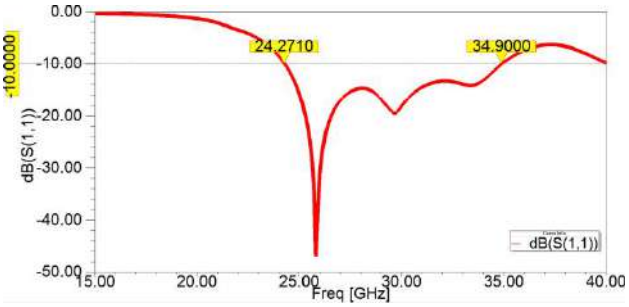

(a)

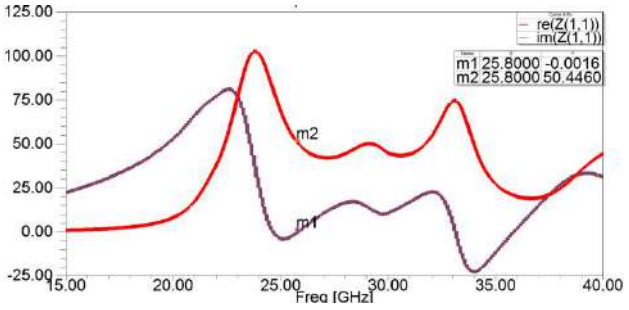

(b)

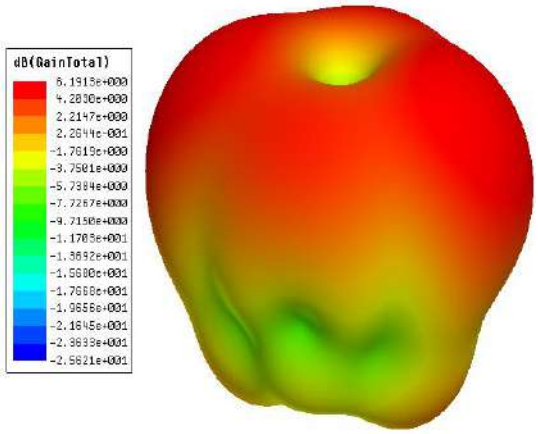

(c)

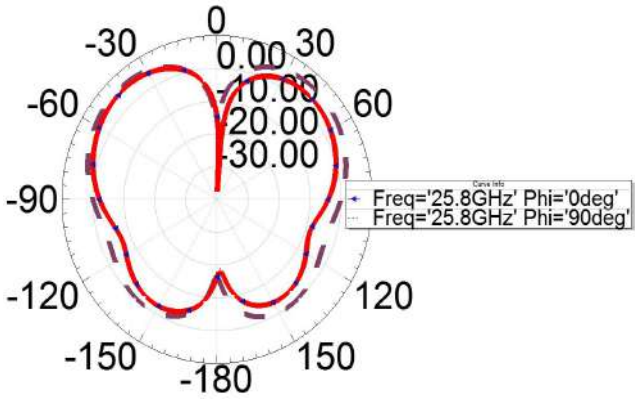

(d)

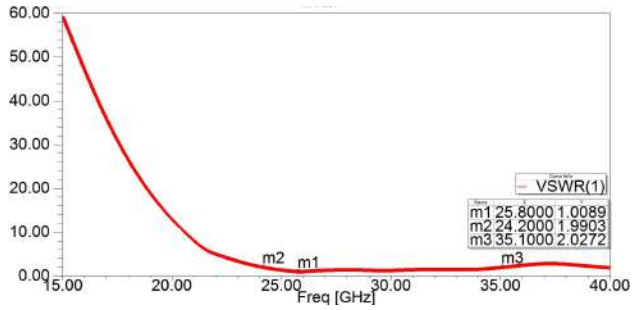

(e)

Figure 2: The simulation results of array element. (a)S11. (b)Z parameter. (c)3D radiation pattern. (d) E-plane and H-plane radiation patterns. (e)VSWR

3. Numerical Result

Two kinds of different linear SIW arrays are devised for better performance in this section. It can be seen from Figure. 3 that the antenna array is composed of the antenna elements proposed in the previous section through the linear arrangement of 1×2 and 1×4.

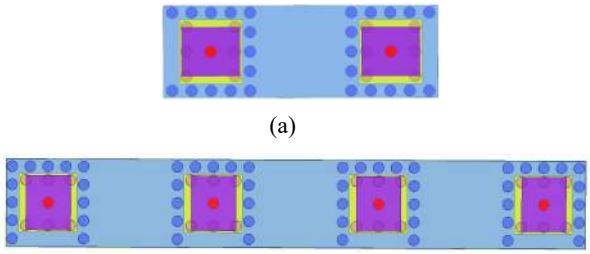

(a)

(b)

Figure 3: The structures of two different arrays. (a)1 × 2 antenna array, (b)1×4 antenna array

The 1×2 array has achieved a gain of 10dB with isolation of more than 15dB at the working frequency as illustrated in Figure. 4(a) and Figure. 4(b). Figure. 4(d) and Figure. 4(e) show the return loss and the gain of the 1×4 array. The 1×4 array has a gain of 13dB and an isolation of more than 15dB which means the interference between different elements is low. The E-plane and H-plane radiation patterns of the 1×2 array and 1×4 array have good symmetry.

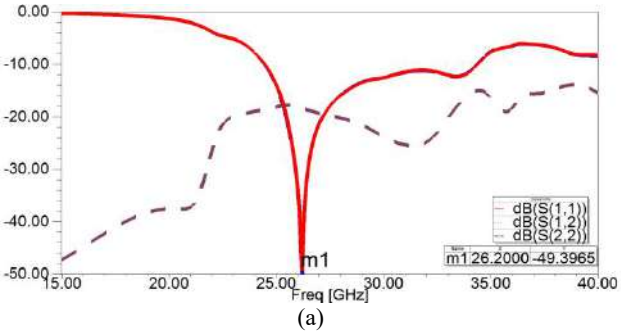

(a)

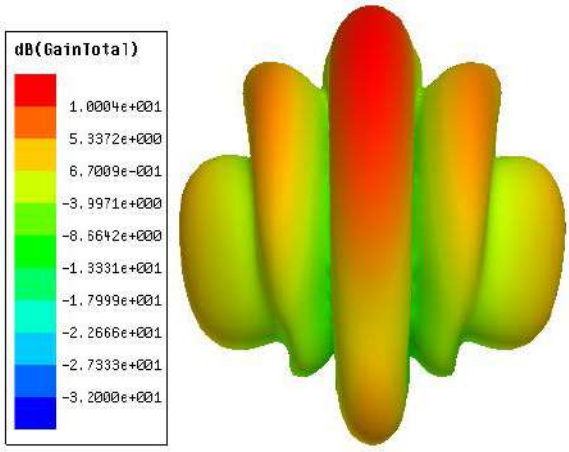

(b)

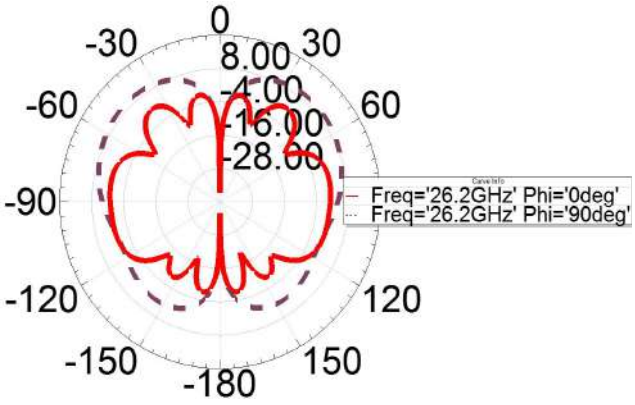

(c)

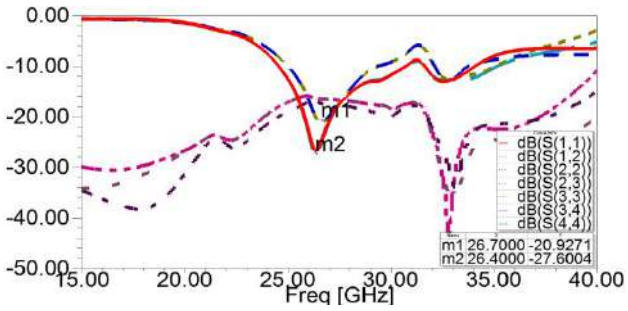

(d)

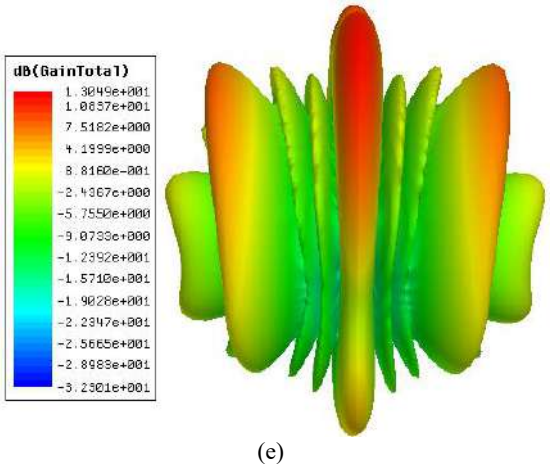

(e)

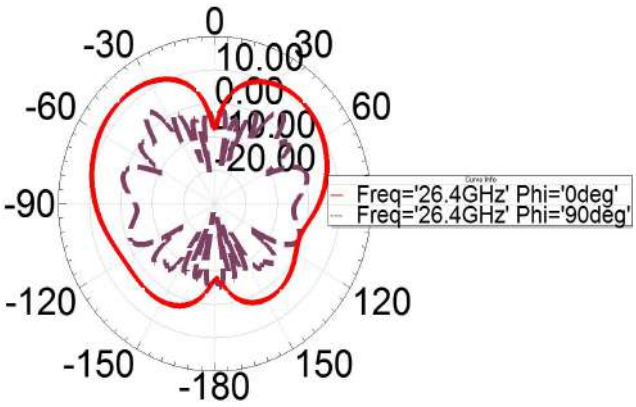

(f)

Figure 4: The simulation results of two arrays. (a)Return loss of two elements array. (b)3D radiation pattern. (c)E-plane and H-plane radiation patterns.(d)Return loss of four elements array. (e)3D radiation pattern. (f)E-plane and H-plane radiation patterns.

4. Conclusions

Several linear SIW millimeter antenna arrays with high gain and symmetric patterns are proposed in this article. To improve the performance of the antenna element, SIW technology is applied in the element design. The simulation results illustrated that the designed array has good characteristics. A gain of 13dB with the isolation of more than 15dB between different elements at the working frequency has been obtained in the 1×4 antenna array by setting the appropriate arrangement and the intervals of antenna elements. The 1×4 antenna array has the advantages of broad bandwidth, high gain, and good symmetry of the pattern which made it suitable for 5G communication applications.

Acknowledgements

This work is supported by the National Project of Innovative Entrepreneurship of Undergraduate (No. 201910399019, 202110399010).

References

[1] M. Shafi, A.F. Molisch, and P.j. Smith, “5G: A Tutorial Overview of Standards, Trials, Challenges, Deployment and Practice,” IEEE Journal on Selected Areas in Communications, 2017, pp. 1201 - 1221.

[2] W. Hong, K.H. Baek, and S. Ko, “Millimeter-Wave 5G Antennas for Smartphones: Overview and Experimental Demonstration,” IEEE Transactions on Antennas and Propagation, 2017.

[3] Marcus and M. J, “5G AND "IMT FOR 2020 AND BEYOND,” IEEE Wireless Communications, 2015.

[4] F. Albagdali, and A. Aydin, “Dual band mmWave 5G antenna,” 2020.

[5] Y.C. Chang, “A Novel Dual-Polarized Wideband and Miniaturized Low Profile Magneto-Electric Dipole

Antenna Array for mmWave 5G Applications," IEEE Open Journal of Antennas and Propagation, 2021.

[6] Y. Li, "Simulation and experiment on SIW slot array antennas," IEEE Microwave and Wireless Components Letters, 2004, pp.446-448.

[7] M. Bozzi, A. Georgiadis, and K. Wu, "Review of substrate-integrated waveguide circuits and antennas," Iet Microwaves Antennas & Propagation, 2011, pp.909-920.

Broadband Anti-Reflection Moth-Eye Structures in the Terahertz Region Fabricated by Ultrashort-Pulsed Laser Processing

Kuniaki Konishi

Institute for Photon Science and Technology, The University of Tokyo, Japan
kkonishi@ipst.s.u-tokyo.ac.jp

Abstract: It is demanded to reduce signal loss due to Fresnel reflections that occur on the surface of optical elements such as lenses and waveplates used to control terahertz waves. In this talk, I will present terahertz moth-eye structures in which several protruding structures are arranged on the material surface, fabricated with ultrashort-pulsed lasers, which almost completely suppresses reflections in the sub-terahertz and terahertz regions, and show their applications.

Terahertz waves, which are in the frequency band between radio waves and visible light, correspond to the frequency band used in cosmic microwave background radiation polarization observation and next-generation wireless communication technologies. In these applications, it is strongly demanded to reduce signal loss due to Fresnel reflections that occur on the surface of optical elements such as lenses and waveplates used to control terahertz waves. Moth-eye structures, in which several protruding structures are arranged on the material surface, are one of the antireflection techniques used to suppress such surface reflections [1]. However, lithography, a technique commonly used to fabricate micro-artificial structures, is difficult to use for this purpose because it is suitable for fabricating quasi-two-dimensional structures that are much thinner than the wavelength of terahertz waves.

In recent years, ultrashort-pulsed laser processing has attracted attention as techniques for producing three-dimensional microstructures enabling extremely high-precision processing. We are developing these technologies and it has become possible to produce a moth-eye structure with a resolution of several tens of micrometers smaller than the wavelength of the THz wave. In this talk, I will present terahertz moth-eye structures fabricated with ultrashort-pulsed lasers, which reaches almost 100% transmission in the sub-terahertz [2] and terahertz regions [3], and show their astronomical applications [4]. Such high-definition microstructures fabricated using laser processing will be an important technology for terahertz wave control.

References

1. S. J. Wilson, M. C. Hutley, “The Optical Properties of 'Moth Eye' Antireflection Surfaces,” Optica Acta, Vol 29, No. 7, 993-1009, 1982.
2. H. Sakurai et al., “Terahertz broadband anti-reflection moth-eye structures fabricated by femtosecond laser processing,” OSA Continuum, Vol 2, 2764 – 2772, 2019.
3. R. Takaku et al., “Broadband, millimeter-wave anti-reflective structures on sapphire ablated with femto-second laser,” Journal of Applied Physics, Vol 128, No. 22, 225302, 2020.
4. R. Takaku et al., “A Large Diameter Millimeter-Wave Low-Pass Filter Made of Alumina with Laser Ablated Anti-Reflection Coating,” Optics Express, Vol 29, No. 25, 41745-41765, 2021.

A Simple mm-Wave Chipless Pressure Sensor

S. Rodini[1*], S. Genovesi[1], G. Manara[1], and F. Costa[1]

[1]Department of Information Engineering, University of Pisa, Italy

[*]corresponding author: sandra.rodini@phd.unipi.it

Abstract Pressure is one of the most frequently measured physical quantities. For this reason, it is useful to have pressure sensors that adapt to the most varied applications. Here a simple wireless pressure sensor based on a mm-wave chipless RFID tag is proposed. The tag is composed of an artificial impedance surface loaded with a superstrate. The combination of the periodic surface with the superstrate results in a frequency shift of the resonant peak when pressure is applied to the tag.

Introduction Pressure sensors are required in a large number of applications ranging from biomedical [1], robotics [2], aerospace industries [3]. Pressure sensors can be classified as capacitive, resistive and piezoelectric according to the characteristics of the active layer [4-5]. Many of the pressure sensors released to date are wired, difficult to install, and require active excitation. One way to make fully wireless, battery-free sensors is through RFID technology [6]. In this case it is possible to interface the sensor with the RFID chip in order to have the sensing functionality in the radio frequency system. Another possibility is to create chipless RFID sensors [7]. In chipless RFID technology the tag has no electronic components and requires no power source. In this case the sensor is based solely on the frequency response of a resonator. Here a chipless pressure sensor composed of a resonator working at mm-wave frequencies is proposed. The resonator operates in conjunction with a dielectric superstrate and pressure is applied to the ground of the resonator. The application of pressure causes a frequency shift of the resonance peak.

Pressure sensor design The design of the proposed pressure sensor is shown in Figure 1(a). The sensor is based on a mm-wave chipless tag. The tag is composed by three dipoles, with different length, separated from a ground plane by a thin Roger 3003 substrate (d=127 μm). The unit cell of the periodic surface (Frequency Selective Surface FSS) is shown in Figure.1(b) The periodicity D of the unit cell is equal to 3.7 mm. In order to be able to use the tag as a pressure sensor a superstrate is applied under the FSS. A gradually increasing pressure is applied to the ground plane. The idea is to place a container on top of the tag and fill that container with water. As the volume of water increases, the pressure exerted on the tag will increase. The applied pressure P, calculated as $P=gM/A$, where g is the earth gravity acceleration, M is the mass of the water in the container and A is the area where pressure is applied. The tag is composed of 10 x 10 cells and therefore the area will be D^2, i.e. $(3.7\ mm)^2$. The proposed sensor can be interrogated with two WR28 standard gain horn antennas operating in the frequency range of interest.

Numerical results In order to evaluate the feasibility of the proposed sensor, numerical electromagnetic simulations are first performed. The numerical simulation has been carried out by using the CST Studio Suite Software. The simulation was performed using periodic boundary conditions. In order to exploit the working principle of the proposed sensor several cases are considered as shown in Figure.1(c): the tag only, the tag with the superstrate and finally the tag with the superstrate filling the space between dipoles

because of the applied pressure. The thickness of the metallic deposition has been considered in the simulation. The results of the numerical simulations are shown in Figure 1 (d). A frequency shift can be observed due to applying pressure to the tag. This shift can be justified by the fact that as the applied pressure increases, considering that the dipoles have a thickness, the spaces between the dipoles are filled with a consequent variation of the effective permittivity. The experimental results, which validate the proposed concept, will be shown at the conference.

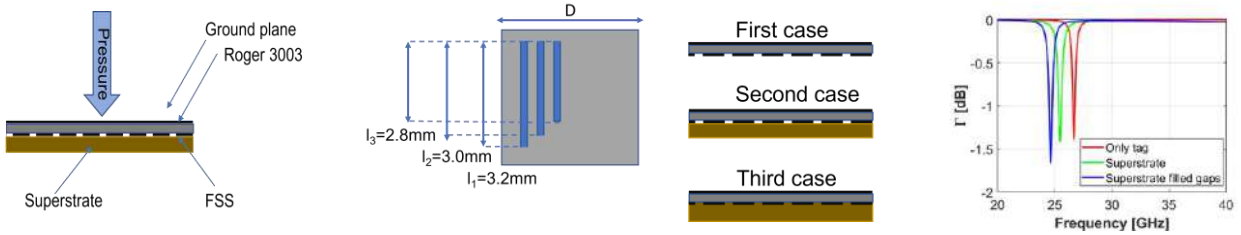

(a) (b) (c) (d)

Figure 1. (a) Lateral view of the proposed pressure(b) top view of the unit cell of the FSS (c) scheme of the three simulated (d) reflection coefficient as the applied pressure varies.

Conclusions An innovative pressure sensor is here proposed. The sensor consists in a mm-Wave chipless tag composed on three metallic dipoles separated by the ground plane from a thin Roger substrate. The combination of the superstrate with the tag results in a frequency shift of the resonance peak proportional to the applied pressure.

Acknowledgements Work partially supported by the Italian Ministry of Education and Research (MIUR) in the framework of both the FoReLab project and the Crosslab project (Departments of Excellence).

References

1. Roriz, P., Frazão, O., Lobo-Ribeiro, A. B., Santos, J. L., & Simões, J. A. (2013). Review of fiber-optic pressure sensors for biomedical and biomechanical applications. *Journal of biomedical optics*, *18*(5), 050903-050903.
2. Almassri, A. M., Wan Hasan, W. Z., Ahmad, S. A., Ishak, A. J., Ghazali, A. M., Talib, D. N., & Wada, C. (2015). Pressure sensor: state of the art, design, and application for robotic hand. *Journal of Sensors*, *2015*.
3. Lin, L., & Yun, W. (1998, March). MEMS pressure sensors for aerospace applications. In *1998 IEEE Aerospace Conference Proceedings (Cat. No. 98TH8339)* (Vol. 1, pp. 429-436). IEEE.
4. Ruth, S. R. A., Feig, V. R., Tran, H., & Bao, Z. (2020). Microengineering pressure sensor active layers for improved performance. *Advanced Functional Materials*, *30*(39), 2003491.
5. Javed, Y., Mansoor, M., & Shah, I. A. (2019). A review of principles of MEMS pressure sensing with its aerospace applications. *Sensor Review*.
6. Brinker, K., & Zoughi, R. (2023). Tunable Chipless RFID Pressure Sensor Utilizing Additive Manufacturing-Model, Simulation, and Measurement. *IEEE Transactions on Instrumentation and Measurement*.
7. Costa, F., Genovesi, S., Borgese, M., Michel, A., Dicandia, F. A., & Manara, G. (2021). A review of RFID sensors, the new frontier of internet of things. *Sensors*, *21*(9), 3138.

Improved Foreign Object Detection Method for Wireless Charging using Balanced and Synchronous Coils

Sehwan Choi[1*], Seunggu Nam[1], Churlseung Lee[1], and Youngkee Ryu[2]

[1]Korea Electronics Technology Institute, Korea
[2]Chungnam Display R&D Cluster Center, Sunmoon University, Korea
[*]corresponding author: shchoi@keti.re.kr

Abstract: In this paper, we propose a new foreign object detection (FOD) structure in which a synchronous coil is added to the balanced coils. The location of the foreign object can be identified by comparing the phase of the added coil with that of the two balanced coils, and using the signal processing method known as the sample and hold method. This paper presents the configuration of the FOD system and the results of the detection method.

The proposed FOD (Foreign Object Detection) method in this paper utilizes a synchronous coil added to the center of the detecting coil to obtain a transmission signal, which allows for the location of a foreign object to be determined using phase detection. The balanced coil method has been used previously, but it has limitations such as low detection rates and an inability to locate foreign objects in certain areas. The proposed method is designed to address these limitations and is applied to mobile phone charging. The location of foreign objects can be identified through simple signal processing.

The FOD structure proposed in this paper is composed of a transmitting coil and a detecting coil. The detecting coil includes two balanced coils and a synchronous coil in the center. The balanced coil generates an electromagnetic field, and when a metal object is placed in the area where the balanced coil is located, the electromagnetic field becomes unbalanced, and current begins to flow. The synchronous coil receives the transmission signal, which is synchronized with the charging signal sent by the transmitting coil, and converts it into a digital signal. This signal is then supplied to the microprocessor, where sample and hold processing is used to create a pulse. The output signal of this method changes its output level and sign depending on the location of the foreign object. The method can determine the presence or absence of a metal object and its location based on the signal change of V^1_{out} and V^2_{out}.

To verify the proposed structure, analog circuits such as filters, amplifiers, and various signal processing functions are required. By using Cypress's PSOC5 microprocessor, it can be configured relatively simply. This processor has built-in high-performance programmable analog blocks that can be configured to perform various signal processing functions. The proposed FOD method can be used to improve the safety and convenience of mobile phone charging by detecting foreign objects and preventing potential hazards.

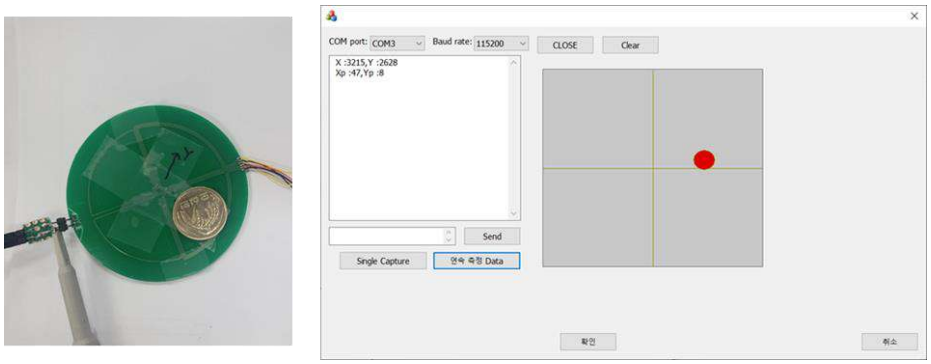

Figure 1. Experimental setup and detection result.

Acknowledgements

This work was supported by ICT R&D program of MSIP/IITP. [2021-0-00259, Development of a Fast Wireless Charging System for Portable Terminals with Improved Heat Dissipation and Shielding Performance]

References

1. L. Lan et al., "Foreign Object Detection for Wireless Power Transfer," 2018 2nd URSI Atlantic Radio Science Meeting (AT-RASC), 2018, pp. 1-2, doi: 10.23919/URSI-AT-RASC.2018.8471551.
2. Y. Zhang et al., “A review of foreign object detection (FOD) for inductive power transfer systems,” eTransportation, Volume 1, August 2019.
3. L. Xiang, Z. Zhu, J. Tian and Y. Tian, "Foreign Object Detection in a Wireless Power Transfer System Using Symmetrical Coil Sets," in IEEE Access, vol. 7, pp. 44622-44631, 2019, doi: 10.1109/ACCESS.2019.2908866.
4. https://www.philips.com/a-w/about/innovation/ips/standardization.html

Analytical, Computational and numerical techniques

A spectral element modal method for the analysis of crossed binary gratings

Gérard Granet[1*] and Kofi Edee[1]

[1]Université Clermont Auvergne, Clermont Auvergne INP, CNRS,

Institut Pascal, F-63000 Clermont−Ferrand, France

[*]corresponding author: gerard.granet@uca.fr

Abstract: A spectral element modal method the originality of which comes from the use of a hierarchical basis built with modified Legendre polynomials is developed in the general case of binary crossed gratings. The big advantage of the spectral element method (SEM) is that it combines the geometric flexibility of finite elements with high precision of spectral methods. Its versatility is illustrated with gratings whose patterns are not aligned with the boundaries of the elementary cell.

Recently, metamaterials and metasurfaces have aroused immense interest because they provide innovative solutions to control electromagnetic waves. We can see in them particular periodic structures and therefore a certain class of gratings. Therefore, the numerical methods developed to calculate the electromagnetic response of the latter is in many cases transposable to metamaterials and metasurfaces. For translation invariant structures, modal methods and mode matching techniques are very interesting in that they avoid discretization along the axis of invariance. Numerical modal methods differ in the choice of expansion and test functions. One can distinguish full domain functions or sub-domain functions according to whether they are defined on the whole domain or only on some part of it. For periodic problems, the most popular method is certainly the well-known Fourier Modal Method (FMM) [1] in which expansion and test functions are pseudo periodic functions. On the contrary, using sub-domain expansions within each domain that constitute the structure allows to express rigorously the different continuity relations that determine the eigenvalue problem and thus leads to exponential convergence for the eigenvalues and eigenvectors. The polynomial modal method [2] is one such method. It was revisited in [3], and [4]. It was shown to outperform all other numerical modal methods for dielectric metallic structures. The aim of the present paper is to reformulate the above polynomial modal method in terms of a Spectral Element Method (SEM).

References

1. Moharam, M.G. and T.K. Gaylord, "Diffraction analysis of dielectric surface-relief gratings," J. Opt. Soc. Am. A, Vol. 72, 1385–1392, 1982.
2. Morf, R.H., "Exponentially convergent and numerically efficient solution of Maxwell's equations for lamellar gratings," J. Opt. Am. A, Vol. 12, 1043-1056, 1995.
3. Edee, K. "Modal method based on sub-sectional Gegenbauer polynomial expansion for lamellar grating," J. Opt. Soc. Am A, Vol. 28, 2006-2013, 2011.
4. Randriamihaja, M.H., G. Granet, K.Edee and K. Raniriharinosy, "Polynomial modal analysis of lamellar diffraction gratings in conical mounting," J. Opt. Soc. Am. A, Vol. 33, 1679-1686, 2016.

Exploring the *Thermally Activated Delayed Fluorescence* Performance for a Phenothiazine Derivative *via* TD-DFT

L. Cascino[1,2*], A. Maggiore[2*], I. Rivalta[3,4], G. P. Suranna[5], R. Grisorio[5], D. Conelli[5], V. Maiorano[2*], and S. D'Agostino[1,2,6]

[1]Mathematics and Physics Department "*E. De Giorgi*", University of Salento, Lecce 73100, Italy

[2]Institute of Nanotechnology, National Research Council (CNR-NANOTEC), Lecce 73100

[3] Dipartimento di Chimica Industriale "Toso Montanari", Università di Bologna, 40136 Bologna, Italy

[4]ENSL, CNRS, Laboratoire de Chimie UMR 5182, 69364 Lyon France

[5]DICATECh, Politecnico di Bari, 70125 Bari, Italy.

[6]Center for Biomolecular Nanotechnologies, Istituto Italiano di Tecnologia, Arnesano (LE) 73010

[*]corresponding author: lucia.cascino@unisalento.it

Abstract: To design new materials for *Thermally Activated Delayed Fluorescence* (TADF) it is necessary to achieve a detailed understanding of the several electronic states involved in such mechanism, which are also very sensitives to environmental effects, such as solvent polarity and rigidity. In such perspective, quantum mechanical calculations are powerful tools to rationalize TADF systems. Herein, we report a computational analysis based on *Time Dependent Density Functional Theory* (TD-DFT) to investigate a phenothiazine derivative that activates TADF only upon aggregation.

In classical fluorescent systems, especially at room temperature, the triplet electronic states can decay only through non-radiative pathways by vibration or phonon interactions, while radiative decay is forbidden. On the other hand, in phosphorescence metalorganic complex featuring heavy metals, the strong spin-orbit coupling enables a radiative emission from triplet excited states. In order to overcome the drawbacks of the latter (toxicity and high costs), new full organic systems that recovering triplet excitation through a delayed fluorescence mechanism have been largely investigated. Such process, namely the TADF, [1] occurs because of a fast reverse intersystem crossing (rISC), which up convert triplet to singlet by thermal energy. Therefore, in order to achieve good TADF performances, besides a large transition dipole moment between excited and the ground singlet states, it is of vital importance to ensure a small enough singlet-triplet energy gap (~ 0.1 eV) [2]. In order to reduce this gap, the exchange energy (J), which is inversely proportional to the spatial separation between the highest occupied molecular orbital (HOMO) and the lowest unoccupied molecular orbital (LUMO), has to be minimized ($2J = \propto \Delta E$). It has been demonstrated that Donor-Acceptor (D-A) molecules presenting strong charge transfer states (CT) are among the most efficient systems to reduce the exchange coupling J.

In this work, we investigated the TADF performance of a phenothiazine derivative consisting of a strong donor (phenothiazine) and acceptor (fluorerone) component, adopting a quasi-equatorial D-A conformation [3] and we analyse the possibility for this molecule to activate TADF by forming aggregated electronic states (Fig. 1a). All simulations were performed by using the ORCA 5.0 package. The geometry of the ground state was optimized in the gas phase by employing the B3LYP functionals and a TZVP basis set, with the def2/*J* auxiliary basis set for the RIJCOSX approximation to the Coulomb integrals [4]. Electronic and optical properties were analysed for the monomer in the quasi-equatorial conformation and in the non-polar cyclohexane solvent. After characterization of

the monomer properties in terms of relative positions of the first singlet (S_1) and triplet (T_3) charge transfer states, we considered three different dimer geometries, analysing their structural and electronic properties as a function of the inter-monomer separation distance (see Fig. 1b).

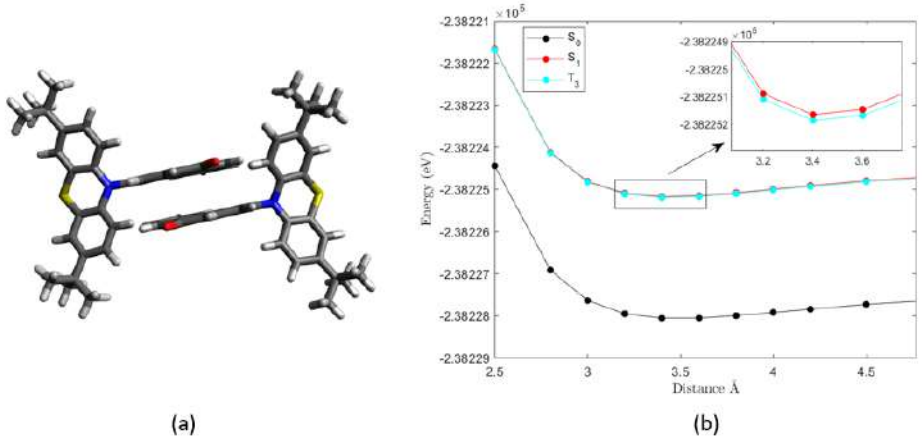

Fig. 1 (a) Sketch of a dimer of phenothiazine derivatives in the quasi-equatorial conformation (3.3 Å, unrelaxed). (b) Energies of S_0, S_1 and T_3 states vs separation distance between molecules (system sketched in panel a) for the monomers relaxed to their ground state geometry.

An important reconstruction in both S_1 and T_3 states was observed, resembling the typical one of dimer electronic state with one monomer in the ground state (S_0) geometry and the other one in the excited state geometry, i.e. S_1 and T_3 geometries, respectively. Moreover, fingerprints of aggregate formation were also tracked down in the nature of *Natural Transition Orbitals* of S_1. With respect to monomer, we registered a promising change in the relative position of the electronic states of interest for TADF. Moreover, coherently with experimental PL spectrum, we observed a red-shift of the emission peak. In addition, to what is well known about the effect of environment conditions (e.g. polarity of solvent affecting the TADF performances), this study attests a new path to activate TADF trough the formation of a new aggregate electronic state. This open new perspective toward an on-demand control of the TADF response in molecules of interest for optoelectronics and nanomedicine.

This work was partially financed by the Research Project "PON ARS01_00951 ECOTEC_ ECO-sustainable and intelligent fibers and fabrics for TEChnic clothing (CUP B66C18000300005)".

References

1. Uoyama, H., K. Goushi, K. Shizu, H. Nomura and C. Adachi, "Highly efficient organic light-emitting diodes from delayed fluorescence", Nature, Vol. 492, No. 7428, 234-238, 2012.
2. Lv, L., K. Yuan, T. Zhao, and G. Dai, "Intrinsic Analysis of Thermally Activated Delayed Fluorescence (TADF) for Ag (I) Complex Based on the Path Integral Approach: Origin of the Effective Spin-Flipping Channel and Vibrational Spin-Orbit Coupling Effect", J. Phys. Chem. A, Vol. 126, No. 38, 6695-6709, 2022.
3. Zhang, J., M. Zhu, Y. Lu, X. Zhang, S. Xiao, H. Lan and T. Yi, "Design of Stimuli-Responsive Phenothiazine Derivatives with Triplet-Related Dual Emission and High-Contrast Mechanochromism Guided by Polymorph Prediction", Eur. J. Chem., Vol. 28, No. 29, 2022.
4. Neese, F., "The ORCA program system", Wiley Interdiscip. Rev. Comput. Mol. Sci., Vol. 2, Issue 1, 73–78, 2012.

Modelling Technique for Finite Length Microstrip Periodic Structures for MMW Filters

A Divsalar and D Mirshekar-Syahkal
RF & Microwave Research Lab, School of Computer Science and Electronic Engineering
University of Essex, United Kingdom
corresponding author: adivsa@essex.ac.uk

Abstract: A technique to analyze MMW microstrip tunable filters with finite number of unit cells is developed. It uses eigen decomposition for factorization of the unit cell transmission matrix to obtain constituent parts and then canonicalize the periodic structure with N unit cells. Based on this concept MATLAB scripts have been developed to determine the dimensions of finite length MMW microstrip periodic structure filter. The results from ADS simulations uphold the validity of the technique.

With the global demands for higher data rate/wider bandwidth networks, most telecommunication service providers are considering wireless MMW technology for mission-critical capabilities including superior speeds and low latencies. Due to their small sizes, development of MMW filters essential for the network transceivers are cumbersome and one promising approach is to use microstrip line periodic structures with finite number of unit cells. As such, the usual theory of periodic structures assuming infinite number of repeated cells is not accurate. In this paper an alternative approach for fast analysis of these structures is proposed.

Periodic structures are modeled based on their unit cells as shown in Fig. 1. In this technique, the reciprocal

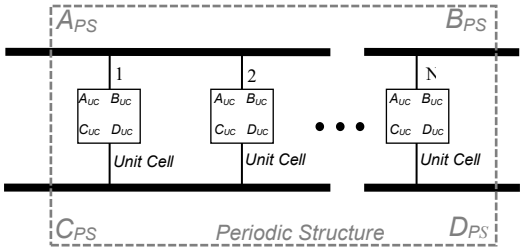

Fig 1, Transmission Matric of Periodic

transmission matrix of a unit cell is factorized into its constituent parts (i.e. canonical and eigenvectors matrix)

$$\begin{bmatrix} A & B \\ C & D \end{bmatrix}^{UC} = \begin{bmatrix} A & B \\ C & D \end{bmatrix}^{UC,canonical} \begin{bmatrix} A & B \\ C & D \end{bmatrix}^{EV} \left(\begin{bmatrix} A & B \\ C & D \end{bmatrix}^{UC,canonical} \right)^{-1} \quad (1)$$

Therefore, the transmission matrix of the unit cell can be expressed as a diagonal matrix. This guarantees a simpler and faster determination of the overall transmission matrix of a periodic structure with finite number of cells. The set of eigen value (EV) solutions (i.e. λ) or the spectrum of the reciprocal transmission matrix is calculated from characteristic eigenvalue equation:

$$\left| \begin{bmatrix} A_{UC} & B_{UC} \\ C_{UC} & D_{UC} \end{bmatrix} - \lambda I \right| = 0 \quad (2)$$

Therefore, the EV and Canonical matrices can be obtained:

$$\begin{bmatrix} A & B \\ C & D \end{bmatrix}^{EV} = \begin{bmatrix} \lambda_1 & 0 \\ 0 & \lambda_2 \end{bmatrix} = \begin{bmatrix} A_{UC} + \sqrt{A_{UC}^2 - 1} & 0 \\ 0 & A_{UC} - \sqrt{A_{UC}^2 - 1} \end{bmatrix} \quad (3)$$

$$\begin{bmatrix} A & B \\ C & D \end{bmatrix}^{UC,canonical} = \begin{bmatrix} -B_{UC} & -B_{UC} \\ -\sqrt{A_{UC}^2 - 1} & \sqrt{A_{UC}^2 - 1} \end{bmatrix} \quad (4)$$

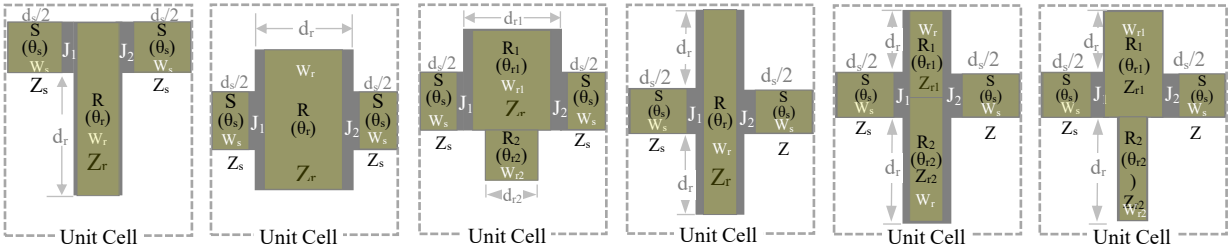

Fig 2, Different analysed microstrip unit cells

Hence, for N unit cells connected in cascade, the overall transmission matrix (where PS represents the overall transmission matrix) will be obtained as follows:

$$\begin{bmatrix} A & B \\ C & D \end{bmatrix}^{PS} = \begin{bmatrix} A & B \\ C & D \end{bmatrix}^{UC,canonical} \left(\begin{bmatrix} A & B \\ C & D \end{bmatrix}^{EV} \right)^{N} \left(\begin{bmatrix} A & B \\ C & D \end{bmatrix}^{UC,canonical} \right)^{-1} \quad (5)$$

Based on the method presented, different unit cells made of microstrip structures for periodic filters are analyzed. MATLAB scripts are written to design a filter based on optimization of the periodic structure transmission matrix. The program receives basic inputs such as desired frequency, bandwidth, input impedance, number of unit cells and the microstrip lines parameters (i.e. substrate permittivity, thickness, conductor height, …) and then by running different loops, it determines the physical dimensions of the microstrip unit cell. Several filters are designed using the MATLAB script. Designed filters are also simulated by ADS which verifies the validity and accuracy of the design method presented here.

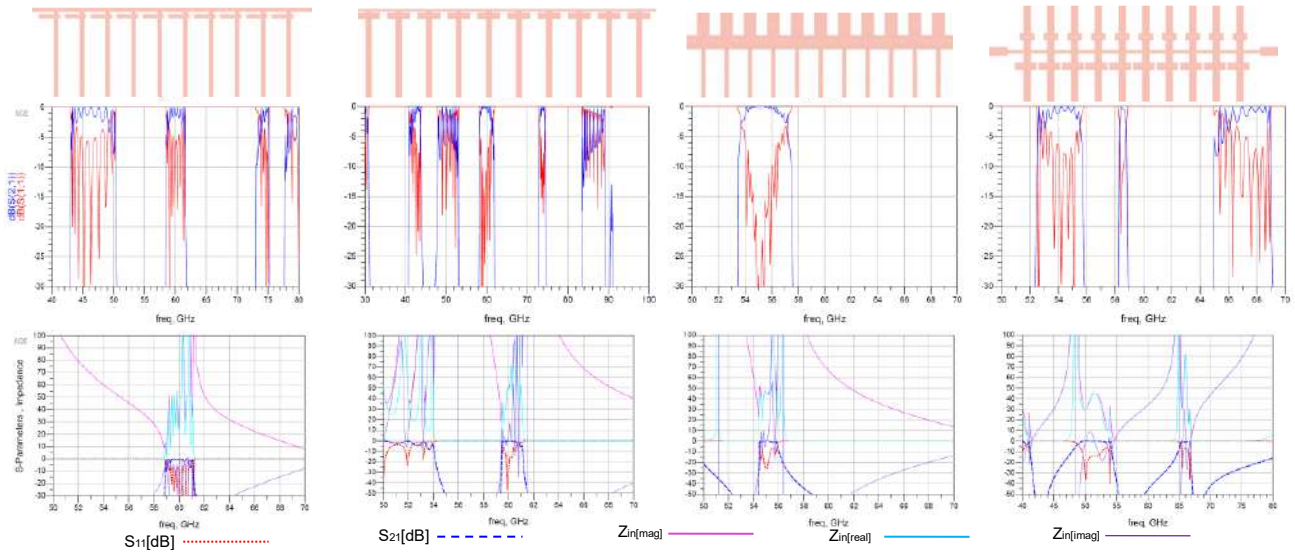

Fig 3, Designed microstrip periodic structures. Their S-parameters and input impedances.

References

1. S. Ba¸skal , Y. S. Kim, “ABCD Matrices as Similarity Transformations of Wigner Matrices and Periodic Systems in Optics”, Journal of the Optical Society of America A · October 2009
2. A. J. Prado, S. Kurokawa, “The eigenvalue analyses for non-symmetric three-phase transmission lines - the Clarke's matrix application” Seventh Latin-American Congress on Electricity Generation and Transmission - CLAGTEE 2007At: Viña del Mar, Chile, October 2007
3. A. Morched, B. Gustavsen and M. Tartibi, “A Universal Model for Accurate Calculation of Electromagnetic Transients on Overhead Lines and Underground Cables”, IEEE Trans. on Power Delivery, vol. 14, no. 3, pp. 1032-1038, July 1999.
4. Hammerstad, E. and Jensen, 0., "Accurate Models for Microstrip Computer- Aided Design", 1980 IEEE M7-7'-S International Microwave Symposium Digest, May 1980, pp. 407-409.

A hybrid wavelet-based method to model the electromagnetic propagation above a polluted sea surface

Thomas Bonnafont[1*], **Ali Khenchaf**[1]

[1]Lab-STICC, UMR CNRS 6285, ENSTA Bretagne, 29806 Brest, France
*corresponding author, E-mail: thomas.bonnafont@ensta-bretagne.fr

Abstract

Electromagnetic propagation above a rough polluted sea surface differs from one above a clean sea. Indeed, a damp effect on the waves appears. This can be used to detect a pollutant leakage. In this article, we model the propagation of electromagnetic waves above a polluted sea using a fast wavelet-based method and a two-scale model. Numerical simulations in S-band are provided.

1. Introduction

In this paper, we are interested in the tropospheric long-range propagation in the maritime environment. In this context, local phenomena such as sea waves, or the presence of a pollutant on the sea have an impact on the measured field. Indeed, waves introduce diffraction for example, while the presence of oil introduces a damping effect [1]. This latter can be used to detect pollutant leakage on the sea [2, 3].

In this framework, a large part of the literature has focused on computing the radar cross section (RCS) of the sea with and without pollutant [4, 5, 6, 7, 3]. Indeed, these methods are appropriate here, since the sea spectrum (and its modified version for an oily sea [1, 6]) can be conveniently introduced in the integral equation [4, 3]. Results have been obtained showing the difference between the RCS of a clean sea and a polluted sea, even leading to the detection of oil leakage from SAR images [2, 3].

Less work [8, 9] has focused on modeling the long-range propagation above a polluted sea surface. In particular, the sea geometry has been assumed to be flat (with the roughness accounted through Ament coefficient [10]), and the oil to cover the whole domain. Nevertheless, the obtained results have highlighted the effect of the oil on the propagated waves and show that detection is feasible.

In this paper, we develop a fast hybrid approach for computing the propagation over a polluted sea surface. The approach is based on the one developed in [11, 12] for propagation above a clean sea, where the sea spectrum [13] is used to generate random surfaces and a roughness coefficient. Besides, the use of the parabolic wave equation model allows taking into account the refraction [14] (due to tropospheric ducts for example), differing from the other proposed works [8, 2, 3]. Furthermore, we show using a Principal Component Analysis (PCA) that a polluted sea can be detected from a clean one using measurements at a given vertical.

The remainder of this paper is organized as follows. Section 2 focuses on the modelization strategy. First, the parabolic wave equation is recalled. After that, both the clean and polluted sea spectra are introduced. Section 3 introduces the computational method. This latter is based on a hybrid approach to introduce the effect of the maritime environment on propagation. Section 4 shows numerical tests performed in the S-band. Besides, a PCA analysis is provided. Finally, Section 5 concludes the paper and gives some perspectives for future works.

2. The model

In the following work, a $\exp(j\omega t)$ time dependence is assumed, where j is the imaginary unit and $\omega = 2\pi f$ is the angular frequency. We also denote by n the refractive index, and this latter is assumed to be slowly varying in the propagation direction. Furthermore, from now on the Cartesian (x, y) coordinate system is used.

2.1. The parabolic wave equation

As a reminder, we want to compute the long-range propagation above a clean or polluted sea surface. A suitable model in this context is the parabolic wave equation [14] (PWE). Indeed, by only accounting for forward propagation, it allows wide steps in the propagation direction, leading to more computationally efficient methods. Besides, the effect of the refraction, the relief, and the terrain can be incorporated. Note that the PWE is only valid in a paraxial cone. Thus for better accuracy, we use its wide-angle PWE version here. This latter is given by

$$\frac{\partial u}{\partial x} = -jk_0 \quad \overline{\frac{1}{k_0^2}\frac{\partial^2}{\partial z^2} + 1 - 1} \quad u - jk_0(n-1)u, \quad (1)$$

with u the reduced field [14], x the propagation direction, and k_0 the wave number. If the backward propagation is of interest, one can use the two-way PWE [15, 12].

2.2. Modeling the waves: the sea spectrum

To model the sea surface along the propagation, a common way is to use a sea spectrum, such as the Elfouhaily one [13], which is used from here on. This latter gives a statistical representation of the sea geometry with respect

to the wind speed. The spectrum S is then expressed as

$$S(K) = \frac{1}{K^3}\left(S_{\mathrm{l}} + S_{\mathrm{h}}\right), \tag{2}$$

where S_{l} and S_{h} correspond to the long and short wave curvature spectrums, respectively. Note that those parameters mostly depend on the wind speed at 10 m (denoted by U_{10}) above the sea, and the interested reader is referred to [13] for more details. An example of the computed sea spectrums for different wind-speed is given in Figure 1.

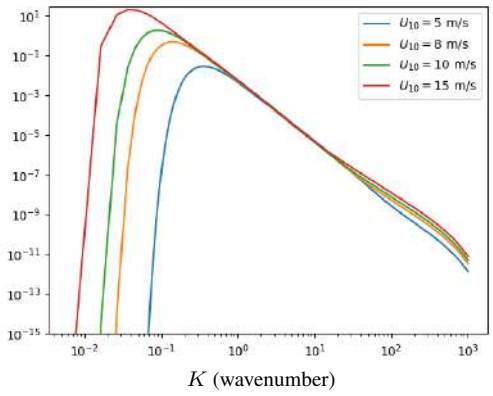

Figure 1: Computed sea spectrums [13] for different wind speeds $U_{10} \in \{5, 8, 10, 15\}$ m/s in a Log/Log scale.

Note that the wind speed has a great influence on the low wavenumber K (i.e. the large scale), thus higher waves are expected.

From this spectrum, one can derive a stochastic process to obtain sea surfaces. Indeed, S describes the statistical properties of the sea surface. The idea is to create a random surface $z_{\mathrm{r}}(x)$, normally distributed with a zero-mean, $\mu = 0$, and centered, $\sigma^2 = 1$. To add the correlation with the sea surface, then z_{r} is convoluted to the inverse Fourier transform of $\sqrt{S}$, such that

$$z(x) = \mathcal{F}^{-1}\left(\sqrt{S}\mathcal{F}(z_{\mathrm{r}}(x))\right), \tag{3}$$

with $\mathcal{F}$ the Fourier transform and z the generated sea surface. Some examples of realizations are given in Figure 2 for different wind speeds.

2.3. Accounting for the pollutant: the dumped spectrum

In this section, we introduce how to model a polluted sea surface. First of all, one can consider, depending on the wind speed U_{10}, whether the oil is soluble or not, meaning that we have an emulsion or not. Here, we focus on the insoluble case, i.e. $U_{10} \leq 8 - 10$ m/s [8], where the damping model [1] can be used.

This latter is based on the following equation

$$S_{\mathrm{po}} = S_{\mathrm{clean}}\left(1 - F + \frac{F}{y}\right), \tag{4}$$

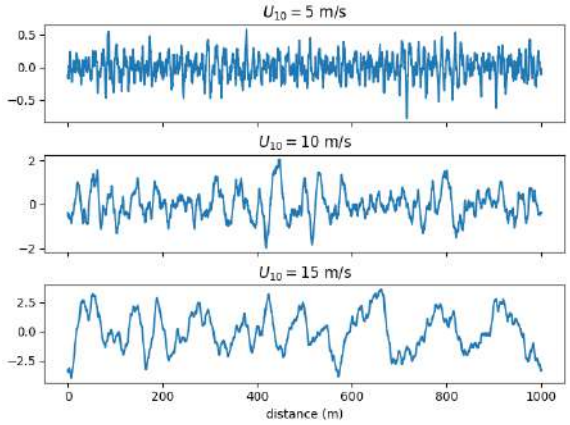

Figure 2: Generated random sea surfaces for different wind speeds $U_{10} \in \{5, 10, 15\}$ m/s using (3).

where S_{clean} corresponds to the clean sea spectrum (see Section 2.2), F to the fraction of oil covered surface, y to a damping ratio and S_{po} to the polluted sea spectrum. Here, we consider only the case where the sea is fully covered, i.e. $F = 1$. In this equation, y introduces the attenuation due to the oil film and depends on the pollutant parameters [4]. In Figure 3, an example of the clean sea spectrum and its polluted counterpart are plotted.

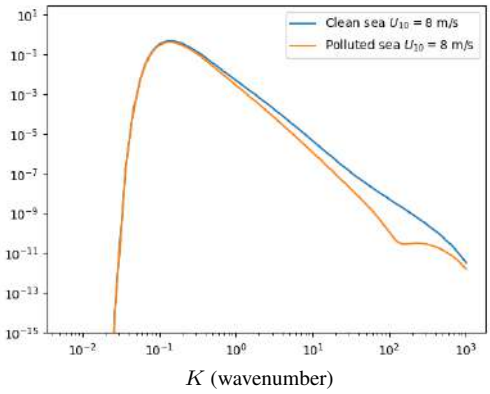

Figure 3: Computed clean and polluted sea spectrum for $U_{10} = 8$ m/s in a Log/Log scale.

One can see that the pollutant affects mainly the capillary waves, even if the maximum is reduced a little.

Using, the polluted sea spectrum S_{po}, we can use the same stochastic method to generate oil-covered sea surfaces. For a wind speed of 8 m/s, an example of the computed clean and polluted sea surface is given in Figure 4.

It should be noted that, as expected [4], the pollutant decreases the waves extremum.

3. The computational method

In this section, we describe the hybrid wavelet-based scheme proposed to solve the PWE (1), while accounting

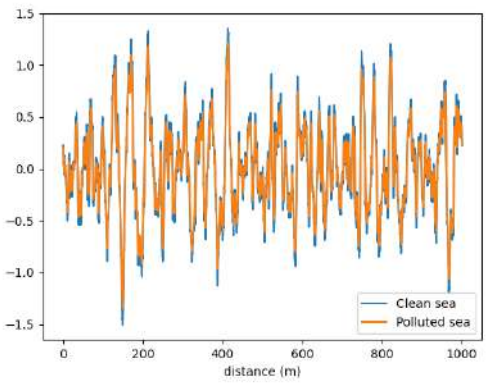

Figure 4: Generated random clean and polluted sea surface for $U_{10} = 8$ m/s.

for refraction, relief (sea surface), and ground composition.

3.1. Discretization

We denote by $x_{\max}$ and $z_{\max}$ the size of the computational domain Ω. The source is placed at $x \leq 0$ and we assume the field at $x = 0$ to be known. Thus, we have $\Omega = [0, x_{\max}] \times [0, z_{\max}]$, since the propagation above the ground is studied. For numerical reasons Ω is discretized along z and x with N_{z} and N_{x} the number of discrete points along each direction. The mesh size is thus given by

$$\Delta z = z_{\max}/N_{\mathrm{z}}$$
$$\Delta x = x_{\max}/N_{\mathrm{x}}$$

Finally, we denote by u_{x} the reduced field u discretized along z at position x.

3.2. An overview of split-step wavelet

In this article, the PWE is solved using the efficient iterative split-step wavelet method (SSW) [16, 17].

This latter allows computing the field marching in on distances by going back and forth in the wavelet and spatial domain. A step of propagation is thus split into two parts. First, the field is propagated in free space in the wavelet domain. Second, the effect of the refraction, the relief, and the ground composition are taken into account in the spatial domain. A step from x to x + Δx can thus be summed up as follows

$$u_{\mathrm{x}+\Delta\mathrm{x}} = \mathbf{R}\mathbf{L}\mathbf{W}^{-1}\mathbf{P}\mathbf{C}_{\mathrm{V_s}}\mathbf{W}u_{\mathrm{x}}, \tag{5}$$

where $\mathbf{W}$ is the wavelet transform, $\mathbf{C}_{\mathrm{V_s}}$ a compression with hard threshold, $\mathbf{P}$ corresponds to the sparse wavelet-to-wavelet propagation [17], and $\mathbf{R}$ and $\mathbf{L}$ ammount for the relief and phase-screen operators, respectively. The latter allows taking into refraction. For the relief, the staircase model is used [14]. Finally, the ground composition is accounted for through the efficient local image method [16].

To conclude on the computational method for the propagation, SSW is efficient both in terms of memory storage and computation time, with a complexity and a memory footprint lower than the conventional split-step Fourier method [16, 17].

3.3. The hybrid approach

In this section, we describe the hybrid approach [11, 12] to accurately model the effect of the sea (polluted or not) on field propagation.

The idea is that given a spatial discretization of N_{x} points (or a step Δx), not all the levels of the sea spectrum, S_{clean} or S_{po}, can be accounted for. Thus, we can compute the cut-off parameter $K_{\max}$, due to the discretization, between the large-scale and low-scale waves. This latter is given by

$$K_{\max} = N_{\mathrm{x}}\frac{2\pi}{x_{\max}}. \tag{6}$$

Using this cut-off the effect of the sea is introduced with a two-scale model. First, the lowest part of the spectrum, with respect to $K_{\max}$, is used to generate the random sea surfaces, as described in 2.2. Second, the highest part of the spectrum is used to compute a new roughness coefficient [11, 12] to take into account the capillary waves effect. This latter is multiplied by the Fresnel coefficient in the local image method.

Nevertheless, the geometry generation is based on a stochastic process, thus a Monte Carlo method is used to compute the mean of the propagation over N_{MC} cases. Therefore, the efficiency of SSW is very interesting here [12], in particular for large N_{MC}.

4. Numerical experiments

The objective of this section is twofold. First, we test that the method works well in different scenarios. Second, a PCA analysis is performed on the constructed database to obtain insights into the pollutant effect.

All the tests are performed in the S-band, at $f = 3$ GHz, in a domain of size $x_{\max} = 5$ km and $z_{\max} = 128$ m. The discretization steps are set to $\Delta x = 50$ m and $\Delta z = 0.05$ m. We also consider a surface duct, as it is frequent above the sea. A complex source point (CSP) placed at $x_s = -50$ m and $z_s = 20$ m with a width of 3 m is considered as the source. Finally, we use the following dielectric constant for the sea (resp. the oil): $\varepsilon_r = 70$ (resp. $\varepsilon_r = 2.2$) and $\sigma = 5$ S/m (resp. $\sigma = 0.0017$ S/m).

4.1. Field propagation results

In this first part, we consider two different pollutants, one with an elasticity $E_0 = 9$ mN/m and a characteristic pulsation $\omega_D = 6$ rad/s, while the other has an elasticity of 25 mN/m and a characteristic pulsation of 11 rad/s.

First, a test with a wind speed of 5 m/s, where with the given parameters, the ground is considered flat. This allows a comparison with the results of [8]. In Figure 5, we plot the field obtained with SSW, with a zoom between 0 and 56 m in altitude, at the last iteration for a clean sea and when both pollutants are considered.

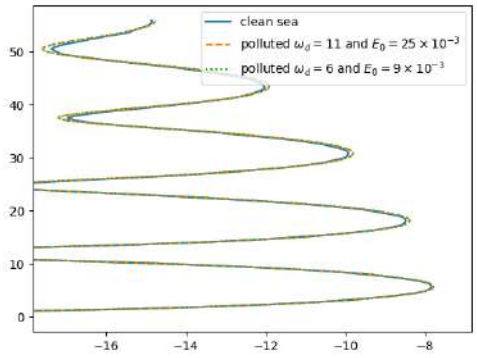

Figure 5: Field at $x = 5$ km computed with SSW for the propagation above a clean and polluted sea.

In Figure 5, one can see the effect of the pollutant on the measured electromagnetic field. Indeed, the extrema are changed when an oil film is considered, as expected since the ground composition is not the same. These results are in line with the one obtained in [8]. In this case, detection seems easy. Nonetheless, it should be recalled that at this wind speed, the sea is considered flat, and one can wonder what happens with a higher U_{10} increasing, and waves appearing.

Therefore, we choose to do the same test, with $U_{10} = 7$ m/s. In this case, since the sea surface is not flat, the mean over the 20 Monte-Carlo simulation of the field computed with SSW at the last iteration is plotted in Figure 6.

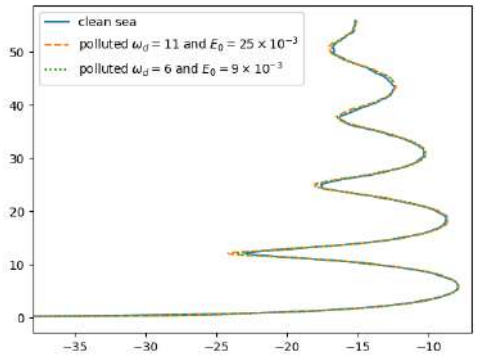

Figure 6: Field at $x = 5$ km computed with SSW for the propagation above a clean and polluted sea when $U_{10} = 7$ m/s.

In this case, we can still see the effect of the oil film but it is less clear than when $U_{10} = 5$ m/s, even if all the area is covered by the pollutant (i.e. $F = 1$). This difference is due to the surface geometry, which is not flat anymore. Note that in different cases (i.e. other surface generation), the detection can be easier or on the contrary more difficult. This is why we decide using a PCA analysis.

4.2. PCA analysis

Here, the goal of the PCA analysis is to obtain features that can help to detect a polluted sea surface. This method has been used in another context in electromagnetic where stochastic processes are studied, see [18].

Given the task, we still study the three cases (clean and polluted sea, with two different pollutants) for different wind speeds. Therefore, we constructed one database per U_{10} as follows. This latter is composed of 100 features per case, thus we have a total of 300 features. These latter shall represent the field propagation as precisely as possible. Therefore, each feature consists of the mean of the computed field at the last iteration over 20 Monte-Carlo simulations, to take into account the stochastic aspect of the surface. Example of these features are given in Section 4.1 for $U_{10} = 5$ m/s and 7 m/s.

Then, a PCA with a given number of 3 components is performed on each dataset. The goal is to find one (or multiple) directions that describe the effect of the pollutant on propagation.

In Figure 7, we plot the transformed features over the first two components of the PCA decomposition. Here, the wind speed is 5 m/s. Note that label 0 is for a clean sea while labels 1 and 2 correspond to the two pollutants with $E_0 = 9$ mN/m and $\omega_D = 6$ rad/s, and $E_0 = 25$ mN/m and $\omega_D = 11$ rad/s, respectively.

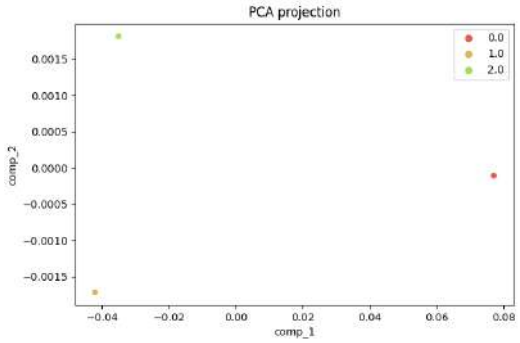

Figure 7: Features transformed onto the PCA components plotted for the first two components when $U_{10} = 5$ m/s.

As expected, the three cases are fully separated, and detection is easy (using for example a logistic regression). Besides, since at this wind speed, the sea surface is flat, all the features for each case are the same. Nevertheless, we can see that the first axis here seems to relate to how close to a clean sea we are.

Therefore, the same analysis is now performed at $U_{10} = 7$ m/s. As before, we plot the transformed features over the two first components of the PCA analysis in Figure 8. The labels remain the same.

In this case, since the surface is not flat anymore, many points are plotted for each label depicting the features in the first two components' axis. Nonetheless, one can see that the three cases are still separated leading to an easy

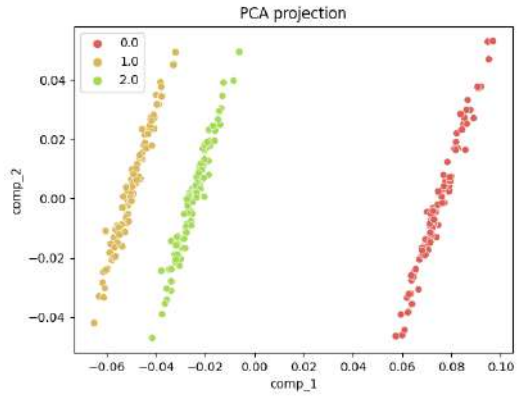

Figure 8: Features transformed onto the PCA components plotted for the first two components when $U_{10} = 7$ m/s.

detection here. Besides, as before, the first axis seems to refer to how close to a clean sea we are.

Other tests have been performed for wind speed upper than $U_{10} = 8$ m/s, upper than the limit for insoluble oil film, and at these speeds, no separation was achieved. This is due to the dominant influence of the sea geometry on the electromagnetic field at these U_{10}.

5. Conclusion

In this article, we studied the tropospheric propagation of the electromagnetic field above a polluted sea.

The propagation model is based on a hybrid approach where the sea spectrum or its damped version to take into account the pollutant, is used to generate random surfaces and to compute a roughness factor.

A wavelet-based computational scheme is used since its efficiency allows fast Monte Carlo simulations. Besides, we constructed a database for different wind speeds to obtain features that help to detect an oil leakage based on electromagnetic measurements.

A PCA analysis, with 3 components, has been performed on these databases, showing that the polluted and clean sea can be detected when the wind speed is below a limit of 8 m/s. Besides, we saw that the first axis of the PCA decomposition could refer to how close we are to a clean see.

Thus, we are currently working on the case where the sea is not fully covered by the pollutant, i.e. $F < 1$. In this case, a new model shall introduce the position of the oil leakage. The same analysis could then be performed to assess the limit of detection. Finally, we are also working on the case where we have an emulsion of oil and water, and when a film and an emulsion are considered.

References

[1] P. P. Lombardini, B. Fiscella, P. Trivero, C. Cappa, and W. Garrett, "Modulation of the spectra of short gravity waves by sea surface films: slick detection and characterization with a microwave probe," *Journal of Atmospheric and Oceanic Technology*, vol. 6, no. 6, pp. 882–890, 1989.

[2] H. Zheng, Y. Zhang, A. Khenchaf, Y. Wang, H. Ghanmi, and C. Zhao, "Investigation of EM backscattering from slick-free and slick-covered sea surfaces using the SSA-2 and SAR images," *Remote Sensing*, vol. 10, no. 12, p. 1931, 2018.

[3] H. Zheng, J. Zhang, A. Khenchaf, and X.-M. Li, "Study on non-Bragg microwave backscattering from sea surface covered with and without oil film at moderate incidence angles," *Remote Sensing*, vol. 13, no. 13, p. 2443, 2021.

[4] H. Ghanmi, A. Khenchaf, and F. Comblet, "Numerical modeling of electromagnetic scattering from sea surface covered by oil," *Journal of Electromagnetic Analysis and Applications*, vol. 2014, 2014.

[5] C.-H. Qi and Z.-Q. Zhao, "Electromagnetic scattering and statistic analysis of clutter from oil contaminated sea surface," *Radioengineering*, vol. 24, no. 1, pp. 87–92, 2015.

[6] T.-H. Kim, C.-S. Yang, and K. Ouchi, "Accuracy improvement of the radar backscatter simulation from sea surface covered by oil slick using fetch-dependent waveheight spectrum: Comparison with the 2007 Heibei Spirit Case in the Yellow Sea," *Ocean Science Journal*, vol. 51, pp. 235–249, 2016.

[7] H. Ghanmi, A. Khenchaf, and F. Comblet, "Electromagnetic characterization of a polluted maritime surface," in *2018 4th International Conference on Advanced Technologies for Signal and Image Processing (ATSIP)*, pp. 1–6, IEEE, 2018.

[8] N. Pinel, C. Bourlier, and J. Saillard, "Forward radar propagation over oil slicks on sea surfaces using the ament model with shadowing effect," *Progress In Electromagnetics Research*, vol. 76, pp. 95–126, 2007.

[9] M. Cui, H. Cha, and B. Tian, "A propagation model for rough sea surface conditions using the parabolic equation with the shadowing effect," *The Applied Computational Electromagnetics Society Journal (ACES)*, pp. 683–689, 2018.

[10] W. Ament, "Toward a theory of reflection by a rough surface," *Proceedings of the IRE*, vol. 41, no. 1, pp. 142–146, 1953.

[11] O. Benhmammouch, A. Khenchaf, and N. Caouren, "Modelling roughness effects on propagation of electromagnetic waves in a maritime environment: A hybrid approach," *IET radar, sonar & navigation*, vol. 5, no. 9, pp. 1018–1025, 2011.

[12] T. Bonnafont, O. Benhmammouch, and A. Khenchaf, "A two-way split-step wavelet scheme for tropospheric long-range propagation in various environments," *Remote Sensing*, vol. 14, no. 11, p. 2686, 2022.

[13] T. Elfouhaily, B. Chapron, K. Katsaros, and D. Vandemark, "A unified directional spectrum for long and short wind-driven waves," *Journal of Geophysical Research: Oceans*, vol. 102, no. C7, pp. 15781–15796, 1997.

[14] M. Levy, *Parabolic equation methods for electromagnetic wave propagation*. No. 45, IET, 2000.

[15] O. Ozgun, "Recursive two-way parabolic equation approach for modeling terrain effects in tropospheric propagation," *IEEE Transactions on Antennas and Propagation*, vol. 57, no. 9, pp. 2706–2714, 2009.

[16] H. Zhou, R. Douvenot, and A. Chabory, "Modeling the long-range wave propagation by a split-step wavelet method," *Journal of Computational Physics*, vol. 402, p. 109042, 2020.

[17] T. Bonnafont, R. Douvenot, and A. Chabory, "A local split-step wavelet method for the long range propagation simulation in 2D," *Radio science*, vol. 56, no. 2, pp. 1–11, 2021.

[18] M. Haider, J. A. Russer, A. Baev, Y. Kuznetsov, and P. Russer, "Principal component analysis applied in modeling of stochastic electromagnetic field propagation," in *Proceedings of the European Microwave Conference (EuMC), EuMC19-1*, 2017.

Higher-order Modes by Misalignment in Transition from Hollow Metallic Waveguides to Dielectric Waveguides

N. Xenidis[1*], S. Smirnov[1], J. Oberhammer[1] and D. Lioubtchenko[1,2]

[1]Division of Micro and Nanosystems, KTH Royal Institute of Technology, Swedem
[2]CENTERA Laboratories, Institute of High Pressure Physics PAS, Poland
[*]corresponding author: xenidis@kth.se

Abstract: In this work, we report the effects of misalignment between a dielectric waveguide and a hollow metallic waveguide in the WR-10 band. The results indicate the excitation of unwanted higher-order modes in the dielectric waveguide that are expected to degrade the performance, especially at higher frequencies.

Dielectric waveguides are a promising guiding structure for THz and sub-THz systems, owing to their low losses and fabrication simplicity. Several platforms to ease integration with standard measurement equipment have been developed, such as effective medium cladded waveguides[1] and unclad dielectric waveguides[2]. However, most dielectric waveguides are excited by a tapered transition structure inserted into a hollow metallic waveguide[3-5]. The manual insertion of the dielectric waveguide into the hollow waveguide can be a source of losses in case of misalignments. If the taper of the dielectric waveguide is not centered in the hollow waveguide, undesired higher-order modes will be excited, an effect especially pronounced at higher frequencies. Fig. 1 shows different kinds of misalignments between a tapered dielectric rod waveguide (DRW) and a hollow metallic waveguide.

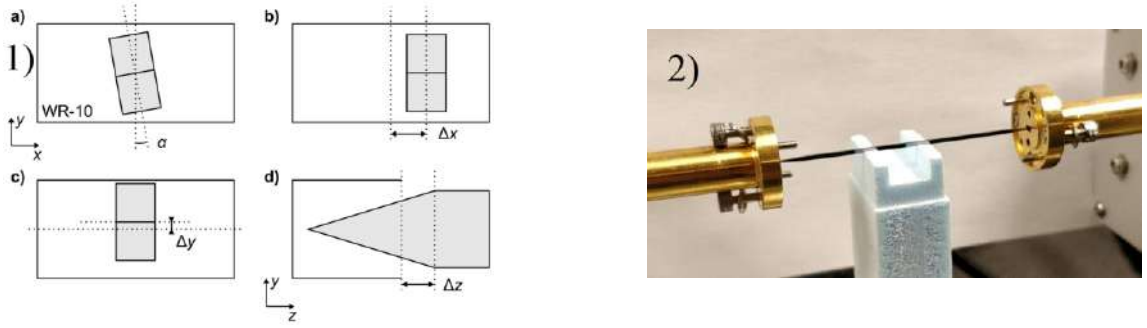

Figure 1: Schematic of misalignments in the transition between the DRW (in grey) and a hollow metallic waveguide (black outline) in a) rotation α, and b-d) linear offsets Δx, Δy, Δz respectively. **Figure 2**: Measurement setup.

A 60 mm silicon DRW with cross section of 1 mm by 0.5 mm and a 6 mm taper in the E-plane was simulated in CST Microwave Studio and fabricated from a high resistivity silicon wafer (10 kΩ cm) by deep reactive ion etching. A WR-10 (67-110 GHz) hollow metallic waveguide operating in the TE_{10} mode was used to excite the DRW, which ideally operates in the fundamental E_{11}^{y} mode. A low loss, low permittivity foam was used as a support structure. A 3-axis positioner stage was used to control for the misalignment in x, y, z. The measurement setup is shown in Fig. 2.

Fig. 3 shows the simulated results for rotational and linear misalignments in x, y, z directions. A rotational misalignment excites the cross-polarized mode E_{11}^{x} with increasing angle α. Linear offsets Δx and Δy excite the E_{21}^{y} and E_{12}^{y} modes, respectively. Linear offset Δz reduces the coupling, with decreasing S_{21} and S_{11} approaching that of an open-ended hollow metallic waveguide.

Fig. 4 shows the measured results, after TRL calibration at the metallic waveguide flanges and time gating. Insertion loss increases up to 0.4 dB at 109 GHz for Δx and up to 1.1 dB at 70 GHz for Δy. Little impact on reflection loss is observed. However, misalignment for Δz results in increased reflection loss, along with insertion loss of up to 15 dB at $\Delta z = 5$ mm.

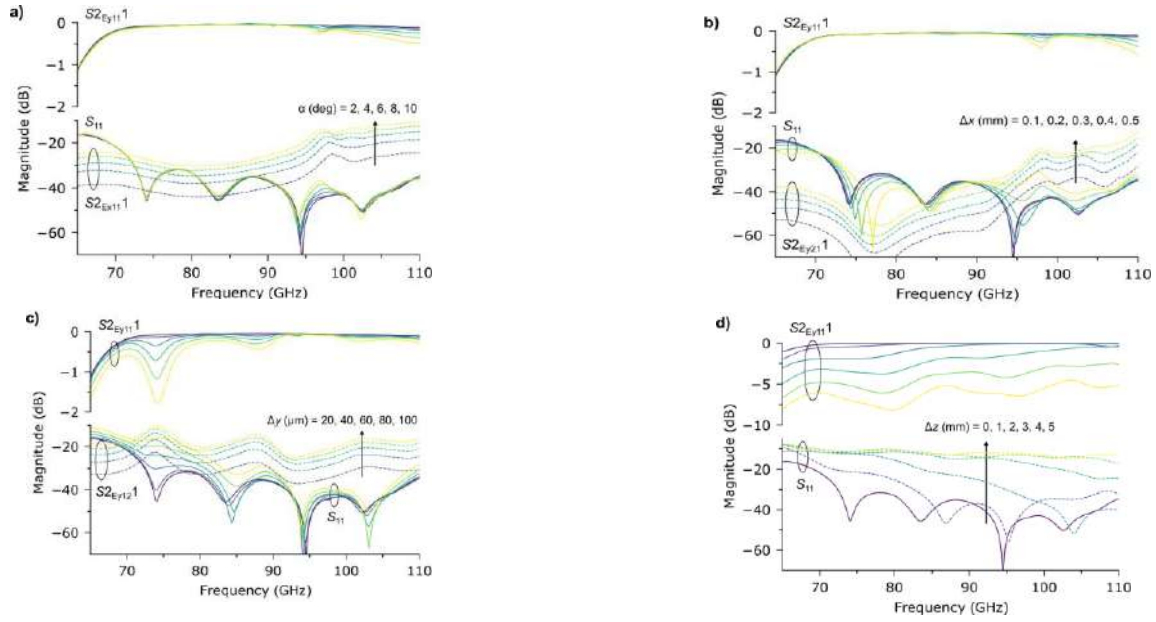

Figure 3: Simulated S-parameters for a) rotational misalignment and b-d) misalignment in x, y, z respectively.

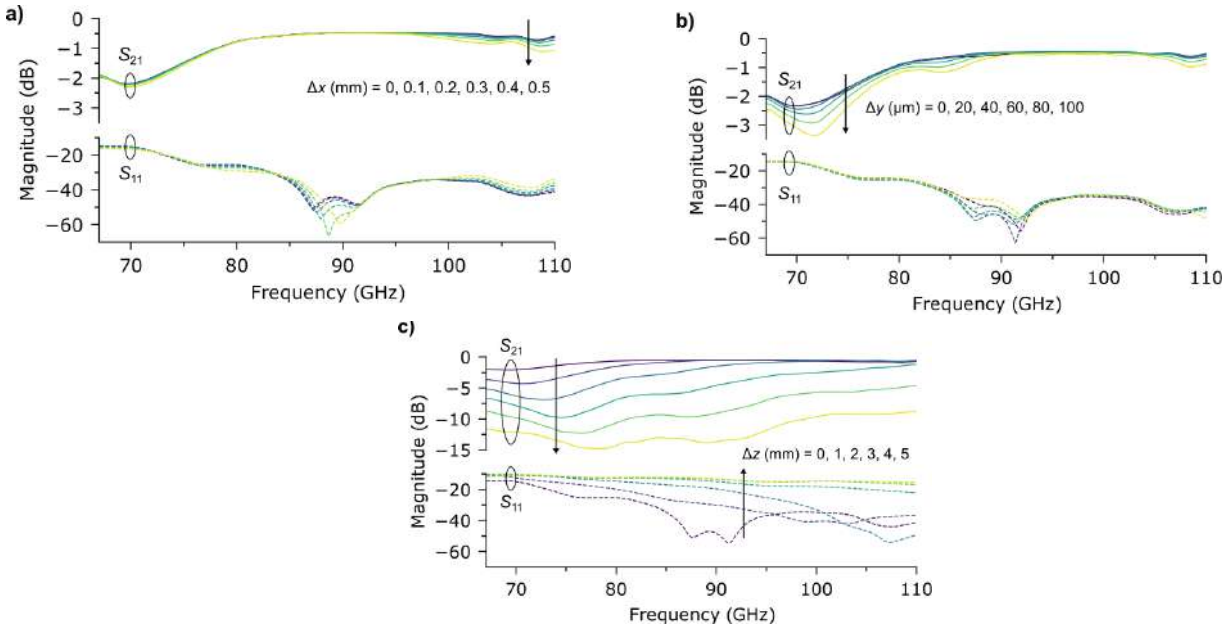

Figure 4: Measured S-parameters of a WR10 – DRW – WR10 transition. a-c) misalignment in x, y, z respectively.

We acknowledge Myfab for provisioning of facilities and experimental support. Myfab is funded by the Swedish Research Council as a national research infrastructure. The work was supported by the European Union's Horizon 2020 FET Open project TERAmeasure (grant agreement No 862788).

References

1. Weijie Gao, Xiongbin Yu, Masayuki Fujita, Tadao Nagatsuma, Christophe Fumeaux, and Withawat Withayachumnankul, "Effective-medium-cladded dielectric waveguides for terahertz waves," Opt. Express 27, 38721-38734 (2019)
2. Daniel Headland, Withawat Withayachumnankul, Xiongbin Yu, Masayuki Fujita, and Tadao Nagatsuma, "Unclad Microphotonics for Terahertz Waveguides and Systems," J. Lightwave Technol. 38, 6853-6862 (2020)
3. Rivera-Lavado, A., García-Muñoz, LE., Generalov, A. et al. Design of a Dielectric Rod Waveguide Antenna Array for Millimeter Waves. J Infrared Milli Terahz Waves 38, 33–46 (2017). https://doi.org/10.1007/s10762-016-0310-9
4. Smirnov, Serguei, Dmitri V. Lioubtchenko, and Joachim Oberhammer. "Single-walled carbon nanotube layers for millimeter-wave beam steering." Nanoscale 11.31 (2019): 14691-14697.
5. Reese, R., Tesmer, H., Jost, M. et al. A Compact Two-dimensional Power Divider for a Dielectric Rod Antenna Array Based on Multimode Interference. J Infrared Milli Terahz Waves 39, 1185–1202 (2018). https://doi.org/10.1007/s10762-018-0535-x

Imaging, inverse scattering and remote sensing

Measuring Free-Space Light Beams with On-Chip Circuitry

P. Banzer[1,2*], V. Sharma[1], J. Bütow[1], D. Brandmüller[1], J. S. Eismann[1,2,3]

[1]Institute of Physics, University of Graz, NAWI Graz, Austria
[2]Max Planck Institute for the Science of Light, Erlangen, Germany
[3]Institute of Optics, Information, and Photonics, University Erlangen-Nuremberg, Germany
*corresponding author, E-mail: peter.banzer@uni-graz.de

Abstract: In this contribution, we discuss how to utilize reprogrammable photonic integrated circuits for the measurement of (structured) free-space light beams. The on-chip super-pixels enable the spatially resolved experimental study of parameters such as intensity, phase, and polarization.

A normal camera usually only measures the spatial distribution of intensity (and colour). However, in countless fields of research and applications, additional information, such as phase or polarization distributions, are of utmost importance because fine details of the interaction of a light field with its environment usually affects those parameters as well. Important examples are free-space communication (via turbulent links), fibre-based endoscopy, nanometrology, and others. The spatial distributions of said parameters, in particular, play a major role [1].

To give a camera the ability to measure also phase and/or polarization, it has to be equipped with extra components, e.g., lenslet arrays (Shack-Hartmann sensors), microscopic polarization elements (polarization cameras), or extra polarimetry and interferometry enabling 'beam-paths'.

Here, we now discuss a fundamentally different and novel approach for the spatially resolved measurement of light's intensity, phase, and polarization [2,3] based on all-integrated and reconfigurable photonic meshes [4,5]. These super-pixels are a powerful and versatile addition to the existing detector toolbox. They pave the way towards intriguing applications in nano-optics and microscopy [5-9] and the fields mentioned. In this presentation, we plan to discuss the underlying principle of this novel detector, its building-blocks, and its calibration, and we show selected applications.

Acknowledgments
We acknowledge the support by the Super-Pixels Consortium. This project has received funding from the European Commission Horizon 2020 research and innovation programme under the Future and Emerging Technologies Open Grant Agreement Super-Pixels No. 829116.

References

[1] H. Rubinsztein-Dunlop et al., "Roadmap on structured light," Journal of Optics 19.1, 013001, 2016.
[2] J. Bütow, J. S. Eismann, M. Milanizadeh, F. Morichetti, A. Melloni, D. A. B. Miller, P. Banzer, "Spatially resolving amplitude and phase of light with a reconfigurable photonic integrated circuit," Optica 9.8, 939-946, 2022.
[3] M. Milanizadeh, F. Toso, G. Ferrari, T. Jonuzi, D. A. B. Miller, A. Melloni, and F. Morichetti, "Coherent self-control of free-space optical beams with integrated silicon photonic meshes," Photon. Res. 9, 2196-2204 (2021)
[4] D. A. B. Miller, "Self-aligning universal beam coupler," Opt. Express 21, 6360-6370, 2013.
[5] D. A. B. Miller, "Self-configuring universal linear optical component," Photonics Res. 1, 1-15, 2013.
[6] J. S. Eismann and P. Banzer, "Sub-diffraction-limit Fourier plane laser scanning microscopy," Optica 9, 455-460 (2022)
[7] P. Beck, M. Neugebauer, P. Banzer, "Toward High-Speed Nanoscopic Particle Tracking via Time-Resolved Detection of Directional Scattering," Laser & Photonics Reviews 14.9, 2000110, 2020.
[8] J. S. Eismann, M. Neugebauer, K. Mantel, P. Banzer, "Absolute characterization of high numerical aperture microscope objectives utilizing a dipole scatterer," Light: Science & Applications, 10(1), 1-7, 2021.
[9] M. Neugebauer, P. Wozniak, A. Bag, G. Leuchs, P. Banzer, "Polarization-controlled directional scattering for nanoscopic position sensing," Nature Commun. 7, 11286, 2016.

The Behaviour of PolInSAR Coherence as a Parameter for Backscattering Analysis and Target Characterization

Sofiane Tahraoui[1,2], **Mounira Ouarzeddine**[2],**Foued Cherchour**[3]

[1]Space Studies Department, Institutes of Aeronautics and Space Studies, University of Blida 1, BP 270, Blida, Algeria.
[2]LTIR, FGE, USTHB, BP N.32 El Alia, Bab Ezzouar, Algiers, Algeria
[3]EMP, Bordj El-Bahri, 16111, Algiers, Algeria.
*corresponding author, E-mail: sofiane.tahraoui@ymail.com

Abstract

This paper investigates the influence of various parameters, such as frequency, polarization, incidence angle, on inversion and analysis for natural media. The primary objective is to examine the distribution of interferometric coherence in the complex plane as a means of discriminating between different media types within forests. Through this analysis, the study uncovers the unique characteristics associated with different forest components. The findings highlight the effectiveness of utilizing interferometric coherence as a discriminative parameter for distinguishing between natural media types. This approach holds significant potential for advancing forest analysis and classification techniques, enabling a more accurate and comprehensive understanding of the intricate interactions between radar signals and diverse media types within forest environments.

1. Introduction

Synthetic Aperture Radars (SAR) are highly efficient and precise tools widely used for retrieving parameters from vegetative media. Studying vegetation targets through scattering modelling allows for understanding the physical properties of the observed medium.

SAR has found applications in various industries, including forestry and farming, due to its versatility. It enables continuous monitoring of crop development, tracking the plant's growth stages, early detection of plant diseases, accurate soil irrigation monitoring for efficient water resource management, estimation of vegetation height, and quantification of biomass densities. However, modelling the vegetative environment is challenging due to its constant evolution.

The combination of SAR Interferometry and SAR Polarimetry techniques, known as **PolInSAR**, offers an effective solution for quantitative and geometric characterization of media. PolInSAR provides 3D spatial information and intrinsic features of the scanned scene, including a Digital Elevation Model (DEM) obtained from the interferogram. The quality and reliability of interferograms are assessed by the magnitude of interferometric coherence at different polarizations. This parameter measures the similarity between two acquisitions of the same scatterer [1, 2]. In the ideal case, this parameter would be equal to 1, indicating perfect coherence.

The interferometric coherence product plays a crucial role in retrieving vegetation parameters. This parameter exhibits high sensitivity to polarization states [3, 4], intrinsic properties of the medium, and radar frequency.

By considering these characteristics, we propose a novel model for the scattering signature of the medium. Our findings indicate that, for specific parameter configurations, the interferometric coherence exhibits distinct forms and positions in the complex plane for each type of medium [5].

In this study, we investigate the potential of utilizing the behaviour (shape and location) of interferometric coherence in the complex plane as a novel signature for natural media. The subsequent section provides a brief overview of the fundamental principles of PolInSAR (polarimetric SAR interferometry). We then examine the scattering behaviour in different polarization states through several examples, and finally present our conclusions.

2. Basic Notions

2.1. The Interferometric coherence

The Interferometric coherence is a measure of the correlation between radar signals obtained from complex SAR images captured at close angles.

Estimation techniques for forest parameters can leverage the significant polarization state dependence observed in the behaviour of interferometric coherence.

To obtain the necessary matrices for analysis, we utilize the outer products of the scattering vector from each antenna, represented as $\rangle Kp1$ and $\rangle Kp2$. These vectors are then expressed in the Pauli basis, resulting in the three 3x3 complex matrices: $[T_{11}]$, $[\Omega_{12}]$, and $[T_{22}]$.

$$\begin{aligned} [T_{11}] &= \rangle K_{p1} \rangle K^*_{p1} \\ [T_{22}] &= \rangle K_{p2} \rangle K^*_{p2} \\ [\Omega_{12}] &= \rangle K_{p1} \rangle K^*_{p2} \end{aligned} \tag{1}$$

The matrices $[T_{11}]$ and $[T_{22}]$ are hermitian coherency matrices that capture the polarimetric properties of each individual acquisition. On the other hand, the matrix $[\Omega_{12}]$ is a

non-hermitian complex matrix that contains interferometric phase information [6].

To further analyze the data, we introduce two unity complex vectors, $\langle\ \rangle_1$ and $\langle\ \rangle_2$, which can be interpreted as generalized scattering mechanisms. By projecting the scattering vectors, $\langle Kp1\rangle$ and $\langle Kp2\rangle$, onto these vectors, we generate two complex scalar images, i_1 and i_2 as:

$$i_1 = \langle\ \rangle_1^{*T} \langle K_{p1}\rangle \qquad i_2 = \langle\ \rangle_2^{*T} \langle K_{p2}\rangle \tag{2}$$

The interferogram related to the scattering mechanisms $\langle\ \rangle_1$ and $\langle\ \rangle_2$ is then given by

$$i_1 i_1^* = (\langle\ \rangle_1^{*T} \langle K_{p1})(\langle\ \rangle_2^{*T} \langle K_{p2})^{*T} = \langle\ \rangle_1^{*T} [\Omega_{12}] \langle\ \rangle_2 \tag{3}$$

And the corresponding interferometric phase is derived as follows:

$$\phi = \arg(i_1 i_1^*) = \arg(\langle\ \rangle_1^{*T} [\Omega_{12}] \langle\ \rangle_2) \tag{4}$$

Thus, an overall expression for the complex interferometric coherence can be obtained for any arbitrary selection of scattering mechanisms, $\langle\ \rangle_1$ and $\langle\ \rangle_2$ as:

$$\gamma = \frac{\left\langle \langle\ \rangle_1^{*T} [\Omega_{12}] \langle\ \rangle_1 \right\rangle}{\left\langle \langle\ \rangle_1^{*T} [T_{11}] \langle\ \rangle_1 \right\rangle \left\langle \langle\ \rangle_2^{*T} [T_{22}] \langle\ \rangle_2 \right\rangle} = \gamma e^{j\phi} \tag{5}$$

where γ is the amplitude of the complex coherence γ, and ϕ is the interferogram phase.

2.2. The sensitivity of the coherence to the polarization

The inversion of physical parameters of the volume relies on the behaviour of interferometric coherence, which exhibits high sensitivity to changes in polarization states of the electromagnetic field [7].

Under the assumption that the polarimetric information obtained from the two interferometric antennas is identical, we have $[T_{11}] = [T_{22}]$. Consequently, the expression for the interferometric coherence (equation 5) can be simplified as:

$$\gamma \approx \frac{\left\langle \langle\ \rangle_1^{*T} [\Omega_{12}] \langle\ \rangle_1 \right\rangle}{\left\langle \langle\ \rangle_1^{*T} [T_{11}] \langle\ \rangle_1 \right\rangle} \tag{6}$$

The interferometric coherence representing a coherent summation of two scatterers S_A and S_B located within the same resolution cell and received by master "m" and slave "s" antennas [2], can be expressed as:

$$\begin{aligned} \gamma &\approx \frac{\left\langle (S_{A_m} + S_{B_m})(S_{A_S} + S_{B_S})^* \right\rangle}{{S_A}^2 + {S_B}^2} \\ &\approx \frac{S_{A_m} {S_{A_S}}^* + S_{B_m} {S_{B_S}}^*}{{S_A}^2 + {S_B}^2} \end{aligned} \tag{7}$$

By assuming that the two contributions (scatterers) originate from the ground S_g and the canopy volume S_v, and that they are uncorrelated, the overall interferometric coherence can be expressed in terms of the individual coherences of these pure contributions γg and γv as follows:

$$\begin{aligned} \gamma &\approx \frac{\mu\gamma_g + \gamma_v}{1+\mu} \\ &\approx \gamma_v + \frac{\mu}{1+\mu}(\gamma_g \langle\ \rangle\ \gamma_v) \end{aligned} \tag{8}$$

where $\mu = \frac{|S_g|^2}{|S_v|^2}$, is the power ratio of these two contributions.

While it is commonly assumed to be equal to 1 regardless of the polarization [7], the contribution of the soil is undesirable as it affects the coherence of the canopy. Consequently, the general interferometric coherence can be expressed as:

$$\gamma = \frac{\gamma_v + \mu(w)}{1+\mu(w)}\, e^{j\phi_0} \tag{9}$$

3. Theoretical Approach

This study focuses on investigating the influence of various parameters on the dispersion of coherence in the complex plane, which can provide valuable insights into the properties of the medium. While the detailed characterization of species signatures is beyond the scope of this paper, we aim to analyse the coherence behaviour in relation to different natural targets.

The selection of appropriate system parameters is crucial to effectively capture the complex properties of natural media and minimize biases in the inversion process. This decision involves careful consideration of trade-offs. Prior knowledge or a priori information plays a vital role in this regard. In this section, we will explore several variables that can introduce distortions in the distribution of coherence within the complex plane.

3.1. Target details and frequency band

The details of the target, such as its scattering characteristics and behaviour, can vary depending on the frequency band used in radar observations. Different frequency bands have different penetration depths and interaction capabilities with the target. Choosing the appropriate frequency/wavelength is crucial. For instance, when the target size is comparable to or smaller than the size of leaves, using X and C wavelength bands, the radar signal does not penetrate deeply into the forest volume. In this case, the primary scattering contributions come from external branches and surrounding leaves. As a result, the volume exhibits inconsistencies due to wind movement, which alters the geometry of scatterers [2]. This randomness in distribution explains the scattered responses observed in the complex plane (Figure 1-a). In contrast, when operating at L and P bands, the radar waves penetrate deeper into the forest and interact with internal branches and trunks. This interaction reduces the decorrelation caused by wind movement and enhances the interferometric coherence within the resolution cell. Consequently, the coherence distribution in the

complex plane becomes more contiguous (Figure 1-b).
Fig. 2 shows the predicted penetration depths as a function

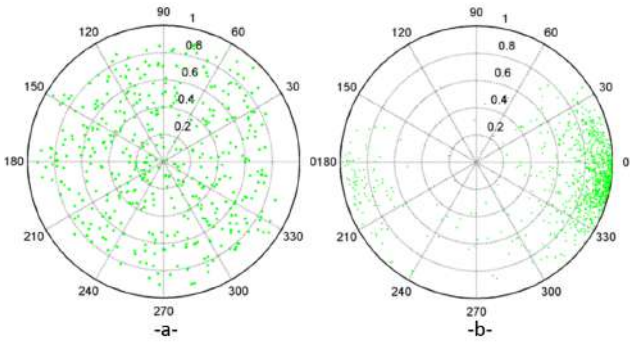

Figure 1: Interferometric Coherence responses of a simulated pine forest (a:X band) and (b:P band) , with heights ranging from 0 to 18m (shown in green)

of frequency calculated using the attenuation rates. Consequently, the average penetration depth, represented by the 50 percent line, varies from 60m in the P band to 40m in the L band and 20m in the C band.
When the volume contains scatterers of different sizes and orientation distributions, the change in extinction with polarization is influenced by the frequency used because the effective scatterers change accordingly. In cases where both ground and volume scattering occur due to penetration, the ground scattering amplitude also varies with frequency, in addition to extinction. This implies that the interferometric coherence exhibits variations with frequency as well [8].

3.2. Target Orientation Analysis

The orientation of the target plays a crucial role in the backscattering response. Consider the case of an oriented volume with uniform density. In this scenario, the backscattering response exhibits minimal dependence on the incident angle, indicating that the orientation of the scatterers has a dominant influence. However, the response strongly varies with polarization, reflecting the interaction between the incident waves and the oriented scatterers. This behaviour has been observed in various applications, such as agricultural fields or plantations, where the alignment of crops or trees results in preferential scattering directions [9]. On the other hand, when dealing with a heterogeneous random volume, the backscattering response shows a different behaviour. Here, the response becomes polarization independent, meaning that the orientation of the scatterers has a negligible effect. Instead, the response becomes more dependent on the incidence angle. In this case, vertically polarized waves tend to interact with the vertical stalks of the plant canopy, resulting in a strong backscattering signal. Conversely, horizontally polarized waves have the ability to penetrate through the plant canopy, resulting in reduced backscattering [9].

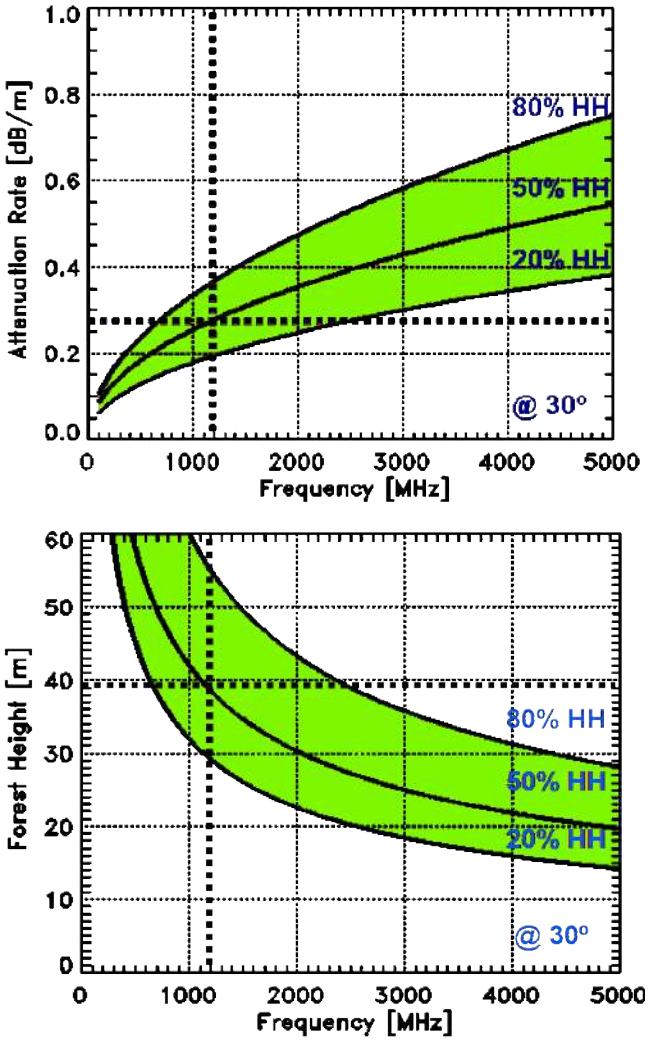

Figure 2: Frequency (for HH at 30° incidence) vs penetration depth (right image) obtained from the attenuation rates (left image) assuming a vegetation height of 20m [8].

3.3. Target Density and Sampling Window Size

When conducting density analysis in a forest, the selection of an appropriate sampling window size plays a critical role. The forest's intricate shapes and structures necessitate careful consideration of this choice. It involves a trade-off between several factors that influence the accuracy and efficiency of the analysis.

Opting for a larger sampling window size can expedite the calculation process. However, it may introduce a merging effect, where multiple scatterers are combined within the same resolution cell. For instance, a large window size could inadvertently merge a tree with the space between trees, which might contain bare soil or stones. Similarly, it could merge different tree species or incorporate contributions from the surrounding soil. This merging effect introduces bias in the characterization and analysis of the targets within the forest.

Nevertheless, using a large window size can prove ad-

vantageous in densely populated forests where trees of the same species and closely spaced. In such cases, the merging of scatterers within the window can actually provide valuable insights into the density and distribution of the dominant species and improve target characterisation.

Conversely, choosing a smaller sampling window size may increase computation time, but it offers the advantage of improved estimation efficiency. The smaller window allows for better separation and identification of individual targets within the resolution cell. However, if the window size becomes too small compared to the wavelength, the estimation may become inefficient. This is particularly true in forests with a stochastic scattering nature, where the diffusion pattern of the dominant species is sought after.

In summary, the selection of an appropriate sampling window size for target density analysis in forests is a delicate balance. Considering the merging effect, computation time, estimation efficiency, and the scattering characteristics of the forest are all vital factors to achieve accurate and meaningful results.

4. Proposed Inversion Models

As mentioned earlier, the coherence distribution pattern in the complex plane can offer valuable insights into natural media. In this regard, we present Figures 3, 4, and 5, which depict the regions of complex interferometric coherence for two simulated forest types generated using the **polsarproSIM** software.

This simulator allow for the manipulation of various parameters, such as incidence angle, polarization, frequency band, and tree species (e.g., Pine, deciduous), as well as stand density. By altering these parameters, we can explore the impact of different factors on the resulting coherence patterns. t is worth noting that these simulation models offer a flexible and controlled environment to study the behaviour of interferometric coherence in different forest scenarios. The inversion results obtained from the simulated

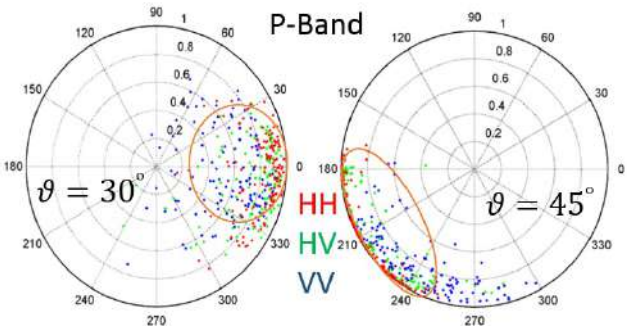

Figure 3: Representation of the interferometric coherence (P-Band) in the complex plane corresponding to Pine Forest.

forests, as shown in Figures 3 and 4, provide valuable insights into the relationship between various parameters and the resulting complex interferometric coherence. The angular distribution of coherence corresponds to the height dispersion of the phase centres within the forest, which is primarily influenced by the density and vertical extent of the volume layer. The simulation models the forest as multiple independent layers of randomly oriented particles, leading to an interferometric phase that is influenced by the vertical position of these layers [7]. This implies that the position of the interferometric coherence in the complex plane is sensitive to both the orientation and vertical location of the target, which represent two distinct parameters. Additionally, the coherence is affected by the polarization of the signal, which in turn is influenced by the intrinsic properties of the target. Consequently, each target within the forest can exhibit a unique **PolInSAR Signature**, which is indicated by the position of the coherence in different polarisations.

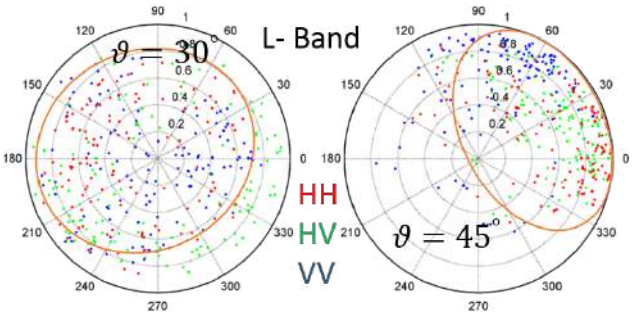

Figure 4: Representation of the interferometric coherence (L-Band)in the complex plane corresponding to Pine Forest.

This observation becomes apparent when analysing the distribution of interferometric coherence in different polarizations and frequency bands within a small selected area containing the same tree species (pine) as shown in Figures 3,5 and 5. It is evident that the coherence distribution of the same population is influenced by the viewing angle, frequency, and polarization. This finding leads us to consider the potential of exploiting these variations for medium characterization and classification purposes. Experimental studies can be conducted on different targets to derive signatures of canonical targets, enabling the development of effective methods for target identification and classification based on their PolInSAR Signatures. In summary, the inversion results from the simulated forests provide a basis

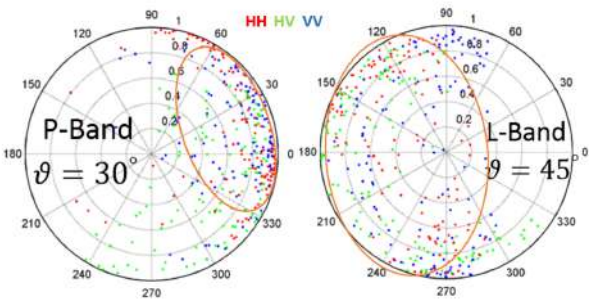

Figure 5: Representation of the interferometric coherence in the complex plane corresponding to Deciduous Forest.

for understanding the relationship between various parameters and the resulting complex interferometric coherence. This knowledge can be leveraged for medium characterization and classification, with the potential to derive target signatures through experimental studies.

5. Analysis Using Real Forest Scenarios

To validate and further explore the insights gained from simulated forest inversion models, it is crucial to conduct tests using real PolInSAR data. Real data enables the analysis of actual forest scenarios, allowing for the verification of the proposed models in practical situations. In this study, we utilize forested area data (BioSAR08) acquired by E-SAR, focusing on the province of Västerbotten in northern Sweden, where the majority of the site is covered by forests. We selected samples of 20 by 20 pixels from three different regions within the study area, using two different wavelengths (Figure 6a). The first region (Region 1) consists of ploughed barren soil with small vegetation, the second region (Region 2) represents a forested zone, and the third region (Region 3) features bare soil. This selection allows for the comparison and analysis of different land cover types. Figures 6b, 6c, and 6d illustrate the dispersion of coherence in the complex plane for the three regions, employing two different frequencies: P band (represented in green) and L band (represented in blue). The coherence distribution provides valuable information about the interaction between the radar signal and the forest structures at various depth levels, as influenced by the penetration capabilities of the chosen frequencies. Consequently, the different scatterer types within the forest can be observed and analysed. By analysing real PolInSAR data in forested areas, we aim to validate the findings obtained from simulated forest inversion models. Additionally, this study provides an opportunity to explore the behaviour of coherence in different land cover types and frequency bands, contributing to a better understanding of forest structure and scattering phenomena.

As illustrated in Figure 5, the same area exhibits two distinct placements and shapes of coherence, indicating different coherence behaviours observed at different frequencies for the same target. However, despite these variations, the concentration of coherence within a specific region in the complex plane suggests the presence of the same type of scatterer within the sampled area.

This observation highlights the importance of considering both frequency and spatial information when analysing coherence patterns. While the specific placement and shape of coherence may differ, the overall concentration within a particular region provides valuable insights into the consistent presence of a particular scatterer type.

6. Conclusions

This work has investigated and discussed various parameters that can affect inversion models in the context of forest analysis. These parameters have been categorized into two groups: media parameters, related to the size of the chosen windows, and sensor parameters, including frequency, polarisation and incidence angle. The distribution of interferometric coherence in the complex plane has been examined to explore its potential as a means to discriminate between different media types within forests. This analysis has been conducted using both simulated PolInSAR data and real data acquired from the BioSAR08 mission.

By analysing the distribution of interferometric coherence, we aim to understand how it varies across different media types within the forest. This information can be valuable for distinguishing between various forest components, such as different tree species, vegetation density, and terrain characteristics. The results indicate that the interaction with the volume structures, such as the vertical orientation of branches and trunks, as well as the incidence angle, play a significant role in shaping the radar signal response. Moreover, the frequency band (L or P) has a noticeable impact on the distribution of coherence responses in the complex plane.

Simulated PolInSAR data provides a controlled environment where we can investigate the coherence distribution under different scenarios by manipulating parameters such as incidence angle, frequency, and media properties. This allows us to gain insights into the expected behaviour of coherence for different media types within the forest.

The presented method effectively utilizes interferometric coherence to distinguish between different types of forests based on its distribution in the complex plane. Future studies will focus on investigating the influence of parameters such as incidence angle and different baseline effects on the shape and region of interferometric coherence. Experimental measurements will also be conducted to validate specific target signatures, further supporting the potential use of coherence as a classifier for media types within forests. This research contributes to advancing forest analysis and classification techniques.

Overall, this research contributes to a better understanding of the parameters influencing inversion models in forest analysis and highlights the potential for using interferometric coherence as a valuable tool for forest characterization and classification.

Acknowledgement

Acknowledgements belong here.

References

[1] K. Papathanassiou and S. Cloude, "Single-baseline polarimetric SAR interferometry," *IEEE Transactions on Geoscience and Remote Sensing*, vol. 39, no. 11, pp. 2352–2363, 2001-11.

[2] K. P. Papathanassiou and S. R. Cloude, "The effect of temporal decorrelation on the inversion of forest parameters from PoI-InSAR data," in *INTERNATIONAL GEOSCIENCE AND REMOTE SENSING SYMPOSIUM*, vol. 3, 2003, pp. III–1429.

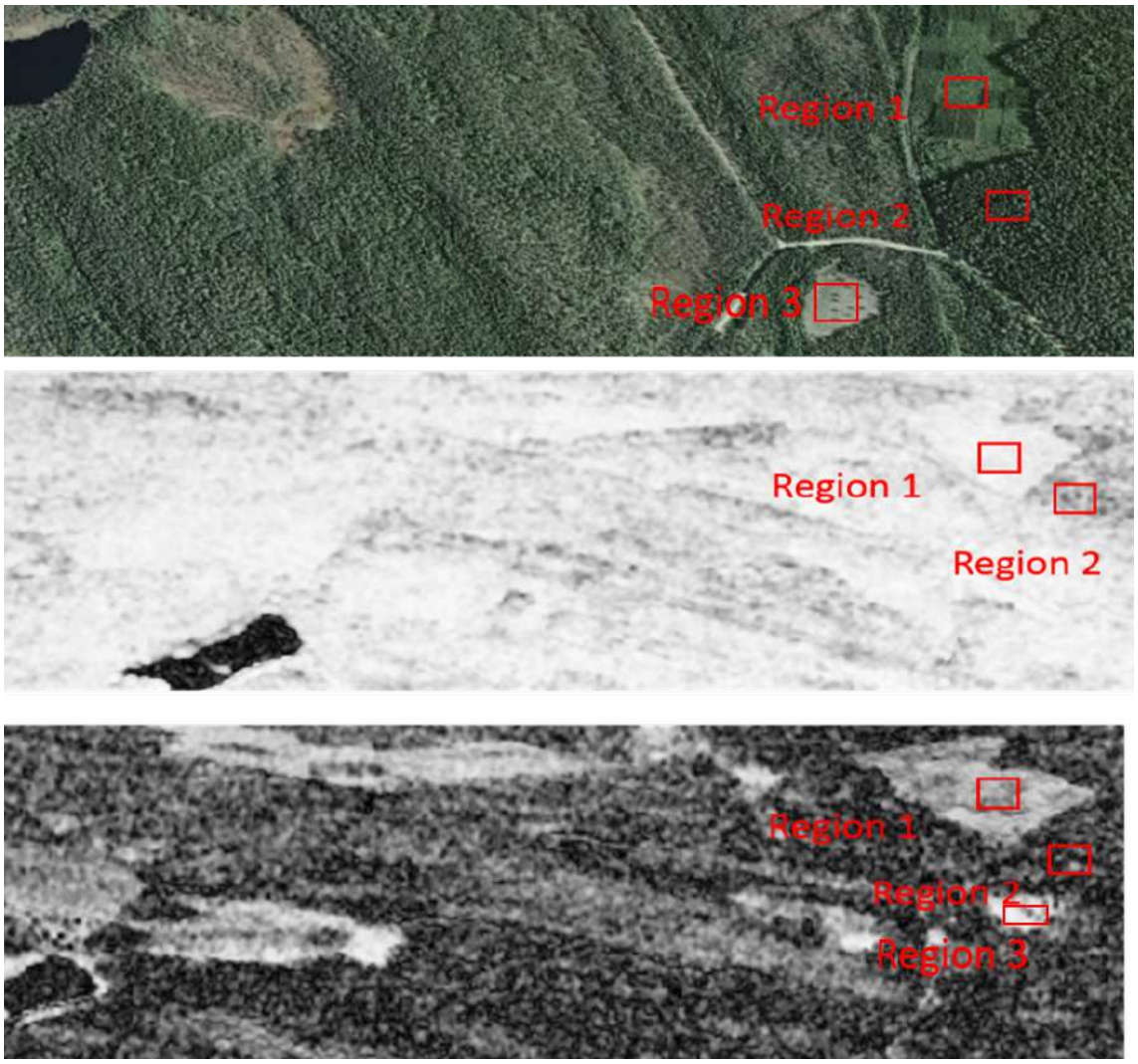

(a) Top: Google Earth site, Middle: Test site at P band, Bottom: Test site at L band

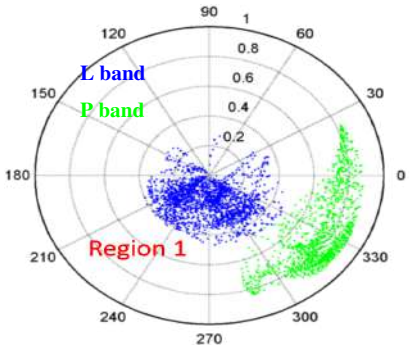

(b) Region 1:**Small vegetation**

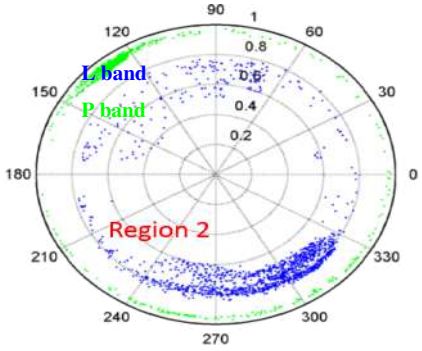

(c) Region 2:**forested area**

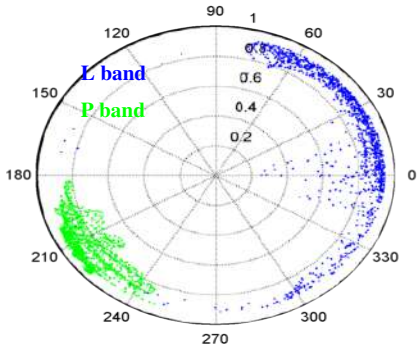

(d) Region 3:**Bare soil**

Figure 6: Coherence Behaviour Across Different Scattering Mechanisms in Three Regions

[3] S. Tahraoui and M. Ouarzeddine, "Assess the effects of wind on forest parameters inversion by using pol-InSAR applications," in *Advanced Control Engineering Methods in Electrical Engineering Systems*, M. Chadli, S. Bououden, S. Ziani, and I. Zelinka, Eds. Springer International Publishing, 2019, pp. 556–564.

[4] S. Tahraoui, "Assessment of polinsar potential for the characterisation of target's parameters," phdthesis, 2019. [Online]. Available: https://repository.usthb.dz/handle/123456789/7863

[5] S. Tahraoui, M. Ouarzeddine, and B. Souissi, "Interferometric coherence optimization: A comparative study." IEEE, 2013-10, pp. 427–431.

[6] K. Papathanassiou, A. V. Reigber, and M. . Coltelli, "On the interferometric coherence: A multifrequency and multitemporal analysis." in *Proc. FRINGE '96 (1996)*, 1996. [Online]. Available: http://elib.dlr.de/33442/

[7] R. N. Treuhaft and P. R. Siqueira, "Vertical structure of vegetated land surfaces from interferometric and polarimetric radar," *Radio Science*, vol. 35, no. 1, pp. 141–177, 2000.

[8] F. Kugler, F. N. Koudogbo, K. P. Papathanassiou, and K. Gutjahr, "Frequency effects in pol-InSAR forest height estimation - conference papers - VDE publishing house," 2006-05.

[9] H. Cai, B. Zou, and M. Lin, "Parameter inversion models based on PolInSAR images," in *1st Asian and Pacific Conference on Synthetic Aperture Radar, 2007. APSAR 2007*, 2007-11, pp. 751–754.

Metamaterials, metasurfaces, FSS and EBG

Roles of spatial symmetries in metamaterials

K. Achouri[1*]

[1]Swiss Federal Institute of Technology in Lausanne (EPFL), Switzerland
[*]corresponding author: karim.achouri@epfl.ch

Abstract: Dielectric metasurfaces are now ubiquitous. However, due to their large electrical size, they require adequate synthesis and analysis techniques that include multipolar contributions to be properly modeled. While such a technique has been recently developed, it faced the issue that a tremendous amount of new material parameters is required to account for multipolar responses. To overcome this issue, we have developed an approach based on spatial symmetries to greatly reduce the complexity of the problem.

Dielectric metasurfaces have attracted major attention over the past few years due to their small footprint, very low loss and excellent wave control capabilities [1]. However, the dielectric resonators that compose them typically have a large electrical size compared to their metallic counterparts. It is in fact so large that the conventionally used dipolar approximations do not apply to them anymore as they exhibit multipolar scattering responses [2]. This implies that metasurface synthesis and analysis techniques, purely based on dipolar approximations, generally fail at properly modeling dielectric metasurfaces especially under oblique wave propagation, where multipolar contributions strongly differ from dipolar ones.

To overcome this issue, we have recently extended our metasurface modeling framework so as to include multipolar contributions. This model, which was originally based on the generalized sheet transition conditions (GSTC) [3], is now able to account for dipolar and quadrupolar responses, which are the dominant contributions in dielectric metasurfaces [2]. However, including quadrupolar responses has led to a major problem. Indeed, it requires considering several hundreds additional effective material parameters compared to the standard dipolar model, which severely complicates the modeling procedure.

To avoid having to deal with so many coefficients, we have developed a simple and straightforward approach to reduce the complexity of the model. This approach relies on the spatial symmetries of the metasurface lattice and that of its scattering particles [4]. While group theory concepts have been used to develop this technique, using it does not require any a priori knowledge of group theory meaning that it is accessible to a very large audience. An illustration of its application is shown in Fig. 1. Two metasurfaces composed of L-shaped scattering particles are considered. In Fig. 1a, the particles lie flat on the metasurface plane, whereas they stand vertical along the *xz*-plane in Fig. 1b. Applying our approach, whose details are provided in [4], to these two metasurfaces yields the two material matrices plotted in Fig. 1c and Fig. 1d, respectively. These matrices connect together the electric dipole, **p**, the magnetic dipole, **m**, the electric quadrupole, **Q**, and the magnetic quadrupole, **S**, to the electric and magnetic fields as well as the spatial derivatives of these fields. The elements of the matrices that appear blank correspond to material parameters that cannot be excited due to the symmetries of the metasurfaces. The numbers within the matrix elements indicate possible connections, i.e., two elements with the same number are equal. We can therefore easily see how this approach help simplify the metasurface modeling procedure.

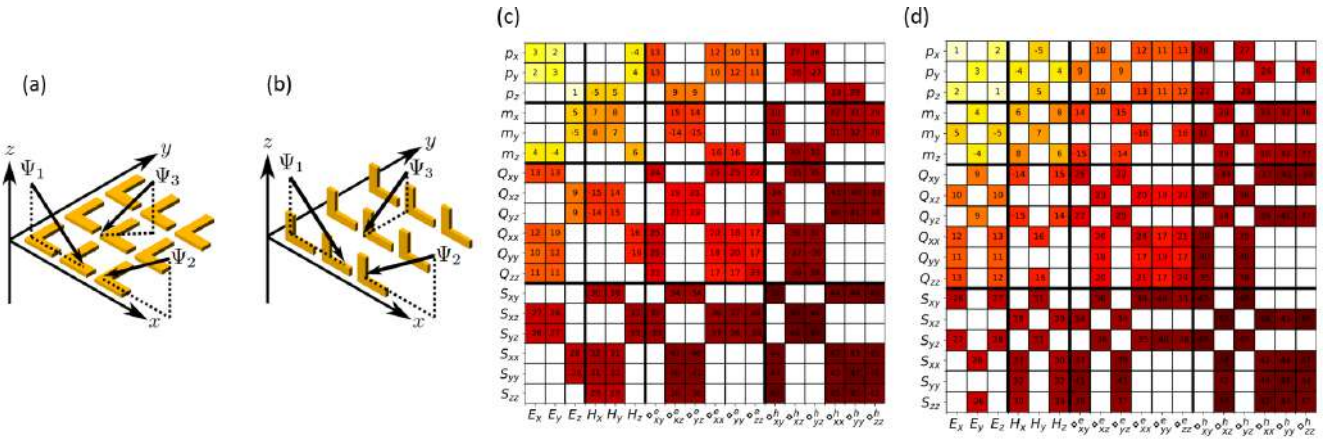

Figure 1. Metasurfaces and their corresponding material parameters.

Note that this approach does not only apply to metasurfaces but also to single isolated particles. As such, we have applied it to the case of helical-shaped nanomotors and were able to explain the existence of an optically driven optical torque in terms of multipolar pseudochiral effects [5], as shall be shown at the conference.

Acknowledgement

We gratefully acknowledge funding from the Swiss National Science Foundation (project PZ00P2_193221).

References

1. Kamali, Seyedeh Mahsa, et al. "A review of dielectric optical metasurfaces for wavefront control." Nanophotonics 7.6 (2018): 1041-1068.
2. K. Achouri, V. Tiukuvaara, and O. JF Martin. "Multipolar Modeling of Spatially Dispersive Metasurfaces." IEEE Transactions on Antennas and Propagation 70.12 (2022): 11946-11956.
3. K. Achouri, and C. Caloz. Electromagnetic Metasurfaces: Theory and Applications. John Wiley & Sons, 2021.
4. K. Achouri, V. Tiukuvaara, and O. JF Martin. "Spatial Symmetries in Multipolar Metasurfaces: From Asymmetric Angular Transmittance to Multipolar Extrinsic Chirality." arXiv preprint arXiv:2208.12504 (2022).
5. M. Chung, K. Achouri, and O. JF Martin. "Optically driven nano-motors designed by machine learning." Optical Trapping and Optical Micromanipulation XIX. SPIE, 2022.

Topologically protected plasmonic edge states in metallic nanostructures

Yuto Moritake[1,2,*]

[1]Department of Physics, Tokyo Institute of Technology, Tokyo, Japan
[2] JST, PRESTO, Tokyo, Japan
[*]corresponding author: moritake@phys.titech.ac.jp

Abstract: Recently, nanophotonics fields called “topological photonics” and “non-Hermitian photonics” have become very active. In these fields, a topological property of the systems is the key concept to realize novel photonic phenomena. In particular, topologically protected edge states have drawn great attentions due to robustness against disorders and chiral dependent controllability. In this presentation, we introduce the studies on topologically protected plasmonic edge states. Our plasmonic platforms would provide new opportunities for photonic functionalities based on the edge states.

Stimulated by materials science, “topological photonics [1]” and “non-Hermitian (NH) photonics [2]” have become very active in the recent years. In these fields, a topological property of the systems is the key concept to realize and manipulate novel photonic phenomena. In topological photonic systems, based on condensed matters physics, band topology plays a central role to form topological edge states (TESs). The TESs have drawn great attentions due to robustness against disorders and chiral dependent controllability. On the other hand, very recently, topologically protected edge state base on non-Hermiticity, called a non-Hermitian skin effect (NHSE), have been found [3]. The NHSE is the phenomena that all bulk eigenstates forming bands localize at the edge of open NH systems and can be understood by topological origin in a complex energy space. In this presentation, we introduce topologically protected plasmonic edge states in topological and NH systems. For topological systems, we used plasmonic zigzag chains [4] and valley plasmonic crystals [5]. We experimentally visualized the plasmonic edge states localized at nano-scale. Next, we present numerical results on NHSE in metallic nanostructures. We show that the simple metal-dielectric structures exhibit NHSE. Our plasmonic platforms would provide new opportunities for novel photonic functionalities based on the edge states.

Since plasmonic edge states localize at nano-scale, their visualization is generally difficult. To do this, for example, scanning near field microscope is effective tool for nano-scale visualization and applied to plasmonic system in the optical region [6]. We proposed the other techniques to visualize the plasmonic edge states in the optical region. The first one is far-field imaging of long connected zigzag chains [5], and the second one is angle resolved cathode luminescence (CL) of valley plasmonic crystals (VPlCs) [6].

Figure 1(a) shows the structure of a zigzag chain composed of gold nanodiscs. When dipole resonance is excited by light incidence, their chain can be regarded as photonic mimic of an SSH model, which is known as the simplest topological model. In this zigzag chain, polarization dependent TESs are expected. And we successfully observed them by using far-field imaging method as shown in Fig. 1(b). The advantage of the method is simple setup which is same as traditional microscope, enabling us to obtain images of many edge states at the same time.

Figure 1(c) shows our valley plasmonic crystal (VPlC) (Figure 2(a)). Our structure is metallic counterpart of valley photonic crystal, which is widely used in topological photonics. The structure is honeycomb lattice with breaking inversion symmetry which is an analogy of valleytronic materials. When we combine the VPlC with

different topologies (valley Chern number), propagating edge states appears in a topological band gap. By using CL imaging, we succeeded to visualize the edge states in nano-scale as shown in Fig. 1(d).

NHSE is unique phenomena in NH system, in which all bulk modes become localized states in open NH systems [3]. Recently, it was found that the NHSE can be obtained simple photonic system with anisotropy and loss (or gain) [7]. We found numerically that NHSE can be achieved in simple multilayered structure with loss and anisotropy, which can be experimentally fabricated. The structure is composed of Cr and SiO2 layers with sub-wavelength thickness. Due to their thinness, the structure can be described by effective medium with averaged anisotropic primitivities. And by tilting the structure along the termination, we can observe the NHSE.

In summary, we introduced our recent results on topologically protected edge states, TESs and NHSE, in metallic nanostructures. Our visualization techniques can be applied to other plasmonic structures possessing TESs. And our prediction of NHSE would lead to experimental observation of optical NHSE and novel photonic devices including waveguides, pulse manipulation, and non-reciprocal devices.

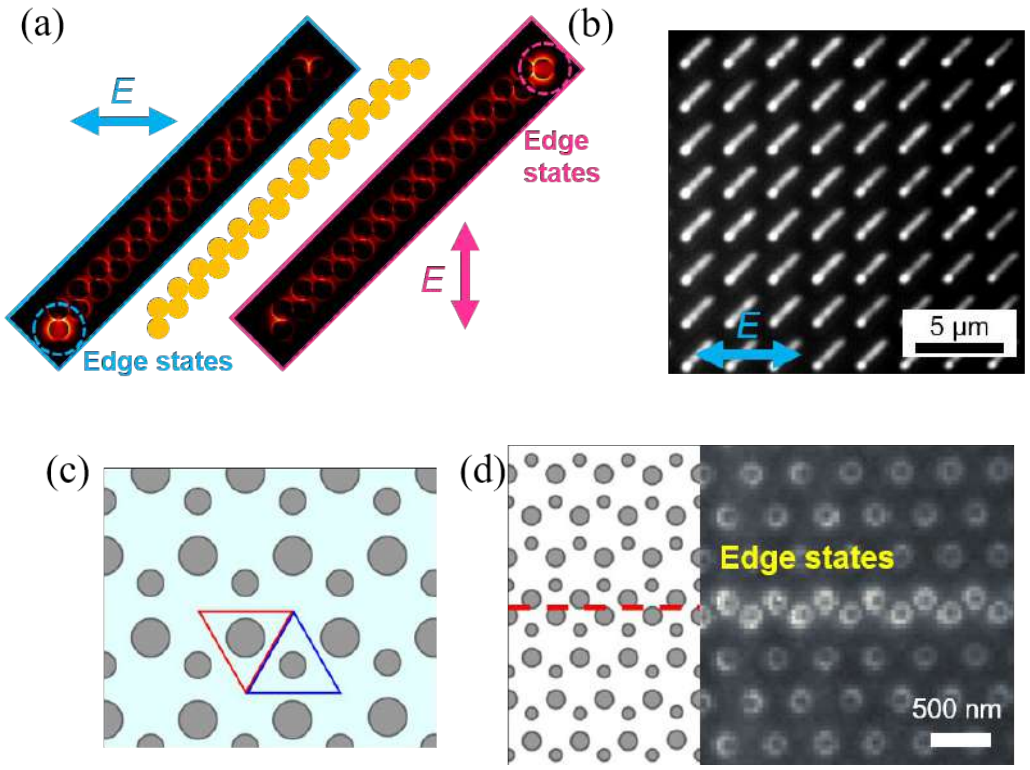

Figure 1 (a) The structure of the zigzag chain. (b) The far-field image of the TESs in many zigzag chains. (c) The structure of the valley plasmonic crystal. (b) The CL image of the TESs at the boundary of bulk topology.

Acknowledgements

This work has been supported by JST, PRESTO Grant Number JPMJPR18L9, Japan, by JSPS, Grant-in-Aid for Scientific Research (S), 20H05641, Japan, and by Grant-in-Aid for Early-Career Scientists, 21K14551.

References

[1] L. Lu *et al.*, Nat. Photon. **8**, 821 (2014). [2] Ş. K. Özdemir *et al.*, Nat. Mater. **18**, 783 (2019).

[3] S. Yao and Z. Wang, Phys. Rev. Lett., **121**, 086803 (2018). [4] Y. Moritake *et al.*, Nanophotonics, **11**(9) 2183 (2022).

[5] H. Saito *et al.*, Nano Lett. **21**(15), 6556 (2021). [6] I. S. Sinev *et al.*, Nanoscale, **7**, 11904 (2015). [6

[7] K. Yokomizo *et al.*, Phys. Rev. Res. **4**, 023089 (2022).

Design and Experimental Demonstration of Optical Cloaking

K. Kajikawa

Tokyo Institute of Technology, Japan
*corresponding author: kajikawa@ee.e.titech.ac.jp

Abstract: The design and experimental demonstration of optical cloaking is presented. In the design, neural network or generic algorism (GA) was adopted to find the optimized structure. A broadband cloaking condition was found using the GA. In the experimental demonstration, the plasmonic cloaking was performed on an Ag nanowire 110 nm diameter, immobilized on an STM probe. The scattering was strongly suppressed, and the wire became invisible.

Cloaking is an optical technique to achieve invisibility by covering an object with a specific medium. Two methods have been proposed to achieve this phenomenon. One is to design the refractive index of the cloaking medium so that light detours the cloaking object [1,2], and the other is to design the refractive index of the cloaking medium so that the polarization in the cloaking medium cancels out the polarization in the object [3]. In my presentation, I will discuss the design of a cloaking medium for a cylinder used as the cloaking object and the experimental demonstration of plasmonic cloaking.

The cloaking method in which light detours the object is designed using coordinate transformation optics. However, the cloaking medium must have an anisotropic dielectric constant, and the dielectric constant must vary within the medium. This is highly challenging to achieve this in the optical domain. A solution to this problem is to use a multilayer structure for the cloaking medium to give anisotropy and distribution of the dielectric constant based on the effective medium approximation [4]. This method achieves a cloaking performance, but not enough. Our research group first designed a clocking structure with higher performance than the design based on the effective medium by using a neural network [5]. Following this, we conducted a design using a genetic algorithm and succeeded in designing a structure in which cloaking can be achieved in a broad bandwidth.

In the second part of my presentation, I will make an experimental demonstration of optical cloaking. Although there have been many studies on the design of cloaking structures, there have been no reports of experimentally demonstrated invisibility of freestanding objects in the visible light range. In this study, we demonstrated cloaking in the visible light region, which has only been studied theoretically and computationally. In the experiment, Ag nanowires with a length of about 20 μm and a diameter of 0.11 μm immobilized on an STM probe were coated with a high-index cloaking medium (MoO_3) by vacuum evaporation. When incident light from a HeNe laser (633 nm) was illuminated, the scattered light intensity was suppressed from the sample with the cloaking medium, and the Ag nanowire became invisible. The results showed that cloaking was achieved as expected in the design.

This work was partially supported by a Grant-in-Aid for Scientific Research (19H02624) from the Japan Society for the Promotion of Science.

References

1. Leonhardt, Y., "Optical Conformal Mapping", Science, Vol. 312, 1777–1780, 2006.
2. Pendry, J. B., Schurig, D. and Smith D. R. “Controlling Electromagnetic Fields,” Science, Vol. 312, 1780–1782, 2006.
3. Alu, A. and N. Engheta “Cloaking and transparency for collections of particles with metamaterial and plasmonic covers,” Optics Express, Vol. 15, 7578-7590, 2007.
4. Huang, Y., Feng, Y. and Jiang, T. “Electromagnetic cloaking by layered structure of homogeneous isotropic materials,” Optics Express, Vol. 15, 11133–1141, 2007.
5. Akashi, N., Toma M., and Kajikawa, K., "Design by neural network of concentric multilayered cylindrical metamaterials", Appl. Phys. Express, Vol. 13, 042003, 2020.

Mechanically tunable multiplexed holographic metasurfaces

Jianling Xiao[1], Robert I. Hunter[1], Duncan A. Robertson[1], Graham M. Smith[1], Simon Horsley[2], Sebastian A. Schulz[1], and Andrea Di Falco [1*]

[1]School of Physics and Astronomy, University of St Andrews, North Haugh, St Andrews, KY16 9SS, UK
[2]Department of Physics and Astronomy, University of Exeter, Stocker Road, Exeter, EX4 4QL, UK
[*]corresponding author: adf10@st-andrews.ac.uk

Abstract: In this paper, we demonstrate a conformable reflective-type holographic metasurface, which can be tuned by altering its shape. Here we show that we can encode two independent holographic images on the metasurface and retrieve them when the substrate is mechanically bent to a convex or a concave shape.

Metasurfaces (MSs) are widely utilized as a functional platform to manipulate the properties of scattered light, such as its phase, amplitude, and polarization [1,2]. Spatial control of the reflected or transmitted wavefront can be achieved by tailoring at a sub-wavelength scale the meta-atoms, which can be programmed as the pixel of a computer-generated holographic plate. Information multiplexing is one of the key strengths of holographic MS technology, where different images can be encoded in the MS and retrieved when illuminated with light of different polarization, helicity, wavelength, angular momentum or for different surrounding media [3,4]. This technology has been applied for uses in data storage, encryption, and optical display [5-7]. In literature, multiplexing has also been achieved by mechanically tuning the MSs, such as via stretching [8]. Here, we present a flexible reflective MS, in which we encoded two independent images that can be retrieved via mechanical tuning, at a frequency of 94GHz [9].

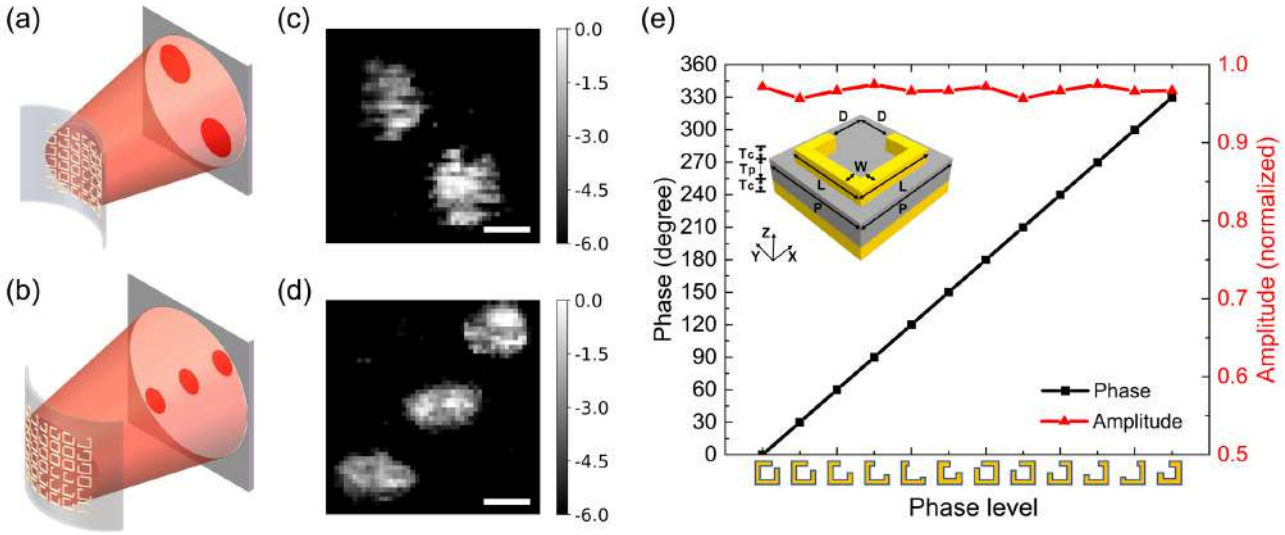

Figure. 1 (a) and (b) are the concept images of mechanical tunable multiplexed holographic MSs; panles (c) and (d) show the experimental images in normalized units, obtained when the MS is bent to convex and concave shape with radii of curvature are 35 mm and -100 mm. The scale bar represents 20 mm. (e) is the simulated phase shift and normalized amplitude of 12-level c-rings at 94 GHz with a unit cell as an insert on the top-left.

The concept of mechanically tunable holographic MSs is shown in Figures 1(a) and 1(b), while the 1(c) and 1(d) are the corresponding normalized experimental results. The 2 dots and 3 dots images can be reconstructed when the substrate of the MS is bent to a convex and concave shape, with radii of curvature of 35 mm and -100 mm, respectively. The experimental results fit well with the simulation.

To achieve the multiplexing, we encoded phase distribution obtained by interleaving two individual phase distributions relative to the two distinct target images, each at their radius of curvature. The pixels and period of the interleaved hologram are 80 × 80 and 0.8 mm and the area of the MS is 64 mm × 64 mm. The unit cell is an inset in Figure 1(e), where a spacer layer of 380 μm PMMA is sandwiched by the top copper c-ring and bottom reflective copper film, both 200 nm thick. The meta-atoms, designed with CST, can cover the phase shift from 0 to 2π, discretized here in 12 levels, and maintain a high reflectivity over the whole phase range, as shown in Figure 1 (e).

The sample was fabricated by photolithography and wet-etching process, using a dry film as a negative photoresist and a UV mask, fabricated with a photoplotter. The experimental results obtained scanning a waveguide over a surface placed 160 mm away from the MS demonstrate the excellent quality of the platform, despite the small number of meta-atoms used to encode the information.

In conclusion, we demonstrated a mechanically tunable MS that can encode and reconstruct two independent images when bending the substrate to specific curvatures. We believe that this will enable new optomechanical sensors and actuators and potential applications in electromagnetic antennas and radar.

Acknowledgements

ADF is supported by the European Research Council (ERC) under the European Union Horizon 2020 research and innovation program (Grant Agreement No. 819346).

References

[1] S. Chen, Z. Li, W. Liu, H. Cheng, and J. Tian, "From single‐dimensional to multidimensional manipulation of optical waves with metasurfaces," *Advanced materials*, vol. 31, no. 16, p. 1802458, 2019.

[2] H. T. Chen, A. J. Taylor, and N. Yu, "A review of metasurfaces: physics and applications," *Reports on Progress in Physics Physical Society*, vol. 79, no. 7, p. 076401, 2016.

[3] S. Chen, W. Liu, Z. Li, H. Cheng, and J. Tian, "Metasurface‐empowered optical multiplexing and multifunction," *Advanced Materials*, vol. 32, no. 3, p. 1805912, 2020.

[4] L. Yan et al., "Two-tier manipulation of holographic information," *Optics Express*, vol. 30, no. 11, pp. 19145-19151, 2022.

[5] X. Fang, H. Ren, and M. Gu, "Orbital angular momentum holography for high-security encryption," *Nature Photonics*, vol. 14, no. 2, pp. 102-108, 2020.

[6] J. Burch and A. Di Falco, "Surface topology specific metasurface holograms," *ACS Photonics*, vol. 5, no. 5, pp. 1762-1766, 2018.

[7] Z. Li et al., "Cryptography Metasurface for One‐Time‐Pad Encryption and Massive Data Storage," *Laser & Photonics Reviews*, vol. 16, no. 8, p. 2200113, 2022.

[8] S. C. Malek et al., “Strain Multiplexed Metasurface Holograms on a Stretchable Substrate”, *Nano Lett.,* vol. 17, no. 6, pp. 3641–3645, 2017.

[8] J. Xiao et al., "Shape Dependent Conformable Holographic Metasurfaces," *Advanced Materials Technologies*, p. 2202006, 2023.

Polarization manipulation and multiplexing in optical metasurfaces

Ruwen Peng[1*], and Mu Wang[1,2]

[1]National Laboratory of Solid State Microstructures, Nanjing University, Nanjing 210093, China
[2]American Physical Society, Hauppauge, NY 11788, USA.
*corresponding author: rwpeng@nju.edu.cn

Abstract: In this talk we present our recent studies on polarization manipulation and multiplexing in optical metasurfaces. One is to realize multichannel distribution and transformation of entangled photons with dielectric metasurface, and the other is to break the limitation of polarization multiplexing in optical metasurfaces with engineered noise. The approaches achieve potential applications on optical display, data storage, information encryption, and quantum information networks.

It is known that manipulating the polarization of light on the microscale or nanoscale is essential for integrated photonics and quantum optics. Yet simultaneously generating different types of polarization states with a single piece of metasurface remains challenging, whereas different types of polarization states are required to encode information for quantum computing and cryptography applications. Recently, by introducing geometrical-scaling-induced phase modulation, we demonstrated the simultaneous generation of arbitrary assembly of polarization states with a single piece of the metasurface. Further, we extended the study from the classic to the quantum system, and realized the transformation and distribution of polarization-entangled photon pairs with multichannel dielectric metasurfaces. The approach may pave the way for the future integration of quantum information networks.

On the other hand, polarization plays an important role in integrated optics and photonics, for example, via polarization multiplexing. Yet in a 2D planar optical system, the number of independent channels is usually limited to three, which roots from the dimension constraints of the Jones matrix. We recently broke this limitation of polarization multiplexing in optical metasurfaces by introducing engineered noise. With polarization multiplexing only, we experimentally demonstrate up to 11 independent holographic images using a single metasurface illuminated by visible light. Furthermore, our polarization multiplexing strategy based on noise engineering can be combined with other multiplexing methods, such as position multiplexing and orbital angular momentum multiplexing, to boost the information-encoding capacity. This approach suggests a new paradigm for high-capacity optical display, information encryption, and data storage.

References

1. Bo Xiong, Yu Liu, Yihao Xu, Lin Deng, Chao-Wei Chen, Jia-Nan Wang, Ruwen Peng, Yun Lai, Yongmin Liu, Mu Wang, “Breaking the limitation of polarization multiplexing in optical metasurfaces with engineered noise”, **Science** 379, 294-299 (2023).
2. Ya-Jun Gao, Zheng Wang, Yue Jiang, Ru-Wen Peng, Zi-Yu Wang, Dong-Xiang Qi, Ren-Hao Fan, Wen-Jie Tang, and Mu Wang, “Multichannel distribution and transformation of entangled photons with dielectric metasurfaces”, **Physical Review Letters** 129, 023601 (2022).
3. Ya-Jun Gao, Xiang Xiong, Zhenghan Wang, Fei Chen, Ru-Wen Peng, and Mu Wang, “Simultaneous generation of

arbitrary assembly of polarization states with geometrical-scaling -induced phase modulation”, **Physical Review X** 10, 031035 (2020).

AES 2023, TORREMOLINOS - SPAIN, 5 – 8 JUNE 2023

Complete control of microwave transmission with double-layer metasurfaces

Jonghwa Shin[1*], Joonkyo Jung[1], and Taeyong Chang[2]

[1]Korea Advanced Institude of Science and Technology, Korea
[2]Nanyang Technological University, Singapore
[*]corresponding author: qubit@kaist.ac.kr

Abstract: We show that a double-layer metasurface can control the amplitude and phase of the transmitted microwave independently in a pixel-by-pixel manner, for two independent polarizations. It is based on the mathematical principle we proposed recently for optical metasurfaces, but requires a different design approach due to the difference in the wavelength-normalized thicknesses.

Metasurfaces have been actively researched in the last two decades with many potential microwave applications. For reflective metasurfaces (with a conducting base layer such that the transmittance is effectively blocked), one can design a single-layer pattern made of conductive materials such as carbon-based ink or graphene on top of a low-loss dielectric spacer for broadband absorption of microwaves[1,2]. For transmissive applications, more complicated designs are necessary in general because the problem becomes a two-port system rather that a one-port system as in the case of reflective metasurfaces and requires simultaneous control of the reflected and transmitted waves. The design can be simplified to some degree if the main focus is the properties of the transmitted wave as we can select from multiple solutions with the same transmission and different reflection characteristics.

The transmission characteristics for paraxial waves can be conveniently represented with a Jones matrix. Depending on the structural symmetry of the metasurface, the matrix can be of a symmetric form (matrix S in Eq. (1)) or a more general form (matrix A in Eq. (2)).

$$S = \begin{pmatrix} a & b \\ b & d \end{pmatrix}, \quad A = \begin{pmatrix} a & b \\ c & d \end{pmatrix} \tag{1}$$

For the systems with no reflection, absorption, or diffraction to other directions, an additional constraint is imposed on these matrices, making them unitary. The goal of a complete control of the transmitted wave is to break this unitary constraint as well as the symmetry of the matrix in a controllable way. In other words, one needs to find a systematic way to realize any arbitrary 2-by-2 matrix (with singular values not larger than one if we do not consider amplification).

Here, we show that a simple, double-layer metasurface can accomplish such a task and can manipulate the amplitude and phase of the transmitted wave independently for two orthogonal input polarizations. The mathematical principle is similar to what we have recently reported for optical metasurfaces[4]. However, if the design approach is applied to microwaves, e.g., X-band, it results in metasurfaces thicker than a centimeter, which is impractical in most applications. On the positive side, at microwave frequencies, the absorption loss in metals are much less of a concern compared to the optical cases, so one can utilize the large permittivity of the metals or other conductive materials for design of compact double-layer metasurfaces. This design approach can serve as a systematic way to realize transmissive microwave metasurfaces for diverse applications.

This research is funded by the Ministry of Science and ICT of the Korean government.

References

1. Jeong, J.-Y. et al., “Fabrication and characterization of resistive double square loop arrays for ultra-wide bandwidth microwave absorption,” Sci. Rep., Vol. 11, No. 1, 12767/1–12, 2021.
2. Kim, Y. et al., “Ultrawideband electromagnetic metamaterial absorber utilizing coherent absorptions and surface plasmon polaritons based on double layer carbon metapatterns,” Sci. Rep., Vol. 11, No. 1, 23045/1–13, 2021.
3. Han, J. S. et al., “Ultrawide meta-film replication process for the mass production of a flexible microwave absorbing meta-surface,” Opt. Express, Vol. 30, No. 16, 29760–29771, 2022.
4. Chang, T et al., “Universal metasurfaces for complete linear control of coherent light transmission,” Adv. Mater., Vol. 34, No. 44, 2204085/1–11, 2022.

Control of the Scattering Properties of a Complex Enclosure by Means of Nonlinear Metasurfaces

Jared Erb[1], and Steven M. Anlage[1*]

[1]Physics Department, University of Maryland, College Park, MD 20742, USA

[*]corresponding author: anlage@umd.edu

Abstract: Through use of the generalized Wigner-Smith operator we experimentally demonstrate control of scattering matrix singularities of a ray-chaotic microwave enclosure through the use of embedded nonlinear metasurfaces.

Our objective is to establish complete control over the wave scattering properties of electrically-large enclosed spaces by means of controlled perturbations to the environment. We use the Generalized Wigner-Smith (GWS) operator $Q_\alpha = -iS^{-1}dS/d\alpha$, where S is the scattering matrix of a ray-chaotic enclosure and α is an arbitrary parameter, to understand the dependence of the scattering matrix on various parameters of interest [1,2]. The GWS allows us to understand how the zeros and poles of the scattering matrix move with respect to a change in a specific parameter. A particular example of the GWS operator is the Wigner time delay operator where α is frequency, and we can use the eigenvalues of that operator to determine the locations of the zeros and poles of S in the complex frequency plane, and to find conditions for coherent perfect absorption (CPA) [3-5]. By using the GWS operator, we can gather more information about how a complex scattering system interacts with incoming waves, and use this information to create conditions for CPA, to create hot or cold spots in specific areas, etc. In our experimental setup, we use a variable globally-biased varactor-loaded metasurface inside a ray chaotic microwave billiard to explore the range of possible scattering behaviors. In this setup we can mold the flow of microwave energy by means of varying the spectral properties of the scattering matrix through systematic variation of varactor bias voltage, rf power, etc. We present our results on achieving control of the wave scattering properties through several examples in the context of wave chaotic microwave enclosures with various types of reconfigurable metasurfaces located inside.

This work was supported by NSF RINGS under grant No. ECCS-2148318, ONR under Grant No. N000141912481, DARPA WARDEN Grant HR00112120021, and the Maryland Quantum Materials Center.

References

1. M. Buttiker and M. L. Polianski, "Charge fluctuations in open chaotic cavities," J Phys A-Math Gen **38** (49), 10559-10585 (2005).
2. Philipp Ambichl, Andre Brandstötter, Julian Böhm, Matthias Kühmayer, Ulrich Kuhl, and Stefan Rotter, "Focusing inside Disordered Media with the Generalized Wigner-Smith Operator," Phys Rev Lett **119** (3), 033903 (2017).
3. Lei Chen, Steven M. Anlage, and Yan V. Fyodorov, "Generalization of Wigner Time Delay to Sub-Unitary Scattering Systems," Phys. Rev. E **103**, L050203 (2021).
4. Lei Chen, Steven M. Anlage, Yan V. Fyodorov, "Statistics of Complex Wigner Time Delays as a counter of S-matrix poles: Theory and Experiment," Phys. Rev. Lett. **127**, 204101 (2021).
5. Lei Chen and Steven M. Anlage, "Use of Transmission and Reflection Complex Time Delays to Reveal Scattering Matrix Poles and Zeros: Example of the Ring Graph," Phys. Rev. E **105**, 054210 (2022).

Electromagnon Excitations and Microwave/Optical Device Functions in Multiferroic Materials

Masahito Mochizuki

Department of Applied Physics, Waseda University, Japan
email: masa_mochizuki@waseda.jp

Abstract: We discuss the results of our theoretical studies on the optical and microwave device functions of multiferroics associated with the electromagnon excitations by particularly focusing on the ultrafast switching of vector spin chirality in the spiral-magnetism-based multiferroics and the giant microwave isolator effect of chiral magnetic insulators.

Spiral- or vortex-type noncollinear magnetic ordering in insulating magnets often generates dielectric polarization through the coupling of electric charges and magnetic dipoles mediated by the relativistic spin-orbit interactions. Materials with such magnetism-derived ferroelectricity are called "multiferroics" and offers a unique stage for rich cross-correlation responses between electricity and magnetism. In particular, the electromagnon excitations, i.e., collective excitations of spins excited by the ac electric-field component of electromagnetic waves such as light and microwaves through the magnetoelectric coupling is of great interest[1].

One interesting subject of the electromagnon excitations is intense excitations. Since the energy scale of the electric field is much larger than that of the magnetic field, the electromagnons excited by the electric-field component of light or microwaves can be intensely excited, which is not possible for conventional magnons excited by the magnetic-field component. The intensely excited electromagnons often give rise to and nontrivial and nonlinear dynamical phenomena. Another interesting subject is the interference of electric and magnetic activation channels. Because the electromagnons can be excited by both magnetic field and electric field of electromagnetic waves, these two activation channels can work cooperatively or destructively depending on the incident direction. which results in rich optical and microwave device functions. As examples of these two subjects, we will discuss the following two topics related with the electromagnon excitations in multiferroics.

Intense Electromagnon Excitations and Ultrafast Chirality Switching in Spin-Spiral Multiferroics [1-3]

Perovskite-type Mn oxides (RMnO$_3$, where R=Tb, Dy, Eu1-xYx.) are typical spin-spiral-based multiferroics, in which the transverse spiral order of Mn spins induces the ferroelectric polarization via the inverse Dzyaloshinskii-Moriya effect. With the specific optical polarization of THz laser pulse, the electromagnon can be excited. It is theoretically demonstrated that application of intense laser pulse with a resonance frequency of the electromagnon excitation can realize the ultrafast switching of the vector spin chirality of the transverse spiral spin order within a few picoseconds. We demonstrate that both the 90-degree flop and the 180-degree reversal can be achieved at will by tuning the amplitude, sign and shape of the laser pulse. Interestingly, dynamical stripe pattern of the vector spin chirality appears during the process of the switching.

Giant Microwave Nonreciprocal Dichroism in an Insulating Chiral Magnets [4-8]

In chiral magnets, the Dzyaloshinskii-Moriya interaction, which favor rotating spin configurations, becomes active because of the broken spatial inversion symmetry. This interaction often stabilizes nontrivial magnetic

orders such as skyrmion crystals, helical magnetism, and conical magnetism. These noncollinear magnetic orders in insulating chiral magnets induce dielectric polarization through magnetoelectric coupling mediated by the relativistic spin-orbit interactions and render the system multiferroic, in which the electromagnon excitations can appear. The electromagnons can be excited both magnetically by the magnetic-field component and electrically by the electric-field component of electromagnetic waves. The interference effect of these two excitation channels manifest itself in the giant microwave nonreciprocal directional dichroism for specific light/microwave polarization configurations with respect to the crystallographic axes or the skyrmion-crystal plane. We discuss a microscopic mechanism of this phenomenon and related experimental results.

Acknowledgements: This work was supported by JSPS KAKENHI (20H00337), JST CREST (JPMJCR20T1), and the Waseda University Grant for Special Research Projects (2022C-139).

References

1. M. Mochizuki, N. Furukawa and N. Nagaosa, Phys. Rev. Lett. **104**, 177206 (2010).
2. M. Mochizuki and N. Nagaosa, Phys. Rev. Lett. **105**, 147202 (2010).
3. M. Mochizuki and N. Nagaosa, J. Phys.: Conf. Sers. **320**, 012082 (2011).
4. M. Mochizuki,Phys. Rev. Lett. 108, 017601 (2012).
5. M. Mochizuki, and S. Seki, Phys. Rev. B **87**, 134403 (2013).
6. Okamura, F. Kagawa, M. Mochizuki *et al.*, Nat. Comm. **4**, 3391 (2013).
7. M. Mochizuki, and S. Seki, J. Phys.: Cond. Matt. **27**, 503001 (2015).
8. M. Mochizuki, Phys. Rev. Lett. **114**, 197203 (2015).

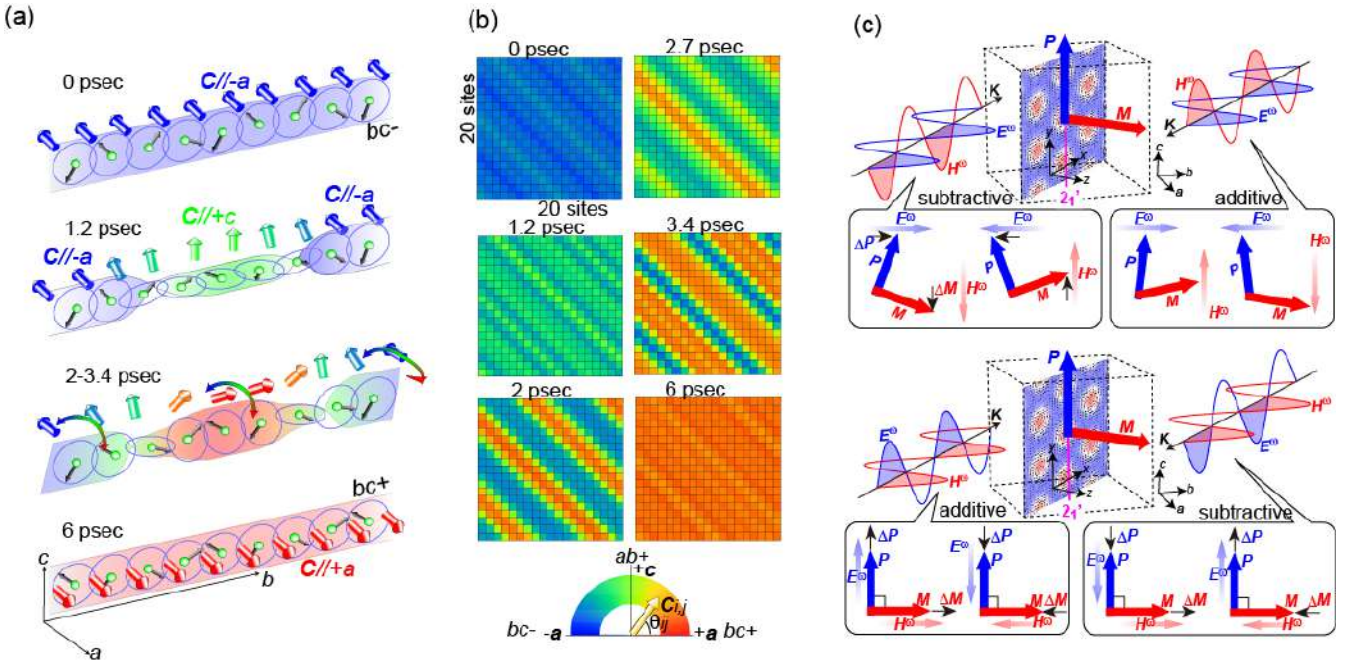

Figure: (a) Schematics of the ultrafast spin chirality switching of transverse spiral magnetism by intense excitation of electromagnons in the spin-spiral-based multiferroic materials. (b) Dynamical spatial-pattern formation in the process of the spin chirality switching. (c) Two configurations of microwave polarization and the skyrmion-crystal plane with which the microwave directional dichroism can be observed.

3D chiral metasurface composed of bidirectional folded split ring resonators

Changzhi Gu[1,2*]

[1] Beijing National Laboratory for Condensed Matter Physics, Institute of Physics, CAS, Beijing, China

[2] CAS Key Laboratory of Vacuum Physics, University of Chinese Academy of Sciences, Beijing, China

[*]corresponding author: czgu@iphy.ac.cn

Abstract: We propose a 3D chiral metasurface composed of bidirectional folded split ring resonators by focused ion beam irradiation (FIB). Our results show that the 3D chiral metasurface exhibits a giant circular dichorism as high as 0.78/0.85 (Experiment/Simulation) in the mid-infrared region. Moreover, we demonstrate that the FIB-induced bidirectional deformation mainly relies on both materials and the ion doses, and the deformation degrees can be tuned by ion irradiated doses, which greatly contributes to construct large numbers of diverse 3D structures.

Summary

Origami allows the transformation of flat sheets into macroscale 3D folding/bending structures, which is always fascinating due to its unique combination of outstanding properties, such as reconfigurability, folding ability, and twistable capability.[1,2] However, the existing folding and bending structures have a single deformation direction, which remains subject to significant restrictions in dexterity.

In this work, an FIB-induced bidirectional origami method is proposed, which can break through the freedom of structural space control and realize challenging 3D micro/nanofabrication and achieve controllable bending/folding directions of different materials.[3] It is found that the initial direction of origami varies with the materials. For the monolayer 50 nm SiNx film, the deformation deviating from the incident direction of ion beam is realized by FIB. Then, the bilayer films are prepared by physical deposition, which not only realized upward deformation, indicating the deformation toward to the ion source, of Au film, but also achieved bidirectional origami for numbers of materials, such as Al, Ti, and Al_2O_3. The behind physics of the bidirectional origami are further discussed by the results of both Monte Carlo simulations and experiments, which indicate that the stresses are mainly caused by the vacancies. Particularly, the key factor in the direction of deformation is atomic sputtering quantity, which can be proved by the surface characterization, for instance the grain sizes change and the surface roughness of the materials during the irradiation. Importantly, based on above FIB origami strategy, a 3D chiral metasurface with bidirectional folded split ring resonators (SRRs) are designed and constructed. Our work broadens greatly the fabrication capacity of FIB-induced origami and lay a new foundation for the design and realization of 3D multifunctional micro/nano photonic devices in the future.

Acknowledgements

This work was supported by the National Natural Science Foundation of China under Grant Nos. 61888102, 11974386, 62174179, 12074420, U21A20140 and 61905274, the National Key Research and Development Program of China under Grant No. 2021YFA1400700.

References

1. Liu, Z., S. Du, A. Cui, Z. Li, Y. Fan, et al., “High-Quality-Factor Mid-Infrared Toroidal Excitation in Folded 3D Metamaterials,” Adv. Mater. 29, 1606298, 2017.
2. Yang, S., Z. Liu, S. Hu, A. Jin, H. Yang, et al., “Spin-Selective Transmission in Chiral Folded Metasurfaces,” Nano Lett., 19, 3432−3439, 2019.

Ultra-sensitive THz biosensors based on metasurfaces

T. -T. Kim[1*]

[1]Department of Semiconductor Physics, University of Ulsan, Republic of Korea
[*]corresponding author: ttkim@ulsan.ac.kr

Abstract: In this presentation, we will discuss the latest research findings on THz metamaterials that allow for highly sensitive biomolecule sensing. Specifically, we will cover two sensing methods: direct absorption fingerprint detection achieved by an individual ring-shaped coaxial aperture resonator in combination with near-field spectroscopy, and early detection of Alzheimer's disease through an abrupt phase transition near an exceptional point in non-Hermitian metasurfaces. The effectiveness of these sensing techniques has been demonstrated through experimental verification, with the ability to detect minuscule amounts of biomolecules at sub-picomole levels.

Terahertz (THz) spectroscopy has shown great promise as an analysis technique for investigating the electromagnetic properties of various media in the fields of physics, chemistry, and biology by observing carrier dynamics, molecules, and lattice vibrations [1]. However, due to the extreme size mismatch between hundreds of micrometers long THz waves and sub-100-nanometer-scale biomolecules, weak light-matter interaction has limited the effectiveness of THz waves in biomolecule sensing. Recently, THz plasmonic metamaterials have emerged as a potential solution to this challenge by enhancing the inherently weak light-molecular interaction. Nevertheless, detecting distinctive THz molecular absorption spectroscopy remains technically challenging, as far-field signals collected from a millimeter-wide THz spot tend to be averaged out. Amyloid beta (Aβ) protein is a primary biomarker for early detection of Alzheimer's disease (AD). Our previous study revealed that the conductance of Aβ protein gradually decreases as they fibrilize [2]. However, the detection of very low molecular levels below picomole is crucial for early diagnosis of Alzheimer's disease. In this talk, we will introduce two types of highly sensitive THz metamaterial sensors for spectrally and spatially selective ultra-sensitive THz fingerprint detection. These sensors integrate a ring-shaped coaxial aperture resonator with a microprobe-based near-field measurement system [3], as well as a non-Hermitian metasurface [4] for detecting a small amount of Aβ protein. The experimentally verified efficacy of these sensors suggests their potential for sub-picomole level biomolecule sensing.

Acknowledgements

This work was supported by National Research Foundation of Korea (NRF) through the government of Korea (NRF-2021R1C1C100631612)

References

1. Ferguson, B. and Zhang, X.-C. "Materials for terahertz science and technology," Nat. Mat. Vol. 1, 26–33, 2002.
2. Heo, C. et al., "Identifying Fibrillization State of Aβ Protein via Near-Field THz Conductance Measurement," ACS Nano, Vol. 14, No. 6, 6548–6558, 2022.
3. Ha, T. et al., "Subwavelength Terahertz Resonance Imaging (STRING) for Molecular Fingerprinting," Nano Lett., Vol.

22, No. 24, 10200–10207, 2022.

4. Park, S. H. et al., “Observation of an exceptional point in a non-Hermitian metasurface,” Nano Photon., Vol. 9, No. 5, 1031–1039, 2020.

Nonlinear Metasurfaces: Third order Nonlinearities of amorphous Composites and structure-induced Second order Surface Nonlinearities

Christin David

Friedrich-Schiller Universität Jena, Institute of Condensed Matter Theory and Optics, 07743 Jena, Germany
Abbe Center of Photonics, 07745 Jena, Germany
christin.david@uni-jena.de

Abstract: My goal is the tailoring of nanostructured and nanocomposite metasurfaces with respect to not only their linear but also their nonlinear optical response. I present studies on gold diffraction gratings and their ability to produce and selectively enhance a second harmonic signal stemming from symmetry breaking at their surface. I discuss third order Kerr nonlinearities and nonlinear polarization holography based on cross-phase modulation (XPM) nonlinear effects.

Nonlinear materials enable ultrafast switching for a wealth of operations such as frequency conversion, pulse generation and signal processing [1, 2]. In addition, structuring can yield enhanced optical nonlinearities and metasurfaces not only allow efficient coupling of light into a nonlinear system boosting the weak multiple photon processes [3], but also controlling the nonlinear fields via beam steering, phase, polarization and amplitude modulation, as well as manipulating their spectral response.

At nanostructured surfaces, (surface) second harmonic generation SHG is the most prominent type of nonlinear response where the symmetry of nonlinear contributions within the bulk is broken. I study SHG from gold nanogratings where the central goals are the efficient nonlinear optical response within higher diffraction orders and the resonant coupling of the macroscopic nonlinear polarization into the grating structure. For optimized geometries, both the fundamental and the second harmonic wavelength can be in resonance simultaneously further enhancing the nonlinear signal through doubly resonant lattice plasmon excitation [4].

Surface second harmonic response from nanogratings is calculated using the Fourier Modal Method (FMM) [5] to obtain local near-fields around the nanostructure from which the second order macroscopic polarization $\mathbf{P}_{2\omega}(\omega)$ is obtained [6]. My theoretical modeling aids explaining resonances, symmetries and field enhancement effects observed in related experiments [4] for various illumination conditions. Exploiting structure-induced diffraction anomalies, the goal is to provide insight into the conditions for doubly resonant structures, i.e., where a surface lattice resonance coincides with the plasmonic excitation of the one-dimensional gold nanograting.

Third order harmonics become important when due to symmetries in the structure the second order response can be neglected. This is the case for centrosymmetric systems such as spherical nanoparticles. For amorphous composites made from metal nanoparticles embedded in a transparent host material, I study the optical Kerr effect where the driving field and nonlinear polarization coincide in frequency as well as the influence of the amorphous mixture on the overall optical and nonlinear properties. For cross-phase modulation (XPM), i.e. cases where the incident and polarization fields are at different frequencies, I study the impact of the metal loading on the dephasing time [7].

I acknowledge funding by the DFG (Deutsche Forschungsgemeinschaft) through the Collaborative Research Center CRC 1375 NOA, 398816777.

References

1. Keren-Zur, S., L. Michaeli, H. Suchowski, and T. Ellenbogen, “Shaping light with nonlinear metasurfaces,” Advances in Optics and Photonics, vol. 10, no. 1, p. 309, 2018.
2. Shaltout, A. M., V. M. Shalaev, and M. L. Brongersma, “Spatiotemporal light control with active metasurfaces,” Science, vol. 364, no. 6441, 2019.
3. Metzger, B., M. Hentschel, and H. Giessen, “Ultrafast Nonlinear Plasmonic Spectroscopy: From Dipole Nanoantennas to Complex Hybrid Plasmonic Structures,” ACS Photonics, vol. 3, no. 8, pp. 1336–1350, 2016.
4. Beer, S., J. Gour, A. Alberucci, C. David, S. Nolte, and U. D. Zeitner, “Second harmonic generation under doubly resonant lattice plasmon excitation,” Optics Express, vol. 30, no. 22, p. 40884, 2022.
5. Liu, V., and S. Fan, “S4: A free electromagnetic solver for layered periodic structures,” Computer Physics Communications, vol. 183, pp. 2233–2244, 2012.
6. Mendoza, B. S., and Mochán, “Exactly solvable model of surface second-harmonic generation,” Phys. Rev. B, vol. 53, no. 8, pp. 4999–5006, 1996.
7. Hazra, M., P. Paul, D. Kim, C. David, S. Gräfe, U. Peschel, M. Kübel, A. Szeghalmi, and A. Pfeiffer, “Nonlinear polarization holography of nanoscale iridium films,” New Journal of Physics (in press) , 2022.

Photonic Metamaterial Continuous Time Crystal

T. Liu[1], V. Raskatla[1], J.-Y. Ou[1, 2], K. F. MacDonald[1*], and N. I. Zheludev[1, 3]

[1]Optoelectronics Research Centre, University of Southampton, Southampton, SO17 1BJ, UK
[2]School of Physics and Astronomy, University of Southampton, Southampton, SO17 1BJ, UK
[2]Centre for Disruptive Photonic Technologies, TPI, SPMS, Nanyang Technological University, Singapore 637371
[*]corresponding author: kfm@orc.soton.ac.uk

Abstract: We report that a classical metamaterial nanostructure, a two-dimensional array of plasmonic metamolecules supported on flexible nanowires, can be driven to a state possessing all the key features of a continuous time crystal: coherent illumination resonant with the metamolecules' plasmonic mode triggers a spontaneous phase transition to a superradiant-like state of transmissivity oscillations resulting from many-body interactions among the metamolecules, and which is characterized by long-range order in space and time.

A time crystal, as originally proposed by Wilczek[1], is a quantum many-body system whose lowest-energy state is one in which the particles are in oscillatory motion. Although it has been shown that such a system, breaking continuous time-translation symmetry by exhibiting oscillatory dynamics, is prohibited by nature, a number of systems which show discrete time-translation symmetry-breaking imposed by an external modulated parametric drive have been recently realized on various platforms, including trapped atomic ions, spin impurities, ultracold atoms, condensates of magnons and quantum computers. Recently, a quantum time crystal that breaks time-translation symmetry *continuously* has been observed in an atomic Bose-Einstein condensate inside an optical cavity. Continuous time crystals are also potentially of great interest in photonics as they can support a variety of new wave propagation phenomena.

We show that a 2D lattice of plasmonic metamolecules supported on doubly-clamped nanowires cut from a semiconductor membrane (Fig. 1a) spontaneously transitions, at room temperature, to a continuous time crystal analogue state characterized by persistent transmissivity oscillations when illuminated by coherent light that stimulates interaction among the metamolecules. Above a threshold of incident optical power, the spectrally dispersed thermal fluctuations of the individual nanowires become spatially coherent synchronous oscillations

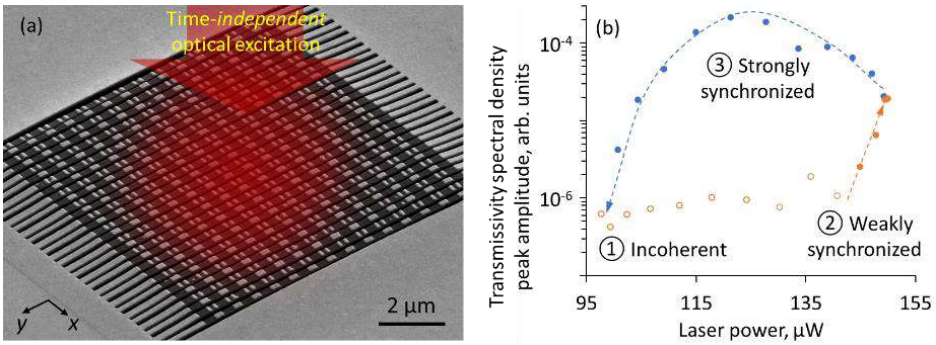

Figure 1: (a) Metamaterial continuous time crystal constructed as an array of nanowires decorated with plasmonic metamolecules. (b) Light-induced interactions among metamolecules lead to synchronized motion of the nanowires via a 1st-order phase transition, resulting in a manifold increase of transmissivity modulation.

over the illuminated ensemble (Fig. 1b).

The phenomenon points to a new mechanism for the synchronization of noise-driven, linear oscillators based upon *non-reciprocal* coupling. The simplicity and control achievable in the nano-opto-mechanical metamaterial platform, offer a new path towards applications in all-optical modulation, frequency conversion and timing, and for the study of dynamic classical many-body states in the strongly correlated regime.

References

1. F. Wilczek, "Quantum Time Crystals," Phys. Rev. Lett. Vol. 109, 160401 (2012).

Advanced wavefront engineering for 6G wireless communications

S. Droulias[1*], G. Stratidakis[1], and A. Alexiou[1]

[1]Department of Digital Systems, University of Piraeus, Piraeus 18534, Greece

[*]corresponding author: sdroulias@unipi.gr

Abstract: The mmWave and terahertz (THz) frequency bands have recently attracted considerable attention in wireless communications, as potential candidates for providing the necessary high bandwidth for demanding applications. Such high frequencies lie in between the bands most commonly used by the wireless and optical communities. In this work we bring together the tools and techniques from the optical regime with the desired functionalities and associated applications in wireless communications, to enable advanced operations for future 6G networks.

The mmWave and terahertz (THz) frequency bands have recently attracted considerable attention in wireless communications, as potential candidates for providing the necessary high bandwidth for demanding applications. With increasing frequency, however, the wavelength becomes comparable to the size of the objects laid in the propagation environment, thus reducing the ability of the signals to diffract around obstacles, and the communication link becomes more vulnerable to blockage [1]. In addition, pathloss increases, and the wireless transmissions can be further attenuated by molecular absorption loss, due to the atmospheric water vapor [2]. Therefore, to take full advantage of the high bandwidth offered by mmWave and THz bands, and to ensure high quality, resilient links, it is necessary to efficiently counteract the sources of blockage and attenuation that lead to signal degradation. The capability to avoid blockages and -in general- flexibly engineer the wavefront taking into consideration environmental parameters and usage scenario characteristics opens up a new ‘beyond communications’ playground, where communication nodes can be employed to identify the shape of surrounding obstacles, map the environment, detect the presence of objects, focus power, localize, track mobility and navigate.

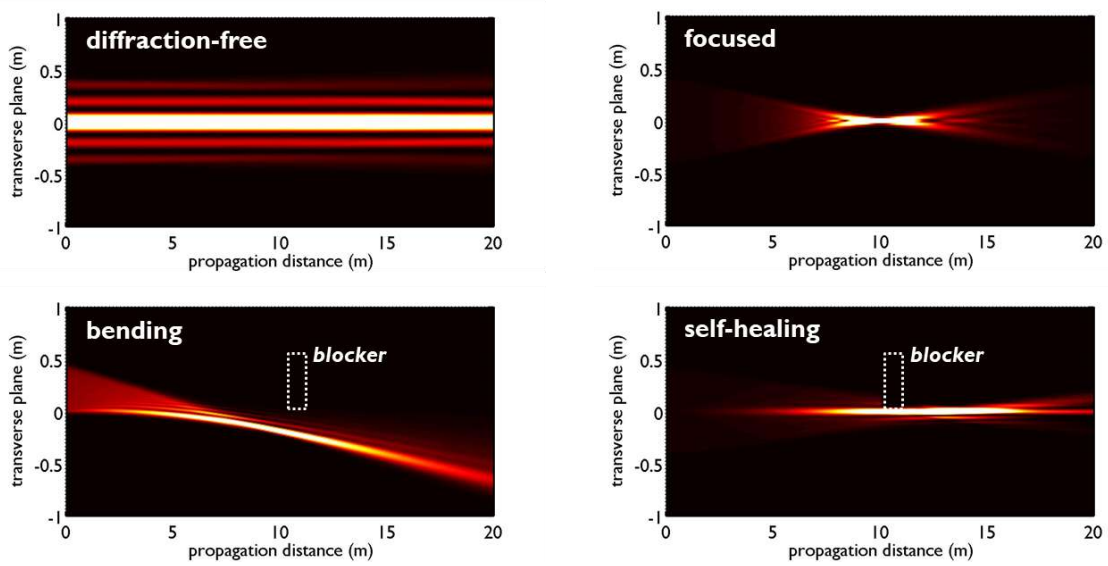

Figure 1. Beam engineering for communication and sensing applications in 6G wireless communications

In this work we extend the beam forming capabilities of reconfigurable intelligent surfaces (RISs) to advanced wavefront engineering, in order to enable precise beam control for communication and sensing applications. Our aim is to bring together the tools and techniques from the optical regime with the desired functionalities and associated applications in wireless communications, in order to enable advanced operations for future 6G networks. We show how non-diffracting beams can mitigate the increased propagation attenuation and how bending beams, that is, beams that are able to propagate along a curved trajectory, enable blockage avoidance. We demonstrate how the link quality is improved with the design of self-healing beams, that is, beams that are able to reconstruct after being interrupted by a small blocker, and how beam focusing enables energy efficient communications and new codebooks for localization and sensing applications.

Acknowledgements

This work has received funding from the European Commission's Horizon 2020 research and innovation programme ARIADNE under grant agreement No. 871464.

References

1. MacCartney, G. R., Deng, S., Sun, S. and Rappaport, T. S., "Millimeter-Wave Human Blockage at 73 GHz with a Simple Double Knife-Edge Diffraction Model and Extension for Directional Antennas," 2016 IEEE 84th Vehicular Technology Conference (VTC-Fall), Montreal, QC, Canada, pp. 1-6, 2016. doi: 10.1109/VTCFall.2016.7881087.
2. Kokkoniemi, J., Lehtomäki, J. and Juntti, M. A "Line-of-sight channel model for the 100–450 gigahertz frequency band," J Wireless Com Network 2021, 88, 2021. https://doi.org/10.1186/s13638-021-01974-8.
3. Stratidakis, G., Droulias, S. and Alexiou, A., "Analytical performance assessment of beamforming efficiency in reconfigurable intelligent surface-aided links," IEEE Access, vol. 9, 115 922–115 931, 2021.
4. Droulias, S. and Alexiou, A., "Reconfigurable Intelligent Surface: an angular spectrum representation approach," 2022 56th Asilomar Conference on Signals, Systems, and Computers, Pacific Grove, CA, USA, pp. 413-418, 2022. doi: 10.1109/IEEECONF56349.2022.10051988.

Machine learning in nanooptics and phonics

M. K. Hedayati[1*]

[1]Department of Engineering, Durham University, UK
[*]corresponding author: mehdi.keshavarz-hedayati@durham.ac.uk

Abstract: The traditional methods for developing optical materials and photonic devices involve a process of trial and error as well as numerical simulations, which can be both time-consuming and resource-limited. This method is also quite expensive and does not always result in the most optimal designs. However, with the advancement of computational power and the availability of sophisticated algorithms, artificial intelligence (AI) has become a new tool in the field of nanophotonics and metamaterials, with deep learning leading the way. nIn recent years, there has been a surge of interest in using AI to design new photonic structures with tailored functionalities. The success of this approach has been attributed to the ability of deep learning models to process vast amounts of data quickly and to learn complex patterns. Additionally, AI can help to overcome some of the limitations of traditional methods, such as the requirement for domain expertise and the need for large amounts of computational resources.

One of the key benefits of AI in the field of nanophotonics and metamaterials is its ability to significantly reduce the computational time required for designing complex structures. For example, a recent paper demonstrated that AI can lead to a 10^5 orders of magnitude decrease in computational time when compared to finite-difference time-domain simulations used in conventional design workflows [1]. This achievement has been made possible by optimizing a fully connected deep neural network (DNN) to predict the structural color parameters while tuning the geometric parameters such as the thickness of resonator, H, and the diameter of the disk, D. It is worth noting that although the input data for these AI models are still produced through simulations, the computational cost only occurs once, and the burden can be distributed across several devices [2].

References

1. Roberts, N; Hedayati MK, “A deep learning approach to the forward prediction and inverse design of plasmonic metasurface structural color,” Applied Physics Letters, Vol. 119, No.6, 061101, 2021.
2. Head, S; Hedayati, MK; “Inverse Design of Distributed Bragg Reflectors Using Deep Learning,” Applied Sciences Vol. 12, No. 10, 4877, 2022.

Microwave Discrete Time Crystal Oscillator

Kyungmin Lee[1], Minwook Kyung[1], Jagang Park[2], Yung Kim[3], Hyuckjoon Cho[3], Joonhee Choi[4], and Bumki Min[1*]

[1]Department of Physics, Korea Advanced Institute of Science and Technology, Daejeon, 34141, Republic of Korea; [2]Department of Electrical Engineering and Computer Sciences, University of California, Berkeley, California 94720, USA; [3]Department of Mechanical Engineering, Korea Advanced Institute of Science and Technology, Daejeon, 34141, Republic of Korea; [4]Department of Electrical Engineering, Stanford University, Stanford, CA 94305, USA

[*]joonhee.choi@stanford.edu, bmin@kaist.ac.kr

Many-body effects in classical systems can be uncovered through nonlinearity. This is particularly evident in periodically driven nonlinear systems, where spontaneous breaking of discrete time translational symmetry can occur. Classical discrete time crystals have provided a new framework for understanding common phenomena like ergodicity breaking and rigid subharmonic response. This concept also unifies our comprehension of diverse periodically driven nonequilibrium matter phases. In this talk, we present a microwave discrete time crystal and quasicrystal oscillators and experimentally demonstrate adjustable commensurate and incommensurate subharmonic oscillations relative to the driving period. These microwave time crystal oscillators are realized by interconnecting an array of periodically-driven nonlinear LC resonators. Intriguingly, the inherent system nonlinearity serves two essential functions: simulating quantum many-body effects in a classical setting and preventing the system from heating to an infinite temperature. We have further verified the stability of these harmonic and anharmonic time crystalline oscillations against spatial and temporal perturbations. This work offers a general design principle for observing controllable commensurate and incommensurate subharmonic signals in a one-dimensional array of driven nonlinear coupled resonators.

Spoof terahertz surface plasmon polaritons on metasurface pathways for network and sensing applications

Sven Becker[1], Tassilo Fip[1], and Marco Rahm[1]*

[1]Department of Electrical and Computer Engineering, State Research Center OPTIMAS, RPTU Kaiserslautern-Landau, Erwin-Schroedinger-Strasse, 67663 Kaiserslautern, Germany

*corresponding author: marco.rahm@eit.uni-kl.de

Abstract: We investigate the routing and frequency-selective manipulation of strongly confined spoof terahertz surface plasmon polaritons (SSPPs) on metasurface pathways of subwavelength width. We also exploit that the impact of objects close to the SSPP route can be directly observed in the far-field after irradiation from an antenna array. As a consequence, such metasurface networks can be used for sensing applications.

Electronic integration is a corner stone in modern electronics that enables the research and development of highly compact devices used daily by millions of customers. By applying a similar concept to optical systems, it is possible to significantly reduce the size of optical networks. Such systems on a chip (SoC) rely on the transmittance of information by using so-called surface plasmon polaritons (SPPs) as a carrier. SPPs can propagate along flat metal surfaces and are tightly bound to the surface in the optical frequency regime, thus allowing a high degree of integration. While a strong confinement can be readily achieved in the optical frequency range, the metal surfaces must be specifically designed and structured to support confined SSPPs at terahertz frequencies. SPPs propagating along specifically tailored meta-surfaces are called spoof surface plasmon polaritons (SSPPs), as they mimic the properties of SSPPs on flat metal surfaces.

Here, we numerically and experimentally study the guiding, routing and manipulation of strongly confined spoof terahertz surface plasmon polaritons (terahertz SSPPs) on metasurface pathways. The pathways are of subwavelength width with respect to the SSPP wavelength and consist of single-, two- or three-cut wires. We electro-optically imaged the spatio- and spectro-temporal dynamics of the electric field of the SSPPs and observed a strong out-of-plane and in-plane confinement of the SSPPs, even on curved routes with subwavelength path width. We proved that SSPPs can be tightly guided within subwavelength space on metasurfaces without loss of the out-of-plane confinement. Due to these beneficial electromagnetic properties, metasurface pathways of subwavelength width seem to be ideally suited for the implementation of on-chip terahertz networks and sensor systems [1]. Furthermore, we designed and implemented an SSPP-based terahertz sensor that transforms on-chip near field information into far-field information by use of a multi-patch antenna array. We show that the impact of objects close to the SSPP route on the spectro-dynamical properties of the SSPPs can be directly observed in the far-field after transformation.

We acknowledge funding by the Deutsche Forschungsgemeinschaft under contract No. RA 1903/4-1.

References

1. Becker S., Fip T., and Rahm M. “Routing of strongly confined terahertz spoof surface plasmon polaritons on metasurfaces along straight and curved pathways with subwavelength width,” Opt. Express, Vol. 28, 6766-6780, 2020.

Weyl Physics and Electromagnetic Metamaterials

Amirullah M.Mamedov, Ekmel Ozbay

Bilkent University, Ankara Türkiye 06800

In this investigation, we present the results of the Weyl physics of narrow band nonlinear materials and their applications in a class of structures that we call Weyl metamaterials.

The Weyl fermion, one of the intriguing particles predicted in the development of quantum field theory and may be realized as emergent quasiparticles in a low-energy condensed matter system. This prediction was first proposed by Conyers Herring, in the context of electronic band structures of solid state systems such as electronic crystals – topological insulators or Weyl semimetals (WSM). Topological materials in the vicinity of band inversion transition became a primary target in search of topologically protected bulk electronic band crossings. Weyl fermion phase exhibits many novel properties such as nonvanishing finite density of states at Fermi level and anomalous chiral Landau levels. These properties together with the topologically protected Fermi-arc surface states, apart from being interesting in fundamental physics, may be useful in the realization of quantum computation and high efficiency circuitry. Tuning the WSM to explore its various properties has remained difficult in condensed-matter systems. Crystalline ZrTe is one of the first discovered topological Weyl fermion semimetal which exhibits topological surface Fermi arcs where Weyl fermion is electrically charged along the line of original suggestion by Herring. An electronic Weyl fermion is not only charged but stable at room temperature where there is no such superfluid or liquid state known.

Topological semimetals are materials whose band structure contains touching points that are topologically nontrivial and can host quasiparticle excitations that behave as Dirac or Weyl fermions [1-3]. These so-called Weyl points not only exist in electronic systems, but can also be found in artificial periodic structures with classical waves such as acoustic waves in phononic crystals - PC [4]

In present investigation we show that Weyl points can be realized in superlattices based on three-dimensional layered photonic crystals. Our approach is based on creating an inversion-breaking array of weakly coupled planar defects embedded in a periodic layered structure with a large omnidirectional photonic band gap. Using detailed band structure calculations, we demonstrate that this class of layered systems can be tailored to display to display 3D point degeneracies between photonic band gaps, without breaking time reversal symmetry. These results open new prospects for the observation of Weyl points and for the application of Weyl physics in photonic devices. Also, we expect our results will stimulate further research on the observation of Weyl points in optic regime, with applications in nano-scale coherent light generation, quantum information processing, and solar energy harvesting.

we study a class of structures that we call Weyl metamaterials [5]. In these systems the chiral Weyl fermions familiar from ferroelectric ceramics.

In summary, we have designed a 3D mechanical structure-analogous to the honeycomb lattice. We show that this relatively simple design carries Weyl points at the vertices of the Brillouin zone and describe the dynamics around the Weyl points and calculate their topological charges. We show the finite boundaries of this structure. Using numerical simulations on a 3D structure, we show the existence of Fermi arcs and compare them with the results obtained from equifrequency-contour analysis. Our design could be easily scaled up or down and can be relevant to applications such as energy harvesting and vibration control on 3D elastic structures.

Multichannel Distribution and Transformation of Polarization-Entangled Photons with Metasurfaces

Ya-Jun Gao[1], Ru-Wen Peng[1,*], and Mu Wang[1,2,*]

[1] National Laboratory of Solid State Microstructures, School of Physics, and Collaborative Innovation Center of Advanced Microstructures, Nanjing University, Nanjing 210093, China
[2] American Physical Society, Editorial Office, Ridge, New York 11961, USA
[*]corresponding author: rwpeng@nju.edu.cn; muwang@nju.edu.cn

Abstract: Photonic quantum information processing relies on operating the quantum state of photons, which usually involves bulky optical components. Here we report on the transformation and distribution of polarization-entangled photon pairs with metasurfaces. Two metasurfaces, each simultaneously distributing polarization-entangled photons to spatially separated multiple channels M (N), accomplish M×N channels of entanglement distribution and transformation. The approach may pave the way for future integration of quantum information networks.

In quantum optics, entanglement-based quantum communication has been extensively studied [1,2]. Although several network configurations have been proposed, bulky optical components remain an obstacle for the miniaturization of optical quantum communication. The metasurfaces may resolve this challenge because of the outstanding light manipulation capability [3-7]. Yet simultaneous entanglement distribution and state transformation with metasurfaces which are essential in constructing integrated quantum networks is challenging. We present a new strategy to realize entanglement distribution and transformation with two metasurfaces, where each comprises resonators with a gradient of geometrical-scaling-induced (GSI) phase [8].

The unit cell in our strategy consists of anisotropic resonators with different geometrical features [6,7]. The interference of the scattering carrying elaborately designed GSI phase from each resonator leads to multiple output beams with different polarization states in the far field (Fig. 1). Meanwhile, the output polarization state is determined by the size , spatial sequence, and separation of the resonators in the unit cell.

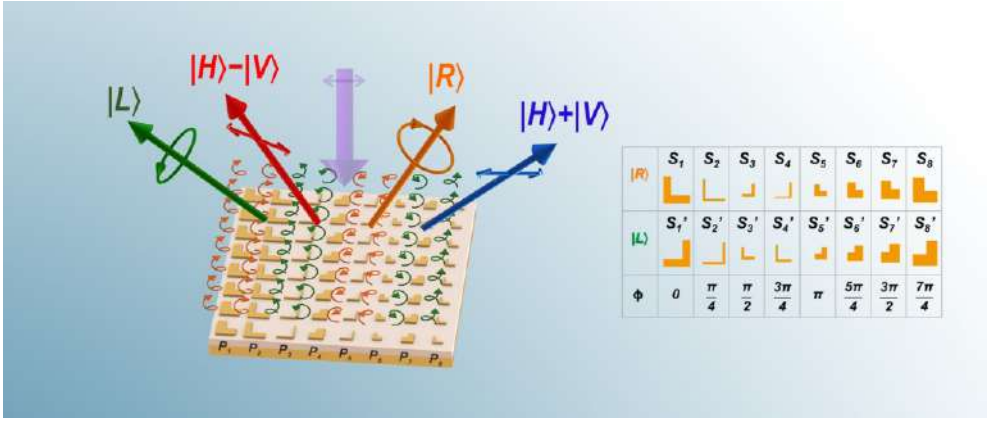

Fig. 1. The schematics showing the generation of multiple polarization states from GSI metasurface. Each resonator diffracts a circularly polarized state with a GSI phase.

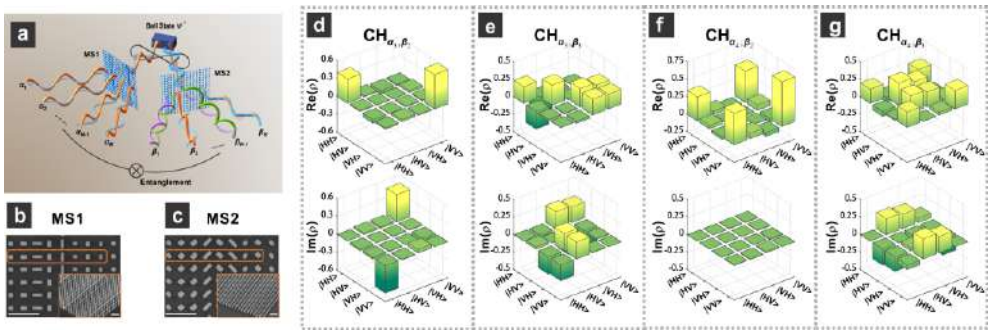

Fig. 2. (a) The schematic of the quantum entanglement distribution and transformation via two metasurfaces composed of silicon resonators with GSI phase. (b)and(c) SEM micrographs of the fabricated metasurfaces, MS1 and MS2. The dash line box marks the unit cell. The inset is the oblique view of the fabricated sample. The white bars all represent 1μm. (d)to(g) The reconstructed density matrices (the real and imaginary part) of the entangled states distributed to 4 among 16 channel combinations.

With this strategy, two metasurfaces with GSI phase can be applied for the integrated entanglement distribution and transformation [8]. Consider the scenario that the non-collinearly entangled photon pairs interact with two metasurfaces MS1 and MS2 respectively. MS1 has *M* output channels, and MS2 has *N* output channels. The photon pairs are coming out probabilistically from each two output channels of MS1 and MS2. Meanwhile, the entangled state can be transformed into different forms, such as $\left(|HV\rangle+|VH\rangle\right)/\sqrt{2}$ (ψ^+), $\left(|HV\rangle-|VH\rangle\right)/\sqrt{2}$ (ψ^-), $\left(|HH\rangle+|VV\rangle\right)/\sqrt{2}$ (ϕ^+), $\left(|HH\rangle-|VV\rangle\right)/\sqrt{2}$ (ϕ^-), or the superposition of these Bell states. (Fig. 2(a)).

Theoretically we can obtain an arbitrary entangled state at the specific output channels by designing the resonators with GSI phase. Figure 2 shows an example where MS1 and MS2 have four output channels respectively. The parametric down-conversion light source generates polarization-entangled photon pairs ψ^+. There should be 16 output states including four Bell states, eight superpositions of the two Bell states, and four superpositions of four Bell states. The unit cell is illustrated in Figs. 2(b) and 2(c). To verify the quantum entanglement, we reconstruct the quantum state with the quantum state tomography. The reconstructed density matrices of four output states (ϕ^++iϕ^-, ϕ^++iϕ^--iψ^+-ψ^-, ϕ^+, and ϕ^+-iψ^+) are provided in Figs. 2(d)-3(g). Most fidelities are above 0.880, with the median at 0.892±0.017. The results confirm the polarization entanglement distribution to every two channels of MS1 and MS2.

The experimental realization of the entanglement distribution and transformation indicates that GSI metasurfaces are suitable for distributing different photon states to a large number of users. This strategy significantly decreases the number of conventional optical components in constructing a quantum network.

References

1. S. Wengerowsky, S. K. Joshi, F. Steinlechner, H. Hübel, and R. Ursin, "An entanglement-based wavelength-multiplexed quantum communication network", Nature, Vol. 564, 225-228 (2018).
2. H.-K. Lo, M. Curty, and K. Tamaki, "Secure quantum key distribution", Nat. Photonics, Vol. 8, 595-604 (2014).
3. T. Stav, A. Faerman, E. Maguid, D. Oren, V. Kleiner, E. Hasman, and M. Segev, "Quantum entanglement of the spin and orbital angular momentum of photons using metamaterials", Science, Vol. 361, 1101-1104 (2018).
4. K. Wang, J. G. Titchener, S. S. Kruk, L. Xu, H.-P. Chung, M. Parry, I. I. Kravchenko, Y.-H. Chen, A. S. Solntsev, Y. S. Kivshar, D. N. Neshev, and A. A. Sukhorukov, "Quantum metasurface for multiphoton interference and state reconstruction", Science, Vol. 361, 1104-1108 (2018).
5. A. S. Solntsev, G. S. Agarwal, and Y. S. Kivshar, "Metasurfaces for quantum photonics", Nat. Photonics, Vol. 15, 327-336 (2021).
6. Y.-J. Gao, X. Xiong, Z. Wang, F. Chen, R.-W. Peng, and M. Wang, "Simultaneous generation of arbitrary assembly of polarization states with geometrical-scaling-induced phase modulation," Phys. Rev. X, Vol. 10, 031035 (2020).
7. Y.-J. Gao, Z. Wang, W. Tang, X. Xiong, Z. Wang, F. Chen, R.-W. Peng, and M. Wang, "Metasurface design for the generation of an arbitrary assembly of different polarization states," Phys. Rev. B, Vol. 104, 125419 (2021).
8. Y.-J. Gao, Z. Wang, Y. Jiang, R. W. Peng, Z.-Y. Wang, D.-X. Qi, R.-H. Fan, W.-J. Tang, and M. Wang, "Multichannel Distribution and Transformation of Entangled Photons with Dielectric Metasurfaces" Phys. Rev. Lett., Vol. 129, 023601 (2022).

FSS-Backed Reflectarray for Millimeter-Wave 5G Applications at the 28 GHz band

Roman Soroka[1*], Eduardo Martinez-de-Rioja[1], Ana Arboleya[1] and Jose A. Encinar[2]

[1] Dept. of Signal Theory and Communications and Telematic Systems and Computing, Universidad Rey Juan Carlos, 28942 Fuenlabrada, Spain
[2] Information, Processing and Telecommunications Center, Universidad Politécnica de Madrid, 28040 Madrid, Spain
[*]corresponding author: r.soroka.2020@alumnos.urjc.es

Abstract: This contribution presents the design of a 30x30-element reflectarray antenna backed by a frequency selective surface (FSS) for millimeter-wave 5G applications at the 28 GHz band. The proposed FSS-backed reflectarray works identically to a conventional metal-backed reflectarray in the 28 GHz band, where it can be used to enhance millimeter-wave coverage. However, in other bands of 5G, such as sub-6 GHz and 39 GHz, the antenna behaves as a transparent structure, suppressing the specular reflections of impinging signals.

The Fifth Generation (5G) of mobile systems is intended to use different frequency bands, such as the sub-6, 28 and 39 GHz bands [1]. The millimeter-wave (mm-wave) bands offer high capacity and low latency for broadband communications [1], which is in high demand today. However, propagation conditions at mm-wave bands are characterized by larger path loss and penetration losses [2]. This may result in zones with poor levels of coverage (no line of sight from the base station), which are called 'death' zones [3]. In the recent years, reflectarray antennas have been applied to design coverage-enhancing panels for mm-wave 5G networks [3]. They can be used to solve the problem of death zones by working as passive reflecting surfaces, exploiting their ability to generate shaped and dual-polarization beams [3]. In conventional metal-backed reflectarrays [3], the out-of-band impinging signals produce undesired specular reflections (since the reflectarray acts as a flat metallic reflector at out-of-band frequencies) that can cause undesired interference and degrade other wireless communication links, see Fig. 1 (a). In this work, the authors propose an FSS-backed reflectarray for mm-wave 5G applications in the 28 GHz band, see Fig. 1(b). The FSS emulates a metallic plate (totally reflective) at 28 GHz, so the FSS-backed reflectarray produces the same beam at 28 GHz than the metal-backed reflectarray. On the other hand, the FSS is practically transparent at other 5G bands (sub-6 GHz and 39 GHz), letting the signals pass through it, and thus, avoiding the specular reflections produced by the metal-backed reflectarray.

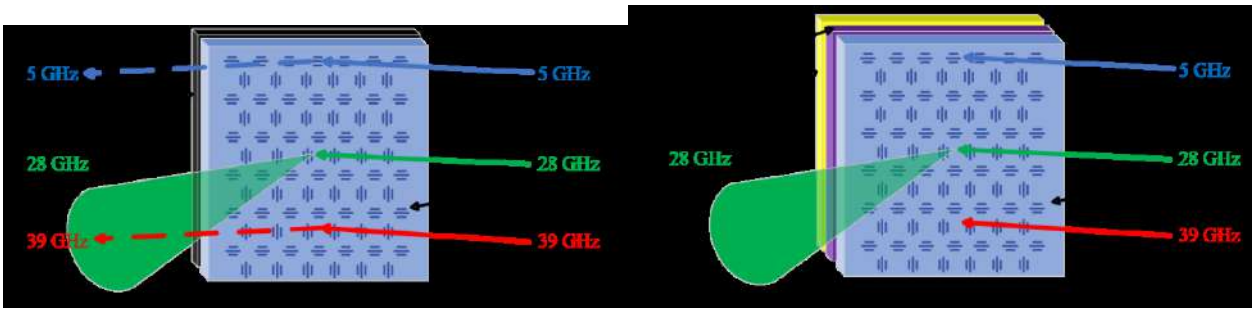

Figure 1. Reflectarray panel designed to produce a focused beam at 28 GHz: (a) metal-backed reflectarray showing specular reflection of out-of-band signals, and (b) FSS-backed reflectarray (the absorber behind the FSS is optional).

The unit-cell is based on the design shown in [4], which combines a dual-layer FSS with a single-layer reflectarray on the top. The unit-cell (with dimensions of 5 mm x 5 mm) contains orthogonal groups of dipole-type elements in both the reflectarray and the FSS layers. The dielectric material of both layers is Arlon AD260A, with thickness of 0.76 mm, relative permittivity of 2.6 and loss tangent of 0.0017. The dimensions of the FSS elements have been optimized to provide the required spectral response: at 28 GHz, reflection losses are less than 0.7 dB, while at the sub-6 GHz 39 GHz bands, transmission losses are below 0.5 dB.

The unit-cell has been used to design a 30x30-element FSS-backed reflectarray antenna for mm-wave 5G applications at the 28 GHz band. The reflectarray is illuminated by a centered feed placed at a distance of 1 m. The dimensions of the reflectarray elements have been optimized so that the antenna produces a collimated beam in the direction $\theta = 20°$. The radiation patterns of the antenna have been simulated at several frequencies and compared with those produced by an equivalent metal-backed reflectarray, see Fig. 2. The results confirm that the proposed FSS-backed reflectarray provides the same performance at 28 GHz than the conventional reflectarray, while being transparent at sub-6 GHz and 39 GHz bands.

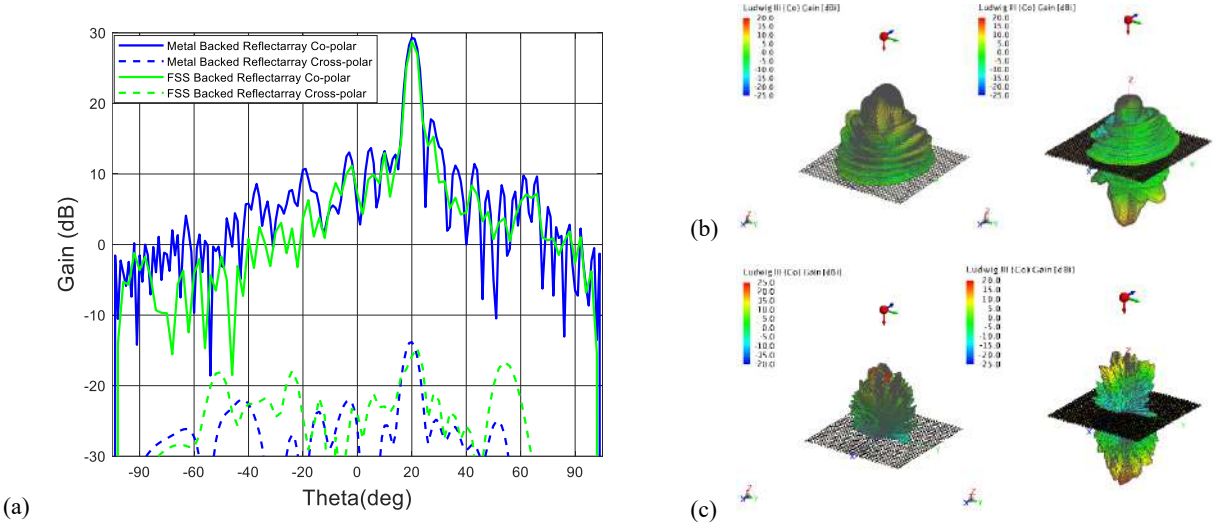

Figure 2. Simulated radiation patterns: (a) cut in the $\varphi = 0º$ plane at 28 GHz (design frequency), and 3D radiation patterns at (b) 5 GHz and (c) 39 GHz (metal-backed reflectarray on the left, FSS-backed reflectarray on the right).

Acknowledgements: Authors are grateful to the Ministry of Science and Innovation and Spanish Research Agency, within projects PID2020-114172RB-C21-2/AEI/10.13039/501100011033 and TED2021-131975A-I00, and to the Comunidad de Madrid, within the Multiannual Agreement Framework with Universidad Rey Juan Carlos, Line of Action 1, Young Researchers R&D Project INCREASE-5G (Ref. F858).

References

1. Wang, Y., J. Li, L. Huang, Y. Jing, A. Georgakopoulos and P. Demestichas. "5G Mobile: Spectrum broadening to higher-frequency bands to support high data rates", IEEE Vehicular Technology Magazine, Vol. 9, No. 3, 39-46, 2014.
2. Shafi, M., *et al*. "Microwave vs. millimeter-wave propagation channels: Key differences and impact on 5G cellular systems", *I*EEE Communications Magazine, Vol. 56, No. 12, 14-20, 2018.
3. Martinez-de-Rioja, E., *et al*. "Passive dual-polarized shaped-beam reflectarrays to improve coverage in millimeter-wave 5G networks", 15th Eur. Conf. Antennas Propag., Dusseldorf, Germany, 2021.
4. Soroka, R., E. Martinez-de-Rioja, A. Arboleya, and J. A. Encinar. "Design of FSS-backed reflectarray cells for coverage-enhancing panels with suppressed out-of-band reflections in millimeter-wave 5G", 16th Eur. Conf. Antennas Propag., Madrid, Spain, 2022.

Soil Moisture Detection Using Metamaterials Based Absorber

Mohammed M. Bait-Suwailam[*1,2], **and Yaseen Al-Mulla**[1,3]

[1]Remote Sensing and GIS Research Center, Sultan Qaboos University, Muscat, Oman
[2]Dept. of Electrical and Computer Eng., Sultan Qaboos University, Muscat, Oman
[3]Dept. of Soils, Water and Agricultural Eng., Sultan Qaboos University, Muscat, Oman
[*]corresponding author: msuwailem@squ.edu.om

Abstract: In this paper, a novel design of a highly electromagnetic absorber is proposed for soil moisture detection. The electromagnetic absorber design consists of a periodic arrangement of Split-Ring Resonator (SRR) metamaterial inclusion. The metamaterial absorber takes advantage from its design and structure in which soil samples are embedded underneath the resonant SRR inclusion. Based on the numerical results, the absorber is able to detect water moisture on Loamy and Sandy soils with 12.6% and 10% shift in its absorption peak, respectively.

Soil moisture is one of the important health and growth indicators of agricultural land cover ecosystems [1], since it can provide necessary information about the need of irrigation and requirements for taking any necessary measures in order to optimize the consumption of water in soil. There have been lots of studies on the sensing, estimation and monitoring of soil moisture, including deployment of microwave antennas and deep analysis of space-borne imagery data [2-5]. However, we believe that much efforts are needed to develop less complex metamaterial-based sensors. In this research work, we propose a novel design for the detection of soil moisture through embedding soil under test (SUT) within a metamaterials-based highly absorber. Numerical full-wave simulations using Ansys HFSS are presented and discussed.

Fig.1 presents the design of a dual-band high absorber metamaterial structure. The absorber consists of a two-layer substrate, where the top substrate is an FR-4 laminate (ε_r = 4.4, tanδ = 0.02) with SRR inclusion printed on it, and the second layer is where the SUT is embedded for detecting any potential soil moisture. The absorber at end is backed with a metallic ground layer. Periodic boundary conditions are then enforced on the four side walls in order to mimic an infinite dual-band metamaterial absorber. For detection purposes, a Floquet port is excited from the top of an air-filled rectangular box, as shown in Fig. 1.

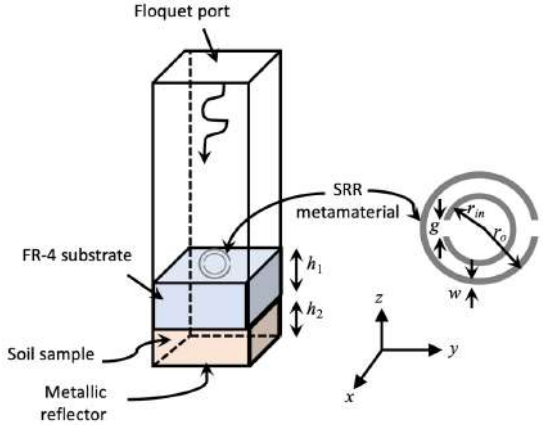

Fig. 1 Schematic of the developed dual-band absorber for soil moisture detection. The absorber cell size is $30mm$, $h_1 = 1.6mm$, $h_2 = 0.5mm$, $r_o = 14mm$, $r_{in} = 11mm$, $g = 0.6mm$, and $w = 1mm$.

In this numerical study, four different soil samples are investigated, namely: Loamy soil (dry and wet), and Sandy soil (dry and wet). The electric properties of the soil samples have been extracted from the simulator's library. Fig. 2(a) depicts the numerical simulation results for the metamaterial absorber alone, which is essential to investigate for calibration purposes. As can be seen, a dual-band resonance is achieved, which can be seen in the reflectance curve, while the absorption level is above 90%, which is an indication of the highly absorption strength of the proposed soil moisture sensor. Fig. 2(b) depicts the soil moisture detection capability of the metamaterial absorber from the four SUT samples and compared against the case of unloaded absorber (reference from Fig. 2(a)). As can be seen from Fig. 2(b), a 10% shift in the frequency of first absorption peak for the case of wet Sandy soil was achievable, while a 12.6% shift was observed for the case of wet Loamy soil, which is due to the accumulated water molecules in the wet soil samples. The case of dry SUT samples showed lower percentage shift in the absorption peaks of the absorber, since the samples are saturated and thus incurs minimal effect to the absorber's resonance shift.

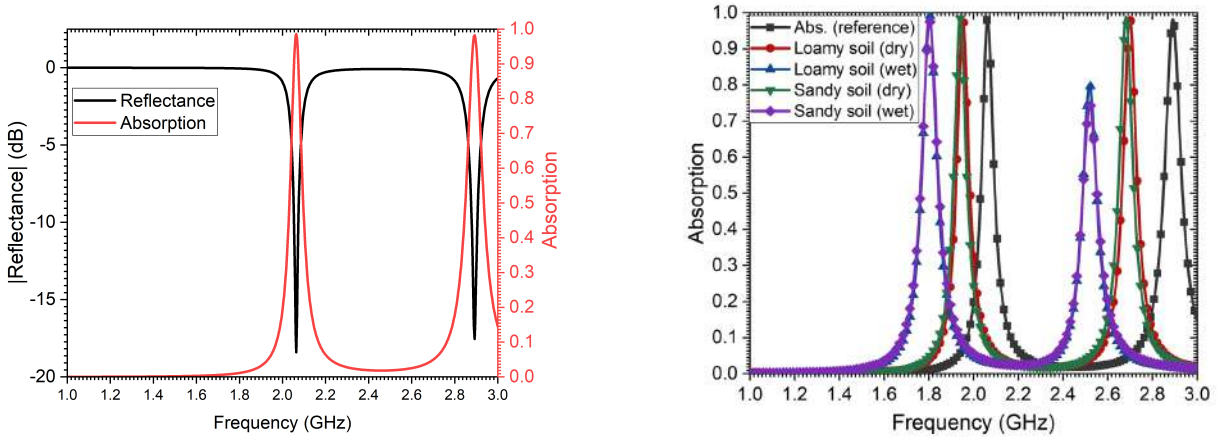

(a) **(b)**

Fig. 2 (a) The reflectance and absorption strength of the proposed (unloaded) soil moisture detector; (b) the absorption strength for 4 different SUT samples.

References

1. Lekshmi, S., Singh, D.N., Baghini, M.S. "A critical review of soil moisture measurement," Measurement, Vol. 54, 92–105, 2014.
2. Skiljo, M., et al. "Self-sensing antenna for soil moisture: beacon approach," Sensors, Vol. 22, 9863–14, 2022.
3. Kashyab, B., and Kumar, R. "Sensing methodologies in agriculture for soil moisture and nutrient monitoring," IEEE Access, Vol. 9, 14095-14121, 2021.
4. Bait-Suwailam, M., et al. "Microwave sensors for soil moisture detection: an application towards healthy date palm," [Edt.] In Soil Moisture, Dec. 2022, doi: 10.5772/intechopen.109152.
5. Narayan, U., Lakshmi, V., Jackson, T.J. "High-resolution change estimation of soil moisture using L-band radiometer and radar observations made during the SMEX02 experiments," IEEE Trans. Geosci. Remote Sens., Vol. 44, 1545-1554, 2006.

One-way Complete Polarization Conversion at the Non-Hermitian Chiral Degeneracy of a Null-eigenvalue

S. Baek[1], D. Oh[2], S. Lee[1], K. Lee[2], J. Park[3], T.-T. Kim[4], B. Min[1,2]

[1]Department of Mechanical Engineering, Korea Advanced Institute of Science and Technology (KAIST), Daejeon 34141, Republic of Korea

[2]Department of Physics, Korea Advanced Institute of Science and Technology (KAIST), Daejeon 34141, Republic of Korea

[3]Department of Electrical Engineering and Computer Sciences, University of California, Berkeley, CA, USA

[4]Department of Physics, University of Ulsan, Ulsan 44610, Republic of Korea

*bmin@kaist.ac.kr

Abstract: We propose a non-Hermitian metasurface that enables one-way complete polarization conversion at a null-eigenvalued EP via the incorporation of gain. We numerically validate this concept by designing a metasurface that allows polarization conversion from right to left circular polarization while blocking the opposite conversion and eliminating co-polarized transmission.

A deeper understanding of non-Hermitian systems provides a unique opportunity to investigate polarization optics from a different perspective [1-3]. At exceptional points (EPs), the eigenpolarization states coalesce into a single eigenpolarization, revealing the singular and topological polarization phenomena. However, it is essential to consider both the coalesced eigenpolarization and the eigentransmission to gain a complete understanding of the polarization-related phenomena at the EP. Here, we propose a non-Hermitian metasurface to accomplish one-way complete polarization conversion (OCPC) at the chiral EP. The OCPC in this work refers to the phenomenon where there is conversion from right (or left) to left (or right) circular polarization, while simultaneously blocking the opposite conversion and eliminating co-polarized transmission. The design simultaneously leverages zero eigentransmission and a coalesced circular eigenpolarization state at the chiral EP, illustrating one intriguing feature of the eigenvalue-dependent polarization phenomena at the EP. Additionally, we show that the OCPC can provide a way of achieving the highest level of circular dichroism even in the absence of a three-dimensional helical chiral arrangement.

To verify the OCPC phenomenon at the chiral EP, we conducted a numerical simulation of a non-Hermitian metasurface composed of two coupled nano-rod plasmonic resonators on a gain substrate designed to operate at near-infrared frequencies. The major axes of the two resonators are orthogonal, and they are engineered to share the same resonance frequency when the incident light is polarized along the major axis (refer to Fig. 1a). In Fig. 1b, the numerically-extracted eigentransmission is plotted in a two-parameter space spanned by the input frequency and the imaginary part of the substrate permittivity. The presence of the chiral EP with zero-valued eigentransmission results in the intended OCPC phenomena, which is supported by the observation that all elements except t_{LR} in the non-Hermitian Jones matrix become almost zero (Fig 1c). It is worth mentioning that the OCPC results in a maximum circular dichroism (CD) in *transmission*, as evidenced by the value approaching a value of -1. This behavior contrasts qualitatively with the CD observed in three-dimensional helical chiral structures, which usually exhibit differences in co-polarized transmission between RCP and LCP incidence and zero-valued cross-polarized transmission. In addition, our proposed metasurface is also defined by its planar chirality, which is caused by a broken mirror symmetry in the plane. This gives it a different response to circularly polarized light coming from either direction. Consequently, asymmetric OCPC is observed, in which incident light

is converted to LCP for forward propagation but to RCP for backward propagation, with the sign of the maximal CD being inverted for forward and backward propagation (Fig. 1d, e). At this point, it is worth mentioning that the asymmetric maximal circular dichroism has also been observed in the metasurface possessing quasi-bound states in the continuum (q-BIC) [4].

In conclusion, we propose a method to achieve OCPC through the utilization of a gain-incorporated metasurface featuring null-eigenvalued chiral EP. This provides the numerical proof of OCPC from a non-Hermitian viewpoint Furthermore, it offers a novel method for achieving asymmetric maximal CD by -1 or 1, without the need for extrinsic chirality or 3D helical structure. The utilization of this non-Hermitian approach presents the possibility of facilitating various applications in polarization optics and photonics, as well as introducing new prospects for engineering polarization-dependent interactions between light and matter.

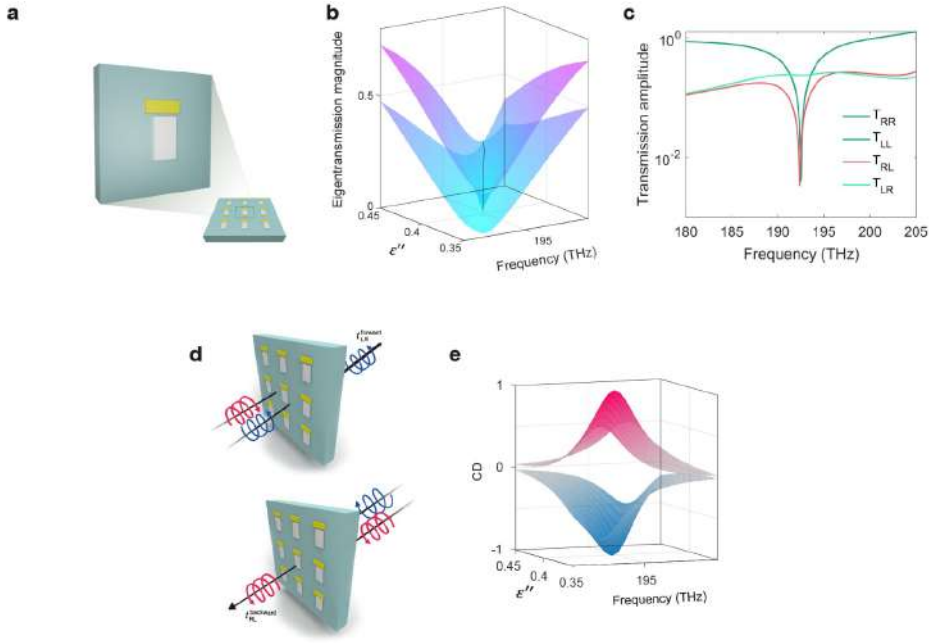

Figure 1 (a) A schematic illustration of the gain-incorporated non-Hermitian metasurfaces. (b) Numerically-extracted eigentransmission surfaces in a two-parameter space spanned by incident frequency and imaginary substrate permittivity. (c) Numerically-extracted transmission amplitudes near a null-eigenvalue chiral EP. (d) A schematic illustration of an asymmetric polarization conversion taking place at a null-eigenvalue chiral EP. (e) A plot of CD in the two-parameter space, where the red and blue surfaces correspond to the CD in the forward and backward propagation direction, respectively.

References

1. M. Kang, J. Chen, and Y. D. Chong, “Chiral exceptional points in metasurfaces,” *Phys. Rev. A*, vol. 94, no. 3, pp. 1–5, 2016
2. M. Lawrence *et al.*, “Manifestation of PT symmetry breaking in polarization space with terahertz metasurfaces,” *Phys. Rev. Lett.*, vol. 113, no. 9, pp. 1–5, 2014
3. S. Baek *et al.*, “Non-Hermitian chiral degeneracy of gated graphene metasurfaces,” *Light: Sci and Appl.*, accepted for publication, 2023
4. Shi, Tan, et al. "Planar chiral metasurfaces with maximal and tunable chiroptical response driven by bound states in the continuum." *Nat. Commun.,* vol. 13, no.1 pp. 4111, 2022

Bi-hyperbolic and tetra-hyperbolic isofrequency topologies in a gyroelectromagnetic medium

V. I. Fesenko[1*], D. M. Vavriv[1], P. Savi[2], and V. R. Tuz[3,4]

[1]Microwave Electronics Department, Institute of Radio Astronomy National Academy of Sciences of Ukraine, Ukraine
[2]Electronics and Telecommunications Department (DET), Politecnico di Torino, Italy
[3]State Key Laboratory on Integrated Optoelectronics, College of Electronic Science and Engineering, International Center of Future Science, Jilin University, China
[4]School of Radiophysics, Biomedical Electronics and Computer Systems, V.N. Karazin Kharkiv National University, Ukraine
[*]corresponding author: volodymyr.i.fesenko@gmail.com

Abstract: Isofrequency topologies are studied for a gyroelectromagnetic medium obtained by stacking optically thin magnetized ferrite and semiconductor layers into a unified structure. In such a structure, both bi-hyperbolic and tetra-hyperbolic isofrequency contours appear as a simultaneous effect of both periodic arrangement of constitutive layers and external magnetic field influence. It is proposed to consider the obtained bi-hyperbolic and tetra-hyperbolic isofrequency contours as new topology classes of the wave dispersion.

A hyperbolic metamaterial (HMM) is a special type of artificial anisotropic structures whose isofrequency contours take the form of an open hyperboloid since the principal components of their constitutive electric or magnetic tensors have opposite signs. By tuning the shape of the hyperbolic dispersion, the propagation of light in HMMs may be flexibly controlled [1]. The hyperbolic dispersion exists also in natural media featuring gyroelectric (e.g., semiconductor) or gyromagnetic (e.g., ferrite) properties under the influence of an external static magnetic field. Under saturated magnetization, aforementioned media become extremely anisotropic in a specific frequency band due to the plasma or ferromagnetic resonance. This leads to the appearance of the hyperbolic topology of isofrequency contours related to particular waves.

In this Report, we demonstrate that the utilization of natural hyperbolicity inherent to magnetized ferrite and semiconductor materials in an artificial finely-stratified structure (superlattice) can result in arising new forms of isofrequency topology. We consider a gyroelectromagnetic medium as a HMM which is described by the constitutive relations $\vec{D} = \hat{\varepsilon}\vec{E}$ and $\vec{B} = \hat{\mu}\vec{H}$, where relative permittivity and permeability tensors are given by $\hat{\eta} = \{\eta_{xx}, \eta_{xy}, 0; -\eta_{xy}, \eta_{yy}, 0; 0, 0, \eta_{zz}\}$ $(\eta = \varepsilon, \mu)$. These tensors are the effective parameters obtained by applying the homogenization procedure (for details, see Ref. [2]) to a finely-stratified structure composed of magnetized ferrite and semiconductor layers [see Fig. 1(a)]. From Maxwell's equations, the dispersion equation, which describes propagation of electromagnetic waves through an unbounded gyroelectromagnetic medium, is derived as follows:

$$\begin{aligned}(\varepsilon_{zz}\mu_{zz})^{-1}\{k_x^4\varepsilon_{xx}\mu_{xx} + k_y^4\varepsilon_{yy}\mu_{yy} + k_z^4\varepsilon_{zz}\mu_{zz} + k_x^2k_y^2(\varepsilon_{xx}\mu_{yy} + \varepsilon_{yy}\mu_{xx}) \\ + k_x^2k_z^2(\varepsilon_{xx}\mu_{zz} + \varepsilon_{zz}\mu_{xx}) + k_y^2k_z^2(\varepsilon_{yy}\mu_{zz} + \varepsilon_{zz}\mu_{yy}) - k_0[k_x^2(\varepsilon_{xx}\varepsilon_{zz}\mu_\perp + \mu_{xx}\mu_{zz}\varepsilon_\perp) \\ + k_y^2(\varepsilon_{yy}\varepsilon_{zz}\mu_\perp + \mu_{yy}\mu_{zz}\varepsilon_\perp) + k_z^2\varepsilon_{zz}\mu_{zz}(\varepsilon_{xx}\mu_{yy} + \varepsilon_{yy}\mu_{xx} - 2\varepsilon_{xy}\mu_{xy})]\} + k_0^4\varepsilon_\perp\mu_\perp = 0,\end{aligned} \quad (1)$$

where $\varepsilon_\perp = \varepsilon_{xx}\varepsilon_{yy} - \varepsilon_{xy}^2$; $\mu_\perp = \mu_{xx}\mu_{yy} - \mu_{xy}^2$; k_x, k_y and k_z are the components of the wavevector.

We assume that the superlattice is composed of BaCo and doped Si layers (see material parameters in Ref. [3]). In the studied case, isofrequency topologies are mostly conditioned by values and signs of the three principal components μ_{xx}, μ_{yy} and ε_{zz} of the constitutive tensors [4]. Several representative regions on the k_0 scale are distinguished in Fig 1(b), namely: Region I where $\mu_{xx} > 0$ and $\mu_{yy} > 0$; Region II where $\mu_{xx} < 0$ and $\mu_{yy} < 0$; Region III where $\mu_{xx} < 0$ and $\mu_{yy} > 0$. In all cases $\varepsilon_{zz} < 0$.

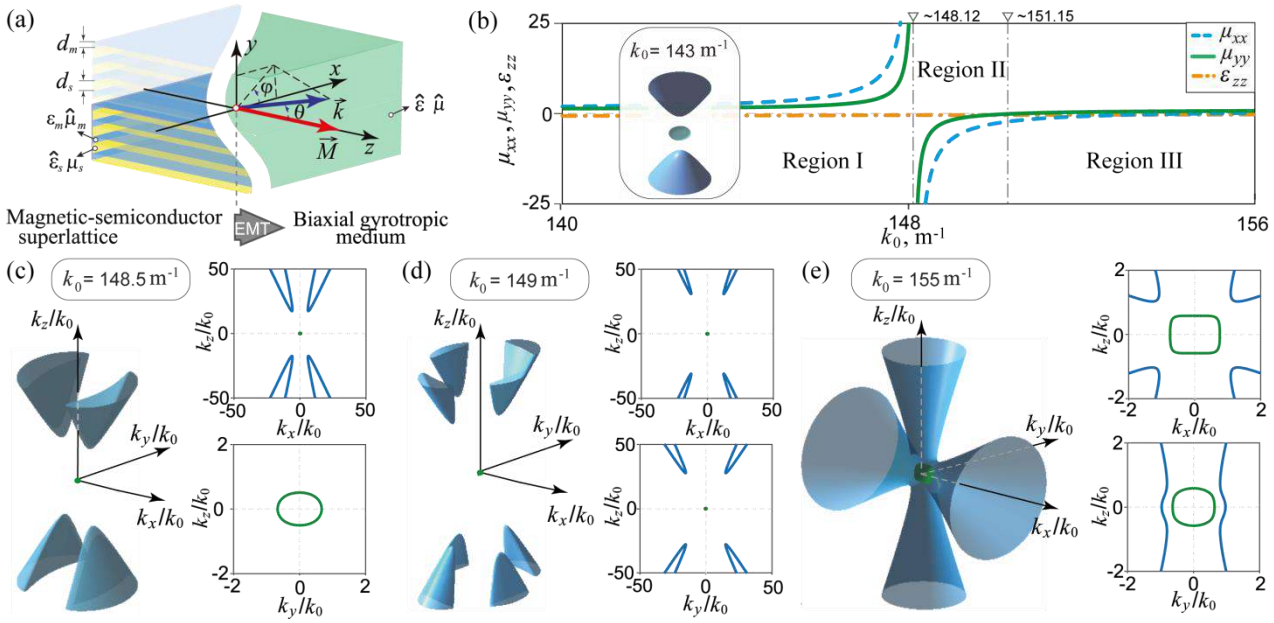

Figure 1: (a) The magnetic-semiconductor superlattice influenced by an external static magnetic field $\vec{M}$ and resulting homogenized biaxial gyrotropic medium. (b) Principal values of the components of relative permittivity ε_{zz} and relative permeability μ_{xx} and μ_{yy} versus k_0 at fixed values $d_m/d = 0.06$ and $d_s/d = 0.94$, where d is the period. (c-e) Topological forms of isofrequency surface, and their cross-sections, related to both extraordinary (blue surfaces) and ordinary (green surfaces) bulk waves propagating through the studied medium for (c, d) Region II and (e) Region III at the fixed values of k_0. The inset of panel (b) shows typical topological forms of isofrequency surfaces in Region I.

In Region I, the isofrequency surface for the extraordinary waves arises in the form of a two-fold Type I uniaxial-hyperboloid [Fig. 1(b)], which is caused by the hyperbolicity of semiconductor subsystem along the z-axis. In Region II, due to the influence of the external static magnetic field, there is a topological transition of the isofrequency surface to the form of cones cut into either two or four parts which are oriented along the z-axis. Obtained forms of isofrequency surface are attributed to the bi-hyperbolic topology [Fig. 1(c)] and tetra-hyperbolic topology [Fig. 1(d)], respectively. In Region III, for the extraordinary waves, the isofrequency contour is in the form of two one-fold Type II hyperboloid with orthogonal revolution axes [Fig. 1(e)]. This isofrequency contour is attributed to the bi-hyperbolic topology. The revealed novel types of topology appear due to the simultaneous effect of both the structure periodicity and an external magnetic field influence. They exist when both relative permittivity and permeability are tensor values, whose principal components have different combinations of signs.

References

1. Guo, Z., H. Jiang and H. Chen. “Hyperbolic metamaterials: From dispersion manipulation to applications”, J. Appl. Phys., Vol. 127, 071101, 2020.
2. Tuz, V. R. “Polaritons dispersion in a composite ferrite-semiconductor structure near gyrotropic-nihility state”, J. Magn. Magn. Mater., Vol. 419, 559–565, 2016.
3. Fesenko, V. I. and V. R. Tuz, “Lossless and loss-induced topological transitions of isofrequency surfaces of a biaxial gyroelectromagnetic medium”, Phys. Rev. B, Vol. 99, 094404, 2019.
4. Tuz, V. R. and V. I. Fesenko. “Magnetically induced topological transitions of hyperbolic dispersion in biaxial gyrotropic media”, J. Appl. Phys., Vol. 128, 013107, 2020.

Tunable THz graphene metasurface beam splitter

Hyeongi Park[1], Sodam Jeong[1], Soojeong Baek[2] and Teun-Teun Kim[1*]

[1]Department of Physics, University of Ulsan, Ulsan 44610, Republic of Korea
[2]Department of Mechanical Engineering, Korea Advanced Institute of Science and Technology (KAIST)
[*]ttkim@ulsan.ac.kr

Abstract: We propose electrically tunable Terahertz (THz) beam splitter based on graphene metasurfaces. The ratio of transmission and reflection of incident THz wave can be dynamically controlled through modulation of graphene's conductivity by gating. The electrically tunable THz beam splitter can be applied to next-generation THz communication and advanced imaging systems.

Beam splitter is an optical device that splits a beam into a transmitted and a reflected beam and is essential part in interferometer that can measure various physical characteristics. However, conventional beam splitter are bulky and heavy, which makes them unsuitable for integrated use of optical devices. Particularly at the THz regime, the spectroscopy is mainly performed at the time-domain, the etalon effect of thick beam-splitters induces time-domain distortion of THz pulse due to the multiple internal reflection. Moreover, once the beam-splitter is fabricated, the ratio of transmission and reflection is intrinsically fixed. Recently, gate-induced switching and linear modulation of THz waves can be achieved in a hybrid material system comprising artificially constructed meta-atoms and an atomically thin graphene layer [1]. Here, we propose electrically tunable transmission and reflection ratio of THz wave by varying the graphene's optical conductivity. An active metasurface is formed by integrating graphene layer with square-shaped thin metallic metasurfaces (fig. 1a). By using a polyimide with thickness of 1 μm as a substrate, the numerically calculated results clearly show that the etalon effect can be significantly reduced (fig. 1b). As shown in fig. 1c, the measured ratio of the transmission and reflection are from 1:1 to 2:3. Our active graphene metasurface beam-splitter can be applied to reconfigurable intelligent surface for THz wireless communication and advanced imaging systems.

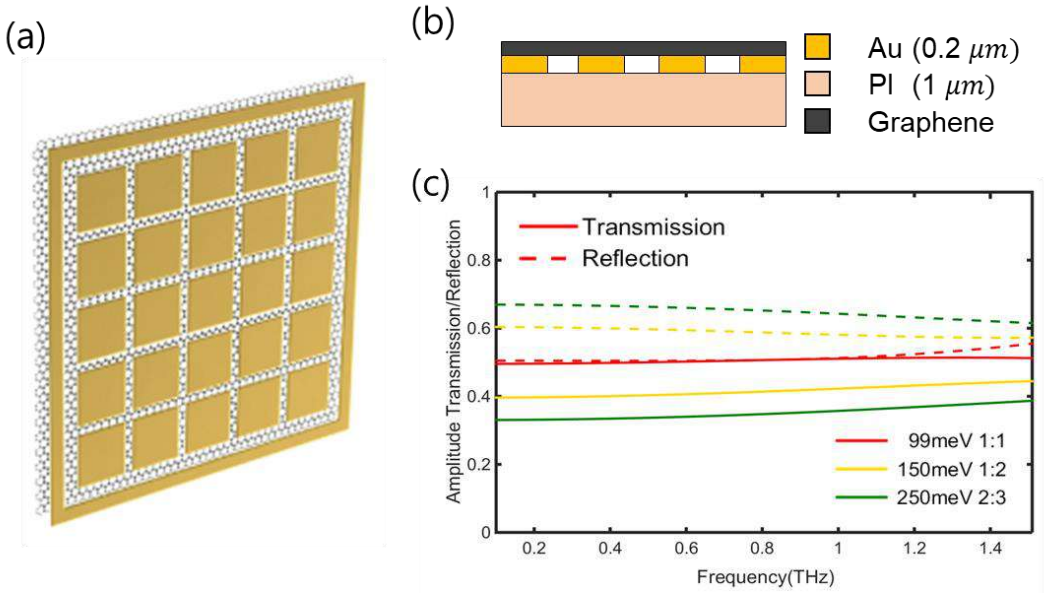

Figure 1. (a, b) Schematic illustration of graphene metasurfaces for active beam-splitter. (c) Simulation result of ratio of transmission and reflaction ratio.

Acknowledgements

This work was supported by National Research Foundation of Korea (NRF) through the government of Korea (NRF-2021R1C1C100631612)

References

[1] S. Lee, *et. al.*, "Metamaterials for enhanced optical responses and their application to active control of terahertz waves" Adv. Mat., **32**, 2000250 (2020).

Nanophotonics, plasmonics and quantum optics

Chiro-optical microscopic imaging of plasmonic materials and chiral near-field interaction with molecules

Hiromi Okamoto*

Institute for Molecular Science, National Institutes of Natural Sciences, Okazaki, Japan
*corresponding author: aho@ims.ac.jp

Abstract: Based on near-field and far-field chiro-optical microscopy, we demonstrate here highly enhanced local chiro-optical effects of plasmonic materials, even in achiral nanostructures, suggesting strong chiral near-field interactions. The strong chiral near-field interaction gave highly circularly polarized luminescence from achiral dye molecules combined with chiral gold nanostructures.

Chirality is an essential property of nanostructured materials, from the viewpoint of not only fundamental nano-optics but also application of their interactions with molecules nearby. It is essential to investigate internal structures (geometrical distributions) of chiro-optical responses in the nano- and micro-structured materials, for the design of their chiral properties and functions. We developed near-field and far-field chiro-optical microscopic imaging systems that allow us to visualize local structures of chiro-optical signals in nano-/micro-materials, which include (i) near-field circular dichroism (CD) microscope, (ii) near-field polarimetry microscope, and (iii) high-precision far-field CD imaging microscope. These methods were applied to observe local chiral fields for plasmonic gold nanostructures, chiral microcrystalline samples, and so forth.[1] We found very different characteristic features of local chiro-optical effects as compared with macroscopic chiro-optical spectroscopic characteristics. The local chiral fields that interact with molecules in the peripheries of the nanomaterials provide characteristic chiro-optical properties the molecules.

Nano/micro-scale chiro-optical imaging of chiral plasmons

Gold nanostructures with chiral geometries are known to exhibit strong optical activity in the wavelength region resonant with some localized surface plasmon modes. Figure 1(a) shows a far-field CD microscopic image of a chiral 4-fold symmetry 2-dimensional pinwheel-shaped gold nanostructure array.[2] The CD signal is inverted when the handedness of the nanostructure is inverted. The CD signal was found to be not uniform and oscillate spatially in the single unit cell.

The image contrast was more prominent in the near-field chiro-optical images, and the amplitudes of local chiral signals were as large as 10^2 times the signal intensities obtained in the macroscopic spectroscopic measurements of the same samples, for 2-dimensional chiral gold nanostructures. Even 2-dimensional achiral nanostructures (that do not give macroscopic CD signals) exhibited strong local chiro-optical effects arising from the local chirality. Figure 1(b) shows an ellipticity (corresponding to CD) image of gold nanorod obtained with near-field polarimetry microscope.[3] Based on the results obtained here, we can provide the controllable local circularly polarized field by a combination of linearly polarized light and a gold nanorod,

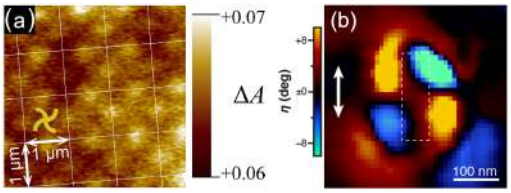

Fig. 1 (a) Far-field CD image (@ 700 nm) of a pinwheel-shaped gold nanostructure array.[2] (b) Near-field ellipticity image (@ 800 nm) of a gold nanorod.[3]

which may give us a chance to pioneer analytical applications of chiral optical fields and novel optical devices.

Highly circularly polarized luminescence from fluorescent molecules induced by chiral plasmons

The strong local chiro-optical activity associated with the chiral plasmons indicates existence of highly chiral local fields, which may induce strong chiral near-field interaction between the plasmons and the materials in the vicinity of the nanostructures. We can thus expect near-field interaction between dye molecules and chiral plasmons, which yields highly circularly polarized luminescence from the dye coexisting with the chiral plasmonic material. In fact, we found that the luminescence from achiral dye molecules combined with chiral plasmonic nanostructure was highly circularly polarized (dissymmetry factor $g > 0.1$, Fig. 2)[4] as compared with luminescence from dyes with chiral molecular structures ($g \sim 10^{-3}$-10^{-2}).

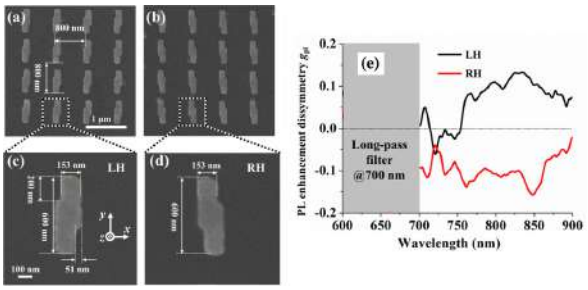

Fig. 2 (a-d) SEM images of 2-dimensional chiral gold nanostructures fabricated by e-beam lithography. (e) Dissymmetry spectra of circularly polarized luminescence from IR-125 dye on the chiral gold nanostructures.[4]

The author thanks Drs. T. Narushima, S. Hashiyada, K. Q. Le, J. Yamanishi, and H.-Y. Ahn for their contributions. This work was supported by Grants-in-Aid for Scientific Research (KAKENHI Nos. JP22225002, JP15H02161, JP15K13683, JP15J01261, JP16H06505, JP17H07330, JP21H04641, JP21K18884, and JP22H05135).

References

1. H. Okamoto, "Local optical activity of nano- to microscale materials and plasmons," *J. Mater. Chem. C* **7**, 14771-14787, 2019.
2. T. Narushima, H. Okamoto, "Circular Dichroism Microscopy Free from Commingling Linear Dichroism via Discretely Modulated Circular Polarization," *Sci. Rep.* **6**, 35731, 2016.
3. S. Hashiyada, T. Narushima, H. Okamoto, Imaging Chirality of Optical Fields near Achiral Metal Nanostructures Excited with Linearly Polarized Light," *ACS Photon.* **5**, 1486-1492, 2018.
4. K. Q. Le, S. Hashiyada, M. Kondo, H. Okamoto, "Circularly Polarized Photoluminescence from Achiral Dye Molecules Induced by Plasmonic Two-Dimensional Chiral Nanostructures," *J. Phys. Chem. C* **122**, 24924–24932, 2018.

Realization of true perfect absorber metasurfaces for perfect thermal radiation in midinfrared wavelength

Y. Nishijima[1*]

[1] Department of Electrical and Computer Engineering, Graduate School of Engineering, Yokohama National University, 79-5 Tokiwadai, Hodogaya-ku, Yokohama, 240-8501, Japan

[*]corresponding author: nishijima-yoshiaki-sp@ynu.ac.jp

Abstract: We have realized true perfect absorption with midinfrared metasurfaces by numerical simulation and experimental measurements in midinfrared wavelength for thermal radiation applications. To realize this feature, we noticed that the controlling of absorption and scattering in metasurface.

Realization of perfect absorption is desirable in the field of photo-thermal, photo-voltaic energy conversion. Especially radiation absorption in metal-insulator-metal (MIM) metasurface, which generally consist of a metal back-plate, dielectric layer, and a metal nano-structure, is currently applied for realizing a great variety of efficient photo-thermal energy converter designs. Such converters also show significant promise in the mid-infrared (IR) wavelength range, where they are used as both IR radiation sources as well as detectors, notably for applications in optical sensing of volatile organic compounds (VOCs)[1-3].

In most studies, the absorbance A exhibited by a MIM metasurface is among its most important properties implicitly treated as $A = I - R$, where I is total incident energy on the sample ($I = 1$ in the normalized presentation), whereas R is the reflectance. The metal back plate is understood as a reflector with negligible transmittance owing to its considerable thickness (Typically, thickness $t > 200$ nm of Au thickness is used as back ground metal). Hence, the scattered portion of radiation energy S is either ignored or not explicitly accounted for, since it is assumed to be incorporated in R or and is distributed among them[4].

However, the origin of plasmon resonance comes from scattering of light by metal nano structures. The absorption part will become the loss of the resonance. Therefore, it is natural to put the scattering as optical power balance equation as $I = A + R + T + S$. Due to a zero transmittance $T=0$ of the MIM metasurface, both R and S manifest as a backward reflection of light. Therefore, it is difficult to identify the true A and S from reflection measurement in experiments, it corresponds to the extinction, $Ext = A + S$.

One of the evidences of this scattering effects can bee seen in thermal radiation measurements. Figure 1 shows reflection spectra and thermal radiation spectra of MIM metasurface with different disc diameter. When the parameters of metasurface, such as thickness and permittivity of insulator layer, disc diameter, periodicity and resonance wavelength, metasurface realized perfect ant reflection R~0 (PAR). However, even such PAR condition, the radiation is reached around 60 ~ 70% and they did not reach to the perfect radiation (PR, Rad ~ 100%). According to the Kirchhoff's thermal law of radiation (absorption coefficient □ = radiation coefficient □), Absorption portion is directly equal to the radiation portion. Therefore, we concluded that PAR condition is not equal to the perfect absorption (PA), and the reflection measurements cannot identify PAR and PA.

In the presentation, we demonstrate the quantitatively analyzed the scattering effects by numerical modeling as well as fabrication and characterization of MIM metasurface. We observed the considerable effect

backwards scattering has on the optical response of metasurface. Also, there is further room for improvement in removing the specular reflection of metasurface, guided by detailed FDTD analysis. Light scattering under slanted incidence is the next required step for analysis of MIM response and can be achieved at a quantitative level using FDTD modeling. Also, we will show that it is possible to increase the PA and PR condition with using of nano-thin layers of metals with strong absorbance such as Cr, and high absorption plasmonic metal, AgAuCuPdPt high entropy alloy as new plasmonic materials.

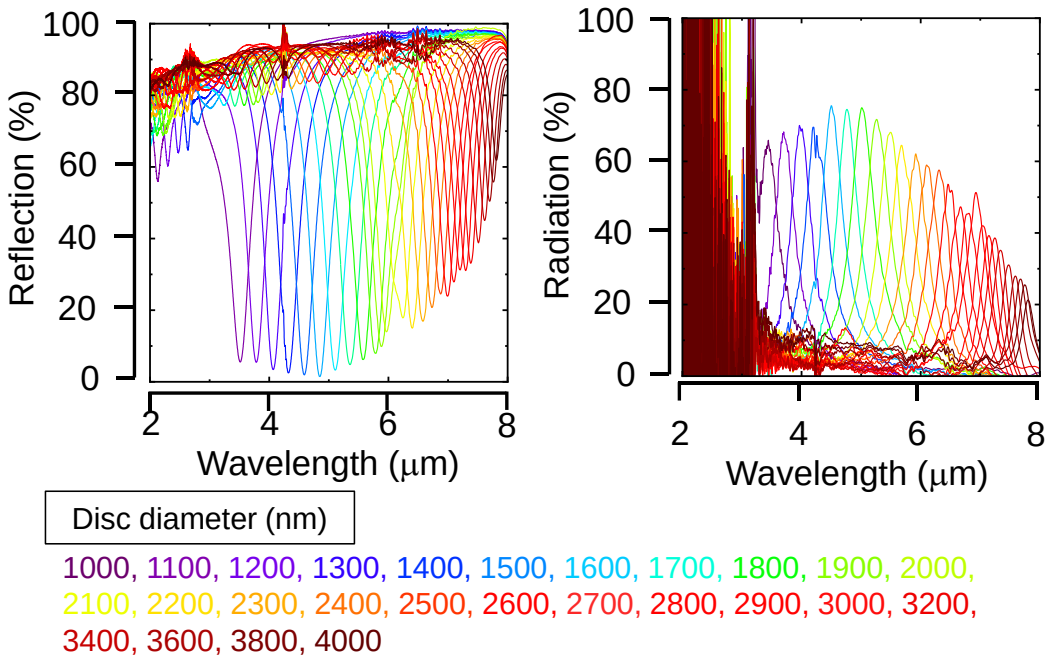

Figure 1: absorption and thermal radiation of metasurfaces with Au-SiO_2-Au nanodisc.

References

1. Y. Nishijima, S. Morimoto, A. Balčytis, T. Hashizume, R. Matsubara, A. Kubono, N. To, M. Ryu, J. Morikawa, and S. Juodkazis, "Coupling of molecular vibration and metasurface modes for efficient mid-infrared emission," J. Mater. Chem. C, 10, 451-462, (2022).
2. Y. Nishijima, S. Juodkazis, "Control of Vibration-Metasurface Coupling at the Mid-Infrared Spectral Window for Inorganic Thermal Emitters," Bull. Chem. Soc. Jpn, 95, 1411-1418, (2022).
3. Y. Nishijima, S. Juodkazis, "The Tunable Coupling between Metasurface and Molecular Vibration towards the Platform of Spectral Analysis," Bull. Chem. Soc. Jpn, 95, 1318-1324, (2022).
4. Y. Nishijima, N. To, A. Balčytis, and S. Juodkazis, "Absorption and scattering in perfect thermal radiation absorber-emitter metasurfaces," 30, 4058-4070 (2022).

Reconfigurable nanoantennas based on conducting polymer plasmonics

S. Chen[1*] and M. P. Jonsson[1]

[1] Laboratory of Organic Electronics, Department of Science and Technology, Linkoping University, Norrkoping SE 602 74, Sweden

[*]corresponding author: shangzhi.chen@liu.se

Abstract: Coinage metals have been the key plasmonic materials for years, but they have issues such as limited tunability. By contrast, conducting polymers exhibit outstanding tunability and were recently introduced as a new category of plasmonic materials. In this talk, I will briefly introduce the emergence, current status, and future prospects of using conducting polymers for dynamic plasmonic nanoantennas.

Conducting polymers are a category of organic conductors possess conjugated backbones with alternating single and double carbon-carbon bonds. Since its discovery in the late 1970s, conducting polymers have been widely used in optoelectronic and flexible devices[1]. We recently demonstrated that conducting polymers can be used for plasmonics with a highly conducting polymer, poly(3,4-ethylenedioxythiophene) doped with Sulf ions (PEDOT:Sulf). Nanoantennas made of PEDOT:Sulf exhibit clear dipolar plasmonic resonance with peak located in near infrared spectral range[2]. Different from conventional plasmonic systems based on metals, our conducting polymer plasmonics exhibit excellent tunability with reversible transition between plasmonic (conducting) and dielectric (insulating) states. The state tuning can be realized *via* either chemical[2] or electrical approaches[3]. Such properties make conducting polymer promising for dynamic optical antennas with spatiotemporal control.

In this talk, I will start from the basic properties of conducting polymers and the emergence of nanoantennas based on conducting polymers, to their applications for dynamic beam steering and tunable meta-lens and future prospects for biomedical and thermoplasmonic devices. In the last part of this talk, I will discuss the challenges as well as fascinating properties (e.g., hyperbolic) of conducting polymer plasmonic nanoantennas that need to be addressed or exploited in the future.

Acknowledgements: financial support from Kunt and Alice Wallenberg Foundation, the Swedish Research Council (VR, No. 2020-00287 and 2022-00211), the Swedish Foundation for Strategic Research (SSF), and the Swedish Government Strategic Research Area in Materials Science on Functional Materials at Linkoping University (Faculty Grant SFO-Mat-LiU No. 2009 00971).

References

1. Shirakawa, H. “Nobel lecture: the discovery of polyacetylene film – the dawning of an era of conducting polymers”, *Rev. Mod. Phys.*, Vol. 73, No. 3, 713, 2001.
2. Chen, S., Kang, E. S. H., Shiran Chaharsoughi, M., Stanishev, V., Kuhne, P., Sun, H., Wang, C., Fahlman, M., Fabiano, S., Darakchieva, V., and Jonson, M. P. “Conductive polymer nanoantennas for dynamic organic plasmonics”, *Nat. Nanotechnol.*, Vol. 15, No. 1, 35-40, 2020.
3. Karki, A., Cincotti, G., Chen, S., Stanishev, V., Darakchieva, V., Wang, C., Fahlman, M., and Jonsson, M. P., “Electrical tuning of plasmonic conducting polymer nanoantennas”, *Adv. Mater.*, Vol. 34, No. 13, 2107272, 2022.

Mode synchronization in GaN ridge polariton lasers

H. Souissi[1*], M. Gromovyi[2,3], T. Gueye[1], C. Brimont[1], L. Doyennette[1], D. Solnyshkov[4,5], G. Malpuech[4], E. Cambril[2], S. Bouchoule[2], B. Alloing[3], J. Zuniga-Perez[3], and T. Guillet[1]

[1]Laboratoire Charles Coulomb (L2C), Université de Montpellier, CNRS, Montpellier, France
[2]Centre de Nanosciences et de technologies, CNRS, Université Paris-Saclay, France
[3]Université Côte d'Azur, CNRS, CRHEA, Rue Bernard Gregory, Valbonne 06560, France
[4]Université Clermont Auvergne, CNRS, Institut Pascal, Clermont-Ferrand, France
[5]Institut Universitaire de France (IUF), 75231 Paris, France
[*]corresponding author: hassen.souissi@umontpellier.fr

Abstract: We experimentally demonstrate polariton laser in a GaN ridge waveguide. The strong-coupling regime is assessed through a comparison of the measured and modeled cavity free spectral range (FSR). The findings reveal that the laser exhibits a transition from monomode to multimode operation as the temperature is increased from 70K to 150K. The transition to multimode lasing is characterized by a flattening of the FSR just above the threshold, which constitutes the signature of mode synchronization induced by polaritonic nonlinearities.

Long-studied, polaritons have been most often studied in vertical microcavities with an active layer sandwiched between two distributed Bragg reflectors (DBR). More recently, polaritonic waveguides in which the photon confinement is achieved by total internal reflection have been introduced and begun to be studied. Polaritons in waveguides offer new possibilities for their use in optoelectronics, built upon the concept of the polariton laser. Unlike a conventional semiconductor laser, a polariton laser does not need a population inversion to stimulate the light emission, potentially enabling the development of laser components that operate with much greater gain and short injection sections. We experimentally evidenced the distinction between a ridge polariton laser and a conventional edge-emitting ridge laser in a Fabry-Perot cavity [1]. The laser effect is accomplished with an exciton reservoir length that constitutes only 15% of the cavity length, a feat that would not be possible in a conventional ridge laser. Recently, polariton lasing in the ultraviolet (UV) spectral range has also been reported in microring resonators that use GaN/AlGaN slab waveguides [2]. Beyond this, a nonlinear effect resulting from polariton nonlinearity, such as ultrafast pulse modulation, has been reported in an AlInGaN polariton waveguide [3]; due to the negative group velocity dispersion, this self-focusing nonlinearity is predicted to lead to frequency combs in such polaritonic devices [4].

In this study, the horizontal laser cavities are GaN etched-ridge structures with vertical Bragg reflectors, measuring 20-60µm in length (inset fig.1(a)). The wide bandgap material GaN has robust excitons and large oscillator strength, making it a suitable choice to maintain the strong coupling regime up to room temperature [5]. The cavity is pumped with a pulsed laser that quasi-resonantly excites the exciton reservoir using a line-shaped spot profile. Figure 1(a,c) shows power-dependent emission spectra across the lasing threshold, for a cavity length Lcav=60µm, at T=70K and 150K. The spectra exhibit Fabry-Perot (FP) modes over a large energy range. Beyond the threshold, a "monomode" laser is demonstrated to operate continuously at 70K [1], whereas "multimode" lasing is observed beyond 150K, due to a spectral broadening of the polaritonic gain. To evaluate the strong coupling between photons and excitons in a waveguide geometry, our analysis will be based on the

cavity free spectral range (FSR). The demonstration of the strong coupling regime is supported by the agreement between the FSRs obtained from the FP transmission below threshold, and the FSR calculated from lower polariton branch (LPB) dispersions (fig.1(b,d)), especially with a decrease of the FSR near the exciton resonance. Just above threshold, the FSR dispersion is unchanged at 70K, whereas it exhibits a flattening at 150K. This provides a first indication of mode synchronization, that would occur based on the polaritonic self-focusing nonlinearity [3,4]. This paves the way to the development of polariton lasers based on harmonic mode locking.

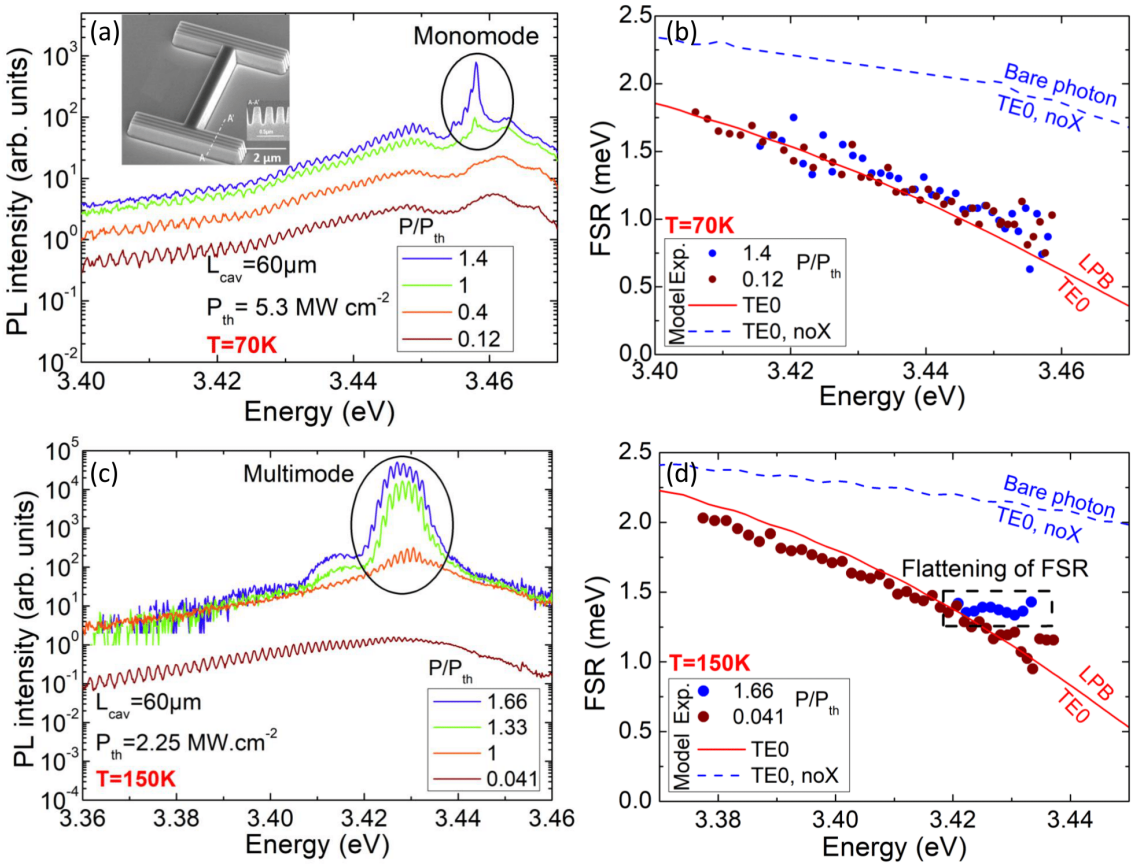

Figure 1: (a,c) Power-dependent PL spectra of the 60-µm-long cavity at 70K and 150K, respectively; Inset: SEM image of a 5-µm-long polariton ridge waveguide. (b,d) Experimental FSR versus excitation power (colored dots) and FSR calculated from LPB dispersions (plain line) at 70K and 150K ,respectively.

The authors acknowledge funding from the French National Research Agency (ANR-16-CE24-0021-03, ANR-11 LABX-0014, ANR-21-CE24-0019-01), the French Renatech network and the Region Occitanie (ALDOCT-001065).

References

1. H. Souissi et al. Phys. Rev. Appl. , Vol. 18, 044029, 2022.
2. A. Delphan et al. APL Photonics, Vol. 8, 021302, 2023.
3. D. M. Di Paola et al. Nat. Commun. , Vol 12, 3504, 2021.
4. O. A. Egorov et al. Optics Express, Vol. 26, 18, 2018.
5. C. Brimont et al. Phys. Rev. Appl. Vol 14, 054060, 2020.

Nonlocal theory of tip-enhanced type microscopies

H. Ishihara[1]*, M. Tamura[1,2], Y. Tomoshige[1], H. Ikagawa[1] and T. Yokoyama[1]

[1]Department of Materials Engineering Science, Osaka University, Japan
[2]Research Institute for Light-induced Acceleration System, Osaka Metropolitan University, Japan
*corresponding author: ishi@mp.es.osaka-u.ac.jp

Abstract: We develop nonlocal response theories of tip-enhanced type microscopies such as photo-induced force microscopy (PiFM), tip-enhanced coherent anti-Stokes Raman scattering (TE-CARS), and tip-enhanced photoluminescence (TEPL). By coupling the nonlocal constitutive equations with Maxwell's equations, we derive self-consistent solutions of electric field and induced polarization. Both the microscopic optical response of single molecules and cavity effect due to the localized surface plasmon resonance sustained by the macroscopic metallic structures are treated in a single framework.

The spectroscopies using tip-enhanced electric fields are actively studied for revealing the physical and chemical functions of single molecules, and recently, relevant technologies have been highly developed. Tip-enhanced Raman Scattering (TERS) spectroscopy and STM luminescence spectroscopy are the representative techniques. These techniques use the localized surface plasmon resonance (LSPR) sustained between the metal-coated probe tip and metal substrate. Extremely localized and enhanced field leads to the sensitive detection of a single molecule with sub-nm spatial resolution. These techniques have elucidated the fine spectra with the spatial dependence with sub-nm resolution [1], and also, revealed possibilities to control the quantum mechanical properties of individual single molecules [2].

The LSPR yields an extremely localized field whose intensity varies even within a single molecule, and hence, the spatial correlation between the field and the wavefunction of induced polarizations of molecules becomes important. Thus, the nonlocal response occurs. We developed a numerical method extending the discrete dipole approximation incorporating the nonlocal response of single molecules under LSPR. We revealed the optical forbidden transition of a single-walled carbon nanotube by analyzing the Raman signals [3]. This method can be applied to developing the nonlocal theories for the tip-enhanced type microscopies.

In the present study, we will present theoretical formulations of tip-enhanced type microscopies such as photo-induced force microscopy (PiFM), tip-enhanced coherent anti-Stokes Raman scattering (TE-CARS), and tip-enhanced photoluminescence (TEPL). In these theories, we derive constitutive equations describing the relation between induced polarization and electric field in a form containing the nonlocal susceptibility. By coupling them with Maxwell's equations, we obtain self-consistent solutions. In this process, it is necessary to include both the microscopic optical response of single molecules and the cavity effect due to LSPR sustained by the macroscopic metallic structures in a single framework.

An example of theoretical demonstration is reproducing PiFM imaging with sub-nm spatial resolution obtained for the quantum dots [4], where the frequency-dependent images of the dumbbell-type quantum dots (developed for highly efficient catalysts) were reproduced. Further, our theoretical studies have predicted PiFM imaging of the optical forbidden transition of single molecules [5] and circular dichroism (CD) of the single

molecules [6]. Another demonstration is for the TE-CARS. CARS is one of the third-order nonlinear Raman scatterings. Its signal is caused by two incident lights, a pump light with the frequency ω_1 and a Stokes light with the frequency ω_2 ($\omega_1 > \omega_2$), which emits anti-Stokes light with the frequency $2\omega_1$-ω_2. The nonlinearity in the CARS is considered to contribute to improving the spatial resolution and intensity of the signal. Our theory reproduces the large enhancement of CARS signal by LSPR even for that associated with the optical forbidden electronic transitions of excitons in a semiconductor quantum dot. The third demonstration is for the TEPL. The molecule is expressed with the nonlocal susceptibility which can describe the optically forbidden transition with several nodes inside the molecule. We can treat Green's function as a function of frequency, which is an advantage over the previous TEPL theory [5]. Because of this, we can correctly calculate photoluminescence even in the case where the resonance levels of the molecule largely shift or split due to the strong coupling between the gap plasmons and the molecule.

We hope that our theoretical methods contribute not only to analyzing the experimental results of tip-enhanced type microscopies but also to proposing novel physical and chemical functions of single molecules and nanostructures.

References

1. B. Yang, G. Chen, A. Ghafoor, Y. Zhang, Y. Zhang, Y. Zhang, Y. Luo, J. Yang, V. Sandoghdar, J. Aizpurua, Z. Dong, and J. G. Hou, "Sub-nanometre resolution in single-molecule photoluminescence imaging," Nature Photonics **14**, 693, 2020.
2. H. Imada, M. Imai-Imada, K. Miwa, H. Yamane, T. Iwasa, Y. Tanaka, N. Toriumi, K. Kimura, N. Yokoshi, A. Muranaka, M. Uchiyama, T. Taketsugu, Y. K. Kato, H. Ishihara, and Y. Kim, "Single-molecule laser nanospectroscopy with micro–electron volt energy resolution," Science **373**, 95, 2021.
3. M. Takase, H. Ajiki, Y. Mizumoto, K. Komeda, M. Nara, H. Nabika, S. Yasuda, H. Ishihara and K. Murakoshi, “Selection-rule breakdown in plasmon-induced electronic excitation of an isolated single-walled carbon nanotube”, Nature Photonics **7**, 550-554 (2013)
4. J. Yamanishi, H. Yamane, Y. Naitoh, Y. J. Li, N. Yokoshi, T. Kameyama, S. Koyama, T. Torimoto, H. Ishihara and Y. Sugawara, “Optical force mapping at the single-nanometre scale”, Nature Communications **12**, 3865 (2021)
5. H. Yamane, J. Yamanishi, N. Yokoshi, Y. Sugawara and H. Ishihara, “Theoretical analysis of optically selective imaging in photoinduced force microscopy”, Optics Express **28**, 34787 (2020)
6. H. Yamane, N. Yokoshi, H. Oka, Y. Sugawara, and H. Ishihara, “Near-field circular dichroism of single molecules”, Optics Express **31**, 3415 (2023)

Near-field manipulation of light via nanoantennas: analytical tools for electromagnetic fields design and potential for photonic integration

M. F. Picardi[1*], C. P. T. McPolin[2], Jack J. Kingsley-Smith[3], Xudong Zhang[4], Shumin Xiao[4], A. V. Zayats[3], and F. J. Rodríguez-Fortuño[3]

[1]ICFO - Institut de Ciencies Fotoniques, The Barcelona Institute of Science and Technology, Castelldefels (Barcelona) 08860, Spain

[2]Digital Catapult, Ormeau Baths, 18 Ormeau Avenue, Belfast BT2 8HS, United Kingdom

[3]Department of Physics and London Centre for Nanotechnology, King's College London, Strand, London, WC2R 2LS, UK

[4]National Key Laboratory of Science and Technology on Advanced Composites in Special Environments, Ministry of Industry and Information Technology Key Lab of Micro-Nano Optoelectronic Information System, Harbin Institute of Technology (Shenzhen), Shenzhen 518055, People's Republic of China

[*]corresponding author: michela.picardi@icfo.eu

Abstract: Owing to its high photonic density of states, the near field of a source offers a remarkable playground for the manipulation of light via designed nanoantennas. Various nanostructures and nanoparticle arrangements have been optimized to achieve tailored behaviors, such as high Q-factor coupling to guided modes, directional near and far-field scattering, polarization-selective routing. In this talk we show how an integrated Janus dipole, embedded between two identical silicon waveguides, couples preferentially to only one of them.

Photonics-based technologies constitute the main platform for information transfer, with light driven communications being significantly faster and cheaper than their electronic counterparts. Similarly, the manipulation and processing of information could benefit from adopting all-optical techniques for signal processing and routing. Nanoantennas, nanostructured materials and nanoparticles provide a platform via which electromagnetic fields can be locally manipulated, so that the signal generated by an optical source can be redirected into different channels or converted into a different signal. In order to do so, the nanoantenna must be tailor-designed to the desired output. A simple local manipulation of electromagnetic fields can be achieved via the interference of multipolar sources, such as electric and magnetic dipoles. These point sources are easy to implement and integrate in photonics platforms. For example, it has been shown that the scattering from high-index dielectric nanoparticles, is accurately described by the superposition of electric and magnetic dipoles.

The interference between the fields of the electric and magnetic dipoles can give rise to interesting near-field directionalities or selective coupling to guided modes. Among the possible sources, a fascinating dipolar superposition is achieved with the Janus dipole. This source, which is comprised of two orthogonal linear electric and magnetic dipoles oscillating 90˚ out-of-phase, earns its name from its dual face behavior. In fact, it will excite a guided mode in a waveguide if facing it from one side, while showing a complete absence of coupling when facing it from the opposite side [1, 2]. Interestingly, when such a source is placed between two identical waveguides, its selective coupling means it will excite a guided mode exclusively in one of the two.
Mathematically, this is due to the matching of the reactive power, $Im(\mathbf{E}^* \times \mathbf{H})$, of the source and that of the excited guided mode. Conversely, the reactive power of the mode that does not get excited is exactly opposite to

that of the source.

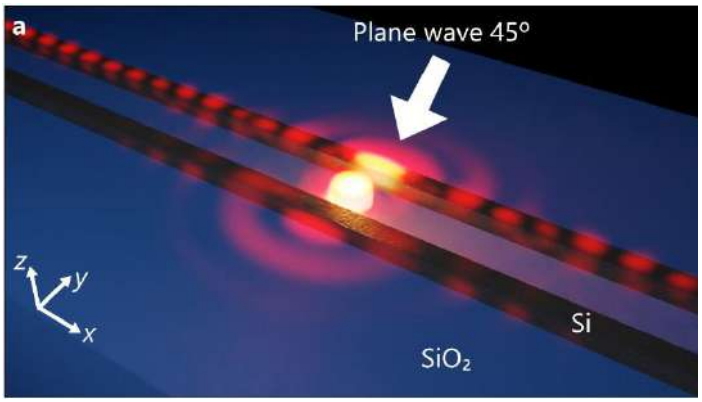

Figure 1: Janus dipole selective coupling to a Si waveguide. The dipole is induced in a Si nanocylinder illuminated by a plane wave (λ=1550 nm) at an angle of 45º.

In this talk we will present an experimental realization of a Janus dipole acting as a selective coupler between two identical waveguides [3]. The dipole is achieved illuminating a silicon nanocylinder placed on a silica substrate, illuminated at 45º by a plane wave at telecom wavelength (λ=1550 nm). Under this illumination, the electric and magnetic dipolar responses induced in the nanocylinder are of comparable amplitudes and 90º out-of-phase, so the scattered field is that of a Janus dipole. The source is embedded between two integrated silicon single-mode waveguides. Due to the selective coupling, the intensity contrast ratio between the modes excited in the two waveguides is measured to exceed threefold. The simulations further show the possibility of tuning this contrast ratio continuously between 1 and 14.

Advances in nanoparticle-mediated light manipulation can surely pave the way for faster and cheaper routing of information. In addition to that, locally modifying an electromagnetic field can facilitate designed energy transfer, for example implementing redirection or polarization conversion of the field emitted by a source. This has the potential to drive advances in light-based energy harvesting and collection.

References

1. Picardi, M. F., Zayats, A. V. and Rodríguez-Fortuño, F. J., "Janus and Huygens dipoles: near-field directionality beyond spin-momentum locking", Phys. Rev. Lett., 120(11), 117402, 2018.
2. Picardi, M. F. et al., "Experimental demonstration of linear and spinning Janus dipoles for polarisation- and wavelength-selective near-field coupling", Light: Sci. Appl. 8, 52, 2019.
3. Picardi, M. F., McPolin, C. P., Kingsley-Smith, J. J., Zhang, X., Xiao, S., Rodríguez-Fortuño, F. J., and Zayats, A. V., "Integrated Janus dipole source for selective coupling to silicon waveguide networks", Applied Physics Reviews, 9(2), 021410, 2022.

Distinguishing Polaritonic from Charge Transfer Excitations in a Metal-Molecule System

L. Cascino[1,2], S. Corni[3,4], and S. D'Agostino[1,2,5*]

[1]Mathematics and Physics Department "*E. De Giorgi*", University of Salento, Lecce 73100, Italy
[2]Institute of Nanotechnology, National Research Council (CNR-NANOTEC), Lecce 73100
[3]Dipartimento di Scienze Chimiche, Università di Padova, 35131 Padova, Italy
[4]CNR Istituto Nanoscienze, 41124 Modena, Italy
[5]Center for Biomolecular Nanotechnologies, Istituto Italiano di Tecnologia, Arnesano (LE) 73010
[*]corresponding author: stefania.dagostino@nanotec.cnr.it

Abstract: Polariton chemistry is a very recent research field exploiting the effects of strong coupling interaction on the chemistry of an emitter which presents a huge plethora of applications in life sciences. In this work, we propose for the first time a fully atomistic computational study within the framework of Time-Dependent Density Functional Theory (TD-DFT) of a selected direction on the potential energy surfaces of the first electronic states of an azobenzene photoswitch interacting with a tetrahedral Ag_{20} nanocluster sustaining plasmons.

Inspired by the pioneering work in 2012 by Ebbesen's group [1], polaritonic chemistry, i.e., the field caring of manipulating chemical structure and reactions through the formation of polaritons, hybrid half-light half-matter states, has become the attraction of several experimental and theoretical researches in the last few years.
From a theoretical point of view, the problem of the perturbations induced on the potential energy surfaces of a molecule by photonic modes has been largely faced in the framework of Quantum Electrodynamics (QED) [2].
In the endeavor to take into account the real atomistic structure of matter in hybrid metal-molecule systems involving charge transfer and tunneling effects, fully quantum-mechanical (QM) approaches seem to overcome QED and other approaches approximating matter component. In this regard, *Time-Dependent Density Functional Theory* (TD-DFT) has been shown to be the unique venue to pursue, given its favorable computational cost, especially in light of the active development for its applicability in large-scale applications.
In this work a fully-QM scheme, based on an atomistic description in the linear response framework of the TD-DFT of both the matter and light components, is proposed to analyze a chosen isomerization pathway for an azobenzene molecule interacting with a plasmonic nanocluster put in its proximities (Fig. 1). Azobenzene represents one of the simplest photochromes able to interconvert between trans- and cis- forms. Despite its isomerization process has not yet been fully understood, numerous applications have been developed: in biomedicine, in bioimaging, in photopharmacology, etc. The metallic counterpart is a tetrahedral cluster of Ag_{20}. This choice is due to the fact that this cluster has a simple spectrum dominated by only one narrow excitation in the same spectra range of Azobenzene which can be associated to a localized plasmon [3]. Recent works have shown that the strong coupling between surface plasmon-polariton mode and excitons could lead to the formation of hybrid states, namely polaritons or plexcitons [4]. Here we show the onset of these new states for particular conditions and how these can modify the potential energy landscape of the molecule. Moreover we introduce a new figure of merit defined *Polaritonic Index* (PI) which allow us to identify all the hybrid excitations and among them to distinguish polaritonic from charge-transfer states.

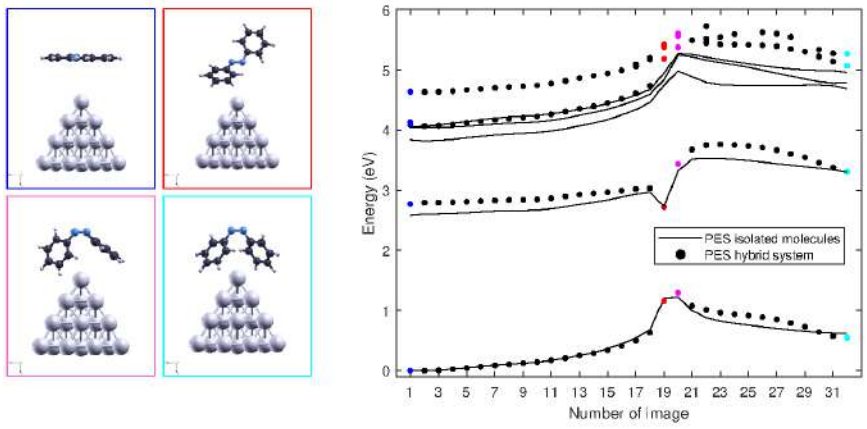

Fig. 1 (a) Sketches of the 4 hybrid systems corresponding to Azobenzene put 5Å away from the cluster. (b) Reconstruction of the first PESs of the hybrid system. Dots represent the TD-DFT collective excitations with a polaritonic index larger than 1.99. Colored ones refer to the configurations shown on the left side. The PESs of the first 5 electronic states of the Azobenzene alone are reported (in black continuous line) for a comparison.

This quantity is a measure of the ratio between the transition density per molecular atom and the one per metallic atom and gives for each frequency the nature of excitation. This quantity revealed to be a good figure of merit to distinguish the nature or the origin of the collective excitation of the entire system: states with PI near to 0 are purely metallic; states with PI near to 1 are half-light half-matter states (where with light we refer to the plasmon); states with PI much larger than 1 are, instead, molecular ones.

Beyond polaritonic states, responsible for the blue-shift and the perturbation of the S_2 and S_3 PoPESs, through a PI-based analysis, a second category of hybrid states appeared: the charge-transfer (CT) states. Distinguished in short-range and long-range CT states, these states involve excitations moving electronic charge from a system (donor) to the other one (acceptor). They represent a cardinal phenomenon in many areas of science and a challenging theoretical issue. Here we demonstrate that an *Ab Initio* modelling of strong coupling between molecular excitations and LSPs discloses a picture of polaritonic chemistry much more richer with respect to that expected on the bases of Jaynes-Cummings like Hamiltonians.

References

1. Henzl, J., M. Mehlhorn, H. Gawronski, K.H. Rieder, and K. Morgenstern, “Reversible cis–trans isomerization of a single azobenzene molecule”, Angew. Chem. Int, Vol. 45, No. 4, 603–606, 2006.
2. Feist, J., J. Galego, and F.J. Garcia-Vidal, “Polaritonic chemistry with organic molecules”, ACS Photonics, Vol. 5, No. 1, 205-216, 2018.
3. D’Agostino, S., R. Rinaldi, G. Cuniberti and F. Della Sala, “Density functional tight binding for quantum plasmonics”, J. Phys. Chem. C ., Vol. 122, No. 34, 19756– 19766, 2018.
4. Giannone, G., F. Della Sala and S. D’Agostino, “Atomistic investigation of hybrid plasmonic systems”, Nanomater. Nanotechnol., Vol. 9, 1847980419856534, 2019.

Symmetry and topology in photonic crystals

Thomas Christensen[1]

[1] Department of Electrical and Photonics Engineering, Technical University of Denmark, Denmark
[*] thomas@dtu.dk

Abstract: Symmetry imposes strong constraints on the frequency dispersion and topology of photonic crystal bands. I will describe several interesting consequences of these constraints, highlighting implications for the connectivity of photonic bands, the prevalence of photonic topology, and the outlook for having frequency-isolated topological degeneracies at high-symmetry points in the Brillouin zone.

The transverse polarization of photons produces a symmetry singularity at zero frequency which distinguishes the lowest bands of photonic crystals from those of other quasiparticles. I will discuss our recent work [1] on how symmetry, topology, and this singularity lead to constraints on where the first photonic band gap can be opened. These constraints can be incorporated and solved by a symmetry-based framework that allows us to determine the minimum connectivity of bands below the first photonic gap as well as the any associated symmetry-identifiable topology. By systematically examining the topology of all possible minimal configurations, we find a new, uniquely photonic topological effect which obstructs symmetry-allowed gap-openings by requiring the presence of topological nodal lines.

The framework developed to answer these questions enables us to leverage recent methods from electronic topology – known as symmetry indicators or topological quantum chemistry – to the photonic context: I will highlight a few interesting examples of the opportunities that this brings, including an assessment of the prevalence of topology in two-dimensional photonic crystals and whether frequency-isolated Weyl points can exist at high-symmetry points of the Brillouin zone.

References

1. T. Christensen, H.C. Po, J.D. Joannopoulos, & M. Soljačić, “Location and Topology of the Fundamental Gap in Photonic Crystals”, Phys. Rev. X **12**, 021066 (2022).

Enhanced and Tunable Kerr effect on InSb/graphene hybrid magnetoplasmonic structure at Terahertz waves

M. Ben Rhouma[1*], K. Edee[2], and B. Guizal[3]

[1] ESYCOM lab, Univ Gustave Eiffel, CNRS UMR 9007, F-77454 Marne-la-Vallee, France
[2]Université Clermont Auvergne, Institut Pascal, BP 10448, F-63000 Clermont-Ferrand, France, CNRS, UMR 6602, France
[3]Laboratoire Charles Coulomb (L2C), UMR 5221 CNRS-Université de Montpellier, F-34095 Montpellier, France
[*]corresponding author: maha.ben-rhouma@univ-eiffel.fr

Abstract: In this work, we propose a novel hybrid magneto-plasmonic structure based on graphene and doped InSb to enhance the magneto-optical Kerr effect at terahertz frequencies. The structure is composed of a 1D periodic doped InSb inlayed between a metallic backgate and a dielectric/doped graphene sheet. By computing the optical response of this structure, we show an enhanced and large Kerr rotation in a wide range of THz frequencies compared to that induced by a single graphene sheet and/or a doped magnetized InSb .

Magneto-optical (MO) effects such as Faraday and Kerr effects are phenomena referring to changes in the polarisation state of light after interacting with a magnetic material and describe the interaction between optical and magnetic materials, which plays a fundamental role in the technological applications, such as optical isolators and magnetic sensors. The ability to enhance MO effects is then crucial for designing several devices. One way to achieve that is to combine plasmonics and magnetics to give rise to the magnetoplasmonics field which became, recently, an active topic of research.

Graphene magneto-plasmonics, the research area that combines magnetic and plasmonic properties of graphene, has attracted considerable interest in recent years, thanks to the unique and unusual properties of the surface magnetoplasmons supported by graphene [1]. These properties have been exploited to design many tunable plasmonic nonreciprocal devices in the terahertz regime which became attractive for its benefits in various applications such as medical imaging, biological studies, space exploration, communications and security. Doped InSb has been recently exploited in magneto-plasmonic devices for the terahertz range as a potential MO material and showed interesting magneto-plasmonic properties in this frequency range. In this work, we propose to combine the interesting properties of both materials in the THz regime by hybridizing their surface magnetoplasmons which give rise to a large and enhanced magneto-optical effect. The studied structure consists of a 1D periodic doped InSb inlayed between a metallic backgate and a dielectric/doped graphene sheet and an external static magnetic field can be applied. We compute the magneto-optical spectra with the Polynomial Modal Method (PMM) and study the magneto-optical Kerr effect on such structures. We show an enhanced and large Kerr rotation in a wide range of THz frequencies compared to that induced by a single graphene sheet and/or a doped magnetized InSb. It is found that the underlying mechanism is due to the hybrid plasmonic waveguide guided modes resulting from the strong coupling between the graphene surface magneto-plasmons (GSMP) and the surface magneto-plasmons across the InSb. Moreover, calculation results demonstrate that this large Kerr rotation can be tuned by optimizing the graphene properties and structure parameters such as the graphene fermi level and the applied magnetic field. Our findings may offer a promising way in the design of new THz magneto-optical devices.

References

1. Jun Guo, Xiaoyu Dai, Yuanjiang Xiang, and Dingyuan Tang , "Excitation of graphene magneto-plasmons in terahertz range and giant Kerr rotation", Journal of Applied Physics 125, 013102 (2019)

Hybrid Anapole States: Theory and Applications

A. S. Shalin[1,2*], A. V. Kuznetsov[1,3] and V. Bobrovs[3]
[1]Center for Photonics and 2D Materials, Moscow Institute of Physics and Technology, Dolgoprudny, Russia
[2]Moscow State University, Faculty of Physics, Moscow, 119991, Russian Federation
[3]Institute of Telecommunications, Riga Technical University, Riga, Latvia
[*]corresponding author: alexandesh@gmail.com

Abstract: In this paper, we propose an alternative approach to Huygens' metasurfaces for implementing phase control of the radiation passing through the metasurface - the hybrid anapole regime. This regime has a number of advantages, which make it possible to significantly simplify the design the new generation of photonic devices.

In recent years, dielectric nanophotonics has become more and more popular. In particular, thanks to the possibility of controlling resonances, it becomes possible to obtain previously inaccessible effects [1-4]. Their use in designing a metasurface makes it possible to create efficient ultra-compact photonic devices of a new generation [5-9].

In particular, the recently discovered hybrid anapole regime has great potential [10-12]. This regime is a resonant combination of multipole minima up to a magnetic quadrupole at one frequency, which can be obtained by careful selection of the geometrical parameters of the nanoscatterer. A metasurface consisting of such metaatoms has a number of useful properties that are not available for the currently used Huygens metasurfaces. For example, metaatoms in the hybrid anapole regime do not have a field in the far zone, which opens up new possibilities for designing metasurfaces. One of the main properties of such meta-atoms is their transparency. Due to the unique combination of multipoles, the metasurface of such metaatoms is practically transparent at a certain wavelength, which makes this regime a promising platform for nanooptics. Using such metaatoms, it becomes possible to create a structure with randomly distributed elements, excluding the lattice effect and to arrange metaatoms close to each other, creating a superdense metasurface. By varying the geometric parameters and staying within the transparency window of the anapole, one can control the phase on each individual metaatom. By changing the radius of the metaatom by 10 nm at its value of 127 nm in the hybrid anapole, it is possible to shift the phase by about 40 degrees. This can be useful in various holographic applications, ultra-thin lenses and other applications that require phase control of the transmitted radiation at full transmission. In addition, the metasurface in the hybrid anapole regime is not sensitive to the substrate material, which makes it possible to use a large library of substrates depending on the tasks and methods set.

Thus, in this paper, we have developed the concept of a metasurface that has a number of properties that are useful for practical applications, such as, for example, almost complete transparency at the anapole wavelength, insensitivity to the environment and neighboring metaatoms. Based on such metasurfaces, it is possible to create various applications for nanophotonics, such as sensors, ultrathin lenses, and various holographic applications.

The authors gratefully acknowledge the financial support from the Ministry of Science and Higher Education of the Russian Federation (Agreement No. № 075-15-2022-1150). The investigation of the hybrid

anapole regimes has been partially supported by the Russian Science Foundation (Grant No. 21-12-00151). V.B. acknowledges the support of the Latvian Council of Science, project: DNSSN, No. lzp-2021/1-0048.

References

1. Barhom, H., A.A. Machnev, R.E. Noskov, A. Goncharenko, E.A. Gurvitz, A.S. Timin, V.A. Shkoldin, S. V. Koniakhin, O.Y. Koval, M. V. Zyuzin, A.S. Shalin, I.I. Shishkin and P. Ginzburg, "Biological Kerker Effect Boosts Light Collection Efficiency in Plants," Nano Lett., Vol. 19, 7062–7071, 2019.

2. Terekhov, P.D., Evlyukhin, A.B., Redka, D., Volkov, V.S., Shalin, A.S. and A. Karabchevsky, "Magnetic Octupole Response of Dielectric Quadrumers," Laser Photon Rev, Vol. 14, 1900331, 2020.

3. Kuznetsov A. V., A. Canós Valero, H. K. Shamkhi, P. Terekhov, X. Ni, V. Bobrovs, M. V. Rybin and Alexander S. Shalin, "Special scattering regimes for conical all-dielectric nanoparticles," Sci. rep., Vol. 12, 21904, 2022.

4. Terekhov, P.D., K. V. Baryshnikova, Y. Greenberg, Y.H. Fu, A.B. Evlyukhin, A.S. Shalin and A. Karabchevsky, "Enhanced absorption in all-dielectric metasurfaces due to magnetic dipole excitation," Sci Rep., Vol. 9, 1–9, 2019.

5. Shamkhi, H.K., A. Sayanskiy, A. Canós Valero, A.S. Kupriianov, P. Kapitanova, Y.S. Kivshar, A.S. Shalin and V.R. Tuz, "Transparency and perfect absorption of all-dielectric resonant metasurfaces governed by the transverse Kerker effect," Phys Rev Mater, Vol. 3, 1–10, 2019.

6. Novitsky, D. V., A. Karabchevsky, A. V. Lavrinenko, A.S. Shalin and A. V. Novitsky, "PT symmetry breaking in multilayers with resonant loss and gain locks light propagation direction," Phys Rev B, Vol. 98, 125102, 2018.

7. Canós Valero, A., D. Kislov, E.A. Gurvitz, H.K. Shamkhi, A.A. Pavlov, D. Redka, S. Yankin, P. Zemánek and A.S. Shalin, "Nanovortex‐Driven All‐Dielectric Optical Diffusion Boosting and Sorting Concept for Lab‐on‐a‐Chip Platforms," Advanced Science, Vol. 7, 1903049, 2020.

8. Kostina, N.A., D.A. Kislov, A.N. Ivinskaya, A. Proskurin, D.N. Redka, A. Novitsky, P. Ginzburg and A.S. Shalin, "Nanoscale Tunable Optical Binding Mediated by Hyperbolic Metamaterials," ACS Photonics, Vol. 7, 425–433, 2020.

9. Novitsky, D. V., A.S. Shalin, D. Redka, V. Bobrovs and A. V. Novitsky, "Quasibound states in the continuum induced by PT symmetry breaking," Phys Rev B, Vol. 104, 085126, 2021.

10. Ospanova, A.K., A. Basharin, A.E. Miroshnichenko and B. Luk'yanchuk, "Generalized hybrid anapole modes in all-dielectric ellipsoid particles [Invited]," Opt Mater Express, Vol. 11, 23, 2021.

11. Canós Valero, A., E.A. Gurvitz, F.A. Benimetskiy, D.A. Pidgayko, A. Samusev, A.B. Evlyukhin, V. Bobrovs, D. Redka, M.I. Tribelsky, M. Rahmani, K.Z. Kamali, A.A. Pavlov, A.E. Miroshnichenko and A.S. Shalin, "Theory, Observation, and Ultrafast Response of the Hybrid Anapole Regime in Light Scattering," Laser Photon Rev., Vol. 15, 2100114, 2021.

12. Kuznetsov, A. V., A. Canós Valero, M. Tarkhov, V. Bobrovs, D. Redka and A.S. Shalin, "Transparent hybrid anapole metasurfaces with negligible electromagnetic coupling for phase engineering," Nanophotonics, Vol. 10, 4385–4398, 2021.

Collective effects in periodic arrays of plasmonic antennas

J. R. Deop-Ruano[1] **and A. Manjavacas**[1, 2*]

[1]Instituto de Óptica (IO-CSIC), Consejo Superior de Investigaciones Científicas, 28006 Madrid, Spain
[2]Department of Physics and Astronomy, University of New Mexico, Albuquerque, New Mexico 87106, USA
*corresponding author: a.manjavacas@csic.es

Abstract: Periodic arrays of metallic nanostructures present collective modes commonly known as lattice resonances, which arise from the coherent scattering between the constituents of the array. Thanks to their collective nature, lattice resonances give rise to strong optical responses with an extremely narrow spectral profile. Despite the large effort devoted to investigating the properties of lattice resonances, many aspects remain unexplored. In this talk, we will discuss fundamental aspects of the optical response of periodic arrays of nanostructures.

Periodic arrays of metallic nanostructures are able to support collective modes commonly known as lattice resonances, which arise from the coherent scattering between the constituents of the array. Thanks to their collective nature, lattice resonances give rise to strong optical responses with an extremely narrow spectral profile. In this talk, we will discuss fundamental aspects of the optical response of periodic arrays of nanostructures. In particular, we will analyze the conditions under which a periodic array of graphene nanodisks can support lattice resonances and characterize their optical properties. Furthermore, we will investigate how these properties change when the array is illuminated with a light beam of finite width. We will also discuss the conditions required for an array to sustain lattice resonances with an out-of-plane nature. The results of this work shed light on the excitation of collective lattice resonances and provide new avenues to exploit their extraordinary properties.

Chiral sensing with semiconductor nanophotonics

Alberto G. Curto[1,2,3]

[1] Photonics Research Group, Ghent University-imec, Ghent, Belgium

[2] Center for Nano- and Biophotonics, Ghent University, Ghent, Belgium

[3] Department of Applied Physics and Eindhoven Hendrik Casimir Institute, Eindhoven University of Technology, Eindhoven, The Netherlands

[*]Corresponding Author: Alberto.Curto@UGent.be

Abstract: Detecting molecular chirality is crucial in biochemistry. It is, however, limited by low sensitivity at low concentrations. I will discuss our progress to push the limits of chiral sensing by exploiting semiconductor nanophotonics.

Chirality plays a pivotal role in the functionality of biomolecules such as proteins, amino acids, and carbohydrates. Circular dichroism can distinguish enantiomers thanks to a small difference in the absorption of circularly polarized light. However, chiral sensing faces significant limitations due to inherently weak chiroptical signals. It is thus severely limited by low sensitivity and low spatial resolution. As a result, it is challenging to resolve the chirality of individual nanoscale objects using light for critical applications such as detecting protein aggregates linked to various diseases. In this presentation, I will discuss our progress in pushing the sensitivity limits of optically resolvable chirality by exploiting semiconductor nanophotonics. I will show several strategies to optimize chiral molecular sensors based on silicon metasurfaces to detect low molecular concentrations. Specifically, I will present our recent results on tailoring silicon nanostructures to enhance polarized fluorescence [1, 2] and Raman spectroscopies, increase optical chirality and maximize chirality transfer [3, 4]. Our results promise an increase in sensitivity towards the detection of single chiral molecules compatible with high-resolution imaging.

Acknowledgements. This work was financially supported by The Netherlands Organisation for Scientific Research (NWO) through an NWO START-UP Grant (740.018.009) and the European Research Council (ERC) under the European Union's Horizon 2020 research and innovation program (grant agreement 948804, CHANSON).

References

1. A.F. Cihan, A.G. Curto, S. Raza, P. G. Kik, M. L. Brongersma “Silicon Mie resonators for highly directional light emission from monolayer MoS_2” *Nature Photonics* 12, 284–290, 2018.
2. S. Murai, G. W. Castellanos, T. V. Raziman, A. G. Curto, J. G. Rivas, “Enhanced light emission by magnetic and electric resonances in dielectric metasurfaces”, *Adv. Opt. Mat.* 8 (16), 1902024, 2020.
3. E. Mohammadi, A. Tittl, K. L. Tsakmakidis, T. V. Raziman, A. G. Curto, “Dual Nanoresonators for Ultrasensitive Chiral Detection,” *ACS Photonics*, 8, 6, 1754, 2021.
4. T. V. Raziman, R. H. Godiksen, M. A. Müller, A. G. Curto, “Conditions for Enhancing Chiral Nanophotonics near Achiral Nanoparticles,” *ACS Photonics* 6, 10, 2583, 2019.

Plasmonics in a variable-temperature thermodynamic bath

M. Magnozzi[1*], M. Ferrera[1], L. Mattera[1], M. Canepa[1] and F. Bisio[2]

[1]Optmatlab, Dipartimento di Fisica, Università di Genova, Italy
[2]CNR-SPIN, Genova, I-16152 Genova, Italy
[*]corresponding author: magnozzi@fisica.unige.it

Abstract: The emerging field of thermoplasmonics requires an accurate understanding of the temperature-dependent complex permittivities of plasmonic materials. We report the temperature-dependent complex permittivities of gold and silver - two of the most widely studied plasmonic materials – in a wide spectral range spanning from the UV to the NIR; we build on this knowledge to discuss fascinating physical mechanisms in plasmonic nanoparticles, such as surface premelting, ultrafast relaxation dynamics, and the comparison between interband and plasmonic excitations.

The conversion of electromagnetic energy into heat within nanosized metallic nanoparticles is the basic working principle of thermoplasmonics. Although many fundamental aspects and applications of thermoplasmonics have been exploited, the possibility of a-priori assessing what temperatures will be achieved by thermoplasmonics heating in a given system is still somewhat out of grasp. One of the factors that play a role in this is the scant knowledge of the temperature-dependent complex permittivities of the plasmonic materials involved.

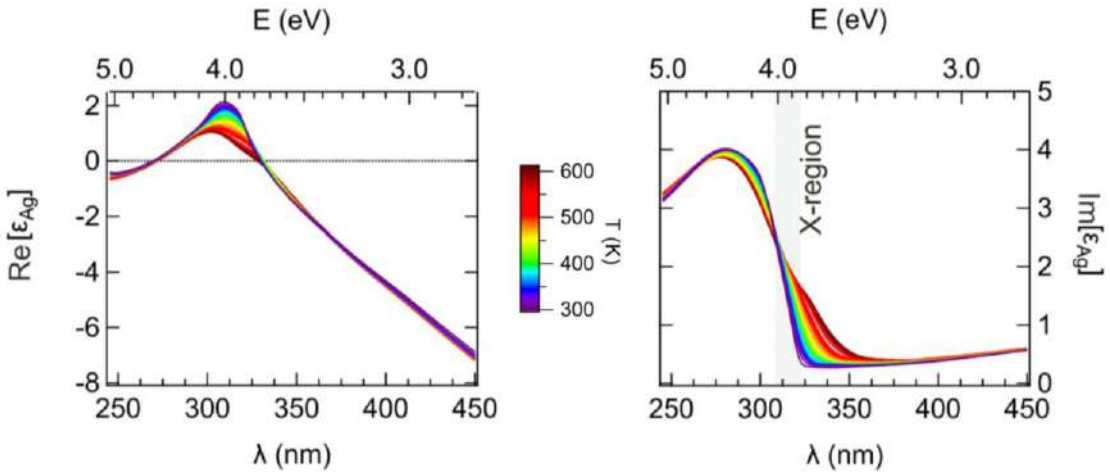

Figure 1. Complex permittivity of silver in the 300 K - 600 K temperature range and 250-450 nm spectral range.

We report the experimental extraction of the temperature-dependent complex permittivities of gold [1] and silver [2] (see also Figure 1), two widely used plasmonic metals, in a spectral range encompassing the UV to the NIR, by means of a customized high-vacuum cell for spectroscopic ellipsometry [3]. For both metals, we address the RT - 600 K range, whereupon sizable and sometimes unexpected variations occur. For instance in silver, the relative increase of the imaginary part of permittivity at 340 nm was found to be around 500% when temperature is raised from room temperature to 600 K, suggesting the possibility of self-limiting plasmonic heating phenomena, or exploitation as self-calibrated nano-thermometers. Such large temperature-dependent variations must be taken into account whenever the performance of Ag- and Au- based thermoplasmonic systems has to be evaluated.

Applications relevant for thermoplasmonics will be discussed that are based on the permittivity data, including the detection of surface premelting[1], the thermometric calibration of the ultrafast relaxation dynamics, the comparison between interband and plasmonic absorption, and the difference between light- and temperature-induced thermal effects in plasmonic Au nanoparticles.

References

1. M. Magnozzi, M. Ferrera, L. Mattera, M. Canepa, F. Bisio. Plasmonic of Au nanoparticles in a hot thermodynamic bath. *Nanoscale*, 11, 1140, 2019
2. M. Ferrera, M. Magnozzi, F. Bisio, M. Canepa. Temperature-dependent permittivity of silver and implications for thermoplasmonics, *Phys. Rev. Mater*., Vol. 3, 105201, 2019.
3. M. Magnozzi, F. Bisio, and M. Canepa, *Appl. Surf. Sci*. 421**,** 651, 2017.

PLASMONIC SENSING AND SWITCHING: FANO, PIT and MIM RESONNANCES

Zouheir Sekkat*
University Mohammed V, Rabat, Morocco;
MAScIR, University Mohammed VI Polytechnic, Ben Guerir, Morocco.

*z.sekkat@mascir.ma

ABSTRACT

In this talk, I will discuss coupling of modes in layered nano-structures which result in Fano resonances as well as plasmon induced transparency (PIT) and metal-insulator-metal (MIM) hybrid modes. Such structures are easy to prepare, i.e. they do not require complicated procedures of nano-fabrication, and they show superior sensing and switching capabilities compared to convensional structures based on conventional surface plasmon resonance.
Keywords: Plasmonic Resonnaces, Switching, Sensing, Fano.

Quasi-BIC on a hybrid anapole regime in silicon metasurfaces

A. V. Kuznetsov[1,2*], **V. Bobrovs**[1] **and A. S. Shalin**[2,3]

[1]Institute of Telecommunications, Riga Technical University, Riga, Latvia
[2]Center for Photonics and 2D Materials, Moscow Institute of Physics and Technology, Dolgoprudny, Russia
[3]Moscow State University, Faculty of Physics, Moscow, 119991, Russian Federation
[*]corresponding author: alexey.kuznetsov98@gmail.com

Abstract: In this work, we show the possibility of simultaneously obtaining a high-Q quasi bound states in the continuum (quasi-BIC) on a silicon conical particle at the wavelength of the hybrid anapole regime. Based on such particles, a metasurface was developed that has a high sensitivity to the refractive index of the environment, which opens up the possibility of creating ultra-compact sensors.

Fully dielectric nanophotonics opens up new horizons in the creation of various new generation devices that surpass existing analogues in terms of efficiency and compactness [1-4]. In particular, various forms of nanoscatterers are of great interest, due to the non-standard geometry of which it becomes possible to obtain a number of new effects due, for example, to breaking the symmetry of an object [5]. Based on such nanoscatterers, it is possible to create metasurfaces, with the help of which controlling the light at the nanoscale can be achieved. For example, using quasi bound states continuum (quasi-BIC) in a metasurface makes it possible to create high-Q resonances in devices [6,7]. To describe the properties of nanoscatterers, a multipole decomposition is used. It has become possible to develop various effects based on different multipoles combinations [8-10], such as a hybrid anapole regime, which can be used to control the phase of the radiation passing through the structure, and there is no strict restriction on the position of the meta-atoms and the substrate material [11-13].

In this paper, we demonstrate the possibility of obtaining a high-quality state, called quasi-BIC, on magnetic quadrupole at a frequency coinciding with the recently discovered hybrid anapole regime (one multipole in q-BIC regime and others are negligible because of the hybrid anapole state) on truncated cone silicon particles. Using such particles as meta-atoms, the optical properties of a structure were investigated numerically.

Due to the unique combination of several effects, it is possible to obtain a completely transparent metasurface, the optical properties of which change significantly when the refractive index of the environment changes. By changing the refractive index of air from 1 to 1.05, the transmission resonance shifts to the red region of 10 nm, and the transmission coefficient at the resonance wavelength changes by about 60%. Based on such a structure, it becomes possible to create an ultrathin sensitive sensor for changing the refractive index of the medium.

The authors gratefully acknowledge the financial support from the Ministry of Science and Higher Education of the Russian Federation (Agreement No. № 075-15-2022-1150). The investigation of the hybrid anapole regimes has been partially supported by the Russian Science Foundation (Grant No. 21-12-00151). V.B. acknowledges the support of the Latvian Council of Science, project: DNSSN, No. lzp-2021/1-0048.

References

1. Shamkhi, H.K., A. Sayanskiy, A. Canós Valero, A.S. Kupriianov, P. Kapitanova, Y.S. Kivshar, A.S. Shalin and V.R. Tuz, "Transparency and perfect absorption of all-dielectric resonant metasurfaces governed by the transverse Kerker effect," Phys Rev Mater, Vol. 3, 1–10, 2019.
2. Novitsky, D. V., A. Karabchevsky, A. V. Lavrinenko, A.S. Shalin and A. V. Novitsky, "PT symmetry breaking in multilayers with resonant loss and gain locks light propagation direction," Phys Rev B, Vol. 98, 125102, 2018.
3. Canós Valero, A., D. Kislov, E.A. Gurvitz, H.K. Shamkhi, A.A. Pavlov, D. Redka, S. Yankin, P. Zemánek and A.S. Shalin, "Nanovortex‐Driven All‐Dielectric Optical Diffusion Boosting and Sorting Concept for Lab‐on‐a‐Chip Platforms," Advanced Science, Vol. 7, 1903049, 2020.
4. Kostina, N.A., D.A. Kislov, A.N. Ivinskaya, A. Proskurin, D.N. Redka, A. Novitsky, P. Ginzburg and A.S. Shalin, "Nanoscale Tunable Optical Binding Mediated by Hyperbolic Metamaterials," ACS Photonics, Vol. 7, 425–433, 2020.
5. Kuznetsov A. V., A. Canós Valero, H. K. Shamkhi, P. Terekhov, X. Ni, V. Bobrovs, M. V. Rybin and Alexander S. Shalin, "Special scattering regimes for conical all-dielectric nanoparticles," Sci. rep., Vol. 12, 21904, 2022.
6. Rybin M. V., K. L. Koshelev, Z. F. Sadrieva, K. B. Samusev, A. A. Bogdanov, M. F. Limonov, and Y. S. Kivshar, "High-Q Supercavity Modes in Subwavelength Dielectric Resonators," Phys. Rev. Lett., Vol. 119, 243901, 2017.
7. Novitsky, D. V., A.S. Shalin, D. Redka, V. Bobrovs and A. V. Novitsky, "Quasibound states in the continuum induced by PT symmetry breaking," Phys Rev B, Vol. 104, 085126, 2021.
8. Barhom, H., A.A. Machnev, R.E. Noskov, A. Goncharenko, E.A. Gurvitz, A.S. Timin, V.A. Shkoldin, S. V. Koniakhin, O.Y. Koval, M. V. Zyuzin, A.S. Shalin, I.I. Shishkin and P. Ginzburg, "Biological Kerker Effect Boosts Light Collection Efficiency in Plants," Nano Lett., Vol. 19, 7062–7071, 2019.
9. Terekhov, P.D., Evlyukhin, A.B., Redka, D., Volkov, V.S., Shalin, A.S. and A. Karabchevsky, "Magnetic Octupole Response of Dielectric Quadrumers," Laser Photon Rev, Vol. 14, 1900331, 2020.
10. Terekhov, P.D., K. V. Baryshnikova, Y. Greenberg, Y.H. Fu, A.B. Evlyukhin, A.S. Shalin and A. Karabchevsky, "Enhanced absorption in all-dielectric metasurfaces due to magnetic dipole excitation," Sci Rep., Vol. 9, 1–9, 2019.
11. Ospanova, A.K., A. Basharin, A.E. Miroshnichenko and B. Luk'yanchuk, "Generalized hybrid anapole modes in all-dielectric ellipsoid particles [Invited]," Opt Mater Express, Vol. 11, 23, 2021.
12. Canós Valero, A., E.A. Gurvitz, F.A. Benimetskiy, D.A. Pidgayko, A. Samusev, A.B. Evlyukhin, V. Bobrovs, D. Redka, M.I. Tribelsky, M. Rahmani, K.Z. Kamali, A.A. Pavlov, A.E. Miroshnichenko and A.S. Shalin, "Theory, Observation, and Ultrafast Response of the Hybrid Anapole Regime in Light Scattering," Laser Photon Rev., Vol. 15, 2100114, 2021.
13. Kuznetsov, A. V. , A. Canós Valero, M. Tarkhov, V. Bobrovs, D. Redka and A.S. Shalin, "Transparent hybrid anapole metasurfaces with negligible electromagnetic coupling for phase engineering," Nanophotonics, Vol. 10, 4385–4398, 2021.

Resonant hot carrier generation due to coherent coupling between plasmon and electron-hole pairs in nano metal array

S. Inoue [1*], T. Yokoyama [1] and H. Ishihara [1,2]

[1] Graduate School of Engineering Science, Osaka Univ., Japan
[2] Center for Quantum Information and Quantum Biology, Osaka Univ., Japan
[*]corresponding author: inoue.s@opt.mp.es.osaka-u.ac.jp

Abstract: Plasmon excitation in the metallic nanostructures generates strong electric fields. In this situation, plasmon can couple with electron-hole pairs via transverse and longitudinal field. In this study, we investigate the relation between this coherence and hot carrier generation in an array of nanoscale metals. As a result, this coherence contributes to a resonant energy transfer from plasmon to electron-hole pairs. When the interactions between plasmons exist, this coherence shows synergetic effect with it as an 'antenna effect'.

Plasmon excitation and plasmonics are one of the most attractive electromagnetic responses in metals. It is utilized for sensor, photovoltaics, photosynthesis, nano heater, etc [1,2]. A hot carrier generation is a significant physics for such light-induced phenomena and applications. The hot carrier is a nonequilibrium electron distribution, where the electrons have exceeded energy more than that of thermal distribution. Then, the hot carriers can be utilized for oxidation-reduction reaction and photocurrent. Therefore, an improvement of efficiency of the hot carrier generation is significant subject. The array structure of nanometals and the hybridization of plasmon excitations in the array could provide such significant achievements for the hot carrier generation [3]. Recently, X. Shi, et al., have studied an enhancement of the hot carrier generation by the design of spatial structure of electromagnetic field based on cavity structures [4].

In previous many theoretical studies for the hot carrier generation mechanism, relaxation and damping processes have been considered [5], where the photon energy of incident light is transferred unidirectionally to the hot carrier. Such mechanisms are based on the electron-electron interaction, which is a part of the longitudinal field. Recently, we have discussed a coherent coupling between the plasmon and electron-hole pair excitations owing to a transverse field in a single nanostructure field [6], where bidirectional energy transfers could be obtained.

In this study, by mimicking [4], we consider a metallic chain array on a cavity structure (Fig. 1), where the plasmon excitations in the metals couple to a photon of the cavity mode. The plasmons in the metals couple directly with each other. Moreover, we assume a novel coherent coupling between the plasmon and electron-hole pairs in respective metals. This coupling is mediated by a radiative field. Based on this minimal model, we investigate the hot carrier generation enhancement

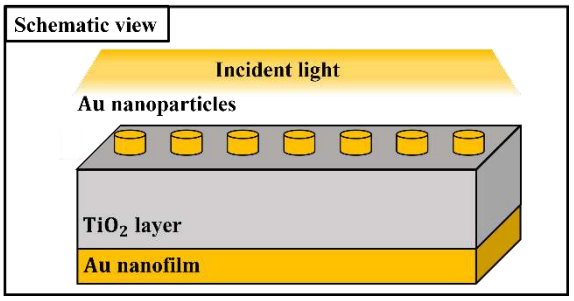

Figure 1: Schematic view of a metallic chain array connected to a cavity structure.

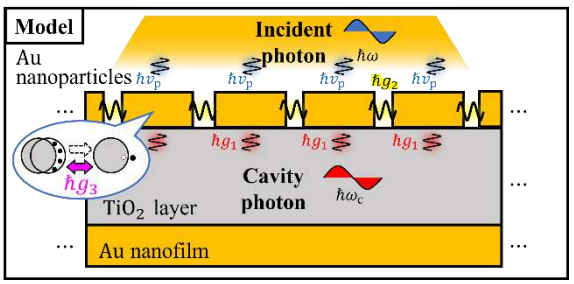

Figure 2: Model for describing coherent couplings between plasmon and electron-hole pairs via radiative field.

owing to coherent couplings between the plasmon and electron-hole pairs. Fig 3 represents a sharp behavior in absorption spectrum at the excitation energy of electron-hole pair. It is found when the plasmon-individual coherent coupling. In addition, a hot carrier generation efficiency form one absorbed photon shows a peak at the electron-hole pair excitation (Fig. 4). This behavior cannot be seen in the absence of coherent couplings between the plasmon and electron-hole pairs. It means that coherent coupling between plasmon and electron-hole pairs induce resonant energy transfer from plasmon to electron-hole pairs, that lead to enhance the efficiency of photoelectric conversion. Moreover, when we consider the hybridization of plasmon excitations as with [3], this novel coherent coupling shows synergetic effect with it and an "antenna effect" are expected to happen. Therefore, by a design of radiative field and metallic structures, the hot carrier generation and light-induced phenomena can be enlarged.

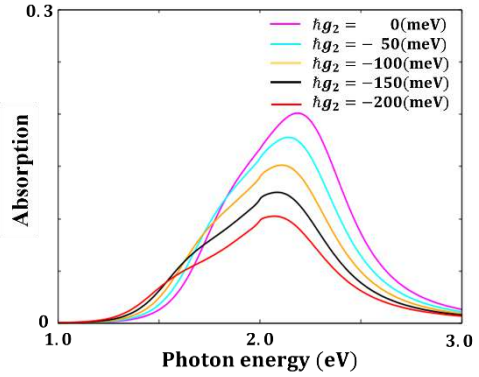

Figure 3: plasmon-plasmon coupling constant dependence of absorption spectra.

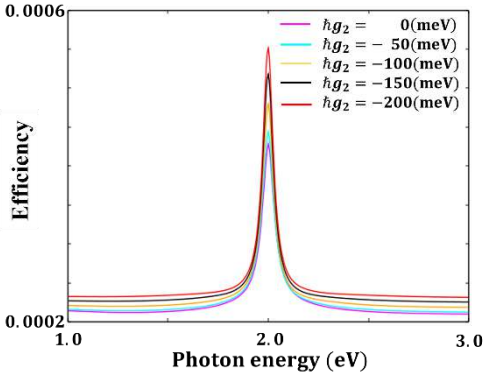

Figure 4: plasmon-plasmon coupling constant dependence of carrier generation efficiency spectra.

References

1. Govorov, A. O., H. Zhang, H. V. Demir and Y. K. Gun'ko, "Photogeneration of hot plasmonic electrons with metal nanocrystals: Quantum description and potential applications," Nano Today Vol. 9, 85-101, 2014.
2. César C., "Plasmon-induced hot-electron generation at nanoparticle/metal-oxide interfaces for photovoltaic and photocatalytic devices," Nat. Photonics vol. 8, 95-103, 2014.
3. Yu, H., Q. Sun, J. Yang, K. Ueno, T. Oshikiri, A. Kubo, Y. Matsuo, Q. Gong and H. Misawa, "Near-field spectral properties of coupled plasmonic nanoparticle arrays," Opt. Express Vol. 25, 6883-6894, 2017.
4. Shi, X., K. Ueno, T. Oshikiri, Q. Sun, K. Sasaki and H. Misawa, "Enhanced water splitting under modal strong coupling conditions," Nat. Nanotechnol. Vol. 13, 953-958, 2018.
5. Brongersma, M. L., N. J. Halas and P. Nordlander, "Plasmon-induced hot carrier science and technology," Nat. Nanotechnol. Vol. 10, 25-34, 2015.
6. Yokoyama, T., M. Iio, T. Kinoshita, T. Inaoka and H. Ishihara, "Comprehensive microscopic theory for coupling of individual and collective excitations via longitudinal and transverse fields," Phys. Rev. B Vol. 105, 165408, 2022.

Pure broadband toroidal source

D. A. Borovkov[1,2*], A. C. Valero[3,4], M. S. Sidorenko[3], A. Kalganov[3], P. Dergachev[5,6], E. Gurvitz[3], L. Gao[7], V. Bobrovs[2], A. Miroshnichenko[8] and A. S. Shalin[1,7,9]

[1]Center for Photonics and 2D Materials, Moscow Institute of Physics and Technology, Dolgoprudny 141700, Russia
[2]Riga Technical University, Institute of Telecommunications, Riga 1048, Latvia
[3]ITMO University, St. Petersburg 197101, Russia
[4]Institute of Physics, University of Graz, and NAWI Graz, 8010, Graz, Austria
[5]National Research University Moscow Power Engineering Institute 14 Krasnokazarmennaya st., Moscow 111250, Russia
[6]National University of Science and Technology (MISIS) 4 Leninsky pr., Moscow 119049, Russia
[7]School of Optical and Electronic Information, Suzhou City University, Suzhou 215104, China
[8]School of Engineering and Information Technology University of New South Wales Canberra Campbell, ACT 2600, Australia
[9]Faculty of Physics, M. V. Lomonosov Moscow State University, 119991 Moscow, Russia
[*]corresponding author: borovkov.da@mipt.ru

Abstract: The idea of creating a source of toroidal dipole radiation excites the scientific community since toroidal dipole was discovered. However, the models existing up until now present the antennas capable of radiating as toroidal dipole only in a limited frequency range. Here we for the first time introduce a model of a source of pure toroidal character followed with the analytical background and the experiment based on our model.

Previous attempts on creating a source of toroidal radiation accomplish origins emitting as toroidal dipole only in narrow range of frequencies [1], [2]. We dedicate our work to the creation of the structure supporting a pure broadband toroidal dipole (**T**) response in the complete absence of the electric dipole (**p**), magnetic dipole (**m**) and other 'ordinary' multipole contributions.

First, we formulated the necessary conditions for the current to support the toroidal dipole, while electric and magnetic dipoles, which commonly have stronger response, would be zero. These conditions are: (i) the absence of surface and volume charges and (ii) the current must be poloidal on surface of imaginary torus. They are fulfilled with the following current:

$$\mathbf{J}_\omega(\rho,\theta)=\frac{K(\rho)}{R_0+\rho cos\theta}\mathbf{e}_\theta \tag{1}$$

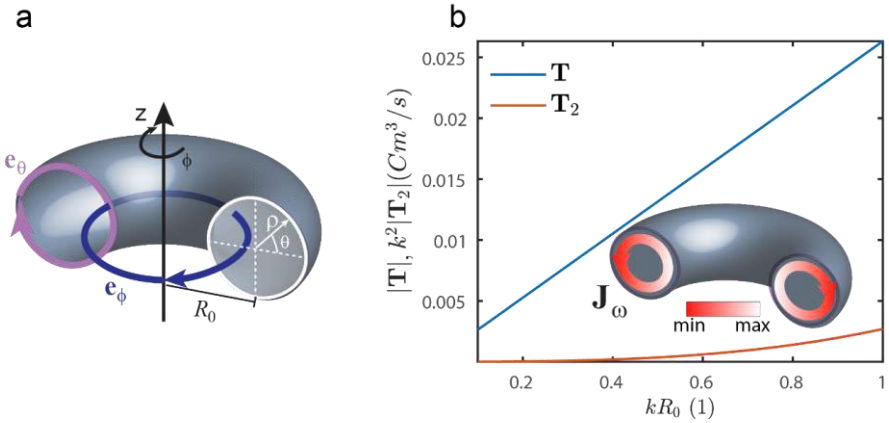

Figure 1. (a) The toroidal coordinate system. $\mathbf{e}_{\theta,\varphi}$ - unit vectors in the poloidal and toroidal directions

respectively. ρ and R_0 are, respectively, the minor and major radius of a torus. (b) Amplitudes of the toroidal dipole and 1st mean square radius ($\mathbf{T}_2$) for the current distribution in Eq.(1).

Then we simulated an antenna based on the mentioned analytics. It consists of 8 metallic loops with current independently exited through input port, each one of them radiates as magnetic dipole (Fig.2a). Combined in a way to create a toroidal-like shape it radiates as pure toroidal dipole of whole simulated region (Fig.2b). Based on this model, we for the first time show experimentally a pure broadband dynamic toroidal dipole source.

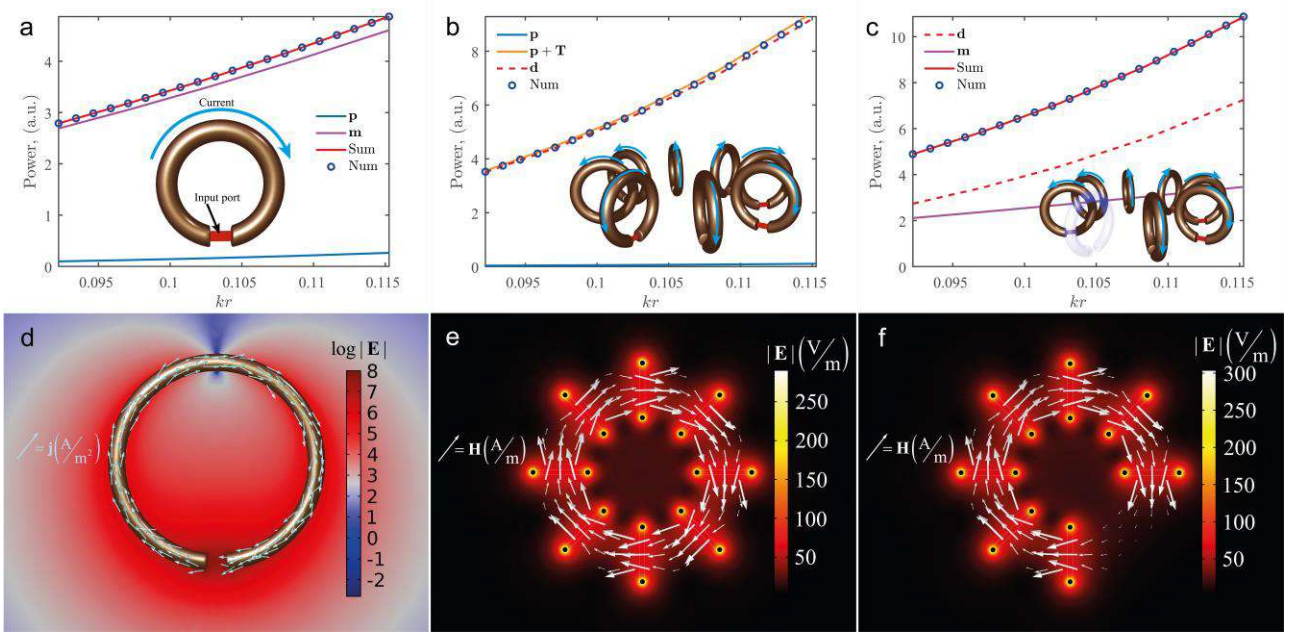

Figure 2. Illustration and multipole decomposition (a) of one loop, (b) whole toroidal dipole antenna (**d**=**p**+**T**+Higher order terms), (c) case with the broken symmetry if one loop is removed, (d) electric field and currents around one loop, (e) and (f) electric and magnetic fields for the structures in (b) and (c) respectively.

Lastly, we further develop our model into a structure formed with point magnetic dipoles supporting a novel tipe of anapole – a toroidal anapole, where the anapole state is achieved due to interference of toroidal dipole with its higher order term – 1st mean square radius.

Our work is submitted, and the preprint is available in the Arxiv [3].

The authors gratefully acknowledge the financial support from the Ministry of Science and Higher Education of the Russian Federation (Agreement No. № 075-15-2022-1150). The investigation of the hybrid anapole regimes has been partially supported by the Russian Science Foundation (Grant No. 21-12-00151). V.B. acknowledges the support of the Latvian Council of Science, project: DNSSN, No. lzp-2021/1-0048.

References

1. Savinov, V., V. A. Fedotov and N. I. Zheludev, “Toroidal dipolar excitation and macroscopic electromagnetic properties of metamaterials”, Phys Rev B, Vol. 89, no 20, p. 205112, 2014.
2. Kaelberer, T., V. A. Fedotov, N. Papasimakis, D. P. Tsai and N. I. Zheludev, “Toroidal Dipolar Response in a Metamaterial”, Science (1979), Vol. 330, no 6010, p. 1510–1512, 2010.
3. Valero, A. C., D. Borovkov et al., “On the existence of pure, broadband toroidal sources in electrodynamics”, 2022, doi: 10.48550/arxiv.2208.02908.

Optothermal non-contact surface cleaning

D. Kislov[1*], D. Ofer[2], A. Machnev[2], H. Barhom[2], V. Bobrovs[4], A. Shalin[1,3] and P. Ginzburg[2]
[1]Country Center for Photonics and 2D Materials, MIPT, Dolgoprudny, 141700, Russia
[2]Tel Aviv University, Ramat Aviv, Tel Aviv, 69978, Israel
[3]Faculty of Physics, M. V. Lomonosov Moscow State University, 119991 Moscow, Russia
[4]Riga Technical University, Institute of Telecommunications, Riga 1048, Latvia
[*]corresponding author: denis.a.kislov@gmail.com

Abstract: Here we develop and demonstrate a new physical mechanism, based on abnormal optothermal expansion of mesoporous microparticles.

We observe vaterite nanoparticles, being fully biocompatible polymorph of calcium carbonate, were placed on a substrate, and accelerated towards it with the aid of a short femtosecond laser pulse. The physical mechanism of the particle propulsion was revealed and attributed to an abnormal anisotropic thermal expansion of the mesoporous microparticle.

The optothermal interaction of ultrashort light pulses with microparticles, depending on the absorption mode, is described using a one-temperature (OTM) [1] or two-temperature model (TTM) [2]. Taking into account the anisotropic properties of a vaterite, the linear momentum can be written as:

$$p_z = \rho V \alpha_{zz} R_0 \frac{dT}{dt} \quad (1)$$

where ρ, V, R_0 the density, volume and radius of particle; α_{zz} the linear thermal expansion coefficient; $\frac{dT}{dt}$ the heating rate.

The authors gratefully acknowledge the financial support from the Ministry of Science and Higher Education of the Russian Federation (Agreement No. № 075-15-2022-1150). V.B. acknowledges the support of the Latvian Council of Science, project: PHOTON, No. lzp-2022/1-0579.

References

1. Tribelsky M. I. and Fukumoto Y. "Laser heating of dielectric particles for medical and biological applications," Biomed. Opt. Express, Vol. 7, 2781-2788, 2016.
2. Rethfeld B. et al. "Modelling ultrafast laser ablation", J. Phys. D: Appl. Phys., Vol. 50, 193001, 2017.

Analysis of tip-enhanced photoluminescence image for allowed and forbidden transition of single molecule based on nonlocal response theory

Y. Tomoshige[1*], M. Tamura[1,2], T. Yokoyama[1], and H. Ishihara[1]

[1]Graduate School of Engineering and Science, Osaka University, Japan
[2] Research Institute for Light-induced Acceleration System, Osaka Metropolitan University, Japan
[*]corresponding author: tomoshige.y@opt.mp.es.osaka-u.ac.jp

Abstract: Tip-enhanced photoluminescence (TEPL) is a microscopy technique enabling the visualization of a single molecule with a high spatial resolution. We have developed the nonlocal theory to evaluate the TEPL. The molecular polarization, expressed with the nonlocal susceptibility originating from the molecular orbital, and Maxwell's equations were solved self-consistently. We could obtain the photoluminescence map by scanning the probe tip, successfully indicating the selective excitation and visualization of molecular modes corresponding to the optically allowed and forbidden transitions.

Tip-enhanced photoluminescence (TEPL) based on scanning probe microscopy can provide microscopic information about light and matter interaction resulting from local excitation near the probe tip. The TEPL experiment demonstrated spectroscopic imaging of a single zinc phthalocyanine with a sub-nm resolution [1]. Furthermore, Imada et al. combined a narrow-line tunable laser with scanning tunneling microscopy to realize the precise TEPL spectroscopy, where the electronic and vibrational states of a single phthalocyanine were characterized and controlled with distinguishing the different states [2].

We have developed the nonlocal theory to evaluate the TEPL. The molecular polarization was expressed with the nonlocal susceptibility originating from the molecular orbitals. The electric field as a solution of Maxwell's equation was given by the Green's function, renormalizing the presence of metallic structure by the discrete dipole approximation (DDA) [3]. We determine the molecular polarization and the electric field self-consistently. In comparison with the previous report of the theoretical study on TEPL [4], we employed the Green's function with a frequency dependence, which provides the correct evaluation of photoluminescence even when, for instance, the strong coupling between the plasmon and the molecule makes the resonance energy shifted or split.

Figure 1 shows the schematic model of TEPL calculation, where the target was a phthalocyanine molecule. The presence of the substrate was ignored, while the silver sphere discretized for the DDA cell was present as a probe tip. The Drude and critical points model was employed as the dielectric function of metal [5]. The transition dipole of the target molecule was obtained from the molecular orbital calculated by GEMASS [6]. For the incident field, we assumed two irradiation cases [A] and [B]: the plane wave propagating for [A] y and [B] x, while its polarization was [A] x and [B] y, respectively, as shown in Figure 1(b). As an elementary calculation at this time, we located the detector at a

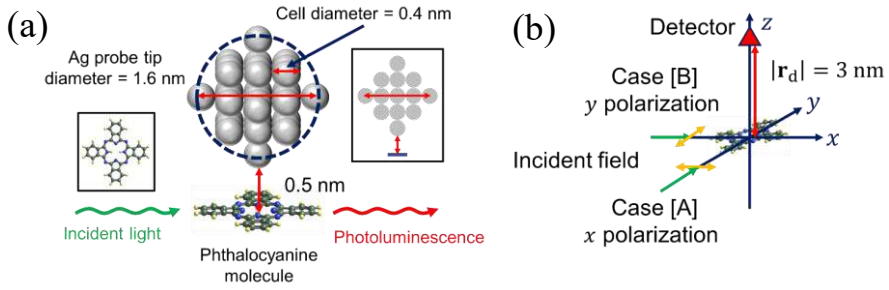

Figure 1 (a) Schematic model of TEPL. The probe tip is considered the silver sphere discretized for DDA calculation. The left inset shows the atomic structure of phthalocyanine. The right inset shows the side view of the system. (b) The irradiation conditions of the incident field and the configuration of the detector toward the phthalocyanine molecule.

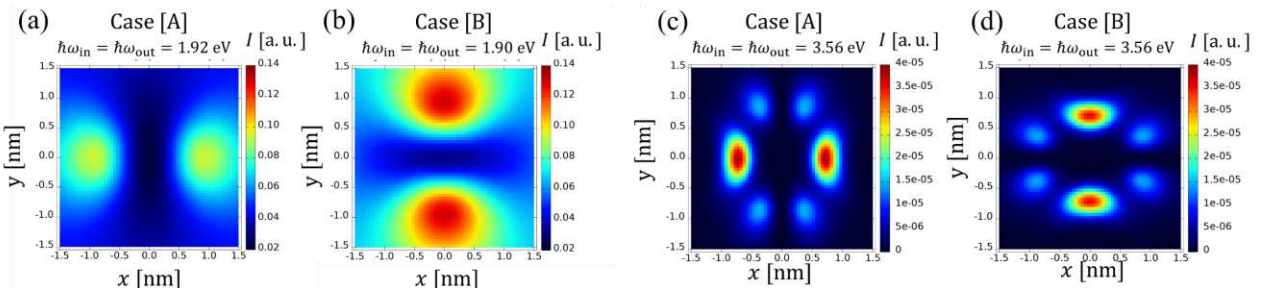

Figure 1 Photoluminescence intensity map. The different mode in single molecule was selectively excited with the incident field of condition [A] x polarization for (a)(c) and [B] y polarization for (b)(d). The transition of (a)(b) is the optically allowed, whereas that of (c)(d) is forbidden.

distance of 3 nm from the sample above the tip. Figure 2 shows a photoluminescence intensity map as a function of the probe tip position, where the energy of incident light was adjusted to each transition of the molecule while the energy of calculated photoluminescence was the same as the incident light. The intensity map reflects the transition dipole, which indicates that the molecule can be selectively excited depending on the energy and the irradiation condition of the incident light. In addition, Figure 2(c)(d) related to the forbidden transition suggests the effect of the nonlocality emerges in the map with several nodes inside the molecule. The map for the forbidden transition can be obtained by far-filed measurement.

In conclusion, we have developed the nonlocal theory to evaluate the TEPL, where we solved the electric field and the induced polarization of the molecule self-consistently. The different condition of the incident field excites the molecular mode selectively. Thus, the obtained photoluminescence intensity map reflects the spatial distribution of each transition dipole moment. In addition, the forbidden transition can be excited by the localized electric field and is detectable by far-field measurement. The developed theory will enable the investigation of photochemical properties inside a single molecule and the contribution of optical scanning microscopy technology.

Acknowledgments: This work was supported by JSPS KAKENHI (Grant Numbers JP16H06504, JP21H05019, JP20K15196), JST-Mirai Program (Grant Numbers JPMJMI18GA and JPMJMI21G1), JST CREST (Grant Number JPMJCR1903), and JST SPRING (Grant Number JPMJSP2138).

References

1. Yang, B., Chen, G., Ghafoor, A. *et al.*, "Sub-nanometre resolution in single-molecule photoluminescence imaging," Nature Photonics 14, 693, 2020.
2. Imada, H., Imai-Imada, M., Miwa, K. *et al.*, "Single-molecule laser nanospectroscopy with micro–electron volt energy resolution," Science 373, 95, 2021.
3. Hoshina, M., Yokoshi, N., Okamoto, H., and Ishihara, H., "Super-Resolution Trapping: A Nanoparticle Manipulation Using Nonlinear Optical Response," ACS Photonics 5, 318, 2018.
4. Lyu, S., Zhang, Y., Zhang, Y., Chang, K., Zheng, G., and Wang, L., "Picocavity-Controlled Subnanometer-Resolved Single-Molecule Fluorescence Imaging and Mollow Triplets," The Journal of Physical Chemistry C 126, 11129, 2022.
5. Barchiesi, D. and Grosges T. "Fitting the optical constants of gold, silver, chromium, titanium, and aluminum in the visible bandwidth" Journal of Nanophotonics, 8, 083097, 2014.
6. Schmidt, M. W., Baldridge, K. K., Boatz, J. A. *et al.*, "General atomic and molecular electronic structure system", The Journal of Computational Chemistry, 14, 1347-1363, 1993

Nonlocal Formulation of Coherent Anti Stokes Raman Scattering for Tip-Enhanced Microscopy

H. Ikagawa[1*], M. Tamura[1,2], T. Yokoyama[1] and H. Ishihara[1]

[1]Department of Materials Engineering Science, Osaka University, Japan
[2]Research Institute for Light-induced Acceleration System, Osaka Metropolitan University, Japan
[*]corresponding author: ikagawa.h@opt.mp.es.osaka-u.ac.jp

Abstract: Combining the coherent anti-Stokes Raman scattering (CARS) with the scanning probe microscopy technique, the tip-enhanced CARS (TE-CARS) has been developed. To examine the characteristics of TE-CARS, we have constructed the theoretical framework. Based on the constitutive equation of sample and the Maxwell's equations, the nonlocal polarization and the electric field are solved self-consistently. The obtained result showed the peak of the phonon mode of sample, and the enhancement of signal owing to the presence of metal tip.

Scanning probe microscopy (SPM) techniques such as the atomic force microscopy (AFM) and scanning tunneling microscopy (STM) enable the visualization of microscopic structures with a highly precise resolution. In addition, the metallic probe tip can be used for the antenna to concentrate the light field at the apex. The various optical SPM techniques, for example, the scanning near-field optical microscopy (SNOM) and tip-enhanced Raman scattering (TERS)[1], have been much developed.

Furthermore, there are the experimental reports of the nonlinear Raman scattering combined with the SPM. Ichimura, et al., realized the spectroscopy with the coherent anti-Stokes Raman scattering (CARS), one of the third order nonlinear responses, called tip-enhanced CARS (TE-CARS)[2]. As shown in Fig. 1(a), the two different light frequencies (ω_1 and ω_2) are involved to excite the CARS process. The intensity of the CARS signal can be stronger than the spontaneous Raman scattering. In addition, it has been considered that the spatial resolution of the TE-CARS can be finer than the TERS by the CARS nonlinearity. However, the detail theoretical discussion of the nature of the TE-CARS has been insufficient. Therefore, we have constructed a theoretical framework to evaluate the TE-CARS from the perspective of the microscopic physics.

To discuss the optical response in TE-CARS of mesoscopic system, first, we derived the nonlocal constitutive equation of sample polarization. The nonlocality originated from the spatial distribution of wave function in the sample. To derive the nonlocal constitutive equations, we assumed the quantum master equation with the

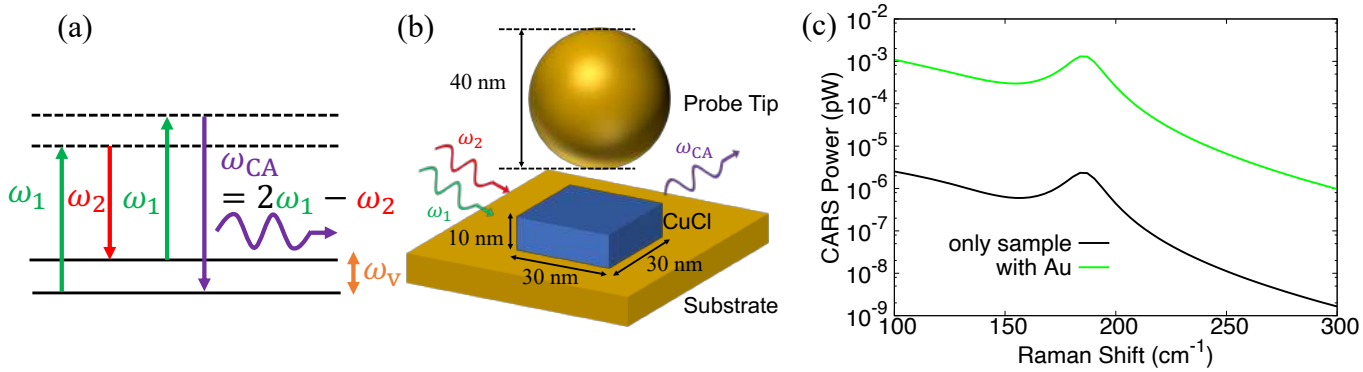

Fig.1. (a) Energy diagram of CARS process. (b) Calculation model. (c) Calculated spectra of CARS power. The green line is a result corresponding to the situation of (b), while the black line is for the sample only (absence of metal). The horizontal axis is the Raman shift $\omega_1 - \omega_2$ in wavenumber. To calculate the spectrum, ω_2 was varied (ω_1 was fixed).

Hamiltonian,

$$\widehat{H} = \widehat{H}_{\mathrm{v}} + \widehat{H}_{\mathrm{ex}} + \widehat{H}_{\mathrm{ex-r}} + \widehat{H}_{\mathrm{ex-v}}, \tag{1}$$

where $\widehat{H}_{\mathrm{v}} = \hbar\omega_{\mathrm{v}}\hat{a}^{\dagger}\hat{a}$ and $\widehat{H}_{\mathrm{ex}} = \hbar\omega_{\mathrm{ex}}\hat{b}^{\dagger}\hat{b}$ are the Hamiltonian of the system of phonons and excitons, respectively (the operator $\hat{a}\ (\hat{a}^{\dagger})$ and $\hat{b}\ (\hat{b}^{\dagger})$ are the annihilation (creation) operator of phonons and excitons), $\widehat{H}_{\mathrm{ex-r}} = -\int d\boldsymbol{r}\widehat{\boldsymbol{P}}(\boldsymbol{r}) \cdot \boldsymbol{E}(\boldsymbol{r})$ is the exciton-electric field interaction, and $\widehat{H}_{\mathrm{ex-v}} = F\hat{a}\,\hat{b}^{\dagger}\hat{b} + \mathrm{H.C.}$ is the exciton-phonon interaction. The expressions of polarization are given by the expectation value of the excitonic polarization operator $\widehat{\boldsymbol{P}}(\boldsymbol{r})$. The expressions for linear and third-order nonlinear polarization were given by the following forms,

$$\boldsymbol{P}^{(1)}(\boldsymbol{r},\omega) = \int d\boldsymbol{r}'\boldsymbol{\chi}^{(1)}(\boldsymbol{r},\boldsymbol{r}',\omega)\boldsymbol{E}(\boldsymbol{r}',\omega), \tag{2}$$

and

$$\boldsymbol{P}^{(3)}(\boldsymbol{r},\omega) = \iiint d\boldsymbol{r}'d\boldsymbol{r}''d\boldsymbol{r}'''\boldsymbol{\chi}^{(3)}(\boldsymbol{r},\boldsymbol{r}',\boldsymbol{r}'',\boldsymbol{r}''',\omega',\omega'',\omega''')\boldsymbol{E}(\boldsymbol{r}',\omega')\boldsymbol{E}(\boldsymbol{r}'',\omega'')\boldsymbol{E}(\boldsymbol{r}''',\omega'''), \tag{3}$$

with the respective susceptibility $\boldsymbol{\chi}^{(1)}$ and $\boldsymbol{\chi}^{(3)}$ including the nonlocality originating from the wave function.

On the other hand, using the Green's function $\boldsymbol{G}(\boldsymbol{r},\boldsymbol{r}',\omega_j)$ of Maxwell's equations, the electric field is,

$$\boldsymbol{E}(\boldsymbol{r},\omega_j) = \boldsymbol{E}_{\mathrm{inc}}(\boldsymbol{r},\omega_j) + \int d\boldsymbol{r}'\boldsymbol{G}(\boldsymbol{r},\boldsymbol{r}',\omega_j)\{\boldsymbol{P}^{(1)}(\boldsymbol{r}',\omega_j) + \boldsymbol{P}_{\mathrm{bg}}(\boldsymbol{r}',\omega_j) + \boldsymbol{P}_{\mathrm{metal}}(\boldsymbol{r}',\omega_j)\}, \tag{4}$$

where $\omega_j = \omega_1, \omega_2, \omega_{\mathrm{CA}}$, $\boldsymbol{E}_{\mathrm{inc}}(\boldsymbol{r},\omega_j)$ is incident field, $\boldsymbol{P}_{\mathrm{bg}}(\boldsymbol{r},\omega_j)$ is the background polarization, $\boldsymbol{P}_{\mathrm{metal}}(\boldsymbol{r},\omega_j)$ is the polarization of metal, and $\boldsymbol{P}^{(1)}(\boldsymbol{r}',\omega_j)$ is the nonlocal polarization. At each frequency, we solved the constitutive equation and Maxwell's equations self-consistently. In this calculation, we treated the nonlinear polarization $\boldsymbol{P}^{(3)}(\boldsymbol{r}',\omega_{\mathrm{CA}})$ as the source of the incident field at the CARS frequency $\boldsymbol{E}_{\mathrm{inc}}(\boldsymbol{r},\omega_{\mathrm{CA}})$.

Fig. 1(b) shows the calculation model, where the rectangular shaped nanoparticle of CuCl was loaded on the substrate metal, and probe sphere was located over the sample. The substrate and probe tip consist of gold. We assumed the presence of LO phonons (eigenenergy 23.1 meV) and Z_3 excitons (3.2022 eV) as an elementally excitation of CuCl. First, we assumed that the motion of the center of the mass of the exciton is ground state. For the irradiation of pump light (frequency ω_1) and Stokes light (ω_2), the calculated CARS Spectra is shown in Fig. 1(c). The result shows the peak of LO phonon and the enhancement due to the metal. Furthermore, the excitation of the forbidden mode of excitonic polarization could be evaluated correctly because of the employment of nonlocal constitutive equations. The obtained results will clarify the capability of TE-CARS, and our theory will contribute the development of optical SPM techniques.

Acknowledgments: This work was supported by JSPS KAKENHI (Grant Numbers JP16H06504, JP21H05019, JP20K15196), JST-Mirai Program (Grant Numbers JPMJMI18GA and JPMJMI21G1), and JST CREST (Grant Number JPMJCR1903).

References

1. N. Hayazawa, Y. Inouye, Z. Sekkat and S. Kawata, "Metallized tip amplification of near-field Raman scattering," Opt. Commun., Vol. 183, 333–336, 2000.
2. T. Ichimura, N. Hayazawa, M. Hashimoto, Y. Inouye and S. Kawata, "Application of tip-enhanced microscopy for nonlinear Raman spectroscopy," Appl. Phys. Lett., Vol. 84, 1768–1770, 2004.

AES 2023, TORREMOLINOS - SPAIN, 5 – 8 JUNE 2023

Simultaneous transfer of energy and angular momentum in a pair of rotating nanostructures

J. R. Deop-Ruano[1], A. Manjavacas[1, 2*]

[1]Instituto de Óptica (IO-CSIC), Consejo Superior de Investigaciones Científicas, 28006 Madrid, Spain
[2]Department of Physics and Astronomy, University of New Mexico, Albuquerque, New Mexico 87106, USA
[*]corresponding author: a.manjavacas@csic.es

Abstract: Radiative heat transfer and Casimir interactions emerge from the fluctuations of the electromagnetic field. Although these phenomena are usually studied separately, their combined effect can lead to exotic phenomena. Here, we perform a simultaneous study of the transfer of energy and angular momentum in a pair of rotating nanostructures. In doing so, we find that the rotation of the nanostructures allows us to increase, reduce or even reverse the heat transfer that occurs for nanostructures at rest.

The fluctuations of the electromagnetic field are at the origin of the radiative heat transfer between material structures. This phenomenon is enhanced at the nanoscale, thanks to the contribution of the near-field components of the electromagnetic field and the strong resonances supported by nanostructures [1, 2]. Another important phenomenon induced by the fluctuations of the electromagnetic field is the Casimir forces and torques between neutral nanostructures, which can be used to enable a transfer of linear and angular momentum in the nanoscale [3, 4]. Despite these phenomena sharing the same physical origin, radiative heat transfer and Casimir interactions are usually investigated separately. For the former, it is common to consider the nanostructures to be at rest, while, to study Casimir interactions, nanostructures are typically assumed to be thermalized. However, as we show in this work, Casimir interactions can remarkably modify the radiative heat transfer, and vice versa.

Here [5], we study the simultaneous transfer of energy and angular momentum in a pair of rotating nanostructures with different temperatures T_1 and T_2 and rotation frequencies Ω_1 and Ω_2, as depicted in Figure 1. We find that, depending on the rotation of the nanostructures, the radiative heat transfer between them can be increased, decreased, or even reversed with respect to the transfer that occurs in absence of rotation, which is given by the difference in the temperature of the nanostructures. We can observe all of these phenomena in Figure 1(b), where we calculate the power transferred between the nanostructures P_1, normalized to the power transferred in the absence of rotation Π_1, as a function of Ω_2 for $\Omega_1 = \pi k_B T_2/\hbar$ and $T_1 = 1.5T_2$. This figure shows that the normalized power transferred can take positive or negative values, which are indicated by the red and blue backgrounds, respectively. That is to say, the heat flow can be reversed and made go from the cold nanostructure to the hot one.

These results show that it is possible to achieve great control of the radiative heat transfer between the nanostructures by exploiting their rotation. Our theoretical model is based on a combination of the fluctuational electrodynamics framework with the dipole approximation. Thanks to this model, we derive fully analytical expressions for the torque and the power transferred between the nanostructures. This work sheds light on the nontrivial phenomena emerging from the interplay between radiative heat transfer and Casimir interactions. Furthermore, it provides the theoretical understanding necessary to use the rotation of nanostructures to control radiative heat transfer.

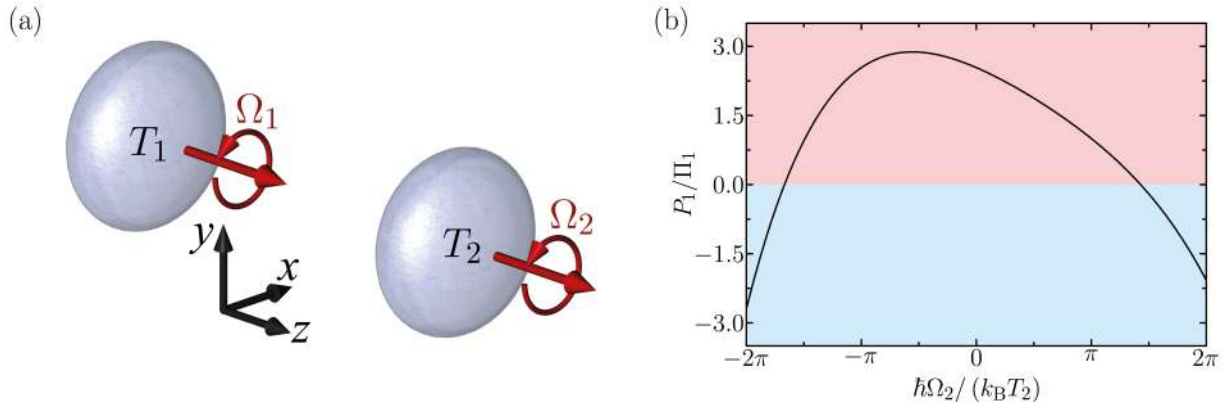

Figure 1. (a) Schematics of the system. (b) Power transferred between the nanostructures P_1, normalized to the power transferred in the absence of rotation Π_1, as a function of Ω_2 for $T_1 = 1.5T_2$, $\Omega_1 = \pi k_B T_2/\hbar$. The red (blue) background indicates positive (negative) values of the normalized power transferred

This work was sponsored by Grant No. TEM-FLU PID2019-109502GA-I00 funded by MCIN/AEI/ 10.13039/501100011033.

References

1. S.-A. Biehs, S..; Messina, R.; Venkataram, P. S.; Rodriguez, A. W.; Cuevas, J. C. and Ben-Abdallah, P. "Near-field radiative heat transfer in many-body systems", Rev. Mod. Phys. 93, 025009, 2021.

2. Manjavacas, A. and García de Abajo, F. J., "Radiative heat transfer between neighboring particles", Phys. Rev. B 86, 075466, 2012.

3. Pendry, J. B., "Shearing the vacuum - quantum friction", J. Phys. Condens. Matter 9, 10301, 1997.

4. Sanders, S.; Kort-Kamp, W. J. M.; Dalvit, D. A. R. and Manjavacas, A., "Nanoscale transfer of angular momentum mediated by the Casimir torque", Commun. Phys. 2, 71, 2019

5. Deop-Ruano, J. R. and Manjavacas, A., "Control of the radiative heat transfer in a pair of rotating nanostructures", Phys. Rev. Lett. (In press)

Optics and Photonics

Detection of concealed reagents using THz parametric generator

K. Kawase*, S. Mine, K. Murate

Department of Electronics, Nagoya University, Japan

*Corresponding author: kawase@nuee.nagoya-u.ac.jp

Abstract: We have studied an injection-seeded terahertz (THz) wave parametric generator (is-TPG) that has a wide dynamic range around the 1-2 THz region and is suitable for measurements through shielding. The multi-wavelength is-TPG has been realized, and it is now possible to acquire fingerprint spectra of reagents in real time. Further, we have developed practical THz tag reading system using combination of a multi-wavelength is-TPG and a machine learning.

For years, we have worked on the development of a high-power THz-wave source, based on parametric processes in a $LiNbO_3$ crystal. In 2001, we created an injection-seeded THz-wave parametric generator (is-TPG) with 300mW output. Recently, the peak output power of is-TPG approached 100 kW by introducing a new pump laser; a microchip YAG laser with shorter pulse width. Is-TPG is a monochromatic widely tunable THz wave source and can obtain THz spectra directly over a relatively wide detection area. Therefore, the spectra from the contents contained in covering materials that refract, diffract, or scatter THz waves can be measured using is-TPG [1-3].

THz wave parametric generation with an is-TPG uses a near-infrared (NIR) pump beam and seed beam input to the MgO:$LiNbO_3$ crystal. In contrast, the THz parametric detector uses a THz wave as the seed beam instead of a NIR beam. In the detection configuration, when the pump beam and THz wave are input into the crystal, the THz wave is upconverted to the NIR Stokes beam by parametric processes in the crystal that are measured using a NIR detector. This THz generation and detection scheme has allowed us to develop a high-dynamic range THz wave spectroscopic system that can be used for spectroscopic imaging of chemicals hidden in thick envelopes.

We have also improved the sensitivity of the THz parametric detector drastically using a multistage configuration to suppress the spontaneous THz emission and enhance the gain [4]. In our new system, the THz parametric detectors were divided into two parts, i.e., for the up-conversion (pre-amplifier) and for the main amplifier as shown in Fig. 1. THz waves were upconverted to a NIR Stokes beam in the first part of the set-up. An iris positioned behind the upconverted region passed the Stokes beam and blocked the broadband spontaneous THz emission. Thus, in the amplification region, only the desired Stokes beam was clearly amplified. The amplified detection Stokes beam was then measured by a NIR beam profiler. This ultra-sensitive detection enables us to see through a thicker obstacle such as EMS envelope or cardboard box in which illicit drugs may be hidden.

Recently, we have developed practical THz tag reading system using combination of a multi-wavelength is-TPG and a machine learning by deep neural network [5, 6]. Reagent pellets with clear fingerprint spectra were used as the THz tag as shown in Fig. 2. Incident angle of THz-wave does not affect the fingerprint spectrum. The tags were swiped by hand at a speed of about 10 cm/sec. along a holder placed at the focal point of THz-wave. The detection Stokes beams, predicted reagent name, and predicted probability were displayed in each captured frame. We achieved accurate and fast tag identification even though the

intensities of the detection Stokes beams were weak and the differences between the images were slight due to the shielding material.

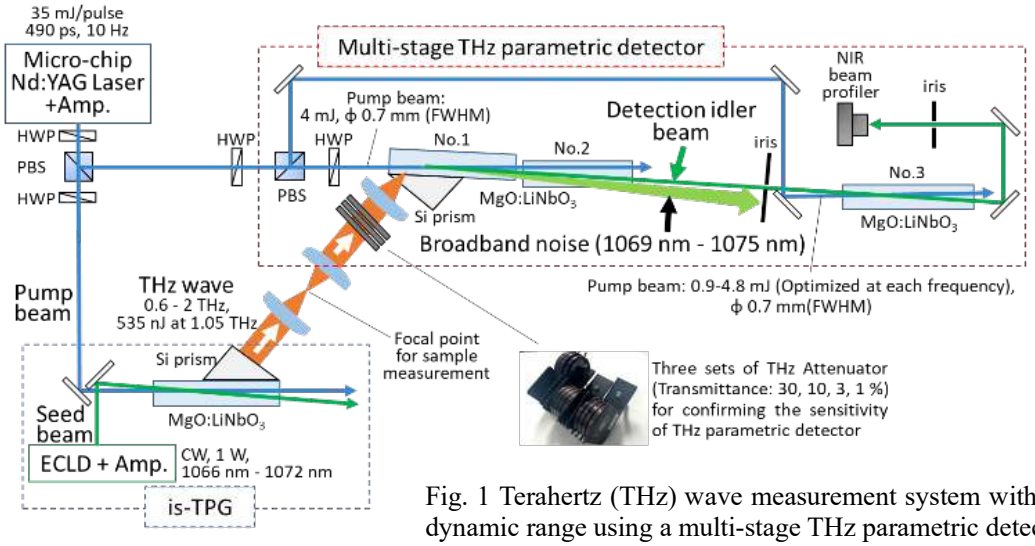

Fig. 1 Terahertz (THz) wave measurement system with a wide dynamic range using a multi-stage THz parametric detector.

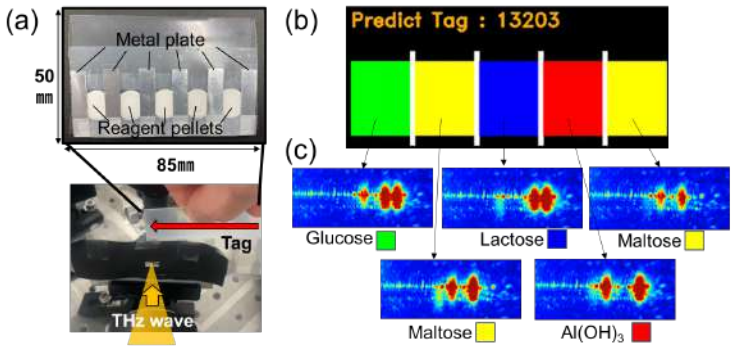

Fig. 2 (a) View of THz-tag and measurement (b) Time-series change of identification results (c) Detection Stokes beam at each reagent position.

References

1. K. Murate, and K. Kawase, “Perspective: Terahertz wave parametric generator and its applications,” Journal of Applied Physics, Vol 124, Issue 16, pp. 160901 (2018).
2. S. Mine, K. Kawase and K. Murate, "Real-time wide dynamic range spectrometer using a rapidly wavelength-switchable terahertz parametric source" Optics Letters, Vol. 46, No. 11, pp.2618-2621, (2021).
3. S. Mine, K. Kawase and K. Murate, "Noise-free terahertz-wave parametric generator," Optics Letters, Vol. 47, No. 5, pp.1113-1116 (2022).
4. H. Sakai, K. Kawase, and K. Murate, “Highly sensitive multi-stage terahertz parametric detector," Optics Letters, Vol. 45, Issue 14, pp. 3905-3908 (2020).
5. R. Mitsuhashi, K. Murate, S. Niijima, T. Horiuchi, and K. Kawase, “Terahertz tag identifiable through shielding materials using machine learning,” Optics Express, Vol 28, Issue 3, pp. 3517-3527 (2020).
6. K. Murate, H. Kanai, K. Kawase, “Application of Machine Learning to Terahertz Spectroscopic Imaging of Reagents Hidden by Thick Shielding Materials,” IEEE Transactions on Terahertz Science and Technology, Vol,11, Issue 6, 620 - 625 (2021)

Symmetry aspects of patterns produced by optical scanners with Risley prisms

V.-F. Duma[1,2,*] **and A.-L. Dimb**[2]

[1]3OM Optomechatronics Group, Faculty of Engineering, Aurel Vlaicu University of Arad, Str. Elena Dragoi no. 2, 310177 Arad, Romania

[2]Doctoral School, Polytechnic University of Timisoara, 1 Mihai Viteazu Ave., 300222 Timisoara, Romania

[*]corresponding author: duma.virgil@osamember.org

Abstract: Symmetries of scan patterns obtained with a pair of rotational Risley prisms are studied. The graphical method we developed is utilized. It has the advantage of generating exact scan patterns (in contrast to approximate methods) and of simplicity (with regard to analytical methods). A multi-parameter analysis is performed with regard to all parameters of such scanners: angles and refractive indexes of the prisms, their rotational velocities, and Marshall's parameters (i.e., ratios of the prism angles and of their rotational velocities).

Rotational Risley prisms are one of the fastest and most employed 2D optical and laser scanning systems [1]. They have been studied with approximate methods [2] or with analytical ones [3]. However, the former does not provide exact scan patterns, while the latter are quite complex. Therefore, we have introduced [4] and developed [5] a novel, graphical method, using a commercially-available mechanical design program, CATIA V5R20 (Dassault Systems, Paris, France). Thus, exact scan patterns can be generated/simulated, in a simple and easy-to-use way. This allows for optimally designing the scanner in order to obtain a required scanning [5].

The present report focuses on the symmetries of the scan patterns obtained with a pair of Risley prisms. We studied in detail these aspects [6], and defined *structures of symmetry* that can be employed by using a finite number of rotations to generate the entire pattern. An example of such structures of symmetry are presented in Fig. 1.

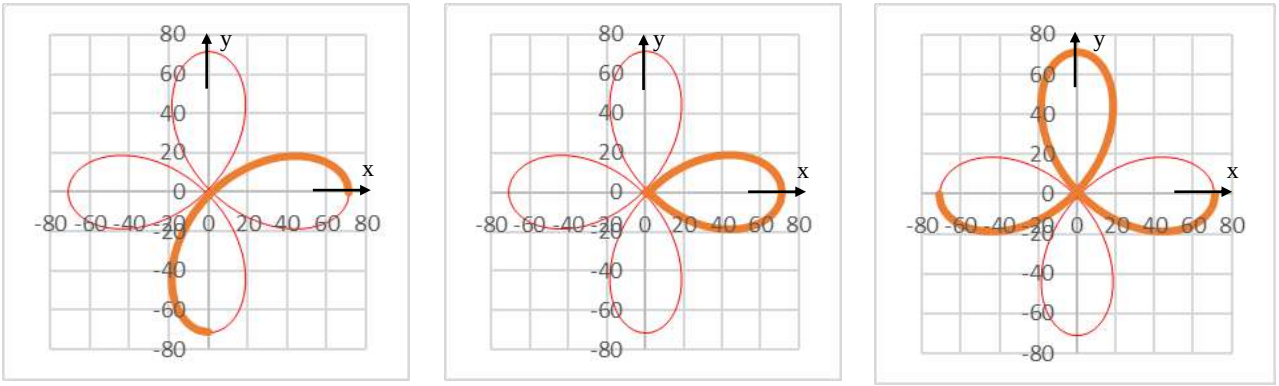

(**a**) (**b**) (**c**)

Figure 1. Study of symmetries in scan patterns of a pair of rotational Risley prisms, simulated for the ratio $M = -3$. Some of the structures of symmetry defined in [6] are highlighted, for several relative rotational angles of the two prisms of the scanner: (a) from 0 to $\pi/2$; (b) from $-\pi/2$ to $\pi/2$; (c) from 0 to π.

A multi-parameter analysis was performed, considering all the characteristic parameters of the scanner (i.e., refractive indexes and angles of the scanner's prisms, their rotational velocities, and the distance between the

prisms), as well as Marshall's ratios of the scanning velocities (M) and of the angles of the two optical prisms (k) of the scanner. We demonstrated that M is the main parameter that determines the symmetries, with the number A of the symmetry axes equal to the number μ of the pattern's loops pointed out in [2,4,5]:

$$A = \mu = |M - 1|, \ \forall |M| \in N^* - \{1\} \quad (1)$$

In order to increase the fill factor (FF) of the patterns in the field-of-view (FOV) of the scanner, using negative values of M is useful, and in this case

$$A(M < 0) = A(|M| + 2) \quad (2)$$

Interesting cases are obtained for particular values of M, equal to 0, ∞, or ±1. Integer values of M are the most useful, as for them closed, repetitive scan patterns are generated. However, in order to provide a comprehensive overview of all possible cases, fractional values of M were considered in [6], as well. They generate multiple spiral-like patterns for rational fraction, while for other values patterns that are not closed can be obtained. The latter have the potential to increase the FF of the patterns, which is useful in certain applications.

All the other parameters of the scanner impact only the size of the patterns, and not their symmetries. In this respect, dimensions of the scan patterns (with intersection points of the pattern's loop and with the widths of these loops, for example) can also be easily obtained using the developed graphical method [6], by extracting the coordinates of the scan trajectories of the laser spot.

Experimental validations of the obtained scan patterns were performed, as in our previous studies [4,5], for different cases of the scanner's parameters and configurations. The results open avenues for precisely obtaining and for analyzing scan patterns of different Risley prisms configurations [7,8].

Acknowledgement: This research was supported by the Romanian Ministry of Research, Innovation and Digitization, CNCS/CCCDI–UEFISCDI, project PN-III-P4-ID-PCE-2020-2600, within PNCDI III (http://3om-group-optomechatronics.ro/, accessed on 1 December 2022).

References

1. G.F. Marshall and G.E. Stutz, Eds., Handbook of Optical and Laser Scanning, 2nd ed., CRC Press: London 2011.
2. G.F. Marshall, "Risley Prism Scan Patterns," Proc. SPIE, Vol. 3787, 74–86, 1999.
3. Y. Li, "Third-order theory of the Risley-prism-based beam steering system," Appl. Opt., Vol. 50, 679–686, 2011.
4. V.-F. Duma and A. Schitea, "Laser scanners with rotational Risley prisms: Exact scan patterns," Proc. Rom. Acad. Ser. A, Vol. 19, 53–60, 2018.
5. V.-F. Duma and A-L. Dimb, "Exact Scan Patterns of Rotational Risley Prisms Obtained with a Graphical Method: Multi-Parameter Analysis and Design," Appl. Sci., Vol. 11, 8451, 2021.
6. A-L. Dimb and V.-F. Duma, "Symmetries of Scan Patterns of Laser Scanners with Rotational Risley Prisms," Symmetry, Vol. 15, No. 2, 336, 2023.
7. Y. Zhou, D. Fan, S. Fan, Y. Chen, G. Liu, "Laser scanning by rotating polarization gratings," Appl. Opt., Vol. 55, 5149–5157, 2016.
8. A. Li, W. Gong, Y. Zhang, X. Liu, "Investigation of scan errors in the three-element Risley prism pair," Opt. Express, Vol. 26, 25322–25335, 2018.

AES 2023, TORREMOLINOS - SPAIN, 5 – 8 JUNE 2023

Fictitious, Physical and Stochastic Sources within Multilayer Optics

C. Amra, P. Rouquette, M. Zerrad, G. Soriano, M. Lequime

Aix Marseille Univ, CNRS, Centrale Marseille, Institut Fresnel, Marseille, France
*corresponding author: claude.amra@fresnel.fr

Abstract: We use the same admittance formalism to design arbitrary huge enhancement and inhibition processes of light scattering, luminescence and thermal radiation in multilayer optical interference filters

Multi-dielectric optics are most often used for the control of light in free space (antireflective coatings, beam splitters and polarizers, mirrors and narrow-band filters…). However for an increasing number of applications these components may support sources in their bulks, which can be fictitious (case of light scattering), physical (case of luminescent micro-cavities) or stochastic (case of thermal radiation). In this talk we present a few analytical techniques to design inhibition or enhancement of the emission pattern from these sources within dielectric multilayers [1].

Fictitious sources are first introduced to describe light scattering processes. All rough surfaces (<1nm) are replaced by fictitious surface currents (electric and magnetic) located on perfectly smooth surfaces. These currents interfere and may lead to inhibition processes, depending on a mutual coherence related to the interface cross-correlation functions. We show how to design specific anti-scattering effects which may open the door to sub-ppm losses in multilayers, a crucial point for the detection of gravitational waves [2].

Micro-cavity patterns are most often emitted by bulk physical sources (electric) inside one volume of the multilayer. We show how to design huge enhancement of evanescent waves for applications in high sensitivity sensors. Enhancement can be analytically simultaneously designed for arbitrary wavelengths, angles and polarizations [3]. Intrinsic and extrinsic limits of these dielectric components are analyzed.

Thermal radiation is the result of stochastic bulk currents (electric and magnetic) within each layer of the stack. These currents take their origins in the temperature that can be photo-induced or ambient [4]. We show how to generalize the previous techniques to create unity emissivity with dielectric multilayers. This emissivity can be chosen in several narrow bandwidths at directions and wavelengths chosen beforehand [5]. Applications concern energy and defense.

The same formalism is used for all processes mentioned above. Eventually the energy balance includes light which merges in free space outside the coatings, as well as the trapped light which is carried by the guided waves inside the multilayer [6]. All predictions are validated with numerical calculation.

References

1. Claude Amra, Michel Lequime, Myriam Zerrad. Electromagnetic Optics of Thin-Film Coatings: Light Scattering, Giant Field Enhancement, and Planar Microcavities. Cambridge University Press, 2020, 9781108772372.
2. Imran Khan, Michel Lequime, Myriam Zerrad, Claude Amra. Detection of Ultralow Light Power Back-Reflected or Back-Scattered by Optical Components Using Balanced Low-Coherence Interferometry. Phys.Rev.Applied, 2021, 16 (4), pp.044055. <10.1103/PhysRevApplied.16.044055>
3. Paul Rouquette, Claude Amra, Myriam Zerrad, and Michel Lequime, "Micro-cavity optimization for ultra-sensitive all-dielectric optical sensors," Opt. Express 30, 15344-15364 (2022)

4. P. Rouquette, C. Amra, M. Zerrad, C. Grèzes-Besset, and H. Krol, "Photo-induced temperature in optical interference coatings," Opt. Express 30, 46575-46601 (2022)
5. P. Rouquette, C. Amra, M. Zerrad, C. Grèzes-Besset, H. Krol, “Thermal Radiation Photo-Induced in Optical Interference Coatings”, submitted to Optics Express
6. Claude Amra, Myriam Zerrad, and Michel Lequime, "Trapped light scattering within optical coatings: a multilayer roughness-coupling process," Opt. Express 29, 25570-25592 (2021)
7. P. Munzert, N. Danz, A. Sinibaldi, F. Michelotti, “Multilayer coatings for Bloch surface wave optical biosensors,” Surface and Coatings Technology, 314, 79-84, (2017).
8. M. Francoeur, M. Pinar Mengüç, and R. Vaillon, "Solution of near-field thermal radiation in one-dimensional layered media using dyadic Green’s functions and the scattering matrix method," Journal of Quantitative Spectroscopy and Radiative Transfer 110, 2002–2018 (2009).
9. B. J. Lee and Z. M. Zhang, "Coherent thermal emission from modified periodic multilayer structures," Journal of Heat Transfer 129, 17–26 (2007).
10. J.-J. Greffet, R. Carminati, K. Joulain, J.-P. Mulet, S. Mainguy, and Y. Chen, "Coherent emission of light by thermal sources," Nature 416, 61–64 (2002).
11. D. L. C. Chan, M. Soljačić, and J. D. Joannopoulos, "Direct calculation of thermal emission for three-dimensionally periodic photonic crystal slabs," Phys. Rev. E 74, 036615 (2006).

Low threshold mode-locking close at an exceptional point in coupled microcavities

[*1]Takasumi Tanabe, [1]Riku Imamura, and [2]Shun Fujii

Department of Electronics and Electrical Engineering, Faculty of Science and Technology, Keio University, Japan

Department of Physics, Faculty of Science and Technology, Keio University, Japan

[*]corresponding author: takasumi@elec.keio.ac.jp

Abstract: We discuss a low-threshold mode-locking in a coupled cavity system, where nonlinear loss and gain are present.

In order to develop ultrahigh repetition rate lasers, we need a system composed of a small cavity, high gain, and nonlinear absorption (i.e., saturable absorption (SA)), which is not usually an easy task to obtain simultaneously [1]. Here we show that a coupled microresonator system with a gain resonator coupled to a nonlinear loss resonator will serve as a good platform for mode-locking at lower gain. It is based on the idea of employing the Q revival of the gain cavity when the loss is increased at the carbon nanotube (CNT) coupled cavity, which will exist in the vicinity of the exceptional point [2].

The model is shown in Fig. 1(a), where a cavity with a gain is coupled with a nonlinear loss cavity. We conducted numerical analyses based on nonlinear Schrödinger equations, as given below.

$$Tr\frac{\partial}{\partial T}A(t,T) = \left(-iL_A\frac{\beta_2}{2}\cdot\frac{\partial^2}{\partial t^2} + iL_A\gamma|A|^2\right)A(t,T) + \{g_{Tr}(T) - l_{TrA}\}A(t,T) + i\frac{\kappa}{2}B(t,T) \quad (1)$$

$$Tr\frac{\partial}{\partial T}B(t,T) = \left(-iL_B\frac{\beta_2}{2}\cdot\frac{\partial^2}{\partial t^2} + iL_B\gamma|B|^2\right)B(t,T) - \{l_{TrB} + \alpha_{Tr}(t,T)\}B(t,T) + i\frac{\kappa}{2}A(t,T) \quad (2)$$

$A(t, T)$ and $B(t, T)$ are the electric field envelope waveforms in the Er-doped microresonator, and the CNT-coated microresonator at time T. g_{Tr}, l_{Tr}, and α_{Tr}, are the gain, linear loss, and saturable absorption induced by the CNTs, respectively. The Q of the CNT-coated (nonlinear loss) cavity is 5×10^6. The two cavities are coupled with a coefficient κ.

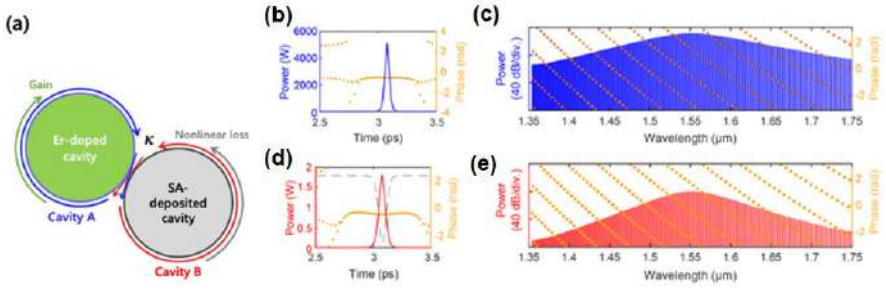

Fig. 1: (a) Schematic illustration of coupled microresonator system including gain and nonlinear loss. (b-e) Temporal waveform and spectrum in Cavity A (b, c) and Cavity B (d, e).

Assuming that Cavity-A was pumped and exhibited gain, we calculated the evolution of the intracavity power inside each resonator. The obtained spectra and temporal waveforms are shown in Figs. 1(b)-1(e). These results indicate that self-starting mode-locking is achieved. Since a Q of $>10^7$ was needed for mode-locking when we use a single cavity system (a CNT is attached to the same cavity that exhibits gain) [1], we obtained a significant

relaxation of the Q requirement, where it is 5×10^6 for the CNT-coated cavity.

The origin that we obtain a mode-locking even in a system with a higher loss and lower gain is due to the suppressed effective loss that appears in the vicinity of the exceptional point. Figure 2(a) is the imaginary part of the system's Eigenfrequency (i.e., the total loss) in function to the additional loss induced by the CNT in Cavity B. We observe explicit behavior of the exceptional point where the total nonlinear loss of the system decreases (i.e., Q_{NL} increases) even when we increase the CNT loss (i.e., reduce the Q_{CNT}). It suggests the existence of suppressed loss at high CNT loss. However, it should be noted that we use a steady-state analysis to obtain this graph, which is not sufficient to study SA, which is a transient phenomenon; hence a transient analysis is required for deeper understanding.

Figures 2(b) and 2(c) are waveforms and temporal loss profiles in Cavity A when the system is still in a transient phase. Since Cavity B functions as the SA component for Cavity A, we monitor the coupling loss of Cavity A (coupling of light from Cavity A to B). Figure 2(c) shows that the background coupling loss is about -2×10^{-5} ps^{-1}, whereas the coupling loss is about -3×10^{-8} ps^{-1} at the position where the pulse starts to form. The loss contrast is about three orders of magnitude, indicating that the SA's effect is pronounced for a coupled cavity system compared to a single cavity system. More interestingly, when the system reached a steady mode-locking state (Fig. 2(d)), the background loss was significantly reduced, as shown in Fig. 2(e). The background loss rate is now at about -1×10^{-10} ps^{-1}, which corresponds to a coupling Q of 10^{12} to 10^{13}. In addition, the phase in the background is shown to split into two components with a separation of π, which indicates the presence of two modes that appear beyond the exceptional point. Such behavior originates from the exceptional point, which will explain why we obtained mode-locking behavior even at a lower gain.

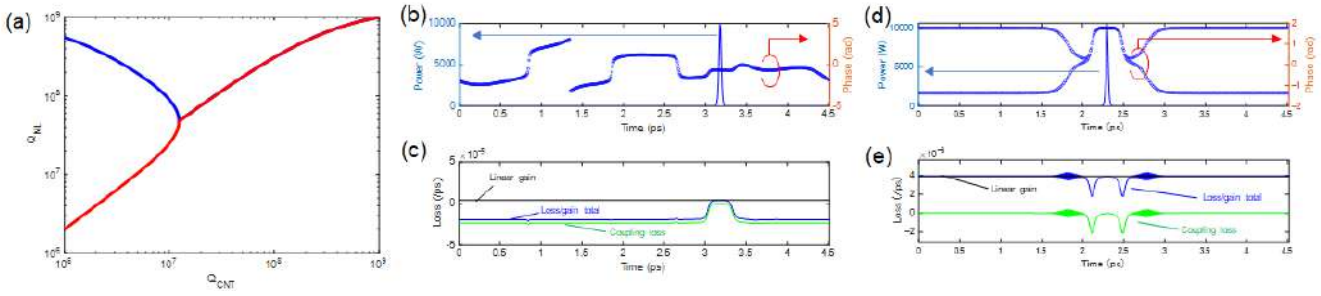

Fig. 2: (a) Imaginary part of the complex Eigenfrequency of the coupled cavity system in function to the additional loss due to CNT (Q^{CNT}). (b) Temporal waveform and phase in Cavity A at transient phase. (c) Corresponding loss profile for (b). (d, e) same as (b, c) but at a steady state.

In summary, we show that mode-locking is possible with a lower Q and lower gain when a coupled cavity system is employed.

Part of this work was supported by the Strategic Information and Communications R&D Promotion Programme (SCOPE) (#JP225003008) from the Ministry of Internal Affairs and Communications

References

1. T. S. P. Suzuki, *et al*., "Design of a passively mode-locking whispering-gallery-mode microlaser," J. Opt. Soc. Amer. B **38**, 3172 (2021)
2. B. Peng, *et al*., "Loss-induced suppression and revival of lasing," Science **346**, 328 (2014).

Galaxy-shaped structures fabricated by irradiation of hybrid vortex modes

T. Omatsu[1,2]

[1]Graudate School of Engineering, Chiba University, Japan
[2]Molecular Chirality Research Center, Chiba University, Japan
*corresponding author: omatsu@faculty.chiba-u.jp

Abstract: Azopolymers allow the development of photo-induced reversible engineered optical materials with exotic physical properties unattainable in natural materials through trans-cis-trans photoisomerization.
We herein report on the first demonstration of the chiral engineered optical materials with $2|\ell|$ spiral arms by employing hybrid optical vortex modes, formed of the coherent superposition of orthogonal $\pm\ell^{th}$ order optical vortices.

Engineered optical materials with artificial physical properties unattainable in natural materials, such as photonic/plasmonic crystals and metasurfaces, have been intensely investigated. Azopolymers have the capacity to develop photo-induced reversible engineered optical materials through trans-cis-trans photoisomerization.

Optical vortex with a helical wavefront carries an annular spatial profile and orbital angular momentum (OAM), characterized by a topological charge ℓ, associated with their on-axis phase singularity. It is discovered that the OAM of optical vortex enables us to twist the irradiated azopolymers to form nano/micron-scale chiral surface structures. This exotic twisting of azopolymers under optical vortex irradiation will offer the development of chiral engineered optical materials. However, the fabricated structures are always singly armed even with the optical vortices with higher topological charge.

In this work, we demonstrate, for the first time to the best of our knowledge, the formation of chiral surface structures with $2|\ell|$ spiral arms of azopolymers by employing spinning hybrid optical vortex modes, formed of the coherent superposition of orthogonal $\pm\ell^{th}$ order optical vortices with circular polarization. Intriguingly, the fabricated structures reflect full geometric parameters, such as handedness (spinning direction), topological charge, and initial azimuthal phase, of the irradiated hybrid optical vortex modes.

This work will open the door towards the advanced development of new photo-induced reversible engineered optical materials with the freedom of chirality, orientation, and spiral arms.

References

1. H. Ishitobi, M. Tanabe, Z. Sekkat, and S. Kawata, "The anisotropic nanomovement of azo-polymers," Opt. Express 15, 652 (2007).
2. D. Barada, G. Juman, I. Yoshida, K. Miyamoto, S. Kawata, S. Ohno, and T. Omatsu, "Constructive spin-orbital angular momentum coupling can twist materials to create spiral structures in optical vortex illumination," Appl. Phys. Lett. 108, 051108 (2016).
3. M. Watabe, G. Juman, K. Miyamoto, and T. Omatsu, "Light induced conch-shaped relief in an azo-polymer film," Sci. Rep. 4, 4281 (2015).
4. A. Ambrosio, L. Marrucci, F. Borbone, A. Roviello, and P. Maddalena, "Light-induced spiral mass transport in azo-polymer films under vortex-beam illumination," Nat. Commun. 3, 989 (2012).
5. T. Omatsu, K. Miyamoto, K. Toyoda, R. Morita, Y. Arita, and K. Dholakia, "A New Twist for Materials Science: The Formation of Chiral Structures Using the Angular Momentum of Light," Adv. Opt. Mater. 7, 1801672 (2019).

6. T. Omatsu, K. Masuda, K. Miyamoto, K. Toyoda, N. M. Litchinitser, Y. Arita, and K. Dholakia, "Twisted mass transport enabled by the angular momentum of light," J. Nanophotonics 14, 1 (2020).
7. M. J. Padgett and J. Courtial, "Poincaré-sphere equivalent for light beams containing orbital angular momentum," Opt. Lett. 24, 430 (1999).

Optical manipulation and fusion of gold particle assemblies by two focal lasers

T. Yokoyama[1*], Y. Tao[1], and H. Ishihara[1,2]

[1]Department of Material Engineering Science, Osaka University, Japan
[2]Center for Quantum Information and Quantum Biology, Osaka University, Japan
yokoyama.t.es@osaka-u.ac.jp

Abstract: Non-contacting manipulate and ordered formation of many nanoparticles are attractive subjects for surface applications because the nanoparticle array induces a photonic crystal effect. In this study, we examine numerically an optical binding and manipulation of many nanoparticles by focal two laser beams. The two lasers form two assemblies of the nanoparticles, then scattered lights from the assemblies cause an interaction between them. We demonstrate such extended optical binding and a fusion of the two assemblies, which is significant for meta-surface.

A formation of ordered structure of nanoscale objects provides rich applications and advantages for surface physics. An optical force accelerates small objects by a light irradiation without physical contact [1]. Hence, optical manipulation can be performed in a vacuum, in a solvent, and applied for wide-range fields [1,2]. Light has many degrees of freedom, e.g., polarization, vortex, focal size, etc, which give rich functionalities on optical manipulation and ordered formations of nanoparticles.

We investigate a generalized extension of optical binding theoretically. Optical binding is a concept to trap small objects (mainly spherical nanoparticles) with a finite distance owing to an interaction between light-induced polarizations on the nanoparticles. A conventional optical binding is examined under a wide-area laser irradiation; hence all bound nanoparticles are irradiated directly. In recent our study [3], we have extended this concept to a local irradiation by a tightly focal laser and indirect mechanism. Under the focal laser beam, only several nanoparticles are irradiated directly. They are trapped by the focal laser. Scattered lights from the directly

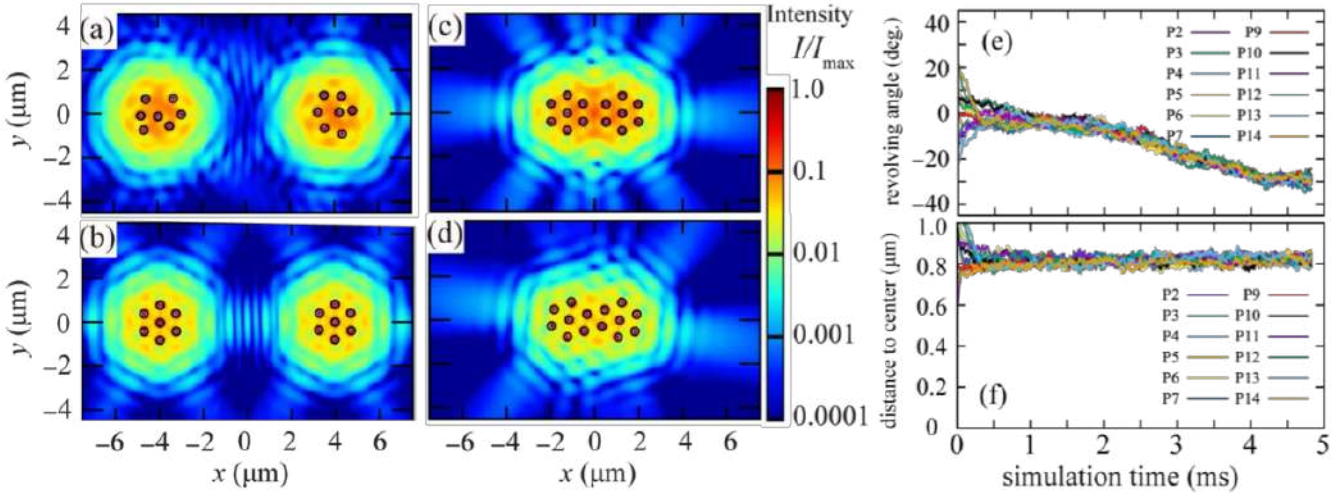

Fig. 1: Simulated results for two focal laser beams. (a,b) Particle position for 7+7 particles at t = 0 (a) and 10 msec (b). (c,d) Fusion of particles by tilting the lasers at t' = 0 (c) and 24 msec (d). Color plots indicate total field intensity. (e) Revolving angle and (f) particle distance from respective focal center when the two lasers are separated.

trapped nanoparticles also contribute to optical trapping and manipulation for surrounding nanoparticles. Then, even at out of the irradiation area, the nanoparticles are optically bound. We have examined a numerical simulation for dynamics of the bound nanoparticles and shown a good agreement with an experimental observation by Kudo, et al. [4].

In this study, we consider optical binding of gold nanoparticles by two focal laser beams. Both lasers have the same circular polarization. The nanoparticles are directly trapped at the two focal laser irradiations as shown in Figs. 1(a) and (b). If the two lasers are far from each other, the particles revolve at the respective irradiation area owing to the spin angular momentum of circular polarized light. When a distance between the laser beams is the order of several times of wavelength, the scattered light affects the particles at other laser spots and the revolving dynamics is stopped (see Figs. 1(e) and (f)). The particles exhibit hexagonal arrays. By tilting the incident angle of the two laser beams and being closer to each other, the two hexagonal arrays show a fusion to one hexagonal array in Figs. 1(c) and (d). This fused assembly is not isotropic but elliptic along the position of two laser beams. Hence, by using this fusion iteratively, we might be able to draw an arbitrary "line" of hexagonal order particle assembly.

This result will lead to a local tuning and switching of meta-surface properties by the laser irradiation.

Acknowledgments: T.Y. is supported by Toyota Riken Scholar. H.I. is supported by JSPS KAKENHI 18H01151.

References

1. Ashkin, A., J. M. Dziedzic, J. E. Bjorkholm and S. Chu, "Observation of a single-beam gradient force optical trap for dielectric particles," Opt. Lett., Vol. 11, 288–290 1986.
2. Zhou, L.-M., Y. Shi, X. Zhu, G. Hu, G. Cao, J. Hu, and C.-W. Qiu, "Recent Progress on Optical Micro/Nanomanipulations: Structured Forces, Structured Particles, and Synergetic Applications," ACS Nano, Vol. 16, 13264–13278 2022.
3. Tao, Y., T. Yokoyama and H. Ishihara, "Rotational dynamics of indirect optical bound particle assembly under a single tightly focused laser," Opt. Exp., Vol. 31, 3804–3820, 2023.
4. Kudo, T., S. F. Wang and H. Masuhara, "A Single Large Assembly with Dynamically Fluctuating Swarms of Gold Nanoparticles Formed by Trapping Laser," Nano Lett., Vol. 18, 5846–5853 2018.

Theoretical analysis of luminescence-induced optical force exerted on micromechanical membranes

H. Arahari[1*], S. Konishi[2], S. Akita[2] and H. Ishihara[1]

[1]Dept. of Materials Engineering Science, Osaka University, Toyonaka, Osaka, 560-8531, Japan
[2]Dept. of Physics and Electronics, Osaka Metropolitan University, Sakai, Osaka, 599-8531, Japan
[*]corresponding author: arahari.h@opt.mp.es.osaka-u.ac.jp

Abstract: We have theoretically evaluated the luminescence-induced optical force (LiOF) on the emitting film. LiOF occurs by designing an anisotropic dielectric structure surrounding an emitter. As a model, we assumed a square-type optomechanical resonator formed with the luminescent nanofilm and a metallic mirror substrate. Then, we theoretically revealed that the LiOF could induce the mechanical frequency shift of the oscillator. This research provides new insights into the development of optomechanics using luminescence.

Optical force, generated by the momentum transfer of light into matter, has been applied in a wide range of fields, including molecular biology [1,2], photochemistry [3,4], and optomechanics [5], as a technique to manipulate small objects from atomic to micrometer sizes. Among such studies, we focus on optical manipulation using the 'luminescence' of materials. When luminescence occurs isotropically, it contributes little to the motion of the emitter. However, we considered that by designing the spatial structure of dielectrics surrounding the emitters so that the luminescent field becomes anisotropic, the luminescence-induced optical force (LiOF) is exerted on the emitter itself, resulting in mechanical motion. From the above perspective, we assumed an optomechanical cavity structure formed by a luminescent nanofilm and a metallic mirror substrate, as shown in Fig 1(a). We theoretically show that luminescence contributes to the mechanical motion of the emitter in such structures. If quantum states of the emitters can be coupled to mechanical modes via luminescence, it leads to quantum systems which control the luminescence properties of materials such as lasing [6].

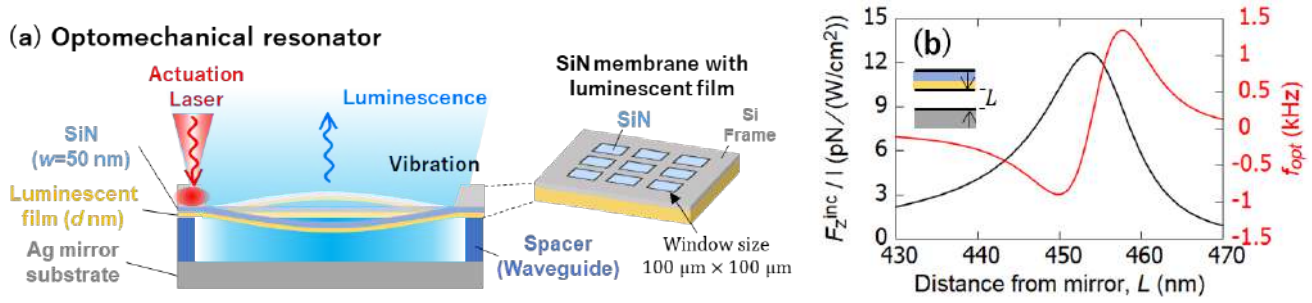

Figure 1. (a) Model diagram of the optomechanical resonator. The size of the membrane window is 100 μm ×100 μm. As the luminescent film, we assumed organic-inorganic layered perovskites $(C_{10}H_{21}NH_3)_2PbI_4$. The system is assumed to have a mechanical frequency f_m = 1 MHz and a film thickness of d=130 nm. (b) Black line: Cavity length L-dependence of LiOF F_z^{inc} when the luminescent film is given steady excitation energy. Here, the excitation energy is the interaction energy between the exciton polarization and the excitation light field that corresponds to the energy when the luminescent film is irradiated with excitation light of intensity I. The results are normalized by I. Red line: Mechanical frequency shift f_{opt} induced by LiOF under I=100 W/cm^2.

As the luminescent film in Fig 1, we assumed organic-inorganic layered perovskites $(C_{10}H_{21}NH_3)_2PbI_4$ [7,8], which is one of the promising light-emitting materials. The cavity structure is constructed by fabricating the luminescent film on a silicon nitride (SiN) membrane and transferring it onto the Ag mirror substrate. Here, the photoluminescence (PL) electric field in the cavity is enhanced or suppressed depending on the distance L between the film and the mirror due to the optical confinement effect. The spatial anisotropy of the PL electric field surrounding the emitter results in LiOF.

In Fig. 1(b), we evaluated the LiOF F_z^{inc} exerted on the luminescent film assuming the situation where only LiOF was exerted on the film by giving steady excitation energy to the luminescent film. Here, as the steady-state excitation energy, we gave the interaction energy between the exciton polarization and the excitation light that corresponded to the energy when the luminescent film was irradiated with excitation light of intensity I. Fig. 1(b) shows that the LiOF is enhanced at a specific cavity length. Such LiOF enhancement occurs at half the emission wavelength period (≅244 nm). As shown in Fig. 1(b) red line, the enhanced LiOF induces the mechanical frequency shift f_{opt} of the luminescent film from the given parameter $f_{\mathrm{m}} = 1$ MHz,

$$f_{\mathrm{opt}} = f_{\mathrm{eff}} - f_{\mathrm{m}}, \dots (1)$$

$$f_{\mathrm{eff}} = f_{\mathrm{m}} \sqrt{1 - \frac{\nabla F_z^{\mathrm{inc}}}{m_{\mathrm{eff}} \omega_{\mathrm{m}}^2}}, \dots (2)$$

which is known as the optical spring effect [9]. We can confirm that LiOF affects the mechanical motion of the emitter by observing this effect in experiments.

These results are promising for new optomechanical applications that convert the modes of luminescence into mechanical vibrational modes. The mechanism can lead to new applications of optical force to transmit the quantum properties of emitters to other quantum systems with different frequency regimes via the induced vibrational modes.

References

1. A. Ashkin, J. M. Dziedzic, J. E. Bjorkholm, and S. Chu, *Observation of a Single-Beam Gradient Force Optical Trap for Dielectric Particles*, Opt. Lett. **11**, 288 (1986).
2. S. Corsetti, and K. Dholakia, *Optical Manipulation: Advances for Biophotonics in the 21st Century*, J. Biomed. Opt. **26**, (2021).
3. S. Ito, Y. Tanaka, H. Yoshikawa, Y. Ishibashi, H. Miyasaka, and H. Masuhara, *Confinement of Photopolymerization and Solidification with Radiation Pressure*, J. Am. Chem. Soc. **133**, 14472 (2011).
4. A.-C. Cheng, H. Masuhara, and T. Sugiyama, *Evolving Crystal Morphology of Potassium Chloride Controlled by Optical Trapping*, J. Phys. Chem. C **124**, 6913 (2020).
5. M. Aspelmeyer, T. J. Kippenberg, and F. Marquardt, *Cavity Optomechanics*, Rev. Mod. Phys. **86**, 1391 (2014).
6. D. Yu and F. Vollmer, *Active Optomechanics*, Communications Physics **5**, 1 (2022).
7. T. Ishihara, J. Takahashi, and T. Goto, *Exciton State in Two-Dimensional Perovskite Semiconductor (C10H21NH3)2PbI4*, Solid State Commun. **69**, 933 (1989).
8. T. Ishihara, J. Takahashi, and T. Goto, *Optical Properties Due to Electronic Transitions in Two-Dimensional Semiconductors (C n H 2 N+ 1 NH 3) 2 PbI 4*, Phys. Rev. B **42**, 11099 (1990).
9. B. S. Sheard, M. B. Gray, C. M. Mow-Lowry, D. E. McClelland, and S. E. Whitcomb, *Observation and Characterization of an Optical Spring*, Phys. Rev. A **69**, 051801 (2004).

Diffractive Optical Elements through Reshaped Photosensitive Materials Platform

S. Moujdi[1*], M. De Oliveira[1], S. L. Oscurato[1, 2], F. Borbone[1,2] and A. Ambrosio[1]

[1]CNST@POLIMI - Fondazione Istituto Italiano di Tecnologia, Via Rubattino 81, 20134, Milano – Italy
[2]Physics Department "E. Pancini", University of Naples "Federico II", Via Cinthia Complesso Universitario di Monte Sant'Angelo, Via Cintia, 80126 Naples, Italy
[*]corresponding author: sara.moujdi@iit.it

Abstract: Diffractive optical elements have been and will be increasingly in demand for various applications in photonics. These devices require surface patterning of materials at the wavelength scale of light. Azopolymers have been considered as promising materials owing to their ability to produce surface reliefs under irradiation of spatially structured optical fields. In this work, the direct realization of reconfigurable diffractive elements is achieved by a single process of photo-structuring a photosensitive material to provide effective optical functionality on demand.

An escalating interest in the realization of diffractive optical elements has witnessed considerable critical attention owing to their potential application in photonics and planar optics. The fabrication of such devices recommends several lithographic processes that provide an accurate surface profile but are not reconfigurable after surface fabrication. Recently, a new approach has been used to directly produce surface reliefs without requiring additional lithographic processes [1]. Photoresponsive materials, also known as Azobenzene-containing polymer films, have drawn tremendous attention as the most promising materials platform that has the ability to form direct surface patterns on the film surface when irradiated to UV/Visible light. The photoinduced surface structuration is due to the reversible light-induced mass movement of the polymer chains triggered by the cyclic photoisomerization of azo chromophores [2,3]. The ability to pattern polymer surfaces directly and reversibly makes azopolymer films a good candidate for use as reshaped planar diffractive optical devices [4]. It is well known that this process is vectorial, which means that the geometry of such patterns is susceptible to the polarization state and intensity of the irradiated light.

In our experiment, we have used a holographic grayscale light-intensity patterning scheme in which we implement a spatial light modulator to project the final light path directly onto the surface of an azo-polymer film in this case the surface relief patterns [1,5]. In a single lithographic step, we formed the surface relief patterns of several flat transmissive diffractive optical elements. For example, when this azopolymer film is irradiated by two interfering light beams with a sinusoidal profile, a sinusoidal topographic diffraction grating is formed. In addition, complex diffraction gratings can also be made with the same configuration. After making the first single diffractive optical element, an additional laser beam is used to erase the patterned area in an all-optical process. This process restores the original profile of the flat surface, making the surface ready to perform a grating with a new periodicity, which is then erased again and transformed into another diffractive optical element.

In conclusion, shape-shifting diffractive optical elements are realized directly in a single step of photo-structuring a photosensitive polymer film. Our approach is an excellent first step towards the fabrication of diffractive optical materials that will serve as the basis for future uses in photonics.

Acknowledgements

This work has been financially supported by the European Research Council (ERC) under the European Union's Horizon 2020 research and innovation programme "METAmorphoses", Grant Agreement No. 817794. This work has been supported by Fondazione Cariplo, Grant No. 2019-3923.

References

1. Oscurato, S.L., Reda, F., Salvatore, M., Borbone, F., Maddalena, P. and Ambrosio, A., "Shapeshifting Diffractive Optical Devices," Laser Photonics Rev, Vol. 16, No. 4, 2022.
2. Oscurato, S.L., Salvatore, M., Maddalena, P. and Ambrosio, A., "From nanoscopic to macroscopic photo-driven motion in azobenzene-containing materials", Nanophotonics, Vol. 7, No. 8, 1387-1422, 2018.
3. Priimagi, A. and Shevchenko, A., "Azopolymer-based micro - and nanopatterning for photonic applications," Journal of Polymer Science Part B: Polymer Physics, 52(3), pp.163-182. 2014. Vol. 52, No. 3, 163-182, 2014.
4. Oscurato, S.L., Reda, F., Salvatore, M., Borbone, F., Maddalena, P. and Ambrosio, A., "Large-Scale Multiplexed Azopolymer Gratings with Engineered Diffraction Behavior," Advanced Materials Interfaces, Vol. 8, No. 21, 2021.
5. Oscurato, S.L., Salvatore, M., Borbone, F., Maddalena, P. and Ambrosio, A., "Computer-generated holograms for complex surface reliefs on azopolymer films," Scientific Reports, Vol. 9, No. 1, 2019.

Comparison between the optical force by the microscopic model of chiral molecules and that based on the phenomenological chiral susceptibility

T. Horai[1*] and H. Ishihara[1,2]

[1] Department of Materials Engineering Science, Graduate School of Engineering Science, Osaka University, 1-3 Machikaneyama-cho, Toyonaka, Osaka 560-8531, Japan
[2] Center for Quantum Information and Quantum Biology, Osaka University, 1-2 Machikaneyama-cho, Toyonaka, Osaka 560-0043, Japan
[*]corresponding author: horai.t@opt.mp.es.osaka-u.ac.jp

Abstract: For calculating the optical force acting on chiral molecules, phenomenological chiral susceptibility is widely used, where the microscopic molecular structures are not treated explicitly. In this contribution, considering the Born-Kuhn model, we compare the optical force obtained based on the microscopic model of chiral molecules with that based on phenomenological chiral susceptibility. As a result, the optical spectra and their difference due to chirality appear differently between both treatments.

Recently, the separation of chiral molecules by optical force has been getting attention and actively researched. However, the separation of nanometer-sized chiral molecules, which are considerably smaller than the wavelength of light, remains challenging. For discussing its feasibility theoretically, it is important to evaluate the optical force accurately acting on chiral molecules. However, in previous studies, the optical force acting on chiral molecules has been evaluated based on a phenomenological susceptibility [1], called chiral susceptibility. The difference in optical response, for example, by a helical structure is expressed in the Pasteur parameter, which expresses the magnitude of chirality, in the chiral susceptibility. Therefore, it is necessary to discuss how this evaluation method is accurate when evaluating the optical force on chiral molecules. Based on this background, in this study, we compare the optical force evaluating it by using phenomenological chiral susceptibility and that obtained considering the microscopic structure of the molecule.

We compare the two cases using the Born-Kuhn model, as shown in Figure 1, which represents coupled two dipoles. We define the pair of dipoles: $\mathbf{d}_i = d\mathbf{e}_x$ and $\mathbf{d}_j = d\mathbf{e}_y$ as the R-enantiomer and $\mathbf{d}_i = d\mathbf{e}_x$ and $\mathbf{d}_{j'} = -d\mathbf{e}_y$ as the S-enantiomer ($\mathbf{e}_k$ is the unit vector along the k-axis), with the electric dipole moment d. The incident light is assumed to be right circularly polarized light.

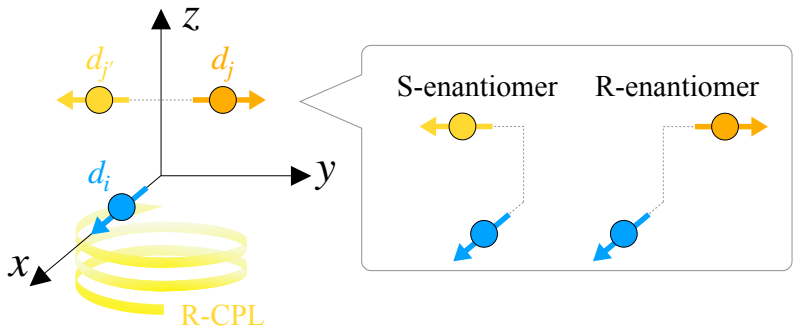

Figure 1 Chiral molecule expressed by the Born-Kuhn model.

When the phenomenological chiral susceptibility is used, the optical force acting on the non-magnetic chiral molecule is expressed as [1],

$$\langle \mathbf{F}_{\mathrm{phen}}(\omega) \rangle = \frac{k|E_0|^2}{2} \left(\mathrm{Im}[\alpha(\omega)] - 2\sqrt{\frac{\varepsilon_0}{\mu_0}} \mathrm{Im}[\chi(\omega)] \right) \mathbf{e}_z, \tag{1}$$

where E_0 is the incident light amplitude, k is the wave number. α, χ satisfy the following equations [2],

$$\alpha(\omega) = \frac{n|\mathbf{d}|^2}{3} \left(\frac{1}{\bar{E} - \hbar\omega + i\gamma} - \frac{1}{\bar{E} + \hbar\omega + i\gamma} \right) - \varepsilon_0, \tag{2}$$

$$\chi(\omega) = -\frac{in\mathbf{d} \cdot \mathbf{m}}{3} \left(\frac{1}{\bar{E} - \hbar\omega + i\gamma} - \frac{1}{\bar{E} + \hbar\omega + i\gamma} \right), \tag{3}$$

where n is the number of molecular dipoles, $\mathbf{d}$ and $\mathbf{m}$ are the electric and magnetic dipole moment, respectively. $\bar{E}$ and γ are the excitation energy and relaxation constant of the molecule. The optical force can be calculated in the Born-Kuhn model by using equations (2), (3).

On the other hand, when the optical force is calculated considering the microstructure of the Born-Kuhn model, the equation is as follows [3]:

$$\langle \mathbf{F}_{\mathrm{micro}}(\omega) \rangle = \frac{kd^2|E_0|^2}{2} \left\{ \frac{\xi_1(\omega)}{\xi_0(\omega)} \pm \frac{\xi_2(\omega)}{\xi_0(\omega)} \sin k(z_i - z_j) \right\}. \tag{4}$$

The explicit expressions for ξ_0, ξ_1 and ξ_2 are not provided here because of the complexity of the tabular expressions. They include information on the interaction between the two dipoles. The second term on the right-hand side of (5) is the contributions that varies according to the handedness of the chiral molecule, indicating that when $z_i - z_j = 0$, i.e. when the chirality disappears, the difference in optical force disappears.

Figure 2 shows the calculation results of (a) the incident light energy dependence of the optical force acting on the R-enantiomer and (b) the incident light energy dependence of the optical force difference between both cases. Here, the parameters of excitation energy, relaxation constant, and dipole moment of the molecule were taken equally. A comparison of these results shows that the orders of the optical force are similar around the resonance region, but a clear difference in peak shape appears. This strongly suggests that the consideration of the microscopic structures of chiral molecules is necessary for the accurate evaluation of chirality-dependent optical forces.

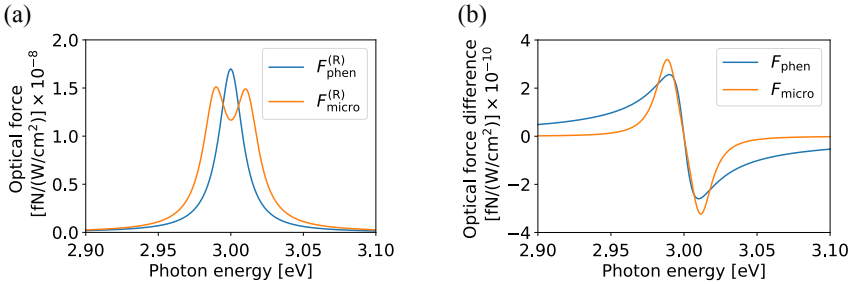

Figure 2 The dependence of (a) the optical force acting on the R-enantiomer on the incident light energy and (b) the optical force difference on the incident light energy for both cases under right circularly polarized light irradiation.

References

1. A. Canaguier-Durand and C. Genet, “Chiral route to pulling optical forces and left-handed optical torques,” Phys. Rev. A Vol. 92, No. 4, 043823, 2015.
2. A. O. Govorov and Z. Fan, “Theory of Chiral Plasmonic Nanostructures Comprising Metal Nanocrystals and Chiral Molecular Media,” Chem. Phys. Chem, Vol. 13, No. 10, 2551–2560, 2012.
3. T. Horai, H. Eguchi, T. Iida, and H. Ishihara “Formulation of resonant optical force based on the microscopic structure of chiral molecules,” Opt. Express, Vol. 29, No. 23, 38824–38840, 2021.

Optoelectronics, Photonic Materials and Devices

VCSEL-based optical Ising solver

A. J. Danner[1,*], S. T. Lim[2]

[1]National University of Singapore, Singapore
[2]Institute for High Performance Computing, Agency for Science, Technology and Research (A*STAR), Singapore
[*]corresponding author: adanner@nus.edu.sg

Abstract: We discuss the use of vertical cavity surface-emitting lasers (VCSELs) and an optical feedback network to implement an all-optical Ising computer. We experimentally demonstrate a proof-of-concept with a small number of qubits.

An Ising computer is a highly parallel form of computer architecture which is well-suited to the solution of large combinatorial optimization problems. In a system with m analog bits σ_m connected to one another by connections J_{mn}, a physical system is sought which serves to minimize the Hamiltonian $\mathcal{H} = \sum_{m,n} J_{mn}\sigma_m\sigma_n$ (the task ultimately being to determine whether $\sigma_m = 1$ or $\sigma_m = -1$). There are several proposals which seek to solve this system electromagnetically, for instance with the use of spatial light modulators [1], Mach-Zehnder modulators [2], and injection locked systems of lasers [3]. In this presentation, we will show how VCSELs are particularly suitable for storing analog bits during computation, and how programmable all-to-all interaction can be achieved. We then show a physical demonstration of the system.

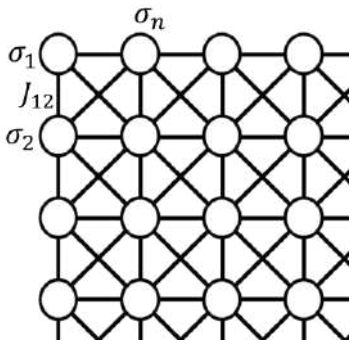

Fig. 1: An array of VCSELs can serve as Ising bits

This research is supported by the National Research Foundation, Singapore and A*STAR under its Quantum Engineering Programme (NRF2021-QEP2-02-P12).

References

1. Pierangeli, D., G. Marcucci, and C. Conti, “Large-Scale Photonic Ising Machine by Spatial Light Modulation,” Physical Review Letters, Vol. 122, 213902 (2019).
2. Böhm, F., G. Verschaffelt, G. and Van der Sande. “A poor man’s coherent Ising machine based on opto-electronic feedback systems for solving optimization problems,” Nat. Commun. 10, 3538 (2019).
3. Utsunomiya S., K. Takata, and Y. Yamamoto. “Mapping of Ising models onto injection-locked laser systems,” Optics Express, Vol. 19, 18091-18108 (2011).

Discovering new high-refractive-index dielectric materials

Søren Raza
Department of Physics, Technical University of Denmark, Fysikvej, DK-2800 Kongens Lyngby, Denmark

E-mail: sraz@dtu.dk

Abstract: Dielectric materials with a high refractive index are key in the design of optical nanoantennas and metasurfaces. Here, we use a high-throughput screening method combined with optical Mie theory to evaluate the performance of more than 2000 materials and discover a new promising material, boron phosphide, which has so far been elusive. We prepare boron phosphide nanoparticles and experimentally demonstrate that they support Mie resonances across the visible and the near ultraviolet using both optical measurements and electron energy-loss spectroscopy.

Optical metasurfaces and nanoantennas based on high-refractive-index materials offer efficient manipulation of light on the nanoscale due to low optical losses and their ability to support both magnetic- and electric-type Mie resonances.[1] The development of all-dielectric nanophotonics has been largely driven by the availability of just a few high-index materials, such as silicon, gallium phosphide, and titanium dioxide, which offer low-loss operation in most of the visible spectral range and where lithographic processing has been well established.[2] For applications in the important ultraviolet spectral range, the availability of high-index materials is even more scarce. Identifying new optical materials that may outperform the ones currently available, offer new functionalities or give access to other spectral regions is critical for many applications.

In this work,[3] we discover new high-index materials using high-throughput screening based on density functional theory (DFT). Starting from a library of more than 2000 thermodynamically stable binary materials, we develop a workflow to identify isotropic high-index dielectric materials across a spectral range spanning from mid infrared to the deep ultraviolet. The wavelength-dependent complex refractive indices of these materials are calculated within the random phase approximation and used as input for Mie scattering calculations to evaluate their optical performance. Our methodology identifies all of the known high-index materials as well as other materials, which have been less investigated. In particular, we identify boron phosphide (BP), which offers a refractive index above 3 with very low absorption losses in a spectral range spanning from the infrared to the near ultraviolet.

To support our computational discovery, we prepare BP nanoparticles and experimentally demonstrate that they support Mie resonances across the visible and ultraviolet spectral ranges using dark-field optical measurements and electron energy-loss spectroscopy. The Mie resonance energies can be tuned with particle size. We also demonstrate a laser reshaping method to realize spherical BP nanoparticles, which host multiple Mie resonances in quantitative agreement with full-field optical simulations. Our experimental measurements of Mie resonances in BP nanoparticles demonstrate the potential of high-index BP across a broad spectral range as well as validate the refractive index obtained from DFT calculations. Besides the discovery of BP, we believe that our high-throughput screening results provide an overview of existing materials as well as a pathway for realizing new high-index materials.

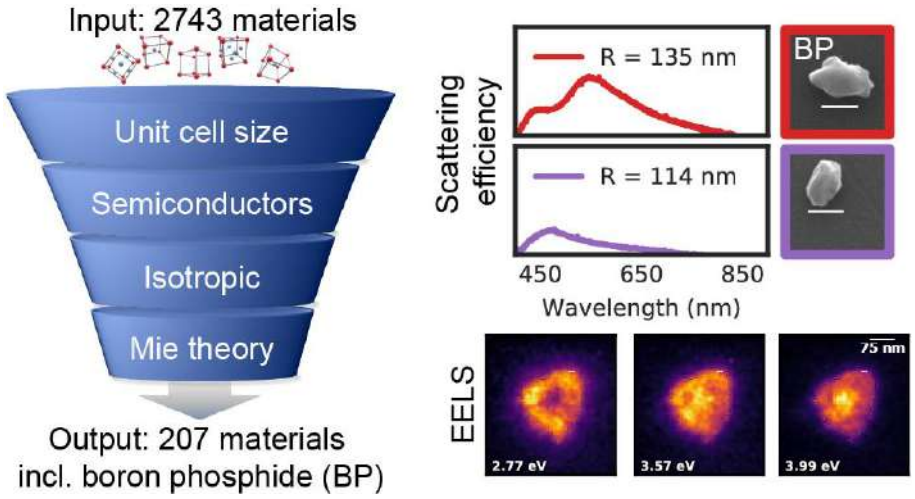

Fig. 1. High-throughput screening of a large library of materials identifies many high-refractive-index materials across a broad spectral range. Boron phosphide (BP) appears particularly promising due to its refractive index above 3 in a spectral range covering the visible and reaching the near ultraviolet. BP nanoparticles are prepared and their scattering properties are measured using far-field dark-field spectroscopy and near-field electron energy-loss spectroscopy (EELS). Combined with full-field optical simulations, these measurements demonstrate that BP nanoparticles support Mie resonances at visible and ultraviolet energies.

References

1. Kuznetsov, A. I., Miroshnichenko, A. E., Brongersma, M. L., Kivshar, Y. S. & Luk'yanchuk, B. Optically resonant dielectric nanostructures. *Science* **354**, aag2472 (2016).
2. Baranov, D. G. *et al.* All-dielectric nanophotonics: the quest for better materials and fabrication techniques. *Optica* **4**, 814 (2017).
3. Svendsen, M. K. *et al.* Computational Discovery and Experimental Demonstration of Boron Phosphide Ultraviolet Nanoresonators. *Adv. Opt. Mater.* **2200422**, 2200422 (2022).

Integration of Mid-index Silicon Nitride Platforms for CMOS Photonic Circuits

T. Domínguez Bucio[1, *], V. Vitali[1,2], I. Skandalos[1], S. T. Ilie[1], T. Rutirawut[1], J. M. Luque González[3], G. Wangüemert Pérez[3], A. Ortega Moñux[3], I. Molina Fernández[3], P. Cheben[4], J. Schmid[4], C. Lacava[1,2], P. Petropoulos[1] and F. Y. Gardes[1]

[1] Optoelectronics Research Centre, University of Southampton, SO17 1BJ UK
[2] *Electrical, Computer and Biomedical Engineering Department, University of Pavia, Pavia 27100, Italy*
[3] *E.T.S.I. Telecomunicación, Universidad de Málaga. Campus de Teatinos, 29071 Málaga, Spain*
[4]*National Research Council Canada, 1200 Montreal Road, Ottawa, Ontario, Canada K1A 0R6*
[*]Corresponding author: T.Dominguez_Bucio@soton.ac.uk

Abstract: We present our progress in the demonstration of novel material integration schemes that facilitate the incorporation of mid-index silicon nitride platforms with a variety of refractive indices in CMOS compatible photonic integrated circuits. The integration of such materials enables the realization of linear and nonlinear devices for a variety of applications, including telecom and all-optical processing.

In recent years, silicon nitride (SiN) platforms with a mid-refractive index (1.7-3.1) have gained interest for the demonstration of photonic integrated circuits. They offer full CMOS compatibility with low propagation losses and flexible optical properties that can be tailored to achieve linear and nonlinear properties suited for a wide range of applications [1-2]. In this work, we present our progress in the incorporation of silicon nitride with two distinct refractive indices for the realisation of advanced telecom and all-optical processing devices [3-4]. Our work includes a novel butt-coupling integration scheme between micro-meter scale SiN and silicon-on-insulator (SOI) waveguides based on N-rich SiN layers with a refractive index of 1.88 at 1310nm. This scheme has been used to seamlessly interface SiN (de)multiplexers with SOI circuits and can be further exploited to integrate active devices with thick material stacks that are often difficult to integrate with thin SOI geometries. We have also demonstrated a Si-rich SiN platform with a refractive index of 2.41 at 1550nm with an enhanced nonlinear Kerr coefficient, negligible two-photon absorption, and low propagation loss. This platform has enabled the demonstration of a fully integrated four-wave-mixing based wavelength converter in the C and L wavelength bands for all-optical signal processing.

This research was supported by the Engineering and Physical Sciences Research Council (EPSRC) with the grants “Rockley Photonics and the University of Southampton: A Prosperity Partnership” (EP/R003076/1) and “Silicon rich silicon nitride Nonlinear Integrated Photonic ciRcuits & Systems (juNIPeRS)”, and by the H2020 EU project “PlasmoniAC” (871391).

References

1. T. Domínguez Bucio et al., “Silicon Nitride Photonics for the Near-Infrared,” *IEEE Journal of Selected Topics in Quantum Electronics*, vol. 26, no. 2, pp. 1–13, 2020.
2. F. Gardes *et al.*, “A Review of Capabilities and Scope for Hybrid Integration Offered by Silicon-Nitride-Based Photonic Integrated Circuits,” *Sensors*, vol. 22, no. 11, p. 4227, 2022.
3. T. Domínguez Bucio et al., “Material and optical properties of low-temperature NH3-free PECVD SiNx layers for photonic applications,” *Journal of Physics D: Applied Physics*, vol. 50, no. 2, 2017.
4. C. Lacava, S. Stankovic, A. Z. Khokhar, T. D. Bucio, F. Gardes, G. T. Reed, D. J. Richardson, and P. Petropoulos, “Si-rich silicon nitride for nonlinear signal processing applications,” *Scientific Reports*, vol. 7, no. 22, pp. 1–13, 2017.

Steering light in flat-optics 2D semiconducting layers

M. C. Giordano[1*], F. Buatier de Mongeot[1]

[1]Dipartimento di Fisica, Università di Genova, Via Dodecaneso 33, 16146 Genova, Italy
[*]corresponding author: maria.caterina.giordano@unige.it

Abstract: The nanoscale reshaping of 2D Transition Metal Dichalcogenide semiconductor layers as flat-optics nanogratings is shown over large-area demonstrating the capability to effectively control light propagation and photon absorption. These flat-optics layers support tunable Rayleigh Anomalies, promoting strong in-plane electromagnetic confinement, directional light scattering, and broadband photon absorption enhancement with strong impact in photoconversion applications. Finally, deterministic 2D TMD semiconductor nanocircuits have been devised via thermal-Scanning Probe Lithography locally tailoring their optoelectronic response for nanophotonic applications.

Two-dimensional (2D) Transition Metal Dichalcogenide (TMD) semiconductors have attracted diffuse interest due to their exceptional optoelectronic properties. However, the inherent low photon absorption of the atomic layers demands for novel light coupling schemes. There is also an urgent request to scale-up the lateral size of the 2D layers, limited in micrometric flakes, and to engineer their shape at the nanoscale. Here the nanoscale reshaping of 2D TMDs layer is shown over large-area (cm^2 scale) demonstrating superior photon harvesting properties and opening new perspectives in photonics [1-4]. In a first activity we show a flat-optics scheme based on large-area few-layers MoS_2 forming periodic nanogratings. These nanopatterned layers can effectively steer the light propagation via Rayleigh Anomalies [2,3], promoting strong in-plane electromagnetic confinement directional light scattering and broadband photon absorption enhancement, with strong impact in photoconversion. In particular, a photo to chemical energy conversion process have been recently boosted in flat-optics few-layer semiconductors lying onto flexible templates, opening new possibilities for large-scale energy storage applications [4]. As a step forward, deterministic nanocircuits devices based on few-layer TMD semiconductors have been fabricated thanks to a new *additive* thermal-Scanning Probe Lithography approach [5]. This way Van der Waals heterostructure devices can be engineered locally tailoring the optoelectronic response of the 2D layers, and opening new perspectives in nanoelectronics, nanophotonics and photoconversion.

References

1. C. Martella et al., Adv. Mater. 30, 1705615, 2018.
2. M. Bhatnagar et al., Nanoscale, 12, 24385, 2020.
3. M. Bhatnagar et al., ACS Appl. Mater. Interf., 13, 11, 13508, 2021.
4. G. Ferrando et al., Nanoscale 2023.
5. M. C. Giordano et al., Adv. Mater. Interf. 2201408, 2023.

Magnonic antenna effect for strong magnon-polariton in magnetic thin layer

T. Yokoyama[1*], K. Kato[1], and H. Ishihara[1,2]

[1]Department of Material Engineering Science, Osaka University, Japan
[2]Center for Quantum Information and Quantum Biology, Osaka University, Japan
yokoyama.t.es@osaka-u.ac.jp

Abstract: Magnon-polariton (MP) is a candidate to store and manipulate quantum information. Therefore, emergence of strong MP is an important subject. In this study, we theoretically investigate strong MP in magnetic layered structure. We discuss a longitudinal coupling between magnons in thin and thick magnetic layers. In the thick layer, strong MPs is formed. Owing to the longitudinal coupling between the layers, we obtain strong and functionalized MPs even in a microscale thin layer, which means magnonic antenna effect.

Magnetism is a one of the most stable quantum phenomena. In ferri- and ferro-magnets, a low-energy excitation can be obtained by a microwave photon incidence, which is called magnon. The magnon excitation is found even at the room temperature [1] and the magnon can carry an information without charge current in magnetic insulators [2]. However, typical magnon velocity and magnon excitation density are ineffective for application using magnon current. To overcome them, strong magnon-polariton (MP) have attracted many attentions and has been studied intensively [3,4]. However, to obtain a strong magnon-photon coupling, more than millimeter-order size of the magnetic material is required, which is not favorable condition for application.

In this study, we investigate theoretically a strong MP in a micrometer-scale thin magnetic layer [5]. Such thickness is favorable to fabricate magnonic circuits by using lithography technique. We propose a layered thin magnet/thin dielectric/thick magnet structure as shown in Fig. 1. In the two magnetic layers, magnons are excited and they are coupled with each other. This coupling is mediated by a longitudinal magnetic field. In the thin magnet, the magnon cannot couple to the microwave directly, whereas a strong microwave-magnon coupling is obtained in the thick layer, hence the MPs are also strong. Note that the microwave is transverse field. Owing to the interlayer magnon-magnon longitudinal coupling, the strong microwave-magnon transverse coupling is mapped to the thin magnetic layer, thus a strong MP is obtained in the thin layer. We refer this indirect mechanism as “magnonic antenna effect.” To discuss the magnonic antenna effect in microscopic description, we formulate a nonlocal response theory for magnons self-consistently coupled with Maxwell’s equations [5]. In our formulation, the spatial correlation between the magnon wavefunction and both longitudinal

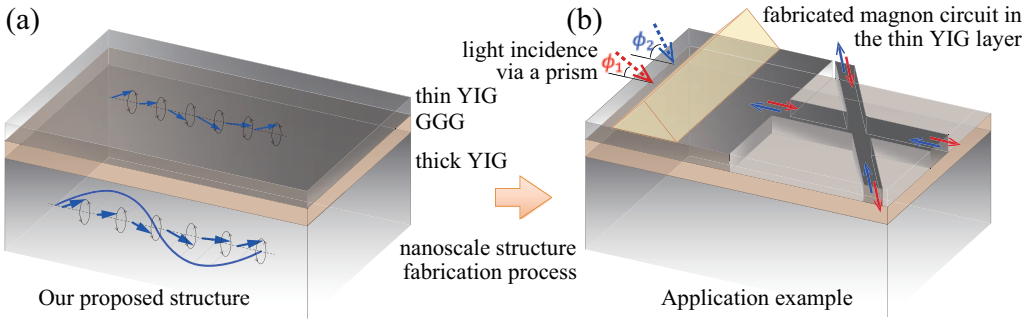

Fig. 1: Schematic of multi-layer structure for magnonic device. (a) Proposed structure comprising thin YIG / thin GGG / thick YIG layers. (b) Imaginary processed structure [5].

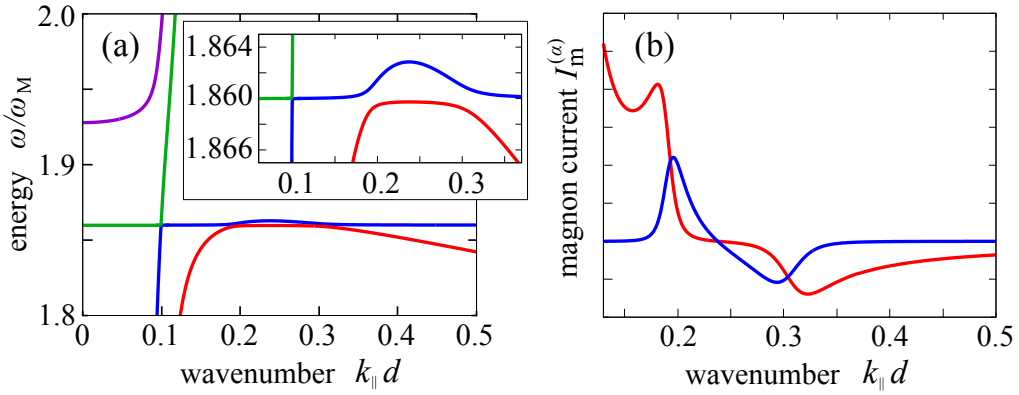

Fig. 2: (a) Dispersion relation of MPs in the proposed structure. Inset is enlarged view. (b) Magnon current evaluated by group velocity of the dispersion and magnon density [5].

and transverse Maxwell fields becomes an essential factor. Especially a waveguide mode formed by the dielectric constants of magnetic and dielectric layers is significant, which supports a long coherence time of photons and enlarges the coupling strength between the magnon and photon.

We assume yttrium iron garnet (YIG) for the magnetic layers and gadolinium gallium garnet (GGG) for dielectric layer. The thicknesses of three thin YIG, thin GGG, and thick YIG layers are 100nm, 1μm, and 500μm, respectively. Figure 2(a) represents the dispersion relation of MPs formed in the proposed layered structure. The strong MPs show a high magnon density and positive/negative dispersion. Around $k_\parallel d$ = 0.19 and 0.30, strong MPs in the thick YIG are coupled with magnons in the thin YIG, which results in strong MPs in the thin YIG as the magnonic antenna effect. From the slope of MP dispersions and magnetization amplitude corresponding to the magnon density, we evaluate the magnon current in Fig. 2(b). If a thin YIG was isolated, the magnon current was not enlarged. In our proposed structure, the magnon current is enlarged even in the thin YIG. A wavenumber $k_\parallel$ of incident microwave can be tuned by an incident angle. Hence, the magnonic current direction is also swichable by the incident angle of microwave.

These our results will give a guideline to examine magnonic circuit fabricated on a thin magnetic layer.

Acknowledgments: T.Y. is supported by JSPS KAKENHI 18K13484 and Toyota Riken Scholar. H.I. is supported by JSPS KAKENHI 18H01151.

References

1. Demokritov, S. O., V. E. Demidov, O. Dzyapko, G. A. Melkov, A. A. Serga, B. Hillebrands and A. N. Slavin, "Bose–Einstein condensation of quasi-equilibrium magnons at room temperature under pumping," Nature, Vol. 443, 430–433, 2006.
2. Kajiwara, Y., K. Harii, S. Takahashi, J. Ohe, K. Uchida, M. Mizuguchi, H. Umezawa, H. Kawai, K. Ando, K. Takanashi, S. Maekawa and E. Saitoh, "Transmission of electrical signals by spin-wave interconversion in a magnetic insulator," Nature, Vol. 464, 262–266, 2010.
3. Tabuchi, Y., S. Ishino, T. Ishikawa, R. Yamazaki, K. Usami and Y. Nakamura, "Hybridizing Ferromagnetic Magnons and Microwave Photons in the Quantum Limit," Phys. Rev. Lett., Vol. 113, 083603, 2014.
4. Zhang, X., C.-L. Zou, L. Jiang, and H. X. Tang, "Strongly Coupled Magnons and Cavity Microwave Photons," Phys. Rev. Lett., Vol. 113, 156401, 2014.
5. Kato, K., T. Yokoyama and H. Ishihara, "Functionalized high-speed magnon-polaritons resulting from magnonic antenna effect," Phys. Rev. Appl, in press.

Scattering and diffraction

Diffraction of Plane Waves by a Junction between Magnetically Conductive and PMC Co-Planar Half-Sheets

G. Riccio[1*], G. Gennarelli[2], F. Ferrara[3], C. Gennarelli[3], and R. Guerriero[3]

[1]D.I.E.M. - University of Salerno, Italy
[2]I.R.E.A. – C.N.R., Italy
[3]D.I.In. - University of Salerno, Italy
[*]corresponding author: griccio@unisa.it

Abstract: This research work deals with the plane wave diffraction due to the discontinuity of a planar junction between a magnetically conductive half-sheet and a perfect magnetic conductor. The uniform asymptotic physical optics approach is used to solve such a diffraction problem in the context of the uniform geometrical theory of diffraction. The corresponding solution results from an analytical procedure and possesses the same simplicity of use of the heuristic solutions.

The plane wave diffraction due to the discontinuity of a planar junction between a magnetically conductive half-sheet and a perfect magnetic conductor (PMC) is studied (see Fig. 1).

The edge diffraction by an isolated magnetically conductive half-screen has been recently solved in the case of skew incidence [1] by employing the Uniform Asymptotic Physical Optics (UAPO) approach in the framework of the Uniform Geometrical Theory of Diffraction (UTD) [2]. A magnetically conductive sheet possesses free-space permittivity ε_0 and complex permeability μ, and is characterized by the surface conductivity $R_m = -j/\left[k_0\zeta_0 d(\mu_r - 1)\right]$ [1], [3], where ζ_0 and k_0 are the impedance and the propagation constant of the free space, respectively, $\mu_r = \mu/\mu_0$ and d is the thickness of the material. A PMC is obtained when $R_m = 0$. The conductive boundary conditions [3] have been exploited in [1] to achieve the expressions of the reflection and transmission coefficients to be used with parallel and perpendicular polarizations of the incident electric field.

A planar junction between a magnetically conductive half-screen (A) and a PMC (B) is lit by an incident plane wave (see Fig.1). The UAPO diffracted field by such a structure is achieved as a linear combination of the contributions associated to the edges of the involved surfaces [4], [5]:

$$\begin{pmatrix} E_\beta^d \\ E_\phi^d \end{pmatrix} = \left[F_A^d \; \underline{\underline{A}} + F_B^d \; \underline{\underline{B}}\right] \begin{pmatrix} E_{\beta'}^i \\ E_{\phi'}^i \end{pmatrix} \frac{\exp(-jk_0 s)}{\sqrt{s}} \tag{1}$$

where s is the distance from the diffraction point to the observation point P. The functions $F_{A,B}^d$ contain the UTD transition function F [2] and write as:

$$F_{A,B}^d = \frac{\exp(-j\pi/4)}{2\sqrt{2\pi k_0}} \; \frac{F\left(2k_0 s \sin^2\beta' \cos^2\left(\dfrac{\phi_{A,B} \pm \phi'_{A,B}}{2}\right)\right)}{\sin^2\beta'(\cos\phi_{A,B} + \cos\phi'_{A,B})} \tag{2}$$

with $\phi'_A = \phi'$, $\phi'_B = \pi - \phi'$, $\phi_A = \phi$ and $\phi_B = \pi - \phi$ if β', ϕ' define the incidence direction and the diffraction direction is given by $\beta = \beta', \phi$. The matrices $\underline{\underline{A}}$ and $\underline{\underline{B}}$ account for the expressions of the magnetic PO equivalent surface currents and for the transformation rules between the local reference systems.

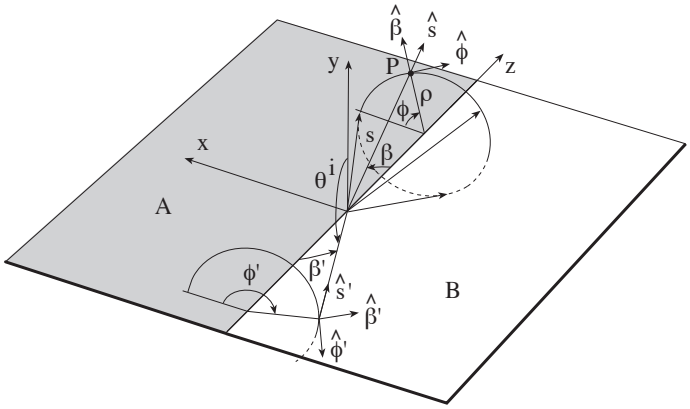

Fig. 1. Reference systems.

Figures 2(a) and 2(b) show the comparisons with the data obtained by running the RF unit of Comsol Multiphysics® when considering $\beta' = 90°, \phi' = 60°$ and $s = \rho = 7\lambda_0$ (λ_0 is the free-space wavelength). The half-sheet A is characterized by $\mu_r = 8$ and $d = 0.02\lambda_0$. The PMC thickness is the same. A good accordance is evident in the full observation range, thus validating the efficiency of the proposed solution.

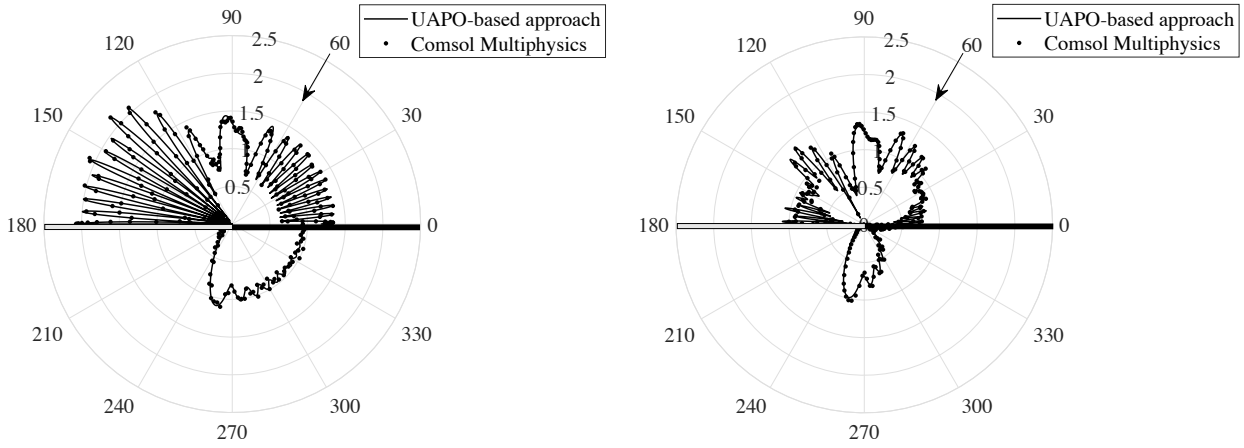

(a) amplitude of the β-component (b) amplitude of the ϕ-component

Fig. 2. Electric field: comparisons with the data resulting from Comsol Multiphysics®.

References

1. Riccio, G., G. Gennarelli, F. Ferrara, C. Gennarelli and R. Guerriero, "A PO-based uniform asymptotic procedure for the scattering from a magnetically conductive half-screen," IEEE Antennas Wireless Propag. Lett., Vol. 22, No. 1, pp. 204-207, Jan. 2023.
2. Kouyoumjian, R.G. and P.H. Pathak, "A uniform geometrical theory of diffraction for an edge in a perfectly conducting surface," Proc. IEEE, Vol. 62, pp. 1448-1461, Nov. 1974.
3. Senior T.B.A. and J.L. Volakis, *Approximate Boundary Conditions in Electromagnetics*, Stevenage: IEE, 1995.
4. Gennarelli, G. and G. Riccio, "Diffraction by a planar metamaterial junction with PEC backing," IEEE Trans. Antennas Propag., Vol. 58, No. 9, pp. 2903-2908, Sept. 2010.
5. Gennarelli, G. and G. Riccio, "A solution for the plane wave diffraction by the discontinuity between two co-planar metamaterial sheets," IEEE Trans. Antennas Propag., Vol. 70, No. 6, pp. 4705-4711, Jun. 2022.

Complex Time Delay of Short Pulses in Scattering Systems

Isabella Giovannelli[1], and Steven M. Anlage[1*]

[1]Physics Department, University of Maryland, College Park, MD 20742, USA

[*]corresponding author: anlage@umd.edu

Abstract: Complex time delay (derived from frequency-domain scattering matrix data) gives a quantitative description of the time delay and amplitude distortion suffered by a pulse as it propagates through a complicated scattering system. However, the physical meaning of negative real parts, and the imaginary part, of the complex time delay is unclear. Here we perform time-domain experiments on pulse propagation through a microwave graph to provide a clear physical interpretation of the complex time delay.

We have further developed the concept of complex time delay for wave scattering [1] and related it to the locations of the poles and zeros of the scattering matrix in the complex frequency plane [2,3]. The complex time delays (Wigner, transmission, reflection) are easily evaluated from measurements of the scattering matrix in the frequency domain. They enable detailed measurements of S-matrix zeros as the condition of coherent perfect absorption is approached, for example. We now address the physical meaning of the real and imaginary parts of the complex time delay through a series of time-domain experiments on pulse propagation through complex scattering systems. Short pulses are sent into microwave graph structures whose complex time delay has been determined from frequency domain measurements. We demonstrate the physical meaning of the real and imaginary parts of the time delays through their effects on the pulse delay and center frequency [1]. The use of complex time delay to manipulate pulses in novel ways will be explored and discussed.

This work was supported by NSF RINGS under grant No. ECCS-2148318, ONR under Grant No. N000141912481, DARPA WARDEN Grant HR00112120021, and the Maryland Quantum Materials Center.

References

1. M. Asano, K. Y. Bliokh, Y. P. Bliokh, A. G. Kofman, R. Ikuta, T. Yamamoto, Y. S. Kivshar, L. Yang, N. Imoto, Ş K. Özdemir, and F. Nori, "Anomalous time delays and quantum weak measurements in optical micro-resonators," Nat. Commun. 7 (1), 13488 (2016).
2. Lei Chen, Steven M. Anlage, and Yan V. Fyodorov, "Generalization of Wigner Time Delay to Sub-Unitary Scattering Systems," Phys. Rev. E **103**, L050203 (2021).
3. Lei Chen and Steven M. Anlage, "Use of Transmission and Reflection Complex Time Delays to Reveal Scattering Matrix Poles and Zeros: Example of the Ring Graph," Phys. Rev. E **105**, 054210 (2022).

Propagation theory

On the Implementation of Large Intelligent Antenna Systems without Equalization

Mário Marques da Silva[1,2,3,4*], **Rui Dinis**[2,3,5]

[1]Universidade Autónoma de Lisboa, Portugal

[2]Autonoma TechLab, Portugal

[3]Instituto de Telecomunicações, Portugal

[4]Ci2 – Centro de Investigação em Cidades Inteligentes, Portugal

[5]Faculty of Sciences and Technology, Universidade Nova, Portugal
[*]Corresponding author: marques.silva@ieee.org

Abstract

This paper studies Large Intelligent Systems (LIS) with different receiver types: Equal Gain Combining (EGC), Maximum Ratio Combining (MRC), Zero Forcing (ZF), and Minimum Mean Squared Error (MMSE). We consider Single Carrier with Frequency Domain Equalization (SC-FDE). It is shown that the MRC receiver is much simpler, from the computational point of view than ZF and MMSE, while performing closer to those. Moreover, the MRC avoids the need to perform equalization and, consequently, the need to make channel estimate.

1. Introduction

5G communications were based on Massive MIMO (Multiple Input Multiple Output) and Millimeter Wave Communications. The new requirements expected for 6G communications demand new transmission techniques and spectrum. LIS systems alongside Terahertz bands are expected to be the key issues to achieving such demanding requirements [1].

m-MIMO (Massive MIMO—Multiple Input Multiple Output), UM-MIMO (Ultra Massive-MIMO), and ELAA (Extremely Large Antenna Arrays) are three of the most significant developments in communication system design in recent decades, and they have significantly improved data rate, network capacity, and performance. In this regard, the LIS concept can be viewed as a beyond-massive MIMO in a telecommunications network with increased capacity and data rate, where the number of antennas is even higher.

Traditionally, wireless communications are established in the far-field, that is, with propagation distances beyond the Fraunhofer distance (the Fraunhofer distance is only a few wavelengths). The LIS system comprises several panels, and each panel includes several antenna elements [2,3,4]. As can be seen from Figure 1, the LIS system acts as a near-field beamforming, that is, the communication is established behind the Fraunhofer distance [5,6]. In this case, the individual array elements are in the far-field but not the array as a whole. Consequently, the focus is established not only in the bearing and elevation planes but also in the distance dimension. This allows for the reduction of interferences between users that are aligned but located at different ranges, bringing another advantage, as compared to traditional beamforming [7]. The typical distance between the antenna elements is λ/2. The channel correlation between the antenna elements allows for the creation of the above-described beam.

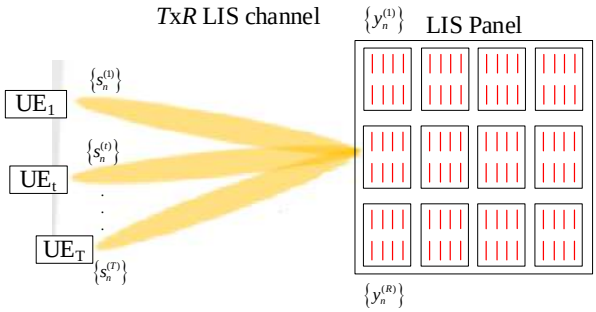

Figure 1 Block diagram of a LIS System

2. System Model

This paper considers the uplink direction of a LIS system, where the link between the Base Station (BS) and the Mobile Terminal (MT) presents two different paths: one direct, and a second through the LIS. In this paper, we focus on the link between the MTs and the LIS system.

This LIS considers a number of *P* panels, where each panel comprises *D* antennas (receiving antennas because we consider the uplink). Moreover, the mobile terminal considers a single transmitting antenna. The total number of receiving antennas, from the LIS side, is equal to $R = P \times D$. Moreover, we consider that *T* MTs transmit simultaneously. This originates a channel of dimension $R \times T$ from the total number of MTs into the LIS system.

In LIS system settings, various receiver design methodologies are possible. Frequency Domain Equalization (FDE) receivers include ZF, MMSE, MRC, and EGC. The ZF and MMSE algorithms, which are based

on matrix inversions, are unquestionably harmful in this type of system, even though their Bit Error Rate (BER) results can be excellent because the computational cost grows exponentially with the number of transmitting and receiving antennas. In contrast, the MRC and EGC procedures are straightforward, resulting in less processing and, as a result, energy savings [8].

For the evaluation of these various receivers, we need to know about feedback matrices (B_k for feedback matrices).

Using the matrix-vector representation, we can express (1) for LIS structure, using the corresponding frequency-domain block as [1]:

$$Y_k = H_k U_k + W_k \tag{2}$$

where H_k denotes the $R \times T$ channel matrix for the k^{th} frequency. W_k denotes the channel noise.

The combined effect of Inter-Symbol Interference (ISI) and channel noise, the equalized samples S_k, is usually found by optimizing the coefficients B_k under a certain criterion.

$$S_k = B_k Y_k \tag{3}$$

where B_k denotes the $R \times T$ precoding matrix, and the data symbols $X_k = \left[X_k^{(1)}, ..., X_k^{(R)} \right]$. Depending on the algorithm employed, the precoding matrix B_k can be computed as [8]:

- ZF employs the Moore-Penrose quasi-inverse matrix technique, also known as the ZF receiver matrix. This approach totally separates the several transmitted data streams by inverting the channel matrix H.

$$B_k = \left(H^H H \right)^{-1} H^H \tag{4}$$

- Employing the MMSE provides estimated signals with the minimum mean squared error.

$$B_k = \left[H^H H + N_o I \right]^{-1} H^H \tag{5}$$

- Using the MRC combines the signals from each branch in order to maximize the received SNR. The inverse of the channel matrix.

$$B_k = H^H \tag{6}$$

- Using the EGC to obtain a high SNR, this equalizer simply uses phase rotations, mixing all received signals with unitary weights.

$$B_k = \exp\left\{ j \cdot \arg\left(H^H \right) \right\} \tag{7}$$

For defining the iterative receiver (interference canceller), used by MRC and EGC, we have:

$$\tilde{X}_k = Y_k - C_k \bar{X}_k \tag{8}$$

where the frequency domain estimated data symbols are $\tilde{X}_k = \left[\tilde{X}_k^{(1)}, ..., \tilde{X}_k^{(R)} \right]^T$. The interference cancellation matrix can be computed by

$$C_k = H_k B_k - I \tag{9}$$

where I is an $R \times R$ identity matrix.

3. Simulation Results

This section studies the BER performance results obtained with Monte Carlo simulations, using LIS systems, in the Uplink direction, associated with SC-FDE block transmission technique. E_b stands for the energy of the transmitted bits, and N_0 is the one-sided power spectral density of the noise. The BER is calculated as a function of E_b/N_0. A block size of N = 256 symbols was used for the QPSK modulation (identical results were seen for different values of N, given that $N >> 1$).

The LIS system comprises several panels, whereas each panel includes several antenna elements. The distance between the antenna elements is λ/2. The channel correlation between the antenna elements allows for the creation of the above-described beam. Five statistically independent equal power paths were considered in the Monte Carlo simulation to translate for an extreme Rayleigh fading channel. The simulations considered four receiver types: ZF, MMSE, MRC and EGC.

Figure 2 shows the performance results for 4X25 LIS system (4 panels, each with 25 antennas, making a total of 200 antennas), with 5 users, with and without equalization, for the ZF, MRC, EGC, and MMSE, four distinct receivers. Note that only the MRC and EGC may avoid equalization, while ZF and MMSE receivers cannot get rid of this. This makes MRC and EGC even simpler, besides the possibility of avoiding the channel matrix inversion for each frequency component of the channel. As can be seen, for the MRC and EGC receivers and 4X25 LIS system, the equalization does not bring any added value in terms of performance improvement, as compared to the results without equalization. Moreover, in this scenario, channel estimation is not required, which is very demanding in previous MIMO systems [8]. From these results we can conclude that the LIS system allows the use of a very simple processing, as equalization and channel estimation are avoided, at least for this LIS configuration. Moreover, it is viewed that the MMSE and ZF are the receivers that achieve the best performance, whose curves are almost superimposed. On the other hand, the MRC performs better than the EGC (whose performance is the worst), but these receivers present a high level of simplicity.

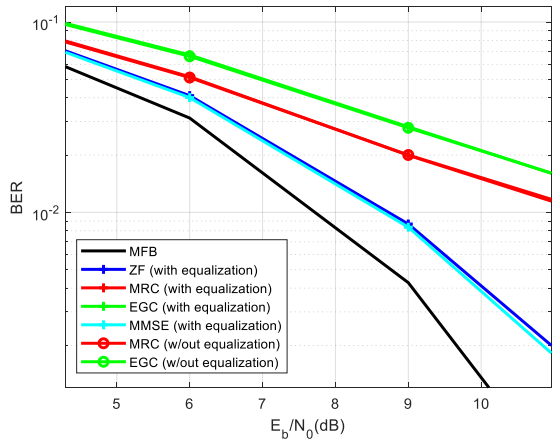

Figure 2. Results for 4X25 LIS System, with 5 users, with and without equalization.

Figure 3 shows the performance results 4X25 versus 4X225 LIS System, with 2 users (1 reference users plus 1 interfering user), for four distinct receivers: the ZF, MRC, EGC, and MMSE, without LDPC codes. As before, the MMSE curve superimpose the ZF one. For all receiver types, the efficiency obtained results with the 4X225 LIS system are better than those achieved with the 4X25 LIS system, as indicated. Nevertheless, it should be mentioned that the MRC, EGC and MMSE are less computational demanding than the ZF. Finally, it should be mentioned that the EGC achieves the worst performance.

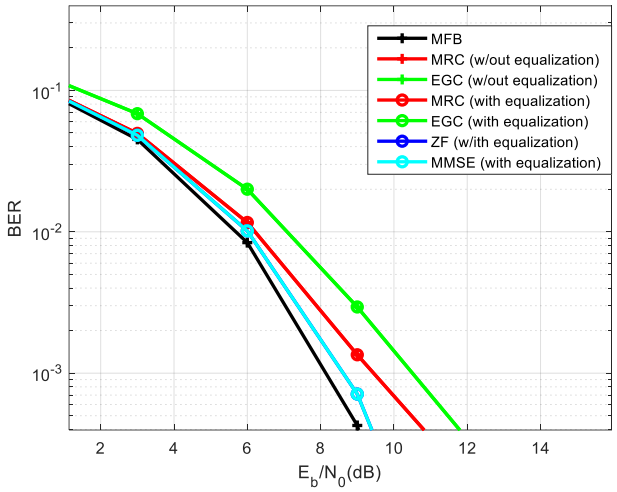

Figure 3. Results for 4X225 LIS System, with 5 users, without LDPC codes, with and without equalization.

4. Conclusions

The paper studied the performance of a LIS system combined with SC-FDE transmission, with several receiver types: ZF, MMSE, MRC and EGC. It was shown that the LIS allows avoiding the use of equalization for the MRC and EGC. Furthermore, it was shown that the MRC and EGC do not require the channel inversion for each frequency component, while the ZF and MMSE do. Moreover, it was viewed that the performance of the MRC approaches that of the MMSE, with a much higher level of simplicity.

Acknowledgements

This work is funded by FCT/MCTES through national funds and when applicable co-funded EU funds under the projects UIDB/EEA/50008/2020 and 2022.03897. PTDC.

References

[1] Pereira, A., Rusek, F., Gomes, M., Dinis, R.: Deployment Strategies for Large Intelligent Surfaces. IEEE Juune 15,2022.

[2] Lu, L., N., Li, Y., G., Swindlehurst, L., A., Ashikhmin, A., Zhang, R.: An Overview of Massive MIMO: Benefits and Challenges, IEEE, Journal of Selected Topics in Signal Processing, Vol. 8, Issue.5, Oct. 2014.

[3] Larsson, E., G., Edfors, O., Marzetta, L., T.: MIMO for Next Generation Wireless Systems. IEEE Communications Magazine, Feb.2014.

[4] Pan, Y., Deng, Z.: Channel Estimation for Wireless Communication Systems Aided By Large Intelligent Reflecting Surface. IEEE, 2nd International Conference on Big Data Artificial Intelligence and Internet of Things Engineering (ICBAIE), 2021.

[5] Bjornson,E.; Özlem, T.;Sanguinetti, L.. A primer on near-field beamforming for arrays and reconfigurable intelligent surfaces. Asilomar Conf. Signals, Syst. Computer (ACSSC), Pacific Grove, CA, USA, pp. 105-112, Mar. 2020.

[6] Dajer, M.;Ma, Z.; Piazzi, L.; Narayan, P.; Qi, X.; Sheen, B.;Yang, J.;Yue, G.. Reconfigurable Intelligent Surface: Design the Channel – a New Opportunity for Future Wireless Networks. arXiv:2010.07408v1 [eess.SP] ,14 Oct 2020.

[7] Gashtasbi, A. Marques da Silva, M., Dinis, R., "IRS, LIS, and Radio Stripes-Aided Wireless Communications: A Tutorial" MDPI, Applied Sciences 12, no. 24: 12696; December 2022; https://doi.org/10.3390/app122412696

[8] Marques da Silva, M.; Dinis, R.; Guerreiro, J.. A Low Complexity Channel Estimation and Detection for Massive MIMO using SC-FDE", MDPI - Telecom, 1(1), 3-17; 14 March 2020 (https://www.mdpi.com/2673-4001/1/1/2/htm).

Review on Ladder Topological Based Microstrip BP-NGD Design

S. Ngoho[1*] and B. Ravelo[2]
[1]Association Française de Science des Systèmes (AFSCET), 151 Bd de l'Hôpital, Paris 75013, France
[2]Nanjing University of Information Science & Technology (NUIST)، Nanjing 210044, Jiangsu, China
[*]Corresponding author: samngoho@yahoo.fr

Abstract: Despite the performed research work, the negative group delay (NGD) microwave function remains unfamiliar to most of electromagnetic engineers. It was introduced with multiple microstrip design that there is a type of bandpass (BP) NGD topologies. The present paper reviews a BP type NGD circuit designed with ladder microstrip circuit. The BP-NGD specifications are presented. The topology of ladder cell with fully distributed transmission line (TL) based structure is described. Some simulations and experimental results highlighting the BP-NGD circuit characterization are discussed.

1. Introduction of BP-NGD type ladder topology

The analogy with filter theory enables to understand the most fundamental NGD topologies [1]. In the RF engineering, the BP type NGD topologies are the most useful [2-3]. Fig. 1(a) represents the two-port black box diagram of f-frequency dependent S-parameters (SP) model of BP-NGD symmetrical topology. The NGD characterization is based on the GD (Fig. 1(b)), S_{21} and S_{11} parameters (Fig. 1(c)) analyses.

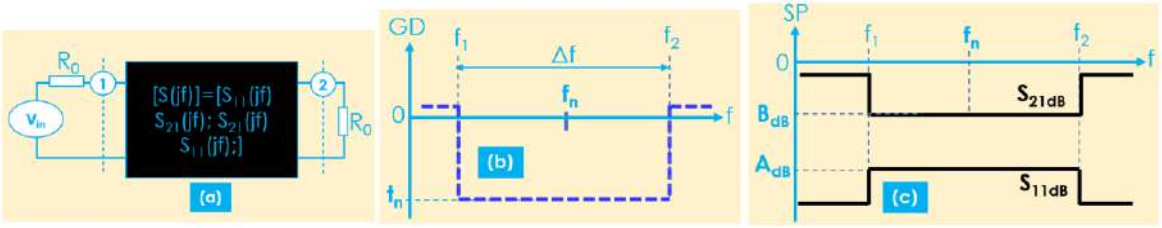

Fig. 1: (a) SP, BP-NGD (b) GD and (c) reflection/transmission diagrams [2-5].

The main parameters of BP-NGD function are i) center frequency f_n, ii) bandwidth $\Delta f=f_2-f_1$ which is associated to the cut-off frequencies $GD(f_1)=GD(f_2)=0$ and iii) value $t_n=GD(f_n)<0$. In the NGD frequency band, reflection and transmission coefficients must respect conditions $S_{11dB}<A_{dB}$ and $S_{21dB}>B_{dB}$.

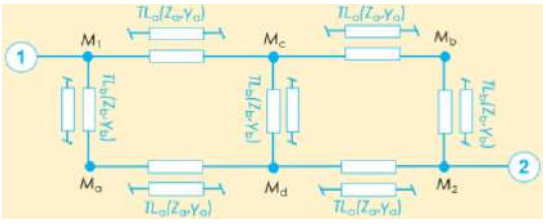

Fig. 2: Two-cell ladder topology [5].

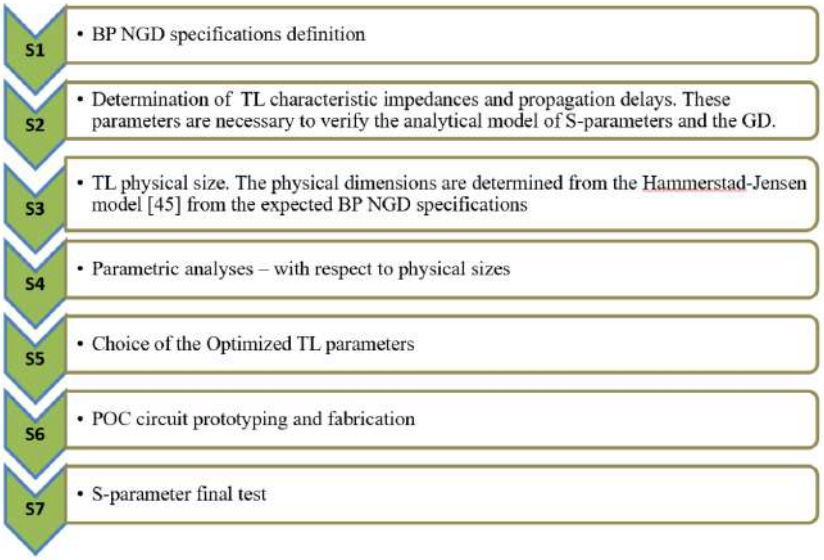

Fig. 3: BP-NGD ladder design flow.

One of simplest TL-based BP-NGD passive topology is the ladder distributed circuit shown by Fig. 2 [5]. The design phases and characterization of the BP-NGD structure are indicated by 7 steps of Fig. 3 [5].

2. BP-NGD feasibility result discussion

As proof-of-concept (PoC), Figs. 4 shows the ADS® schematic, HFSS© layout and photo of the fabricated microstrip prototype on Cu-metallized F4BK substrate. The BP-NGD behavior was verified according to the analytical principle introduced in Figs. 1. Figs. 5 depict the f_n=3.645 GHz and t_n=-3 ns validation results showing good correlation between simulations. The passive circuit presents insertion loss of about 5 dB and reflection loss better than 10 dB at f=f_n.

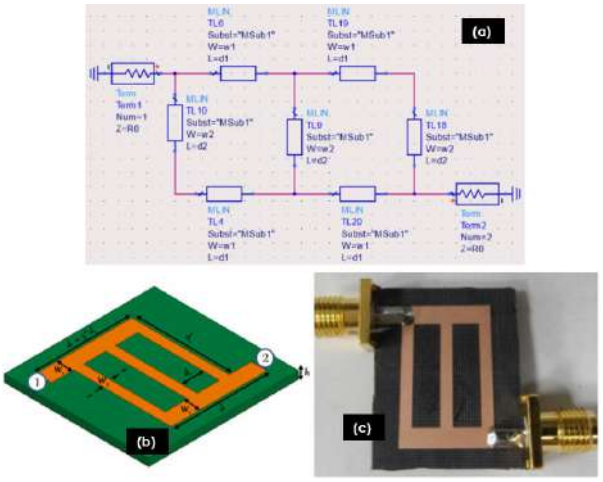

Fig. 4: (a) Schematic, (b) 3-D design and (c) photo of BP-NGD ladder PoC [5].

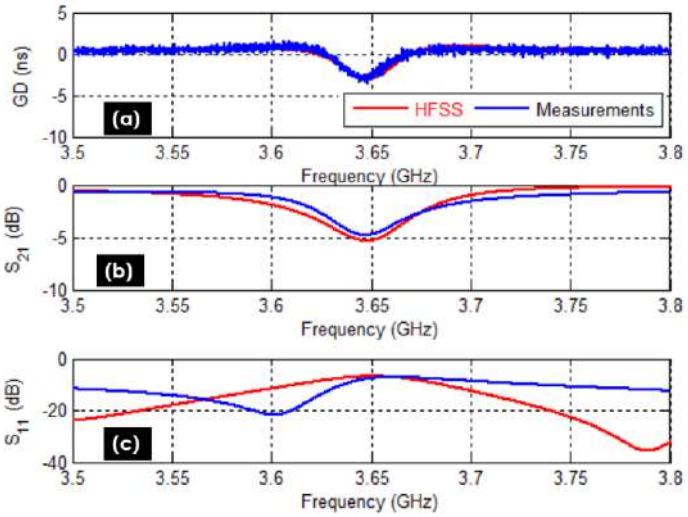

Fig. 5: Simulated and measured (a) GD, (b) S_{21} and (c) S_{11} [5].

3. Conclusion

The design approach of ladder BP-NGD topology is reviewed. The design principle, PoC and validation results are described. The BP-NGD circuits are potentially useful for future 5G and 6G communication systems.

References

1. Ravelo, B., "Similitude between the NGD function and filter gain behaviours," Int. J. Circ. Theor. Appl., Vol. 42, No. 10, 1016–1032, 2014.
2. Sambatra, E., S. Ngoho, F. E. Sahoa, G. Fontgalland, V. Mordachev, N. M. Murad, F. Wan, and B. Ravelo, "Literature review on RF and microwave design of passive microstrip circuit with bandpass type NGD behavior," Smart systems: Theory and Advances, Book chapter I, Amplla Editora, Campina Grande – Brazil, pp. 9-36, 2022.
3. Ravelo, B., "Negative Group-Delay Phenomenon Analysis with Distributed Parallel Interconnect Line", IEEE Tran. EMC, Vol. 58, No. 2, 573-580, 2016.
4. Ngoho, S., M. D. Camara, Y. Dong, A. Douyère, N. M. Murad, P. Thakur, A. Thakur, R. Randriatsiferana and B. Ravelo, "S-matrix based bandpass negative group delay innovative model of inverted parallel arm distributed topology," Journal of Electromagnetic Waves and Applications, Vol. 36, No. 12, pp. 1745-1759, 2022.
5. Ngoho, S., Y. C. Mombo Boussougou, S. S. Yazdani, Y. Dong, N. M. Murad, S. Lalléchère, W. Rahajandraibe and B. Ravelo, "Design and modelling of ladder-shape topology generating bandpass NGD function," PIER C, Vol. 115, pp. 145-160, 2021.

Analysis of Propagation Mechanisms in Different Tunnel Environments for LOS and NLOS Scenarios

Enes Aksoy[1,2,3,*], Allan Wainaina Mbugua[1], Yun Chen[1], Haroon Khan[1], Leszek Raschkowski[2], Lars Thiele[2], Slawomir Stanczak[2,3]

[1]Huawei Munich Research Center, Germany
[2]Fraunhofer Institute for Telecommunications, Germany
[3]Technical University of Berlin, Germany
[*]corresponding author: enes.aksoy@huawei.com

***Abstract*— Wireless communications in tunnel scenarios is a challenging research area. Often times, specific measurements and simulation tools are needed to model the effects on communication channels. This paper analyzes the different propagation mechanisms for tunnel geometries with and without traffic, by using ray tracing simulations for vehicle to vehicle (V2V) communications in line of sight (LOS) and non line of sight (NLOS) scenarios. The most important propagation mechanisms are highlighted, providing the best possible simulation results in tunnel environments.**

1. Introduction

The increasing frequencies for fifth generation (5G) communications and beyond, lead to ever decreasing wavelengths. Hence, the behavior of communication channels is also significantly changing for different areas, such as tunnel environments [1]. The tunnel acts like an oversized waveguide for the high frequency signals and the propagation mechanisms are significantly different, than for low frequency signals [2]. Recently, the IEEE 802.11p standard determined a carrier frequency of 5.9 GHz for vehicular communications. So specific methods and tools are required to characterize the communication channels in tunnel environments for these higher frequencies [3].

Several studies utilize ray tracing for this purpose, since most effects on the communication channel can be captured, while the computational complexity of the tool is manageable [1], [3] . This paper analyzes a rectangular and arched tunnel environment, by utilizing ray tracing simulations. Vehicle to vehicle (V2V) scenarios, without and with additional traffic in these tunnels, are simulated and the main propagation mechanisms in the environment are presented, to obtain the most accurate simulation results and channel characterization.

2. Methodolody

In general, realistic tunnel models are rectangular or arched [3]. Therefore, these two different geometries are analyzed in this paper. Furthermore, each of these two tunnel environments are evaluated, by either using only a transmitting and receiving car, maintaining a line of sight (LOS) path; or by also using additional vehicles, obstructing the line of sight, leading to a non line of sight (NLOS) scenario, as depicted in Fig. 1. So in total four different simulations are performed to assess the effects of the tunnel geometry and traffic within the tunnel scenarios.

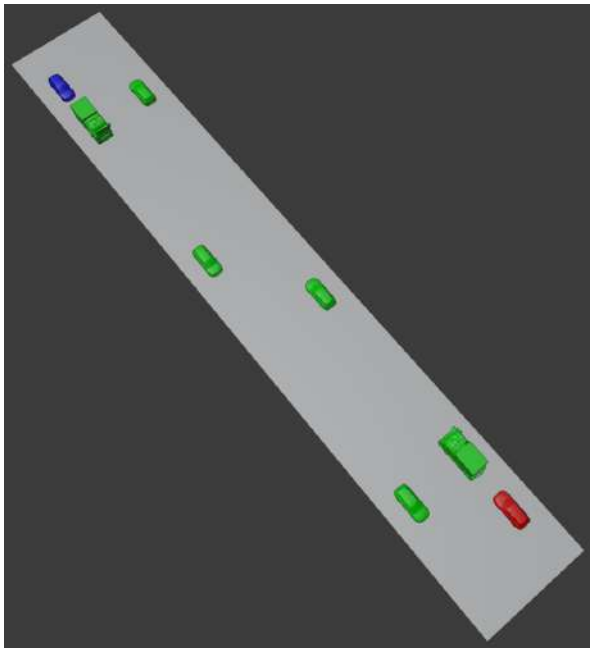

Fig. 1. The transmitting car (red) is at the beginning of the tunnel, while the receiving car (blue) is at the end. They have a distance of 80m to each other. Furthermore, several different obstructing vehicles (green) are used for the with traffic case, while all obstructing vehicles are removed for the without traffic case.

Fig. 1 shows the V2V simulation model with traffic. Most importantly, obstructing trucks between the transmitting and receiving car lead to a NLOS scenario. The same tunnel environment is also analyzed without further traffic, only including the transmitting and receiving car. The vehicles for the simulation are 3D scanned models with a sub-mm accuracy [4]. All vehicles are modeled as perfect electrical conductors (PECs), while the tunnel is made of concrete, using the complex permittivity specified by the ITU at 5.9 GHz [5]. Finally, all interaction mechanisms, e.g. reflections, diffractions and scattering are utilized during the ray tracing simulations and the IEEE 802.11p standardized frequency of 5.9 GHz for vehicular communications is used.

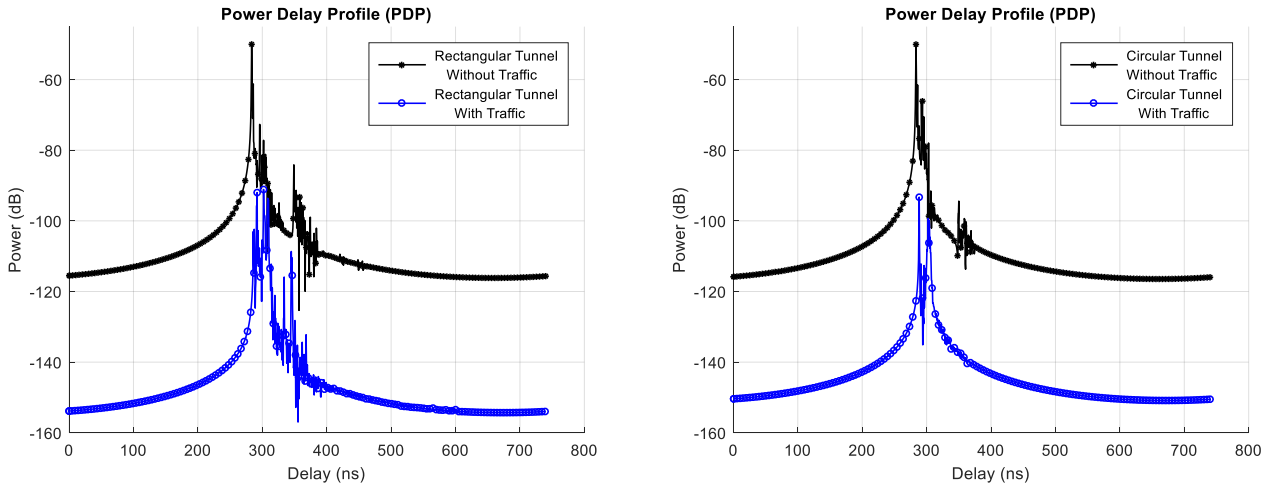

Fig. 2. This figure shows the PDP for the rectangular and arched tunnel. Each scenario is analyzed without and with traffic, as depicted in Fig. 1.

3. Results

Fig. 2 shows the power delay profile (PDP) of each scenario, in this case with six orders of interaction for all propagation mechanisms. For the without traffic scenarios, some of the most dominant paths are coming from the reflection interactions, while the tunnel is acting similar to a waveguide, directing the signal towards the receiver and amplifying them through the multipath components [2]. However, once the LOS path is obstructed and other vehicles are also in the tunnel, the scattering interactions get significantly more important, providing most of the received power. So vehicles act as scatterers and disturb the guided reflections within the tunnel. Over 80% of the received power comes from the LOS and reflection paths in the without traffic cases, while around 80% of the received power stems from scattering interactions for the with traffic NLOS scenarios. In general, diffractions have a negligible impact during all simulations and measurements [3].

For the without traffic cases, it can be seen, that the received power is significantly amplified, due to the reflections off the tunnel, acting like a waveguide between the receiver and transmitter. This phenomenon is also observed during measurement campaigns, performed in several different studies [1], [6]. Therefore, through the superposition of all the different multipath components, the received power is significantly higher than only the LOS path. Additionally, it can be seen, that the shape of the tunnel has a significant impact on the signal behavior [3], [6]. The arched tunnel is focusing the signals, while the rectangular tunnel has a higher spread over time for the received power [6].

4. Conclusion

This paper compares rectangular and arched tunnel geometries; with traffic in NLOS and without traffic in LOS scenarios; with each other, while analyzing the dominant propagation mechanisms for the communication channel. It is shown, that reflections have a high importance for no or low traffic scenarios, while obstructing vehicles and additional traffic increases the importance of scattering mechanisms. So during the ray tracing simulations of tunnel scenarios, a high order of reflections, e.g. 5 or more, should be chosen for relatively empty environments, while a high order of scattering calculations, e.g. 4 or more, is required for packed environments with more traffic.

Furthermore, as stated in previous studies [6], the importance of the tunnel geometry is shown for the communication channel. A rectangular tunnel leads to a higher spread of the received power, while arched tunnels lead to focusing of the received signal. These insights enable us to develop more specific and tailored simulation tools, adjusting their settings for tunnel environments and to obtain more accurate results for future studies.

References

[1] Chen, S. & Jeng, S. SBR image approach for radio wave propagation in tunnels with and without traffic. *IEEE Transactions On Vehicular Technology*. **45**, 570-578 (1996)

[2] Lienard, M. & Degauque, P. Propagation in wide tunnels at 2 GHz: a statistical analysis. *IEEE Transactions On Vehicular Technology*. **47**, 1322-1328 (1998)

[3] Masson, E., Combeau, P., Berbineau, M., Vauzelle, R. & Pousset, Y. Radio wave propagation in arched cross section tunnels-simulations and measurements. *Journal Of Communication*. **4**, 276-283 (2009)

[4] Best-Form, Sep. 20, 2022. [Online]. Available: https://best-form.de/3d-scan/

[5] Series, P. Effects of building materials and structures on radiowave propagation above about 100 MHz. *Recommendation ITU-R*. pp. 2040-2 (2021)

[6] Didascalou, D., Maurer, J. & Wiesbeck, W. Subway tunnel guided electromagnetic wave propagation at mobile communications frequencies. *IEEE Transactions On Antennas And Propagation*. **49**, 1590-1596 (2001)

Amplitude-time characteristics of mobile phone emissions in 5G versus 4G networks

Delia Bianca Deaconescu[1], David Vatamanu[1*], Andreea Maria Buda[1], Paul Bechet[2] and Simona Miclaus[1,2*]

[1]Doctoral School of Electrical Engineering, Technical University of Cluj-Napoca, Cluj-Napoca, Romania
[2]"Nicolae Balcescu" Land Forces Academy, Sibiu, Romania
* simo.miclaus@gmail.com

Abstract

4G and 5G emissions of a mobile phone are quantified by means of Amplitude Probability Distribution (APD) function and Complementary Cumulative Distribution Function (CCDF) capabilities of a real-time signal and spectrum analyzer. The aim is to emphasize the differences during real-life usage of either of the standards while running various mobile applications, from the point of view of the user's electromagnetic exposure. Knowing the average power of a signal within a given bandwidth and the probability that the instantaneous power of the signal to exceed a certain threshold contribute to expressing the dynamic range of the signal, its peak-to-average power ratio, with consequences on an increasingly refined dosimetric characterization.

1. Introduction

One of the interesting features of the last generations of mobile communication's signals is their time variability. This one is important from the perspective of the characterization of the electromagnetic exposure of users. With the major change of waveforms emitted in the fifth generation - 5G standard versus the earlier fourth generation - 4G, it became challenging to probe, in certain situations, the variableness of the signals, its magnitude and its distribution.

Some authors have recently measured time variability of 5G pilot signals [1]. Here, we start from the idea that knowing the time variability of emissions may be energetically connected with radiation fluence and to fluence rate, therefore to human exposure level.

On the other hand, there are several approaches in which different measurements are performed to characterize the human exposure to 4G and 5G emissions. In [2] authors revealed that 5G exposure was overall very low when they extensively considered an urban location. In another work it was revealed that the peak dose of absorbed radiation is always dominated by an individual's mobile phone and, in the case of non-users, by the bystanders' mobile phones [3]. Adda et. al. [4] proved that dynamic spectrum sharing (DSS) and maximum-power extrapolation techniques can be used to estimate maximum exposure levels also for 5G signals. Since now it is demonstrated that smartphone exposure dominates over the base stations [5], it is deduced that the phone's emissions should be carefully characterized in multiple situations. To assess the exposure levels in different 5G scenarios, for mobile applications, Bonato et. al. [6] designed a phased-array antenna with eight elements and different types of skin models on Sim4Life platform. The results emphasized that for a person passing nearby the phone, the exposure levels were even slightly higher than those experienced by the mobile phone user himself. In [7] authors proved that the time-averaged output levels of the phone were significantly lower than the maximum available time-averaged output power, respectively below 43% of the maximum value.

The study of the time variability of the radiated power dynamics for 3G+/4G+ mobile generations and for IEEE 802.11n communications standards were performed in [8] and [9]. By using the complementary cumulative distribution function (CCDF) the authors proved that for 4G+ emissions the power density in the near field of a mobile terminal was the highest during the following application running (in descendent order): file upload, voice over IP, video call, file download, streaming and browsing. Amplitude probability distribution (APD) function was used in [10] in order to demonstrate the differences in exposure due to five different mobile applications running in Long Term Evolution (LTE) standard. Authors concluded that this method proves a high agility in tracing the microsecond variability of emitted power level. In [11] authors made measurements in different configurations of fourth and fifth generation wireless fidelity (Wi-Fi) standards near of a mobile phone. They used the APD capability of a real-time spectrum analyzer to highlight different user exposure profiles.

Due to different time-structure and time-dynamics of 4G and 5G mobile communication standards, an analysis is made here, based on real emissions of a mobile phone in its vicinity, with the objective of emphasizing the dissimilarities of the electromagnetic exposure of the user. Due to differences in the modulation and coding schemes, in the peak-to-average power ratio (PAPR), in the resource allocation techniques, and in the power control mechanisms, the statistic features of the signals are characteristic. Moreover, they are specific to each mobile application running. Therefore, here we assessed the dynamics of the emitted field by means of statistic instruments like: APD, CCDF, channel power variance.

2. Experimental set-up and methodology

Here we have experimentally evaluated the time-amplitude variation of the radiated power level and of the electric (E) field strength nearby a mobile terminal connected sequentially to one of the two networks: a) 4G LTE at a

central frequency f1=1.75 GHz and a bandwidth of 40 MHz; b) 5G NR FR1 at a central frequency f1=3.58 GHz and a bandwidth of 100 MHz. The following receiving instruments were used (Fig.1): a receiving antenna Aaronia model OmniLOG 30800 and a real-time signal & spectrum analyzer model FSV3013 from R&S, with an analysis bandwidth of 40 MHz. The emission source was an Iphone 14 Pro phone.

Figure 1: Measurement set-up showing the receiving omnidirectional antenna connected to the signal analyzer and the Iphone 14 Pro phone

The receiving antenna was positioned at a distance d = 22 cm from the phone's front surface. Four mobile applications were used as sources of field emissions, for both 4G and 5G connections: file download, video streaming, file upload and video call. For each mobile application, the measurements were performed in five repetitions and we calculated the median of the results. For both connections we used the following settings of the signal analyzer: resolution bandwidth (RBW) = 1 MHz, video bandwidth (VBW) = 10 MHz, sweep time = 1 ms, sweep count = 50, measurement time = 2.5 s, analysis bandwidth = 40 MHz, number of samples = 100.000, preamp = 15 dB. In 4G standard case we used a 40 MHz span compared to 5G where we used a 120 MHz span.

Statistical analysis made use of APD and CCDF. The APD function describes the probability distribution of the amplitude of a signal. It shows how frequently a particular amplitude occurs in the signal. APD is useful for determining the signal strength, noise level, and other signal characteristics. In general, a signal with a larger amplitude will have a higher probability of occurrence in the signal than a signal with a smaller amplitude. The CCDF is a measure of the probability that the amplitude of a signal will exceed a certain level. It is the complement of the cumulative distribution function (CDF) and is often used to characterize the behavior of signals that have non-Gaussian (non-normal) distributions, such as those encountered in communication systems. The CCDF is useful in determining the peak-to-average power ratio (PAPR) of a signal. In general, a signal with a high PAPR will have a steep CCDF curve, while a signal with a low PAPR will have a flatter CCDF curve.

From the measured power levels we calculated E-field strength afterwards based on the antenna factor (AF) of the receiving antenna at the two central frequencies of emission, following the formula:

$$AF = \frac{E}{U} = \frac{9.73}{\lambda\sqrt{G}}, \quad (1)$$

where E is the electric field strength, U is the voltage (calculated from the received power), λ represents the wavelength and G is the antenna gain at the respective frequency.

3. Results and discussion

APD distributions show in both standards two humps (Fig. 2, Fig. 3): the first one, at lower powers, correspond to noise/interferences, while the second one, at power levels higher tha -50 dBm correspond to interest mobile phone signals. In the case of 4G, the sharpest and highest distributions of power levels is found for the download and upload applications (Fig. 2). Above all, upload has the highest probability of apparition of the largest powers emitted. For the 5G emissions (Fig.3), we notice that all four applications conduct to similar probability of appearance (0.002) of the highest powers emitted, compared to the 4G network where there are obvious differences between the applications - for example 10 times higher between the upload/download applications and streaming respectively. We also note that the highest probability of occurrence in the case of the download application in both standards groups at the power of -30 dBm, and for the other applications the probability of occurrence groups around the power value of -20 dBm. We can state that 5G signals have a lower probability of occurrence at the same power levels if compared against 4G signals, and for all applications a similar probability of occurrence is kept, while for the 4G signals a greater probability of occurrence is observed, marked by clear differences between the used applications.

The CCDF function of 4G signals are shown in Fig. 4 and Fig. 5.

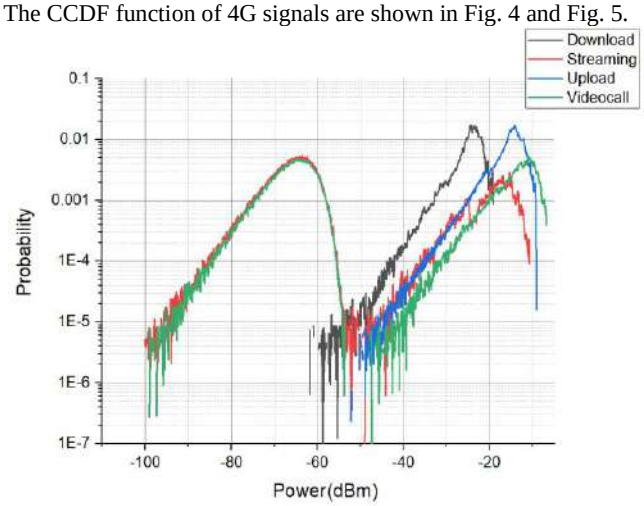

Figure 2: Median of Amplitude Probability Distribution function (APD) for 4G emissions corresponding to four applications

Fig. 4 corresponds to 4G standard and we see the highest probability that the signal strength exceeds the average value, for video streaming and videocall applications. We also observe the lowest probabilities in case of upload and download applications, which are similar. In the case of 5G (Fig.5), we notice that

streaming and videocall applications have a similar probability of exceeding the average, which is similar with the correspondent application in 4G. Although in the 4G network for the upload and download we observe a similar trend of power level variation, in the 5G network the signals related to the two applications vary differently, having a very different probability of occurrence. For example, in the 4G network, the probability of exceeding the average power value, for the upload application, appears at 6 dBm while in the 5G network at 16 dBm power level.

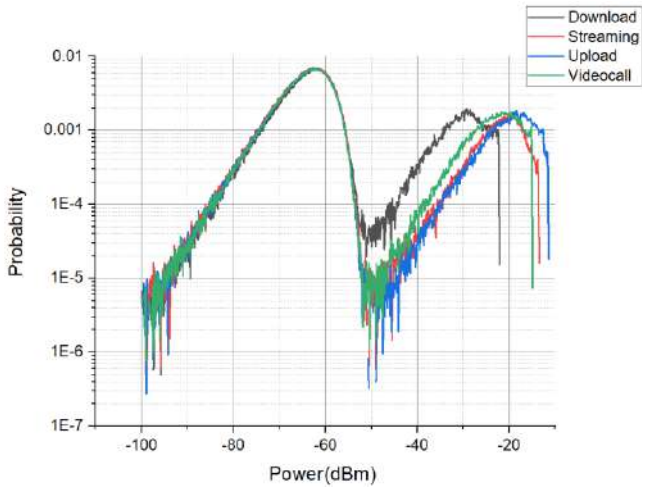

Figure 3: Median of Amplitude Probability Distribution function (APD) for 5G emissions corresponding to four applications

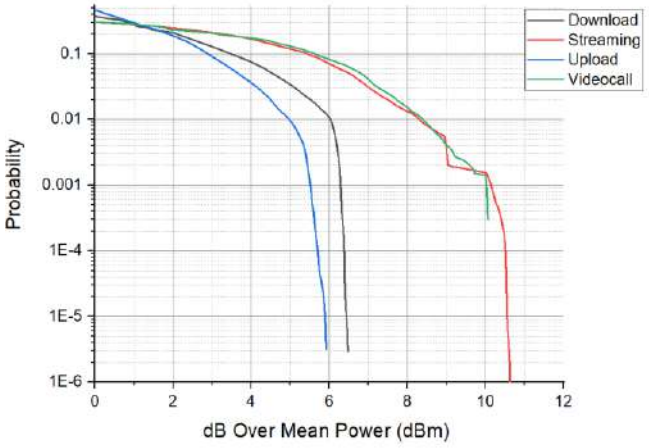

Figure 4: Median of Complementary Cumulative Distribution Function (CCDF) for 4G applications

For each application running, we took the Amplitude Probability Distribution over 50 counts which lasted 2.5 s. In this sense, we obtained average and peak values of the power level, which was further transformed into E-field strengths, so as to compare correctly the two emitting frequency bands. In Fig. 6 we can observe the average values of E-field strengths (rms) emitted for each application. Higher values of E-field strengths are observed for the 4G cases compared to the 5G cases. For 4G the mean field levels at 22 cm from the phone vary between 0.6 – 1.83 V/m, while for 5G they vary between 0.2 – 0.56 V/m.

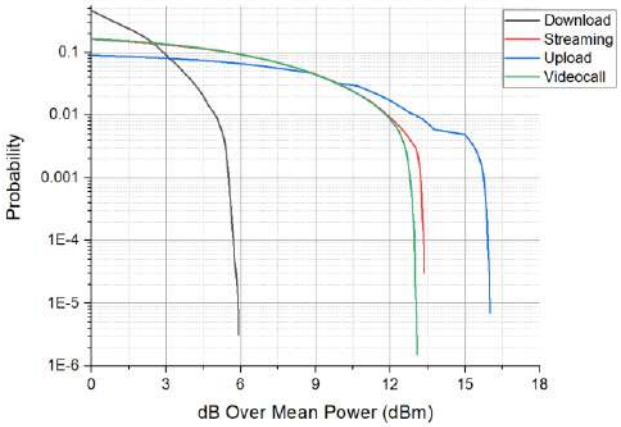

Figure 5: Median of Complementary Cumulative Distribution Function (CCDF) for 4G applications

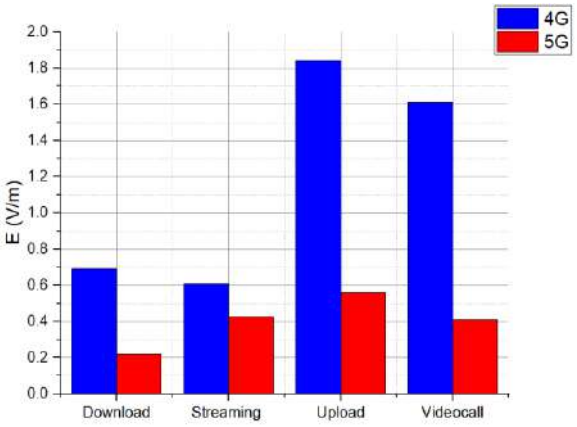

Figure 6: Mean values of rms E-field strengths after 50 counts of the spectrum at 22 cm from the phone

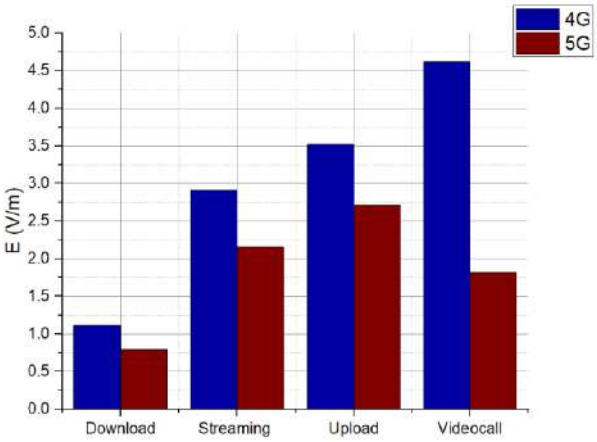

Figure 7: Peak values of rms E-field strengths after 50 counts of the spectrum at 22 cm from the phone

In Fig. 7, we represented the peak values of E-fields; they vary between 1.2 - 4.6 V/m for the 4G case and between 0.7

- 2.7 V/m for the 5G case. Again, peak field is greater in 4G than in 5G for all applications. Also, both for mean- and for peak-values, the variation of 4G signals is larger than that of 5G signals. Crest factor represents the PAPR and is indicated in Fig. 8. We notice that for all the running applications, for 5G emissions, the crest factor values are higher compared to those related to 4G emissions, for example for upload it is more than double in 5G than in 4G. Similar to the previous cases of mean and peak values, also in case of the crest factor, we observe that 4G signals have a higher variation inter-applications than 5G signals.

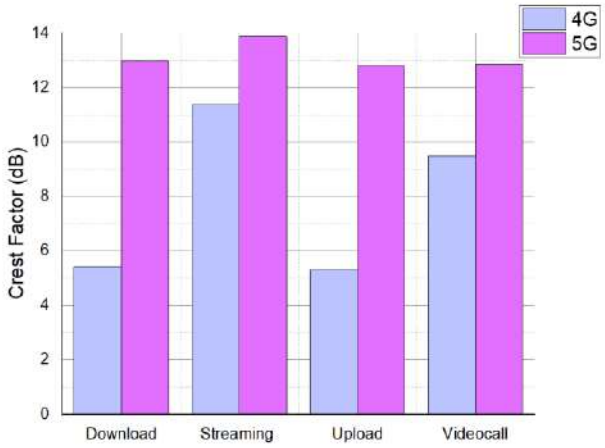

Figure 8: Peak to average power ratio after 50 counts of the spectrum

4. Conclusions

When comparing 4G and 5G mobile signals, the APD and CCDF distributions provide insights into the time-amplitude differences between the two signal types. In terms of APD, 4G signals seem to have a slight higher probability of occurrence of higher amplitudes compared to 5G. This effect is due to the lower real-time analysis bandwidth used for the 5G signal capture (analyzer's capability limitation). We would have expected that 5G signals, which typically use higher carrier frequencies, wider bandwidths, and more advanced modulation schemes, to contribute to a lower signal strength. Regarding CCDF, with the same real-time analysis bandwidth limitation, our results show that 4G signals have a more significant reduction in the PAPR compared to 5G signals. However, because 5G uses advanced techniques such as beamforming, massive MIMO, and OFDM, CCDF curves should have been steeper than for 4G. Opposite, flatter CCDF curves indicate a more stable and predictable signal that is less likely to cause interference with other devices or degrade the overall system performance.

5G signals have a higher PAPR compared to 4G signals. This is because 5G uses more advanced modulation schemes, such as 256-QAM (Quadrature Amplitude Modulation), which allow for higher data rates but also result in higher PAPR. Additionally, 5G also utilizes larger bandwidths, which further increases the PAPR. The impact of PAPR on mobile applications depends on the specific application and its requirements. Applications that require high data rates, such as video streaming or large file transfers, benefit from the higher PAPR of 5G signals, as it allows for higher data rates.

References

[1] G. Betta, D. Capriglione, G. Cerro, G. Miele, M. D. Migliore and D. Šuka, Experimental analysis of 5G pilot signals' variability in urban scenarios, *IEEE International Symposium on Measurements & Networking (M&N)*, Padua, Italy, pp. 1-6, 2022.

[2] L. Chiaraviglio *et al.*, Massive measurements of 5G exposure in a town: methodology and results, *IEEE Open Journal of the Communications Society*, vol. 2, pp. 2029-2048, 2021.

[3] S. Kuehn, S. Pfeifer, N. Kuster, Total local dose in hypothetical 5G Mobile Networks for varied topologies and user scenarios, *Applied Sciences*, 10(17):5971, 2020.

[4] S. Adda *et al.*, Assessment of population exposure to electromagnetic fields due to systems that implement dynamic spectrum sharing between 4G and 5G: definition of methods and on-site measurements, *IEEE International Workshop on Metrology for Living Environment (MetroLivEn)*, Cosenza, Italy, pp. 263-268, 2022.

[5] L. Chiaraviglio, C. Lodovisi, S. Bartoletti, A. Elzanaty and M. Slim-Alouini, Dominance of smartphone exposure in 5G mobile networks, *IEEE Trans. Mob. Comput.* [in press], 2023.

[6] M. Bonato, L. Dossi, S. Gallucci, M. Benini, G, Tognola, M. Parazzini, Assessment of human exposure levels due to mobile phone antennas in 5G networks, *Int. J. Environ. Res. Public Health*, vol. 19, 2022.

[7] P. Joshi, F. Ghasemifard, D. Colombi and C. Törnevik, Actual output power levels of user equipment in 5G commercial networks and implications on realistic RF EMF exposure assessment, *IEEE Access*, vol. 8, pp. 204068-204075, 2020.

[8] A. Sarbu, A. Bechet, T. Balan, D. Robu, P. Bechet and S. Miclaus, Using CCDF statistics for characterizing the radiated power dynamics in the near field of a mobile phone operating in 3G+ and 4G+ communication standards, *Measurement*, vol. 134, pp. 874-887, 2019.

[9] A. C. Beehet, R. Helbet, S. Miclaus, I. Bouleanu, A. Sarbu and P. Bechet, Comparative WLAN exposure analysis: weighted channel power method versus CCDF method, *2019 8th International Conference on Modern Power Systems (MPS)*, pp. 1-4, Cluj-Napoca, Cluj, Romania, 2019.

[10] S. Miclaus and P. Bechet, Non-stationary statistics with Amplitude Probability Density Function for exposure and energy density reporting near a mobile phone running 4G applications, *Electromagnetics Research*, vol. 89, pp. 151-159, 2020.

[11] A. Sarbu, S. Miclaus, A. Digulescu and P. Bechet, Comparative Analysis of user exposure to the electromagnetic radiation emitted by the fourth and fifth generations of Wi-Fi communication devices, *Int. J. Environ. Res. Public Health*, 17, 2020.

Classification of IEEE 802.11ax Emissions by Using YOLOv7 Real-Time Detection Algorithm

A. M. Buda[1], D.B. Deaconescu[1], D. Vatamanu[1] and S. Miclaus[1,2*]

[1]Doctoral School of Technical University of Cluj-Napoca, Romania
[2] "Nicolae Balcescu" Land Forces Academy, Sibiu, Romania
[*]simo.miclaus@gmail.com

Abstract

Present work aimed at highlighting the possible use of YOLOv7 deep learning algorithm in classification of IEEE 802.11ax emissions based on spectrograms recognition. Here we used a very simple case, a unidirectional communication between a WIFI 6 router and a mobile phone, to transmit four types of different signals: video streaming, upload, download and videocall. It resulted that the algorithm is feasible for time-frequency imprint recognitions and the approach can be further exploited in more complex situations.

1. Introduction

The increased development of Deep Learning (DL) has accelerated the progress of related methods and algorithms used in the fields of image processing and computer vision [1]. Nowadays, signals classification is an important task which needs specific capabilities proper to certain applications.

Before classification of the signal, we should decompose it using some techniques like Fast Fourier Transform (FFT) or other statistical methods intended to individual modulation features.

In the last years, we have seen a rapid development of neural network architectures, algorithms, and optimization techniques commonly known as DL. The state-of-the-art DL methods can be applied to the same problem of signal classification and show excellent results while completely avoiding the need of difficult handcrafted feature selection [2]. One of the most important deep learning tasks that currently has an increased number of requests is computer vision. Object detection is a computer vision task that involves identifying and locating objects in images or videos. It is an important part of many applications, such as surveillance, self-driving cars, or robotics [3].

The outcomes of the current paper will demonstrate the capability of object detection models in real-time signal recognition applications based on spectrogram images.

Object detection algorithms can be divided into two main categories: single-shot detectors and two-stage detectors [4].

You Only Look Once (YOLO) is a popular object detection model known for its speed and accuracy [5]. This model works using an end-to-end neural network that makes predictions of bounding boxes and class probabilities all at once.

YOLO v7, the latest version (2022) [6] of YOLO, comes with some improvements over the previous versions, the most important one being the use of anchor boxes. Anchor boxes represent a set of predefined boxes with different aspect ratios that are used to detect objects with different shapes. Nine anchor boxes are used, which allows it to detect an increased number of object shapes and sizes compared to previous versions, thus helping to decrease the number of false positive detections [7].

The main purpose of this paper is to apply YOLOv7 in classification of IEEE 802.11 ax signals emitted by a WiFi6 router in case of four different mobile applications requested by a mobile phone connected to the router. Practically, the recorded images of spectrograms captured by a spectrum analyzer are used for training and recognition with this deep learning object detection algorithm.

2. Materials and methods

2.1. Signal detection

To obtain the spectrograms, we prepared an experimental setup composed of the emitter - a ZTE WIFI 6 router, and a receiving system based on the Aaronia 70600 omnidirectional receiving antenna connected to a Spectran V5 real-time spectrum analyzer. A Samsung Galaxy S21 Ultra smartphone with WIFI 6 capabilities was connected to the router for wireless applications requests. First, we operated the network between the smartphone and the WIFI 6 router in the 5 GHz frequency range. The network was deployed indoor, in a "quiet" Wi-Fi area with no other 5 GHz Wi-Fi network present. The position of the smartphone and router was not changed during the measurements. The emitted signal occupied a bandwidth of 100 MHz, centered at 5.29 GHz and uses orthogonal frequency-division multiplexing (OFDM) modulation.

Figure 1 indicates the experimental setup used for signal detection and spectrogram analysis. Spectrograms of the emitted signals were recorded using the RTSA Suite Pro software. The settings of the analyzer were: center frequency of 5291 MHz, 224 FFT bins, real-time bandwidth of 88 MHz (max of the analyzer) and a frequency step of 100 KHz.

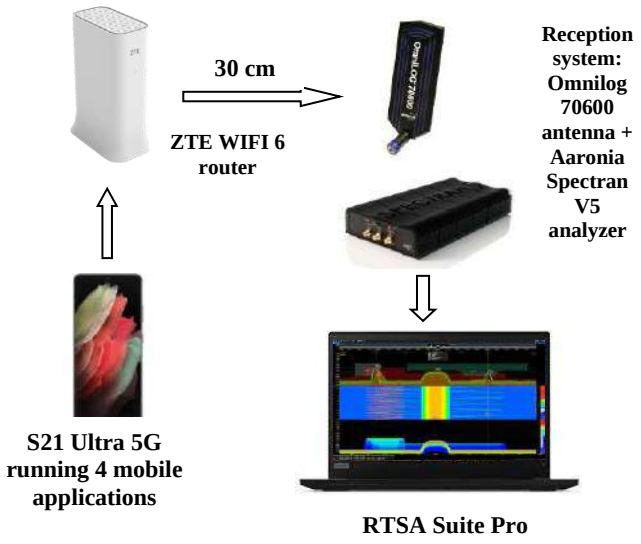

Figure 1: The measurement setup

2.1. Signal classification

For signal classification stage, based on the recorded spectrograms, we trained a YOLO v7 model using PyTorch framework on an NVIDIA Tesla T4 GPU.
As a first step in the training process, we defined the classes that the output model must "learn". The classes have the same names as the mobile application previously mentioned: streaming, upload, download and videocall.
To train the spectrograms recognition model, a total number of 2368 images were used as follows: 2168 for training process and 200 images (50 for each class) for validation process.
After the training, the resulting model was used to run a number of inferences. These inferences define the new images that our output model must identify. As a result, Figure 2 shows an image example with a bounding boxes which comprise the detected object and the identification percentage.

3. Results and discussion

After the training and validation process, the achieved results were statistically analyzed based on the four types of mobile applications checked. As we can observe in Fig. 2, the signal bandwidth is perfectly framed in the bounding box. Also, in the upper left part of the spectrogram we can notice a flag which indicates the type of mobile application that the YOLO V7 model has identified and the recognition percentage.
Fig. 3 shows the overall results by indicating the average +/- standard deviations of the recognition percentages for each of the four types of emissions. We used 20 inferences (5 for each type of mobile application). The recognition percentages are very high (> 97 %) for all four types of emissions, while the standard deviation is null for download and streaming.

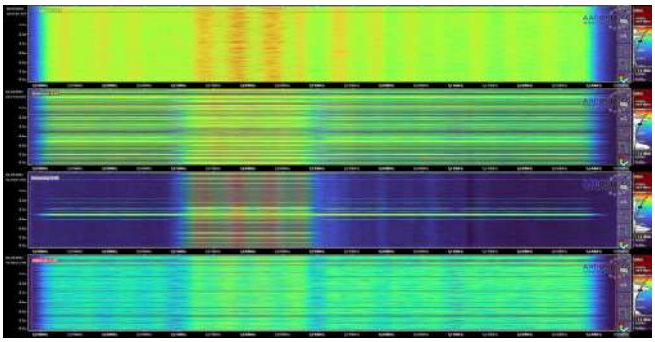

Figure 2: The result of running inferences (image to recognize) using YOLO v7 trained model

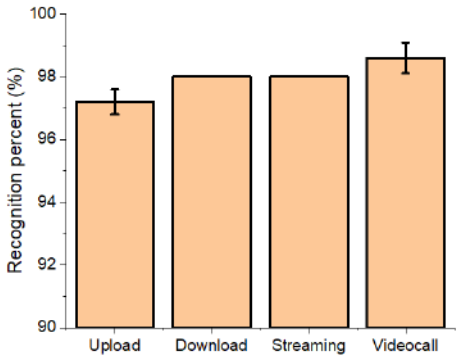

Figure 2: Percentage of recognized spectrograms per each WIFI 6 emitted signal

These results can be attributed to the fact that, from a visual point of view, the WIFI 6 signal spectrograms for the considered wireless applications are very different. So, the neural network used by YOLO very easily identifies the differences in these simple cases. Therefore, this incipient tested situation designed to check the preliminary capability of YOLOv7 for being used with spectrograms provides a very good prognostic. However, the "quite" and controlled electromagnetic environment is not a realistic case, so that further development of the procedure will be destined for more complex situations of emissions.

4. Conclusions

Nowadays, specific machine learning algorithms have become used more and more, thus being applied for different types of situations.
In this work, a different approach of using automatic object recognition algorithms was presented, namely their use for the automatic recognition of signals based on recorded spectrograms of the signals. As a result, it was observed that the YOLO V7 algorithm offers very good performances in terms of spectrogram recognition, but considering how the underlying neural network is built, it can be said that this algorithm is limited by the visual characteristics and the differences between images assigned to different classes.

References

[1] A. I Khan, S. Al-Habsi, Machine Learning in Computer Vision, *Procedia Computer Science, Elsevier BV*, Vol. 167, pp. 1444–1451, 2020.

[2] J. Xu., Z. Lin, Modulation and Classification of Mixed Signals Based on Deep Learning (Version 1), *arXiv*, 2020.

[3] A. Vagollari, V. Schram, W. Wicke, M. Hirschbeck and W. Gerstacker, "Joint Detection and Classification of RF Signals Using Deep Learning," *2021 IEEE 93rd Vehicular Technology Conference*, Helsinki, Finland, 2021.

[4] B. Vaidya, C. Paunwala, Deep Learning Architectures for Object Detection and Classification. In Smart Techniques for a Smarter Planet, *Springer International Publishing*, pp. 53–79, 2019.

[5] P. Jiang, D. Ergu, F. Liu, Y. Cai, B. Ma, "A Review of Yolo Algorithm Developments", *Procedia Computer Science*, Volume 199, pp. 1066-1073, 2022.

[6] C-Y. Wang, A. Bochkovskiy, H-Y. M. Liao, "YOLOv7: Trainable bag-of-freebies sets new state-of-the-art for real-time object detectors*", Computer Vision and Pattern Recognition*, July 2022.

[7] L. Cao, X. Zheng, L. Fang, The Semantic Segmentation of Standing Tree Images Based on the Yolo V7 Deep Learning Algorithm, *Electronics*, Vol. 12, Issue 4, p. 929, 2023.

Material Characterization and non-destructive testing

Ultra-wideband graphene-based absorbers for THz integrated waveguide systems

N. Xenidis[1], A. Przewłoka[2,3], A. Krajewska[2], P. Drozdz[2], J. Oberhammer[1], D. Lioubtchenko[1,3*]

[1]KTH Royal Institute of Technology, Malvinas vag , Stockholm, SE-100 44, Sweden
[2]CENTERA Laboratories, Institute of High Pressure Physics PAS, ul. Sokołowska, Warsaw, 01-142, Poland
[3]Institute of Optoelectronics, Military University of Technology, ul. gen. Sylwestra Kaliskiego 2, Warsaw, 00-098, Poland
[*]corresponding author: dml@kth.se

Abstract: Here we present novel graphene-based absorber materials and a simple method to measure its properties by direct integration in terahertz waveguide systems. In contrast to existing absorbers, the ability to embed such materials in a metallic waveguide allows them to be integrated into complete terahertz systems for large-scale applications.

Historically, terahertz science and technology has been restricted to specialized applications such as radio astronomy due to various technological challenges. Hollow rectangular waveguides are the primary transmission line medium in many terahertz systems due to their mechanical stability, low electromagnetic losses, enclosed nature, and compatibility with active circuit elements. Electromagnetic wave devices such as circulators, couplers and power dividers require that one or more of their ports be terminated to eliminate unwanted signals and ensure correct operation. Waveguide terminations are often realized by short-circuited waveguide sections that present low reflection and absorb the incident energy due to the presence of an absorbing material inside the waveguide [1]. We proposed a new kind of ultra-wideband THz absorber which can be directly integrated into a standard metallic waveguide (Fig.1a-c) [2,3], allowing it to be used in conventional THz systems.

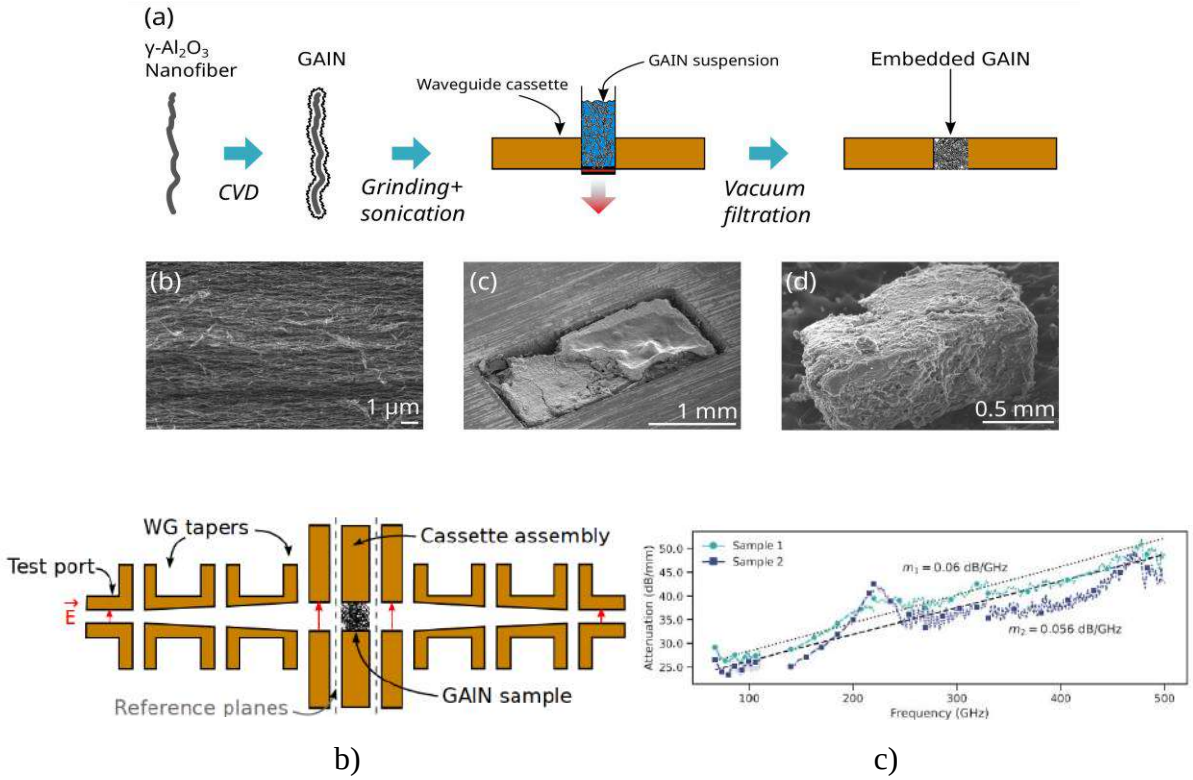

Fig.1. Schematic of a) method of deposition, b) wideband waveguide measurement setup. c) Measured attenuation of the absorbers

In order to analyze the electromagnetic properties of the absorbing materials in the frequency range from 67 GHz to 500 GHz, the absorbing material has to be embedded inside a waveguide. At the sub-millimeter frequencies, these dimensions get too small to insert any absorber material; therefore, we use vacuum filtration to directly deposit the absorber material inside a specialized waveguide cassette. This cassette can then be integrated with a waveguide system for material characterization. The integration method developed here is easily scalable to different frequency ranges and waveguide geometries and requires only standard laboratory equipment and techniques, making it viable for high-volume production. In addition, by utilizing the same method with precision silicon micromachined components [4], our approach could be used to develop compact, low-cost THz waveguide absorbers of complex geometry.

The attenuation of the embedded samples across a wide band of frequencies is shown in Fig.1e. The measured insertion loss between 67 GHz to 110 GHz is greater than 20 dB and exceeds 40 dB at frequencies above 400 GHz. The reflection coefficient of the samples measured below 200 GHz is in excess of −10 dB, indicating that much of the incident energy is reflected by the step change in impedance at the material's interface at these frequencies. The short electrical length of the samples at these frequencies (0.2λ0 at 88.5 GHz) leads to a relatively low insertion loss, despite the material's high reflectivity. Above 200 GHz, the GAIN samples exhibit a reflection coefficient below −10 dB.

Acknowledgements

This work was supported by CENTERA Laboratories in frame the International Research Agendas program for the Foundation for Polish Sciences co-financed by the European Union under the European Regional Development Fund (No. MAB/2018/9), by the European Union's Horizon 2020 FET Open project TERAmeasure (grant agreement No 862788) and A. Krajewska was supported by the Foundation for Polish Science (FNP; grant agreement No START 44.2021). The authors wish to acknowledge B. Stonio and M. Filipiak for their support with the preparation of SWCNT transistor structures. S. Smirnov acknowledges Myfab for provisioning of facilities and experimental support; Myfab is funded by the Swedish Research Council as a national research infrastructure.

References

1. Anoshkin, I.V., J. Campion, D.V. Lioubtchenko and J. Oberhammer "Freeze-dried carbon nanotube aerogels for high frequency absorber application" ACS Applied Materials & Interfaces, Vol. 10 No. 3, 19806–19811, 2018.
2. Campion, J., N. Xenidis, S. Smirnov, R. Ivanov, J. Oberhammer, I. Hussainova, D. Lioubtchenko "Ultra‐Wideband Integrated Graphene‐Based Absorbers for Terahertz Waveguide Systems" Advanced Electronic Materials, Vol 8, No 9, 2200106, 2022.
3. Dróżdż, P.A., N. Xenidis, J. Campion, S. Smirnov, A. Przewłoka, A. Krajewska, M. Haras, A. Nasibulin, J. Oberhammer, D. Lioubtchenko "Highly efficient absorption of THz radiation using waveguide-integrated carbon nanotube/cellulose aerogels", Applied Materials Today, Vol. 29, 101684, 2022.
4. Campion, J. and J. Oberhammer "Silicon Micromachined Waveguide Calibration Standards for Terahertz Metrology", IEEE Transactions on Microwave Theory and Techniques, Vol. 69, No 8, 3927-3942, 2021.

Intelligent Testing Environments for the Over-The-Air Characterization of Intelligent Wireless Devices

A. Alayón Glazunov

Linköping University, Department of Science and Technology, Sweden
andres.alayon.glazunov@liu.se

Invited Talk

Abstract: Over-The-Air (OTA) measurements are becoming key to the realistic, accurate, and cost-efficient characterization of the radiated performance of antennas, antenna systems, and wireless devices in general. In this talk, we present a summary of our latest results and the main ideas behind the OTA characterization based on different measurement philosophies. Fundamentally, the testing environments' electromagnetic design and main characteristics are explained.

Mainly two types of testing environments have dominated the existing OTA measurement technologies, i.e., the anechoic chamber (AC) and the reverberation chambers (RC). For example, traditionally, AC-based techniques have provided the high accuracy required in determining the gain and nulls of antennas and array antenna systems in predominantly free space channels with no reflections from the testing environment. This remains the focus for such applications as space and defense communications, sensing, and localization. On the other hand, the rapid development of wireless cellular communications technology in the past few decades, and lately with the Internet-of-Things applications, has increased the demands for fast yet accurate OTA techniques. RC-based techniques offer considerably faster, cost-effective, yet highly accurate, measurements of communication performance based on isotropic radiated power figures of merit as compared to ACs. RCs are the antithesis of ACs because they rely on the generation of multiple reflections in the test environment. RCs are highly suitable to characterize the diversity gain and multiplexing efficiency gain as well as the actual throughput performance of multiple-input multiple-output (MIMO) wireless devices operating in rich multipath (RIMP) environments [1].

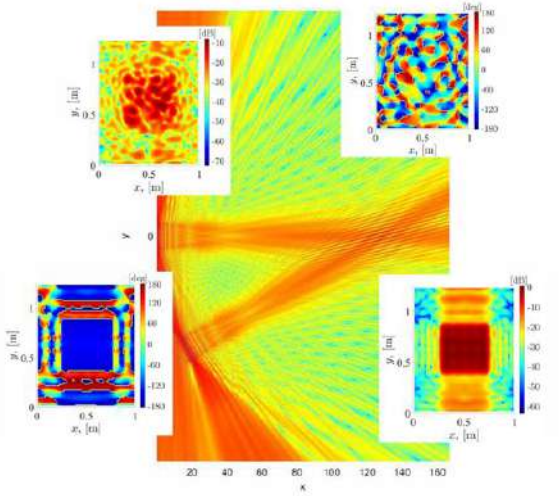

Fig. 1 Illustration of various electric field amplitude distributions that may be achieved by exciting the elements of a chamber antenna within the test zone of an OTA measurement chamber

5G and beyond wireless systems employ electrically large multiple-antenna systems for communications, sensing, and localization applications either as stand-alone systems, but trends are going towards the consolidation of their convergence into a single multi-capable system. Antennas are at the core of these systems that need to operate under various propagation conditions with different degrees of spatial, temporal, and polarization adaptivity. Hence, depending on the specific application advanced multiple antenna devices may be required to perform under different requirements [1, 2]. The objective of over-the-air (OTA) characterization is, in this context, to ensure that radiated performance of wireless devices, including the antennas, while complying with disparate standardized requirements in order to deliver the promised quality of service.

AC- and RC-based OTA technologies provide excellent radiated characterization in two limiting propagation environments, i.e., the free-space [3], and in the RIMP propagation channel, channels are more complex in many practical situations. Indeed, the complex dynamic environments need to be reproduced in laboratory conditions too (see Fig. 1). Automated, accurate, dependable, and time- and cost-efficient OTA characterization techniques and technologies are in high demand. Hence, in order to meet the various demands of communication, sensing, and localization performance imposed on multiple antenna systems a novel OTA technique i.e., the hybrid anechoic-reverberation chamber, has been recently introduced that provides high deployment flexibility [4, 5]. In this paper, we will present the main results on AC, RC, and HARC. We focus on providing insights into the physical principles governing the emulation of different OTA measurement environments and their application to multiple antenna performance evaluation.

Acknowledgments: The contribution of my students and collaborators in industry and academia is highly appreciated as well as the collaboration with and the support of companies such as Ericsson AB, Gapwaves AB, Bluetest AB, Ranlos AB, and Ranplan Wireless. Research funding received through the EU Commission especially, the Marie Skłodowska-Curie Actions within the Horizon 2020 research and innovation program under the grant agreements No. 734798 is3DMIMO H2020-MSCA-RISE-2016, No. 766231 WAVECOMBE H2020-MSCA-ITN-2017, and No. 955629 5VC H2020-MSCA-ITN-2020 are highly appreciated.

References

1. A. Hussain, P. -S. Kildal and A. A. Glazunov, "Interpreting the Total Isotropic Sensitivity and Diversity Gain of LTE-Enabled Wireless Devices from Over-the-Air Throughput Measurements in Reverberation Chambers," in IEEE Access, vol. 3, pp. 131-145, 2015.
2. M. Z. Mahfouz, R. Vogt-Ardatjew, A. B. J. Kokkeler and A. A. Glazunov, "Measurement and Estimation Methodology for EMC and OTA Testing in the VIRC," in IEEE Transactions on Electromagnetic Compatibility, vol. 65, no. 1, pp. 3-16, Feb. 2023
3. M. S. Kildal, S. Mansouri Moghaddam, A. Razavi, J. Carlsson, J. Yang and A. Alayón Glazunov, "Verification of the Random Line-of-Sight Measurement Setup at 1.5-3 GHz Including MIMO Throughput Measurements of a Complete Vehicle," in IEEE Transactions on Vehicular Technology, vol. 69, no. 11, pp. 13165-13179, Nov. 2020.
4. R. Maaskant, O. A. Iupikov, P. S. Krasov, R. Rehammar, A. A. Glazunov and M. V. Ivashina, "A New Hybrid Chamber for Generating a Spectrum of Oblique Incident Plane Waves at the DUT," in IEEE Transactions on Antennas and Propagation, vol. 69, no. 10, pp. 6806-6815, Oct. 2021.
5. O. A. Iupikov, P. S. Krasov, A. A. Glazunov, R. Maaskant, J. Fridén and M. V. Ivashina, "Hybrid OTA Chamber for Multidirectional Testing of Wireless Devices: Plane Wave Spectrum Generator Design and Experimental Demonstration," in IEEE Transactions on Antennas and Propagation, vol. 70, no. 11, pp. 10974-10987, Nov. 2022

Non-Axial Aligned Biaxial Material Characterization Using a Focus Beam System

N. A. O'Gorman[1*], **M. J. Havrilla**[2]

[1]Air Force Institute of Technology, United States
[2]Air Force Institute of Technology, United States
[*]corresponding author: nicholas.o'gorman@afit.edu

Abstract: As the complexity of materials increases, the ability to determine material parameters for samples of greater complexity with non-destructive testing becomes of greater importance. Aligning these samples with the axes of the measurement device for testing is not always easy or possible. This paper discusses a method using a second sample with known axial orientation for calibration to calculate the Z-axis material parameters of a sample with no cross-polarization terms without knowing its axial orientation.

When measuring the material parameters for a sample, it is required for the axis of the antenna to be aligned with the axis of the sample so that the various parameters can be calculated separately. This can become more difficult with increasingly complex metamaterial designs, especially when measuring the parameters along the samples thickness. For metamaterials that do not possess cross-polarization terms, the induced cross-polarization from misalignment can be used to remove the unknown angle of rotation from the measurements to calculate the unrotated equivalent values. To do this, a second sample (S2) with a known axial rotation around the Z-axis is used to isolate the focus beam system measurements relating to the test sample (S) rotated around the Z-axis at an unknown angle (ϕ) and rotated around the Y-axis at a known angle (θ) as depicted in Fig 1.

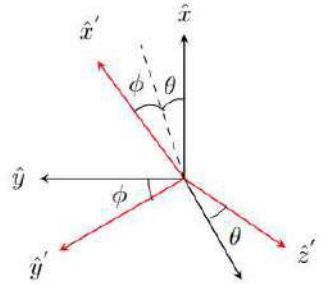

Fig. 1. Rotated Axis Around Z and Y Axis [1]

The S2 sample measurements are used to isolate the S parameters relating to the test sample using Equations 1 and 2. The $S_{21\theta\phi}^{x'x'S}$ and $S_{21\theta\phi}^{y'y'S}$ can be calibrated using the same method as when the axes are aligned [2].

$$S_{21\theta\phi}^{x'y'S} = e^{-jK_0 d(\sec(\theta)-1)} \sqrt{\left|\frac{S_{21}^{xyMS} S_{12}^{xyMS}}{S_{21}^{xyMS2}}\right| \left|\frac{S_{21\phi_2}^{x'y'S2} S_{12\phi_2}^{x'y'S2}}{S_{12}^{xyMS2}}\right|} \exp\left\{\frac{j}{2}\left(\angle\frac{S_{21}^{xyMS} S_{12}^{xyMS}}{S_{21}^{xyMS2}} + \angle\frac{S_{21\phi_2}^{x'y'S2} S_{12\phi_2}^{x'y'S2}}{S_{21}^{xyMS2}}\right\}\right. \quad (1)$$

$$S_{21\theta\phi}^{y'x'S} = e^{-jK_0 d(\sec(\theta)-1)} \sqrt{\left|\frac{S_{21}^{yxMS} S_{12}^{yxMS}}{S_{21}^{yxMS2}}\right| \left|\frac{S_{21\phi_2}^{y'x'S2} S_{12\phi_2}^{y'x'S2}}{S_{12}^{yxMS2}}\right|} \exp\left\{\frac{j}{2}\left(\angle\frac{S_{21}^{yxMS} S_{12}^{yxMS}}{S_{21}^{yxMS2}} + \angle\frac{S_{21\phi_2}^{y'x'S2} S_{12\phi_2}^{y'x'S2}}{S_{21}^{yxMS2}}\right\}\right. \quad (2)$$

The aligned cross-polarization S parameters for the sample can be written in terms of the S parameters for the

sample rotated around the Z and Y-axis as shown in Equation 3. Setting this equation to zero allows the angle around the Z-axis (ϕ) to be calculated.

$$S_{21\theta}^{x'y'S} = cos(\phi)\sin(\phi)\left(S_{21\theta\phi}^{x'x'S} - S_{21\theta\phi}^{y'y'S}\right) + \cos^2(\phi)\ S_{21\theta\phi}^{x'y'S} - \sin^2(\phi)\, S_{21\theta\phi}^{y'x'S} = 0 \tag{3}$$

A similar relationship can be found for S^{yy}(Equation 4) and S^{xx}(Equation 5). Plugging ϕ into these equations solves for the material parameters corresponding to the sample being aligned with the measurement device.

$$S_{21\theta}^{y'y'S} = \sin^2(\phi)\, S_{21\theta\phi}^{x'x'S} - \sin(\phi)\cos(\phi)\left(S_{21\theta\phi}^{y'x'S} + S_{21\theta\phi}^{x'y'S}\right) + \cos^2(\phi)\, S_{21\theta\phi}^{y'y'S} \tag{4}$$

$$S_{21\theta}^{x'x'S} = \cos^2(\phi)\, S_{21\theta\phi}^{x'x'S} - \sin(\phi)\cos(\phi)\left(S_{21\theta\phi}^{y'x'S} + S_{21\theta\phi}^{x'y'S}\right) + \sin^2(\phi)\, S_{21\theta\phi}^{y'y'S} \tag{5}$$

With $S_{21\theta}^{y'y'S}$ and $S_{21\theta}^{x'x'S}$, the material parameters of the sample can be solved for using the same method used when the antenna is aligned with the axis of the sample [2]. To isolate the material parameters for the Z-axis of the sample, the method outlined in [3] must be used with a Y-axis rotation of zero.

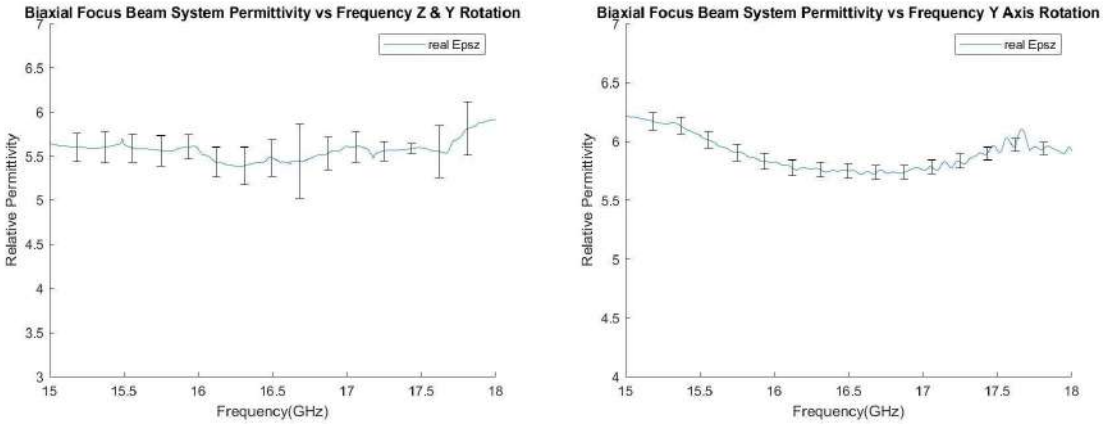

Fig. 2. Calculated Permittivity [1]

Figure 2 shows the results for this method on the left and the results for when the sample is aligned with the antenna on the right. These graphs show that this calibration technique, for an unaligned sample, produced similar results when compared to an aligned sample. It can also be seen that the unaligned sample method produced a more consistent value across frequencies when compared to the axially aligned method. These fluctuations in the aligned sample can be caused by the sample not perfectly aligning with the antenna, causing interference from cross-polarization. Without assuming axial alignment, these induced errors are removed from the results giving a more consistent value for material parameters.

References

1. O'Gorman, N.A. "Focused Beam System Biaxial Material Characterization," master's thesis, EENG AFIT.
2. O'Gorman N. A. and Havrilla M. J. " Biaxial Material Characterization Utilizing A Focus Beam System," EMC EUROPE, 2020, pp. 1-4, doi: 10.1109/EMCEUROPE48519.2020.9245835.
3. O'Gorman, N. A." Focus Beam System Biaxial Cross-Polarization 2nd Sample Method," ICEAA, 2021, pp. 053-053, doi: 10.1109/ICEAA52647.2021.9539819.

Artificial intelligence optical hardware for ultra-sensitive detection

Q. Wang[1*], N. Li[1], Z. He[1], A. B. Lopez[1], F. Xiang[1], and A. Fratalocchi[1]

[1] PRIMALIGHT, Faculty of Electrical Engineering, King Abdullah University of Science and Technology (KAUST), Thuwal 23955-6900, Saudi Arabia

[*]qizhou.wang@kaust.edu.sa

Abstract: This work proposes an artificial intelligence (AI)-based platform for ultra-sensitive detection, combining a wet chemistry-based optical sensor for signal collection and optical AI hardware for fast data pre-processing. This technology does not employ costly instruments like spectrum analyzers. It achieves real-time data readout through off-the-shelf conventional monochrome cameras.

Recent years have seen thriving studies and applications on biochemical sensing, ranging from fields such as concentration quantification [1], dynamic biomarkers monitoring [2], and molecular identification [3]. The research proposes various sensing models and metrics, ranging from spectrum peak shift, intensity variations, and line widths [4]. While these approaches provide a straightforward pathway for the sensor design, they have poor detection sensitivity at specific concentrations of analytes. The leading cause is that most standard analysis models only extract the essential features based on prior knowledge, implying a strong influence of human bias.

Artificial Intelligence (AI) is one of the most promising techniques to address this issue by learning hidden feature representations from large datasets [5]. By leveraging these features, a well-trained AI-sensing model can significantly surpass traditional models and enhance the limits of detection concentration. Presently, a challenge of these techniques is the need for expensive data collection instruments such as spectrum analyzers. This can limit the generalization ability of the models, as it becomes more difficult and costly to gather sufficient data for training the models. Furthermore, the limited availability of these instruments can restrict the scope and scale of potential applications.

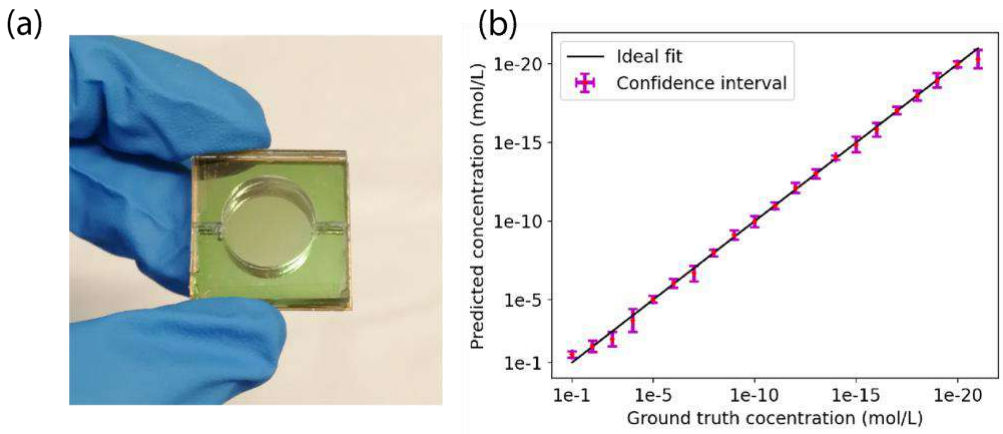

(a) A fabricated reusable optical sensor. (b) Examples of the prediction results on the test dataset, with concentrations ranging from 10^{-1} mol/L to 10^{-20} mol/L. For a more intuitive visualization, the plotted confidence interval is magnified by 30 times.

In this work, we implement a framework for large-scale real-time sensing, addressing data collection and analysis issues that widely exist in AI-based sensing methods. This technology uses a wet chemistry-based scalable manufacturing technique for a reusable optical sensor. As shown in Figure 1a, the fabricated sensor comprises a microfluidic cell and gold plasmonic structures deposited to a silicon substrate. Our design ensures minimal residual analytes after each measurement and enables multiple measurements using a single device. Inspired by the wide implementations of dielectric metasurfaces [6,7], we sequentially designed and fabricated a hardware optical AI component for pre-processing data. This component is mounted on a regular monochrome camera and extracts in hardware the sparse feature from the spectra before imaging. The recorded image is seen as the output of this AI model and used as the input of a consecutive regression network. The network trains on 79 glucose solution samples. It demonstrates precise prediction of the concentrations down 10^{-20} mol/L, the lowest concentration level ever reported for this analyte. Figure 1b shows the model's performance at each concentration level. As an overview, the overall R^2 score on 30 test samples reaches 0.9965. This platform exhibits high sensitivity, making it applicable for large-scale sensing applications in areas such as drug discovery and development, industrial process monitoring, and personalized healthcare.

References

1. M. Erzina, A. Trelin, O. Guselnikova, A. Skvortsova, K. Strnadova, V. Svorcik, and O. Lyutakov, "Quantitative detection of A1-acid glycoprotein (AGP) level in blood plasma using SERS and CNN transfer learning approach," Sensors and Actuators B: Chemical 367, 132057 (2022).
2. H. Lee, W. J. Rhee, G. Moon, S. Im, T. Son, J.-S. Shin, and D. Kim, "Plasmon-enhanced fluorescence correlation spectroscopy for super-localized detection of nanoscale subcellular dynamics," Biosensors and Bioelectronics 184, 113219 (2021).
3. H. Kim, W. Seong, E. Rha, H. Lee, S. K. Kim, K. K. Kwon, K.-H. Park, D.-H. Lee, and S.-G. Lee, "Machine learning linked evolutionary biosensor array for highly sensitive and specific molecular identification," Biosensors and Bioelectronics 170, 112670 (2020).
4. Y. Xu, P. Bai, X. Zhou, Y. Akimov, C. E. Png, L.-K. Ang, W. Knoll, and L. Wu, "Optical refractive index sensors with plasmonic and photonic structures: promising and inconvenient truth," Advanced Optical Materials 7, 1801433 (2019).
5. Z. Ballard, C. Brown, A. M. Madni, and A. Ozcan, "Machine learning and computation-enabled intelligent sensor design," Nature Machine Intelligence 3, 556–565 (2021).
6. M. Makarenko, Q. Wang, A. Burguete-Lopez, F. Getman, and A. Fratalocchi, "Robust and scalable flat-optics on flexible substrates via evolutionary neural networks," Advanced Intelligent Systems 3, 2100105 (2021).
7. M. Makarenko, A. Burguete-Lopez, Q. Wang, F. Getman, S. Giancola, B. Ghanem, and A. Fratalocchi, "Real-time Hyperspectral Imaging in Hardware via Trained Metasurface Encoders," in 2022 IEEE/CVF Conference on Computer Vision and Pattern Recognition (CVPR), pp. 12682–12692.